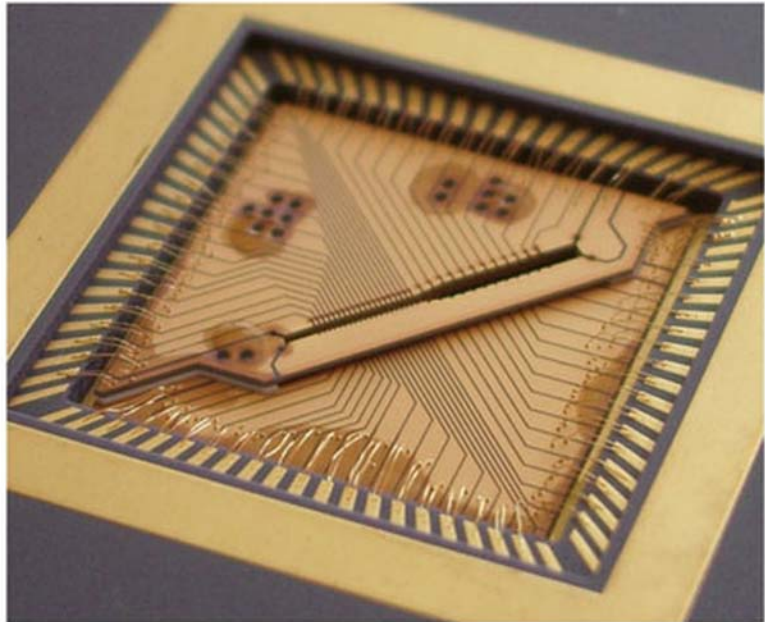


W. P. Schleich  
H. Walther (Eds.)

WILEY-VCH

# Elements of Quantum Information



## **Elements of Quantum Information**

*Edited by*

*Wolfgang P. Schleich and*

*Herbert Walther*

## 1807–2007 Knowledge for Generations

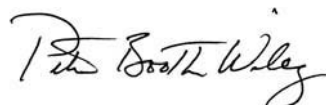
Each generation has its unique needs and aspirations. When Charles Wiley first opened his small printing shop in lower Manhattan in 1807, it was a generation of boundless potential searching for an identity. And we were there, helping to define a new American literary tradition. Over half a century later, in the midst of the Second Industrial Revolution, it was a generation focused on building the future. Once again, we were there, supplying the critical scientific, technical, and engineering knowledge that helped frame the world. Throughout the 20th Century, and into the new millennium, nations began to reach out beyond their own borders and a new international community was born. Wiley was there, expanding its operations around the world to enable a global exchange of ideas, opinions, and know-how.

For 200 years, Wiley has been an integral part of each generation's journey, enabling the flow of information and understanding necessary to meet their needs and fulfill their aspirations. Today, bold new technologies are changing the way we live and learn. Wiley will be there, providing you the must-have knowledge you need to imagine new worlds, new possibilities, and new opportunities.

Generations come and go, but you can always count on Wiley to provide you the knowledge you need, when and where you need it!



William J. Pesce  
President and Chief Executive Officer



Peter Booth Wiley  
Chairman of the Board

# Elements of Quantum Information

*Edited by*

*Wolfgang P. Schleich and Herbert Walther*



WILEY-VCH Verlag GmbH & Co. KGaA

## The Editors

*Prof. Dr. Wolfgang P. Schleich*  
Universität Ulm  
Abteilung f. Quantenphysik  
Albert-Einstein-Allee 11  
89069 Ulm  
Germany

*Prof. Dr. Herbert Walther* †  
MPI für Quantenoptik  
Hans-Kopfermann-Str. 1  
85748 Garching  
Germany

## Cover Image

Segmented linear Paul trap, University of Ulm, Germany (2006) by S. Schulz and F. Schmidt-Kaler.

The trap is fabricated from gold coated ceramic wafers which are structured by fs-laser pulses. The large number of 12 segments in the 500 µm wide loading zone – at the right hand side of the slit – and 19 segments in the 250 µm wide processor zone of this trapping device allow to scale-up quantum computing with trapped ions.

The article *Optimization of Segmented Linear Paul Traps and Transport of Stored Particles* by S. Schulz, U. Poschinger, K. Singer, and F. Schmidt-Kaler explains how to transport ions in this device fast but without any heating effects.

All books published by Wiley-VCH are carefully produced. Nevertheless, editors, authors and publisher do not warrant the information contained in these books to be free of errors. Readers are advised to keep in mind that statements, data, illustrations, procedural details or other items may inadvertently be inaccurate.

**Library of Congress Card No.:**  
applied for

**British Library Cataloguing-in-Publication Data:**  
A catalogue record for this book is available from the British Library.

**Bibliographic information published by the Deutsche Bibliothek**

The Deutsche Bibliothek lists this publication in the Deutsche Nationalbibliografie; detailed bibliographic data is available in the Internet at <http://dnb.d-nb.de>

© 2007 WILEY-VCH Verlag GmbH & Co KGaA, Weinheim

All rights reserved (including those of translation into other languages). No part of this book may be reproduced in any form – by photocopying, microfilm, or any other means – nor transmitted or translated into a machine language without written permission from the publishers. Registered names, trademarks, etc. used in this book, even when not specifically marked as such, are not to be considered unprotected by law.

Printed in the Federal Republic of Germany  
Printed on acid-free paper

**Composition:** Steingraeber Satztechnik GmbH, Ladenburg

**Printing:** Strauss GmbH, Mörlenbach

**Bookbinding:** Litges & Dopf Buchbinderei GmbH, Heppenheim

**ISBN:** 978-3-527-40725-5

## Contents

**Preface to the Book** XVII

**Preface to the Journal** XIX

**List of Contributors** XXI

<b>1</b>	<b>The Deterministic Generation of Photons by Cavity Quantum Electrodynamics</b>	<b>1</b>
	<i>H. Walther</i>	
1.1	Introduction	1
1.2	Oscillatory Exchange of Photons Between an Atom and a Cavity Field	1
1.2.1	Experimental Set-up of the One-atom Maser	3
1.2.2	One-atom Maser as a Source of Non-classical Light	5
1.2.3	Review of Experiments on Basic Properties of the One-atom Maser	8
1.2.4	Statistics of Detector Clicks	12
1.2.5	Trapping States	13
1.2.6	Trapping State Stabilization	17
1.2.7	Fock States on Demand	17
1.2.8	Dynamical Preparation of $n$ -photon States in a Cavity	18
1.2.9	The One-atom Maser Spectrum	24
1.3	Other Microwave Cavity Experiments	26
1.3.1	Collapse-and-revival of the Rabi Oscillations in an Injected Coherent Field	26
1.3.2	Atom-photon and Atom-atom Entanglement	27
1.3.3	Atom-photon Phase Gate	28
1.3.4	Quantum Nondestructive-measurement of a Photon	28
1.3.5	Wigner-function of a One-photon State	29
1.3.6	Multiparticle Entanglement	29
1.3.7	Schrödinger Cats and Decoherence	29

1.4	Cavity QED Experiments in the Visible Spectral Region	30
1.4.1	The One-atom Laser	30
1.4.2	Atoms Pushed by a Few Photons	31
1.4.3	Single-photon Sources	33
1.4.4	Single-atom Laser using an Ion Trap	34
1.5	Conclusions and Outlook	38
	References	39
<b>2</b>	<b>Optimization of Segmented Linear Paul Traps and Transport of Stored Particles</b>	<b>45</b>
	<i>Stephan Schulz, Ulrich Poschinger, Kilian Singer, and Ferdinand Schmidt-Kaler</i>	
2.1	Introduction	45
2.2	Optimization of a Two-layer Microstructured Ion Trap	46
2.2.1	Design Objectives	47
2.2.2	Operating Mode and Modeling of the Segmented Linear Paul Trap	49
2.2.3	Optimization of the Radial Potential	51
2.2.4	Optimization of the Axial Potential	52
2.3	Open Loop Control of Ion Transport	54
2.3.1	Non-adiabatic Heating Sources	54
2.3.2	Overview of the Applied Optimization Strategies	55
2.3.3	The Optimal Control Method	55
2.3.4	Optimization Results	58
2.3.5	Ion Heating due to Anharmonic Dispersion	59
2.3.6	Quantum Mechanical Estimate of Non-adiabatic Parametric Heating	59
2.3.7	Improved Initial Guess Function and Ultra-fast Transport	60
2.3.8	Discussion of the Open-loop Result	62
2.4	Outlook	64
A	Appendix	65
	References	66
<b>3</b>	<b>Transport Dynamics of Single Ions in Segmented Microstructured Paul Trap Arrays</b>	<b>69</b>
	<i>R. Reichle, D. Leibfried, R. B. Blakestad, J. Britton, J. D. Jost, E. Knill, C. Langer, R. Ozeri, S. Seidelin, and D. J. Wineland</i>	
3.1	Introduction	69
3.2	Classical Equations of Motion	71
3.3	Classical Dynamics of Ion Transport	72
3.3.1	Homogeneous Solution	73
3.3.2	Green's Function and General Solution	74

3.3.3	Adiabatic Limit	75
3.4	Quantum and Classical, Dragged Harmonic Oscillators with Constant Frequency	76
3.5	The Dragged Quantum Harmonic Oscillator	78
3.6	Transport Dynamics in a Well-controlled Regime	81
3.6.1	Two Analytical Examples	82
3.6.2	Near-optimum Transport Functions	86
3.6.3	High-frequency Limit, Adiabatic Transport, and Approximate Trajectories	86
3.7	Please supply a short title	87
3.7.1	Determination of Waveforms	87
3.7.2	Potential Fluctuations and Aspect-ratio Rule	90
3.8	Conclusions	95
A	Appendix	96
	References	96
<b>4</b>	<b>Ensemble Quantum Computation and Algorithmic Cooling in Optical Lattices</b>	<b>99</b>
	<i>M. Popp, K. G. H. Vollbrecht, and J. I. Cirac</i>	
4.1	Introduction	99
4.2	Physical System	102
4.2.1	Bose-Hubbard Model	102
4.2.2	Initial State Properties	103
4.2.3	Entropy as Figure of Merit	105
4.2.4	Basic Operations	106
4.3	Ensemble Quantum Computation	108
4.4	Cooling with Filtering	112
4.5	Algorithmic Ground State Cooling	114
4.5.1	The Protocol	114
4.5.2	Theoretical Description	115
4.6	Conclusion	118
	References	119
<b>5</b>	<b>Quantum Information Processing in Optical Lattices and Magnetic Microtraps</b>	<b>121</b>
	<i>Philipp Treutlein, Tilo Steinmetz, Yves Colombe, Benjamin Lev, Peter Hommelhoff, Jakob Reichel, Markus Greiner, Olaf Mandel, Artur Widera, Tim Rom, Immanuel Bloch, and Theodor W. Hänsch</i>	
5.1	Introduction	121
5.2	Optical Lattices	122
5.2.1	Preparation of a Qubit Register	122
5.2.2	A Quantum Conveyer Belt for Neutral Atoms	123

5.2.3	Controlled Collisions	124
5.3	Magnetic Microtraps	127
5.3.1	Qubit States on the Atom Chip	128
5.3.2	State-dependent Microwave Potentials	132
5.3.3	Qubit Readout in Microtraps	135
5.3.3.1	Stable fiber Fabry-Perot Cavities	137
5.3.3.2	FFP Cavity Fabrication and Performance	137
5.3.4	On-chip Atom Detection with a FFP Cavity	138
5.3.5	Single Atom Preparation	141
5.4	Conclusion	142
	References	142
<b>6</b>	<b>Two-dimensional Bose-Einstein Condensates in a CO<sub>2</sub>-laser Optical Lattice</b>	<b>145</b>
	<i>Giovanni Cennini, Carsten Geckeler, Gunnar Ritt, Tobias Salger, and Martin Weitz</i>	
6.1	Introduction	145
6.2	Experimental Setup and Procedure	146
6.3	Experimental Results	148
6.4	Conclusions	151
	References	153
<b>7</b>	<b>Creating and Probing Long-range Order in Atomic Clouds</b>	<b>155</b>
	<i>C. von Cube, S. Slama, M. Kohler, C. Zimmermann, and Ph. W. Courteille</i>	
7.1	Introduction	155
7.2	Collective Coupling	157
7.2.1	Experimental Setup	158
7.2.1.1	Ring Cavity	159
7.2.1.2	Dipole Trap for <sup>85</sup> Rb	160
7.2.1.3	Optical Molasses	162
7.2.2	Signatures of Collective Atomic Recoil Lasing	163
7.2.2.1	Beat Note of Field Modes	163
7.2.2.2	Spectra of Recoil-induced Resonances	165
7.2.2.3	Atomic Transport	166
7.3	Creating Long-range Order	168
7.3.1	Analytic Treatment for Perfect Bunching	168
7.3.1.1	Radiation Pressure	170
7.3.1.2	Phase-locking by Imperfect Mirrors	171
7.3.2	Simulations of Atomic Trajectories with Friction and Diffusion	172
7.3.2.1	Lasing Threshold	173
7.3.2.2	Self-synchronization	174

7.4	Probing Long-range Order	176
7.4.1	Bragg Scattering	176
7.4.2	Heterodyned Bragg Spectra	178
7.4.3	Measuring the Bragg Scattering Phase	179
7.5	Conclusion	180
	References	181
<b>8</b>	<b>Detecting Neutral Atoms on an Atom Chip</b>	<b>185</b>
	<i>Marco Wilzbach, Albrecht Haase, Michael Schwarz, Dennis Heine, Kai Wicker, Xiyuan Liu, Karl-Heinz Brenner, Sönke Groth, Thomas Fernholz, Björn Hessmo, and Jörg Schmiedmayer</i>	
8.1	Introduction	185
8.2	Detecting Single Atoms	186
8.2.1	Measuring the Scattered Light: Fluorescence Detection	186
8.2.2	Measuring the Driving Field	187
8.2.2.1	Absorption on Resonance	187
8.2.2.2	Refraction	189
8.2.3	Cavities	189
8.2.3.1	Absorption on Resonance	189
8.2.3.2	Refraction	190
8.2.3.3	Many Atoms in a Cavity	190
8.2.4	Concentric Cavity	191
8.2.5	Miniaturization	191
8.3	Properties of Fiber Cavities	192
8.3.1	Loss Mechanisms for a Cavity	193
8.3.2	Losses due to the Gap Length	194
8.3.3	Losses due to Transversal Misalignment	195
8.3.4	Losses due to Angular Misalignment	196
8.3.5	Fresnel Reflections	197
8.4	Other Fiber Optical Components for the Atom Chip	199
8.4.1	Fluorescence and Absorption Detectors	199
8.4.2	A Single Mode Tapered Lensed Fiber Dipole Trap	199
8.5	Integration of Fibers on the Atom Chip	201
8.5.1	Building Fiber Cavities	201
8.5.2	The SU-8 Resist	203
8.5.3	Test of the SU-8 Structure	204
8.6	Pilot Test for Atom Detection with Small Waists	205
8.6.1	Dropping Atoms through a Concentric Cavity	205
8.6.2	Detecting Magnetically Guided Atoms	207
8.7	Conclusion	208
	References	209

<b>9</b>	<b>High Resolution Rydberg Spectroscopy of Ultracold Rubidium Atoms 211</b>
	<i>Axel Grabowski, Rolf Heidemann, Robert Löw, Jürgen Stuhler, and Tilman Pfau</i>
9.1	Introduction 211
9.2	Experimental Setup and Cold Atom Preparation 212
9.2.1	Vacuum System and Magneto Optical Trap (MOT) 212
9.2.2	Rydberg Laser System and Rydberg Excitation 215
9.2.3	Detection of the Rydberg Atoms 216
9.2.4	Excitation Sequence 217
9.3	Spectroscopy of Rydberg States, $ m_j $ Splitting of the Rydberg States 219
9.4	Spatial and State Selective Addressing of Rydberg States 220
9.4.1	Spatial Selective Rydberg Excitation 220
9.4.2	Hyperfine Selective Rydberg Excitation 221
9.5	Autler-Townes Splitting 222
9.6	Conclusion and Outlook 224
	References 224
<b>10</b>	<b>Prospects of Ultracold Rydberg Gases for Quantum Information Processing 227</b>
	<i>Markus Reetz-Lamour, Thomas Amthor, Johannes Deiglmayr, Sebastian Westermann, Kilian Singer, André Luiz de Oliveira, Luis Gustavo Marcassa, and Matthias Weidemüller</i>
10.1	Introduction 227
10.2	Excitation of Rydberg Atoms from an Ultracold Gas 229
10.3	Van-der-Waals Interaction 230
10.3.1	Blockade of Excitation 231
10.3.2	Ionization 232
10.4	States with Permanent Electric Dipole Moments 234
10.5	Förster Resonances 236
10.6	Conclusion 239
	References 241
<b>11</b>	<b>Quantum State Engineering with Spins 243</b>
	<i>Andreas Heidebrecht, Jens Mende, and Michael Mehring</i>
11.1	Introduction 243
11.1.1	Quantum States of Spins 244
11.2	Deutsch-Josza Algorithm 246
11.2.1	The Deutsch-Josza Algorithm 246
11.2.2	Implementation of the 3-qubit Deutsch-Josza Algorithm Using Liquid State NMR 247

11.2.2.1	2,3,4-Trifluoroaniline	247
11.2.2.2	Preparation of Pseudo-pure States	248
11.2.2.3	Results on the 3-qubit DJ-algorithm	249
11.3	Entanglement of an Electron and Nuclear Spin in $^{15}\text{N}@\text{C}_{60}$	251
11.4	Spin Quantum Computing in the Solid State: S-bus	253
11.4.1	The S-bus Concept	253
11.4.2	Single Crystal $\text{CaF}_2 : \text{Ce}^{3+}$ as an S-bus system	255
11.4.3	Experimental Details	256
11.4.4	3-qubit Pseudo-pure States	258
11.4.5	2-qubit Deutsch-Josza Algorithm	259
11.4.5.1	Controlling Nuclear Spin Decoherence in $\text{CaF}_2 : \text{Ce}$	260
11.5	Summary and Outlook	263
	References	263
<b>12</b>	<b>Improving the Purity of One- and Two-qubit Gates</b>	<b>265</b>
	<i>Sigmund Kohler and Peter Hänggi</i>	
12.1	Introduction	265
12.2	Quantum Gate with Bit-flip Noise	266
12.2.1	Bloch-Redfield Master Equation	267
12.2.2	Purity Decay	268
12.2.3	Numerical Solution	269
12.3	Coherence Stabilization for Single Qubits	270
12.3.1	Dynamical Decoupling by Harmonic Driving	271
12.3.2	Coherent Destruction of Tunneling	272
12.4	Coherence Stabilization for a CNOT Gate	275
12.4.1	Heisenberg vs. Ising Coupling	276
12.4.2	Coherence Stabilization by an AC Field	278
12.4.3	Numerical Solution	279
12.4.4	Implementation with Quantum Dots	282
12.5	Conclusions	282
A	Appendix	283
	References	284
<b>13</b>	<b>How to Distill Entanglement from a Finite Amount of Qubits?</b>	<b>287</b>
	<i>Stefan Probst-Schendzielorz, Thorsten Bschorr, and Matthias Freyberger</i>	
13.1	Introduction	287
13.2	Entanglement Distillation	288
13.2.1	The Protocol	289
13.3	CNOT Distillation for a Finite Set of Entangled Systems	293
13.3.1	Iterative Distillation	294
13.4	Example of the Iterative Distillation for Small Finite Sets	297

13.5	Conclusions	299
A	Appendix	300
	References	301

**14 Experimental Quantum Secret Sharing 303**

*Christian Schmid, Pavel Trojek, Sascha Gaertner, Mohamed Bourennane, Christian Kurtsiefer, Marek Zukowski, and Harald Weinfurter*

14.1	Introduction	303
14.2	Theory	304
14.2.1	The GHZ-protocol	304
14.2.2	The $ \Psi_4^-\rangle$ -protocol	305
14.2.3	The Single Qubit Protocol	306
14.2.4	Security of the Protocols	307
14.3	Experiment	309
14.3.1	The $ \Psi_4^-\rangle$ -protocol	309
14.3.2	The Single-qubit Protocol	310
14.4	Conclusion	312
	References	314

**15 Free Space Quantum Key Distribution:  
Towards a Real Life Application 315**

*Henning Weier, Tobias Schmitt-Manderbach, Nadja Regner, Christian Kurtsiefer, and Harald Weinfurter*

15.1	Introduction	315
15.2	Setup	316
15.2.1	Transmitter Unit	316
15.2.2	Free Space Link	317
15.2.3	Receiver Unit	318
15.2.4	Synchronisation and Automatic Alignment Control	319
15.2.5	Sifting, Error Correction and Privacy Amplification	319
15.2.6	Experimental Results	320
15.3	Conclusion	322
	References	323

**16 Continuous Variable Entanglement Between Frequency  
Modes 325**

*Oliver Glöckl, Ulrik L. Andersen, and Gerd Leuchs*

16.1	Introduction	325
16.2	Sideband Separation	327
16.2.1	Theory	328
16.2.2	Pictorial Description	331
16.3	Experiment and Results	331

16.4	Conclusion and Discussion	335
	References	336
<b>17</b>	<b>Factorization of Numbers with Physical Systems</b>	<b>339</b>
	<i>Wolfgang Merkel, Ilya Sh. Averbukh, Bertrand Girard, Michael Mehring, Gerhard G. Paulus, and Wolfgang P. Schleich</i>	
17.1	Introduction	339
17.2	Chirping a Two-photon Transition	340
17.2.1	Chirped Laser Pulses	340
17.2.2	Excitation Probability Amplitude	341
17.2.3	Example for Factorization	342
17.3	Driving a One-photon Transition	343
17.3.1	Model	344
17.3.2	Floquet Ladder	345
17.3.3	Pulse Train	346
17.4	Factorization	347
17.4.1	Factorization with Floquet Ladder	348
17.4.2	Factorization with a Pulse Train	349
17.5	NMR-experiment	350
17.6	Conclusions	352
	References	353
<b>18</b>	<b>Quantum Algorithms for Number Fields</b>	<b>355</b>
	<i>Daniel Haase and Helmut Maier</i>	
18.1	Introduction	355
18.1.1	Outline of the Survey	355
18.1.2	Why Number Fields?	356
18.1.3	Some History of the Subject	356
18.2	Geometry of Numbers	357
18.2.1	Number Fields	357
18.2.2	Lattices	358
18.2.3	Integral Elements	359
18.2.4	The Class Number	360
18.2.5	The Regulator	361
18.2.6	Complexity Results	361
18.3	Reduction	362
18.3.1	Reduced Ideals	362
18.3.2	Infrastructure	363
18.3.3	Geometric Interpretation of $\mathbf{G}$	364
18.4	Results from Analytic Number Theory	366
18.4.1	Distribution of Prime Numbers	366
18.4.2	Class Number Formulas	367

18.5	Examples of Minima Distributions	368
18.6	Computing the Regulator	370
18.6.1	Real Quadratic Case	370
18.6.2	Hallgren's Algorithm	371
18.6.3	Generalization of the Weak Periodicity Condition	372
18.7	Computation of Other Invariants	374
18.7.1	The Principal Ideal Problem	374
18.7.2	Computing the Class Number	375
	References	376
<b>19</b>	<b>Implementation Complexity of Physical Processes as a Natural Extension of Computational Complexity</b>	<b>377</b>
	<i>Dominik Janzing</i>	
19.1	Introduction	377
19.2	Similar Complexity Bounds for Different Tasks	379
19.3	Relating Control Problems to Hard Computational Problems	385
19.4	The Need for a Control-theoretic Foundation of Complexity	388
19.5	Hamiltonians that Compute Autonomously	393
	References	396
<b>20</b>	<b>Implementation of Generalized Measurements with Minimal Disturbance on a Quantum Computer</b>	<b>399</b>
	<i>Thomas Decker and Markus Grassl</i>	
20.1	Introduction	399
20.2	Minimal-disturbing Implementations of POVMs	401
20.2.1	Generalized Measurements of Quantum Systems	401
20.2.2	Positive-operator Valued Measures	402
20.2.3	Orthogonal Measurements	403
20.2.4	Disturbance of a Generalized Measurement	404
20.2.5	Minimal-disturbing Implementation of a POVM	405
20.3	Symmetric Matrices and their Structure	406
20.3.1	Representations of Finite Groups	407
20.3.2	Projective Representations	408
20.3.3	Symmetry of a Matrix and Schur's Lemma	410
20.3.4	Symmetric POVMs Define Matrices with Symmetry	411
20.4	Implementation of Symmetric POVMs	413
20.5	Cyclic and Heisenberg-Weyl Groups	416
20.5.1	Cyclic Groups	416
20.5.2	Heisenberg-Weyl Groups	419
20.6	Conclusions and Outlook	423
	References	424

<b>21</b>	<b>Full Counting Statistics of Interacting Electrons</b>	<b>425</b>
	<i>D. A. Bagrets, Y. Utsumi, D. S. Golubev, and Gerd Schön</i>	
21.1	Introduction	425
21.2	Concepts of FCS	428
21.3	Full Counting Statistics in Interacting Quantum Dots	435
21.3.1	FCS of a Set for Intermediate Strength Conductance	437
21.3.2	Non-Markovian Effects: Renormalization and Finite Lifetime Broadening of Charge States	440
21.3.3	Keldysh Action and CGF in Majorana Representation	442
21.4	FCS and Coulomb Interaction in Diffusive Conductors	443
21.4.1	Model and Effective Action	445
21.4.2	“Cold Electron” Regime	447
21.4.3	“Hot Electron” Regime	453
21.5	Summary	454
	References	455
<b>22</b>	<b>Quantum Limit of the Carnot Engine</b>	<b>457</b>
	<i>Friedemann Tonner and Günter Mahler</i>	
22.1	Introduction	457
22.2	Spin-oscillator Model	458
22.2.1	Basic Definitions	458
22.2.2	Thermodynamic Variables for $G$	461
22.3	Master Equation	462
22.3.1	Lindblad Superoperator	462
22.3.2	Time Slot Operators	463
22.4	Machine Cycles	465
22.4.1	Choice of Amplitudes $a_{\pm}^{(j)}$ and Control Functions $\theta^{(j)}(\tau)$	465
22.4.2	Heat and Work	467
22.4.3	Energy Balance	468
22.4.4	Fluctuations	468
22.5	Numerical Results	470
22.5.1	Heat Engine	470
22.5.2	Heat Pump	474
22.5.3	Longtime Limit	475
22.5.4	Quantum Limit and Classical Limit	475
22.6	Summary and Conclusions	477
	References	479
<b>Appendix: Colour Plates</b>		<b>481</b>
<b>Index</b>		<b>491</b>



## Preface to the Book Edition

*Elements of Quantum Information* is based on a collection of articles previously published in a special issue of *Fortschritte der Physik/Progress of Physics*. It summarizes the results obtained in a collaboration of scientists from Bavaria and Baden-Württemberg working in the field of quantum information processing. This research effort was coordinated by H. Walther and W.P. Schleich. Despite his illness H. Walther was part of the project until his un-timely death on July 22, 2006, at which time all manuscripts were already in press. Unfortunately, he never saw the special issue nor the present book in their final forms.

Ulm, November 2006

W.P. Schleich



## Preface to the Journal Edition

Quantum information processing has come a long way – from the early ideas of a quantum computer, put forward by Richard Feynman and David Deutsch in the early eighties, via the factorization algorithm of Peter Shor, to the present day quantum optical realisations of quantum gates. This newly emerging branch of quantum physics has united many disciplines by encompassing computer science, physics, mathematics as well as engineering. The potential gain in using the resources of quantum mechanics is enormous.

The governments of Baden-Württemberg and Bavaria have recognized the importance of quantum information and have dedicated substantial support to its development. Four years ago 12 groups from Baden-Württemberg and 6 groups from Bavaria joined forces to collaborate on this topic. Since all groups were located (more or less) along the highway A8 the descriptive title *Quantum Information Highway A8* was chosen for this project. We are also very proud that our colleague and collaborator in the *Quantum Information Highway A8*, Prof. Dr. Theodor Hänsch, Munich, was awarded the Nobel Prize 2005.

The present special issue represents a state of the art summary of the various projects of the *Quantum Information Highway A8*. The contribution by Reichle et al. is a slight exception to this program. It summarizes the approach taken by the Wineland group in Boulder (Colorado) and, therefore, lies outside of the *Quantum Information Highway A8*. Since the theme of this work complements that of the article by Schulz et al. and the paper was prepared in Ulm with the assistance of the *Quantum Information Highway A8* we have decided to include it in this issue. Moreover, it demonstrates clearly one of the many international connections of this collaboration.

We take this opportunity to express our sincere thanks to our sponsors and the enthusiastic support of Dr. Heribert Knorr from the Ministerium für Wissenschaft, Forschung und Kunst Baden-Württemberg and the late Dr. Christian Schuberth and his successor Felix Köhl from the Bayerisches Staatsministerium für Wissenschaft, Forschung und Kunst, without them the idea of a quantum information highway would have never materialized. We are most grateful for the financial support provided by the Landesstiftung Baden-

Württemberg as well as from the Ministerium für Wissenschaft, Forschung und Kunst Baden-Württemberg and the Bayerisches Staatsministerium für Wissenschaft, Forschung und Kunst. Moreover, the continuously kind assistance of Clemens Benz and Irene Purschke from the Landesstiftung made it an enjoyable working environment.

Thomas Beth, a strong proponent of quantum computing from its infant days, deserves a lot of credit for establishing quantum information processing in Germany; the community rightfully considers him a true pioneer of this field. For example, Thomas Beth was one of the initiators of the Schwerpunkt-Programm of the Deutsche Forschungsgemeinschaft in this area. Likewise, in the *Quantum Information Highway A8* he was a major player. The world of science has suffered a tragic loss when Thomas passed away August 2005. In memory of his achievements and prominent role in the A8 the present special issue of *Fortschritte der Physik* becomes a living testimony to his drive in pushing new ideas to their limits. We were all privileged to have his company in this enterprise of quantum information and dedicate this special issue to his memory.

Wolfgang P. Schleich and Herbert Walther

## List of Contributors

**Thomas Amthor**

Physikalisches Institut  
 Universität Freiburg  
 Hermann-Herder-Str. 3  
 79104 Freiburg  
 Germany  
 t.amthor@physik.uni-freiburg.de

**Ulrik L. Andersen**

Building 309  
 Danmarks Tekniske Universitet  
 (DTU)  
 2800 Lyngby  
 Denmark  
 ulrik.andersen@fysik.dtu.dk

**Ilya Sh. Averbukh**

Department of Chemical Physics  
 Weizmann Institute of Science  
 Rehovot 76100  
 Israel  
 ilya.averbukh@weizmann.ac.il

**Dmitry A. Bagrets**

Institut für Nanotechnologie  
 Forschungszentrum Karlsruhe  
 Postfach 3640  
 76021 Karlsruhe  
 Germany  
 dmitry.bagrets@int.fzk.de

**Brad Rodney Blakestad**

Time and Frequency Division  
 National Institute of Standards and  
 Technology  
 325 Broadway  
 Boulder, CO 80305  
 USA  
 brad.blakestad@nist.gov

**Immanuel Bloch**

Max-Planck-Institut für Physik  
 Johannes-Gutenberg-Universität  
 Staudingerweg 7  
 55099 Mainz  
 Germany  
 bloch@uni-mainz.de

**Mohamed Bourennane**

Physics Department  
 Stockholm University  
 10691 Stockholm  
 Sweden  
 boure@physto.se

**Karl-Heinz Brenner**

Lehrstuhl für Optoelektronik  
 Universität Mannheim  
 B 6, 27–29  
 68131 Mannheim  
 Germany  
 brenner@rumms.uni-mannheim.de

***Joe Britton***

Time and Frequency Division  
National Institute of Standards and  
Technology  
325 Broadway  
Boulder, CO 80305  
USA  
britton@nist.gov

***Thorsten Bschorr***

Institut für Quantenphysik  
Universität Ulm  
89069 Ulm  
Germany

***Giovanni Cennini***

Philips Research  
High Tech Campus 37  
5656AE Eindhoven  
The Netherlands  
giovanni.cennini@philips.com

***Ignacio Cirac***

Max-Planck-Institut für  
Quantenoptik  
Hans-Kopfermann-Str. 1  
85748 Garching  
Germany  
ignacio.cirac@mpq.mpg.de

***Yves Colombe***

Laboratoire Kastler Brossel de  
l'E.N.S.  
24 Rue Lhomond  
75231 Paris Cedex 05  
France  
yves.colombe@lkb.ens.fr

***Philippe Courteille***

Physikalisches Institut  
Universität Tübingen  
Auf der Morgenstelle 14  
72076 Tübingen  
Germany  
courteille@pit.physik.uni-tuebingen.de

***André Luiz de Oliveira***

UDESC – Universidade do Estado  
de Santa Catarina  
Departamento de Física  
Joinville, SC 89223-100  
Brazil  
andre@joinville.udesc.br

***Thomas Decker***

Institut für Algorithmen und  
Kognitive Systeme (IAKS)  
Fakultät für Informatik  
Universität Karlsruhe (TH)  
Postfach 6980  
76128 Karlsruhe  
Germany  
decker@ira.uka.de

***Johannes Deiglmayr***

Physikalisches Institut  
Universität Freiburg  
Hermann-Herder-Str. 3  
79104 Freiburg  
Germany  
j.deiglmayr@physik.uni-freiburg.de

***Thomas Fernholz***

Van der Waals-Zeeman Instituut  
Universiteit van Amsterdam  
1018 XE Amsterdam  
The Netherlands  
tfernhol@science.uva.nl

**Matthias Freyberger**

Institut für Quantenphysik  
Universität Ulm  
89069 Ulm  
Germany  
matthias.freyberger@uni-ulm.de

**Sascha Gaertner**

Ludwig-Maximilians-Universität  
80799 Munich  
and  
Max-Planck-Institut für  
Quantenoptik  
Hans-Kopfermann-Str. 1  
85748 Garching  
Germany  
s.gaertner@mpq.mpg.de

**Carsten Geckeler**

Physikalisches Institut  
Universität Tübingen  
Auf der Morgenstelle 14  
72076 Tübingen  
Germany  
geckeler@pit.physik.uni-tuebingen.de

**Bertrand Girard**

Laboratoire Collisions, Agrégats,  
Réactivité  
CNRS UMR 5589 – IRSAMC  
Université Paul Sabatier  
118 route de Narbonne  
31062 Toulouse Cedex 04  
France  
bertrand.girard@irsamc.ups-tlse.fr

**Oliver Glöckl**

Institut für Optik, Information und  
Photonik  
Max-Planck-Forschungsgruppe  
Universität Erlangen-Nürnberg  
Günther-Scharowsky-Str. 1  
91058 Erlangen  
Germany

**Dmitri S. Golubev**

Institut für Nanotechnologie  
Forschungszentrum Karlsruhe  
Postfach 3640  
76021 Karlsruhe  
Germany  
dmitri.golubev@int.fzk.de

**Axel Grabowski**

Physik Instrumente (PI) GmbH &  
Co. KG  
Auf der Römerstraße 1  
76228 Karlsruhe  
Germany

**Markus Grassl**

Institut für Algorithmen und  
Kognitive Systeme (IAKS)  
Fakultät für Informatik  
Universität Karlsruhe (TH)  
Postfach 6980  
76128 Karlsruhe  
Germany  
grassl@ira.uka.de

**Markus Greiner**

Department of Physics  
Harvard University  
17 Oxford Street  
Cambridge, MA 02138  
USA  
greiner@physics.harvard.edu

**Sönke Groth**

Physikalisches Institut  
Universität Heidelberg  
Philosophenweg 12  
69120 Heidelberg  
Germany  
groth@physi.uni-heidelberg.de

**Albrecht Haase**

ICFO – Institut de Ciències  
Fotòniques  
Parc Mediterrani de la Tecnologia  
Av. del Canal Olímpic s/n  
08860 Castelldefels, (Barcelona)  
Spain  
albrecht.haase@icfo.es

**Daniel Haase**

Institut für Zahlentheorie und  
Wahrscheinlichkeitstheorie  
Universität Ulm  
Helmholtzstraße 18  
89069 Ulm  
Germany  
daniel.haase@uni-ulm.de

**Peter Hänggi**

Institut für Physik  
Universität Augsburg  
Universitätsstraße 1  
86135 Augsburg  
Germany  
peter.hanggi@physik.uni-augsburg.de

**Theodor W. Hänsch**

Max-Planck Institut für  
Quantenoptik und  
Sektion Physik der Ludwig-  
Maximilians-Universität  
Schellingstr. 4  
80799 München  
Germany  
t.w.haensch@physik.lmu.de

**Andreas Heidebrecht**

2. Physikalisches Institut  
Universität Stuttgart  
Pfaffenwaldring 57  
70569 Stuttgart  
Germany  
a.heidebrecht@physik.uni-  
stuttgart.de

**Rolf Heidemann**

5. Physikalisches Institut  
Universität Stuttgart  
Pfaffenwaldring 57  
70569 Stuttgart  
Germany  
R.Heidemann@physik.uni-  
stuttgart.de

**Dennis Heine**

Physikalisches Institut  
Universität Heidelberg  
Philosophenweg 12  
69120 Heidelberg  
Germany  
heine@physi.uni-heidelberg.de

**Björn Hessmo**

Atomic Institute of the Austrian Universities  
 Vienna University of Technology  
 Stadionallee 2  
 1020 Vienna  
 Austria  
 hessmo@atomchip.org

**Peter Hommelhoff**

Varian Physics Building  
 382 Via Pueblo Mall  
 Stanford University  
 Stanford, CA 94305  
 USA  
 hommelhoff@stanford.edu

**Dominik Janzing**

Institut für Algorithmen und  
 Kognitive Systeme  
 Fakultät für Informatik  
 Universität Karlsruhe (TH)  
 Am Fasanengarten 5  
 76131 Karlsruhe  
 Germany  
 janzing@ira.uka.de

**John D. Jost**

Time and Frequency Division  
 National Institute of Standards and  
 Technology  
 325 Broadway  
 Boulder, Colorado 80305  
 USA  
 john.jost@nist.gov

**Emanuel (Manny) Knill**

Mathematical and Computational  
 Sciences Division  
 National Institute of Standards and  
 Technology  
 325 Broadway  
 Boulder, Colorado 80305  
 USA  
 knill@boulder.nist.gov

**Markus Kohler**

Physikalisches Institut  
 Universität Tübingen  
 Auf der Morgenstelle 14  
 72076 Tübingen  
 Germany  
 kohler@pit.physik.uni-tuebingen.de

**Sigmund Kohler**

Institut für Physik  
 Universität Augsburg  
 Universitätsstraße 1  
 86135 Augsburg  
 Germany  
 sigmund.kohler@physik.uni-augsburg.de

**Christian Kurtsiefer**

Department of Physics  
 National University of Singapore  
 Singapore 117 542  
 Singapore  
 phyck@nus.edu.sg

**Chris Langer**

Time and Frequency Division  
 National Institute of Standards and  
 Technology  
 325 Broadway  
 Boulder, Colorado 80305  
 USA  
 chris.langer@nist.gov

**Dietrich Leibfried**

Time and Frequency Division  
National Institute of Standards and  
Technology  
325 Broadway  
Boulder, Colorado 80305  
USA  
dil@boulder.nist.gov

**Gerd Leuchs**

Institut für Optik, Information und  
Photonik  
Max-Planck-Forschungsgruppe  
Universität Erlangen-Nürnberg  
Günther-Scharowsky-Strasse 1  
91058 Erlangen  
Germany  
leuchs@physik.uni-erlangen.de

**Benjamin Lev**

Department of Physics  
UCB/JILA  
Boulder, CO 80309-0440  
USA  
benlev@jila.colorado.edu

**Xiyuan Liu**

Lehrstuhl für Optoelektronik  
Universität Mannheim  
B 6, 27-29  
68131 Mannheim  
Germany  
xiyuani@rumms.uni-mannheim.de

**Robert Löw**

5. Physikalisches Institut  
Universität Stuttgart  
Pfaffenwaldring 57  
70550 Stuttgart  
Germany  
r.loew@physik.uni-stuttgart.de

**Günter Mahler**

1. Institut für Theoretische Physik  
Universität Stuttgart  
Pfaffenwaldring 57  
70550 Stuttgart  
Germany  
guenter.mahler@itp1.uni-  
stuttgart.de

**Helmut Maier**

Institut für Zahlentheorie und  
Wahrscheinlichkeitstheorie  
Universität Ulm  
Helmholtzstraße 18  
89069 Ulm  
Germany  
hamaier@mathematik.uni-ulm.de

**Olaf Mandel**

Varian Physics Building  
Stanford University  
382 Via Pueblo Mall  
Stanford, CA 94305  
USA  
mandel@stanford.edu

**Luis Gustavo Marcassa**

USP – Universidade de São Paulo  
Istituto de Física  
São Carlos, SP 13560-970  
Brazil  
marcassa@if.sc.usp.br

**Michael Mehring**

2. Physikalisches Institut  
Universität Stuttgart  
Pfaffenwaldring 57  
70569 Stuttgart  
Germany  
m.mehring@physik.uni-stuttgart.de

***Jens Mende***

Institut für Technische Physik  
Deutsches Zentrum für Luft- und  
Raumfahrt e.V.  
Pfaffenwaldring 38-40  
70569 Stuttgart  
Germany  
jens.mende@dlr.de

***Wolfgang Merkel***

Institut für Quantenphysik  
Albert-Einstein-Allee 11  
89081 Ulm  
Germany  
wolfgang.merkel@uni-ulm.de

***Roee Ozeri***

Time and Frequency Division  
National Institute of Standards and  
Technology  
325 Broadway  
Boulder, Colorado 80305  
USA  
roee.ozeri@nist.gov

***Gerhard G. Paulus***

Department of Physics  
Texas A&M University  
College Station, TX 77843  
USA  
ggpaulus@tamu.edu

***Tilman Pfau***

5. Physikalisches Institut  
Universität Stuttgart  
Pfaffenwaldring 57  
70550 Stuttgart  
Germany  
t.pfau@physik.uni-stuttgart.de

***Markus Popp***

Max-Planck-Institut für  
Quantenoptik  
Hans-Kopfermann-Str. 1  
85748 Garching  
Germany  
markus.popp@mpq.mpg.de

***Ulrich Poschinger***

Abteilung Quanten-  
Informationsverarbeitung  
Universität Ulm  
Albert-Einstein-Allee 11  
86069 Ulm  
Germany  
ulrich.poschinger@uni-ulm.de

***Stefan Probst-Schendzielorz***

Institut für Quantenphysik  
Universität Ulm  
89069 Ulm  
Germany  
Stefan.probst@uni-ulm.de

***Markus Reetz-Lamour***

Universität Freiburg  
Physikalisches Institut  
Hermann-Herder-Str. 3  
79104 Freiburg  
Germany  
m.rlamour@physik.uni-freiburg.de

***Nadja Regner***

Department für Physik  
Ludwig-Maximilians-Universität  
München  
Oettingenstr. 67  
80538 Munich  
Germany  
nadja.regner@physik.uni-  
muenchen.de

**Jakob Reichel**

Laboratoire Kastler Brossel de l'E.N.S  
24 Rue Lhomond  
75231 Paris Cedex 05  
France  
jakob.reichel@ens.fr

**Wolfgang P. Schleich**

Institut für Quantenphysik  
Universität Ulm  
Albert-Einstein-Allee 11  
89081 Ulm  
Germany  
wolfgang.schleich@uni-ulm.de

**Rainer Reichle**

Abteilung Quanten-  
Informationsverarbeitung  
Universität Ulm  
Albert Einstein Allee 11  
89069 Ulm  
Germany  
rainer.reichle@uni-ulm.de

**Christian Schmid**

Ludwig-Maximilians-Universität  
80799 Munich  
and  
Max-Planck-Institut für  
Quantenoptik  
Hans-Kopfermann-Straße 1  
85748 Garching  
Germany  
christian.schmid@mpq.mpg.de

**Gunnar Ritt**

Forschungsinstitut für Optronik und  
Mustererkennung  
Gutleuthausstr. 1  
76275 Ettlingen  
Germany  
ritt@fom.fgan.de

**Ferdinand Schmidt-Kaler**

Abteilung Quanten-  
Informationsverarbeitung  
Universität Ulm  
Albert-Einstein-Allee 11  
89069 Ulm  
Germany  
ferdinand.schmidt-kaler@uni-  
ulm.de

**Tim Rom**

Institut für Physik  
Johannes-Gutenberg-Universität  
Staudingerweg 7  
55099 Mainz  
Germany  
rom@uni-mainz.de

**Jörg Schmiedmayer**

Atomic Institute of the Austrian  
Universities  
Vienna University of Technology  
Stadionallee 2  
1020 Vienna  
Austria  
schmiedmayer@atomchip.org

**Tobias Salger**

Institut für Angewandte Physik  
Universität Bonn  
Wegelerstr. 8  
53115 Bonn  
Germany  
Salger@iap.uni-bonn.de

**Tobias Schmitt-Manderbach**

Department für Physik  
Ludwig-Maximilians-Universität  
München  
Schellingstraße 4  
80799 Munich  
Germany  
tobias.schmitt-  
manderbach@physik.uni-  
muenchen.de

**Gerd Schön**

Institut für Theoretische  
Festkörperphysik  
Universität Karlsruhe  
76128 Karlsruhe  
Germany  
gerd.schoen@phys.uni-karlsruhe.de

**Stephan Schulz**

Abteilung Quanten-  
Informationsverarbeitung  
Universität Ulm  
Albert-Einstein-Allee 11  
89069 Ulm  
Germany  
stephan.schulz@uni-ulm.de

**Michael Schwarz**

Institut für Technische Physik  
Forschungszentrum Karlsruhe  
Hermann-von Helmholtz-Platz 1  
76344 Eggenstein-Leopoldshafen  
Germany  
Michael.Schwarz@itp.fzk.de

**Signe Seidlin**

Time and Frequency Division  
National Institute of Standards and  
Technology  
325 Broadway  
Boulder, Colorado 80305  
USA  
seidelin@boulder.nist.gov

**Kilian Singer**

Abteilung Quanten-  
Informationsverarbeitung  
Universität Ulm  
Albert-Einstein-Allee 11  
89069 Ulm  
Germany  
kilian.singer@uni-ulm.de

**Sebastian Slama**

Physikalisches Institut  
Universität Tübingen  
Auf der Morgenstelle 14  
72076 Tübingen  
Germany  
slama@pit.physik.uni-tuebingen.de

**Tilo Steinmetz**

Laboratoire Kastler Brossel de  
l'E.N.S  
24 Rue Lhomond  
75231 Paris Cedex 05  
France  
tilo.steinmetz@lkb.ens.fr

**Jürgen Stuhler**

TOPTICA Photonics AG  
Lochhamer Schlag 19  
82166 Gräfelfing  
Germany  
juergen.stuhler@toptica.com

**Friedemann Tonner**

1. Institut für Theoretische Physik  
Universität Stuttgart  
Pfaffenwaldring 57  
70550 Stuttgart  
Germany  
friedemann.tonner@itp1.uni-stuttgart.de

**Philipp Treutlein**

Max-Planck-Institut für  
Quantenoptik  
and  
Sektion Physik  
Ludwig-Maximilians-Universität  
Schellingstr. 4  
80799 Munich  
Germany  
philipp.treutlein@physik.lmu.de

**Pavel Trojek**

Ludwig-Maximilians-Universität  
80799 Munich  
and  
Max-Planck-Institut für  
Quantenoptik  
Hans-Kopfermann-Straße 1  
85748 Garching  
Germany  
pavel.trojek@mpq.mpg.de

**Yasuhiro Utsumi**

Condensed Matter Theory  
Laboratory, RIKEN  
2-1 Hirosawa, Wako  
Saitama 351-0198  
Japan  
utsumi@riken.jp

**Karl Vollbrecht**

Max-Planck-Institut für  
Quantenoptik  
Hans-Kopfermann-Str. 1  
85748 Garching  
Germany  
karl.vollbrecht@mpq.mpg.de

**Christoph von Cube**

Physikalisches Institut  
Universität Tübingen  
Auf der Morgenstelle 14  
72076 Tübingen  
Germany  
cube@pit.physik.uni-tuebingen.de

**Herbert Walther** †

Max-Planck-Institut für  
Quantenoptik  
Hans-Kopfermann-Str. 1  
85748 Garching  
Germany

**Matthias Weidemüller**

Universität Freiburg  
Physikalisches Institut  
Hermann-Herder-Str. 3  
79104 Freiburg  
Germany  
m.weidemueller@physik.uni-freiburg.de

**Henning Weier**

Department für Physik  
Ludwig-Maximilians-Universität  
München  
Schellingstraße 4  
80799 Munich  
Germany  
henning.weier@physik.uni-muenchen.de

**Harald Weinfurter**

Department für Physik  
Ludwig-Maximilians-Universität  
München  
Schellingstraße 4  
80799 Munich  
and  
Max-Planck-Institut für  
Quantenoptik  
Hans-Kopfermann-Straße 1  
85748 Garching  
Germany  
harald.weinfurter@physik.uni-muenchen.de

**Martin Weitz**

Institut für Angewandte Physik  
Universität Bonn  
Wegelerstr. 8  
53115 Bonn  
Germany  
weitz@iap.uni-bonn.de

**Sebastian Westermann**

Physikalisches Institut  
Universität Freiburg  
Hermann-Herder-Str. 3  
79104 Freiburg  
Germany  
Sebastian.westermann@physik.uni-freiburg.de

**Kai Wicker**

Physikalisches Institut  
Universität Heidelberg  
Philosophenweg 12  
69120 Heidelberg  
Germany  
wicker@physi.uni-heidelberg.de

**Arthur Widera**

Max-Planck Institut für  
Quantenoptik und  
Sektion Physik der Ludwig-Maximilians-Universität  
Schellingstr. 4  
80799 München  
Germany

**Marco Wilzbach**

Physikalisches Institut  
Universität Heidelberg  
Philosophenweg 12  
69120 Heidelberg  
Germany  
wilzbach@physi.uni-heidelberg.de

**David J. Wineland**

Time and Frequency Division  
National Institute of Standards and  
Technology  
325 Broadway  
Boulder, Colorado 80305  
USA  
djw@boulder.nist.gov

**Claus Zimmermann**

Physikalisches Institut  
Universität Tübingen  
Auf der Morgenstelle 14  
72076 Tübingen  
Germany  
clz@pit.physik.uni-tuebingen.de

**Marek Zukowski**

Instytut Fizyki Teoretycznej i  
Astrofizyki  
Uniwersytet Gdańskie  
80-952 Gdańsk  
Poland  
marek.zukowski@univie.ac.at



# 1

## **The Deterministic Generation of Photons by Cavity Quantum Electrodynamics**

*H. Walther*

### **1.1**

#### **Introduction**

Cavity quantum electrodynamics allows the study of strong coupling between excited atoms and a single mode of a resonant cavity. As a consequence of the strong coupling the cavity field and the atom are entangled. The system thus provides important ingredients necessary for studies of quantum information processing. In addition the periodic exchange of a photon between atom and cavity can be studied. It thus represents the ideal system to investigate the Jaynes-Cummings model and to study a variety of phenomena related to the dynamics of the photon exchange such as collapse and revivals depending on the statistics of the photon field. Furthermore, it is an ideal system to study the quantum measurement process. The system leads to masers and lasers which sustain oscillations with less than one atom on average in the cavity and can, in addition, be used as a deterministic photon source. The setup allows to study in detail the conditions necessary to obtain nonclassical radiation, i.e. radiation with sub-Poissonian photon statistics and even photon number states; this is the case even when Poissonian pumping is used.

This paper reviews the work on cavity quantum electrodynamics performed with the one-atom maser and with a single ion trap laser. We will start with the discussion of the one-atom maser. For a more detailed discussion of those experiments see also [1].

### **1.2**

#### **Oscillatory Exchange of Photons Between an Atom and a Cavity Field (Strong Coupling) – the One-atom Maser or Micromaser**

The single-mode radiation field of the one-atom maser, or *micromaser*, is the prototype of an open driven quantum system. It has been successfully used for studies – both experimental and theoretical – of the quantum interaction

between two-level Rydberg atoms and one privileged microwave mode of the radiation field.

In a one-atom maser (or laser)For laser see Sect. 1.4.1, simple two-level atoms are strongly coupled to a single mode of the radiation field that is resonant, or nearly resonant, with the atomic transition. This situation is described by the Jaynes-Cummings Hamiltonian [2],

$$H = \hbar\omega a^\dagger a + \hbar(\omega + \Delta)\sigma^\dagger\sigma - \hbar g(t)(a^\dagger\sigma + \sigma^\dagger a), \quad (1.1)$$

where  $a$ ,  $a^\dagger$  are the photon annihilation and creation operators,  $\sigma^\dagger$  and  $\sigma$  are the raising and lowering operators of the atomic transition, and  $g(t)$  is the time-dependent coupling strength between the atomic transition and the cavity mode. The frequency of the cavity mode is  $\omega$ , and the atomic transition differs from this by the detuning  $\Delta$ . The time dependence of  $g(t)$  originates in the passage of the atom through the resonator. Typically, the simple form

$$g(t) = \begin{cases} 2\Omega & \text{for } t_0 < t < t_0 + t_{\text{int}}, \\ 0 & \text{otherwise,} \end{cases} \quad (1.2)$$

describes matters sufficiently well. Here  $\Omega$  is the (effective) Rabi frequency,  $t_0$  is the instant when the atom in question enters the cavity, and  $t_{\text{int}}$  is the duration of the interaction.

Although several experiments have been published in which the strong coupling between atoms and a single cavity mode is exploited, the micromaser is the only strongly coupled system in which a steady-state quantum field has been created with single atoms or less simultaneously in the cavity. The first paper on the one-atom maser was published in [3]. The experiment on the realization of the two-photon maser-oscillator [4] which is based on a related scheme as the one-atom maser also produces a steady-state field, however, the average number of atoms at threshold is about five. Excited-state atoms entering the cavity drive the micromaser field, each atom contributing to the quantum cavity field. Above the threshold of maser action, the steady-state field can be strongly non-classical depending on the particular parameters of the system.

The one-atom maser or micromaser was for a long time the only experimental apparatus that distinctly passes the quantum threshold and enters the non-classical regime. (For a detailed discussion see [1]). The single atom laser recently described by Kimble and coworkers [5] also reaches the quantum limit. The quantum threshold strictly only applies to systems with only one atom at a time in the cavity, since collective atom effects act to destroy quantum effects (see, for example, [6]). A detailed comparison of the different micromaser systems is given in [1]. This shows that the very high  $Q$  factor of the micromaser cavity is the feature that allows a steady-state field to be generated with properties that can only be described by quantum mechanics. The

cavity lifetime of the one-atom maser is more than two orders of magnitude larger than in other related experiments [7]. Work in the optical spectral region is being very actively pursued at the moment (see Sect. 1.4). Furthermore, quantum dots embedded in a semi-conductor micro-cavity [8–10] are another important field of activity as well as semiconductor cavity systems [11].

An important feature of the one-atom maser is its ability to generate steady-state sub-Poissonian (and hence non-classical) fields in the cavity. The extreme sub-Poissonian state is a Fock state, or number state. A Fock state is a state with a fixed number of photons and is maximally distant from what is typically known as a classical light field. These states are the quantum mechanical basis states of the electromagnetic field and are used in nearly all aspects of quantum optics. However, the extreme non-classical nature of these states has made them difficult to produce experimentally, and current sources are limited to the production of single photons [12], see also Chap. 1.4. The one-atom maser, with its high  $Q$  factor and hence long photon lifetime, is the most suitable experimental apparatus to produce such states, and their production has therefore been a major focus of recent work on this apparatus, whereby evidence of up to 5-photon Fock states could be achieved. In the following we will describe the micromaser in some detail and provide a review of the recent work on the production of Fock states.

### 1.2.1

#### Experimental Set-up of the One-atom Maser

The scheme of the experimental set-up of the one-atom maser used in our laboratory is displayed in Fig. 16.4. The shown set-up is more elaborate than the system described in the first publication [3]. The standard set-up of the one-atom maser employs the effusive output of a rubidium oven, which is collimated into two atomic beams: a central one passing directly into a  ${}^3\text{He}-{}^4\text{He}$  dilution refrigerator and a second one directed to an auxiliary excitation region. The central beam passes through the superconducting niobium cavity and the state-selective field ionization apparatus housed in the cryostat. The superconducting cavity has a  $Q$ -factor of up to  $4 \times 10^{10}$ , which corresponds to an average lifetime of a photon in the cavity of 0.3 s [13]. The photon lifetime is therefore much longer than the interaction time of an atom with the maser field, being approximately  $30\text{--}130\,\mu\text{s}$  for a thermal atomic beam, and therefore the atomic beam is sufficiently weak to make the probability of two atoms being in the cavity at the same time negligible.

The two-level transitions used in the experiments are between  ${}^{85}\text{Rb}$  Rydberg levels. The rubidium atoms are excited by laser excitation into the  $63P_{3/2}$  upper maser level. A frequency-doubled dye laser ( $\lambda = 297\,\text{nm}$ ) is used to excite the atoms to the Rydberg state from the  $5S_{1/2}$  ( $F = 3$ ) ground state.

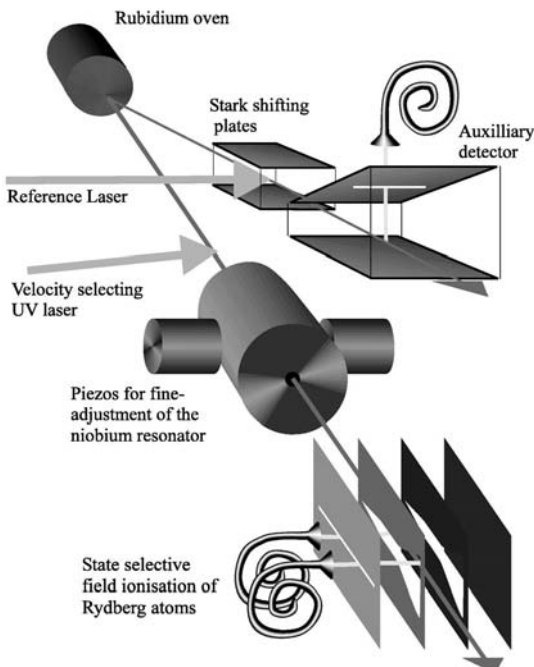


**Fig. 1.1** The atoms leaving the rubidium oven are excited into the  $63P_{3/2}$  Rydberg state by means of a UV laser at an angle of  $11^\circ$ . After the cavity the atoms are detected by state-selective field ionisation. The cavity is tuned with two piezo translators. An auxiliary atomic beam is used to stabilise the laser frequency.

The laser is locked to a Stark-shifted atomic resonance of the auxiliary beam, thus allowing the velocity subgroup selected by excitation to be continuously changed within the range of the velocity distribution of the atoms. In this way the interaction time of the atoms with the cavity is controlled.

The lower maser level is either the  $61D_{5/2}$  or the  $61D_{3/2}$  for cavity frequencies of 21.456 GHz and 21.50658 GHz, and the vacuum Rabi frequencies of these transitions are 44 kHz and 20 kHz, respectively. Surface impurities in the cavity tend to alter the values of these parameters and therefore some calibration is required. In more recent experiments, trapping states (see below) have been used to provide accurate values of the parameters. Velocity selection is provided by angling the excitation laser towards the main atomic beam at  $11^\circ$  to the normal. The dye laser was locked, by means of an external feedback control [14], to the  $5S_{1/2}(F = 3)$ - $63P_{3/2}$  transition of the reference atomic beam excited at normal incidence. The exciting laser light from the frequency-doubled laser is linearly polarized and aligned with the linear polarization of the microwave cavity. Only transitions  $\Delta m = 0$  are thus allowed. This guarantees the two-level nature of the microwave interaction. For a recent paper on this fact see [15].

Tuning the laser, which changes the velocity of the beam and thus the interaction time, was performed by Stark shifting the resonance frequency with a stabilized voltage source. This enabled the laser to be tuned while remaining locked to an atomic transition.

Collective effects caused by the entry of more than one atom into the cavity reduce the appearance of quantum effects in the cavity field. An upper limit for the one-atom condition can be arbitrarily considered to be 0.2 atoms on average in the cavity. For a cavity decay time of 0.3 s this corresponds to a pump rate  $N_{\text{ex}} = 1500$ , whereby  $N_{\text{ex}} = R \cdot \tau_{\text{cav}}$  with  $R$  for the atomic flux. Above this limit collective effects play an increasingly larger role in the maser dynamics and the detailed predictions of the theory become increasingly inaccurate [6, 16–19]. In fact, for some special conditions as in the case of quantum mechanical states (for example, in the case of the trapping states) even this limit is too high. Some care therefore needs to be taken to ensure that these collective effects do not significantly influence the maser field statistics.

### 1.2.2

#### One-atom Maser as a Source of Non-classical Light

In the typical operation of the one-atom maser, when collective effects can be ignored and the interaction time is much shorter than the cavity photon lifetime, the strategy to describe the one-atom maser is straightforward. While an atom flies through the cavity the coupled atom field system is described by the Jaynes-Cummings Hamiltonian (equation 1.1), and during the intervals between the successive atoms the evolution of the field is governed by the master equation of a harmonic oscillator damped by a thermal bath. The derivation of the steady-state photon statistics has turned from a research topic [20, 21] to a textbook matter (see, for example, [22, 23]; and [24] is a tutorial on micromaser physics). The problem can be solved analytically, and one obtains the following probability for finding  $n$  photons in the cavity when the maser has reached steady state:

$$P_n = P_0 \left( \frac{n_{\text{th}}}{1 + n_{\text{th}}} \right)^n \prod_{k=1}^n \left( 1 + \frac{N_{\text{ex}} \mathcal{A}_k}{k n_{\text{th}}} \right), \quad (1.3)$$

where  $\mathcal{A}_k = \sin^2(\Omega t_{\text{int}} \sqrt{k+1})$  is the emission probability and  $n_{\text{th}}$  is the thermal photon number. The normalized pump rate  $N_{\text{ex}}$  is the dimensionless parameter that is used in Fig. 1.2 to compare different operating conditions of the one-atom maser. It is given by  $N_{\text{ex}} = R \tau_{\text{cav}}$ , where  $R$  is the atomic rate and  $\tau_{\text{cav}}$  is the cavity photon lifetime. The probability of zero photons,  $P_0$ , is determined by normalization to unit total probability,  $\sum_{n=0}^{\infty} P_n = 1$ .

With the probabilities  $P_n$  at hand, one can calculate moments of the photon number, in particular the mean photon number  $\langle n \rangle$  and the variance  $\langle n^2 \rangle -$

$\langle n \rangle^2$ . Following Fano [25] and Mandel [26], we use the normalized variance, the so-called  $Q$  parameter,

$$Q = \frac{\langle n^2 \rangle - \langle n \rangle^2}{\langle n \rangle} - 1, \quad (1.4)$$

as a convenient numerical measure of the photon number variance. A Poissonian distribution has  $Q = 0$ ; for  $Q < 0$  one speaks of a sub-Poissonian distribution, and for  $Q > 0$  one has a super-Poissonian distribution. Fig. 1.2 shows the normalized mean photon number ( $\langle n \rangle / N_{\text{ex}}$ ) and the normalized variance ( $Q$ ) as functions of (top) the interaction time of the atoms with the cavity photons, and (bottom) the pump rate, which are the two experimentally variable parameters.

A parameter that provides a good qualitative comparison of different one-atom maser regimes is the so-called *pump parameter*, given by  $\Theta = \sqrt{N_{\text{ex}}} \Omega t_{\text{int}}$ . It is useful for locating features of the maser operating under a wide variety of conditions. For example, one can see in Fig. 1.2 that the maxima of the  $Q$  parameter occur when  $\Theta$  is (roughly) a multiple of  $2\pi$ .

When the value of the pump parameter is  $\Theta = 1$ , the average photon number starts to rise steeply, the photon-statistical parameter  $Q$  reaches a local maximum, and the one-photon probability  $P_1$  becomes larger than the no-photon probability  $P_0$  for the first time. This point is therefore known as the *maser threshold*. Another position of interest is where the statistical parameter  $Q$  crosses zero for the first time. There the photon distribution passes from a classically shaped super-Poissonian distribution to a sub-Poissonian distribution. This quantum threshold lies at approximately  $\Theta = \pi/2$ . At this point nearly all atoms deposit photons in the cavity and the field has a Poissonian distribution with an average value equal to that of the atomic pump rate  $N_{\text{ex}}$ . Above this point the maser field becomes sub-Poissonian and therefore distinctly quantum mechanical, since the average energy in the cavity field is stabilized by the one-atom maser interaction. Some super-Poissonian peaks appear above this position; these are bistable points in which quantum jumps between two sub-Poissonian distributions occur. The statistics are therefore quantum mechanical in origin, even if they lie in a classical region. The atomic rate, as a function of the interaction time, required to cross the maser threshold and quantum thresholds are indicated in Fig. 1.2 by the lines  $R_{\text{th}}$  and  $Q_{\text{th}}$ , respectively.

The threshold for quantum behavior is really only applicable to the single-atom regime, in which the possibility of collective effects is very low. When collective effects cannot be ignored, the position of this line is somewhat modified. Moreover, while some basic parameters may still apply at this value, the upper bound of collective effects for more exotic states such as trapping states

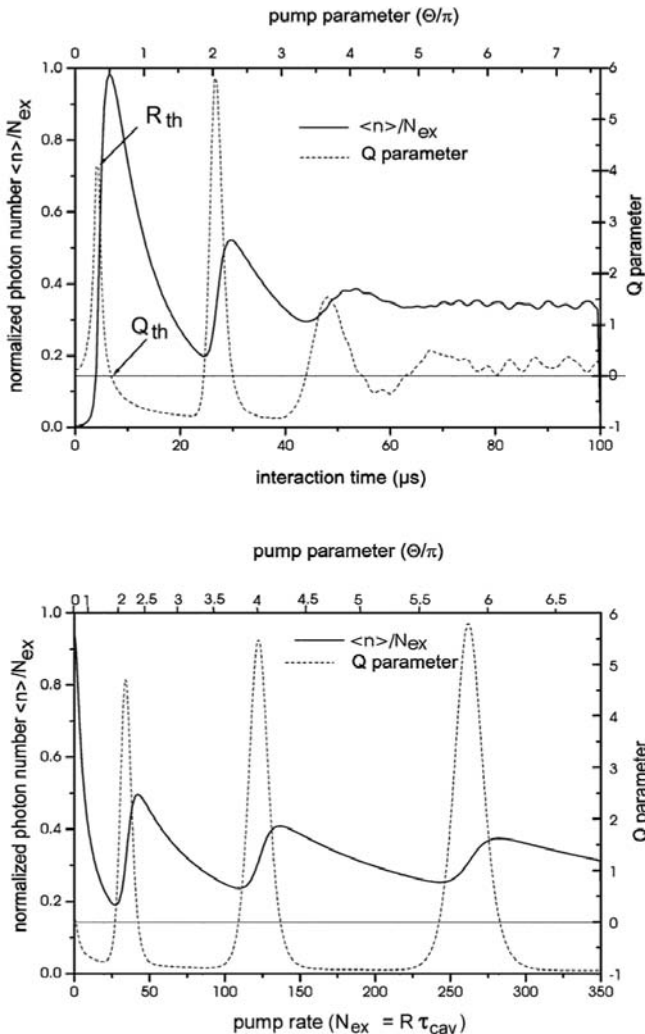


**Fig. 1.2** The pump curve of the one-atom maser as obtained from equation (1.3). In both plots, the temperature is set at 0.5 K, which corresponds to  $n_{\text{th}} = 0.1$  thermal photons. **Top:** The normalized photon number as a function of the interaction time (bottom axis), for a pump rate  $N_{\text{ex}} = 40$ . **Bottom:** The normalized photon number as a function of the pump rate  $N_{\text{ex}}$  (bottom axis), for an

interaction time  $t_{\text{int}} = 30 \mu\text{s}$ . The top axis of both plots shows the equivalent value of the pump parameter,  $\Theta$ , for these conditions (see text). The thresholds of maser action ( $R_{\text{th}}$ ) and quantum field statistics ( $Q_{\text{th}}$ ) are indicated. Note that the micromaser exhibits thresholdless behavior for the parameters of the bottom plot.

is considerably lower since they are completely obliterated by even low levels of collective effects.

Above the threshold ( $R_{\text{th}}$ ), the field in the cavity is a steady-state phenomenon and is thus available for study in some detail. Below threshold, the cavity field is dominated by cavity decay and is therefore a transient effect lasting for a cavity decay time after the interaction of the atom. This is the single-atom-effect region. As the evolution of the atom and cavity field is fully coherent, the atom and cavity field are entangled after their interaction. This entanglement is used, for example, to probe the cavity field in the normal operation of the maser. In the single-atom regime this can be exploited to create a transient field that exists in the cavity for a photon lifetime. As the atomic beam has a Poissonian distribution of arrival times, it can happen that, even in operation well below threshold, several atoms enter the cavity within a cavity decay time. Post-selective detection of such events has been used to observe the interaction of the field with up to three atoms under these conditions [7, 27–30].

### 1.2.3

#### **Review of Experiments on Basic Properties of the One-atom Maser**

Atoms interacting with the cavity field undergo Rabi oscillations and their emission probability is determined by the accumulated Rabi phase when they leave the cavity. When the cavity field is initially in a coherent field state, the photon probability distribution is Poissonian, which results in dephasing of the Rabi oscillations causing their subsequent collapse. After collapse, the evolution of the atom and quantized cavity field results in a revival of the Rabi oscillations. These revivals occur periodically with a period determined by the square root of the average photon number. This phenomenon is known as “collapse-and-revival” and is a purely quantum mechanical feature with no classical counterpart [31].

Collapse-and-revival can also occur in the case of a thermal Bose-Einstein field, where the spread in the photon number is much larger than that of the coherent state. In this case, the pattern of oscillations is more complicated, and the pattern never collapses quite completely – but this is also an inherently quantum mechanical phenomenon since the classical counterpart to this field would cause the oscillation to decay to zero with no revival at all. Collapse-and-revival in the presence of a thermal field was first observed by Rempe et al. in 1987 [32]. Elmfors et al. [33] subsequently performed a theoretical analysis of the experimental conditions and found excellent agreement between theory and experiment, thus clearly showing that the interpretation of the data as collapse-and-revival was accurate. In 1996, collapse-and-revival was also observed in the presence of a coherent field by Brune et al. [34] (see also Sect. 1.3.1).

The coherent interaction of atoms with the cavity field produces non-classical states in the cavity. Fig. 1.2 shows that over a wide range of interaction times a relatively low  $N_{\text{ex}}$  is already sufficient to generate a non-classical maser field. This is the case because the vacuum field initiates transitions to the lower maser level. The sub-Poissonian statistics can be understood from Fig. 1.2, where the normalized average photon number  $\langle n \rangle / N_{\text{ex}}$  is shown on the right as a function of the pump rate  $N_{\text{ex}}$ . An increase in the photon number decreases the emission probability, driving the photon number to a smaller value. A decrease in the photon number, by contrast, increases the emission probability, driving the photon number up. This is a coherent interaction and it is therefore a quantum mechanical stabilization of the photon number, producing sub-Poissonian statistics. As the atoms are the source of the field, the field statistics can be related to the atomic statistics in a systematic manner [35]. The observation of sub-Poissonian atomic statistics was reported by Rempe, Schmidt-Kaler and Walther [36], and its relation to the sub-Poissonian photon distribution was first studied by Rempe and Walther [37] and later by Briegel et al. [35].

The reason for the sub-Poissonian atomic statistics is as follows: A changing flux of atoms changes the Rabi frequency via the stored photon number in the cavity. Adjusting the interaction time allows the Rabi nutation cycle to be chosen such that the probability of the atoms leaving the cavity in the upper maser level increases when the flux, and hence the photon number in the cavity, is raised. This leads to sub-Poissonian atomic statistics since the number of atoms in the lower state decreases with increasing flux and photon number in the cavity. This feedback mechanism can be neatly demonstrated through the anticorrelation of atoms leaving the cavity in the lower state. The fact that anticorrelation is observed indicates that the atoms in the lower state are more equally spaced than expected for a Poissonian distribution of the atoms in the beam. This means that when, for example, two atoms in the upper state enter the cavity close to each other, the second one performs a transition to the lower state with reduced probability.

The interaction with the cavity field thus leads to an atomic beam with atoms in the lower maser level showing number fluctuations which are up to 40 % below those of a Poissonian distribution usually found in atomic beams. This is interesting because atoms in the lower level have emitted a photon to compensate for cavity losses inevitably present. Although this process is induced by dissipation giving rise to fluctuations, the atoms still obey sub-Poissonian statistics. As discussed above, this can also be seen as a consequence of the quantum-non-demolition situation achieved in the region  $\Theta \approx 2\pi$  and multiples thereof.

The field strongly fluctuates at positions where phase transitions occur, these being caused by the presence of two maxima in the photon number distri-

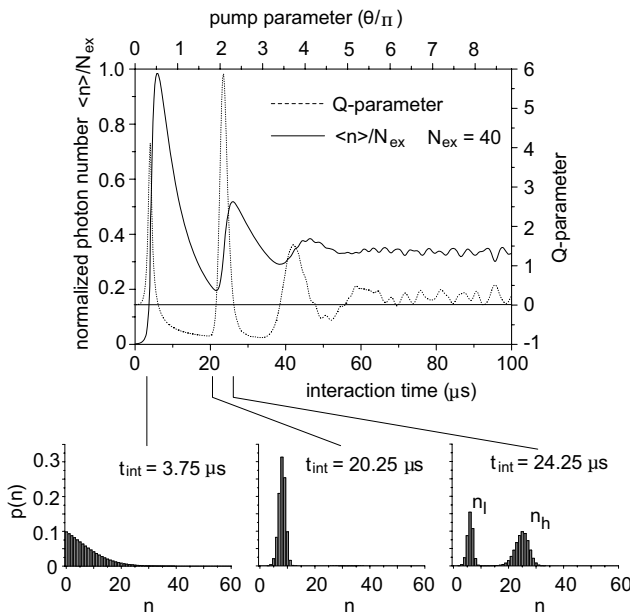


**Fig. 1.3** One-atom maser or micromaser characteristics. The upper part of the figure shows the average photon number versus interaction time (solid curve) and the photon number fluctuations represented by the  $Q$ -factor (dotted line). In the lower part of the figure the steady-state photon number distribution  $P(n)$  is shown for three values of  $t_{\text{int}}$ . The distribution on the left side corresponds to the maser threshold, that on

the right gives an example of the double-peaked distribution associated with the quantum jump behavior. In this situation, the atom is back in the excited state and can again emit, leading to a higher steady-state photon number  $n_h$ . With increasing  $t_{\text{int}}$  this part will grow and  $n_l$  will decrease and disappear. A new jump occurs for pump parameters  $\theta > 3\pi$ .

bution  $P(n)$  at photon numbers  $n_l$  and  $n_h$  ( $n_l < n_h$ ); see Fig. 1.3. The phenomenon of two coexisting maxima in  $P(n)$  was also studied in a semiheuristic Fokker-Planck (FP) approach [20]. There, the photon number distribution  $P(n)$  is replaced by a probability function  $P(\nu, \tau)$  with continuous variables  $\tau = t/\tau_{\text{cav}}$  and  $\nu = n/N_{\text{ex}}$ , the latter replacing the photon number  $n$ . The steady-state solution obtained for  $P(\nu, \tau), \tau \gg 1$ , can be constructed by means of an effective potential  $V(\nu)$  showing minima at positions where maxima of the probability function  $P(\nu, \tau)$  are found. Close to  $\Theta = 2\pi$  and multiples thereof, the effective potential  $V(\nu)$  exhibits two equally attractive minima located at stable gain-loss equilibrium points of maser operation (see Fig. 1.3). The mechanism at the phase transitions is always the same: A minimum of  $V(\nu)$  loses its global character when  $\Theta$  is increased, and is replaced in this role by the next one. This reasoning is a variation of the Landau theory of first-order phase transitions, with  $\sqrt{\nu}$  being the order parameter. This analogy actually leads to the notion that, in the limit  $N_{\text{ex}} \rightarrow \infty$ , the change of the

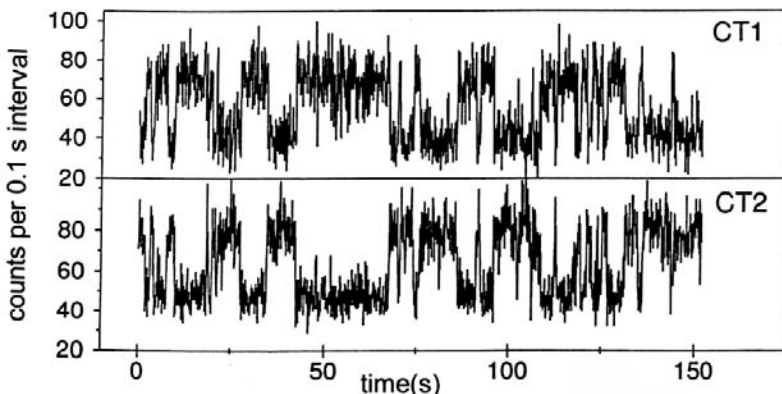


**Fig. 1.4** Quantum jumps between two equally stable operation points of the one-atom-maser field. CT1 is the measurement of the upper state atoms, and CT2 that of the lower state atoms. It can be seen that both signals show counterphase behavior.

micromaser field around integer multiples  $\Theta = 2\pi$  can be interpreted as first-order phase transitions [38].

Close to first-order phase transitions long time constants of the field evolution are expected. This phenomenon was experimentally demonstrated, along with related phenomena such as spontaneous quantum jumps among equally attractive minima of  $V(\nu)$ , bistability, and hysteresis. Some of these phenomena are also predicted in the two-photon micromaser, for which qualitative evidence of first-order phase transitions and hysteresis has been reported. One example of this switching behavior will be discussed in the following. The maser was operated under steady-state conditions close to a first-order phase transition. The two maxima in  $P(n)$  are manifested in spontaneous jumps of the maser field between the two maxima, with a time constant of 10 sec. This fact, and the relatively large pump rate, led to the clearly observable field jumps shown in Fig. 1.4. The two discrete values of the counting rates correspond to the metastable operating points of the maser, these being ca. 70 and ca. 140 photons: these two values correspond to two equally attractive minima in the FP potential  $V(\nu)$ . If one considers, for instance, the counting rate of lower-state atoms (CT2 in Fig. 1.4), the lower (higher) plateaus correspond to time intervals in the low (high)-field metastable operating point. If the actual photon number distribution is averaged over a time interval containing many spontaneous field jumps, the steady-state result  $P(n)$  of the micromaser theory is recovered [38].

As noted above, between the regions of sub-Poissonian statistics, there are narrow regions of super-Poissonian statistics coinciding with thresholds in the photon number. These features are due to photon number phase transitions.

In these regions, the steady-state photon distribution of equation (1.3) has two sub-Poissonian peaks that are well separated, so that the Fano-Mandel  $Q$  parameter is positive (and relatively large). A photon number distribution of this particular kind gives rise to quantum jumps between these two sub-Poissonian peaks. This effect and the associated bistability that one would expect from this system have indeed been observed in the one-atom maser [39, 40].

### 1.2.4

#### Statistics of Detector Clicks

In these experiments all information about the radiation field is second-hand, inasmuch as the experimenter can examine only atoms emerging from the resonator, but not the field itself. The Fock-state Rabi oscillations clearly show this. Although we do not measure the field itself, we are able to determine the photon distribution by analysis of an atom used as a probe of the field. Accordingly, in the steady-state maser dynamics, the atoms play a double role: (i) they pump the cavity and (ii) they provide the interaction diagnostics. The two roles interfere with one another because detection of the atom in a known final state leads to a quantum mechanical reduction of the photon state inside the resonator. Frequent detection is accompanied by quasi-permanent state reduction which can prevent the cavity field from relaxing to the steady state that would be reached if the atoms were left unobserved. Nevertheless, the steady-state properties determine the statistics of clicks recorded by the atom detectors. This method of calculation has been used rather successfully for determining the photon distribution in the cavity in recent experiments [30, 41]. Furthermore, an extended analysis [42] predicts the probabilities of specific sequences of atoms (or, rather, of detector clicks) and therefore provides predictions of correlations between the internal state of the atoms that are successively detected in the field ionization zone. Measurement of these correlations therefore provides a method of assessing the accuracy of the formalism, and then other predictions of the model, which cannot be readily observed, such as the presence of entanglement, can be trusted as well.

The so-called “damping-bases method” [43] has been instrumental in extracting from the one-atom-maser theory predictions about atomic correlations and observed photon distributions [30, 41, 44]. These correlations have recently been observed and the correspondence between theory and experiment determined [44]. The success of this correspondence strongly suggests that other aspects of the theory, such as predictions of multiple atom entanglement, are also true.

## 1.2.5

**Trapping States**

Trapping states are a feature of steady-state operation of the one-atom maser, in which the field is peaked at a single photon number [13]. They occur in the one-atom maser as a direct consequence of the quantization of the cavity field. In fact, in the trapping states the quantum states of the radiation field become directly visible. The one-atom maser is the only system we know allowing to observe the quantum states of the radiation field directly. At low cavity temperatures the number of black-body photons in the cavity mode is reduced and trapping states begin to appear [45, 46]. Under these conditions the sharp spikes appear that were not present in Fig. 1.2. These are the signature of the trapping states that occur at low temperatures because the emission probability  $\mathcal{A}_k$  of equation (1.3) is then a dominant effect. The top plots in Figs. 1.5 and 1.6 show the effect of reduced temperature on the shape of the normalized photon number and the  $Q$  parameter by comparing the curves expected for 100 mK ( $n_{\text{th}} = 10^{-4}$ ) and 500 mK ( $n_{\text{th}} = 0.1$ ). The two bottom plots show blown-up sections of the top plots to make the details clearer. In this case all of the curves are calculated for a cavity temperature of 100 mK, and we compare two pump rates,  $N_{\text{ex}} = 20$  and  $N_{\text{ex}} = 40$ . With a change of pump rate, the trapping states remain fixed in position but their visibility changes dramatically. In the bottom plot of Fig. 1.6 the trapping states are manifested as regions of sub-Poissonian statistics with super-Poissonian regions on either side (this is seen more clearly in the curve for the lower pump rate).

Trapping states occur when  $\mathcal{A}_k = 0$ , i.e. when, for zero thermal photons, emission of an atom is forbidden, so that the Fock space is effectively truncated and the photon number therefore naturally accumulates at this upper limit. Zero emission occurs when the atoms perform an integer number ( $k$ ) of Rabi cycles, i.e. when

$$\sqrt{n_k + 1}\Omega t_{\text{int}} = k\pi \quad (1.5)$$

holds.

In fact, even for certain realistic steady-state operating conditions with a non-zero thermal photon number, the photon distribution can approximate a Fock state very well. Trapping states are characterized by the number of photons  $n_k$  and the number of Rabi cycles  $k$ . The trapping state  $(n_k, k) = (1, 1)$  therefore refers to the one-photon, one-Rabi-oscillation trapped-field state. Equation 1.5 shows that a reliable indication of trapping states is that, unlike other features of the maser pump curve, they are independent of the pump rate, and thus a signature of trapping states is the observation of features in the maser pump curve, as a function of the interaction time, which will not move as a function of the pump rate. A second indication is the characteristic

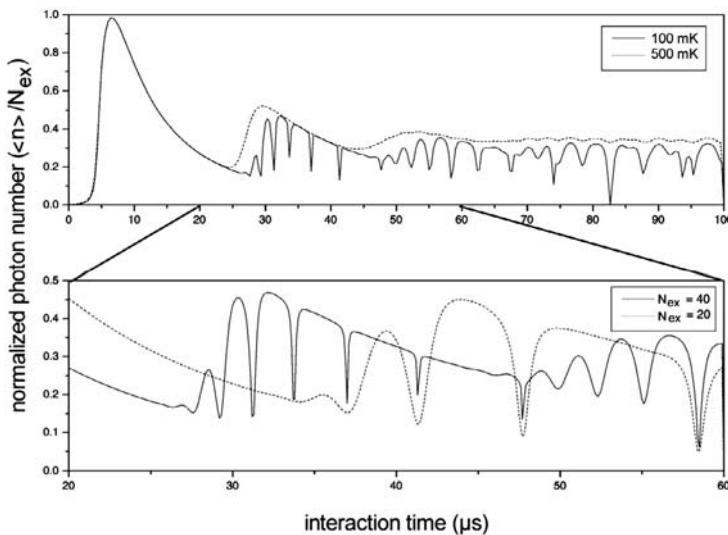


**Fig. 1.5** One-atom maser at low temperature and high temperature. The top plot shows the effects of reduced temperature on the normalized photon number by comparing the expected curves for 100 mK ( $n_{\text{th}} = 10^{-4}$ ) and 500 mK ( $n_{\text{th}} = 0.1$ ). The bottom plot, which

shows a blown-up section of the top plot to make the details clearer, refers to 100 mK and the curves compare two pump rates,  $N_{\text{ex}} = 20$  and  $N_{\text{ex}} = 40$ . The trapping states remain fixed in position but their visibility changes dramatically.

oscillation of the statistical  $Q$  parameter, as seen in the bottom plots of Figs. 1.5 and 1.6.

The effect of thermal photons (always present at finite temperatures) is to violate the trapping condition, so that the Fock space is no longer truncated. To observe trapping states, one therefore requires very low temperatures and highly stable conditions. Avoiding collective atomic effects and the effect of a finite atomic lifetime is also critically important for the realization of trapping states [6, 16–19, 47]. Trapping states are self-stabilizing against the decay of photons from the mode, since atoms are always available to replace photons lost to decay, thus restoring the trapping condition. With a careful choice of parameters, this self-stabilization can be exploited to produce photon number states in a wide range of operating conditions. This has recently been exploited for producing stable trapping state features [48] and also for creating photon number states on demand [49, 50].

The one-atom maser is the ideal system to realize trapping states. The cavity is operated at a temperature of 0.3 K, leading to a thermal field of about  $3 \times 10^{-2}$  photons per mode.

The first indication of trapping states in the maser field was reported in [46]. These results (corrected for the finite atomic lifetimes) are presented in Fig. 1.7 for two values of  $N_{\text{ex}}$  as a function of the interaction time. The cavity tem-

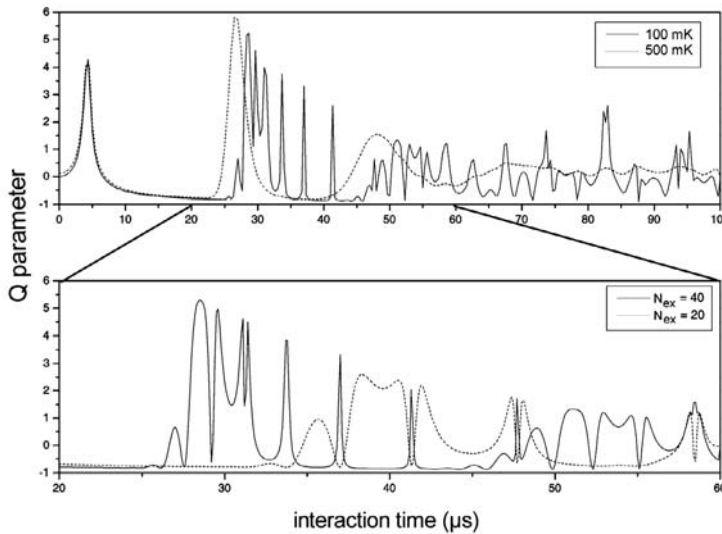


**Fig. 1.6** One-atom maser at low temperature and high temperature. Same as Fig. 1.5, but here the  $Q$  parameter is plotted. Note, in particular, that in the bottom plot the trapping states are manifested as regions of sub-Poissonian statistics with super-Poissonian regions on either side (this is seen more clearly in the lower-pump-rate curve).

perature was about 340 mK, which corresponds to a thermal photon number of 0.054. This result shows good qualitative agreement with the Monte Carlo simulations by Raithel et al. [51]. The positions of the dips are preserved at increased pumping strength, as predicted. The reduction in visibility occurs for two reasons: Firstly due to narrowing of the peaks that occurs for increased pump rates (see Figs. 1.5 and 1.6) and secondly due to increased incidence of collective atom effects which act to reduce the visibility of the trapping state.

As the arrival times of the ground-state atoms were also collected in this experiment, it was possible to use equation 1.4 to extract the lower-state statistics of atoms leaving the cavity. The evaluation of this parameter from the experimental data is presented in the bottom plot of Fig. 1.7. For most of the positions where there is a trapping state sub-Poissonian statistics are also found. As the atom statistics and photon statistics are related, this is to be expected if the photon field is truly sub-Poissonian. One also finds a good qualitative relationship with the rapidly varying  $Q$  parameter of the bottom plots in Figs. 1.5 and 1.6. Note that the vacuum is a coherent state and therefore the lower-state atom statistics should be Poissonian, as they are.

The trapping condition given in equation (1.5) is only accurate when the atoms are resonant with the cavity field. With detuning  $\Delta \neq 0$ , the vacuum

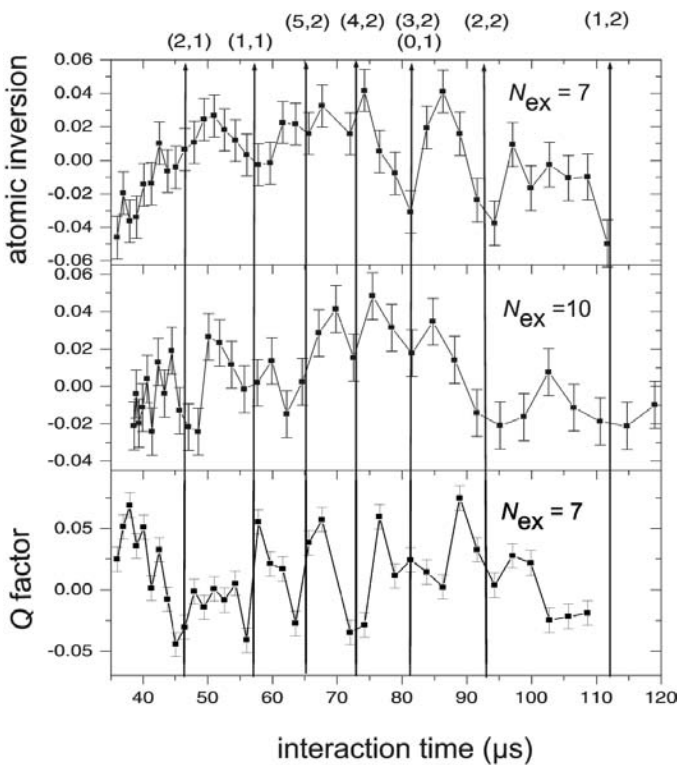


**Fig. 1.7** Experimental measurement of trapping states in the maser field. The various trapping states are labeled by their  $(n_k, k)$  pair of quantum numbers. **Top and center:** Trapping states appear as a reduced probability of finding a ground-state atom. **Bottom:** Trapping states appear as regions

of sub-Poissonian statistics between regions of super-Poissonian statistics. An exception is the vacuum trapping state, which is the ground state of a coherent field, and therefore the atom counting should have Poissonian statistics. (Reproduced from [46].)

emission probability is given by

$$P_g(\Delta, t_{\text{int}}) = \frac{4\Omega^2}{\Delta^2 + \Omega^2} \sin^2 \left( \frac{1}{2} \sqrt{\Delta^2 + 4\Omega^2} t_{\text{int}} \right). \quad (1.6)$$

This exhibits oscillatory behavior that results from Rabi flopping, but, since there is detuning, the observed flopping frequency is higher than that of the vacuum Rabi frequency. When detuning is used in an off-resonant situation, much more periods are thus observed than would occur when the experiment is performed on resonance.

In previous experiments, trapping states and thus the influence of Fock states, could be identified up to  $n = 5$  [46]. The set-up currently in use does not permit investigation of the purity of the Fock states obtained under the

trapping condition. The dynamic generation of Fock states described in the next section, however, does allow the purity of Fock states to be measured.

### 1.2.6

#### Trapping State Stabilization

Trapping states are self-stabilizing in that any photon loss due to cavity decay is replaced by a new photon from the pump atoms and, when the cavity field is in the trapping state, the field distribution is localized to a Fock state, where it will remain for a time determined by the rate of entry of thermal photons into the cavity. As shown above, thermal photons destroy the trapping condition. The best stability is thus achieved by adding a new loss mechanism that can remove any build-up of a field beyond the trapping state. This could be done by adding either lower state atoms to the beam (ground states in the trapping states) or a feedback mechanism that reduces the pump rate to compensate for increased emission [52].

However, a simpler and ultimately highly effective method is to operate the micromaser in cyclic operation, where the pump atoms are turned on and off for short periods (in comparison with the rate of the build-up of the thermal field) for pump and relaxation cycles. During the pumping cycle the cavity begins to fill with photons, approaching the corresponding CW condition; the pump rate is then turned off for a period to allow the field to relax a little before the next pumping cycle, thus correcting for the entry of thermal photons and allowing the field to resume the trapping condition in the next pulse. After many such cycles the field reaches a steady state that is a combination of the pumping cycle and the relaxation cycle. In this mode of operation, the entry of thermal photons only affects a single pulse, after which the cavity is allowed to relax to a photon number below the steady-state value. In such operation trapping states are a dominant feature of micromaser dynamics for a wide range of pump rates and thermal photon numbers.

The theoretical model for calculating the cyclically steady state of the maser (the steady state produced for a pulsed pump cycle) was developed to calculate photon distributions for the analytical analysis of Fock states and can be found in [41] and in a detailed review by Walther et al. [1]. See also [48, 49] and [50] for more details.

### 1.2.7

#### Fock States on Demand

In recent years there has been increasing interest in systems capable of generating photon fields containing a preset number of photons. This has chiefly arisen from applications requiring single photons, such as secure quantum communication and quantum cryptography. Fock states are also useful for

generating multiple-atom entanglements in systems like the micromaser. In the micromaser the generated field and the pumping atoms are in an entangled state. This entanglement can be transferred by the field to subsequent atoms, leading to applications such as basic quantum logic gates.

A basic requirement for *reliably* preparing a field in a preset quantum state is the ability to choose the field state in a controllable manner [30]. Trapping states provide this means. Under trapping-state conditions, quantum feedback between the atoms and the field acts to control the cavity photon number. Trapping states can thus be used to provide photons on demand. Under ideal conditions, the micromaser field in a trapping state is a Fock state, but when the micromaser is operated in a continuous-wave mode, the field state is very fragile and highly sensitive to external influences and experimental parameters. However, in pulsed operation, as opposed to continuous-wave operation, trapping states are more stable and more practical, and can be used over a much broader parameter range than in continuous-wave operation [49]. An additional advantage is that the number of photons generated can be investigated by a probe atom after preparation.

To demonstrate the principle of Fock state preparation, Fig. 1.8 shows a simulation of a sequence of 20 pulses of the pumping atoms in which an average of seven excited atoms per pulse are present. Two operating conditions are present to compare conditions outside trapping conditions ( $gt_{int} = 1.67$ ) with the (1,1) trapping states ( $gt_{int} = 2.2$ ). Below the pulse sequences, two distributions show the probability of finding 0–5 atoms (and hence photons) per pulse in the cavity.

Under the trapping condition, only a single emission event occurs, which produces a single lower-state atom, leaving a single photon in the cavity. As during an atom pulse the atom-cavity system is in the trapping condition, the emission probability is reduced to zero after that and the photon number is stabilized. The variation of the time when an emission event occurs during the atom pulses in Fig. 1.8 is due to the Poissonian spacing of upper-state atoms entering the cavity and the stochasticity of the quantum process. The lower part of Fig. 1.8 shows the photon number distribution resulting from this process. In Fig. 1.8a the broader photon number distribution is due to the absence of a feedback stabilization.

### 1.2.8

#### Dynamical Preparation of $n$ -photon States in a Cavity

In this section we describe an alternative method of generating number states that also permits the analysis of the purity of the states generated to be unambiguously determined. We start the discussion of the method with some general remarks.

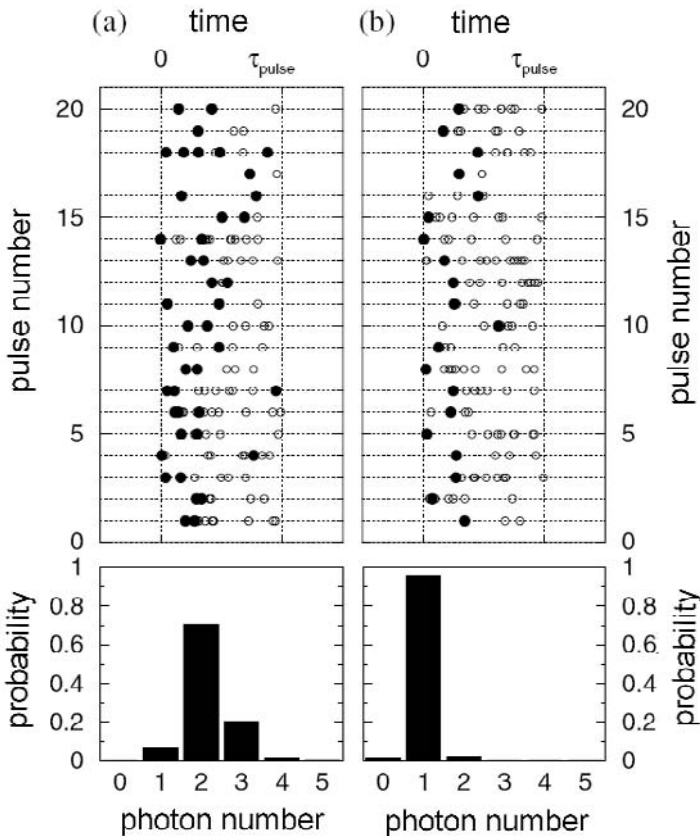


**Fig. 1.8** A simulation of a subset of twenty successive pulses of the excitation laser and the associated probability distribution for photons or lower-state atom production (solid circles represent lower-state atoms and blank circles represent excited-state atoms). The start and finish of each pulse is indicated by the vertical dotted lines marked 0 and  $\tau_{\text{pulse}}$ ,

respectively. The two operating conditions are (a) outside the trapping-state conditions ( $gt_{\text{int}} = 1.67$ ), resulting in a broad photon number distribution, and (b) the (1, 1) trapping state ( $gt_{\text{int}} = 2.2$ ) with a near-Fock-state distribution. Both distributions are sub-Poissonian but they are readily distinguishable experimentally. The figure is taken from [49].

When the atoms leave the cavity in a one-atom maser experiment, they are in an entangled state with the field. If the field is in an initial Fock state  $|n\rangle$ , then the interaction of an atom with the cavity leaves the cavity field in a superposition of the states  $|n\rangle$  and  $|n+1\rangle$  and the atom in a superposition of the internal atomic states  $|e\rangle$  and  $|g\rangle$ . The entangled state can be described by

$$|\Psi\rangle = \cos(\phi) |e\rangle |n\rangle - i \sin(\phi) |g\rangle |n+1\rangle, \quad (1.7)$$

where the phase parameter  $\phi$  depends on the interaction time. The state-selective field ionization measurement of the internal atomic state reduces the field to one of the states  $|n\rangle$  or  $|n+1\rangle$ . State reduction is independent of the

interaction time, hence a ground-state atom always projects the field onto the  $|n + 1\rangle$  state independently of the time spent in the cavity. This results in an *a priori* probability of the maser field being in a specific but unknown number state [53]. If the initial state is the vacuum,  $|0\rangle$ , then a number state is created in the cavity that is equal to the number of ground state atoms that were collected within a suitably small fraction of the cavity decay time. This is the essence of the method of preparing Fock states by state reduction that was proposed by Krause et al. [53].

In a system like the micromaser there is no dissipative loss during the interaction and an atom in the cavity undergoes Rabi oscillations. That is, the relative populations of the excited and ground states of the atom oscillate at a frequency  $\Omega\sqrt{n + 1}$ . As mentioned above, the atomic inversion has been experimentally investigated. In the presence of dissipation, a fixed photon number  $n$  in a particular mode is not observed and the field always evolves into a mixture of such states. The inversion is therefore generally given by

$$I(t_{\text{int}}) = - \sum_n P_n \cos(2\Omega\sqrt{n + 1} t_{\text{int}}) , \quad (1.8)$$

where  $P_n$  is the probability of finding  $n$  photons in the mode.

The method used in this experiment corresponds to a pump-probe experiment in which pump atoms prepare a quantum state in the cavity which is subsequently measured by a probing atom by studying the Rabi nutation. The signature that the quantum state of interest has been prepared is simply the detection of a definite number of ground-state atoms. To verify that the correct quantum state has been projected onto the cavity, a probe atom is sent into the cavity with a variable, but well-defined, interaction time in order to allow measurement of the Rabi nutation. As the formation of the quantum state is independent of the interaction time, we need not change the relative velocity of the pump and probe atoms, thus reducing the complexity of the experiment. In this sense, we are performing a reconstruction of a quantum state in the cavity using a method similar to that described by Bardoff et al. [54]. This experiment reveals the maximum amount of information on the cavity photon number that can be found.

The laser beam populating the upper state was pulsed to create short excitation pulses with only a small probability of exciting one atom; thus when two were observed (i.e. the pump and probe), it is highly probable that not more than two were excited. In fact, to create and detect an  $n$  photon number state in the cavity,  $n + 1$  atoms are required. That is,  $n$  atoms to create the number state and the final atom as a probe of the state. With 40% detector efficiency and the assumption that the probability of missing a count is statistically independent, there is an approx. 1% probability of the state preparation being incorrect because an atom escapes detection. Figs. 1.9(a–c) displays three Rabi

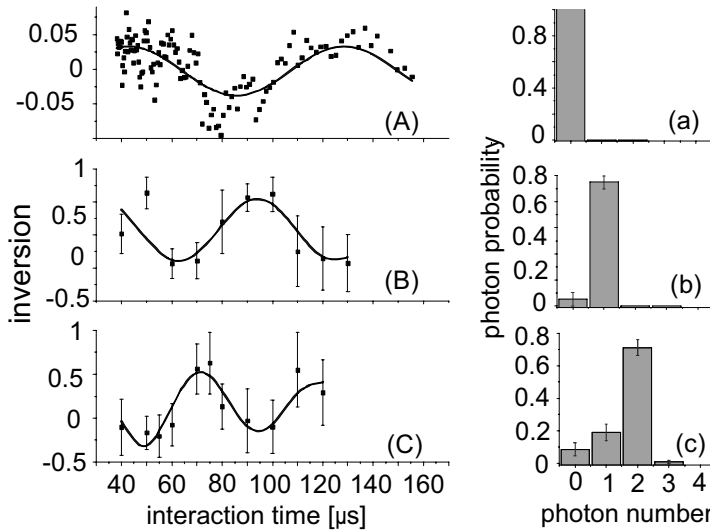


**Fig. 1.9** Plots (A), (B) and (C) on the left present three Rabi oscillations for the number states  $n = 0, 1$ , and  $2$ . Plots (a), (b) and (c) on the right plots display the coefficients  $P_n$ . The photon distribution  $P_n$  was calculated for each Rabi cycle by fitting equation (1.7) to each plot for the set of photon numbers,  $n = 0$  to  $n = 3$ . The relative phase of the Rabi oscillation was fixed since all the atoms enter in the excited state of the maser transition. In each fit, the highest probability was obtained for the target number state. Unlike the  $n = 1$  and  $n = 2$  Rabi cycles, the  $n = 0$  oscillation of plot (A) was obtained in the steady-state operation

of the micromaser in a very low-flux regime. The fit to this curve was performed for Rabi cycles from  $n = 0$  to  $n = 2$ . The low visibility of this curve was due to the low flux (one atom per second) which was required to reduce the steady-state operation of the micromaser to below-threshold behavior; hence detector dark counts become comparable to the real count rates and therefore contribute to a large background. During the Rabi cycle the cavity photon number changes periodically. At the maxima there is one photon more than at the minima. (Reproduced from [30].)

cycles obtained by measuring the inversion of a probe atom that followed the detection of  $n = 0, 1$ , and  $2$  ground-state atoms, respectively.

Because of the long waiting times for three atom events, the  $n = 2$  Rabi data were more difficult to collect than the other two measurements. The data collection time became substantially longer as the interaction time was increased, and then background effects have a higher impact on the data. The fit to the  $n = 2$  data includes an exponentially decreasing weight, so that measurements obtained for longer interaction times have less significance than those at short times.

The fact that pure number states were not obtained here is due to dissipation in the time interval between production and analysis of the cavity field. The simulations described in the following demonstrate that one could generate number states with a purity of 99% for the  $n = 1$  state and 95% for the  $n = 2$

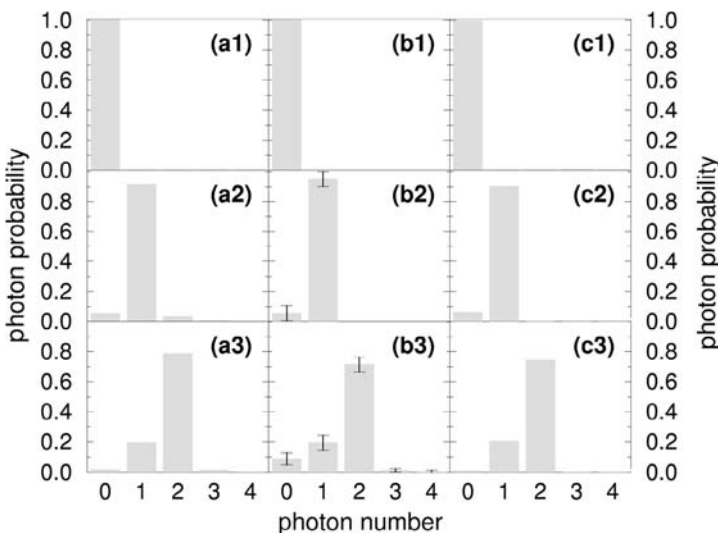


**Fig. 1.10** Comparison between theory and experimental results on the purity of number states. The columns represent photon distributions obtained from: (a) a theoretical simulation of the current experiment; (b) the current experimental results; and (c) a theoretical model that extends the current experiment to the steady state at the positions

of the trapping states. The agreement between the two theoretical results and the experimental result is remarkable, indicating that dissipation is the most likely loss mechanism. Without dissipation, i.e. at the moment of generation the purity of the states is 99% for  $n = 1$  and 95% for  $n = 2$ . (Reproduced from [30].)

state at the time of generation, which is then modified by dissipation between production and measurement.

For the simulations two idealizing assumptions were made: thermal photons are only taken into account for the long-term build-up of the cyclically steady state and Gaussian averaging over the velocity spread of the atoms is considered to be about 3%. Included in the calculations are the exponential decays for the cavity field during the pulse when either one photon (for  $n = 1$ ) or two photons were deposited one by one (for  $n = 2$ ), changing the photon number distribution. The simulations also average over the Poissonian arrival times of the atoms. The details of the calculation are discussed in [41]. They are compared with the experimental results in Fig. 1.10(a) and (b).

As dissipation is the most essential loss mechanism, it is interesting to compare the purity of the number states generated by the current method with that expected for trapping states (cf. Fig. 1.10(c)). The agreement of the purity of the number states is striking. The trapping state photon distribution is generated in steady state, which means that whenever the loss of a photon occurs the next incoming atom will restore the old field with a high probability. The non-zero amplitudes of the states  $|0\rangle$  in Fig. 1.10(c2) and  $|1\rangle$  in Fig. 1.10(c3) are due to dissipative losses before restoration of a lost photon

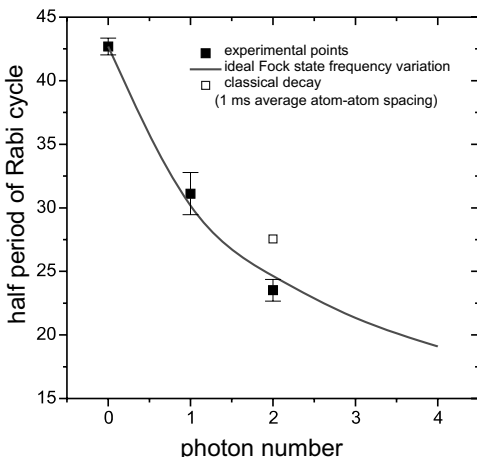


**Fig. 1.11** Dependence of the Rabi frequency on the photon number. A single sine fit to each of the three Fock states is plotted versus the theoretical variation of frequency as a function of photon number. The coupling constant  $36.8 \text{ krad/s}^{-1}$  is the optimum fit to the data. The figure is taken from [48].

which is not replaced immediately but after a time interval dependent on the atom flux. The atom rate used in these calculations was 25 atoms per cavity decay time, or an average delay of 1 ms. This can be compared to the delay between the preparation and probe atoms in the present experiment. In the steady-state simulation loss due to cavity decay determines the purity of the number state; in the limit of zero loss the state measurement is perfect. It can therefore be concluded that dissipative loss due to cavity decay in the delay to a probe atom largely determines the measured deviation from a pure number state. There is, of course, the question of the influence of the thermal field on the photon distribution. By virtue of the selection process in the current experiment we reduce the influence of the thermal field by only performing measurements of the field state following a trigger of ground-state atoms. Hence the state of the field is well known. The simulations for the steady-state case were therefore performed for a temperature of 100 mK, which makes the influence of the thermal field on the steady state correspondingly low. While this is not the first observation of Fock states in general (the  $n = 1$  Fock state having been observed earlier [55]), it is the most detailed study of the interaction of an atom with a quantized mode that has been carried out to date. Here we see the creation of a field state by state reduction and the observation of the interaction of this state with a probe atom.

The unambiguous generation of Fock states of the radiation field described in the previous section allows an interesting observation concerning the decay of the photons. Quantum fields decay discretely. This can be neatly observed

by looking at the variation of the Rabi frequency in time observed after the Fock state generation. The results are shown in Fig. 1.11. The discrete decay follows the solid curve in the figure, whereas a classical and continuous decay would result in a larger period of the Rabi frequency given by the square at photon number state  $n = 2$  [48].

### 1.2.9

#### The One-atom Maser Spectrum

The properties of the micromaser we have discussed so far were all connected with the population of the maser levels or with the diagonal elements of the radiation-density matrix. In the following we would like to discuss a feature – the micromaser spectrum – which depends on the nondiagonal elements [56].

The micromaser spectrum is determined by the decay of the expectation value of the electric field [57] of the maser field

$$\langle E(t) \rangle \sim \sum_{n=0}^{\infty} (n+1)^{1/2} \rho_{n,n+1}(t) \quad (1.9)$$

In order to calculate the spectrum and the linewidth  $D$  of the micromaser an analytical approach was used [56] whereby two novel features, quite dis-

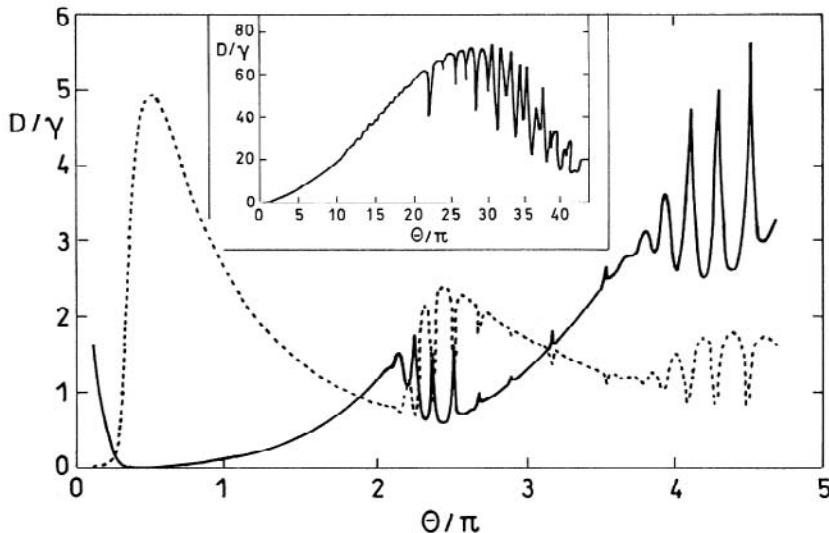


**Fig. 1.12** The relative linewidth  $D/\gamma$  based on equation 1.10 (solid curve and mean photon number  $\langle n \rangle/10$  (dotted curve) as a function of the pump parameter  $\Theta = N^{1/2}g\tau$  for  $N = 50$  and mean thermal photon number  $n_b = 10^{-4}$ . The inset shows the exact relative linewidth  $D/\gamma$  based on a numerical solution of the density matrix for large pump parameter  $\Theta$  for  $N = 20$  and  $n_{th} = 1$ .

tinct from the familiar Schawlow-Townes linewidth [57], show up. As can be seen in Fig. 1.12 (i) the trapping states impress sharp resonances onto  $D$  as a function of the pump parameter  $\Theta$ . (ii) For large values of  $\Theta$  the linewidth  $D$  decreases, and can even oscillate, a phenomenon alien to the monotonic dependence of the Schawlow-Townes linewidth.

Fig. 1.12 is based on the equation for the linewidth [56]:

$$D = 4r\sin^2 \left[ \frac{g\tau}{4\sqrt{\langle n \rangle}} \right] + \frac{\gamma(2n_{th} + 1)}{4\langle n \rangle}. \quad (1.10)$$

This equation is derived from the exact spectrum using a detailed balance condition and the fact that the equation of motion for the density matrix elements  $\rho_{n,n}$  only couples to the nearest neighbors  $\rho_{n,n+1}$  and  $\rho_{n,n-1}$ . For the exact numerical treatment of the relevant density-matrix equations see [58,59]

In Fig. 1.12 the detailed behavior of the phase diffusion constant  $D$  is depicted (solid line) as a function of the pump parameter  $\Theta = \sqrt{N}g\tau$  for  $N = 50$  and  $n_{th} = 10^{-4}$  thermal photons. The sharp resonances in the monotonic increase of  $D$  are reminiscent of the trapping states. To bring out this similarity in the same figure, the average photon number as a function of  $\Theta$  (dotted curve) is shown. We note that the phase diffusion is especially large when the maser is locked to a trapping state, that is, when  $\langle n \rangle$  is caught in one of those sharp minima. The equation 1.10 for  $D$  reveals this behavior in the limit of short interaction times or large photon numbers, that is when  $g\tau/4\langle n \rangle^{1/2} \ll 1$ . If the sine function is expanded, the familiar Schawlow-Townes linewidth [57] is obtained

$$D = \frac{\alpha + \gamma(2n_{th} + 1)}{4\langle n \rangle} \quad (1.11)$$

where  $\alpha = \gamma(N^{1/2}g\tau)^2 = \gamma\Theta^2$ .

The complicated pattern of the micromaser linewidth results from the complicated dependence of  $\langle n \rangle$  on the pump parameter indicated in Fig. 1.12 by the dotted curve which enters in the denominator. We emphasize that the maser linewidth for the micromaser goes beyond the standard Schawlow-Townes linewidth. The sine function in the formula for  $D$  suggests in the limit of large  $\Theta$  values an oscillatory behavior of the linewidth. The exact numerical result shown in the inset of Fig. 1.12 confirms that.

The experimental investigation of the micromaser spectrum is of great fundamental interest. As the nondiagonal field elements are involved, their measurement is not so easy to perform with the present set-up as the holes in the cavity for the atomic beam may perturb the nondiagonal contributions. Therefore several methods have been proposed allowing to measure the phase diffusion despite those perturbing effects [60–62]. All those methods are based on a heterodyne scheme. The maser field is displaced by an injected field and

then afterwards measured by a probe atom. In this way a reconstruction of the field is possible just by the determination of the atomic inversion.

### 1.3

#### Other Microwave Cavity Experiments

In the following, we briefly review the cavity QED work performed by the group of S. Haroche and co-workers at ENS in Paris.

The cavity of the ENS group has an open geometry made of two spherical superconducting mirrors in a Fabry-Perot configuration marked by C in Fig. 1.13. The transitions investigated by this group are at 51.1 GHz, corresponding to a transition between circular Rydberg states with principal quantum numbers 51 and 50. The circular states are characterized by maximum orbital and magnetic quantum numbers. The valence electron is a thin torus centered on the atom's core. They are produced in the CB unit using velocity-selective laser excitation. The velocity-selected atoms cross the cavity perpendicularly to the axis; the interaction length is about 6 mm in diameter. The decay time of the cavity is typically 1 ms (corresponding to  $Q = 3 \cdot 10^8$ ). The entire set-up is cooled to about 1 K to minimize thermal noise [7, 29, 63]. At the thermal equilibrium the cavity mode contains about 0.7 thermal photons on the average, originating from the thermal field leaks. In order to remove this field at the beginning of each sequence atoms prepared in the lower state are transmitted through the cavity to absorb the thermal photons. At the end of this cooling sequence the mean photon number is reduced to 0.1 per mode. Detection of the Rydberg atoms is performed as in the Munich set-up by field ionization which can be done state-selectively (Sect. D, Fig. 1.13). Experiments are also performed where superpositions of the states are investigated. The set-up has for this purpose two additional classical fields  $R_1$  and  $R_2$  coupled to the atoms via two spherical cavities to allow Ramsey-type two-field interaction ([64]). The signal fringes can be investigated to study changes of the phase and amplitude of the interaction between atom and cavity [65].

With this set-up a variety of experiments on the atom-cavity interaction were performed. A survey is given in the following. For a detailed review see [66].

##### 1.3.1

###### **Collapse-and-revival of the Rabi Oscillations in an Injected Coherent Field**

As discussed above, the quantum dynamics depends on the photon statistics of the interacting field. We have already described the measurement of the dynamics in a thermal field in the micromaser cavity [32] and in a number

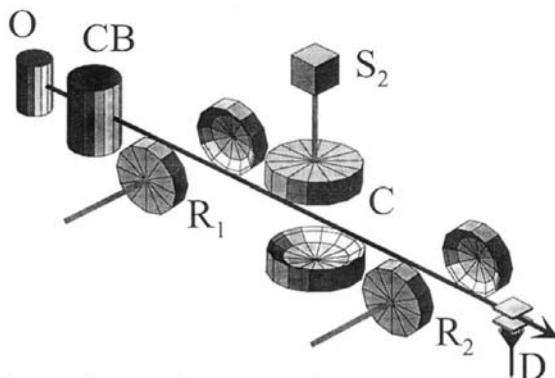


**Fig. 1.13** Cavity-QED set-up used by the group of S. Haroche et al. at the Ecole Normale Supérieure.

state field up to  $n = 2$  [30]. Further experiments have been performed with the spherical cavity and an injected coherent field with an average photon number of  $n = 2$  [34]. The expected collapse-and-revivals [31] were observed.

Revivals of Rabi oscillations can also be induced by a time reversal pulse [67]. The technique was first proposed by Morigi et al. [68] and is suitable to distinguish contributions from coherent and incoherent processes in the evolution of the system. For this purpose the system is exposed to a short electromagnetic pulse after a free evolution during the time  $T$  leading to a reversal of the system's unitary evolution. At time  $2T$  the system then resumes the initial state if no decoherence is present. This scheme was applied to investigate the atomic Rabi oscillations in a mesoscopic coherent field [67] with an average of 13 photons. The oscillation undergoes collapse due to the dispersion of the Rabi frequencies. This effect is unitary and reversible. After a time proportional to the field amplitude, the oscillation is expected to revive. When a  $\pi$  phase shift is applied to the atomic coherence after the collapse time, an early induced Rabi revival is observed. The amplitude of this echo signal is sensitive to non-unitary decoherence processes.

### 1.3.2

#### Atom-photon and Atom-atom Entanglement

It has already been mentioned above that quantum Rabi oscillations provide a simple and flexible tool to entangle atoms and photons (see Sect. 1.2.2). If the Rabi oscillation in vacuum is interrupted mid-way ( $\pi/2$  pulse) between the upper and lower atomic states, the final state of the atom-cavity field system is a maximally entangled state. In the event of the Rabi oscillation lasting twice as long ( $\pi$ -pulse) the cavity and atom exchange their energy with maximum probability. An atom initially in the lower state of the transition when it

enters the cavity containing one photon will end up with high probability in the upper state, leaving the cavity empty. This process can be used to transform an atom-field entanglement into an atom-atom one. When in the experiments two atoms cross the cavity one after the other, the first is initially in the upper level and the second in the lower one. The first atom undergoes a  $\pi/2$  Rabi pulse and gets entangled with the cavity. The second is subjected to a  $\pi$  pulse, copying the cavity state and getting entangled in the process with the first atom. This entanglement was checked in various measurements on the final states of the two atoms and in studying their correlations [27,28]. See also [66] in connection with the generation of EPR pairs. For related work on entanglement with the micromaser see [44]. The generation of a GHZ state and EPR tests in the micromaser is described in [69] and [70].

### 1.3.3

#### **Atom-photon Phase Gate**

An atom-photon phase gate can be realized since after a full cycle of quantum Rabi oscillation ( $2\pi$  Rabi pulse) the system reaches the initial state, but the phase of the wave function of the atom has undergone a  $\pi$ -shift. See also [71]. An atom initially in the lower state of the transition with one photon in the cavity therefore emerges in the same state, the photon being left in the cavity with high probability, but with the sign of the wavefunction of the atom being changed. If the cavity is initially empty, the sign of the atomic state is unaltered. When photon and atom are considered as quantum-bits carrying binary information, the  $2\pi$  Rabi pulse couples them according to the conditional dynamics of a quantum phase gate [63].

### 1.3.4

#### **Quantum Nondestructive-measurement of a Photon**

The principle of a quantum phase gate described above can also be used for nondestructive measurement of single photons in a cavity [7]. The phase change of the wavefunction of the atom occurring when exposed to a  $2\pi$  Rabi pulse can be transferred into an inversion of the phase of the fringe pattern of a Ramsey interferometer sandwiching the microwave cavity (Fig. 1.13). When the interferometer is adjusted to a fringe maximum, the photon number 0 or 1 is correlated to the final state of the atom. The method, however, does not allow one to measure deviations from a single photon state (see Sect. 1.2.6). See also [71].

Recently, it was also demonstrated that an experiment analogous to the photon detection described is also possible for nondestructive Rydberg atom counting using a mesoscopic field in a cavity [72]. The state-dependent atomic index of refraction being proportional to the atomic number shifts the classical

field phase, which is changed into intensity information by a phase-sensitive homodyne procedure. This method may open the possibility of using Rydberg atoms for more applications in quantum information processing.

### 1.3.5

#### **Wigner-function of a One-photon State**

Rydberg atoms are sensitive probes of a microwave cavity field that make it possible to determine its quantum state through determination of quasi-probability distributions which contain the information on the field density distribution. Furthermore, they exhibit the quantum properties of the field if present. The Husimi Q and Wigner functions have been measured for atom cavity systems [73]. For direct determination of the Wigner function of a one-photon Fock state, by a method proposed in [71], see also Bertet et al. [74]. Lougovski et al. [75] showed that the Fresnel transform of measured Rabi oscillations provides an especially simple means of determining the Wigner function, being a much faster method than depending on the dispersive interaction between atoms and field. For the reconstruction of the Wigner function in the one-atom maser see [60] and [61].

### 1.3.6

#### **Multiparticle Entanglement**

When quantum Rabi pulses of variable duration and auxiliary Ramsey pulses are applied to successive atoms crossing a set-up of the kind displayed in Fig. 1.13, one can generate and analyze entangled states involving more than two particles. Such a procedure was demonstrated for the entanglement of up to three atoms [29]. The disadvantage of the experiment is that the atomic coherences cannot exit cavity C, which was modified in relation to Fig. 1.13 by an additional ring structure to increase the photon lifetime. A further limitation is that circular atoms are prepared with Poissonian statistics with a low mean value, requiring long data acquisition times. For a review on the multiparticle entanglement in the micromaser see [44].

### 1.3.7

#### **Schrödinger Cats and Decoherence**

For this experiment a small coherent field containing an average of 3 to 10 photons is prepared in cavity C (Fig. 1.13) by coupling it to an external coherent source. This field interacts with a single atom in a state superposition (produced by a  $\pi/2$  pulse in cavity R). The atomic transition and the cavity frequency are slightly off resonance so that the atom and the field cannot exchange energy but undergo dispersive frequency shifts. The atom-field

coupling during the interaction time produces atomic-level-dependent dephasing of the field and generates an entangled state with the phase  $\phi = g^2 t / \delta$  ( $t$ : interaction time,  $\delta$ : detuning). After leaving field C the atom undergoes another  $\pi/2$  pulse in cavity  $R_2$  identical to R (Fig. 1.13). The signal in the field ionization detector shows Ramsey fringes [64] since the transition monitored can occur either in field  $R_1$  or  $R_2$  and these two “paths” are indistinguishable. The fringe contrast depends on  $\phi$  and decreases with increasing  $\phi$  due to decoherence since the “distance” between the interfering states varies as  $D = 2\sqrt{n} \sin\phi$ . The result obtained for the decoherence time is shorter than the photon decay time in the cavity [76]. The result agrees with simple decoherence theories. The open cavity C leads to a rather strong coupling to the environment, and so investigations with a better closed cavity would be desirable and this is being pursued by the ENS group.

## 1.4

### Cavity QED Experiments in the Visible Spectral Region

The QED experiments in the optical region aimed at achieving strong coupling between atom and cavity field started in the early 1990s with experiments involving atomic beam transits through the mode of a high-finesse cavity [77, 78]. The flux of atoms was small enough to make the average intracavity number roughly one. The one-atom vacuum Rabi splitting for the Cs transition ( $6S_{1/2}, F = 4 \rightarrow 6P_{3/2}, F' = 5'$ ) was observed. Similar observations were made by Feld et al. using Ba atoms [79]. The brief interaction time was a limitation in these experiments, and so subsequent experiments with clouds of cold atoms cooled to sub-Doppler temperatures were prepared in a magneto-optical trap (MOT) located a few millimeters above the cavity and released into the cavity. It was possible to observe in real time their individual trajectories and the duration of their transits [80]. This technique was used to extract the vacuum Rabi spectrum from the transmission of a weak probe.

#### 1.4.1

##### The One-atom Laser

The one-atom laser is the optical analog of the one-atom maser. It has been theoretically discussed in many papers [81–90]. The gain medium is a single atom which couples photons into the resonant mode of the optical cavity. As expected, it is very different from a conventional and semi-classical laser and shows a variety of quantum properties.

The first laser oscillation with a single atom was observed by An et al. [91]. In this experiment a beam of Ba atoms transverses a single mode cavity with a finesse of  $8 \cdot 10^5$ . The atoms are excited by a  $\pi$ -pulse from the  $^1S_0$  ground

state to the  ${}^3P_1$  excited state before they enter the cavity. The mean number of photons inside the cavity was 0.14 to 11.

In a recent experiment [5,92] a Raman-type transition was investigated where a pump beam from the  $(6S_{1/2}, F = 3)$  ground state of the Cs atom to the  $(6P_{3/2}, F' = 3')$  excited state is applied perpendicularly to the cavity. The atomic population is transferred to  $(6S_{1/2}, F = 4)$  via strong coupling to the cavity emitting a single excitation in the laser mode. A repumping beam is necessary to bring the population in the  $6S_{1/2}F = 4$  state back to the ground state. With the set-up thresholdless lasing is observed. Furthermore, the one-atom laser exhibits photon antibunching and sub-Poissonian photon statistics. For further work on the one-atom laser see Sect. 1.4.4

#### 1.4.2

#### Atoms Pushed by a Few Photons

The attractive potential in which the dressed states move, suggests that one could trap neutral atoms in potential wells of this kind, thereby exploiting the forces of just a few photons. This has indeed been suggested in [93]. The gravitational pull just mentioned is, however, much too strong. It cannot be compensated for by the forces that a few microwave photons could provide, and so one would need the microgravity environment of a satellite experiment to demonstrate the reality of these forces.

Circumstances are much more favorable in the optical domain. The light field of a small high-finesse optical resonator can catch a slowly moving atom. This was recently demonstrated in two experiments, one performed with cesium atoms at Caltech [94], the other with rubidium atoms at Garching [95].

In both experiments, single atoms were trapped by one or a few photons and, very impressively, the motion of the atom was tracked by analyzing the light transmitted through the resonator.

The actual atom-light interaction in these experiments needs to take into account the fact that the atoms may scatter the photons out of the resonator.

This is a rapidly developing and intense field of research, both experimentally and theoretically, and we refer the interested reader to the pertinent publications of recent years [94–103]. Let us just note that, in addition to the passive observation, active feedback has been successfully implemented [103], allowing the experimenters to prolong the storage time of the atom substantially.

While atomic confinement with quantized QED field offers an important advance in obtaining well-localized, trapped atoms, it remains preferable to decouple the trap from the QED interaction. A number of groups [104–107] have therefore realized optical dipole force traps, also known as far off-resonant traps or FORTs. They use a far-detuned optical beam inducing a dissipative, attractive force on an atom and since they are operated far off-resonance, they

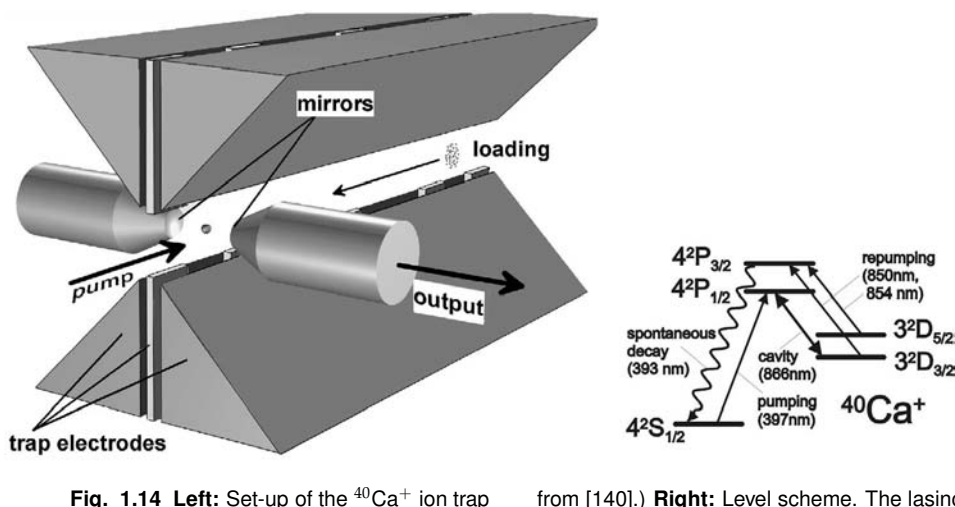


**Fig. 1.14 Left:** Set-up of the  $^{40}\text{Ca}^+$  ion trap laser at Garching. The loading trap at the rear is used to catch ions and cool them. A single ion is then transferred to the front trap between the mirrors of the optical cavity, where the ion is pumped and emits into the resonant resonator mode. (Reproduced

from [140].) **Right:** Level scheme. The lasing transition is  $4^2\text{P}_{1/2} \rightarrow 3^2\text{D}_{3/2}$ ; the major pump transition is  $4^2\text{S}_{1/2} \rightarrow 4^2\text{P}_{1/2}$ ; the (re-)repumping from levels  $3^2\text{D}_{3/2}$  and  $3^2\text{D}_{5/2}$  to  $4^2\text{P}_{3/2}$  prevents the accumulation of population in dead ends; spontaneous decay from  $4^2\text{P}_{3/2}$  to the  $4^2\text{S}_{1/2}$  ground state closes the cycle.

cause practically no atomic excitation. Examples where FORT traps were used in QED experiments are [104, 106, 108]. Using these arrangements allows one to keep an atom inside the cavity for a longer period, as was done in the experiments on single-photon generation [109] or on the one-atom laser [110]. Some considerable progress was recently achieved concerning the trapping time of an atom in a cavity [111]. In this paper it was shown that an orthogonal arrangement of cooling laser, trapping laser and cavity vacuum field gives rise to a combination of friction forces that act along all the three directions so that a single atom can be cooled in a high-finesse cavity, resulting in a trapping time of up to 17 s. In a subsequent paper [112] using the same set-up atoms were repetitively moved out and back into the cavity mode with a repositioning precision of 135 nm. This makes it possible either to selectively address one atom or a string of atoms by the cavity field or to simultaneously couple two precisely separated atoms to a higher mode of a cavity.

Raman transitions have also been used to cool atoms in a cavity. This method was used to investigate the vacuum Rabi spectrum for one-and-the-same atom, as opposed to other experiments using a FORT [78, 113, 114] requiring averaging over a large ensemble of atoms. In the experiment investigating the Rabi splitting a single atom loaded into the FORT is irradiated with a probe beam whose frequency is varied over a range near the atom-cavity resonance, and the transmission of the probe beam is measured. This measurement cycle has

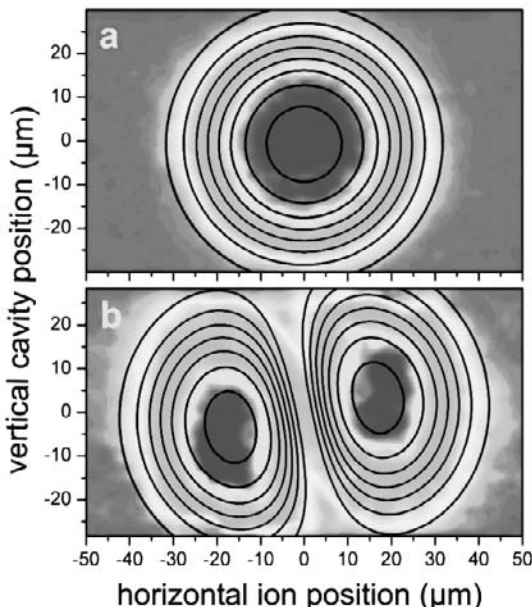


**Fig. 1.15** Two-dimensional images of the cavity field taken over an area of  $100 \times 60 \mu\text{m}^2$ . a)  $\text{TEM}_{00}$  mode. b)  $\text{TEM}_{01}$  mode. In the horizontal direction the ion was moved, while vertically the cavity position was changed relatively to the ion. False colors represent the measured fluorescence count rate; the contour lines indicate the theoretical fluorescence pattern. Cf. the coloured plates in the Appendix.

to be interated with Raman cooling periods. The result agrees very well with the solution of the steady-state master equation of the system [115].

#### 1.4.3

#### Single-photon Sources

The controlled production of single photons is of fundamental and practical interest; they represent the lowest excited quantum states of the radiation field and have applications in quantum cryptography [116] and quantum information processing [117]. Common approaches use the fluorescence of single ions [118], single molecules [119, 120], color centers [121, 122] and semiconductor quantum dots [123–127]. However, the lack of control over such irreversible emission processes precludes the use of these sources in applications (such as quantum networks [128]) that require coherent exchange of quantum states between atoms and photons. The necessary control may be achieved in principle in cavity quantum electrodynamics. In these systems the directed emission can be controlled through the modes of the cavity.

Sources of this kind have been proposed by different authors, e.g. [129–132]. All those schemes are based on a technique known as STIRAP (stimulated Raman scattering involving adiabatic passage) [133, 134] or variants thereof. The first observation of stimulated Raman scattering from a  $\Lambda$ -type three-level atom where the vacuum field of a high-finesse optical cavity is involved was realized by Hennrich et al. [99]. This scheme produces from a single atom one intracavity photon by means of an adiabatic passage sequence consisting of pump laser and cavity field. This photon is transmitted through a less reflecting mirror of the cavity. The transitions used were between hyperfine levels of the  $^{85}\text{Rb}$  atom. The atoms used were pre-cooled in a MOT and released into the cavity. The experiment produced at most one photon per passing atom, but did not operate as a single photon source, since the continuous driving scheme simply mapped the random (Poissonian) atom statistics to the photons. This was later improved in a further experiment where pulsed driving was used together with pulsed recycling to allow a stream of several single-photon pulses to be produced on demand from one and the same atom, triggered by the detection of a first photon emitted from the cavity [135].

#### 1.4.4

#### Single-atom Laser Using an Ion Trap

The ultimate limit of ultra-slowly moving atoms are atoms at rest. A single atom that stays put inside a high- $Q$  resonator will interact with the cavity mode for a long time and, provided the atom is suitably driven, may play the role of the active medium of a laser. This is the situation of the *one-atom laser*. Theoretical studies [87, 136, 137] eventually confirmed that it is indeed possible to get laser operation with a single atom, as discussed in Sect. 1.4.1. Actual realization would require appropriate mechanical forces to keep the atom in place, and such forces are not easily provided.

A much more practical variant of this idea is therefore the *ion-trap laser* [88], where the active medium is a single ion trapped in a standard ion trap around which one positions the mirrors of the optical resonator; see Fig. 1.14. Careful studies [89, 90, 138, 139] demonstrate that the  $^{40}\text{Ca}^+$  ion is well suited to this purpose. One finds, for example, that a mean number of 5–10 photons builds up in the resonator (which corresponds to about  $5 \times 10^5$  photons coupled out per second) and that, in some parameter ranges, the photon statistics may be sub-Poissonian. Experiments for actual realization of an ion-trap laser of this kind are well under way at Garching.

The strength of the ion-photon coupling depends on the location of the ion relative to the nodes and anti-nodes of the mode function in question. It is therefore mandatory to have good control of the ion's position. In fact, the experimenters are able to push the ion around at will (or, equivalently, to

change the mirror positions), as is demonstrated by the measurement reported in Fig. 1.15. This plot shows a two-dimensional map of the mode function obtained by recording the fluorescence light while scanning the ion's position across a plane perpendicular to the resonator axis. The trapped ion can thus serve as a high-resolution probe of the optical field inside the cavity [140]. Owing to the rest motion of the trapped ion a resolution of the order of 40 nm has been achieved. The permanent and fully controllable coupling of a particle to the field with a well-defined strength is a unique property of ion-trap cavity quantum electrodynamics and provides the basis for the ion-cavity experiments described here. In the following, we would like to discuss a single photon source on the basis of a trapped single ion.

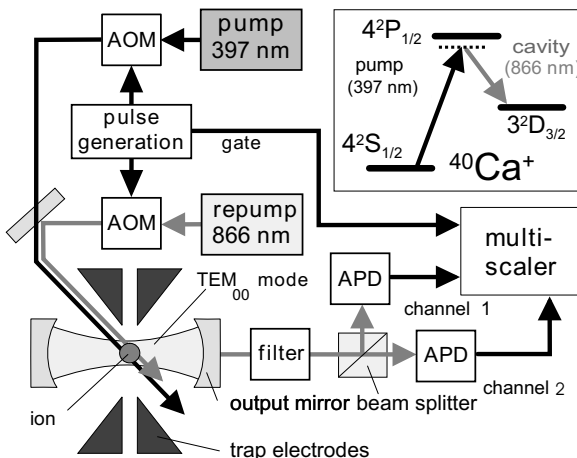


**Fig. 1.16** Experimental set-up outlining the excitation and detection scheme for single photons. Not shown is an additional laser at 894 nm which is resonant with a cavity mode not coupled to the ion and which is used for stabilizing the cavity length. In the path to the detectors, this locking beam is suppressed by a series of filters, providing

an attenuation of  $10^{11}$  at 894 nm. The laser intensities are controlled with acousto-optic modulators (AOMs). The inset shows the relevant levels of the  $^{40}\text{Ca}^+$  ion used for single-photon production. The pump laser and cavity are red-detuned with respect to the  $P_{1/2}$  level.

The first step of the protocol for generating a single-photon pulse is to apply radiation at 397 and 866 nm for  $3\ \mu\text{s}$  from the side of the cavity to laser-cool the ion and thus ensure its proper localization. Subsequently, the initial electronic state  $S_{1/2}$  is prepared by optical pumping at 866 nm for  $0.5\ \mu\text{s}$ . A single photon is produced by driving a cavity-assisted Raman transition to the  $D_{3/2}$  level by means of a pump pulse at 397 nm with a predefined intensity profile of up to  $6\ \mu\text{s}$  duration. The sequence is repeated at a rate of 100 kHz. The photon pulse is emitted from the cavity through one mirror with a transmissivity of 600 p.p.m., 100 times larger than that of the opposite mirror. The Gaussian mode emanating from this mirror is focused on an avalanche photodiode (APD)

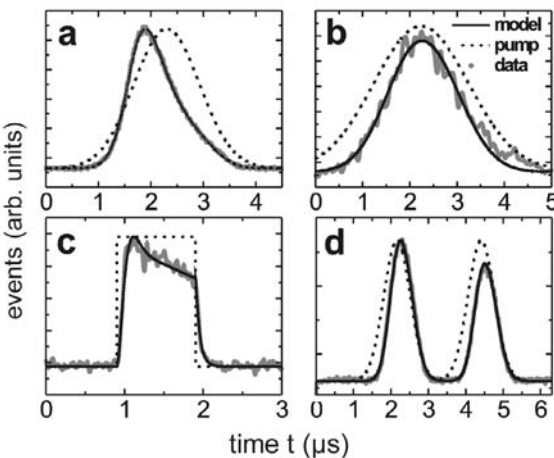


**Fig. 1.17** Single-photon pulse shapes (gray line) for different pump laser profiles, indicated by the dotted line (not to scale). a) Strong Gaussian pump. b) Weak Gaussian pump. c) Square-wave pump. d) Double-peaked pump. The superimposed black curves show the results of a density-matrix calculation, taking into account the full Zeeman structure of the  $^{40}\text{Ca}^+$  levels, as well as the polarization of

the optical fields. Plots a) and d), obtained with the best statistics, demonstrate the nearly perfect agreement between the model and the experimental data, confirming that the waveform of a single photon can be deterministically controlled. In Figs. a) and d) the experimental and theoretical curves are practically identical so that they do not show up as separate curves.

after passing a series of four optical filters and a spatial filter. In this way, light from an auxiliary laser used for locking the cavity length and from other sources of stray light is reduced to a level well below the dark-count rate of the detectors used.

With the position of the ion and hence the ion-field coupling fixed, the distribution of photon detection times exactly follows the shape of the single-photon pulse. By tailoring the intensity profile of the driving pulse, we can imprint an arbitrary temporal structure on the waveform of the photon, which is then precisely reproduced in every emission event. The single-photon pulse shape is extracted from the time records by accumulating the probability distribution of photon arrival times relative to the pump-pulse trigger. Experimental data obtained for intense Gaussian pumping based on the evaluation of over 400,000 photons continuously generated from a single ion are presented in Fig. 1.17a. Because the photon pulses are identical, the time distributions obtained constitute a measurement of the waveform of a single photon. This is confirmed by comparing the data with calculated single-photon pulse shapes, based on coherent Raman coupling of a calcium ion to a single cavity mode [141].

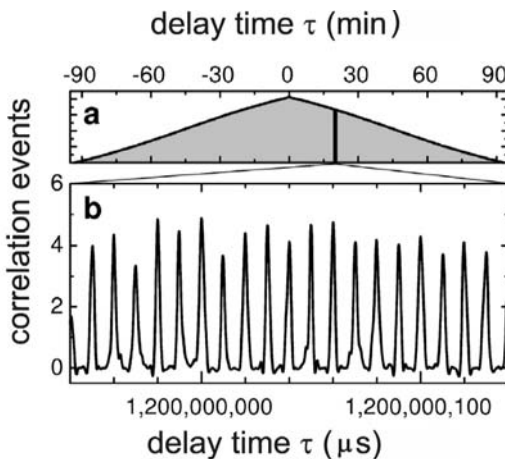


**Fig. 1.18** Long-term correlations of photon arrival times at the two detectors. a) Envelope of two-photon correlations recorded over the entire sampling interval, demonstrating the continuous emission of single photons in our system. b) Zooming in at a delay of  $\tau = 20$  min reveals individual peaks as in Fig. 1.19 for  $\tau \neq 0$ .

Fig. 1.17b shows a symmetric Gaussian output pulse generated with a weak Gaussian pump pulse. The arbitrary control of the photon pulse shape in the set-up is limited only by the time constants associated with ion and cavity dynamics. This is apparent from the response of the system to a pump pulse with a square profile (Fig. 1.17c). The trailing edge of the pulse decreases exponentially at the cavity decay rate, whereas the onset of the pulse is delayed by the time required to excite the electronic transition. As an example of a more complex pulse shape, we generated a twin-peaked single-photon pulse (Fig. 1.17d). The photon detection times are distributed over two well-separated maxima, reflecting the structure of the pump pulse. Spreading a single photon over two distinct time bins may be exploited as a way to encode quantum information in the time domain [142].

Apart from the control of the photon's waveform and the suppression of two-photon events, an important accomplishment for applications in quantum information processing is the continuous, uninterrupted operation of our source, allowing correlations to be measured on very long time scales. Fig. 1.18a shows a measurement of correlations sampled over a time of 90 min. The linear decrease of the envelope of the correlation function is a consequence of the finite duration of the measurement. No individual lines are resolved on the time scale shown, but when an arbitrary point on the time axis is zoomed in, the same peak structure is found as in Fig. 1.19 on either side of the origin. As an example, Fig. 1.18b shows correlations between photons detected 20 min apart. The operation of the system for 90 min represents

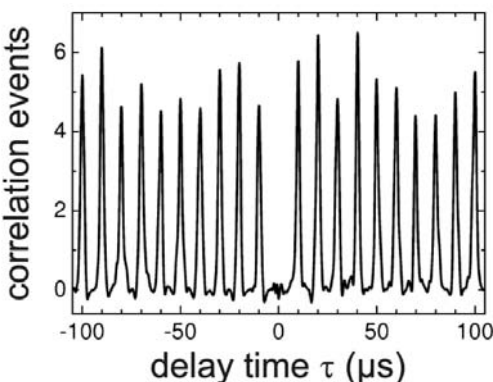


**Fig. 1.19** Cross-correlations of photon arrival times at the two detectors (counts in 100-ns time bins) around zero delay. Dark-count events were eliminated with the help of an independent measurement for the data including dark-counts). The absence of a peak at  $\tau = 0$  confirms that the source emits single photons.

the longest continuous generation of single photons from an atomic source [143]. With ion trapping times of many hours, single-photon emission in the described system can be maintained for even longer periods.

The striking feature of this new single photon source is the fact that it is possible not only to generate a photon on demand or deterministically but also to preselect the duration of the generated photon wavepacket. The latter means that the coherence length of the photon can be preselected. These properties of the single photon source described here will make it a unique source for many applications. The coupling of ions and photons in a controlled way is required in schemes linking optical long-distance quantum communication with ion-trap quantum processors, both of which have been successfully demonstrated in the past. The result could be a quantum version of the internet in which local processing sites are connected with each other by photonic channels.

## 1.5

### Conclusions and Outlook

This paper reviews the work on cavity quantum electrodynamics with free atoms. Emphasis is placed on the work performed with the one-atom maser and the ion-trap laser in our laboratory, but a survey on the work done in other laboratories is also given in order to show the large variety of problems being treated with the very fundamental system of an atom interacting with a single mode of a cavity. (For a more detailed review see also [1]).

The experiments on cavity quantum electrodynamics started with studies of free atoms, but meanwhile the field has expanded to include solid-state

systems, as briefly discussed in the review. Furthermore, new applications are emerging in various directions. First, there are interesting developments of new cavity structures which are leading to new possibilities [144–146]. A further active field is cavity quantum electrodynamics in semiconductors in combination with quantum dots or semiconductor microcavity structures [11, 147]. The latter systems promise application in many areas of optical communication and possibly also in quantum information processing.

The experiments with free atoms will also be further developed. Interesting results may be expected especially in connection with studies of decoherence. The cavity quantum electrodynamical systems with free atoms seem to be the only ones where the phenomenon can be investigated in detail and free of perturbing influences. Furthermore, in connection with the one-atom maser another interesting problem under study is the investigation of the phase diffusion of the maser field.

Phase diffusion of a maser or laser determines the natural linewidth of these systems. In the standard maser/laser, this is caused by spontaneous transitions. In the one-atom maser, spontaneous transitions play no role; there it is the thermal noise which determines the phase diffusion. As this parameter can easily be controlled by changing the cavity temperature, this phenomenon can be nicely investigated. The exploration of phase diffusion is also interesting in the vicinity of trapping states, which were described in Sect. 1.2.5. As shown, the trapping states display the quantum states of the maser field. The behavior of phase diffusion should therefore follow the amplitude-phase uncertainty when the field approaches a trapping state. This phenomenon should be measurable with the available set-up [56].

From the few examples given in this outlook it is obvious that the field of cavity quantum electrodynamics will continue in the future to be as interesting and lively as it has been in the past.

## Acknowledgement

The one atom maser and the trapped ion work is supported by the European Community and the Quantum Information Highway A8 project of the State of Bavaria.

## References

- 1 H. Walther, B. T. H. Varcoe, B.-G. Englert, and T. Becker, *Rep. Prog. Phys.* **69** 1325–1382 (2006).
- 2 E. T. Jaynes and F. W. Cummings, *Proc. IEEE* **51**, 89–109 (1963).
- 3 D. Meschede, H. Walther, and G. Müller, *Phys. Rev. Lett.* **54**, 551–554 (1985).

- 4 M. Brune, J. M. Raimond, P. Goy, L. Davidovich, and S. Haroche, *Phys. Rev. Lett.* **59**, 1899–1902 (1987).
- 5 J. McKeever, A. Boca, A. D. Boozer, J. R. Buck, and H. J. Kimble, *Nature* **425**, 268–271 (2003).
- 6 E. Wehner, R. Seno, N. Sterpi, B.-G. Englert, and H. Walther, *Opt. Commun.* **110**, 655–669 (1994).
- 7 G. Nogues, A. Rauschenbeutel, S. Osnaghi, M. Brune, J. M. Raimond, and S. Haroche, *Nature (London)* **400**, 239–242 (1999).
- 8 A. Imamoglu, D. D. Awschalom, G. Burkard, D. P. DiVincenzo, D. Loss, M. Sherwin, and A. Small, *Phys. Rev. Lett.* **83**, 4204–4207, (1999).
- 9 M. Sherwin, A. Imamoglu, and T. Montraj, *Phys. Rev. A* **60**, 3508–3514 (1999).
- 10 G. S. Solomon, M. Pelton, and Y. Yamamoto, *Phys. Rev. Lett.* **86**, 3903–3906 (2001).
- 11 Y. Yamamoto, F. Tassone, and H. Cao, *Semiconductor Cavity Quantum Electrodynamics*, in: *Springer Tracts in Modern Physics*, Vol. 169 (Springer, Berlin, 2000).
- 12 M. Oxborrow and A. G. Sinclair, *Contemp. Phys.* **46**, 173–206 (2005).
- 13 B. T. H. Varcoe, S. Brattke, and H. Walther, *Fortschr. Phys.* **48**, 679–687 (2000).
- 14 B. T. H. Varcoe, B. Hall, G. Johnson, P. Johnson, W. R. MacGillivray, and M. C. Standage M C, *J. Meas. Sci. and Tech.* **11**, N111–N116 (2000).
- 15 V. A. Reshetov and I. V. Yevseyev, *Laser Phys.* **10**, 916–922 (2000).
- 16 M. Orszag, R. Ramirez, J. C. Retamal, and C. Saavedra, *Phys. Rev. A* **49**, 2933–2937 (1994).
- 17 M. E. Kolobov and F. Haake, *Phys. Rev. A* **55**, 3033–3041 (1997).
- 18 F. Casagrande, M. Garavaglia, and A. Lulli, *Opt. Commun.* **151**, 395–405 (1998).
- 19 F. Casagrande, A. Lulli, and S. Ulzega, *Phys. Rev. A* **60**, 133–141 (1999).
- 20 P. Filipowicz, J. Javanainen, and P. Meystre, *Phys. Rev. A* **34**, 3077–3087 (1986).
- 21 L. A. Lugiato, M. O. Scully, and H. Walther, *Phys. Rev. A* **36**, 740–743 (1987).
- 22 P. Meystre and M. III Sargent, *Elements of Quantum Optics* (Springer-Verlag, Berlin, 1990).
- 23 M. O. Scully and M. S. Zubairy, *Quantum Optics* (Cambridge University Press, Cambridge 1997).
- 24 B.-G. Englert, *Elements of Micromaser Physics*, preprint, [quant-ph/0203052](http://quant-ph/0203052) (1994/2002).
- 25 U. Fano, *Phys. Rev.* **72**, 26–29 (1947).
- 26 L. Mandel, *Opt. Lett.* **4**, 205–207 (1979).
- 27 E. Hagley, X. Maître, G. Nogues, C. Wunderlich, M. Brune, J. M. Raimond, and S. Haroche, *Phys. Rev. Lett.* **79**, 1–5 (1997)
- 28 X. Maître, E. Hagley, G. Nogues, C. Wunderlich, P. Goy, M. Brune, J. M. Raimond, and S. Haroche, *Phys. Rev. Lett.* **79**, 769–772 (1997).
- 29 A. Rauschenbeutel, G. Nogues, S. Osnaghi, P. Bertet, M. Brune, J. M. Raimond, and S. Haroche, *Science* **288**, 2024–2028 (2000).
- 30 B. T. H. Varcoe, S. Brattke, M. Weidinger, and H. Walther, *Nature (London)* **403**, 743–746 (2000).
- 31 J. H. Eberly, N. B. Narozhny, and J. J. Sanchez-Mondragon, *Phys. Rev. Lett.* **44**, 1323–1326 (1980).
- 32 G. Rempe, H. Walther, and N. Klein, *Phys. Rev. Lett.* **58**, 353–356 (1987).
- 33 P. Elmfors, B. Lautrup, and B.-S. Skagerstam, *Phys. Rev. A* **54**, 5171–5192 (1996).
- 34 M. Brune, F. Schmidt-Kaler, A. Maali, J. Dreyer, E. Hagley, J. M. Raimond, and S. Haroche, *Phys. Rev. Lett.* **76**, 1800–1803 (1996).
- 35 B.-J. Briegel, B.-G. Englert, N. Sterpi, and H. Walther, *Phys. Rev. A* **49**, 2962–2985 (1994).
- 36 G. Rempe, F. Schmidt-Kaler, and H. Walther, *Phys. Rev. Lett.* **64**, 2783–2786 (1990).
- 37 G. Rempe and H. Walther, *Phys. Rev. A* **42**, 1650–1655 (1990).
- 38 P. Meystre, *Cavity Quantum Optics and the Quantum Measurement Process*, in: *Progress in Optics*, vol. 30, edited by E. Wolf (North Holland, Amsterdam, 1992), pp. 261–355.

- 39** O. Benson, G. Raithel, and H. Walther, Phys. Rev. Lett. **72**, 3506–3509 (1994).
- 40** G. Raithel, O. Benson, and H. Walther, Phys. Rev. Lett. **75**, 3446–3449 (1995).
- 41** S. Brattke, B.-G. Englert, B. T. H. Varcoe, and H. Walther, J. Mod. Opt. **47**, 2857–2867 (2000).
- 42** C. Bracher, private communication (2000).
- 43** H.-J. Briegel and B.-G. Englert, Phys. Rev. A **47**, 3311–3329 (1993).
- 44** B.-G. Englert, M. Löffler, O. Benson, B. T. H. Varcoe, M. Weidinger, and H. Walther, Fortschr. Phys. **46**, 897–926 (1998).
- 45** P. Meystre, G. Rempe and H. Walther, Opt. Lett. **13**, 1078–1080 (1988).
- 46** M. Weidinger, B. T. H. Varcoe, R. Heerlein, and H. Walther, Phys. Rev. Lett. **82**, 3795–3798 (1999).
- 47** S.-Y. Zhu, L. Z. Wang and H. Fearn, Phys. Rev. A, **44**, 737–746 (1991).
- 48** B. T. H. Varcoe, S. Brattke, and H. Walther, New J. Phys. **6**, 97 (2004).
- 49** S. Brattke, B. T. H. Varcoe, and H. Walther, Phys. Rev. Lett. **86**, 3534–3537 (2001).
- 50** S. Brattke, B. T. H. Varcoe, and H. Walther, Opt. Express **8**, 131–144 (2001).
- 51** G. Raithel, C. Wagner, H. Walther, L. M. Narducci, and M. O. Scully, The Micromaser: A Proving Ground for Quantum Physics,” in: Supplement 2 to Advances in Atomic, Molecular and Optical Physics, edited by Paul R. Berman (Academic, New York, 1994), pp. 57–121.
- 52** H. Wiseman and G. Milburn, Phys. Rev. Lett. **70**, 548–551 (1993).
- 53** J. Krause, M. O. Scully, and H. Walther, Phys. Rev. A **36**, 4547–4550 (1987).
- 54** P. J. Bardoff, E. Mayr, and W. P. Schleich, Phys. Rev. A **51**, 4963–4966 (1995).
- 55** C. K. Hong and L. Mandel, Phys. Rev. Lett. **56**, 58–60 (1986).
- 56** M. O. Scully, H. Walther, G. S. Agarwal, Tran Quang, and W. Schleich, Phys. Rev. A **44**, 5992–5996 (1991).
- 57** M. O. Scully and W. E. Lamb, Jr., Phys. Rev. **159**, 208–226 (1967); see especially M. Sargent, M. O. Scully, and W. E. Lamb, Laser Physics (Addison-Wesley, Reading, MA, 1974) p. 292.
- 58** Tran Quang, G. S. Agarwal, J. Bergou, M. O. Scully, H. Walther, K. Vogel, and W. P. Schleich, Phys. Rev. A **48**, 803–812 (1993).
- 59** K. Vogel, W. P. Schleich, M. O. Scully, and H. Walther, Phys. Rev. A **48**, 813–817 (1993).
- 60** C. T. Bodendorf, G. Antesberger, M. S. Kim, and H. Walther, Phys. Rev. A **57**, 1371–1378 (1998).
- 61** M. S. Kim, G. Antesberger, C. T. Bodendorf, and H. Walther, Phys. Rev. A **58**, R65–R68 (1998).
- 62** F. Casagrande, A. Ferraro, A. Lulli, and R. Bonifacio, Phys. Rev. Lett. **90**, 183601 (2003).
- 63** A. Rauschenbeutel, G. Nogues, S. Osnaghi, P. Bertet, M. Brune, J. M. Raimond, and S. Haroche, Phys. Rev. Lett. **83**, 5166–5169 (1999).
- 64** N. F. Ramsey, Molecular Beams (Oxford University Press, New York, 1956).
- 65** M. Brune et al., Phys. Rev. Lett. **72**, 3339–3342 (1994).
- 66** J. M. Raimond, M. Brune, and S. Haroche, Rev. Mod. Phys. **73**, 565–582 (2001).
- 67** T. Meunier, S. Gleyzes, P. Maioli, A. Auffeves, G. Nogues, M. Brune, J. M. Raimond, and S. Haroche, Phys. Rev. Lett. **94**, 010401 (2005).
- 68** G. Morigi, E. Solano, B.-G. Englert, and H. Walther, Phys. Rev. A **65**, 040102 (2002).
- 69** B.-G. Englert and H. Walther, Opt. Commun. **179**, 283–288 (2000).
- 70** M. Löffler, B.-G. Englert, and H. Walther, Appl. Phys. B **63**, 511–516 (1996).
- 71** B.-G. Englert, N. Sterpi, and H. Walther, Opt. Commun. **100**, 526–535 (1993).
- 72** P. Maioli, T. Meunier, S. Gleyzes, A. Auffeves, G. Nogues, M. Brune, J. M. Raimond, and S. Haroche, Phys. Rev. Lett. **94**, 113601 (2005).
- 73** J. M. Raimond, T. Meunier, P. Bertet, S. Gleyzes, P. Maioli, A. Auffeves, G. Nogues, M. Brune, and S. Haroche, J. Phys. B: At. Mol. Opt. Phys. **38**, S535–S550 (2005).
- 74** P. Bertet, A. Auffeves, P. Maioli, S. Osnaghi, T. Meunier, M. Brune, J. M. Raimond, and S. Haroche, Phys. Rev. Lett. **89**, 200402 (2002).
- 75** P. Lougovski, E. Solano, Z. M. Zhang, H. Walther, H. Mach, and W. P. Schleich, Phys. Rev. Lett. **91**, 010401 (2003).

- 76** M. Brune, E. Hagley, J. Dreyer, X. Maître, A. Maali, C. Wunderlich, J. M. Raimond and S. Haroche, *Phys. Rev. Lett.* **72**, 4887–4890 (1996).
- 77** R. Miller, T. E. Northup, K. M. Birnbaum, A. Boca, A. D. Boozer, and H. J. Kimble, *J. Phys. B: At. Mol. Opt. Phys.* **38**, S551–S565 (2005).
- 78** R. J. Thompson, G. Rempe, and H. J. Kimble, *Phys. Rev. Lett.* **68**, 1132–1135 (1992).
- 79** J. J. Childs, K. An, M. S. Otteson, R. R. Dasari, and M. S. Feld, *Phys. Rev. Lett.* **77**, 2901–2904 (1996).
- 80** H. Mabuchi, Q. A. Turchette, M. S. Chapman, and H. J. Kimble, *Opt. Lett.* **21**, 1393–1395 (1996).
- 81** Y. Mu and C. Savage, *Phys. Rev. A* **49**, 5944–5954 (1992).
- 82** T. Pellizzari and H. Ritsch, *Phys. Rev. Lett.* **72**, 3973–3976 (1994).
- 83** P. Horak, K. M. Gheri, and H. Ritsch, *Phys. Rev. A* **51**, 3257–3266 (1995).
- 84** G. M. Meyer and H.-J. Briegel, *Phys. Rev. A* **58**, 3210–3220 (1998).
- 85** B. Jones, S. Ghose, J. P. Clemens, P. R. Rice, and L. M. Pedrotti, *Phys. Rev. A* **60**, 3267–3275 (1999).
- 86** S. Ya. Kilin and T. B. Karlovich, *JETP* **95**, 805–819 (2002).
- 87** C. Ginzel, H.-J. Briegel, U. Martini, B.-G. Englert, and A. Schenzle, *Phys. Rev. A* **48**, 732–738 (1993).
- 88** G. M. Meyer, H.-J. Briegel, and H. Walther, *Eur. Phys. Lett.* **37**, 317–322 (1997).
- 89** M. Löffler, G. M. Meyer, and H. Walther, *Phys. Rev. A* **55**, 3923–3930 (1997).
- 90** G. M. Meyer, M. Löffler, and H. Walther, *Phys. Rev. A* **56**, 1099–1102 (1997).
- 91** K. An, J. J. Childs, R. R. Dasari, and M. S. Feld, *Phys. Rev. Lett.* **73**, 3375–3378 (1994).
- 92** A. D. Boozer, A. Boca, J. R. Buck, J. McKeever, and H. J. Kimble, *Phys. Rev. A* **70**, 023814 (2004).
- 93** S. Haroche, M. Brune, and J. M. Raimond, *Eur. Phys. Lett.* **14**, 19–24 (1991).
- 94** C. J. Hood, T. W. Lynn, A. C. Doherty, A. S. Parkins, and H. J. Kimble, *Science* **287**, 1447–1453 (2000).
- 95** P. H. W. Pinkse, T. Fischer, P. Maunz, and G. Rempe, *Nature (London)* **404**, 365–368 (2000).
- 96** G. Rempe, *Phys. World* **13**(12), 37–42 (2000).
- 97** P. Münstermann, T. Fischer, P. Maunz, P. W. H. Pinkse, and G. Rempe, *Phys. Rev. Lett.* **84**, 4068–4071 (2000).
- 98** A. C. Doherty, T. W. Lynn, C. J. Hood, and H. J. Kimble, *Phys. Rev. A* **63**, 013401 (2000).
- 99** M. Hennrich, T. Legero, A. Kuhn, and G. Rempe, *Phys. Rev. Lett.* **85**, 4872–4875 (2000).
- 100** P. W. H. Pinkse, T. Fischer, P. Maunz, T. Puppe, and G. Rempe, *J. Mod. Opt.* **47**, 2769–2787 (2000).
- 101** T. Fischer, P. Maunz, T. Puppe, P. H. W. Pinkse, and G. Rempe, *New J. Phys.* **3**, 11.1–11.20 (2001).
- 102** P. Horak, H. Ritsch, T. Fischer, P. Maunz, T. Puppe, P. H. W. Pinkse, and G. Rempe, *Phys. Rev. Lett.* **88**, 043601 (2002).
- 103** T. Fischer, P. Maunz, P. H. W. Pinkse, T. Puppe, and G. Rempe, *Phys. Rev. Lett.* **88**, 163002 (2002).
- 104** J. McKeever, J. R. Buck, A. D. Boozer, A. Kuzmich, H.-C. Nägerl, D. M. Stamper-Kurn, and H. J. Kimble, *Phys. Rev. Lett.* **90**, 133602 (2003).
- 105** J. A. Sauer, K. M. Fortier, M. S. Chang, C. D. Hamley, and M. S. Chapman, *Phys. Rev. A* **69**, 051804 (2004).
- 106** P. Maunz, T. Puppe, I. Schuster, N. Syassen, P. W. H. Pinkse, and G. Rempe, *Nature (London)* **428**, 50–52 (2004).
- 107** J. Ye, D. W. Vernooij, and H. J. Kimble, *Phys. Rev. Lett.* **83**, 4987–4990 (1999).
- 108** S. Kuhr, W. Alt, D. Schrader, M. Müller, V. Gomer, and D. Meschede, *Science* **293**, 278–280 (2001).
- 109** J. McKeever, A. Boca, A. D. Boozer, R. Miller, J. R. Buck, A. Kuzmich, and H. J. Kimble, *Science* **303**, 1992–1994 (2004).
- 110** J. McKeever, A. Boca, A. D. Boozer, J. R. Buck, and H. J. Kimble, *Nature (London)* **425**, 268–271 (2003).
- 111** S. Nussmann, K. Murr, M. Hijlkema, B. Weber, A. Kuhn, and G. Rempe, *Nature Physics* **1**, 122–126 (2005).
- 112** S. Nussmann, M. Hijlkema, B. Weber, F. Rohde, G. Rempe, and A. Kuhn, *Phys. Rev. Lett.* **95**, 173602 (2005).

- 113** C. J. Hood, T. Lynn, M. Chapman, and H. J. Kimble, *Phys. Rev. Lett.* **80**, 4157–4160 (1998).
- 114** P. Maunz, T. Puppe, I. Schuster, N. Syassen, P. W. H. Pinkse, and G. Rempe, Preprint quant-ph/045136 (2004).
- 115** A. Boca, R. Miller, K. M. Birnbaum, A. D. Boozer, J. McKeever, and H. J. Kimble, *Phys. Rev. Lett.* **93**, 233603 (2004).
- 116** C. H. Bennett and G. Brassard, in: *Proc. IEEE Int. Conf. on Computers, Systems, and Signal Processing* (Bangalore, India) (IEEE, New York, 1984), pp. 175–179.
- 117** E. Knill, R. Laflamme, and G. J. Milburn, *Nature* (London) **409**, 46–52 (2001).
- 118** F. Diedrich and H. Walther, *Phys. Rev. Lett.* **58**, 203–206 (1987).
- 119** T. Basché, W. E. Moerner, M. Orrit, and H. Talon, *Phys. Rev. Lett.* **69**, 1516–1519 (1992).
- 120** B. Lounis and W. E. Moerner, *Nature* (London) **407**, 491–493 (2000).
- 121** C. Kurtsiefer, S. Mayer, P. Zarda, and H. Weinfurter, *Phys. Rev. Lett.* **85**, 290–293 (2000).
- 122** R. Brouri, A. Beveratos, J.-P. Poizat, and P. Grangier, *Opt. Lett.* **25**, 1294–1296 (2000).
- 123** P. Michler et al. *Science* **290**, 2282–2286 (2000).
- 124** C. Santori, M. Pelton, G. Solomon, Y. Dale, and Y. Yamamoto, *Phys. Rev. Lett.* **86**, 1502–1505 (2001).
- 125** E. Moreau et al., *Appl. Phys. Lett.* **79**, 2865–2867 (2001).
- 126** Z. L. Yuan et al. *Science* **295**, 102–105 (2002).
- 127** C. Santori, D. Fattal, C. J. Vučković, G. Solomon, and Y. Yamamoto, *Nature* (London) **419**, 594–597 (2002).
- 128** J. I. Cirac, P. Zoller, H. J. Kimble, and H. Mabuchi, *Phys. Rev. Lett.* **78**, 3221–3224 (1997).
- 129** A. S. Parkins, P. Marte, P. Zoller, and H. J. Kimble, *Phys. Rev. Lett.* **71**, 3095–3098 (1993); A. S. Parkins, P. Marte, P. Zoller, O. Carnal, and H. J. Kimble, *Phys. Rev. A* **51**, 1578–1596 (1995).
- 130** W. Lange and H. J. Kimble, *Phys. Rev. A* **61**, 63817 (2000).
- 131** C. K. Law and J. H. Eberly, *Phys. Rev. Lett.* **76**, 1055–1058 (1996); C. K. Law and H. J. Kimble, *J. Mod. Opt.* **44**, 2067–2074 (1997).
- 132** A. Kuhn, M. Hennrich, T. Bondo, and G. Rempe, *Appl. Phys. B* **69**, 373–377 (1999).
- 133** For a review, see K. Bergmann and B. W. Shore, in: *Molecular Dynamics and Stimulated Emission Pumping*, edited by H. L. Dai and R. W. Field (World Scientific, Singapore, 1995) pp. 315–373.
- 134** A. Kuhn, S. Steuerwald, and K. Bergmann, *Eur. Phys. J. D* **1**, 57–70 (1998).
- 135** A. Kuhn, M. Hennrich, and G. Rempe, *Phys. Rev. Lett.* **89**, 067901 (2002).
- 136** A. M. Smith and C. W. Gardiner, *Phys. Rev. A* **41**, 2730–2748 (1990).
- 137** G. S. Agarwal and S. D. Gupta, *Phys. Rev. A* **42**, 1737–1741 (1990).
- 138** G. M. Meyer, *Der Ionenfallenlaser: Einfluß von Dissipation und Pumpdynamik in mikroskopischen Vielniveausystemen*, MPQ report 221 (Garching, 1997).
- 139** M. Löffler, *Korrelationen und Bewegungsquantisierung im Ein-Atom-Maser und -Laser*, MPQ report 235 (Garching, 1998).
- 140** G. R. Guthöhrlein, M. Keller, K. Hayasaka, W. Lange, and H. Walther, *Nature* (London) **414**, 49–51 (2001).
- 141** M. Keller, B. Lange, K. Hayasaka, W. Lange, and H. Walther, *Nature* (London) **431**, 1075–1078 (2004).
- 142** J. Brendel, W. Tittel, H. Zbinden, and N. Gisin, *Phys. Rev. Lett.* **82**, 2594–2597 (1999).
- 143** L.-M. Duan, A. Kuzmich, and H. J. Kimble, *Phys. Rev. A* **67**, 032305 (2003).
- 144** see e. g. R. K. Chang and A. J. Campillo, *Optical Processes in Microcavities*, in: *Advanced Series in Applied Physics*, Vol. 3 (World Scientific, 1996).
- 145** K. Vahala, *Optical Microcavities*, in: *Advanced Series in Applied Physics*, Vol. 5 (World Scientific, 2004).
- 146** J. Rarity and C. Weisbuch, *Microcavities and Photonic Bandgaps* (Kluwer Academic Publishers, 1986).
- 147** H. Deveaud-Pledran, *The Physics of Semiconductor Microcavities* (Wiley-VCH, New York, 2006).



## 2

# Optimization of Segmented Linear Paul Traps and Transport of Stored Particles

*Stephan Schulz, Ulrich Poschinger, Kilian Singer, and Ferdinand Schmidt-Kaler*

### 2.1

#### Introduction

With a series of spectacular experiments the ion trap based quantum computing has proven its prominent position for a future quantum computer among the list of candidates [1]. Starting with two-qubit gate operations [2, 3], long lived two-qubit entanglement [4–6], teleportation experiments [7, 8], and different sorts of multi-qubit entangled states [4, 9–11], the record for qubit-entanglement is currently presented in a 6-qubit cat state and a 8-qubit W-state [12, 13]. Future improvement is expected using the technique of segmented linear Paul traps which allow to shuttle ions from a “processor” unit to a “memory” section [14]. In such a quantum computer, strategies of quantum error correction will be critical for the successful operation. However, as a result, many additional ancilla qubits are required and a large fraction of the computational time will be consumed by shuttling ions between different segments. Detailed simulations [15] show that as much as 99% of the operating time would be spent with the transportation processes. The time required for the transport should be reduced such that the gate times are improved and decoherence processes are reduced.

Thus, we assume that the improvement of these transport processes is necessary. In recent experiments [12, 16], the shuttling has been carried out within the adiabatic limit, such that the time required for the transport by far exceeds the oscillation time of the ion in the potential. It is a common misbelief that this adiabatic transport is necessary to avoid the excitation of vibrational quanta. In this spirit, we investigate in this paper the optimization of fast and non-adiabatic transportation by applying classical optimal control theory. Our simulations allow to predict the time sequence of control voltages such that ion heating is suppressed.

Certainly, non-optimized fast transport of qubit ions into the processor unit followed by sympathetic cooling of a different ion species [17, 18] would be

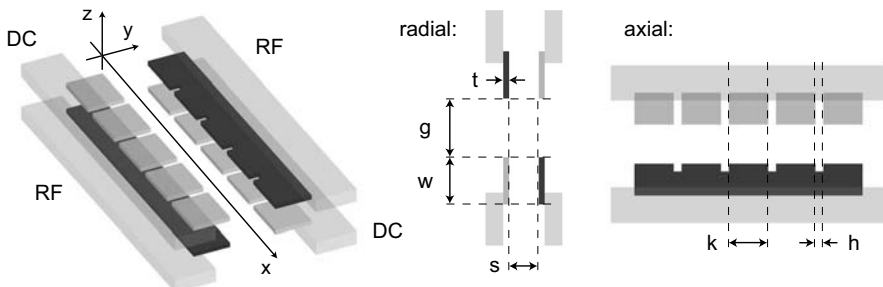


**Fig. 2.1** Scheme of a two-layer microstructured segmented linear trap: The two electrode layers have a thickness  $t$  and are separated by the distance  $s$ . The length of the trapping electrodes is  $w$ , the radio frequency electrodes (RF) and the segmented electrodes (DC) are separated on each layer by the

gap  $g$  (radial direction). The RF voltage is applied on two continuous electrodes (black) and the static voltages are applied on the segmented DC electrodes (gray). The DC electrode segments have the length  $k$  and are separated by a gap  $h$ . The symmetry axis is later denoted as the x- or axial direction.

an alternative strategy. However, the necessary cooling time would render the overall computational time even slower. First experiments show that the qubit coherence is maintained during a transport, but that the vibrational quantum state may typically not be well conserved after a fast shuttle of the ions. This impedes further qubit operations.

In the first section of this paper we start by numeric calculations of the electric trapping potential for ions and show how to optimize the geometry of a two-layer microstructured segmented trap [19, 20]. The same techniques may be applied for the optimization of planar ion traps [21–24]. In the second section we optimize the transport of a single ion between two regions and illustrate the application of optimal control theory [25]. Even though shuttling is fast, we can show that an optimized non-adiabatic transport does not lead to significant heating.

## 2.2

### Optimization of a Two-layer Microstructured Ion Trap

The idea of segmented linear Paul traps has been proposed to realize a scalable quantum computer [14, 26, 27]. Typically, these trap structures are fabricated out of etched semiconductor structures [20] or gold plated insulators structured by microfabrication techniques [28]. Segmented traps come in various shapes and can be categorized by the number of electrode layers forming the trapping potential: Planar traps with one layer only, two-layer traps that are composed of two microstructured planar chips and traps with a higher number of electrode layers. In our discussion, we will focus on the two-layer geometry which is shown in Fig. 2.1. To illustrate the methods of fabrication,

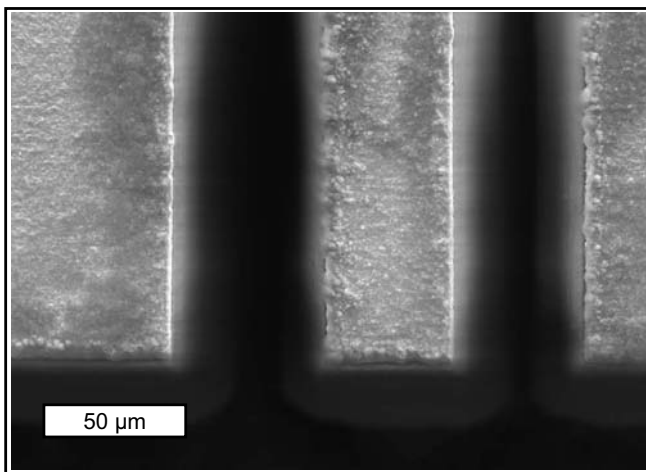


**Fig. 2.2** Detail view on the trap chip, 5  $\mu\text{m}$  gold plated alumina of 125  $\mu\text{m}$  width cut by a fs-pulsed Ti:Sapphire laser. The scanning electron microscope picture shows several DC electrode segments of a single layer.

Fig. 2.2 gives an SEM picture of a gold plated laser cut alumina wafer. Here, with fs-laser ablation [29], the cuts are clean and show a spatial resolution of about 2  $\mu\text{m}$ . The DC-electrodes may be cut in form of “fingers” to reduce the insulating surface seen directly from the ion position. This reduces the influence of the possibly charged surfaces to the trap potential and has also been shown to reduce heating effects of the ion motion. Two structured wafers are assembled to form a two-layer trap geometry as shown in Fig. 2.1.

### 2.2.1

#### Design Objectives

What are the optimal dimensions and aspect ratios in such an ion trap structure? What are the optimal electric trap parameters?

**Radial Configuration** At first, we aim for a high secular trap frequency  $\omega_{\text{sec}}/2\pi$ , such that there is a tight dynamical confinement of the ions within the Lamb-Dicke regime. The confinement should typically reach frequencies of several MHz in the radial direction. The required radial frequencies should be achieved with moderate voltages on the electrodes of several hundred volts. Therefore, the RF trap drive may not exceed the break-through voltage – a limitation which plays a significant role in the case of very small traps [20, 21].

A second aspect is the anharmonicity of the radial trapping potential. From the fact that linear traps with optimized electrode shapes have been shown

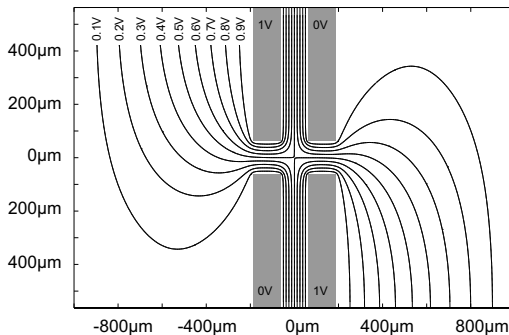


**Fig. 2.3** Electric potential of the two-layer microstructured trap in radial direction ( $yz$  cross section). Ions are confined by a pseudopotential on the  $x$ -axis. Here, the potential lines are normalized to a trap drive amplitude  $U_{rf}$  of 1V. In the central trapping region near the  $x$ -axis the electric potential may be approximated by a quadrupole potential as the radial harmonic pseudopotential for single ions.

to load large crystals of ions [30], we would try to improve the loading rate by reducing non-harmonic contributions to the potential. Especially for larger  $q$ -values when the trap drive power is chosen relatively high, non-linear resonances have been observed [31]. This confirms that even small anharmonicities are relevant in the case of large crystals.

**Axial Configuration** In order to maintain the linear appearance of the ion crystals, the axial trap frequencies have to be lower than the radial frequency. Nevertheless, the axial frequencies  $\omega_{ax}/2\pi$  should exceed a few MHz. Then, cooling techniques are simpler [32], gate operations may be driven faster, and a faster adiabatic transport of ions between segments may be achieved. Ion transport between axial segments requires a fast temporal change of the trap control voltages on the order of several  $\mu$ s. This is accomplished by controlling the DC-electrode voltages by means of fast digital-to-analog converters (DAC) and would be technically much more involved for high voltages.<sup>1</sup>

Furthermore, single ions will have to be split off and merged to ion strings throughout the operation of a segmented ion trap quantum computer. The investigation of splitting and merging operations is not within the scope of this paper [33], however, it was pointed out that a highly non-harmonic axial potential improves this situation [34]; it implies certain geometrical ratios in the axial trap construction.

<sup>1)</sup> Therefore the geometry should also take into account the limited voltage range of the DACs.

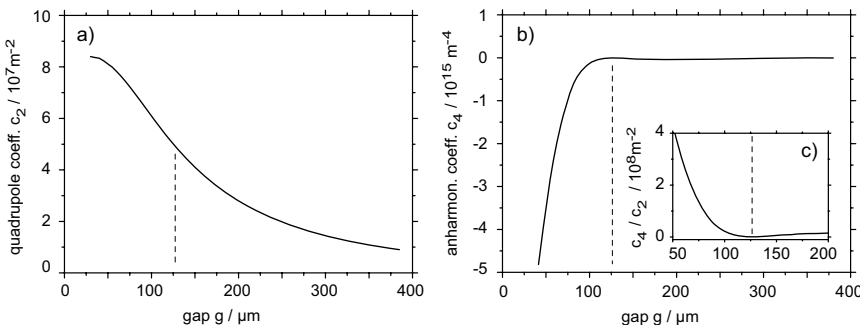


**Fig. 2.4** a) Numerical simulation of the trap stiffness  $c_2$  in radial direction as a function of the slit width. For a slit width of  $126 \mu\text{m}$  we estimate a value of  $5.5 \cdot 10^7 \text{ m}^{-2}$  which corresponds to a radial frequency of  $\omega_{\text{rad}}/2\pi = 5 \text{ MHz}$ . b) Dependence of the

fourth-order parameter  $c_4$  to the slit width  $g$ . The dashed line near  $126 \mu\text{m}$  indicates the optimization result. c) The normalized hexapole coefficient  $c_4$  normalized by the quadrupole coefficient  $c_2$  indicates the decreased loss of the trap drive power.

## 2.2.2

### Operating Mode and Modeling of the Segmented Linear Paul Trap

Linear Paul traps are characterized by a two-dimensional dynamical confinement in the radial direction ( $yz$  plane) and a static confinement in the axial direction ( $x$ -axis). The applied radio frequency  $\omega_{\text{rf}}/2\pi$  to the RF electrodes (see Fig. 2.1) generates a dynamical electric potential  $\phi_{\text{rad}}(y, z, t)$  which leads to a strong confinement of single ions along the axial direction at the radio frequency node. Typically, the axial potential  $\phi_{\text{ax}}(x, t)$  formed by the quasistatic voltages applied to the segmented DC electrodes is weaker than the radial confinement to support a robust alignment of the linear ion string. The shape of this axial potential depends on the geometry of the segmented DC electrodes. The time-dependent variation of the DC control voltages allows to transport ions in the axial direction without micromotion. We separate the numerical optimization of the linear Paul trap into a radial and axial calculation – first, the radial geometry configuration is optimized for strong confinement in the RF node, then the axial electrode geometry is calculated based on the radial geometry.

The lowest-order approximation of the dynamical trap potential  $\phi_{\text{rad}}(y, z, t)$  in radial direction is similar to that of a quadrupole mass filter [35]. The geometric factor  $c_2$  describes the quadrupole potential strength in both radial directions for a symmetric radial electrode geometry:

$$\phi_{\text{rad}}(y, z, t) = c_2/2 (y^2 - z^2) (U_{\text{dc}} + U_{\text{rf}} \cdot \cos(\omega_{\text{rf}} t)) \quad (2.1)$$

An ion trajectory is described as a superposition of a harmonic secular motion at frequency  $\omega_{\text{sec}} = \omega_{\text{rf}}/2 \sqrt{a + q^2/2}$  (lowest order approximation) and the superposed micromotion at the radio frequency  $\omega_{\text{rf}}$ . The frequency of the

secular motion is characterized by the dimensionless stability parameters  $a$  and  $q$  of the radial motion [36] which depends on mass  $m$  and charge  $e$  of the ion, the RF amplitude  $U_{\text{rf}}$  applied to the RF electrodes and the static voltages  $U_{\text{dc}}$  applied to the segmented electrodes of the trap:

$$a = \frac{4e U_{\text{dc}}}{m \omega_{\text{rf}}^2} c_2 \quad , \quad q = \frac{2e U_{\text{rf}}}{m \omega_{\text{rf}}^2} c_2 \quad (2.2)$$

A two-dimensional domain of the stability parameters  $a$  and  $q$  defines a region of stable trajectories as solutions of the classical equations of motion<sup>2</sup>. In general, the electrode configurations result in an electric potential that may be expanded in spherical multipole components, where the quadrupole contribution  $c_2$  represents the dominating part for reasonable Paul trap geometry; the hexapole contribution  $c_4$  contributes mainly to the non-harmonic part.

The quadrupole approximation of the confining potential is inaccurate if the electrode shapes deviate strongly from the ideal hyperbolic form. As a result, anharmonicities and coupling terms appear inside the stability region [31]. As the radio frequency voltage is portioned to various higher order terms and not only to the quadrupole contribution of the potential a loss of the trap stiffness  $c_2$  is observed (Fig. 2.4). For simplicity we idealize  $U_{\text{dc}}$  as zero and characterize the anharmonicity of the pseudopotential in radial direction along the two radial principal axes, here denoted by a radial coordinate  $r(y, z)$ , by the leading terms of the following polynomial expansion:

$$\phi_{\text{rad}}(r(y, z), t) \propto \sum_n c_n r^n \quad (2.3)$$

Because of the radial electrode symmetry the odd-numbered terms  $c_1, c_3, \dots$  are negligible and the potential offset  $c_0$  is irrelevant. The optimization of the radial trap potential leads to a suppression of the higher order potential contribution, such that the hexapole term  $c_4$  as the leading non-harmonic contribution is small.

Based on the geometry for an optimized radial confinement the axial static trap potential along the symmetry axis  $x$  can be analogously expanded,

$$\phi_x(x, t) \propto \sum_n d_n x^n. \quad (2.4)$$

The axial potential properties are determined by the segmented electrode geometry, especially the axial width of the individual electrode segments. An optimal axial confinement of the ion requires a maximum quadratic term  $d_2$ . The transport of a single ion between axial segments is facilitated if the potentials from adjacent segments exhibit a large overlap. For the splitting operation

2) We discuss the optimization in the so-called lowest stability region including  $a = 0$  and  $q \leq 0.9$

**Tab. 2.1** Trap design parameters of several types of linear ion traps: The geometric trap size  $R$  is given by the minimal distance between ion position and electrode surface, the quadratic geometry factor  $c_2$  of the radial cross section describes the magnitude of the radial confinement at the given electrode voltage, the trap drive frequency  $\omega_{\text{rf}}/2\pi$  together with the trap drive voltage  $U_{\text{rf}}$  and the RF stability parameter  $q$  results in the radial motional frequency  $\omega_{\text{rad}}/2\pi$ . For comparison the axial motional frequency  $\omega_{\text{ax}}/2\pi$  is shown. The trap depth  $\Delta$  summarizes the confinement of a single ion.

		$R$ [μm]	$c_2$ [1/m <sup>2</sup> ]	$\omega_{\text{rf}}/2\pi$ [MHz]	$U_{\text{rf}}$ [V]	$q$	$\omega_{\text{rad}}/2\pi$ [MHz]	$\omega_{\text{ax}}/2\pi$ [MHz]	$\Delta$ [meV]
Aarhus [37]	<sup>24</sup> Mg <sup>+</sup>	1750	$1.6 \cdot 10^5$	4.2	$2 \cdot 50 \dots 2 \cdot 150$	$0.2 \dots 0.6$	$0.3 \dots 0.8$	$\leq 0.4$	$\leq 10^5$
Innsbruck [38]	<sup>40</sup> Ca <sup>+</sup>	800	$3.9 \cdot 10^6$	23.5	700	0.6	5.0	1.0	1000
Michigan [39]	<sup>112</sup> Cd <sup>+</sup>	100	$2.2 \cdot 10^7$	48.0		0.3	5.0	2.5	
Simulation	<sup>40</sup> Ca <sup>+</sup>	89	$5.3 \cdot 10^7$	50.0	120	0.3	5.0	2.5	300
Michigan [40]	<sup>112</sup> Cd <sup>+</sup>	30	$4.7 \cdot 10^8$	15.9	8	0.6	4.3	1.0	80

of an aligned two-ion crystal into single ions in independent axial potentials, Steane et al. [34] suggest a potential shape with a maximum quartic term  $d_4$  and minor quadratic contribution  $d_2$ .

Relevant parameters of various linear ion traps are summarized in Table 2.1. The Aarhus hexapole design with endcaps [37] and the Innsbruck blade design [38] show a traditional macroscopic approach of mm-size linear trap design without segmentation of the control electrodes. The Michigan trap designs, the microstructured three-layer trap [39] and the semiconductor two-layer trap [40], represent the progress in the miniaturization of linear ion traps and the segmentation of the control electrodes for the transport of single ions and the splitting of ion crystals.

### 2.2.3

#### Optimization of the Radial Potential

In the first step we optimize the radial confinement of the trap. The width of the slit is varied and the electric potential is calculated, see Fig. 2.3. The distance of the two layers is fixed to the thickness of a commercial alumina wafer (125 μm) which acts as a spacer. Then a variable parameter is the width  $g$  of the lateral laser cut in the trap chips, respectively the distance between the RF and the DC-electrodes of the trap chips. We find that the radial confinement increases with decreasing slit width  $g$ , see Fig. 2.4. Interestingly, for

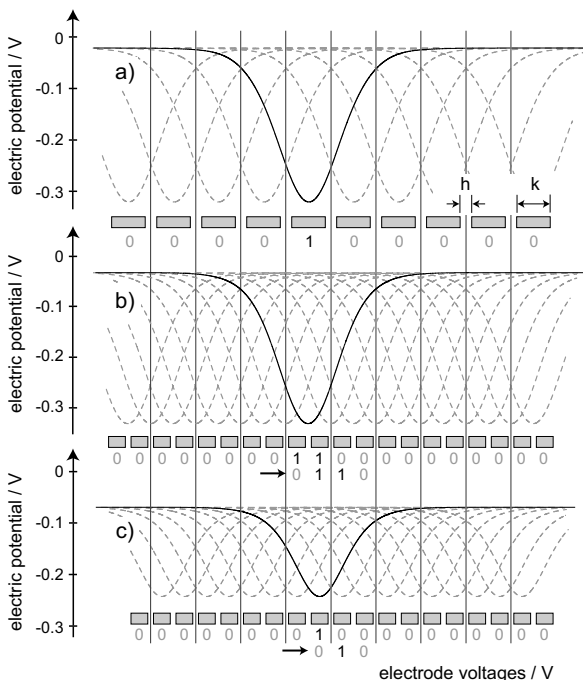


**Fig. 2.5** Numerical calculation of the axial electric potentials  $\phi_{ax}$ , all cases (a) to (c) for the optimized radial slit width of  $g = 126 \mu\text{m}$ .

a) DC segments with a width of  $k = 90 \mu\text{m}$  and gaps between axial electrodes of  $h = 30 \mu\text{m}$  result in a maximal  $d_2$  coefficient. The potential of the adjacent electrode is plotted and shows only partial overlap (dashed gray).

b) Optimized transport scheme: The DC electrodes are divided into equal parts with  $k = 45 \mu\text{m}$  and  $h = 15 \mu\text{m}$ . If both electrodes are at the same voltage of 1V, the potential is

nearly identical to the optimized case (a). For transporting an ion, the potential minimum is shifted by changing the voltages from  $..0/0/1/1/0/0.. \rightarrow ..0/0/0/1/1/0..$  continuously. The axial potentials exhibit a large overlap which improves the transport of the ions. c) Simplified transport scheme: Axial potential for DC segments with  $k = 45 \mu\text{m}$  and  $h = 15 \mu\text{m}$ . Now, only a single segment is at 1 V. For transporting the voltages are changed from  $..0/1/0/0/.. \rightarrow ..0/0/1/0/..$

this geometry, the radial potential is almost harmonic since the fourth-order parameter  $c_4$  is nearly vanishing. For a width of 126  $\mu\text{m}$  the radial frequency of  $\omega_{\text{rad}}/2\pi = 5 \text{ MHz}$  is reached for a singly charged  $^{40}\text{Ca}^+$  ion with a peak RF voltage of 120 V at 50 MHz.

## 2.2.4

## Optimization of the Axial Potential

The optimization of the axial potential determines the performance of the fast ion transport. Additional requirements are a deep axial potential even with moderate DC control voltages and the capability of the segments to split a

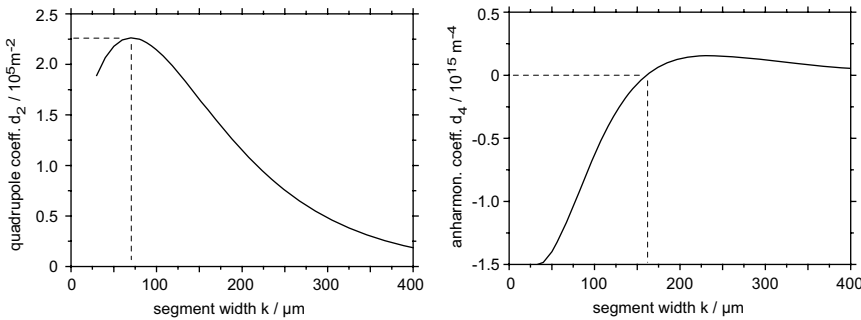


**Fig. 2.6** a) Numerical simulation of the axial trap stiffness  $d_2$  as a function of the segment width  $k$  with  $h = 30 \mu\text{m}$ . b) Dependence of the fourth-order parameter  $d_4$ , the dashed line near  $k = 160 \mu\text{m}$  indicates the zero crossing.

two-ion crystal into two single ions trapped independently in distinct potential minima.

In a first step we investigate the maximization of the axial trap frequency  $\omega_{\text{ax}}$  as a function of the segment width  $k$  and the cut width  $h$ , see Fig. 2.1. The numerical three-dimensional electric potential simulation is depicted in Fig. 2.6 which shows the expected result. For a large width of the segments, the potential is expected to be shallow, and for a very short width the electric potential falls rapidly off from the electrode tips such that again, a weak confinement is found. The maximum axial trap frequency is reached for a segment width  $k_{\text{opt}} \simeq 70 \mu\text{m}$ , a gap between DC and RF electrode  $g = 126 \mu\text{m}$  between DC and RF electrode and a cut width of  $h = 30 \mu\text{m}$ . Changing the size of the segment width by 50% results only in a 20% variation of  $d_2$  which is easily compensated by the DC voltage.

The trapping of single ions and transport require a different electrode configuration. For the transport problem, it is important that the potentials generated by adjacent DC segments exhibit a large spatial overlap (see Fig. 2.5). To achieve both ideal trapping and transport conditions we split each electrode into two parts (b). For trapping we bias two neighboring electrodes with an equal voltage in order to obtain a larger “effective” electrode. Due to the smaller segmentation a better overlap of the individual potentials is provided during transport. As the ion is displaced during the transport process we expect that the anharmonic terms  $d_4, d_5, \dots$  of the potential will cause heating, see Sect. 2.3.5. Therefore we have determined the optimal effective segment width such that the  $d_4$  term is minimized. The results are shown in Fig. 2.6.

In the following, we will use the simplified transport scheme in Fig. 2.5 (c) with one start and one target electrode only and investigate the necessary time dependence of both DC segment control voltages.

## 2.3

### Open Loop Control of Ion Transport

After the optimization of all geometric trap parameters we now focus on the optimization of the time dependent trap control voltages which are applied on the DC segments in order to transport the ion: Our goal will be to decrease the time required for the transport far below the limit of adiabaticity, such that the transport is finished within a single oscillation period only, with the constraint to avoid vibrational excitation. To a good approximation the radial ion confinement does not influence the axial transport between two segments as the ion is moving along the central RF-node with negligible micromotion. Note, that our calculation takes into account two axial segments but may be adapted to a larger number of segments, see Fig. 2.5 (c). The potential which we use for the optimization of the ion transport is the result of a boundary element calculation, see appendix A. In order to transport the ion, the potential minimum is shifted by changing the DC control voltages  $u_i(t)$ . Intuitively, we estimate that a smooth acceleration and a smooth deceleration of the ion is advantageous. Searching for the precise shape of the segment control non-adiabatic heating due to fast transport has to be minimized.

#### 2.3.1

##### Non-adiabatic Heating Sources

For a transport duration approaching the timescale given by the axial trap frequency, the following non-adiabatic effects are expected to occur:

1. *Classical displacement error:* The ion cannot adiabatically follow the potential minimum and starts oscillating, such that it possesses excess energy after the transport process. This behavior may be understood classically. In the quantum picture it corresponds to the buildup of a nonvanishing displacement  $\alpha$  during transport.
2. *Wavepacket dispersion heating:* With a spatial extension of about 10 to 20 nm, the undisplaced wavefunction hardly senses any anharmonicity in an electric potential that is generated by 50 to 100  $\mu\text{m}$  sized electrode structures. However, during the transport the wavepacket undergoes significant excursions of a few  $\mu\text{m}$  out of the minimum of the potential. Here, exposed to higher anharmonic  $d_4$  contributions, the shape of the ion wavepacket disperses which results in vibrational excitation.
3. *Parametric heating:* As the control voltages are changed, the harmonic frequency  $\omega$  of the instantaneous potential is temporarily varying. If the width of the wavepacket can not follow the variation of  $\omega(t)$  adiabatically, parametric heating to higher vibrational states will occur.

### 2.3.2

#### Overview of the Applied Optimization Strategies

In the following Sect. 2.3.3 we minimize the classical displacement error by applying the optimal control method. For the optimization of this entirely classical error source we need to optimize the ion's classical trajectory such that a cost function – weighting the ion's phase space displacement after the transport – is minimized. The solution obtained by the optimal control algorithm does not show considerable heating by wavepacket dispersion. However, we find a significant contribution of parametric heating. A first guess would be to include an additional term in the cost function to prevent parametric heating, involving time derivatives of the control fields.

As this approach fails due to implementational difficulties, we suppress parametric heating by an appropriate initial guess which keeps the trap frequency perfectly constant. This is achieved by a variable transformation from  $u_{1,2}(t)$  to new parameters that allow to decouple the strength of the potential and its minimum position. Starting now the optimal control method yields a solution that reduces the displacement error. Since the control parameters are only slightly modified by the optimization algorithm, the parametric heating and also the wavepacket dispersion heating are negligible.

We conclude that in our case, the choice of variables that decouple the essential optimization parameters [41,42] and a well suited initial guess function are helpful and maybe critical for the success of the optimal control method.

### 2.3.3

#### The Optimal Control Method

This section will give an introduction to optimal control theory applied to single ion transport. We use the method derived from a variational principle with unbounded controls and fixed final time [43]. We consider the dynamics of a singly charged single  $^{40}\text{Ca}^+$  ion confined in a segmented linear Paul trap. We assume that the ion is laser cooled to its motional ground state<sup>3</sup> pertaining to the axial degree of freedom. Neglecting the radial motion, the motional state of a trapped ion is classically represented by a coordinate vector  $\vec{\zeta}(t) = (x, v)^T$  in a two dimensional phase space.

The equation of motion under consideration of two uniform electrode segments with arbitrary voltages applied on them reads

$$\dot{\vec{\zeta}} = \vec{a}(\vec{\zeta}, \{u_i\}) = \begin{pmatrix} v \\ -\frac{q}{m} \sum_i \frac{\partial V_i(x)}{\partial x} u_i(t) \end{pmatrix}. \quad (2.5)$$

3) The calculation is valid also for thermal and coherent states with modest excitation.

Here, the index  $i$  runs over the two electrodes and  $V_i(x)$  are the normalized electrostatic potentials at electrode  $i$ . Eq. (2.5) then holds for arbitrary electrode voltages due to the linearity of the Laplace equation.

Our goal is now to find time-dependent control voltages  $u_i(t)$  that move the ion from the center of electrode 1 to the center of electrode 2. We desire to have the ion at rest after the transport process. The performance of a given control field is judged by the cost function

$$h(\vec{\xi}(t_f)) = \alpha (x(t_f) - x_f)^2 + \beta v(t_f)^2, \quad (2.6)$$

which is a measure of the phase space displacement at the final time  $t_f$ .  $\alpha$  and  $\beta$  weight the contributions relative to each other. Taking Eq. (2.5) as a constraint for all times  $t$ , we obtain the cost functional

$$J(\vec{\xi}, \vec{\xi}_p, \{u_i\}) = \int_{t_0}^{t_f} \frac{\partial h}{\partial \vec{\xi}} \cdot \dot{\vec{\xi}} + \vec{\xi}_p \cdot \left( \vec{a}(\vec{\xi}, \{u_i\}) - \dot{\vec{\xi}} \right) dt \quad (2.7)$$

where we have introduced the costate vector  $\vec{\xi}_p = (x_p, v_p)^T$  as a Lagrange multiplier in order to guarantee that the optimization result obeys the equation of motion Eq. (2.5). The time dependence of all variables has been dropped in the notation. For an optimal control field,  $\delta J = 0$  has to hold, therefore the variational derivatives with respect to  $\vec{\xi}$ ,  $\vec{\xi}_p$  and  $\vec{u}$  have to vanish. The derivative with respect to  $\vec{\xi}_p$  restores the equations of motion Eq. (2.5) for the state vector, the derivative with respect to  $\vec{\xi}$  yields equations of motion for the costate vector:

$$\begin{aligned} \dot{\vec{\xi}}_p &= -\frac{\partial \vec{a}}{\partial \vec{\xi}} \cdot \vec{\xi}_p \Rightarrow \\ \dot{x}_p &= v_p \frac{q}{m} \sum_i \frac{\partial^2 V_i(x)}{\partial x^2} u_i \\ \dot{v}_p &= -x_p. \end{aligned} \quad (2.8)$$

Variation of  $J$  with respect to the control field leads to an additional algebraic equation:

$$\frac{\partial \vec{a}}{\partial u_i} \cdot \vec{\xi}_p = 0 \Rightarrow -\frac{q}{m} \frac{\partial V_i(x)}{\partial x} v_p = 0. \quad (2.9)$$

The boundary condition for  $\vec{\xi}_p$  is derived by variation with respect to the final state:

$$\left. \frac{\partial h}{\partial \vec{\xi}} \right|_{t_f} = 0. \quad (2.10)$$

If we let the ion start at rest in the potential well pertaining to the first electrode, the set of boundary conditions for the state and costate vector reads

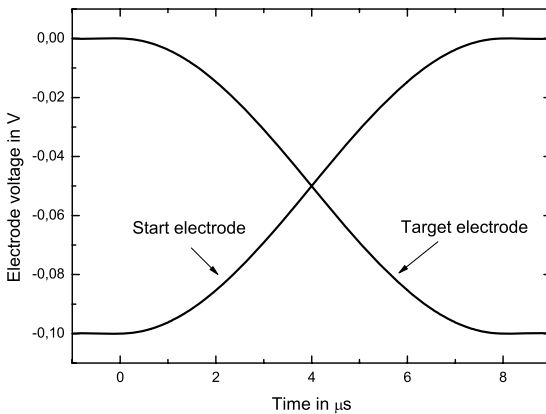


**Fig. 2.7** Initial guess for the control voltages, corresponding to Eq. (2.13).

$$\begin{aligned}
 x(t_0) &= 0 \\
 v(t_0) &= 0 \\
 x_p(t_f) &= 2\alpha (x - x_f) \\
 v_p(t_f) &= 2\beta v. \tag{2.11}
 \end{aligned}$$

Eqs. (2.5), (2.8) and (2.11) together with (2.9) represent a system of coupled ordinary nonlinear differential equations with split boundary conditions, i.e. for two of the variables, initial conditions are given whereas for the other two, the values at the final time are specified. This makes a straightforward numerical integration impossible. The system is therefore solved in an iterative manner by means of a gradient search method. The scheme of this steepest descent algorithm is as follows:

1. Choose an initial guess for the control field  $u_i(t)$ .
2. Propagate  $x$  and  $v$  from  $t = t_0$  to  $t = t_f$  while using  $u_i(t)$  in the corresponding equations of motion. At each time step, save the value of  $x(t)$ .
3. Determine  $x_p(t_f)$  and  $v_p(t_f)$  according to (2.11).
4. Propagate  $x_p$  and  $v_p$  backwards in time from  $t = t_f$  to  $t = t_0$ . At each time step, save the value of  $v_p(t)$ .
5. For each time step, update the control field according to

$$u_i^{new}(t) = u_i^{old}(t) + \tau v_p \frac{q}{m} \frac{\partial V_i(x)}{\partial x} \tag{2.12}$$

6. Repeat steps 2 to 5 until the specified threshold fidelity is reached.

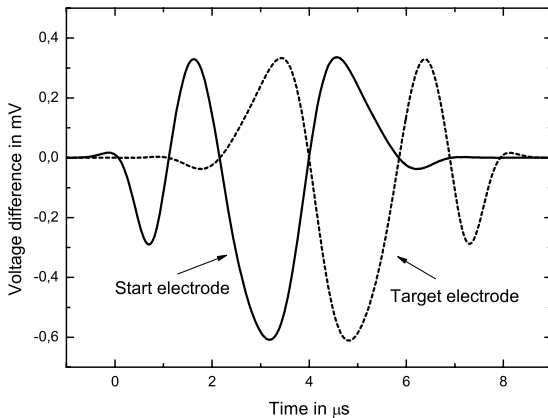


**Fig. 2.8** Optimized control voltages given in terms of change with respect to the initial guess values. The solid curve indicates the voltage  $u_1(t)$  at the start electrode, the dashed one the voltage  $u_2(t)$  at the destination electrode.

In Eq. (2.12), the gradient search step width  $\tau$  is simply chosen by trial and error. If it is too small, the algorithm converges too slowly, if it is too large, the algorithm starts to oscillate. The values of  $\alpha$  and  $\beta$  in Eq. (2.6) are determined based on experience. For the data presented in the following section, these values are  $\alpha = 10$ ,  $\beta = 1$  and  $\tau = 5 \cdot 10^{-8}$ . The algorithm converged after about 200 iterations.

### 2.3.4

#### Optimization Results

For the initial guess the control field is chosen as follows:

$$u_1^{(0)}(t) = \begin{cases} V_0 & \text{for } t \leq 0 \\ V_0 \sin^2\left(\frac{\pi t}{2\Delta t}\right) & \text{for } 0 < t \leq \Delta t \\ 0 & \text{for } t > \Delta t \end{cases}$$

$$u_2^{(0)}(t) = V_0 - u_1^{(0)}(t) \quad (2.13)$$

This provides on the one hand a smooth and symmetric acceleration and deceleration of the ion, on the other hand the potential minimum exactly coincides with the desired positions at the initial and final times. In principle, other initial guess voltages like Gaussian flanks can be used as well. The reference voltage is  $V_0 = -0.1V$ , corresponding to  $\omega \approx 2\pi \cdot 0.5$  MHz in the initial and final potential wells. The switching time is set to  $\Delta t = 8.0 \mu\text{s}$ , the total time interval runs from  $-1.0 \mu\text{s}$  to  $9.0 \mu\text{s}$ .

### 2.3.5

#### Ion Heating due to Anharmonic Dispersion

Quantum mechanically we describe the system with a Hamiltonian operator pertaining to a time-dependent harmonic oscillator with an anharmonic perturbation:

$$H_0(t) = \frac{\hat{p}^2}{2m} + \frac{m\omega(t)^2}{2}(\hat{x} - x_0(t))^2 + \kappa(t)(\hat{x} - x_0)^4. \quad (2.14)$$

Without temporal variation of  $\omega$  and the anharmonic part<sup>4</sup> of the potential, the solution of the time-dependent Schrödinger equation is simply given by a coherent state  $|\alpha(t)\rangle$ , where the displacement parameter  $\alpha(t)$  can be inferred from the classical trajectory. Anharmonic dispersion of a wavepacket occurs at a timescale given by  $T_{\text{rev}}/(\Delta n)^2$  [44], with the revival time

$$T_{\text{rev}} = 2\hbar \left( \frac{d^2 E_n}{dn^2} \right)^{-1} \quad (2.15)$$

and the spread over the vibrational levels  $\Delta n = \alpha(t)$ . The shift of the energy levels  $E_n$  induced by the anharmonic contribution causes a finite dispersion time and can be calculated in first order stationary perturbation theory:

$$\Delta E_n(t) = \frac{5}{4} \frac{\hbar^2 \kappa(t)}{m^2 \omega(t)^2} n^2. \quad (2.16)$$

We now define a generalized dispersion parameter

$$\int_{t_0}^{t_f} dt \frac{\Delta n^2}{T_{\text{rev}}} = \frac{5\hbar}{4\pi m^2} \int_{t_0}^{t_f} dt \frac{\kappa(t) |\alpha(t)|^2}{\omega(t)^2}. \quad (2.17)$$

If this parameter is sufficiently small, anharmonic dispersion will not contribute to heating.

### 2.3.6

#### Quantum Mechanical Estimate of Non-adiabatic Parametric Heating

We now check if the width of the wavepacket adiabatically follows the harmonic frequency  $\omega(t)$ . The adiabatic theorem states that if

$$\hbar \langle \phi_m(t) | \phi_n(t) \rangle \ll |E_n(t) - E_m(t)| \quad (2.18)$$

is fulfilled, transitions between eigenstates can be neglected. The parametric time dependence of the eigenstates states in Eq. (2.18) is the implicit time

4) In contrast to  $d_4$ ,  $\kappa(t)$  is given by expanding the potential around the instantaneous potential minimum.

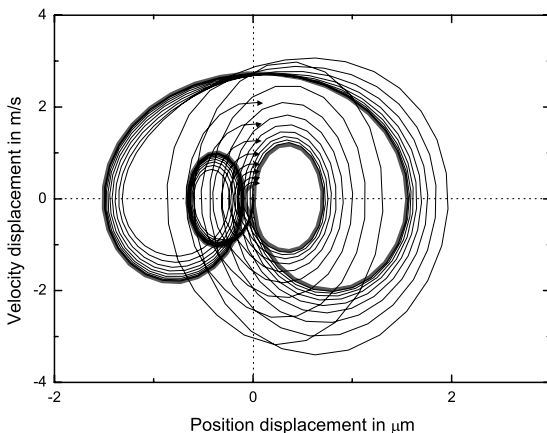


**Fig. 2.9** Phase space trajectories in the frame co-moving with the potential minimum. The figure shows the trajectories pertaining to iterations 0, 10, ..., 100. At iteration 100, the ion arrives close to the origin. Note that the trajectory tends to be symmetrized by the optimization algorithm.

dependence via  $\omega(t)$ . We find the following nonvanishing matrix elements:

$$\begin{aligned}\langle \phi_{n+1} | \dot{\phi}_n \rangle &= \frac{\dot{\omega}}{\sqrt{2\pi^3\omega}} n \sqrt{n+1} \\ \langle \phi_{n+2} | \dot{\phi}_n \rangle &= \frac{\dot{\omega}}{4\omega} \sqrt{(n+1)(n+2)}\end{aligned}\quad (2.19)$$

and similar expressions for  $m = n-1, n-2$ . Thus, parametric heating can be neglected if

$$n^{3/2} \frac{\dot{\omega}}{\omega^2} \ll 1. \quad (2.20)$$

Numerical evaluation of the matrix elements yields the result that the adiabatic following condition is fulfilled for  $n = 0$ , but is clearly violated for the high  $n$  occurring for large excursion of the wavepacket, for example  $\bar{n} \approx 2000$  for  $\Delta x = 1 \mu\text{m}$  at a transport time of 10  $\mu\text{s}$ , see Fig. 2.10.

### 2.3.7

#### Improved Initial Guess Function and Ultra-fast Transport

We therefore have to refine our optimization strategy: As can be seen in Fig. 2.8, the control voltages changes are symmetric, which indicates that one control degree of freedom can be sacrificed in order to keep  $\omega(t)$  constant. This is achieved as follows: The initial guess voltages Eq. (2.13) are normalized to a constant  $\omega$  before the optimization. The optimization process then leads to variations in  $\omega(t)$  that are negligibly small – typically leading to maximum

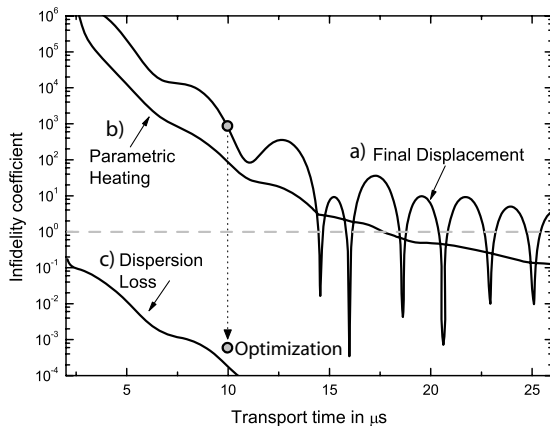


**Fig. 2.10** Non-optimized transport, heating effects, and optimization result: Indicated is the excess energy as a function to transport time, if the initial guess function is used for the transport. The curve (a) describes the energy at the final time in vibrational quanta. The approximate zeros occur when the deceleration of the potential minimum coincides with the ion oscillation. Curve (b) displays the maximum non-adiabaticity parameter Eq. (2.20) for parametric heating

and the (c) the anharmonic dispersion loss parameter from Eq. (2.17). The grey dashed horizontal line indicates a heating of one phonon and the borderline to non-adiabatic behavior in curve (b). The optimization algorithm decreases the excess displacement by more than 6 orders of magnitude. The circles indicate the squared phase space displacement for the guess function and the final optimized control voltages.

values of  $\dot{\omega}/\omega^2$  on the order of  $10^{-5}$  such that according to Eq. (2.20) the adiabatic theorem is fulfilled even after the optimization algorithm has cured the classical phase space displacement heating. This is in strong contrast to the unconstrained, previous guess function, where we obtain  $\dot{\omega}/\omega^2 \simeq 10^{-2}$ . It should be noted that parametric heating can be completely suppressed as well for optimized control voltages. This can be achieved by changing the set of control parameters to  $\tilde{u}_1 = u_1 + u_2$  and  $\tilde{u}_2 = u_1/\tilde{u}_1$ . The new parameter  $\tilde{u}_2$  is now directly related to the instantaneous potential minimum  $x_0$ . If only  $\tilde{u}_2$  is incorporated in the optimization process,  $\tilde{u}_1$  can be readjusted at each step to keep  $\omega$  constant.

The optimization results for the improved initial guess voltages are shown in Fig. 2.12. The transport time could now be reduced to 5  $\mu$ s which corresponds to roughly two oscillation periods. For the improved guess function the wave packet dispersion appears now as the dominant heating source. This process could be suppressed either by further geometric optimization of the trap segments or by including a corresponding additional term into the cost function of the optimization routine.

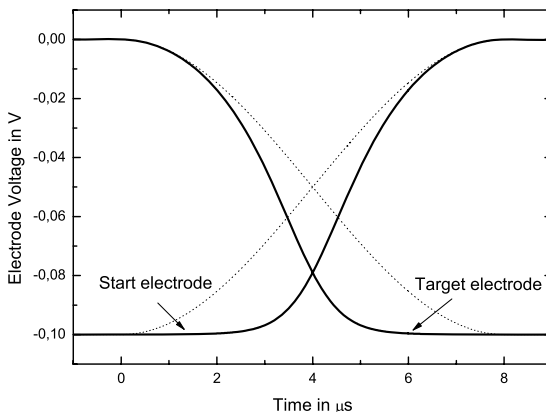


**Fig. 2.11** Initial guess voltages normalized to keep trap frequency constant. The old initial guess voltages are indicated as dashed curves. Note that the dynamics of the potential minimum is unaffected by the normalization.

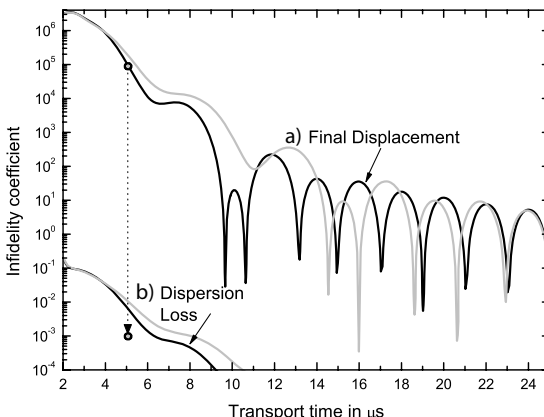


**Fig. 2.12** Nonadiabatic effects versus transport time for the improved initial guess voltages. Here, only the (a) excess displacement and the (b) dispersion parameter are shown, parametric heating is not relevant anymore. The values for the old initial guess voltages are indicated in grey. The improved

initial guess allows for successfull optimization at a transport time of 5  $\mu$ s and an optimization of about eight orders of magnitude in classical phase space displacement. Now, with a few  $\mu$ s transport, anharmonic dispersion becomes the predominant heating source.

### 2.3.8

#### Discussion of the Open-loop Result

Our optimization results indicate that unwanted heating during ion transport can be suppressed by many orders of magnitude by the application of

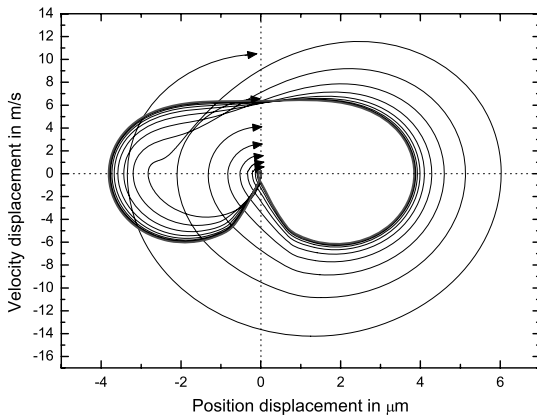


**Fig. 2.13** Phase space trajectories in the frame co-moving with the potential minimum for the improved initial guess voltages. The optimization is now carried out for a transport time of only 5  $\mu$ s corresponding to about two oscillation periods in the harmonic

trap potential. The thin lines indicate the optimization progress and the fat line shows the final result after 100 iterations. Again, the optimization routine symmetrized the trajectory.

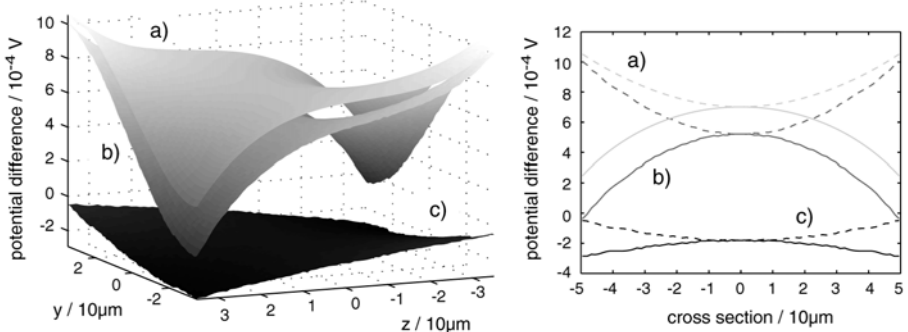


**Fig. 2.14** a) Numeric result obtained by FEMLAB subtracted from the result of BEM [55], b) FEMLAB – CPO, c) CPO – BEM [55]. The left graph shows a 2D potential surface plot in the y-z plane. The right graph shows a line plot in the same plane in the direction of the two diagonal directions.

appropriate time-dependent control voltages. Technically, one would achieve this using a fast high-resolution digital-to-analog converter (DAC) with subsequent scaling to the required voltage range. The small correction voltages obtained from the optimization algorithm might represent a problem, however a 16 bit DAC with an appropriate scaling circuit would allow for a discretization step of roughly 1.5  $\mu$ V for a maximum voltage change of 0.1V. We have also checked the robustness of the control field solutions against noise

by calculating the trajectories with white noise of variable level added on the voltages. We found a quadratic dependence of the excess displacement on the noise level. The deviation of the final displacement from the noise-free case was negligibly small at a noise level of 20  $\mu\text{V}$ . Experimental values for non-adiabatic heating effects in ion transport are given in [16]. The comparison with our theoretical values is hampered by the fact that these measurements have carried out at higher axial trap frequency and the lighter ion species  $^9\text{Be}^+$ , but over a much longer transport distance of 1.2 mm. However, low heating rates were obtained in those experiments only if the transport duration corresponds to a relatively large number of about  $\simeq 100$  of trap periods, whereas in our case, a transport within only *two trap periods* was simulated.

## 2.4 Outlook

The optimization of ion transport beyond the speed limits given by the anharmonic terms of the axial trapping potentials and parametric heating would be most efficient and accurate if a full quantum mechanical equation of motion was employed. Quantum mechanical optimal control methods are based on the same variational principle as presented here for a classical problem, with the only difference that the terms in the penalty functional are functionals on Hilbert space. Algorithms for quantum mechanical optimal control are well developed and were applied to variety of different problems [41, 45]. In our case however, the application of quantum mechanical optimal control was not yet possible for simply a technical reason: The iterative solution via repeated solution of Schrödinger equation over distances on the order of 200  $\mu\text{m}$  and time spans on the order of 20  $\mu\text{s}$  takes too much computational effort, even with highly efficient methods like the Fourier Grid Hamiltonian combined with the Chebyshev propagator technique [46]. On the other hand, we have seen that for the typical electric potentials of segmented Paul traps, the possibility to exert *quantum* control on the system is very restricted since the wavefunction of the ion mainly senses a harmonic potential. The classical approach is therefore well suited to the problem.

In future work, we will investigate whether quantum control could be exerted during short time spans when the ion is displaced from the potential minimum and therefore senses anharmonic contributions to the potential. Extended Gaussian wave packet dynamics [47] could be used to take anharmonic terms efficiently into account. Thus, the application of quantum mechanical optimal control methods also opens new possibilities, for example the control voltages could be used to devise new schemes for quantum computational gates. In this case, the target wave function for the optimization routine could be the first excited motional state or even a superposition of

different motional Fock states. To fulfill this aim, anharmonic contributions to the trapping potentials are crucial.

Open loop optimal control methods will also be applied to the splitting of two ions [33]. With this problem the benefit of going beyond the adiabatic limit will be even more promising. In an adiabatic manner the splitting is initiated by lowering the steepness of the potential in order to increase the separation of the two ions due to their mutual repulsion. This decreases the trapping frequency and as a consequence the speed of the procedure has to be decreased in order to stay adiabatic.

Open loop optimal control has proved to be successful for the optimization of short broadband RF pulses in NMR experiments [48]. In a similar manner in ion trap based quantum computing tailored, light pulses can speed up and improve manipulation of the ions [49,50]. In cases where analytical solution to the control problem is not available open loop optimal control methods could be applied to get optimized light pulses or electrostatic field configurations for multi ion gate operations and entangled state preparation.

Another promising strategy that could be employed to avoid heating during ion transport is the closed loop control technique. Here, the experimental results are fed back into e.g. an evolutionary algorithm to obtain improved values of the control parameters. The heating rate can be measured by comparing the strengths of the red and blue motional sidebands after the transport process [51]. The key problem for applying closed loop control to ion transport lies in finding an appropriate parametrization of the control voltages in order to keep the parameter space small.

This technique may be applied equally well to the problem of separation of two ions from one common potential into two independent sections of the linear trap.

This work has merely started to apply the optimal control theory for ion trap based quantum computing. Not only the motion of ions between trap segments, but the entire process including shaped laser pulses [49] and motional quantum state engineering might be improved with this technique.

## Acknowledgement

We acknowledge support by the European commission within the framework "EMALI", the Deutsche Forschungsgemeinschaft and by the Landesstiftung Baden-Württemberg within the frameworks "quantum highway A8" and "atomics". We thank D. J. Tannor and T. Calarco for stimulating discussions.

## A Comparison of our Boundary-element-package with Commercial Software

Accurate values of the electrostatic potentials are of paramount importance for the determination of the harmonic and the anharmonic terms of the trapping potentials. An adequate choice of a numerical solving method is the Boundary Element Method (BEM) [52, 53]. BEM is a fast and more accurate method compared to the Finite Element Method (FEM) or Finite Difference Method (FDM). This is due to the fact that BEM only needs to solve for the surface charges on the electrode surfaces. With FEM/FDM the Laplace equation has to be solved on a three dimensional mesh. Comparison of the speed and accuracy can be found in [54]. In order to simplify the variation and optimization of the trap geometry we have implemented a free scriptable object-oriented BEM package for 3D and 2D [55]. We have verified the results for the geometry of Fig. 2.3 of our package against the results of the commercial BEM program CPO [56] (see Fig. 2.14 c) and against the results of the commercial FEM program FEMLAB [57] (see Fig. 2.14 a). The higher values in the latter case are due to the inaccuracy of the finite element method itself.

## References

- 1 The roadmaps of US and EU are found at <http://qist.lanl.gov/> and <http://qist.ect.it/>.
- 2 F. Schmidt-Kaler, H. Häffner, M. Riebe, S. Gulde, G. P. T. Lancaster, T. Deusdle, C. Becher, C. F. Roos, J. Eschner, and R. Blatt, *Nature* **422**, 408 (2003).
- 3 D. Leibfried, B. DeMarco, V. Meyer, D. Lucas, M. Barrett, J. Britton, W. M. Itano, B. Jelenkovic, C. Langer, T. Rosenband, and D. J. Wineland, *Nature* **422**, 412 (2003).
- 4 C. F. Roos, M. Riebe, H. Häffner, W. Hänsel, J. Benhelm, G. P. T. Lancaster, C. Becher, F. Schmidt-Kaler, and R. Blatt, *Science* **304**, 1478 (2004).
- 5 H. Häffner, F. Schmidt-Kaler, W. Hänsel, C. F. Roos, T. Körber, M. Chwalla, M. Riebe, J. Benhelm, U. D. Rapol, C. Becher, and R. Blatt, *Appl. Phys. B* **81**, 151 (2005).
- 6 C. Langer, R. Ozeri, J. D. Jost, J. Chiaverini, B. DeMarco, A. Ben-Kish, R. B. Blakestad, J. Britton, D. B. Hume, W. M. Itano, D. Leibfried, R. Reichle, T. Rosenband, T. Schaetz, P. O. Schmidt, and D. J. Wineland, *Phys. Rev. Lett.* **95**, 060502 (2005).
- 7 M. Riebe, H. Häffner, C. F. Roos, W. Hänsel, J. Benhelm, G. P. T. Lancaster, T. W. Körber, C. Becher, F. Schmidt-Kaler, D. F. V. James, and R. Blatt, *Nature* **429**, 734 (2004).
- 8 M. D. Barrett, J. Chiaverini, T. Schaetz, J. Britton, W. M. Itano, J. D. Jost, E. Knill, C. Langer, D. Leibfried, R. Ozeri, and D. J. Wineland, *Nature* **429**, 737 (2004).
- 9 C. A. Sackett, D. Kielpinski, B. E. King, C. Langer, V. Meyer, C. J. Myatt, M. Rowe, Q. A. Turchette, W. M. Itano, D. J. Wineland, and C. Monroe, *Nature* **404**, 256 (2000).
- 10 P. C. Haljan, K.-A. Brickman, L. Deslauriers, P. J. Lee, and C. Monroe, *Phys. Rev. Lett.* **94**, 153602 (2005).
- 11 D. Leibfried, M. D. Barrett, T. Schätz, J. Britton, J. Chiaverini, W. M. Itano, J. D. Jost, C. Langer, and D. J. Wineland, *Science* **304**, 1476 (2004).
- 12 D. Leibfried, E. Knill, S. Seidelin, J. Britton, R. B. Blakestad, J. Chiaverini,

- D. B. Hume, W. M. Itano, J. D. Jost, C. Langer, R. Ozeri, R. Reichle, and D. J. Wineland, *Nature* **438**, 639 (2005).
- 13** H. Häffner, W. Hänsel, C. F. Roos, J. Benhelm, D. Chek-al-kar, M. Chwalla, T. Körber, U. D. Rapol, M. Riebe, P. O. Schmidt, C. Becher, O. Gühne, W. Dür, and R. Blatt, *Nature* **438**, 643 (2005).
- 14** D. Kielpinski, C. R. Monroe, and D. J. Wineland, *Nature* **417**, 709 (2002).
- 15** I. Chuang, private communication.
- 16** M. A. Rowe, A. Ben-Kish, B. DeMarco, D. Leibfried, V. Meyer, J. Beall, J. Britton, J. Hughes, W. M. Itano, B. Jelenkovic, C. Langer, T. Rosenband, and D. J. Wineland, *Quantum Inf. Comput.* **2**, 257 (2002).
- 17** M. Barrett, B. L. DeMarco, T. Schätz, V. Meyer, D. Leibfried, J. Britton, J. Chiaverini, W. M. Itano, B. M. Jelenkovic, J. D. Jost, C. Langer, T. Rosenband, and D. J. Wineland, *Phys. Rev. A* **68**, 042302 (2003).
- 18** M. Drewsen, A. Mortensen, R. Martinussen, P. Staananum, and J. L. Soerensen, *Phys. Rev. Lett.* **93**, 243201 (2004).
- 19** D. Leibfried and T. Schätz, *Phys. J.* **3**, 23 (2004).
- 20** D. Stick, W. K. Hensinger, S. Olmschenk, M. J. Madsen, K. Schwab, and C. Monroe, *Nature Physics* **2**, 36 (2006).
- 21** J. Chiaverini, R. B. Blakestad, J. Britton, J. D. Jost, C. Langer, D. Leibfried, R. Ozeri, and D. J. Wineland, *arXiv:quant-ph/0501147* and *Quant. Inf. Comput.* **5**(6), 419 (2005).
- 22** M. J. Madsen, W. K. Hensinger, D. Stick, J. A. Rabchuk, and C. Monroe, *Appl. Phys. B* **78**, 639 (2004).
- 23** C. E. Pearson, D. R. Leibrandt, W. S. Bakr, W. J. Mallard, K. R. Brown, and I. L. Chuang, *Phys. Rev. A* **73**, 032307 (2006), *arXiv:quant-ph/0511018*.
- 24** S. Seidelin, J. Chiaverini, R. Reichle, J. J. Bollinger, D. Leibfried, J. Britton, J. H. Wesenberg, R. B. Blakestad, R. J. Epstein, D. B. Hume, J. D. Jost, C. Langer, R. Ozeri, N. Shiga, D. J. Wineland, *arXiv:quant-ph/0601173*.
- 25** H. Mabuchi, N. Khaneja, *Int. J. Robust Nonlinear Control* **15**, 647 (2005).
- 26** I. Cirac and P. Zoller, *Phys. Rev. Lett.* **74**, 4091 (1995).
- 27** D. J. Wineland, C. Monroe, W. M. Itano, D. Leibfried, B. E. King, and D. M. Meechhof, *J. Res. Natl. Inst. Stand. Tech.* **103**, 259 (1998).
- 28** W. K. Hensinger, S. Olmschenk, D. Stick, D. Hucul, M. Yeo, M. Acton, L. Deslauriers, C. Monroe, and J. Rabchuk, *App. Phys. Lett.* **88**, 034101 (2006).
- 29** B. N. Chichkov, C. Momma, S. Nolte, F. von Alvensleben, and A. Tünnermann, *Appl. Phys. A* **63**, 109 (1996).
- 30** A. Mortensen, F. Nielsen, T. Matthey, and M. Drewsen, *Phys. Rev. Lett.* **96**, 103001 (2006).
- 31** R. Alheit, Th. Gudjons, S. Kleineidam, and G. Werth, *Rapid Commun. Mass Spectrom.* **10**, 583 (1996).
- 32** J. Eschner, G. Morigi, F. Schmidt-Kaler, and R. Blatt, *J. Opt. Soc. Am. B* **20**, 1003 (2003).
- 33** U. Poschinger et al., in preparation.
- 34** J. P. Home and A. M. Steane, *arXiv:quant-ph/0411102*.
- 35** W. Paul, Q. Osbergerhaus, and E. Fischer, *Forschungsberichte des Wirtschafts- und Verkehrsministeriums Nordrhein-Westfalen*, Vol. 415 (1958).
- 36** D. Leibfried, R. Blatt, C. Monroe, and D. Wineland, *Rev. Mod. Phys.* **75**, 281 (2003).
- 37** M. Drewsen, C. Brodersen, L. Hornekaer, J. S. Hangst, and J. P. Schiffer, *Phys. Rev. Lett.* **81**, 2878 (1998) and private communication: For this trap the drive  $U_{rf}$  is applied also to the DC electrodes with opposite phase (see Fig. 1).
- 38** F. Schmidt-Kaler, H. Häffner, S. Gulde, M. Riebe, G. P. T. Lancaster, T. Deusche, C. Becher, W. Hänsel, J. Eschner, C. F. Roos, and R. Blatt, *Appl. Phys.* **77**, 789 (2003).
- 39** W. K. Hensinger, S. Olmschenk, D. Stick, D. Hucul, M. Yeo, M. Acton, L. Deslauriers, J. Rabchuk, and C. Monroe, *Appl. Phys. Lett.* **88**, 034101 (2006).
- 40** D. Stick, W. K. Hensinger, S. Olmschenk, M. J. Madsen, K. Schwab, and C. Monroe, *Nature Physics* **2**, 36 (2006).
- 41** T. Calarco, U. Dorner, P. S. Julienne, C. J. Williams, P. Zoller, *Phys. Rev. A* **70**, 012306 (2004).

- 42** U. Dorner, T. Calarco, P. Zoller, A. Browaeys, and P. Grangier, *J. Opt. B* **7**, 341 (2005).
- 43** D. Kirk, *Optimal Control Theory – An Introduction* (Dover Publications, Mineola, New York, 2004).
- 44** D. J. Tannor, *Introduction to Quantum Mechanics: A Time-dependent Perspective* (University Science Books, Sausalito, 2006).
- 45** S. E. Sklarz and D. J. Tannor, *Phys. Rev. A* **66**, 053619 (2002).
- 46** R. Kosloff, *J. Phys. Chem.* **92**, 2087 (1988).
- 47** B. M. Garraway, *J. Phys. B* **33**, 4447 (2000)
- 48** T. E. Skinner, T. O. Reiss, B. Luy, N. Khaneja, and S. J. Glaser, *J. Magn. Reson.* **172**, 17 (2005).
- 49** J. J. García-Ripoll, P. Zoller, and J. I. Cirac, *Phys. Rev. Lett.* **91**, 157901 (2003).
- 50** C. Rangan, A. M. Bloch, C. Monroe, and P. H. Bucksbaum, *Phys. Rev. Lett.* **92**, 113004 (2004).
- 51** Ch. Roos, Th. Zeiger, H. Rohde, H. C. Nägerl, J. Eschner, D. Leibfried, F. Schmidt-Kaler, and R. Blatt, *Phys. Rev. Lett.* **83**, 4713 (1999).
- 52** C. Pozrikidis, *A Practical Guide to Boundary Element Methods* (Chapman & Hall/CRC, Boca Raton, London, New York, Washington D.C., 2002).
- 53** B. Brkić, S. Taylor, J. F. Ralph, and N. France, *Phys. Rev. A* **73**, 012326 (2006).
- 54** D. Cubric, B. Lencova, F. H. Read, and J. Zlamal, *Nucl. Instr. Meth. Phys. Res. A* **427**, 357 (1999).
- 55** URL: <http://www.uni-ulm.de/qiv/staff/ksinger/bem>.
- 56** CPO program, available at [www.electrooptics.com](http://www.electrooptics.com).
- 57** FEMLAB program, available at [www.femlab.com](http://www.femlab.com).

### 3

## Transport Dynamics of Single Ions in Segmented Microstructured Paul Trap Arrays

*R. Reichle, D. Leibfried, R. B. Blakestad, J. Britton, J. D. Jost, E. Knill, C. Langer, R. Ozeri, S. Seidelin, and D. J. Wineland*

### 3.1

#### Introduction

Quantum information processing is a rapidly evolving field of physical science. Its practical importance arises from the exponential speedup in computation of certain algorithmic tasks over classical computation [3]. Building an actual device that can process quantum information, however, is technologically difficult due to the need for qubits that can be processed and read out with high fidelities and the extreme sensitivity of the quantum mechanical states stored in these units against external uncontrolled perturbations. A promising technical approach as shown over the last decade, is to use strings of ions as physical qubits confined in linear electromagnetic Paul traps [1, 4]. These strings are stored in a single trap and constitute a one dimensional crystallized structure whose vibrational modes can be laser cooled to their ground states. The strong mutual coupling of the ions by Coulomb forces in such a crystal has been proposed and utilized to create arbitrary superpositions of quantum states of the ionic internal states ( [4–6]). In the last few years methods were developed that enable quantum state engineering with high precision and long coherence times [7–11]. The necessary criteria [12] for large-scale quantum computation have been demonstrated in the past years, and small algorithms have been implemented successfully [13–17]. However, as in other approaches aiming towards quantum computation, scaling to many qubits is challenging. Considerable overhead is required by quantum error correcting schemes that permit robust quantum computation and make large-scale implementations feasible. To scale up a linear string of many ions, a rapidly growing number of vibrational degrees of freedom needs to be controlled and cooled to the ground state for reliable processing. This is extremely difficult to realize. A more recent proposal [1, 2] has been made to circumvent this problem by using small arrays of a few qubits that are shuttled around

in two-dimensional microstructures to process and store quantum states at various locations.

An initial systematic study showed that coherent transport of ions in linear trap arrays is possible with nearly no loss in contrast during the motion [18]. In this experiment an adiabatic transport of a qubit was performed over a distance of 1.2 mm in a time span of about 54  $\mu$ s with negligible heating. Currently, there are strong efforts under way to demonstrate the possibility of building large-scale ion trap structures. For example, suggestions have been made to combine miniaturized ion chips directly with CMOS electronics to handle the resources required to control the many electric potentials [19]. Moreover, fast transport requires excellent experimental control of all these potentials.

A detailed scheme of how a viable architecture of an ion trap processor could look has been recently studied by Steane [20], fully incorporating quantum error correcting codes. The physical gate rate of this proposed 300 qubit processor unit was found to be limited by

$$\tau_g = \frac{2}{\nu_{\text{COM}}} + \frac{10}{\nu_r} + \tau_{\text{cool}} + \tau_p \approx \text{a few } \mu\text{s}, \quad (3.1)$$

with the first two terms being an average time of the part of a typical gate that involve motion that is times for splitting ( $\sim 2\nu_{\text{COM}}^{-1}$ ), recombining and moving ( $\sim 10\nu_r^{-1}$ ) a small ion string, where  $\nu_{\text{COM}}$  and  $\nu_r$  are typical axial and radial trapping frequencies, respectively. The last two terms correspond to cooling after the transport has been done, and the time duration of conducting the actual phase gate, respectively. On the other hand, if large amounts of energy are transferred to the ions, longer cooling times might be needed. Inserting typical operating conditions shows that the first two terms make up a considerable part of the performance of the physical gate rate. In order to keep this part as small as possible we need designs for electrode structures enabling fast qubit transport.

In the following we present a theoretical framework that governs the transport dynamics of ions trapped in a time varying external potential. In Sect. 2 the equations of motion for the transport are derived. Sect. 3 discusses the general classical solution in terms of an Ermakov parametrization. This approach is useful to express the quantum approach presented in Sect. 5, which uses the Heisenberg picture following the approach of Kim et al. [21]. In Sect. 4 we point out some well-known properties of a quantum harmonic oscillator exposed to a transporting force for the simpler case when its frequency is kept constant. Sect. 5 presents the general quantum solutions and the interrelation between classical and quantum transport. Based on this framework we discuss in Sect. 6 a well-controlled regime for the transport and also include first order perturbations to the transport dynamics. In Sect. 7, we present

numerical optimization routines to extract optimum switching of potentials for the transport and study miniaturization of electrode structures to estimate the required resources for a well-controlled transport. Finally, a simple electrode model is used to find a practical rule for the segmentation of ion traps revealing insight into the resources needed for large-scale layouts, that should be also applicable for more general trap arrays.

## 3.2

### Classical Equations of Motion

A linear segmented Paul trap, e.g. as used in recent experiments [5, 14–16, 22, 24], consists typically of two alumina wafers with gold coated electrode surfaces of a few micrometer thickness. The slotted wafers provide electrical RF and DC fields for 3D confinement of ions. The arrangement for control electrodes is schematically sketched in Fig. 3.3 where only a single layer is shown. The confinement along the  $x$ -axis is achieved solely by electrostatic fields whereas the remaining two orthogonal radial directions correspond to a dynamical trapping by ponderomotive RF forces. In this article we limit ourselves to transport along a single dimension  $x$  from  $-b/2$  to  $b/2$ . If we denote the coordinate of the ion in the laboratory frame by  $q$  then we have from Newton's equation of motion

$$\ddot{q}(t) + \frac{Q}{m} \frac{\partial \phi(q, t)}{\partial q} = 0, \quad q(-t_0) = -\frac{b}{2}, \quad \dot{q}(-t_0) = 0, \quad (3.2)$$

with two initial conditions as the equations on the rhs;  $Q$  is the elementary charge and  $m$  the mass of the transported ion. We assume a time interval and location of the ion starting at  $-t_0$  and  $-b/2$ , and ending at  $+t_0$  and  $b/2$ , respectively. In order to make use of coherent states of a harmonic oscillator (that do not spread in time) we are interested in designing the time-dependent electrical potential as

$$\phi(q, t) = \phi_{\text{local}}(q - q_0(t)) + \varphi_0(t), \quad (3.3)$$

where  $\phi_{\text{local}}(q) \sim m\omega_0^2 q^2 / 2Q$  is purely quadratic with constant curvature in a sufficiently large range around the minimum, and  $\varphi_0(t)$  is a time-dependent offset with no influence on the dynamics. Here, we prescribe the dynamics by specifying a desired harmonic frequency  $\omega_0$  and the temporal shift of the harmonic well by a *transport function*  $q_0(t)$ . The residual, uncontrolled force caused by insufficient flexibility in creating the desired harmonic potential deteriorates the transport performance. Its effect can be described by the dif-

ference potential or residual acceleration, i.e.

$$\begin{aligned}\phi_{\text{res}}(q, t) &= \phi(q, t) - \varphi_0(t) - \frac{m\omega_0^2(q - q_0(t))^2}{2Q} \quad \text{and} \\ a_{\text{res}}(q) &= -\frac{Q}{m} \frac{\partial \phi_{\text{res}}(q)}{\partial q},\end{aligned}\quad (3.4)$$

respectively. Due to imperfect realization of the harmonic well  $\phi_{\text{res}}(q, t)$  adds fluctuating parts to the ideal harmonic potential as a function of position or time, critically depending on the electrode structure used. In Sect. 3.7 we will discuss a numerical scheme for approximating  $\phi(q, t)$  based on superpositions of individual electrode potentials in an optimal way.

We finally can write down the classical equation of motion

$$\ddot{u} + \omega_0^2 u = -\ddot{q}_0(t) + a_{\text{res}}(u + q_0(t)) \quad (3.5)$$

which we transformed into a frame moving with  $q_0(t)$  by  $u = q - q_0$ . The net acceleration on the rhs corresponds to an external force and displaces the ion from its equilibrium position  $u = 0$  in this frame. Since we will treat only the first two perturbation terms we expand the final equation of motion around the minimum of the well and rearrange some terms to get

$$\ddot{u} + \omega_0^2 \left(1 - a'_{\text{res}}[q_0(t)]/\omega_0^2\right) u - a''_{\text{res}}[q_0(t)]/2 u^2 + \dots = -\ddot{q}_0(t) + a_{\text{res}}[q_0(t)] \quad (3.6)$$

where primes denote differentiation with respect to  $u$ . For the following discussion we abbreviate  $\omega^2(t) = \omega_0^2(1 - a'_{\text{res}}[q_0(t)]/\omega_0^2)$  and write  $f(t) = -\ddot{q}_0(t) + a_{\text{res}}[q_0(t)]$  for the rhs of Eq. (3.6). For certain electrode structures, we can disregard terms involving the second and higher order derivatives of  $a_{\text{res}}(q)$  (cf. Sect. 3.7). We will make this assumption throughout the paper. In that case Eq. (3.6) simplifies to the equation of motion of a parametrically driven and forced harmonic oscillator with the Hamiltonian

$$\mathcal{H}(t) = \frac{p^2}{2m} + \frac{m\omega^2(t)}{2} u^2 - mf(t)u \quad (3.7)$$

and  $p = m\dot{u}$ .

### 3.3

#### Classical Dynamics of Ion Transport

To obtain a general classical solution with an arbitrary frequency modulation we first consider the formalism which is most often used in conjunction with time-dependent invariants within so called Lewis-Riesenfeld methods [30]. These approaches have been shown to be successful in the quantization

of time-dependent harmonic oscillators with many different kinds of time-dependencies. Here, we discuss the general classical solution using the Ermakov equation and its generalized phase equation for time-dependent frequencies. We then employ in Sect. 3.5 the approach of Kim et al. [21] to express the general quantum solution in terms of its classical solution.

### 3.3.1

#### Homogeneous Solution

Neglecting higher order terms we find the homogeneous part of the solution of Eq. (3.6) by setting  $f(t) = 0$ , thus solving

$$\ddot{u}_c + \omega^2(t)u_c = 0 \quad (3.8)$$

for an arbitrary time-dependent frequency  $\omega(t)$ . For this, it is most convenient to make the ansatz

$$u_1 = \rho(t)e^{i\mu(t)} \quad u_2 = \rho(t)e^{-i\mu(t)}, \quad (3.9)$$

introducing an amplitude function  $\rho(t)$  and a phase function  $\mu(t)$ , both real. Inserting Eq. (3.9) into Eq. (3.8) and considering real and imaginary parts results in the two equations

$$\ddot{\rho} - \rho\dot{\mu}^2 + \omega^2(t)\rho = 0, \quad 2\dot{\rho}\dot{\mu} + \rho\ddot{\mu} = 0. \quad (3.10)$$

$\rho$  is an integrating factor for the second equation on the right so that we can write

$$\rho^2\dot{\mu} = 1, \quad (3.11)$$

where we have chosen the integration constant as 1. The constant on the rhs of Eq. (3.11) has the SI units  $m^2 \text{ rad/s}$  that should be taken into account at the end. If we substitute this back into the first equation of Eq. (3.10) we obtain the Ermakov equation for the amplitude function  $\rho(t)$

$$\ddot{\rho} + \omega^2(t)\rho = 1/\rho^3. \quad (3.12)$$

For periods of constant frequency  $\omega = \omega_0$  the general solution is<sup>1</sup>

$$\rho(t) = \pm\omega_0^{-1/2}\sqrt{\cosh\delta + \sinh\delta\sin(2\omega_0t + \theta)}, \quad (3.13)$$

1) The general solution of this equation is easily obtained by first using  $\dot{\rho}$  as an integrating factor with the integration constant  $2\omega \cosh\delta$ . This equation is immediately transformed to a harmonic oscillator by  $x = \rho^2 - \cosh\delta/\omega$ .

where  $\delta, \theta$  are constants of integration, their values depend on the past evolution [30]. The solution for the generalized phase is easily obtained once  $\rho$  is known. From Eq. (3.11) we have

$$\mu(t) = \int_{-t_0}^t dt' \rho(t')^{-2}. \quad (3.14)$$

The general homogeneous solution is then given by

$$u_h(t) = a_c \rho(t) \cos(\mu(t) + \varphi), \quad (3.15)$$

with the classical amplitude  $a_c$  and initial phase  $\varphi$  fixed by the initial conditions.

### 3.3.2

#### Green's Function and General Solution

We use the general framework of Green's functions to define a particular solution to the inhomogeneous case of Eq. (3.6), where we again terminate the expansion, i.e.  $a_{\text{res}}^{(n)}[q] = 0$  for  $n \geq 2$ , to stay in a harmonic regime. Using the two independent homogeneous solutions of Eq. (3.9) we can determine the causal Green's function

$$G(t, t') = \theta(t - t') \rho(t) \rho(t') \sin(\mu(t) - \mu(t')), \quad (3.16)$$

with  $\theta(t - t')$  the Heaviside function. Employing  $G(t, t')$ , a particular solution is given by

$$u_p(t) = \int_{-t_0}^t dt' G(t, t') f(t') = \rho(t) \int_{-t_0}^t dt' \sin(\mu(t) - \mu(t')) \rho(t') f(t'). \quad (3.17)$$

For later convenience we define the auxiliary function

$$\zeta(t) = ie^{-i\mu(t)} \int dt' e^{i\mu(t')} \rho(t') f(t')$$

which will be useful for expressing the general quantum solution. In this notation we can abbreviate the particular solution by  $u_p(t) = \rho(t) \{\zeta(t) + \zeta^*(t)\} / 2$ .

Thus, we obtained the general solution as the sum of the general homogeneous solution Eq. (3.15) and a particular solution

$$u_c(t) = u_h(t) + u_p(t) \equiv \rho(t) / 2 \left\{ a_c e^{i(\mu(t) + \varphi)} + \zeta(t) \right\} + c.c. \quad . \quad (3.18)$$

Higher derivatives, like velocity and acceleration, can easily be found from the general solution in Eq. (3.18) by using the Leibniz rule. For initial conditions where we start in the classical ground state  $a_c = 0$  we define the quantity  $\Xi(t) = \dot{u}_p(t) + i\omega(t)u_p(t)$ , assuming that the transport starts at  $-t_0 > -\infty$ ,

i.e. later than the infinite past, and demand that it takes a finite amount of time. With the help of the last definition the energy transferred to the oscillator at instants  $t_1$  (where  $f(t_1) \equiv 0$ ) is then given by

$$\mathcal{W}(t_1) = m |\Xi(t_1)|^2 / 2, \quad (3.19)$$

with

$$\begin{aligned} \Xi(t_1) = \int_{-t_0}^{t_1} dt' \rho(t') & \left( \rho(t_1) \dot{\mu}(t_1) \cos(\Delta\mu_{1t'}) \right. \\ & \left. + \{\dot{\rho}(t_1) + i\omega(t_1)\rho(t_1)\} \sin(\Delta\mu_{1t'}) \right) f(t'), \end{aligned} \quad (3.20)$$

and  $\Delta\mu_{1t'} = \mu(t_1) - \mu(t')$ . We will call  $\Xi(t)$  the adiabatic suppression amplitude and its absolute square the adiabatic suppression factor. Thus, we have derived the classical energy transfer for arbitrary frequency evolutions and arbitrary external transport forces. To evaluate this expression one first must solve for the explicit time-dependence of  $\rho$  and  $\mu$  according to Eqs. (3.12), (3.14) by integrating the Ermakov equation and the phase equation, and finally compute the transferred energy at different times using Eqs. (3.19), (3.20).

### 3.3.3

#### Adiabatic Limit

Since we are mainly interested in an adiabatic solution we can simplify the last expression by considering adiabatic expansions of the homogeneous solution for a parametrically driven harmonic oscillator. We introduce an adiabatic time scale  $\mathcal{T}$  such that

$$\dot{\omega}/\omega = \mathcal{T}^{-1} \quad \text{for} \quad \mathcal{T} \gg \omega^{-1}. \quad (3.21)$$

The general adiabatic expansion of the differential equations Eqs. (3.11), (3.12) is readily obtained [29]

$$\begin{aligned} \rho(t) &= \frac{1}{\sqrt{\omega(t)}} + \frac{1}{8} \frac{\ddot{\omega}(t)}{\omega(t)^{7/2}} - \frac{3}{16} \frac{\dot{\omega}(t)^2}{\omega(t)^{9/2}} + \dots \quad \text{and} \\ \dot{\mu}(t) &= \omega(t) - \frac{1}{4} \frac{\dot{\omega}(t)}{\omega(t)^2} + \frac{3}{8} \frac{\dot{\omega}(t)^2}{\omega(t)^3} + \dots \end{aligned} \quad (3.22)$$

This procedure is equivalent to a perturbative approach on the first term in Eq. (3.12) [30]. We require that at instants  $-t_0, t_1$ , i.e. at times when we measure the oscillator's energy, the frequency has settled into a constant. Also for the following discussion we define that the oscillator's initial frequency at  $-t_0$  is  $\omega(-t_0) = \omega_0$ , so that  $\rho(-t_0) = 1/\sqrt{\omega_0}$ ,  $\dot{\rho}(-t_0) = 0$ . Taking into account

only the lowest order of the expansion in Eq. (3.22) the expression in Eq. (3.20) reduces to

$$\Xi(t_1) = \sqrt{\omega(t_1)} \int_{-t_0}^{t_1} dt' f(t') \omega(t')^{-1/2} e^{i\Delta\mu_{1t'}} \quad \text{with} \quad \Delta\mu_{1t'} = \int_{t'}^{t_1} d\tau \omega(\tau) \quad (3.23)$$

providing the adiabatic energy transfer in the first order of frequency modulation.

### 3.4

#### Quantum and Classical, Dragged Harmonic Oscillators with Constant Frequency

Husimi [27] and Kerner [28] independently considered the forced quantum mechanical oscillator and found exact analytical expressions for their wavefunctions and propagators. We review some of their early ideas because they provide insight into the close relationship of the quantum and classical solution. In this paragraph we assume the frequency is independent of time. The corresponding Hamiltonian is given by Eq. (3.7) with  $\omega(t) = \omega_0$ .

Following Husimi and Kerner, we can "uncouple" the classical oscillation by the transformation

$$\Psi(u, t) = \phi(u', t) \exp(im\dot{u}_c u' / \hbar), \quad (3.24)$$

with  $u' = u - u_c$  and  $u_c$  at first undefined. Inserting Eq. (3.24) into the time-dependent Schrödinger equation gives

$$\begin{aligned} i\hbar \frac{\partial \phi}{\partial t} &= \left( -\frac{\hbar^2}{2m} \frac{\partial^2}{\partial u'^2} + \frac{1}{2} m\omega_0^2 u'^2 \right) \phi + m(\ddot{u}_c + \omega_0^2 u_c - f) u' \phi \\ &\quad - (m/2)(\dot{u}_c^2 - \omega_0^2 u_c^2 + 2f u_c) \phi. \end{aligned} \quad (3.25)$$

On the rhs we see that we can make the second term vanishing if we choose  $u_c$  to satisfy

$$\ddot{u}_c + \omega_0^2 u_c - f = 0,$$

i.e. if  $u_c$  satisfies the classical solution of Eq. (3.7). With this choice one can easily identify the classical action  $L(t) = (m/2)(\dot{u}_c^2 - \omega_0^2 u_c^2 + 2f u_c)$  of a forced harmonic oscillator in the third term on the rhs of Eq. (3.25). Furthermore, if we make the ansatz

$$\phi(u', t) = \chi(u', t) \exp \left[ \frac{i}{\hbar} \int_{-\infty}^t dt' L(t') \right],$$

we can absorb this term as a time-dependent phase into  $\phi$ . The remaining part of the wavefunction,  $\chi$ , then needs only to obey the usual harmonic oscillator wave equation in the frame defined by the classical trajectory with its internal coordinate  $u'$

$$i\hbar \frac{\partial \chi}{\partial t} = \left( -\frac{\hbar^2}{2m} \frac{\partial^2}{\partial u'^2} + \frac{1}{2} m\omega_0^2 u'^2 \right) \chi. \quad (3.26)$$

In this way one can achieve a separation of the forced harmonic oscillator from the unforced oscillator in a frame moving with the classical trajectory. The wavepacket does not become deformed by the homogeneously acting force. The quantum solution becomes displaced and only a phase is accumulated.

To determine further properties we can assume now a stationary state with energy  $\epsilon_n$  for the solution of Eq. (3.26)

$$\chi_n(u', t) = u_n(u') \exp(-i\epsilon_n t) \quad \epsilon_n = (n + \frac{1}{2})\hbar\omega_0,$$

and evaluate transition probabilities at time  $t$  for the oscillator to be in the number state  $u_m$  if it was initially in the number state  $u_n$

$$P_{mn}(t) = \left| \int_{-\infty}^{\infty} u_m(u - u_c(t)) u_n(u) e^{im\dot{u}_c(t)u/\hbar} du \right|^2.$$

Husimi and Kerner showed that these transition moments can be evaluated analytically

$$P_{mn}(t) = (\mu!/\nu!) \gamma^{\nu-\mu} e^{-\gamma} (L_{\mu}^{\nu-\mu}(\gamma))^2 \quad \text{with} \quad (3.27)$$

$$\gamma(t) = m/2\hbar\omega_0 |\dot{u}_c + i\omega u_c|^2$$

by using generating functions for the Hermite polynomials [27,28]. In Eq. (3.27),  $\nu$  is the greater while  $\mu$  is the lesser of  $m$  and  $n$ , respectively.  $L_{\mu}^{\nu-\mu}$  denote the associated Laguerre polynomials, and its time-dependent argument  $\gamma(t)$  describes the classical energy transfer in units of  $\hbar\omega_0$ . From Eq. (3.27) we see the classical character of the quantum solution: the transition probabilities are solely defined by the classical quantity  $\gamma(t)$ . Also, if we consider starting from the ground state  $n = \mu = 0$  and using  $L_0^{\nu}(\gamma) \equiv 1$  the probability distribution  $P_{m0}$  becomes a Poissonian, and thus we find the signature of a coherent state.

With this relation the expectation values for the mean energy and the dispersion of the energy distribution are then immediately obtained

$$\langle E_m \rangle_n \equiv \hbar\omega_0 \left( \sum_m m P_{mn} + 1/2 \right) = \hbar\omega_0 \left( n + \gamma + 1/2 \right) = \epsilon_n + \hbar\omega_0 \gamma \quad (3.28)$$

$$\langle(\Delta E_m)^2\rangle_n \equiv (\hbar\omega_0)^2 \langle(m - \langle m \rangle)^2\rangle = (\hbar\omega_0)^2(2n + 1)\gamma = 2\epsilon_n \hbar\omega_0\gamma,$$

where  $\epsilon_n$  is the initial energy before the force acts on the wavepacket. This is indicated in Eq. (3.28) by the subscripts on the lhs. Corresponding expressions for the classical solution

$$\langle E \rangle_{E_0} = E_0 + \mathcal{W} \quad \langle(\Delta E)^2\rangle_{E_0} = 2E_0\mathcal{W} \quad (3.29)$$

are found if we average over the initial classical phase that are completely analogous to the quantum solutions.<sup>2</sup>  $E_0$  is the classical energy before the transport and  $\mathcal{W} \equiv \hbar\omega_0\gamma(t)$  the classical energy transfer. The mean energy and the energy spread increase linearly with the energy transfer in both solutions although the energy distributions of the classical and quantum solution are quite different [27]. Also, the zero point energy makes a difference between the classical and quantum description. If the system is initialized in its quantum ground state, transport can create a dispersion of the wavepacket due to  $\epsilon_0 > 0$ , while this is not the case for the classical ground state, i.e. if  $E_0 = 0$ .

### 3.5

#### The Dragged Quantum Harmonic Oscillator

Many methods have been developed to find exact quantum states of time-dependent oscillators. The generalized invariant method by Lewis and Riesenfeld [30] has been very successful in finding exact quantum motion in terms of wavefunctions and propagators. For the interpretation of time-dependent quantum systems and for showing its relationships to their classical solution, however, the Heisenberg picture is more appropriate since the Heisenberg operators for position and momentum obey similar equations of motion than the corresponding classical quantities. In this paragraph we aim to interpret the quantum solution using its classical analogue and therefore use the general approach of Kim et al. [21] that is based on the general invariant theory but acts in a Heisenberg picture, in contrast to the original approach.

The general invariant theory starts out by defining an invariant operator  $I(t)$  that satisfies the Heisenberg equation of motion. Ji et al. [23] used a Lie algebra approach to find the most general form of the solution with some integration constants  $c_i$ ,  $i = 1, 2, 3$ , arbitrary defining the initial conditions (see discussion at the end of this paragraph). If we fix these parameters according to the conditions of Eq. (3.4) in [25] the generalized invariant is of the form

$$I_T(t) = \omega_I \left( B^\dagger(t)B(t) + \frac{1}{2} \right), \quad (3.30)$$

2) This result is easily derived by averaging the general classical solution in Eq. (3.18) given in Sect. 3.4 for a constant frequency over the phase interval  $[0, 2\pi]$ .

with  $\omega_I$  as a constant of motion, and the annihilation and creation operators are

$$\begin{aligned} B(t) &= \sqrt{\frac{m}{2}} \left\{ \left( \rho^{-1} - i\dot{\rho} \right) \hat{q}(t) - \zeta \right\} + i \frac{\rho}{\sqrt{2m}} \hat{p}(t) \\ B^\dagger(t) &= \sqrt{\frac{m}{2}} \left\{ \left( \rho^{-1} + i\dot{\rho} \right) \hat{q}(t) - \zeta^* \right\} - i \frac{\rho}{\sqrt{2m}} \hat{p}(t). \end{aligned} \quad (3.31)$$

It holds that  $[B(t), B^\dagger(t)] = 1$ , where  $B(t), B^\dagger(t)$  are solely represented by the classical quantities  $\rho = \rho(t), \mu = \mu(t), \zeta = \zeta(t)$  as introduced in previous paragraphs.  $\hat{q}(t), \hat{p}(t)$  refer here to the Heisenberg operators for position and momentum and we have assumed in addition that  $f(-t_0) = 0$ .

From the Heisenberg equations of motion for  $B$ , i.e.  $dB(t)/dt = -i[B(t), \mathcal{H}(t)]$ , one can obtain the simple time evolution for these annihilation and creation operators

$$B(t) \equiv e^{-i\mu(t)} B(-t_0) \quad B^\dagger(t) \equiv e^{i\mu(t)} B^\dagger(-t_0), \quad (3.32)$$

with  $\mu(t)$  the phase function. Their evolution in time is a simple time-dependent phase-shift mediated by the generalized classical phase referenced to the initial time  $-t_0$ . This last property guarantees the time-independence of the invariant and the equivalence to the Hamiltonian (if  $f(-t_0) = 0$ ) at the time  $-t_0$ :

$$I_T(t) = I_T(-t_0) = \mathcal{H}(-t_0). \quad (3.33)$$

Following Kim et al. we can equate hermitian and anti-hermitian parts on both sides of Eqs. (3.32) by using the relations Eqs. (3.31) to determine the time-dependent Heisenberg operators for position and momentum

$$\hat{q}(t) = \rho(t) \left\{ \hat{q}(-t_0) \sqrt{\omega_0} \cos \mu(t) + \frac{\hat{p}(-t_0)}{m\sqrt{\omega_0}} \sin \mu(t) \right\} + u_p(t) \quad (3.34)$$

$$\begin{aligned} \hat{p}(t) &= \hat{q}(-t_0) m \sqrt{\omega_0} \left[ \dot{\rho}(t) \cos \mu(t) - \rho(t)^{-1} \sin \mu(t) \right] \\ &\quad + \frac{\dot{\rho}(-t_0)}{\sqrt{\omega_0}} \left[ \rho(t)^{-1} \cos \mu(t) + \dot{\rho}(t) \sin \mu(t) \right] + m \dot{u}_p(t), \end{aligned} \quad (3.35)$$

where  $\hat{q}(-t_0), \hat{p}(-t_0)$  denote position and momentum operator at time  $-t_0$ , respectively. Similar as  $u_p(t)$ , the classical velocity can be expressed as  $2\dot{u}_p(t) = \{(\dot{\rho} - i\rho^{-1})\zeta + (\dot{\rho} + i\rho^{-1})\zeta^*\}$ .

Our chosen initial conditions, Eq. (3.33), cast momentum and position operators into their standard form

$$\hat{q}(-t_0) = \frac{1}{\sqrt{2m\omega_0}} \left\{ B + B^\dagger \right\} \quad \hat{p}(-t_0) = -i \sqrt{\frac{m\omega_0}{2}} \left\{ B - B^\dagger \right\} \quad (3.36)$$

taking  $\hbar = 1$ . Kim et al. define a more general Fock state space based on number states of the invariant rather than on the Fock state space of the Hamiltonian and point out its importance and advantageous properties. However, due to our choice of the initial conditions these two state spaces are identical and their distinction is irrelevant for our discussion. We can define the Fock basis in the usual way by taking the operators at  $-t_0$  according to

$$|n\rangle_B = |n, -t_0\rangle_B \quad \text{with} \quad |n, t\rangle_B = \frac{B^{\dagger n}(t)}{\sqrt{n!}} |0, t\rangle_B, \quad (3.37)$$

where the vacuum state  $|0, t\rangle_B$  is extracted from  $B(t)|0\rangle_B = 0$ . Furthermore, we introduce the time-independent coherent states in this Fock basis

$$|\alpha\rangle = e^{-|\alpha|^2/2} \sum_{n=0}^{\infty} \frac{\alpha^n}{\sqrt{n!}} |n\rangle_B, \quad (3.38)$$

with the complex amplitude  $\alpha = |\alpha|e^{-i\varphi}$ , because these states are the closest quantum equivalent to the classical solution and include the oscillator ground state for  $\alpha = 0$ . With these definitions the expectation values for the Heisenberg position and momentum operators from Eqs. (3.34,3.35) can be calculated using Eq. (3.36) and Eq. (3.38)

$$\begin{aligned} \langle \alpha | \hat{q}(t) | \alpha \rangle &= \sqrt{\frac{2}{m}} \rho(t) |\alpha| \cos[\mu(t) + \varphi] + u_p(t) \\ \langle \alpha | \hat{p}(t) | \alpha \rangle &= \sqrt{2m} |\alpha| \left\{ \dot{\rho}(t) \cos[\mu(t) + \varphi] - \rho^{-1}(t) \sin[\mu(t) + \varphi] \right\} + m\dot{u}_p(t) \\ &\equiv m \frac{d}{dt} \langle \alpha | \hat{q}(t) | \alpha \rangle. \end{aligned} \quad (3.39)$$

This way we retrieve exactly the same form for the mean values of position and momentum for the quantum solution as we obtained in Eq. (3.18) for the classical solution. If we disregard the zero point energy in  $\langle \alpha | \mathcal{H}(-t_0) | \alpha \rangle / \omega_0 = |\alpha|^2 + 1/2 \sim |\alpha|^2$  and set the matrix element equal to the potential energy at a classical turning point, we have  $a_c \approx \sqrt{2}x_0|\alpha|$  making the homogeneous solution of the classical and quantum formulations and hence the total solution identical. Here,  $x_0 = \sqrt{\hbar/\omega_0 m}$  is the extension of the ground state wave function of the harmonic oscillator. Alternatively, a full quantum description in the Schrödinger picture can be obtained by employing the time evolution operator that can be represented as a product of time-dependent displacement and squeezing operators [21,27].

Similarly we can compute the dispersions of  $\hat{q}(t), \hat{p}(t)$  in the coherent state

$$\langle \alpha | (\Delta q(t))^2 | \alpha \rangle = \rho^2/2m \quad \langle \alpha | (\Delta p(t))^2 | \alpha \rangle = (\rho^{-2} + \dot{\rho}^2)m/2. \quad (3.40)$$

From the dispersion for the momentum we see that the wavepacket generally spreads solely due to the presence of the terms  $\rho^2$  and  $\dot{\rho}^2$ . These matrix elements do not depend on the force because the force acts homogeneously in space and equally on the whole wavepacket. After periods of frequency modulations the dispersions in Eq. (3.40) are both time-dependent and exhibit oscillatory behaviour revealing a certain amount of squeezing [23]. For example, if we assume that after the transport we end up with a nonzero  $\delta$  we can use the exact solution in Eq. (3.13) and evaluate the rhss of Eqs. (3.40). Then, the dispersions for  $q(t), p(t)$  are proportional to

$$(\cosh \delta \pm \sinh \delta \sin(2\omega_0 t + \theta)), \quad (3.41)$$

distinguishable only by the  $+$  and  $-$  sign and constant prefactors, respectively. Therefore after the transport, the dispersions oscillate with twice the harmonic frequency and a relative phase shift of  $\pi$ . The strength of this squeezing oscillation is thus solely ruled by the classical quantity  $\delta$ .

Finally, our classical initial conditions  $\rho(-t_0) = 1/\sqrt{\omega_0}$  together with the choice of the free parameters  $c_1 = c_3 = \omega_0/m, c_2 = 0$  which we used to define the annihilation and creation operators in Eqs. (3.34), (3.35), provide the correct initial dispersions of the quantum formulation in this approach

$$\langle \alpha | (\Delta q(-t_0))^2 | \alpha \rangle = x_0^2/2 \quad \langle \alpha | (\Delta p(-t_0))^2 | \alpha \rangle = \hbar^2/2x_0^2. \quad (3.42)$$

### 3.6

#### Transport Dynamics in a Well-controlled Regime

In the following we consider an idealized situation for the transport, i.e. we assume that we could produce arbitrarily shaped external potentials in the experiment while locally maintaining parabolic potentials around  $q_0$ , i.e.  $1 \gg |a'_{\text{res}}(q_0)|/\omega_0^2$  and  $|\ddot{q}_0| \gg |a_{\text{res}}(q_0)|$  for all positions  $q_0$  or times  $q_0(t)$ . Deviations from these ideal conditions due to constraints in realistic trap configurations will be evaluated in Sect. 3.7. In the ideal case we find from Eq. (3.23)

$$\Xi(t_1) = -e^{i\omega_0 t_1} \int_{-t_0}^{t_1} dt' e^{-i\omega_0 t'} \ddot{q}_0(t'). \quad (3.43)$$

For  $t_0, t_1 \rightarrow \infty$  we arrive at the well-known result that the transferred energy corresponds to the squared modulus of the Fourier transform of the time-dependent force at frequency  $\omega_0$  [34]. Since we can decompose any function into a sum of symmetric and anti-symmetric parts  $q_0(t) = (q_0(t) + q_0(-t))/2 + (q_0(t) - q_0(-t))/2 \equiv q^S(t) + q^A(t)$  we can write

$$|\Xi(t_1)|^2 = \left| \int_{-t_0}^{t_1} dt' \sin(\omega_0 t') \ddot{q}_0^A(t') \right|^2 + \left| \int_{-t_0}^{t_1} dt' \cos(\omega_0 t') \ddot{q}_0^S(t') \right|^2. \quad (3.44)$$

The two parts increase the amount of the transferred energy independently. For a real transport, where start and stop positions differ from each other, we need anti-symmetric parts in the transport function. A simple conclusion from this is that any symmetric part of the transport function can only increase the transferred energy while not contributing to the purpose of the transport, therefore we only need to consider anti-symmetric functions as candidates for transport, i.e. we take  $q_0^S(t) \equiv 0$ . By partially integrating Eq. (3.43) two times and using initial conditions for the start and stop position and velocities Eq. (3.2), we can also rewrite the integral in Eq. (3.43) as a direct functional of  $q_0(t)$  that has a similar appearance but with an additional term. By symbols in this text with an extra tilde we denote quantities that are divided by the half of the transport distance  $b/2$ , e.g.  $\tilde{q}_0(\pm t_0) = q_0(\pm t_0)/(b/2) = \pm 1$ .

The average number of vibrational quanta transferred during transport can now be calculated from Eq. (3.19)

$$\gamma(t_0) = mb^2\omega_0|\tilde{\Xi}(t_0)/\omega_0|^2/8\hbar. \quad (3.45)$$

The energy increase in a transport therefore scales quadratically with the transport distance if the time span is fixed. Before we systematically study expression Eq. (3.43) we will consider two examples for which analytical solutions exist.

### 3.6.1

#### Two Analytical Examples

First we take a sine function for the transport function  $q_0(t)$  as used in the experiments described in [18]

$$\tilde{q}_0(t) = \sin(t\pi/2t_0) \quad \text{for} \quad -t_0 < s < t_0.$$

A graph of this function is given in Fig. 3.1(a). Inserting  $\tilde{q}_0(t)$  into Eq. (3.43) we find

$$\tilde{\Xi}(t_0) \equiv \tilde{\Xi}(x/\omega_0) = \omega_0 \frac{2 \cos(x)}{1 - (2x/\pi)^2} \times \text{phase} \quad \text{with} \quad x = \omega_0 t_0, \quad (3.46)$$

where we converted the time variables to dimensionless units,  $x \equiv \omega_0 t_0$ , so that  $x/2\pi$  corresponds to the number of oscillation cycles. In these variables,  $|\tilde{\Xi}(t_0)/\omega_0|^2$  is independent of the frequency and plotted in Fig. 3.1(b). The energy transfer is decaying overall, but shows some oscillations arising from the dependence on the energy transfer on the phase of the internal oscillation at  $t_0$ . From Eq. (3.45) we see that for an extreme nonadiabatic transport, i.e.  $x \approx 0$ , we have gained the full potential energy of  $m\omega_0^2 b^2/2$ . Depending on the exact transport duration we observe regular intervals where the energy drops to zero and no energy remains in the internal oscillator's motion after the

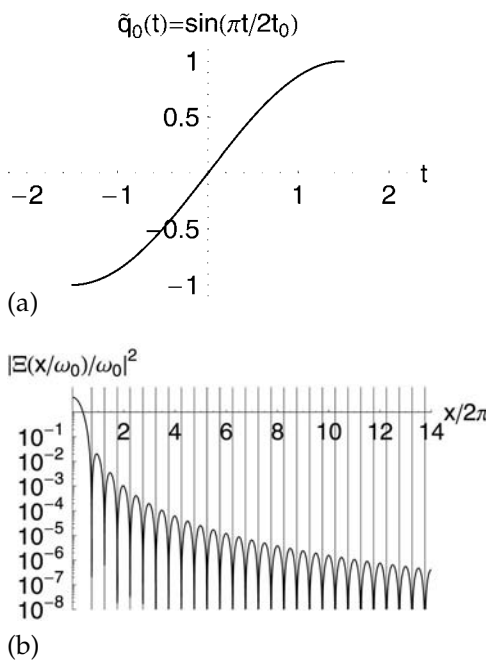


**Fig. 3.1** Sinusoidal transport. In (a) a normalized transport function for a sine transport is shown with a transport in  $2t_0 = 3$  time units. (b) shows the energy transfer as a function of  $x/2\pi = t/T$ , with  $T = 2\pi/\omega$  the period of the associated oscillation frequency. Zeros occur at the positions  $x/2\pi = (2n + 3)/4$  with  $n = 0, 1, \dots$ . See text for details.

interval length  $2t_0$ . This is due to the phase sensitivity of the transport. From Eq. (3.46) we have the proportionality  $|\tilde{\Xi}|^2 \propto (1 + \cos(2x))$ , so that we expect the first zero for  $x/2\pi = 1/4$ . However, for a transport in a harmonic well we need at least half an oscillation period for the ion to move to the other turning point, therefore we have instead  $x/2\pi = 3/4$  which is seen in Fig. 3.1(b) as the first root of the adiabatic factor. The denominator in Eq. (3.46) cancels the first root. The adiabatic energy transfer corresponds to the envelope of this function and is given by  $4/(1 - (2x/\pi)^2)^2$ . As we will see in the following the decay of the envelope can be sped up for different choices of the transport function.

Ideally, we want to have  $mb^2\omega_0|\tilde{\Xi}/\omega_0|^2/8\hbar < 1$  in order to limit the maximum transferred energy to a few vibrational quanta. Let us consider some typical parameters for traps currently in use; we choose the axial frequency  $\omega = 2\pi \cdot 3$  MHz, a typical average transport distance of about four traps (= control electrode widths), i.e.  $b = 400$   $\mu\text{m}$ , and  $m = 9.01218$   $u$  equal to the mass of a Beryllium ion. Then the adiabatic suppression factor should obey

$$|\tilde{\Xi}/\omega_0|^2 < 2 \cdot 10^{-8}. \quad (3.47)$$

In Fig. 3.1(b) we have not plotted the whole range until this criterion is fulfilled. It is satisfied for about  $x/2\pi > 30$ . Thus, for the given case adiabatic transport happens on a rather long time scale, i.e. durations of  $2 \cdot x/2\pi = 2t_0/T = 60$  cycles. The transport in the experiment [18] which has used this transport function was performed over three times this distance requiring that  $|\Xi/\omega_0|^2$  is lower by a factor of 9 more. The adiabatic envelope has decayed to this value at about  $x/2\pi \approx 52$  yielding a transport duration of  $2t_0/T \approx 104$  cycles. Using a sine transport function the experimentally measured limit was around  $2t_0/T \approx 157$  oscillation cycles (where  $2t_0 = 54 \mu\text{s}$  and  $\omega_0 = 2\pi \cdot 2.9 \text{ MHz}$ ). This appears reasonable because the electrode array that was used in [18] was rather sparse, thus not allowing for full control and maintaining the conditions assumed in this paragraph properly. Also, the envelope in this region is quite flat; so within the uncertainties of the experiment, the experimentally observed limit is in reasonable agreement with our estimation.

We will look at an error function transport which turns out to be advantageous to the sine function in the second example

$$\tilde{q}_0(s) = \text{Erf}(2s/t_p)/\text{Erf}(2t_0/t_p) \quad \text{for} \quad -t_0 < s < t_0, \quad (3.48)$$

where we renormalized it to arrive at the times  $\pm t_0$  at the start and end position. In addition we have introduced another time  $t_p$  which is nearly reciprocal to the slope of the transport function at the central point  $t = 0$ . Fig. 3.2(a) is a graph of this function for  $(t_p = 1, t_0 = 3/2)$  in arbitrary time units. Since we truncate the error function, we violate the second initial condition in Eq. (3.2) in a strict sense. However, we are interested only in settings where  $t_p/2t_0 < 1$ , so that this constraint for the velocity can be satisfied arbitrarily well. The adiabatic suppression factor can be evaluated analytically

$$\tilde{\Xi}(x/\omega_0)/\omega_0 \approx 2e^{-y^2/16} \text{Re} \{ \text{Erf}[2x/y + iy/4] \} / \text{Erf}[2x/y] \quad \times \text{phase factor} \quad (3.49)$$

$$\xrightarrow{2x/y \rightarrow \infty} 2e^{-y^2/16} \quad \times \text{phase factor},$$

neglecting the part resulting from the finite initial and final velocities, and using the dimensionless variable  $y = \omega_0 t_p$ . Fig. 3.2(b) illustrates the situation for  $y = 12$  and  $x/2\pi$  in a range of time intervals the same as for the sine transport but also satisfying  $2t_0/t_p > 1$ . It is clear that by using the error function the transport can be performed much faster than with a sine transport function, while still satisfying inequality Eq. (3.47). The full transport can now be performed in  $2x/2\pi \approx 6$  cycles with tolerable energy transfer. Interestingly, taking the limit for large  $2x/y$  ratios in Eq. (3.49) removes the phase-sensitivity completely. However, we also want to note that the differences observed in these examples depend on experimental circumstances, e.g. for very short transport distances, the adiabatic suppression factor does not have

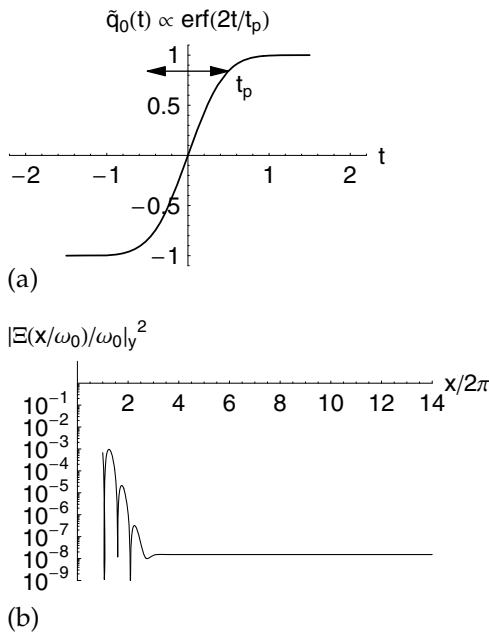


**Fig. 3.2** Error function transport. (a) Graph of the renormalized error function. (b) Adiabatic suppression factor for the error function transport. Details are given in the text.

to be small. In this case the differences between the adiabatic suppression factors is marginal in a qualitative sense. This can be seen in comparing Fig. 3.1(b) and Fig. 3.2(b) for cases when only about  $|\Xi/\omega_0|^2 < 10^{-3}$  is required, e.g. occurring for transport distances much less than an electrode width. On the other hand we find an interesting and advantageous distance scaling behaviour from Eq. (3.49): transporting longer distances does not require much longer time intervals. For example, Steane [20] estimated that within large-scale operation for the processing of a typical gate an average transport distance of  $\approx 22$  traps is needed. By employing an error function transport we find that this is feasible with less than a quantum of transferred energy using the parameters ( $y = 13, x/2\pi = 4$ ), i.e. in already about 8 oscillation cycles, only about a third more time than for a transport over 4 traps. The average velocity for such a transport is then considerably higher.

## 3.6.2

**Near-optimum Transport Functions**

In an attempt to optimize the transport function we can expand expression Eq. (3.49) up to the first order correction [31]

$$\Xi(x/\omega_0)_y \xrightarrow{r \rightarrow \infty} 2\omega_0 \left( e^{-b^2} - \frac{e^{-r^2}}{\sqrt{\pi}\sqrt{r^2 + b^2}} \cos(2rb + \arctan(b/r)) \right) / \text{Erf}[r]$$

× phase factor, (3.50)

with  $r = 2x/y \equiv 2t_0/t_p$ ,  $b = y/4$ . Because of  $2rb = x$  the zeros of the suppression factor  $|\Xi|^2$  are equally spaced as in the sinusoidal example if we disregard the phase in the cosine function, i.e. half periods  $\Delta(x/2\pi) = 1/2$  since the particle can arrive from two different turning points at the end of the transport. From this expansion it is clear that the ratio  $r$  basically determines the magnitude of the second term on the rhs of Eq. (3.50) and suppresses the phase sensitivity as it increases. If  $r$  is chosen large enough the energy transfer is dominated by  $b$ . To find some conditions that are close to optimum we proceed in the following way: first, from the transport distance and achievable frequency we can evaluate the upper bound for the adiabatic suppression factor as in Eq. (3.47). Because we have to satisfy  $2t_0 > t_p$  we then choose  $b$  large enough to suppress the first exponential factor to fulfill the given criterion. This procedure defines the asymptotic value of energy transfer for large  $x/2\pi$  as shown in Fig. 3.2(b). We then choose the interval length  $x/2\pi = rb/\pi$  by defining  $r$  such that we are just in the asymptotic range. The near phase-insensitivity can then be thought of as a result of the extremely slow start where the phase information in the limiting case  $r \rightarrow \infty$  in Eq. (3.49) gets totally lost.

## 3.6.3

**High-frequency Limit, Adiabatic Transport, and Approximate Trajectories**

To better understand the behaviour discussed in previous sections, we present a few more general considerations. We write the time-dependence of the transport function according to  $q_0(t) = \vartheta_0(t/t_0) = \vartheta_0(\tau)$  so that  $\vartheta_0$  only depends on the dimensionless variable  $\tau$  (for the error function example we also keep the ratio  $t_p/t_0$  fixed). Making the substitution  $t' \rightarrow \tau$  in the integral in Eq. (3.43) we find

$$\Xi(t_0)/\omega_0 = (\omega_0 t_0)^{-1} \int_{-1}^1 d\tau e^{-i\omega_0 t_0 \cdot \tau} \vartheta_0''(\tau) \times \text{phase factor} \quad (3.51)$$

$$\xrightarrow{\omega_0 t_0 \rightarrow \infty} 2 \cdot \sum_{n=0}^N \frac{\vartheta_0^{(n+2)}(-1)}{(-\omega_0 t_0)^{n+2}} \cos(\omega_0 t_0 + n\pi/2) \times \text{phase factor.}$$

The exponent in the integral relates the two time scales in  $\omega_0$  and  $t_0$ . Using the method outlined in appendix A we expand it into the sum given in the second line in the limit  $\omega_0 t_0 \rightarrow \infty$  assuming that  $\vartheta_0$  is sufficiently smooth. In this expansion the derivatives at the start position (and end position due to anti-symmetry) define the energy transfer in the transport, and thus fully characterize the transport function for the transferred energy in the adiabatic limit. This provides us with a reason for the difference we observed above for the error function and sine examples. The second derivative for the sinusoidal transport is nonzero at  $\pm t_0$  and much larger than in the case of the error function. In the latter all derivatives are damped by a gaussian while the ones for the sine transport alternate. Furthermore, we see that we can in general decrease the transferred energy for larger values of the product  $\omega_0 t_0$ , i.e. by taking  $\omega_0$  to infinity (high-frequency limit), we can lower the adiabatic suppression arbitrarily, on the other hand, slowing down the motion by increasing the length of the duration of the transport  $2t_0$ , we move into the adiabatic regime. For infinitely slow motion we end up with zero transferred energy. These two limiting cases are formally equivalent because the energy transfer depends only on their relative time scale. We can perform the same expansion starting from Eq. (3.43) directly and use the relation  $u_c(t) = [\Xi(t) - \Xi^*(t)]/2i\omega_0$  to find approximate trajectories valid in the same limits

$$u_c(t) = - \sum_{n=0}^N \frac{1}{\omega_0^{n+2}} \left[ \cos\left(\frac{n\pi}{2}\right) q_0^{(n+2)}(t) - \cos\left(\omega_0(t+t_0) - \frac{n\pi}{2}\right) q_0^{(n+2)}(-t_0) \right].$$

### 3.7

## Regularized Trap-electrode Waveforms, Potential Fluctuations and Aspect-ratio Rule

### 3.7.1

#### Determination of Waveforms

So far, we have said nothing about how to determine the waveforms applied to the electrodes. As soon as we have the waveforms at hand for a given model electrode configuration we can determine the magnitudes of perturbations. This is done in the next section. Here, we seek optimum solutions for a given electrode structure in order to keep the uncontrolled part  $\phi_{\text{res}}(q)$  of the total potential in Eq. (3.4) small. The time-dependent electric potential is created by a linear superposition of the available control potentials  $\phi_m(q)$  and dimen-

sionless time-dependent amplitudes  $a_m(t)$  of the form

$$\phi(q, t) = \sum_m a_m(t) \phi_m(q). \quad (3.52)$$

To optimize waveforms for the time-dependent amplitudes for the transport problem we find a measure of the discrepancy by integrating over the residual non-matched part according to

$$\min_{a_m, \varphi_0} \int_{q_0(t) - \delta q}^{q_0(t) + \delta q} |\phi_{\text{res}}(q, t)|^2 dq \quad \forall t \quad (3.53)$$

while  $\phi(q, t)$  from Eq. (3.52) enters here through Eq. (3.4). For any time  $t$  we want to find a set  $a_m, \varphi_0$  for which expression Eq. (3.53) is minimal. The integration is performed over an interval moving with the minimum of the parabolic potential well, i.e.  $[q_0(t) - \delta q, q_0(t) + \delta q]$  and assuming a unity weight factor in the integrand. We do not consider in this range any lag of the ion due to acceleration and deceleration since for an adiabatic transport and experimental conditions the lag is much smaller compared to the optimization range.  $\varphi_0(t)$  represents here another degree of freedom that does not perturb the dynamics but might allow one to more optimally choose the harmonic potential well by arbitrarily offsetting the desired parabolic potential for best fit. Condition Eq. (3.53) is readily converted into a linear system of equations by taking partial derivatives for the amplitudes  $a_m$  and  $\varphi_0$ , and setting them all equal to zero. The minimization problem in Eq. (3.53) then reads

$$\sum_{m=1}^{n_{\text{el}}} a_m(t) \underbrace{\int dq \phi_m \phi_j}_{\mathbf{S}_a} + \varphi_0(t) \underbrace{\int dq \phi_j}_{\underline{\mathbf{S}}_{\varphi_0}} = \frac{m\omega^2}{2Q} \underbrace{\int dq (q - q_0(t))^2 \phi_j}_{\mathbf{K}} \quad \forall j, \quad (3.54)$$

where we dropped the explicit integral bounds and arguments of the potentials  $\phi_m(q)$  for the sake of simplicity. Bold symbols denote matrices, underlined symbols vectors.

The optimization problem can then be formulated in terms of the linear system

$$\mathbf{S}_{+0} \cdot \underline{\mathbf{a}}_{+0} \equiv \begin{pmatrix} \mathbf{S}_a & \underline{\mathbf{S}}_{\varphi_0} \end{pmatrix} \cdot \begin{pmatrix} \underline{\mathbf{a}} \\ \varphi_0 \end{pmatrix} = \eta \underline{\mathbf{K}} \quad \forall t, \quad (3.55)$$

with  $\eta = m\omega^2/2Q$ . All quantities are functionals of  $q_0$  and for a given transport function  $q_0(t)$ , we need to solve the equations at every point in time. As a result we obtain the waveforms  $a_m(t) \equiv a_m[q_0(t)]$ .

Typically we choose an optimization range of  $2\delta q = 0.5W$  for electrodes of width  $W$ . This is usually much smaller than the mean distance between most of the contributing electrodes to the center of the parabolic well. Thus, due to

the slow decay of the axial potentials, the curvatures of distant electrodes are similar, and their contribution differs locally only by a multiplication constant. This is particularly true for experimental situations where the high electrode density typically makes the system Eq. (3.55) nearly singular. A straightforward least-square method, such as

$$\underline{a}_{+0} = \arg \min_{\underline{a}, \varphi_0} \left\{ \|\mathbf{S}_{+0} \cdot \underline{a}_{+0} - \eta \underline{K}\|^2 \right\}, \quad (3.56)$$

is therefore not well suited for finding waveform amplitudes. For high electrode density, a tiny step  $q_0 \rightarrow q_0 + \delta$  might change the individual electrode amplitudes exponentially fast. In these cases the matrix  $\mathbf{S}_{+0}$  in Eq. (3.55) filters out too much information from  $\underline{a}_{+0}$  to invert this system properly. In mathematical language these kind of problems belong to the family of *discrete ill-posed problems* that can be numerically solved using regularization approaches [35]. Here, the lost information is fed back in the minimization process via a Lagrangian multiplier concerning the smoothness of  $a_m(t)$ , or curvature etc. in amplitude space. If we apply a Tikhonov regularization to the given problem we have to solve

$$\underline{a}_{+0, \nu} = \arg \min_{\underline{a}, \varphi_0} \left\{ \|\mathbf{S}_{+0} \cdot \underline{a}_{+0} - \eta \underline{K}\|^2 + \nu^2 \|\mathbf{L}(\underline{a}_{+0} - \underline{a}_{+0}^*)\|^2 \right\} \quad (3.57)$$

in order to determine smooth time-dependent waveform amplitudes  $a_m(t)$ . In Eq. (3.57) the regularization parameter  $\nu$  corresponds to a weight factor between the original least-square minimization and the additional side constraints, while  $\underline{a}_{+0}^*$  can be used to find solutions near a prescribed setting. The smoothing properties of this optimization originate from a common and simultaneous minimization of both terms.  $L$  is a linear operator that can be used to feed back different kinds of information to the amplitudes. For the results given here we took for  $L$  the unity operator, and also  $\underline{a}_{+0}^* = 0$ . Since we only want to limit the amplitudes  $a_m$  to some appropriate experimental values and stabilize the solution, our interest is not to determine the overall minimum of Eq. (3.57) in a self-consistent way. For our convenience we choose  $\nu$  manually to make the parameters compatible with available technology.

We can summarize the advantages of these methods to the current optimization problem:

1. The regularization method selects only nearby electrodes for creating a local parabolic potential, and disregards tiny linear contributions from distant electrodes which would require large amplitudes to effect small changes.
2. The choice of the regularization parameter limits the amplitudes  $a_m$  to practical experimental values.

3. It is robust against changing the electrode density (here, governed by the widths  $W$ ). This will be of importance in the next section.
4. It stabilizes the output waveforms and smoothes sharp features in the time-dependence of the amplitudes. Different constraints can be set via the  $L$  operator, defining bounds or curvatures in the amplitude space.

For more detailed information we refer the reader to the mathematical literature [35]. A typical example of a parabolic potential created through superposition of an array of electrodes and the time-dependence of amplitudes is shown in Fig. 3.4 and further discussed in the next section.

### 3.7.2

#### Potential Fluctuations and Aspect-ratio Rule

Based on a reasonable multi-electrode structure we want to estimate how well we can meet the requirements on transport potentials stated above, in particular, how stringently we can meet  $|a'_{\text{res}}(q_0)|/\omega_0^2 \ll 1$  and  $|a_{\text{res}}(q_0)| \ll |\dot{q}_0|$ . We employ the definition of waveforms and the method from the previous section for extracting the residual, uncontrolled potential  $\phi_{\text{res}}$  from which we perturbatively derive the effect of imperfections on the transport. As a simple model electrode structure for transport in single and multi-layer traps, we use the “railway track” electrode configuration sketched in Fig. 3.3(a) which might be a simple model for transport in single and multi-layer traps [19, 22, 32, 33]. The transport occurs along the long arrow where we assume the ion is held radially by RF fields and controlled axially by the electrical fields arising from the potentials of the “stripe” electrodes depicted in Fig. 3.3(a). We are mainly interested in the scaling behaviour as a guideline for general design rules. Waveforms that are actually used in experiments should be based on more accurate numerical potentials and generalized versions of Eq. (3.54) for all three dimensions. We are finally interested in the trade off between adding electrodes, by shrinking the electrode distances/widths along  $x$ , and the amount of control that is gained in that way.

We can model this arrangement as a sum over the potentials  $\phi_m(x)$  of several infinitely long (in the  $y$ -direction) stripe electrodes that are distributed along the  $x$ -axis

$$\phi(\hat{x}) = \sum_m a_m \phi_m(\hat{x}) = \frac{1V}{\pi} \sum_m a_m \arctan \left( \frac{\hat{W}}{1 + (\hat{x} - m\hat{W})^2 - \hat{W}^2/4} \right), \quad (3.58)$$

where each  $\phi_m(x)$  is the exact solution of the Poisson equation for an infinitely long stripe at position  $m \cdot W$  that is embedded in a ground plane. For convenience we choose for the individual potentials in this basis set a potential on the electrodes of 1 Volt = 1 V. We denote symbols with a hat as quantities

normalized to the ion distance  $z_{\text{ion}}$  to the surface, e.g. the normalized electrode width  $\hat{W} = W/z_{\text{ion}}$ . Fig. 3.3(b) shows the behaviour of  $\phi_0(\hat{x})$  for various geometric aspect ratios  $\hat{W}$ . We see that a plateau-like structure starts to form for  $\hat{W} \sim 2$  and larger resulting in small field gradients along the transport direction in the center of each stripe electrode. The maximum frequency at the center of electrode  $m = 0$  is obtained from

$$\omega^2(\hat{W}, z_{\text{ion}}) = \frac{Q}{mz_{\text{ion}}^2} \frac{\partial^2}{\partial \hat{x}^2} \phi_0(\hat{x}) \Big|_{\hat{x}=0} = -\frac{2a_0}{\pi m} \frac{1eV}{z_{\text{ion}}^2} \frac{\hat{W}}{(\hat{W}/2)^4 + 3\hat{W}^2/2 + 1}. \quad (3.59)$$

The proportionality  $\omega \propto z_{\text{ion}}^{-1}$  is rather unusual and stems from the fact that we scale only a single dimension (along  $x$ ). The last factor of the second equation is solely defined by the aspect ratio  $\hat{W}$  and thus by the geometry of the trap. It exhibits a maximum for  $\hat{W} \approx 0.78$  and decreases only significantly for small width-distance ratios  $\hat{W} < 0.5$ . Using the mass of Beryllium,  $\hat{W} = 1$ , amplitude  $a_0 = -2$  and  $z_{\text{ion}} = 40 \mu\text{m}$  as the ion surface distance for the surface-electrode trap as used in [32], we find an axial frequency of about  $\omega_0 \approx 2\pi \cdot 9 \text{ MHz}$ . We chose this low value for  $|a_0|$  to be compatible with typical maximum voltages as created by CMOS electronics [19]. With these parameters we have created waveforms for the transport of a confining harmonic well utilizing the regularization approach of the last section. We used a set of 41 electrodes while the transport was over four electrode widths,  $\hat{b} = 4$ , around the central electrode 21 of this array. For the transport we used the error function Eq. (3.48) of Sect. 3.6 with a transport duration of 8 oscillation cycles  $x/2\pi = 4$  and  $y = 12$ . We then determined the lowest order deviations from an ideal harmonic potential with constant trap frequency and controlled acceleration,  $\omega(t)/\omega_0$  and  $-a_{\text{res}}(q_0)/\omega_0^2$ , respectively, in Eq. (3.6) for the aspect-ratios  $\hat{W} = (0.5, 1.0, 1.5, 2.0)$ . Figs. 3.4(a) and (b) illustrate an example for the superposed potentials, and for a set of waveform amplitudes for an error function transport in 8 oscillation cycles.

The choice of the regularization parameter  $\nu$  is not obvious, because we have to deal with a set of near-singular matrices all at once. As mentioned earlier we do not aim for self-consistent methods to determine  $\nu$  and an absolute minimum of the expression Eq. (3.57) [35]. In our context we are more interested in a feasible implementation compatible with given experimental constraints. The choice of the regularization parameter affects both the stability of the linear system and the size and smoothness of the amplitude vector  $a_m$ . In a strongly regularized inversion more stability is added to the solution, forcing the amplitudes to be of limited size. Because of this bound the solution can not closely approximate the desired shape of the potential anymore, so the deviations from the ideal case increase. A weak regularization scheme, on the other hand, adapts more closely to the desired potential shape, but

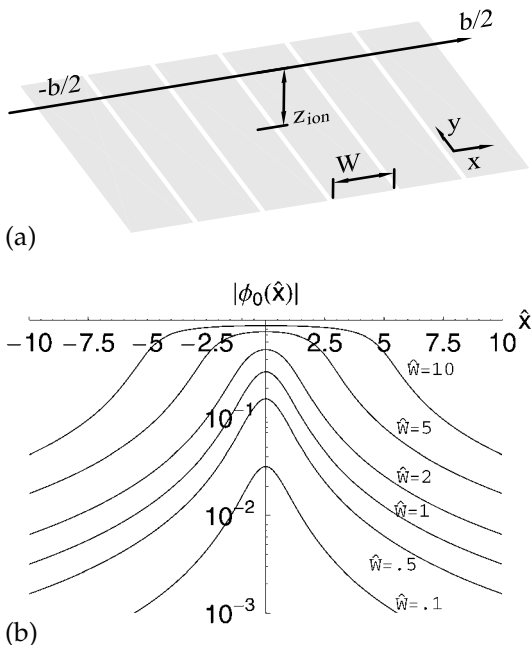


**Fig. 3.3** (a) The electrode array model discussed in the text with  $x$  the axial coordinate,  $z_{\text{ion}}$  the vertical distance of trapped ions to the electrode plane, and  $W$  width of an electrode. The electrode 'stripes' are assumed infinitely extended along  $\pm y$ , and arbitrarily

many along  $\pm x$ . Ions are transported along the long arrow. (b) Modulus of the electric potential of a single electrode at height  $z_{\text{ion}}$  along  $x$  (relative to the center of that electrode and normalized to  $z_{\text{ion}}$ ). The electrode is held at  $-1V$  and  $\hat{W} = W/z_{\text{ion}}$ .

reveals random fluctuations and noise on the solution waveforms  $a_m(t)$ . Also the singular behaviour increases dramatically with an increase of the number of electrodes, and larger parameters  $\nu$  have to be chosen. This latter property makes a direct comparison of the results among various aspect-ratios  $\hat{W}$  difficult. Nevertheless, we can make some qualitative and general statements.

The results for our sample configuration are summarized in Fig. 3.5. The upper graph in Fig. 3.5 displays the uncontrolled acceleration  $-a_{\text{res}}(q_0)/\omega_0^2$ , and the middle and lower graphs the frequency modulation  $\omega(t)$  for various aspect ratios. In both figures a dramatic change of the curves is observed around  $\hat{W} \sim 1$ . While for smaller ratios the frequency fluctuations are in the percentage range (middle panel), the emulation of the potential for larger ratios is much worse due to the constraint  $|a_m| \leq 2$  (lower panel). Frequencies drop by more than 90% already for the  $\hat{W} = 2$  calculation. Only in the strongly regularized scheme, did we find a direct correlation of the solution vector  $a_m$  to the choice of the regularization parameter. In the weakly regularized scheme the amplitudes were limited by other lower bounds, and the wave-

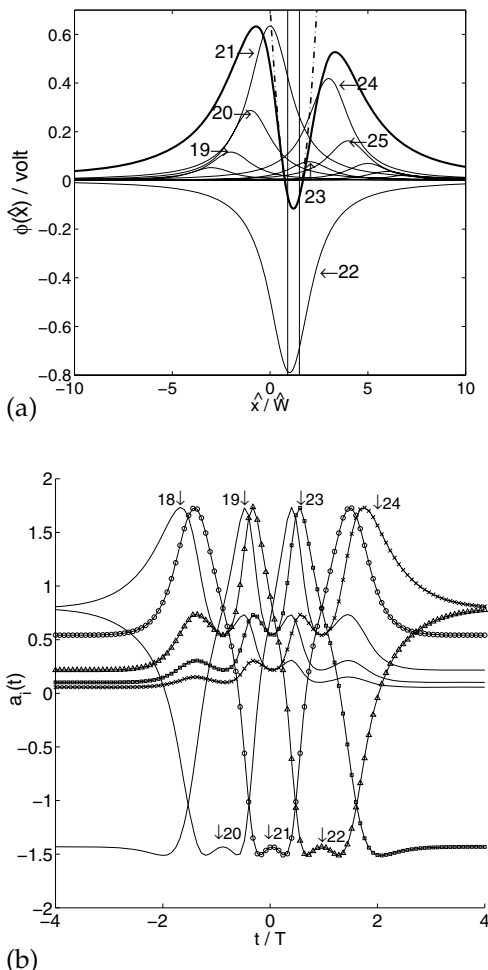


**Fig. 3.4** (a) Creation of a harmonic well by superposing potentials of the electrodes of the stripe configuration of Fig. 3.3(a). The fine lines represent individual electrode potentials that sum up to the total potential represented by the thicker line. The dashed-dotted line shows the ideal harmonic potential and the two vertical lines indicate the range of optimization at this given location. (b)

Waveform amplitudes of electrodes 18 to 24 for a transport from trap 19 to 23 for  $\hat{W} = 1$ . Waveforms from more distant electrodes still contribute but are not shown for the sake of clarity. Amplitudes 21–24 are marked by symbols for better visualizing their traces. The transport is done according to an error function, while the abscissa represents time in units of oscillation periods  $t/T$ .

form solution appeared similar over a large range of  $\nu$ , but exhibited a much noisier behaviour. This enhanced sensitivity is an indication that inclusion of more electrodes (smaller  $\hat{W}$ ) does not improve the quality of the solution anymore. The linear system becomes more singular and exhibits more rank-deficiency, i.e. rows and columns become more equal and their inclusion adds

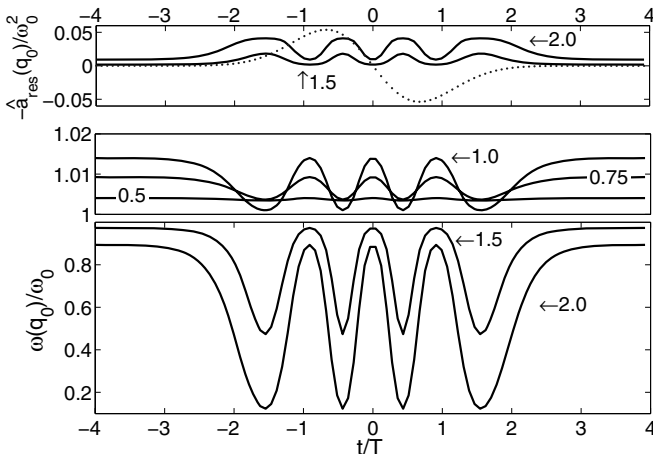


**Fig. 3.5** First and second order perturbation to the transport (thick lines), and their dependence on various aspect ratios  $\hat{W}$ . The abscissa  $t/T$  corresponds to the number of oscillation cycles with period  $T = 2\pi/\omega_0$ . The labels on the graphs annotate the value of  $\hat{W}$ . (Upper panel) Residual, uncontrolled acceleration  $-\hat{a}_{\text{res}}(q_0)/\omega_0^2$  (dimensionless)

which should be compared to  $\ddot{q}_0/\omega_0^2$  (dotted line). This is only given for the large aspect ratios  $\hat{W} = 1.5, 2.0$ . The graphs for smaller ratios would be close to zero on this scale. (Lower panel) Relative frequency modulation  $\omega(q_0)/\omega_0$  during an error function transport for various aspect ratios. For explanations see text.

more redundancy. For the given parameters we observed that for  $\hat{W} = 0.5$  the transition from a regularized to a weakly regularized solution occurred. Therefore, our results indicate that  $\hat{W} = 0.5 - 1.0$  should be optimal for the configuration discussed here. For larger aspect ratios we found that the coverage of curvatures of the individual potentials along the transport axis is not sufficient for the necessary amount of control.

The other constraint, i.e.  $|\hat{a}_{\text{res}}(q_0)| \ll |\ddot{q}_0|$ , of a controlled transport force, has to be interpreted dynamically. Since the acceleration force depends on the time duration in which the transport is performed, this requirement can be violated for a slower transport. In Fig. 3.5 we show that in the initial phase the perturbations overwhelm the transporting acceleration for aspect ratios  $\hat{W} \geq 1.5$  or larger. Results for smaller aspect ratios are not given in this figure because the transport force by far dominates the excess force and lead to a fully controlled transport.

In general, fluctuations in the frequency and transport force affect an energy transfer according to Eq. (3.23). This introduces violations to the symmetry of the transporting force and leads to an enhanced energy transfer as seen from Eq. (3.44). We have not included higher order terms in our discussion, because we aim for experimental conditions to perform a transport in the well-controlled regime. However, they are inevitable for longer transport distances

and other types of motion, such as nonadiabatic transport, or splitting of ion groups where they might lead to large energy transfers.

### 3.8 Conclusions

In conclusion, we have analyzed the dynamics of single ion transport in microstructured linear Paul trap arrays. We have modeled the transport by a forced and parametrically excited harmonic oscillator and have presented a theoretical framework for its description. We have derived exact analytical expressions for the classical as well as quantum dynamics and reviewed their related properties. In particular we have expressed the Heisenberg operators by the approach of Kim et al. [21] through the dynamical quantities of the related classical solution. We have given explicit analytical expressions for the classical energy transfer involved in these transport phenomena and derived expressions for the lowest order deviations from ideal transport that will necessarily appear for unfavourable ion trap layouts. For current trap technology we have evaluated durations for a fast adiabatic transport and found that they depend strongly on the external force employed in the transport. According to these results, the adiabatic single ion transports of reference [18] could be sped up by more than an order of magnitude with negligible energy transfer to the motion. We determined appropriate transport waveforms and found that with an adiabatic transport over four electrode stripes of size roughly equal to the distance of the ion to the nearest electrode and frequencies in the range of  $\approx 9$  MHz is feasible in about 6 oscillation cycles. Our results also indicate that a full control over the transport is available, where perturbations to a harmonic oscillator potential are negligible at all positions and times. By directly relating deviations from these ideal potentials to the aspect ratio of the trap, we have found a practical design rule that should be valid for trap layouts more general than the one given here. The ratio of a control electrode width to the distance to the ion should be in the range  $0.5 - 1$  for a well-controlled regime. Our example suggests that a higher electrode density does not appreciably improve transport performances. This provides important insight into the amount of resources needed to realize large scale implementations of ion trap based quantum computers. Transport in a confining well of constant frequency might also enable continuous cooling processes during the transport. If eventually experiments allow one to maintain a well-controlled regime during the transport, performing quantum processing during transport is conceivable, possibly leading to appreciably shorter processing times.

## Acknowledgement

R.R. acknowledges support by the Alexander von Humboldt Foundation during the course of this work. Work also supported by DTO and NIST. We thank A. Steane, T. Rosenband and J. Wesenberg for helpful comments on the manuscript.

## A Integral Expansion

We employ a mathematical theorem proven within the formalism of h-transforms, see for example theorem 3.2 of [36]: If  $g(\tau)$  has  $N + 1$  continuous derivatives while  $g^{(N+2)}$  is piecewise continuous on the real axis  $[a, b]$  then

$$I(\lambda) = \int_a^b e^{-i\lambda\tau} g(\tau) d\tau \xrightarrow{\lambda \rightarrow \infty} \sum_{n=0}^N \frac{(-1)^n}{(-i\lambda)^{n+1}} \left[ g^{(n)}(b) e^{-i\lambda b} - g^{(n)}(a) e^{-i\lambda a} \right]. \quad (3.60)$$

If we also require  $\lim_{\tau \rightarrow a+} g^{(n)}(\tau) = \lim_{\tau \rightarrow b-} g^{(n)}(\tau) = 0$  for  $n = 0, \dots, N - 1$  it holds that  $I(\lambda) = o(\lambda^{-N})$ .

## References

- 1 D. J. Wineland, C. Monroe, W. M. Itano, D. Leibfried, B. E. King, and D. M. Meekhof, J. Res. Natl. Inst. Stand. Technol. **103**, 259 (1998).
- 2 D. Kielpinski, C. Monroe, and D. J. Wineland, Nature **417**, 709 (2002)
- 3 M. A. Nielsen and I. L. Chuang, Quantum Computation and Quantum Information (Cambridge University Press, Cambridge, 2000).
- 4 J. I. Cirac and P. Zoller, Phys. Rev. Lett. **74**, 4091 (1995).
- 5 D. Leibfried, E. Knill, S. Seidelin, J. Britton, R. B. Blakestad, J. Chiaverini, D. B. Hume, W. M. Itano, J. D. Jost, C. Langer, R. Ozeri, R. Reichle, and D. J. Wineland, Nature **438**, 639 (2005).
- 6 H. Häffner, W. Hänsel, C. F. Roos, J. Benhelm, D. Chek-al-kar, M. Chwalla, T. Körber, U. D. Rapol, M. Riebe, P. O. Schmidt, C. Becher, O. Gühne, W. Dür, and R. Blatt, Nature **438**, 643 (2005).
- 7 D. Leibfried, B. DeMarco, V. Meyer, D. Lucas, M. Barrett, J. Britton, W. M. Itano, B. Jelenkovic, C. Langer, T. Rosenband, and D. J. Wineland, Nature **422**, 412 (2003).
- 8 C. Langer, R. Ozeri, J. D. Jost, J. Chiaverini, B. DeMarco, A. Ben-Kish, R. B. Blakestad, J. Britton, D. B. Hume, W. M. Itano, D. Leibfried, R. Reichle, T. Rosenband, T. Schaetz, P. O. Schmidt, and D. J. Wineland, Phys. Rev. Lett. **95**, 060502 (2005).
- 9 H. Häffner, F. Schmidt-Kaler, W. Hänsel, C. F. Roos, T. Körber, M. Chwalla, M. Riebe, J. Benhelm, U. D. Rapol, C. Becher, and R. Blatt, Appl. Phys. B **81**, 151 (2005).
- 10 P. C. Haljan, P. J. Lee, K.-A. Brickman, M. Acton, L. Deslauriers, and C. Monroe, Phys. Rev. A **72**, 062316 (2005).
- 11 M. J. McDonnell, J.-P. Stacey, S. C. Webster, J. P. Home, A. Ramos, D. M. Lucas, D. N. Stacey, and A. M. Steane, Phys. Rev. Lett. **93**, 153601 (2004).
- 12 D. P. DiVincenzo, Fortschr. Phys. **48**, 771 (2000).
- 13 M. Riebe, H. Häffner, C. F. Roos, W. Hänsel, J. Benhelm, G. P. T. Lancaster,

- T. W. Körber, C. Becher, F. Schmidt-Kaler, D. F. V. James, and R. Blatt, *Nature* **429**, 734 (2004).
- 14** M. D. Barrett, J. Chiaverini, T. Schaetz, J. Britton, W. M. Itano, J. D. Jost, E. Knill, C. Langer, D. Leibfried, R. Ozeri, and D. J. Wineland, *Nature* **429**, 737 (2004).
- 15** J. Chiaverini, D. Leibfried, T. Schaetz, M. D. Barrett, R. B. Blakestad, J. Britton, W. M. Itano, J. D. Jost, E. Knill, C. Langer, R. Ozeri, and D. J. Wineland, *Nature* **432**, 602 (2004).
- 16** J. Chiaverini, J. Britton, D. Leibfried, E. Knill, M. D. Barrett, R. B. Blakestad, W. M. Itano, J. D. Jost, C. Langer, R. Ozeri, T. Schaetz, and D. J. Wineland, *Science* **308**, 997 (2005).
- 17** K.-A. Brickman, P. C. Haljan, P. J. Lee, M. Acton, L. Deslauriers, and C. Monroe, *Phys. Rev. A* **72**, 050306(R) (2005).
- 18** M. A. Rowe, A. Ben-Kish, B. DeMarco, D. Leibfried, V. Meyer, J. Beall, J. Britton, J. Hughes, W. M. Itano, B. Jelenkovic, C. Langer, T. Rosenband, and D. J. Wineland, *Quant. Inf. Comput.* **4**, 257 (2002).
- 19** J. Kim, S. Pau, Z. Ma, H. R. McLellan, J. V. Gates, A. Kornblit, R. E. Slusher, R. M. Jopson, I. Kang, and M. Dinu, *Quant. Inf. Comput.* **5**, 515 (2005).
- 20** A. Steane, quant-ph/0412165
- 21** Hyeong-Chan Kim, Min-Ho Lee, Jeong-Young Ji, and Jae Kwan Kim, *Phys. Rev. A* **53**, 3767 (1996).
- 22** D. Stick, W. K. Hensinger, S. Olmschenk, M. J. Madsen, K. Schwab, and C. Monroe, *Nature Physics* **2**, 36–39 (2006).
- 23** Jeong-Young Ji, Jae Kwan Kim, and Sang Pyo Kim, *Phys. Rev. A* **51**, 4268 (1995).
- 24** W. K. Hensinger, S. Olmschenk, D. Stick, D. Hucul, M. Yeo, M. Acton, L. Deslauriers, C. Monroe, and J. Rabchuk, *App. Phys. Lett.* **88**, 034101 (2006).
- 25** Jeong-Young Ji and Jae Kwan Kim, *Phys. Rev. A* **53**, 703 (1996).
- 26** D. J. Wineland et al., *Proc. 2005 ICOLS conf.*, available at <http://tf.nist.gov/timefreq/general/pdf/2078.pdf>.
- 27** K. Husimi, *Prog. Theor. Phys.* **9**, 381 (1953).
- 28** E. H. Kerner, *Can. J. Phys.*, **36**, 371 (1958).
- 29** R. M. Kulsrud, *Phys. Rev.* **106**, 205 (1957).
- 30** H. R. Lewis, *J. Math. Phys.* **9**, 1976 (1968).
- 31** H. O. Di Rocco and M. Aguirre Tellez, *Acta Physica Polonica A* **106** (6), 817 (2004).
- 32** S. Seidelin, J. Chiaverini, R. Reichle, J. J. Bollinger, D. Leibfried, J. Britton, J. H. Wesenberg, R. B. Blakestad, R. J. Epstein, D. B. Hume, J. D. Jost, C. Langer, R. Ozeri, N. Shiga, and D. J. Wineland, quant-ph/0601173.
- 33** J. P. Home, and A. M. Steane, quant-ph/0411102.
- 34** L. D. Landau and E. M. Lifshitz, *Mechanics* (Pergamon Press, Oxford, 1991).
- 35** P. C. Hansen, *Rank-Deficient and Discrete Ill-Posed Problems: Numerical Aspects of Linear Inversion* (SIAM, Philadelphia, 1998).
- 36** N. Bleistein and R. A. Handelsmann, *Asymptotic Expansions of Integrals* (Dover, New York, 1986).



## 4

## Ensemble Quantum Computation and Algorithmic Cooling in Optical Lattices

*M. Popp, K. G. H. Vollbrecht, and J. I. Cirac*

### 4.1

#### Introduction

Ultracold atoms stored in optical lattices can be controlled and manipulated with a very high degree of precision and flexibility. This places them among the most promising candidates for implementing quantum computations [1–6] and quantum simulations of certain classes of quantum many–body systems [7–14]. However, both quantum simulation and quantum computation with this system face a crucial problem: the temperature in current experiments is too high. In this paper we review two methods that allow to overcome this obstacle. First we show how to perform *ensemble quantum computation* [6]. This method works also in the presence of defects arising from finite temperatures and does not require cooling. The second scheme [15] aims at cooling the system close to the ground state. It combines translation invariant quantum operations with algorithms inspired by quantum computation and will therefore be termed *algorithmic cooling of atoms* [16].

So far, several experimental groups have been able to load bosonic or fermionic atoms in optical lattices and reach the strong interaction regime [17–24]. In those experiments, the typical temperatures are still relatively high. For instance, the analysis of experiments in the Tonks gas regime indicates a temperature of the order of the width of the lowest Bloch band [18], and for a Mott Insulator with harmonic confinement, a temperature of the order of the on-site interaction energy has also been reported [25]. Those temperatures put strong restrictions on the physical phenomena that can be observed with those systems and also on the quantum information tasks that can be carried out with them. They stem from the fact that atoms are loaded adiabatically starting from a Bose–Einstein condensate (in the case of bosons). On the one hand, the original condensate has a relatively high entropy [26] that is inherited by the atoms in the lattice in the adiabatic process. On the other hand, the process may not be completely adiabatic, which gives rise to heating. Thus, it

seems that the only two ways of overcoming these problems are either finding algorithms that are robust against imperfections or to cool the atoms once they have been loaded in the optical lattice.

Let us first consider the case of quantum computation. Once the Mott-Insulator (MI) regime of almost unit occupation per lattice site has been reached, a universal set of quantum gates can then be implemented by individual laser manipulation and inducing cold collisions between the atoms. At the moment, quantum computation with atoms in optical lattices is hindered by three major obstacles: (1) Lack of addressability; (2) Presence of defects; (3) Uncontrolled number of atoms. The first obstacle is due to the fact that the separation between atoms is of the order of an optical wavelength (that of the laser which creates the confining potential) so that in order to address them with a laser one has to focus it close to (or even beyond) the diffraction limit. A possible way to circumvent this problem consists of using optical superlattices [27], or other optical micro traps [28], in which the separation between atoms increases. Quantum gates in these set-ups, however, may become harder than in the standard optical lattice. The second obstacle occurs due to the fact that at finite temperatures there always exist sites that have either no atom or more than one. A single defect will unavoidably spoil any quantum computation, and may also have important consequences in quantum simulations. In present experiments one can estimate that the number of defects is relatively high [29]. This last obstacle can be to a very large extent overcome by a filtering process [30], where the lattice sites in which there is more than one atom are emptied until a single atom remains there. Alternatively, one can define collective qubits independent of the number of atoms per sites [31]. Both procedures should avoid situations in which there exist a defect with no atom present. Finally, the number of atoms which form the quantum computer must be well defined since, otherwise, when performing quantum gates the rest of the atoms will act as an environment. In this paper we review the method in [6] of performing quantum computations in optical lattices (or, more generally, periodic potentials) which circumvents the above mentioned obstacles. One of the fundamental ideas of this scheme is to use defects (which are delocalized in the lattice) in order to mark the atoms that build the quantum computer and to break the translational symmetry in order to obtain addressability. Note that we do not know where the defects are, but their only presence (wherever they are) is sufficient for our purposes. On the other hand, the defects allow us to build "pointer" sites, also delocalized, which will be used to perform a universal set of quantum gates. Note also that since there will be several defects in the atomic sample, we will have several quantum computers running in parallel, randomly distributed all over the optical lattice. This situation resembles the ensemble quantum computation set-up [32], and in fact some of the ideas developed there can be directly incorporated in our method to make it more

efficient. As we will show, the method alone suffers, parallel to what happens in ensemble quantum computation, from the scalability problem. Here we will also present a method to overcome it and to make the present proposal scalable. Note that even though our method is developed for atoms in optical lattices, some of its ideas may also apply to very different implementations where similar obstacles are present.

Let us now consider the case of quantum simulation. Here it is indeed essential that the system is cooled very close to its ground state. One may think of several ways of cooling atoms in optical lattices. For example, one may use sympathetic cooling with a different Bose–Einstein condensate [14, 36]. Here we discuss the algorithmic cooling scheme in [15] which does not require the addition of a condensate. It aims at cooling atoms to the ground state of the Mott-insulating (MI) regime and allows one to predict temperatures which are typically low enough for practical interests. This protocol is based on translation invariant operations (i.e. do not require single–site addressing) and include the presence of an additional harmonic trapping potential, as it is the case in present experiments. Although we will be mostly analyzing their effects on bosonic atoms, they can also be used for fermions. The central idea is to split the atomic cloud into two components and to use particles at the border of one component as "pointers" that remove "hot" particles at the borders of the other component. We provide a detailed theoretical description of this cooling scheme and compare our theory with exact numerical calculations. In particular, we quantify the cooling efficiency analytically in terms of the initial and final entropy. We also compare the efficiency of algorithmic cooling with the one of occupation number filtering as it was first proposed in [30]. In addition, experimental requirements and time scales are discussed.

The paper is organized as follows. We start in Sect. 4.2 with reviewing the physical system in terms of the Bose–Hubbard model. We discuss realistic initial state variables such as entropy and particle number and present a set of available quantum operations. In Sect. 4.3 we show how to perform ensemble quantum computation. Then we turn to the problem of ground state cooling. After analyzing the cooling performance of occupation number filtering in Sect. 4.4 we present the method of algorithmic cooling in Sect. 4.5. We conclude with some remarks concerning possible variants and extensions of these methods.

## 4.2

### Physical System

#### 4.2.1

#### Bose-Hubbard Model

We consider a gas of ultra-cold bosonic atoms which have been loaded into a three dimensional (3D) optical lattice of the form:

$$V(x, y, z) = V_0 (\sin^2(kx) + \sin^2(ky) + \sin^2(kz)). \quad (4.1)$$

This configuration can be created by three orthogonal standing wave laser fields with wave vector  $k = 2\pi/\lambda$ . The lattice depth  $V_0$  is proportional to the dynamic atomic polarizability times the laser intensity. We further account for an additional harmonic trapping potential which either arises naturally from the Gaussian density profile of the laser beams or can be controlled separately via an external magnetic or optical confinement [18, 39].

In the following we will mostly be concerned with one-dimensional (1D) lattices, i.e. we assume that tunnelling is switched off for all times along the transversal lattice directions. This system is most conveniently described in terms of a single band Bose-Hubbard model. For a lattice of length  $L$  the Hamiltonian in second quantized form reads

$$H_{BH} = \sum_{k=-L/2}^{L/2} \left[ -J(a_k^\dagger a_{k+1} + h.c.) + \frac{U}{2} n_k(n_k - 1) + bk^2 n_k \right]. \quad (4.2)$$

The parameter  $J$  denotes the hopping matrix element between two adjacent sites,  $U$  is the on-site interaction energy between two atoms and the energy  $b$  accounts for the strength of the harmonic confinement. Operators  $a_k^\dagger$  and  $a_k$  create and annihilate, respectively, a particle on site  $k$ , and  $n_k = a_k^\dagger a_k$  is the occupation number operator. When raising the laser intensity the hopping rate decreases exponentially, whereas the interaction parameter  $U$  stays almost constant [40]. Therefore we have adopted  $U$  as the natural energy unit of the system.

In the following we will consider 1D thermal states in the grand canonical ensemble, which are characterized by two additional parameters, temperature  $kT = 1/\beta$  and chemical potential  $\mu$ . We are particularly interested in the no-tunnelling limit [41],  $J \rightarrow 0$ , in which the Hamiltonian (4.2) becomes diagonal in the Fock basis of independent lattice sites:  $\{|n_{-(L-1)/2} \dots n_0 \dots n_{(L-1)/2}\}\}$ . The density matrix then factorizes into a tensor product of thermal states for each lattice site:

$$\rho = \frac{1}{\Theta} e^{-\beta(H_{BH} - \mu N)} = \bigotimes_{k=-L/2}^{L/2} \rho_k. \quad (4.3)$$

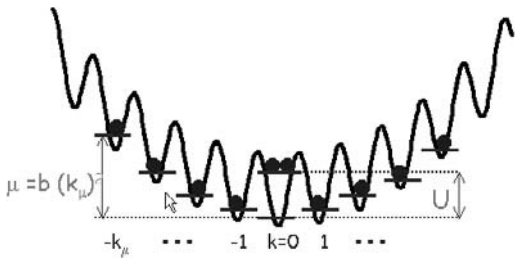


**Fig. 4.1** Illustration of important energy scales for bosonic atoms in an optical lattice in the no-tunnelling regime: on-site interaction energy  $U$ , chemical potential  $\mu$ , and harmonic confinement  $V_{ho} = bk^2$ . The characteristic size of the atomic cloud is given by  $k_\mu = \sqrt{\mu/b}$ .

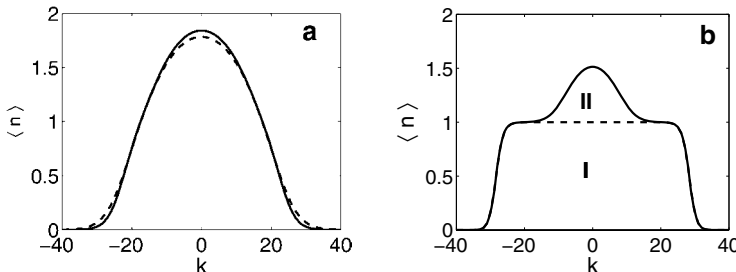


**Fig. 4.2** (a) Density distribution of two thermal states with equal Rényi entropy  $S_2/N = 0.82$  ( $S/N = 1$  in MI phase) and equal particle number  $N = 65$ . At hopping rate  $J/U = 0$  (solid) the temperature is given by  $kT/U = 0.32$  and at  $J/U = 0.16$  ( $V_0 = 5E_r$ ) (dashed) one obtains  $kT/U = 0.46$ . The

harmonic confinement is fixed at  $U/b = 370$  ( $V_0 = 22E_r$  in transverse direction). (b) The separation into two fermionic phases becomes clearly visible in the density profile of a thermal state at low temperatures. Numerical parameters:  $J = 0$ ,  $kT/U = 0.072$ ,  $\mu/U = 1$ ,  $U/b = 800$ , ( $N = 65$ ,  $s = 0.5$ ).

#### 4.2.2

#### Initial State Properties

Let us now study thermal states of the form (4.3) in more detail. In Fig. 4.1 we have depicted graphically all relevant energy scales in the no-tunnelling limit. The chemical potential determines the size of the cloud via the relation  $\mu = bk_\mu^2$ , where  $k_\mu$  denotes the site at which  $\langle n \rangle_{k_\mu} = 0.5$ . For  $\mu \approx U$  singly occupied sites at the border of the cloud become energetically degenerate with doubly occupied sites in the center.

The analysis of recent experiments in the Mott regime [18, 25] implies a substantial temperature of the order of the on-site interaction energy  $U$ . This result is consistent with our own numerical calculations and translates into an entropy per particle  $s := S/N \approx 1$ . The particle number in a 1D tube of a 3D lattice as in [17] typically ranges between  $N = 10$  and  $N = 130$  particles. A representative density distribution corresponding to such initial conditions (with  $N = 65$ ) is plotted in Fig. 4.2a. In this example the inverse

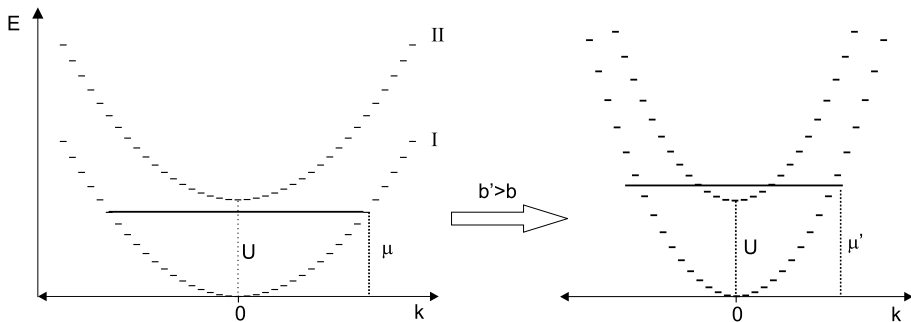


**Fig. 4.3** Effective description of thermal states in the no-tunnelling limit in terms of non-interacting fermions occupying two energy bands. The dispersion relations are  $\varepsilon_I = bk^2$  and  $\varepsilon_{II} = bk^2 + U$ , where  $k$  denotes the lattice site and  $U$  is the interaction energy.

Increasing the harmonic trap strength from  $b$  to  $b'$  increases the chemical potential to  $\mu'$  so that the population of the upper band becomes energetically favorable. In the bosonic picture this process corresponds to the formation of doubly occupied sites.

temperature is given by  $\beta U = 3.1$ . Since our cooling protocols lead to even lower temperatures, we will from now on focus on the *low temperature regime*,  $\beta U \gg 1$ . Moreover, we will only consider states with at most two particles per site, which puts the constraint  $\mu \lesssim 2U - 1/\beta$  on the chemical potential. Such a situation can either be achieved by choosing the harmonic trap shallow enough or by applying an appropriate filtering operation [30].

Under the assumptions  $e^{\beta U} \gg 1$  and  $\mu - U/2 \gtrsim b + 1/(2\beta)$  we have shown in [15] that the density distribution of the initial state (4.3) can be separated into regions that are completely characterized by fermionic distribution functions of the form:

$$f_k(b, \beta, \mu) = \frac{1}{1 + e^{\beta(bk^2 - \mu)}}. \quad (4.4)$$

To be more precise, for sites at the borders of the density distribution,  $bk^2 \gg \mu - U/2 + 1/(2\beta)$ , the mean occupation number is given by  $\langle n_k \rangle \approx n_I(k)$  with  $n_I(k) := f_k(b, \beta, \mu)$ . In the center of the trap,  $bk^2 \ll \mu - U/2 - 1/(2\beta)$ , one has:  $\langle n_k \rangle \approx 1 + n_{II}(k)$  with  $n_{II}(k) := f_k(b, \beta, \mu_{II})$  and effective chemical potential  $\mu_{II} := \mu - U$ . Note also that the underlying MI phase in the center of the trap is well reproduced by the function  $n_I(k)$ , which originally has been derived for the border region. As a consequence, the density distribution for the whole lattice can be put in the simple form:  $\langle n_k \rangle \approx n_I(k) + n_{II}(k)$ , which corresponds to two fermionic phases I and II, sitting on top of each other (Fig. 4.2b). In other words, the initial state of our system can effectively be described in terms of non-interacting fermions, which can occupy two different energy bands I and II, with dispersion relations  $\varepsilon_I = bk^2$  and  $\varepsilon_{II} = bk^2 + U$ , respectively (Fig. 4.3).

In the general case of non-zero tunnelling we can compute 1D thermal states numerically using the matrix-product state (MPS) representation of mixed states [47]. This allows us to estimate how the temperature of a 1D tube

changes when the lattice potential is lowered adiabatically until the superfluid regime is reached. To this end we match the entropy and particle number of two thermal states, one in the tunnelling regime and one in the no-tunnelling regime. Starting from a representative state in the no-tunnelling regime with  $s = 1$  and  $N = 65$  we find a temperature of  $kT = 0.46U = 2.9J$  at  $J/U = 0.16$  ( $V_0 = 5E_r$ ) (Fig. 4.2a). Hence, one faces a substantial temperature of the order of the width of the lowest Bloch band. Note, however, that this is only a lower bound to the true temperature, because our approach does not include any sort of heating processes induced by the adiabatic evolution.

#### 4.2.3

##### Entropy as Figure of Merit

We will show below that algorithmic protocols are suited both for ground state cooling and the initialization of quantum registers. The goal in both cases is to create a pure state under the constraint of keeping a large number of particles. Hence, the performance of our cooling protocol will be characterized by the mixedness of the state. This is measured by the von-Neumann entropy,

$$S(\rho) = \text{tr}(\rho \log_2 \rho) = \sum_k S(\rho_k). \quad (4.5)$$

Outside of the insulator regime ( $J > 0$ ) we cannot compute the von-Neumann entropy  $S$  efficiently. However, we can always use the Rényi entropy

$$S_2 = -\log_2(\text{tr}\rho^2) \quad (4.6)$$

which is a lower bound  $S_2 \leq S$  and can be computed efficiently based on MPS [47].

In order to assess the efficiency of a protocol in achieving our objectives we define two figures of merit: (i) The ratio of the entropies *per* particle after and before invoking the protocol,  $s_f/s_i$ , quantifies the amount of cooling. (ii) The ratio of the final and initial number of particles,  $N_f/N_i$ , quantifies the particle loss induced by the protocol. Note that these figures of merit can sometimes be misleading and should therefore be applied with care. In the case of ground state cooling the entropy is only a good figure of merit if the state of the system after the cooling protocol,  $\rho_f$ , is close to thermal equilibrium. If this is not fulfilled, we compute an effective thermal state,  $\rho_f \rightarrow \rho_{\text{eff}}$ , by accounting for particle number and energy conservation in closed, isolated systems. Our figures of merit can then be calculated from  $\rho_{\text{eff}}$ . For instance, the final entropy is given by  $S(\rho_{\text{eff}})$ . It constitutes the maximum entropy of a state which yields the same expectation values for energy  $E$  and particle number  $N$  as the final state after the protocol. In this context it is important to point out, that other variables, like energy or temperature, are not very well suited as figures of

merit, because they depend crucially on external system parameters like the trap strength.

Note also that in the case of quantum registers it can be erroneous to assume that a finite value of the final entropy implies the existence of defects. For example, we will propose a protocol below that generates a state, whose residual entropy results merely from an incoherent superposition of perfect quantum registers which differ in their length and position.

#### 4.2.4

#### Basic Operations

We present here a collection of available quantum operations in optical lattices which will later be used for quantum computation and cooling. The atoms have three internal states,  $|a\rangle$ ,  $|b\rangle$  and  $|p\rangle$ . In the case of quantum computation the first two will store the qubit, whereas the third one will be used by the pointer. We will consider each 1D lattice independently, i.e. we assume that tunneling is switched off for all times along the  $y$  and  $z$  directions. For the resulting set of 1D periodic lattices we will use a second quantization description of the states. For each lattice site  $k$  we will write a state  $|m_k, m'_k, n_k\rangle_k$ , where  $m_k$ ,  $m'_k$ , and  $n_k$  are natural numbers that indicate the occupation number of levels  $|a\rangle$ ,  $|b\rangle$  and  $|p\rangle$ , respectively. Thus, a typical product state of one 1D lattice will be

$$\otimes_k |m_k, m'_k, n_k\rangle_k. \quad (4.7)$$

We will assume that five kind of basic operations are available. These operations act in exactly the same way in each lattice site, since we do not assume that the sites can be individually addressed. On the other hand, they are based on physical processes which have been demonstrated in the current experimental set-ups:

**(i) Particle transfers** in between internal states. We will consider two kinds:  
**(i.1)** Those in which an integer number of particles is transferred between states  $a$  and  $p$ . For example,

$$U_{m,n}^{m+x, n-x} : |m, 0, n\rangle \leftrightarrow |m+x, 0, n-x\rangle, \quad (4.8)$$

where  $x$  is an integer. Note that for the unitary operator which describes this process at each site holds  $U_{m,n}^{m+x, n-x} = U_{m+x, n-x}^{m, n}$ . Another example that we will use later on will be  $W : |1, 0, 1\rangle \leftrightarrow |0, 1, 1\rangle$ . These operations can be carried out using the blockade mechanisms which is present due to atom–atom interactions [30]. Note also that certain operations, like  $U_{2,0}^{0,2}$  or  $U_{1,0}^{0,1}$ , have already been demonstrated experimentally using an entanglement interferometer [42].

**(i.2)** Those which generate superpositions. For example,  $V = \exp(-iH_{ab}\pi/8)$ , which acts only on the  $a$  and  $b$  levels, with  $H_{ab} = \hat{a}^\dagger \hat{b} + \hat{b}^\dagger \hat{a}$ , where  $\hat{a}$  and  $\hat{b}$

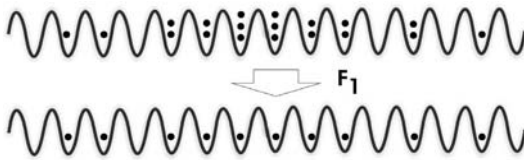


**Fig. 4.4** Illustration of filter operation  $F_1$  which aims at producing a uniform filling of one atom per site. Defects arising from holes cannot be corrected.

are the annihilation operators for particles in states  $|a\rangle$  and  $|b\rangle$ , respectively. These operations can be easily carried out using laser or rf fields [42].

**(ii) Collisional shifts:** They are due to the interactions between particles in the states  $a$  and  $p$ . For example, the unitary operation  $C(\varphi) : |1,0,1\rangle \leftrightarrow e^{i\varphi}|1,0,1\rangle$  can be obtained by waiting the appropriate time [1–4].

**(iii) Lattice shifts:** We denote by  $S_x$  the operations which shift the  $|b\rangle$  lattice  $x$  steps to the right. For example,  $S_{-1}$  transforms the state  $\otimes_k |m_k, n_k\rangle_k$  into  $\otimes_k |m_k, n_{k+1}\rangle_k$ . They can be realized by changing the intensity and polarization of the lasers [1–4, 33].

**(iv) Emptying sites:** All atoms in internal states  $a$ ,  $b$  or  $p$  are thrown away. This can be done, for example, by switching off the lattice potential for the corresponding internal state. We will denote them by  $E_a$ ,  $E_b$  or  $E_p$ . For instance, the operation  $E_b$  transforms the state in Eq. (4.7) into  $\otimes_k |m_k, 0, n_k\rangle_k$ .

**(v) Filtering:** This means particle transfer operations of the form  $U_{m,0,0}^{M,m-M,0}$ , followed by  $E_b$ , for all  $m > M$ . After tracing out the subsystems  $b$  and  $p$ , the filter operation is described by a completely positive map acting solely on atoms in state  $|a\rangle$ :

$$\begin{aligned} F_M[\rho] : \sum_{n,m} \rho_{n,m} |n\rangle \langle m| &\rightarrow \\ &\rightarrow \sum_{n,m \leq M} \rho_{n,m} |n\rangle \langle m| + \sum_{n > M} \rho_{n,n} |M\rangle \langle M|. \end{aligned} \quad (4.9)$$

The filtering operation  $F_1$  (Fig. 4.4) has been first considered in [30]. Recently, an alternative scheme based on resonant control of interaction driven spin oscillations has been put forward [37]. In [15] we have proposed an ultra-fast coherent implementation of  $F_1$  relying on optimal laser control. In the next section we will propose an incoherent realization of filtering, which has the special virtue that it can be applied continuously.

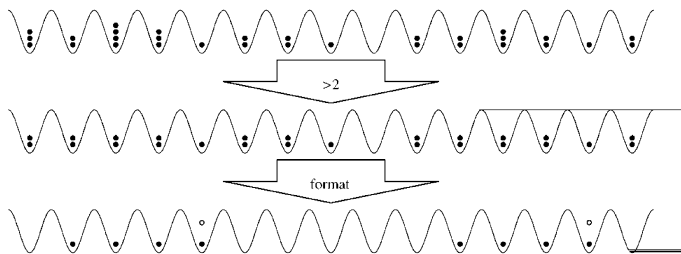


**Fig. 4.5** First, the sites with more than two atoms are depopulated. The “format” step ( $n=3$ ) produces sites with two atoms in levels  $a$  and  $p$ , surrounded by a “reserved area” to their left which contains exactly  $n$  sites with a single atom.

### 4.3

#### Ensemble Quantum Computation

Initially, all atoms are in the internal state  $|a\rangle$ , distributed along the lattice according to some probability distribution, i.e., the state will be a mixture of states in the form of Eq. (4.7) with  $m'_k = n_k = 0$ . Thus, the goal is to show how with these random states, and without requiring individual addressing, we can perform arbitrary quantum computations. This will be achieved in two steps. First there will be a preparation step, and then a computation step. At the end we will show how to include an additional step to make the system scalable. In the preparation stage of our protocol, only states  $a$ , and  $p$  will be occupied. Thus, we will simplify our notation denoting  $|m, n\rangle := |m, 0, n\rangle$ . Moreover, the states that we will use now will be product states, i.e. of the form

$$|m_1, n_1\rangle \otimes |m_2, n_2\rangle \dots \otimes |m_N, n_N\rangle \quad (4.10)$$

where we have not included the subscript  $k$  to simplify the notation. This step starts out by reducing all occupation numbers  $> 2$  to two (Fig. 4.1). This is done by applying the operation  $U_{x,0}^{2,x-2}$  first and then  $E_p$ , and then repeating those actions for  $x > 2$  (up to some value of  $x$  in which we are confident that no site with this number of particles is present).

The next step is to “format” the lattice. We produce several areas, randomly distributed across the lattice, with exactly  $n$  neighboring sites having a single atom in  $a$  and one site at the right edge with two atoms, one in  $p$  and the other in  $a$  (see Fig. 4.1). In order to accomplish this, we have to keep only the areas in which initially there are  $n$  neighboring two-atom sites and a one-atom site at the edge. The rest of the atoms are thrown away, and then we manipulate the remaining atoms to obtain the desired states. The sites in which initially there was a single atom that has survived will now contain the “pointers” (the extra atom in level  $p$ ). This atom will then be used to perform the quantum gates.

First, we change the internal states of the 1-atom sites from  $a$  to  $p$ . These atoms are now called the “pointers”. They will be essential to create the quantum computers in the lattice. Each of those atoms mark the position where we try to establish one of those quantum computers. We want that such a pointer survives during the following protocol if it has on its left at least  $n$  sites with exactly 2-atoms in each. We thus proceed as follows. We shift the pointer one lattice site to the left. We transfer the pointer atom to the state  $a$  iff there are two atoms in that site by applying  $U_{2,1}^{3,0}$ . By emptying the internal states  $p$  we delete all pointers which fail to have a 2-atom site next to their starting position. Then we raise the pointer again by  $U_{2,1}^{3,0}$ . By repeating this procedure for the next  $n - 1$  sites we delete all pointers that fail to have  $n$  2-atom sites on the left of their starting position. Note that this also implies that every pointer in one of the  $n$  sites on the right of each surviving pointer is deleted. This means that every pointer can act on its own “reserved”  $n$  sites, i.e. there are no overlapping reserved areas. Having the pointer and the reserved  $n$  2-atom sites, we can effectively address single sites of this reserved space. This enables us to reduce the number of atoms in each site in this reserved areas to one and afterwards to empty the remaining sites that are not reserved by any pointer. In terms of the operations described above, the protocols is given by a sequence of the following operators: 1)  $U_{1,0}^{0,1}$ ; 2)  $S_{-1}, U_{2,1}^{3,0}, E_p, U_{2,1}^{3,0}$ , and then repeat this whole step  $n - 1$  times; 3)  $U_{2,1}^{1,2}$ ; 4)  $S_1, U_{2,2}^{3,1}, E_p, U_{3,0}^{1,2}$ , and then repeat this whole step  $n - 2$  times; 5)  $S_1, U_{2,0}^{0,2}, E_p, U_{2,0}^{1,1}$ .

The randomly distributed quantum computers consist of  $n$  sites, all of them with a single atom in state  $|a\rangle$ , and the pointer atom in state  $|p\rangle$  in the right-most site (see Fig.21.2). The first atoms store a qubit each, with states  $|\downarrow\rangle = |1,0,0\rangle$  and  $|\uparrow\rangle = |0,1,0\rangle$ , whereas the pointer atoms in state  $|0,0,1\rangle$  carry out the quantum gates.

Now we show how to carry out a universal set of quantum gates using the operations defined above. The idea is to move the pointer atom to the sites which participate in the quantum gate and then apply the appropriate operations. The set is composed of [34] (a) control- $\pi$  phase gate on two arbitrary qubits, at the conventional locations “first site” and “second site”: we move the pointer to the first site, and apply the operator  $U_{1,1}^{2,0}$ . This turns the pointer to the level  $a$ , iff the qubit-atom is in level  $a$ . After this operation, the pointer can be found in any superposition of levels  $p$  and  $a$ . In the next step we move the pointer to the second site and we wait until the collisional shift operation  $C(\pi)$  is applied. Here, “moving the pointer” means displacing the lattice associated with the pointer level  $p$ . Finally, we move the pointer back to the first site and apply again  $U_{1,1}^{2,0}$ . It is simple to show that this will only add a  $\pi$  phase if both qubits are in the state  $|\uparrow\rangle$ ; (b) Phase-gate  $\varphi$  on an arbitrary qubit (see Fig. 4.6): We bring the pointer to the corresponding site and wait for the appropriate collisional shift operation  $C(\varphi)$ ; (c) Hadamard

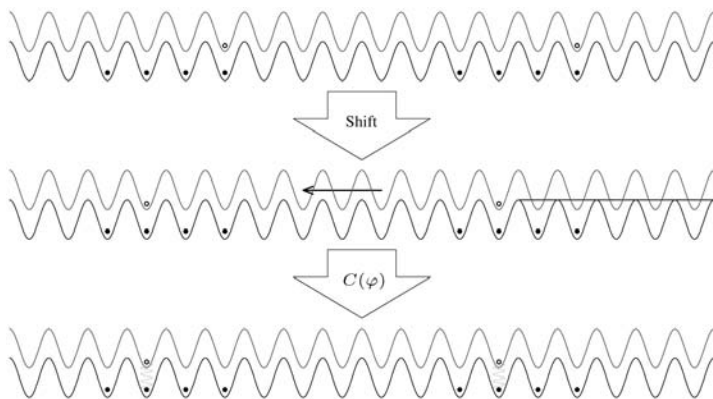


**Fig. 4.6** The levels  $a, b$  will store the qubits, and the  $p$ -level will contain the pointer, which can be moved around allowing us to address single sites, e.g., applying a phase-gate  $\varphi$  on an arbitrary qubit.

gate on an arbitrary qubit: We first bring the pointer to the site. Then we apply the following sequence of operations:  $C(\pi/2), V, C(\pi), V^\dagger, C(\pi/2)$ .

Measurement on an arbitrary qubit in the  $\{| \downarrow \rangle, | \uparrow \rangle\}$  basis can be performed as follows. We promote the corresponding atom to the pointer level provided it is in state  $|a\rangle$ , i.e., if the qubit is in the state  $| \downarrow \rangle$ . For the measurement, we count the numbers of atoms in the pointer level (by analyzing the fluorescence coming from that level) and drop them afterwards. Note that this occurs in the same way as in usual ensemble quantum computation [34], in which we get the global information about all quantum computers. To save the original pointer from being emptied we need an extra resting-site, with one atom in the ground state (for example, the rightmost qubit can be reserved for this purpose). In summary, we: 1) move the pointer to the corresponding site and apply  $U_{1,1}^{0,2}$ ; 2) move the pointer to the resting-site and apply  $U_{1,1}^{2,0}$  and  $U_{1,2}^{2,1}$ ; 3) count atoms in pointer level and apply  $E_p$ ; 4) apply  $U_{2,0}^{1,1}$ . The measured qubit-site is emptied, iff the qubit was found in state  $| \downarrow \rangle$ , while the pointer and the resting-qubit survived unchanged. We can continue by moving the pointer back to the target qubit, applying  $W$  and then repeating the above protocol. The number of atoms counted in the pointer-level is equal to the number of qubits with measured in state  $| \uparrow \rangle$ . Alternatively, we can leave out this step and relate the number of qubits found in  $| \downarrow \rangle$  to the total number of quantum computers in the lattice. This number can be estimated either by the statistic of the initial distribution or by counting the pointers/atoms at the end of the computation.

So far we have shown how to build a quantum register of  $n$  qubits, for any arbitrary integer  $n$ , and how to perform quantum computations. Note that in order to prepare the initial state it is necessary that there are areas in the lattice

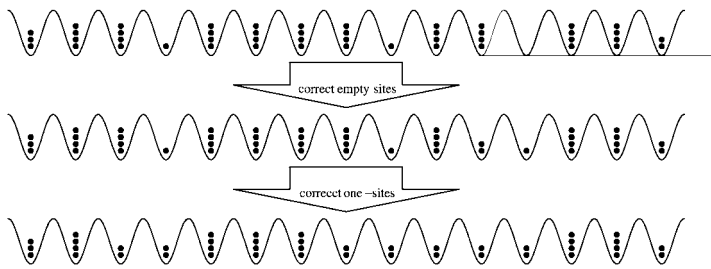


**Fig. 4.7** Overpopulated sites are used to first fill empty sites and then to put two atoms in sites with one atom.

which have no defects, i.e. no empty sites nor 1 atom sites. If the number of such defects well inside the lattice is larger than the number of 1D lattices, then the probability of ending up with at least one quantum computer will decrease exponentially with  $n$ , and thus the method proposed here will not be scalable. In detail, if we assume that every site of the lattice is filled independently with zero, one or two atoms, according to the probabilities distribution  $p_0, p_1, p_2$ , then the expected number of quantum computer of length  $n$  in a 1D lattice can be estimated by  $Np_1p_2^n = Np_1(1 - p_0 - p_1)^n$ , where the length  $N$  of the lattice has to be much larger than  $n$ . This quantity decreases exponentially with  $n$  which makes the proposed method not scalable.

In the following we show how to boost the probability of creating a quantum computer in the lattice by correcting the defects, i.e., making  $p_0$  and  $p_1$  arbitrarily small. Having this possibility, we change the probabilities to  $p_0 = 0$  and  $p_1 = 1/n$ . The resulting expected number of quantum computers in a lattice of size  $N$  is then given by  $N/n(1 - 1/n)^n$ , which goes to  $N/(n \cdot e) \sim 1/n$  for large  $n$ , i.e. our method becomes scalable. The procedure of correcting the defects will also be useful if one would like to perform quantum simulations with large spin chains.

The main idea of the protocol is to first fill all sites which are empty with one atom coming from a different site, which is overpopulated. Then, the sites with one atom are filled with another atom also coming from overpopulated sites (see Fig. 4.3). Thus, we have to assume that there are as many overpopulated sites as defects, an achievable requirement for sufficiently high densities.

First, we reduce all occupation number  $> 4$  to four [35]. Then, the protocol starts out by promoting two atoms to the state  $p$  whenever a site has four atoms. Then we shift the lattice corresponding to level  $p$  by a random amount  $x$  and try to deposit one of such atoms in an empty site. The remaining atom in the  $p$  level is thrown away. Note, that for every corrected defect we lose one atom in this protocol. Losing atoms while correcting defects is unavoidable, since it is the only way to reduce the entropy of the state in our setup. We proceed in the same vein until we make the probability of having sites with

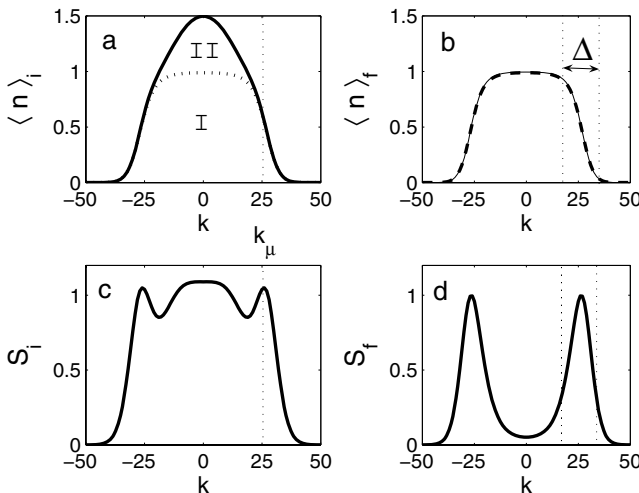


**Fig. 4.8** Spatial dependence of the mean occupation number  $\langle n \rangle$  and entropy  $S$  before (left) and after (right) the application of the filter operation  $F_1$ . The final particle distribution can be well described by Eq. (4.4) (dashed line). Numerical parameters for initial state:  $N_i = 65$ ,  $s_i = 1$ ,  $U/b = 700$ ,  $\beta U = 4.5$  and  $\mu/U = 1$ . Figures of merit:  $s_f/s_i = 0.56$  and  $N_f/N_i = 0.80$ .

no atoms vanishingly small. In more detail, we apply the following sequence of operations several times:  $U_{4,0}^{2,2}$ ,  $S_x$ ,  $U_{0,2}^{1,1}$ ,  $S_{-x}$ ,  $U_{4,0}^{2,2}$ ,  $E_p$ . With this we will have filled the empty sites. Now, we can do the same but replacing  $U_{4,0}^{2,2}$  and  $U_{0,2}^{1,1}$  by  $U_{x,0}^{x-2,2}$  and  $U_{1,2}^{1,1}$ , so that sites with a single atom get double occupation. For a finite lattice of length  $N$  there are only  $N$  different possibilities for the  $x$ , so the protocol requires at most  $N$  repetitions.

We still need some defects to act as pointers. So we either do not fill up all the one-atom defects or we have to create new defects. The latter can be done by first reducing all occupation numbers to two and then applying a unitary operation that changes  $|2,0,0\rangle$  to the superposition state  $\sqrt{\varepsilon}|1,1,0\rangle + \sqrt{1-\varepsilon}|2,0,0\rangle$  followed by  $E_b$ . With probability  $\varepsilon$  a one-atom-site defect is created out of a 2-atom site.

#### 4.4

#### Cooling with Filtering

Let us study the filtering operation  $F_1$  in Eq. (4.9) in more detail. This operation is especially relevant for cooling, because it produces a state close to the ground state of the MI regime. Thus, it also serves as a benchmark which has to be beaten by alternative cooling schemes.

In Fig. 4.8 we have depicted the spatial occupation number and entropy distribution before and after the action of  $F_1$ . One observes that a nearly perfect MI phase with filling factor  $\nu = 1$  is created in the center of the trap. Defects in this phase are due to the presence of holes and preferably locate at the borders of the trap. This behavior is reminiscent of fermions, for which excitations can only be created within an energy range of order  $kT$  around the Fermi level. This numerical observation can easily be understood with our previous analysis of the initial state. Filtering removes phase II, which is due to doubly occupied sites, and leaves the fermionic phase I unaffected (Fig. 4.8a).

For an initial thermal state, defined by parameters  $b$ ,  $\beta$  and  $\mu$ , the final entropy per particle is given by:

$$s_f = \frac{S_f}{N_f} \approx \frac{\sigma_I}{2} \frac{1}{\beta\mu}, \quad (4.11)$$

where  $\sigma_I = \pi^2/3 \ln 2$ . This residual entropy is localized around the Fermi level  $k_\mu$  within a region of width  $\Delta$  (Fig. 4.8d):

$$\Delta = \frac{1}{\beta\sqrt{b\mu}}. \quad (4.12)$$

This parameter is characteristic for the tail width of the density distribution and will in the following be central for the analysis of our protocols. For the special choice  $\mu = U$  (or equivalently  $\langle n_0 \rangle = 1.5$ ) one finds the following expressions for our figures of merit:

$$\frac{s_f}{s_i} \approx \left( \frac{2\sqrt{\beta U}}{\sigma_I} \frac{\sigma_{II}\sqrt{\beta U} + \sigma_I}{\eta_{II} + 2\sqrt{\beta U}} \right)^{-1}, \quad (4.13)$$

$$\frac{N_f}{N_i} \approx \frac{1}{1 + \frac{\eta_{II}}{2\sqrt{\beta\mu}}}, \quad (4.14)$$

with numerical coefficients  $\sigma_{II} \approx 2.935$  and  $\eta_{II} = (1 - \sqrt{2})\sqrt{\pi}\zeta(1/2) \approx 1.063$ . This analysis shows that filtering becomes more efficient with decreasing temperature, since  $s_f/s_i \propto 1/\sqrt{\beta U} \rightarrow 0$  and  $N_f/N_i \rightarrow 1$  for  $\beta U \rightarrow \infty$ .

It is important to note that the state after filtering is not an equilibrium state, because it is energetically favorable that particles tunnel from the borders to the center of the trap, thereby forming doubly occupied sites. According to the discussion in the previous section this implies that the final entropy, which enters the cooling efficiency, should be calculated from an effective state  $\rho_{\text{eff}}$  after equilibration. However, this would yield a rather pessimistic estimate for the cooling efficiency. One can easily come up with a much simpler (and faster) way to reach a thermodynamically stable configuration. While tunnelling is

still suppressed, one has to decrease the strength of the harmonic confinement to a new value  $b'$ , with  $b' \leq b U/(2\mu)$ . The system is then in the equilibrium configuration  $f_k(b', \beta', \mu')$  (4.4) with rescaled parameters  $T' = T b'/b$  and  $\mu' = \mu b'/b \leq U/2$ . This observation shows that it is misleading to infer the cooling efficiency solely from the ratio  $T'/T$ , because it depends crucially on the choice of  $b'$ .

## 4.5

### Algorithmic Ground State Cooling

#### 4.5.1

##### The Protocol

We now propose a cooling scheme, which we have termed algorithmic cooling, because it is inspired by quantum computation. As before the goal is to remove high energy excitations at the borders of the atomic cloud, which have been left after filtering. We restrict ourselves to a sequence of quantum operations that operate solely in the no-tunnelling regime. The central idea is to make use of spin-dependent lattices. A part of the atomic cloud can then act as a "pointer" in order to address lattice sites which contain "hot" particles. In this sense our scheme is similar to evaporative cooling, with the difference that an atomic cloud takes the role of the rf-knife. Another remarkable feature of our protocol is that the pointer is very inaccurate in the beginning (due to some inherent translational uncertainty in the system), but becomes sharper and sharper in the course of the protocol.

The steps of this algorithmic protocol are: (i) We begin with a thermal equilibrium cloud with two or less atoms per site, all in internal state  $|a\rangle$ , and without hopping. This can be ensured with a filtering operation  $F_2$ . (ii) We next split the particle distribution into two, with an operation  $U_{2,0}^{1,1}$  (Fig. 4.9a). (iii) The two clouds are shifted away from each other until they barely overlap. Then we begin moving the clouds one against each other, emptying in this process all doubly occupied sites. This sequence sharpens the density distribution of both clouds. It is iterated for a small number of steps, of order  $\Delta$  (4.12) (Fig. 4.9c). (iv) The atoms of type  $|b\rangle$  are moved again to the other side of the lattice and a process similar to (iii) is repeated (Fig. 4.9d). (v) Remaining atoms in state  $|b\rangle$  can now be removed.

The final particle distribution cannot be made arbitrarily sharp (Fig. 4.9d), due to the particle number uncertainty in the tails of the distribution. In the following we will consider this argument more rigorously and develop a theoretical description of the protocol.

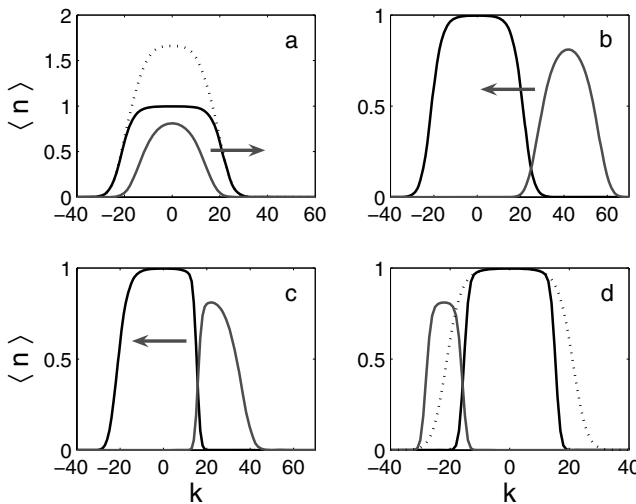


**Fig. 4.9** Illustration of the protocol. The state is initialized with the filter operation  $F_2$ . (a) Particles from doubly occupied sites are transferred to state  $|b\rangle$  (red) using operation  $U_{2,0}^{1,1}$ . (b) The lattice  $|b\rangle$  has been shifted  $2k_\epsilon$  sites to the right, so that the two distributions barely overlap. (c) Density distribution after  $k_s$  lattice shifts. After each shift doubly occupied

sites have been emptied. Afterwards lattice  $|b\rangle$  is shifted  $4k_\epsilon - k_s$  sites to the left and an analogous filter sequence is applied. (d) The final distribution of atoms in state  $|a\rangle$  is sharper compared to the initial distribution (dotted). Numerical parameters:  $N_i = 65$ ,  $s_i = 1$ ,  $U/b = 300$ ,  $k_\epsilon = 21$ ,  $k_s = 20$ ,  $N_f = 30.2$ ,  $s_f = 0.31$  (after equilibration). Cf. the coloured plates in the Appendix.

#### 4.5.2

#### Theoretical Description

For the sake of simplicity we consider a slightly modified version of the protocol. The particle distributions  $|a\rangle$  and  $|b\rangle$  are now two identical but independent distributions of hard-core bosons of the form (4.4) [44]. The lattice  $|b\rangle$  is shifted  $2k_\epsilon$  sites to the right. For given  $\epsilon$  the value  $k_\epsilon = \sqrt{\mu/U} \sqrt{1 - \ln \epsilon / \beta U}$  is chosen such that for atoms  $|a\rangle$  it holds  $\langle n_{k_\epsilon}^a \rangle = \epsilon$ . This initial situation is depicted schematically in Fig. 4.10. The cutoff  $\epsilon$  defines also the width of the region with non-integer filling:

$$\delta_\epsilon = \sqrt{\mu/b} \left( \sqrt{1 - \ln \epsilon / \beta U} - \sqrt{1 + \ln \epsilon / \beta U} \right). \quad (4.15)$$

We analyze first a protocol that involves  $k_s = 3\delta_\epsilon$  lattice shifts and after each shift doubly occupied sites are emptied. Our goal is to compute the final shape of the density profile of atoms in state  $|a\rangle$  (red line in Fig. 4.10). It is sufficient to consider only the reduced density matrices  $\hat{\rho}_a$  and  $\hat{\rho}_b$ , which cover the range  $k \in [k_\epsilon - 2\delta_\epsilon; k_\epsilon]$  and  $k \in [k_\epsilon; k_\epsilon + 2\delta_\epsilon]$ , respectively. These density matrices can

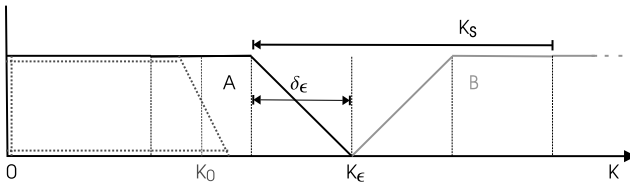


**Fig. 4.10** Schematic description of the initial state for lattice sites  $k \geq 0$ : Two identical density distributions for hard-core bosons, belonging to different species A (black) and B (blue), are shifted  $2k_\epsilon$  lattice sites apart. The region of non-integer filling has width  $\delta_\epsilon$ . In the course of the protocol the lattice of species B is shifted  $k_s = 3\delta_\epsilon$  sites to the left. Cf. the coloured plates in the Appendix.

be written in terms of convex sums over particle number subspaces:

$$\hat{\rho}_a = \sum_{N_a=0}^{2\delta_\epsilon} p_a(N_a) \hat{\rho}_a(N_a), \quad (4.16)$$

$$\hat{\rho}_b = \sum_{N_b=0}^{2\delta_\epsilon} p_b(N_b) \hat{\rho}_b(N_b). \quad (4.17)$$

The further discussion is based on the following central observation. If a state  $\hat{\rho}_a(N_a)$  interacts with a state  $\hat{\rho}_a(N_b)$  then our protocol produces a perfect MI state  $\hat{\rho}'_a(N'_a)$  composed of  $N'_a = (N_a - N_b)/2$  particles. The factor  $1/2$  arises from the fact that  $k_s$  lattice shifts remove at most  $k_s/2$  particles from distribution  $|a\rangle$ . Note that this relation also allows for negative particle numbers, because  $N'_a$  merely counts the number of particles on the right hand side of the reference point  $k_0 = k_\epsilon - 3/2\delta_\epsilon$ . The final density matrix after tracing out particles in  $|b\rangle$  can then be written as a convex sum over nearly perfect (up to the cutoff error  $\epsilon$ ) MI states

$$\hat{\rho}'_a = \sum_{N'_a=-\delta_\epsilon/2}^{\delta_\epsilon/2} p'_a(N'_a) \hat{\rho}'_a(N'_a), \quad (4.18)$$

with probabilities

$$p'_a(N'_a) \simeq 2 \sum_{N_b=\delta_\epsilon}^{2\delta_\epsilon} p_a(2N'_a + N_b) p_b(N_b). \quad (4.19)$$

The factor two is due to the fact that states with  $N_a - N_b = 2M$  and  $N_a - N_b = 2M + 1$  are collapsed on the same MI state with  $N'_a = M$ . Since Lyapounov's condition [46] holds in our system, we can make use of the generalized central limit theorem and approximate  $p_a(N) = p_b(N)$  by a Gaussian distribution with variance  $\sigma^2 = \delta N^2 = \Delta/4 = 1/(2\beta\sqrt{b\mu})$ . Evaluation of Eq. (4.19) then yields a Gaussian distribution with variance  $\sigma'^2 = \sigma^2/2$ . Since MI states do not

contain holes, one can infer the final density distribution  $\langle n_k^a \rangle'$  directly from  $p'_a(N)$  by simple integration. This distribution can then be approximated by the (linearized) thermal distribution:

$$\langle n_k \rangle' \simeq \frac{1}{1 + e^{2(k-k_0)/\Delta'}}. \quad (4.20)$$

The new effective tail width  $\Delta' = \sqrt{\Delta\pi/8}$  of the distribution is roughly the square root of the original width  $\Delta$  (4.12). This effect leads to cooling, which we will now quantify in terms of the entropy.

When applying similar reasoning also to the left side of distribution  $|a\rangle$  one ends up with a mixture of MI states, which differ by their length *and* lateral position. This results in an extremely small entropy of the order  $S_{\text{MI}} \sim \log_2 \Delta$ . However, this final state is typically far from thermal equilibrium. In order to account for a possible increase of entropy by equilibration, we have to compute the entropy of a thermal state, which has the same energy and particle number expectation values as the final state. In our case this is equivalent to computing the entropy directly from the density distribution (4.20):

$$S' \approx \sigma_I \Delta' = \frac{\sigma_I \sqrt{\pi}}{2\sqrt{2}} \frac{1}{(\beta^2 b \mu)^{1/4}} = \frac{\sqrt{\pi}}{2} \frac{\sqrt{\beta \mu}}{\sqrt{N}} S, \quad (4.21)$$

where  $N$  and  $S$  correspond to the expectation values before invoking the algorithmic protocol. The final particle number is given by:  $N' \simeq 2k_0 \approx N(1 + \ln \varepsilon/\beta U)$ .

A significant improvement can be made by shifting the clouds only  $k_s = 2\delta_\varepsilon$  sites. This prevents inefficient particle loss, which has been included in our previous analysis in order to make the treatment exact. With this variant the final particle number increases to  $N'' = 2(k_\varepsilon - \delta_\varepsilon)$ , while in good approximation the final entropy is still given by  $S'$ . Hence, the final entropy per particle can be lowered to:

$$s' = \frac{S'}{N''} \approx \frac{\sqrt{\pi}}{2} \frac{\sqrt{\beta \mu}}{1 + \frac{\ln \varepsilon}{2\beta U}} \frac{1}{\sqrt{N}} S. \quad (4.22)$$

This expression, which holds strictly only in the limit  $\beta U \gg 1$ , shows that for fixed  $N$  the ratio  $s'/s$  becomes smaller at higher temperatures. Even more important, for fixed  $\beta U$ , the entropy per particle  $s'$  decreases with  $1/\sqrt{N}$  as the initial particle number in the system increases. Thus, in the thermodynamic limit our protocol would create a final state asymptotically close to the ground state.

Finally, let us remark that the final entropy can be further reduced, when the protocol is repeated with two independent states of the form (4.18). In practice, this could be achieved with an ensemble of non-interacting atomic species in different internal levels. According to Eq. (4.19), each further iteration of the protocol decreases the total entropy by a factor  $1/\sqrt{2}$ .

## 4.6

### Conclusion

We have shown that it is possible to perform quantum computations in optical lattices in the presence of lattice defects and without the necessity to address single lattice sites, nor to specify the total number of atoms in the lattice. In practice, a very high degree of control is required, something which is being achieved in current experiments with optical lattices. The ideas presented here not only apply to the field of quantum computation but they can also be used to prepare and manipulate the states in the lattice, and to build some prescribed atomic patterns [30]. Furthermore, all these methods can be generalized in a straight forward way to 2-dimensional or 3-dimensional lattices. Finally, note that some of the protocols given here require a large number of steps, something which is experimentally demanding. We are currently using the ideas of quantum compression in order to develop new efficient methods for loading the lattices [48].

We have further given a detailed analytical analysis of filtering operations in the no-tunnelling regime and in the presence of a harmonic trap. We have found that the residual entropy after filtering is localized at the borders of the trap, quite similar as in fermionic systems. Inspired by this result we have proposed a protocol for algorithmic cooling that aims at removing particles from the borders and thus leads to cooling. In this protocol particles from the system itself take the role of the rf-knife in evaporative cooling and remove directly particles at the borders. A special virtue of our schemes is that they rely on general concepts which can easily be adapted to different experimental situations. For instance, our protocols can easily be extended to fermionic systems (for details see [45]). Moreover, the algorithmic protocol can be improved considerably by the use of an ensemble of non-interacting atomic species in different internal states. In this context one should also keep in mind that a 3D lattice structure offers a large variety of possibilities, which have not been fully explored yet. Since we have identified the limitations of filtering, one can immediately think of alternative or supporting cooling schemes. For instance, one might use ring shaped lasers beams to remove particles at the borders of a 3D lattice. Equivalently, one can use a transition, which is resonant only for atoms with appropriate potential energy [45]. Although these methods do not allow to address individual lattice sites, they might still be useful as preliminary cooling steps for the protocols proposed in this article.

We believe that the ideas introduced in this article greatly enhance the potential of optical lattice setups for future applications and might pave the way to the experimental realization of quantum simulation and quantum computation in this system. We also hope that our analytical analysis of the virtues and limitations of current proposals, especially filtering, might trigger further research in the direction of ground state cooling in optical lattices.

## Acknowledgement

Work supported by EU IST projects, the DFG, and the “Kompetenznetzwerk Quanteninformationsverarbeitung der Bayerischen Staatsregierung”.

## References

- 1 D. Jaksch, H.-J. Briegel, J. I. Cirac, C. W. Gardiner, and P. Zoller, Phys. Rev. Lett. **82**, 1975 (1999).
- 2 J. Mompart, K. Eckert, W. Ertmer, G. Birkl, and M. Lewenstein, Phys. Rev. Lett. **90**, 147901 (2003).
- 3 G. K. Brennen, I. H. Deutsch, and C. J. Williams, Phys. Rev. A **65**, 022313 (2002)
- 4 O. Mandel, M. Greiner, A. Widera, T. Rom, T. W. Hänsch, and I. Bloch, Phys. Rev. Lett. **91**, 010407 (2003).
- 5 O. Mandel, M. Greiner, A. Widera, T. Rom, T. W. Hänsch, and I. Bloch, Nature **425**, 937 (2003).
- 6 K. G. H. Vollbrecht, E. Solano, and J. I. Cirac, Phys. Rev. Lett. **93**, 220502 (2004).
- 7 J. I. Cirac and P. Zoller, Science **301**, 176 (2003); Phys. Today **57**, 38 (2004).
- 8 J.-J. García-Ripoll and J. I. Cirac, New J. Phys. **5**, 76 (2003); L.-M. Duan, E. Demler, and M. D. Lukin, Phys. Rev. Lett. **91**, 090402 (2003).
- 9 J.-J. García-Ripoll, M. A. Martin-Delgado, and J. I. Cirac, Phys. Rev. Lett. **93**, 250405 (2004).
- 10 L. Santos, M. A. Baranov, J. I. Cirac, H.-U. Everts, H. Fehrmann, and M. Lewenstein, Phys. Rev. Lett. **93**, 030601 (2004).
- 11 H. P. Büchler, M. Hermele, S. D. Huber, M. P. A. Fisher, and P. Zoller, Phys. Rev. Lett. **95**, 040402 (2005).
- 12 A. Micheli, G. K. Brennen, and P. Zoller, preprint quant-ph/0512222.
- 13 R. Barnett, D. Petrov, M. Lukin, and E. Demler, preprint cond-mat/0601302.
- 14 W. Hofstetter, J. I. Cirac, P. Zoller, E. Demler, and M. D. Lukin, Phys. Rev. Lett. **89**, 220407 (2002).
- 15 M. Popp, J.-J. García-Ripoll, K. G. H. Vollbrecht, and J. I. Cirac, preprint cond-mat/0603859 (2006).
- 16 Note that our concept of *algorithmic cooling of atoms* has to be clearly distinguished from *algorithmic cooling of spins* which is a novel technique that allows to create highly polarized ensembles of spins in the context of NMR experiments, see e.g. P. O. Boykin, T. Mor, V. Roychowdhury, F. Vatan, and R. Vrijen, Proc. Natl. Acad. Sci. USA **99**, 3388 (2002).
- 17 M. Greiner, O. Mandel, T. Esslinger, T. W. Hänsch, and I. Bloch, Nature **415**, 39 (2002).
- 18 B. Paredes, A. Widera, V. Murg, O. Mandel, S. Fölling, I. Cirac, G. V. Shlyapnikov, T. W. Hänsch, and I. Bloch, Nature **429**, 277 (2004).
- 19 H. Moritz, T. Stöferle, M. Köhl, and T. Esslinger, Phys. Rev. Lett. **91**, 250402 (2003); T. Stöferle, H. Moritz, C. Schori, M. Köhl, and T. Esslinger, Phys. Rev. Lett. **92**, 130403 (2004).
- 20 B. L. Tolra, K. M. O’Hara, J. H. Huckans, W. D. Phillips, S. L. Rolston, and J. V. Porto, Phys. Rev. Lett. **92**, 190401 (2004).
- 21 M. Köhl, H. Moritz, T. Stöferle, K. Günter, and T. Esslinger, Phys. Rev. Lett. **94**, 080403 (2005).
- 22 K. Xu, Y. Liu, J. R. Abo-Shaeer, T. Mukaiyama, J. K. Chin, D. E. Miller, W. Ketterle, K. M. Jones, and E. Tiesinga, Phys. Rev. A **72**, 043604 (2005).
- 23 C. Ryu, X. Du, E. Yesilada, A. M. Dudarev, S. Wan, Q. Niu, D. J. Heinzen, preprint cond-mat/0508201.
- 24 G. Thalhammer, K. Winkler, F. Lang, S. Schmid, R. Grimm, and J. Hecker Denschlag, Phys. Rev. Lett. **96**, 050402 (2006).
- 25 A. Reischl, K. P. Schmidt, and G. S. Uhrig, cond-mat/0504724.
- 26 see e.g. L. Pitaevskii and S. Sringari, *Bose-Einstein Condensation* (Oxford University Press, Oxford, 2003).

- 27** S. Peil, J. V. Porto, B. Laburthe Tolra, J. M. Obrecht, B. E. King, M. Subbotin, S. L. Rolston, and W. D. Phillips, *Phys. Rev. A* **67**, 051603(R) (2003).
- 28** R. Dumke, M. Volk, T. Mütter, F. B. J. Buchkremer, G. Birkl, and W. Ertmer, *Phys. Rev. Lett.* **89**, 097903 (2002).
- 29** A method requiring addressability has been proposed in: J. Vala, A. V. Thapliyal, S. Myrgren, U. Vazirani, D. S. Weiss, and K. B. Whaley, *quant-ph/0307085* (2003).
- 30** P. Rabl, A. J. Daley, P. O. Fedichev, J. I. Cirac, and P. Zoller, *Phys. Rev. Lett.* **90**, 6 (2003).
- 31** J. J. García-Ripoll and J. I. Cirac, *Phys. Rev. Lett.* **90**, 127902 (2003).
- 32** N. A. Gershenfeld and I. L. Chuang, *Science* **275**, 350 (1997).
- 33** G. K. Brennen, C. M. Caves, P. S. Jessen, and I. H. Deutsch, *Phys. Rev. Lett.* **82**, 1060 (1999).
- 34** See, e.g., M. A. Nielsen and I. L. Chuang, *Quantum Computation and Quantum Information* (Cambridge University Press, Cambridge, 2000).
- 35** Alternatively, we can repeat the whole protocol with occupation number 4, 5, 6, ... as overpopulated resource.
- 36** A. J. Daley, P. O. Fedichev, and P. Zoller, *Phys. Rev. A* **69**, 022306 (2004).
- 37** F. Gerbier, A. Widera, S. Foelling, O. Mandel, and I. Bloch, preprint *cond-mat/0601151* (2006).
- 38** L. Viverit, C. Menotti, T. Calarco, and A. Smerzi, *Phys. Rev. Lett.* **93**, 110401 (2004).
- 39** F. Gerbier, A. Widera, S. Foelling, O. Mandel, T. Gericke, and I. Bloch, *Phys. Rev. Lett.* **95**, 050404 (2005).
- 40** D. Jaksch, C. Bruder, J. I. Cirac, C. W. Gardiner and P. Zoller, *Phys. Rev. Lett.* **81**, 3108 (1998).
- 41** The condition for the no-tunnelling regime in the presence of a harmonic trap is given by  $|J/(bN)|^2 \ll 1$ , i.e. the hopping matrix element is much smaller than the average energy spacing between single particle states located at the borders of the trap. If desired one can also demand  $|J/b|^2 \ll 1$ , which ensures that single particle eigenfunctions even at the bottom of the trap are localized on individual lattice wells [38].
- 42** A. Widera, O. Mandel, M. Greiner, S. Kreim, T. W. Hänsch, and I. Bloch, *Phys. Rev. Lett.* **92**, 160406 (2004).
- 43** It has turned out that this choice, incidentally, yields the best cooling result [45] for a wide range of initial conditions. In practice, it will therefore be the most relevant case.
- 44** In practice, this can be achieved by applying  $F_1$  to two non-interacting bosonic clouds in different internal states.
- 45** M. Popp, K. G. H. Vollbrecht, J.-J. García-Ripoll, and J. I. Cirac, in preparation.
- 46** see e.g. P. Billingsley, *Probability and Measure* (Wiley, New York, 1995).
- 47** F. Verstraete, J.-J. García-Ripoll, and J. I. Cirac, *Phys. Rev. Lett.* **93**, 207204 (2004).
- 48** K. Vollbrecht et al. (in preparation).

## 5

# Quantum Information Processing in Optical Lattices and Magnetic Microtraps

Philipp Treutlein, Tilo Steinmetz, Yves Colombe, Benjamin Lev, Peter Hommelhoff, Jakob Reichel, Markus Greiner, Olaf Mandel, Artur Widera, Tim Rom, Immanuel Bloch, and Theodor W. Hänsch

## 5.1 Introduction

Neutral atoms present two essential advantages for quantum information processing (QIP). They are relatively weakly coupled to the environment, so that decoherence can be controlled better than in most other systems. Furthermore, complete control of all quantum-mechanical degrees of freedom is already a reality, and is used in experiments with great success, most notably in Bose-Einstein condensation.

Theoretical approaches have been developed to use atoms in well-defined states of controllable potentials for creating many-particle entanglement, and qubit operations in particular. Experimentally realizing these proposals is a major challenge and requires new ideas to overcome the subtle problems occurring in real atomic systems. Requirements on stability and control of environmental conditions, such as electric and magnetic stray fields, are equally demanding.

In the theoretical investigations already, two experimental systems emerged as particularly promising embodiments for neutral-atom QIP. *Optical lattices* allow for a large number of qubits due to their three-dimensional, periodic structure. In *magnetic microtraps (atom chips)*, complex potentials can be realized, and lithographic fabrication techniques enable scalability and modularity in analogy with microelectronics. In the following, we review experimental progress achieved in our group with both systems.

## 5.2

### Optical Lattices

#### 5.2.1

#### Preparation of a Qubit Register

Starting point for the preparation of the neutral atom qubit register is an atomic Bose-Einstein condensate. This is placed in an artificial crystal of light – a so called optical lattice – which is formed by standing wave laser fields along all three space dimensions. By continuously increasing the lattice depth of the optical potentials, one can drive the system through a quantum phase transition from a superfluid to a Mott insulator [1,2], where a defined number

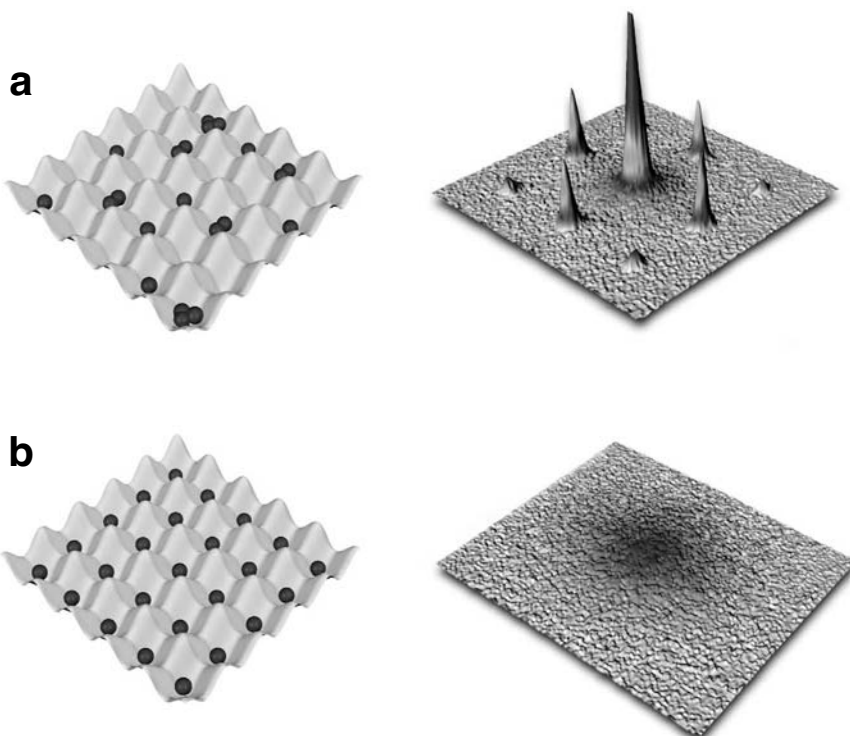


**Fig. 5.1** (a) In the superfluid state of a Bose-Einstein condensate, the underlying atoms can be described as a giant macroscopic matter wave. When such a condensate is released from the periodic potential, a multiple matter wave interference pattern is formed due to the phase coherence between the atomic wavefunctions on different lattice sites. In this case the phase of the macroscopic matter wave is well defined. However, the number

of atoms at each lattice site fluctuates. (b) In the limit of a Mott insulating state, each lattice site is filled with a fixed number of atoms but the phase of the matter wave field remains uncertain. As a result, no matter wave interference pattern can be seen when the quantum gases are released from the lattice potential. Cf. the coloured plates in the Appendix.

of atoms is placed on each lattice site (see Fig. 5.1). By controlling the initial total number of atoms and the confinement parameters of the lattice trap, it is possible to have a large connected region to be populated by single atoms on each lattice site. On each of these sites, the atoms occupy the ground state of the trapping potential and their internal state is initialized to a defined state as well.

### 5.2.2

#### A Quantum Conveyer Belt for Neutral Atoms

So far the optical potentials used for optical lattices with Bose-Einstein condensates have been mostly independent of the internal ground state of the atom. However, it has been suggested that by using spin-dependent periodic potentials one could bring atoms on different lattice sites into contact and thereby realize fundamental quantum gates [3–6], create large scale entanglement [7, 8], excite spin waves [9], study quantum random walks [10] or form a universal quantum simulator to simulate fundamental complex condensed matter physics hamiltonians [11]. Here we show how the wave packet of an atom that is initially localized to a single lattice site can be split and delocalized in a controlled and coherent way over a defined number of lattice sites.

In order to realize a spin dependent transport for neutral atoms in optical lattices, a standing wave configuration formed by two counterpropagating laser beams with linear polarization vectors enclosing an angle  $\theta$  has been proposed [3, 7]. Such a standing wave light field can be decomposed into a superposition of a  $\sigma^+$  and  $\sigma^-$  polarized standing wave laser field, giving rise to lattice potentials  $V_+(x, \theta) = V_0 \cos^2(kx + \theta/2)$  and  $V_-(x, \theta) = V_0 \cos^2(kx - \theta/2)$ . By changing the polarization angle  $\theta$ , one can control the separation between the two potentials  $\Delta x = \theta/180^\circ \cdot \lambda_x/2$  (see Fig. 5.2b). When increasing  $\theta$ , both potentials shift in opposite directions and overlap again when  $\theta = n \cdot 180^\circ$ , with  $n$  being an integer. For a spin-dependent transfer, two internal spin states of the atom should be used, where one spin state dominantly experiences the  $V_+(x, \theta)$  dipole potential and the other spin state mainly experiences the  $V_-(x, \theta)$  potential. Such a situation can be realized in rubidium by tuning the wavelength of the optical lattice laser to a value of  $\lambda_x = 785$  nm between the fine structure splitting of the rubidium D1 and D2 transition. If an atom is now first placed in a coherent superposition of both internal states  $1/\sqrt{2}(|0\rangle + i|1\rangle)$  and the polarization angle  $\theta$  is continuously increased, the spatial wave packet of the atom is split with both components moving in opposite directions.

With such a quantum conveyer belt, atoms have been moved over a defined number of lattice sites. In the experiment a coherent transport of the atoms over a distance of up to 7 lattice sites has been demonstrated [12] (see Fig. 5.3).

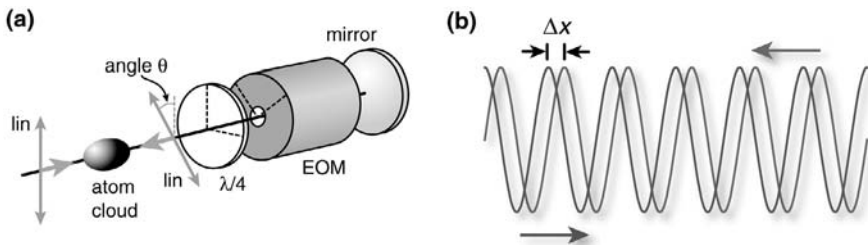


**Fig. 5.2** (a) Schematic experimental setup. A one dimensional optical standing wave laser field is formed by two counterpropagating laser beams with linear polarizations. The polarization angle of the returning laser beam can be adjusted through an electro-optical

modulator. The dashed lines indicate the principal axes of the wave plate and the EOM. (b) By increasing the polarization angle  $\theta$ , one can shift the two resulting  $\sigma^+$  (blue) and  $\sigma^-$  (red) polarized standing waves relative to each other. Cf. the coloured plates in the Appendix.

### 5.2.3

#### Controlled Collisions

In order to realize a controlled interaction between the particles on different lattice sites in a 3D Mott insulating quantum register, the above spin dependent transport sequence can be used. This leads to collisions between neighbouring atoms and can be described through an ensemble of quantum gates acting in parallel [4,7]. Alternatively, these quantum gates can be described as a controllable quantum Ising interaction [8]:

$$H_{\text{int}} \propto g(t) \sum_j \frac{1 + \sigma_z^{(j)}}{2} \frac{1 - \sigma_z^{(j+1)}}{2} \quad (5.1)$$

Here  $g(t)$  denotes the time dependent coupling constant and  $\sigma_z^{(j)}$  is the Pauli spin operator acting on an atom at the  $j^{\text{th}}$  lattice site. For an interaction phase of  $\varphi = 2\pi \times \int_0^{t_{\text{hold}}} g(t) dt / \hbar = (2n + 1)\pi$  one obtains a maximally entangled cluster state, whereas for  $\varphi = 2n\pi$  one obtains a disentangled state [8]. Here  $t_{\text{hold}}$  denotes the time for which the atoms are held together at a common site,  $\hbar$  is Planck's constant and  $n$  is an integer. Let us point out that the creation of such highly entangled states can be achieved in a single lattice shift operational sequence described above and depicted in Fig. 5.4, independent of the number of atoms to be entangled [7,8].

A  $\pi/2$  pulse allows us to place the atom in a coherent superposition of the two states  $|0\rangle \equiv |F = 1, m_F = -1\rangle$  and  $|1\rangle \equiv |F = 2, m_F = -2\rangle$  within a time of  $6\mu\text{s}$ . After creating such a coherent superposition, we use a spin-dependent transfer to split and move the spatial wave function of the atom over half a lattice spacing in two opposite directions depending on its internal state (see Fig. 5.4). Atoms on neighbouring sites interact for a variable amount of time  $t_{\text{hold}}$ . This leads to a controlled conditional phase shift of the

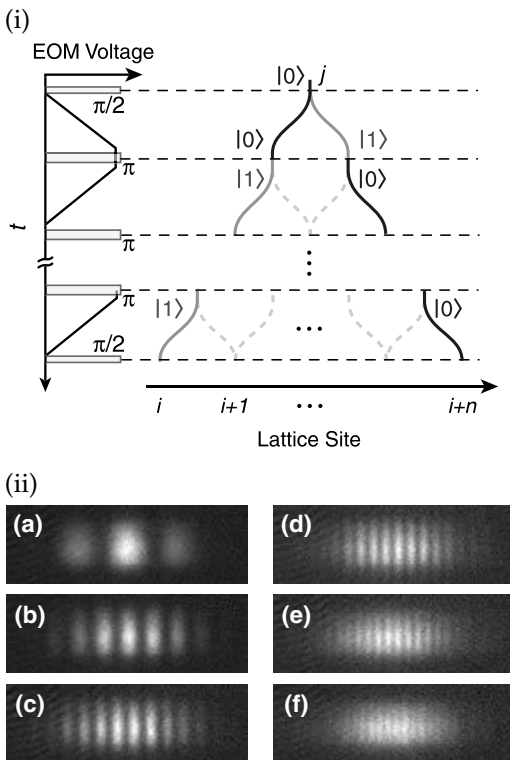


**Fig. 5.3** (i) Schematic sequence used for the quantum conveyor belt. A single atom on lattice site  $j$  can be transported over an arbitrary number of lattice sites depending on its spin state (marked as blue and red curves). (ii) This has allowed us to split the wave function of the atom in a coherent way, such that a single atom simultaneously

moves to the left and to the right. The coherence of the split wave-packets has been demonstrated in an interference experiment. For larger distances between the split wavefunctions, the period of the interference pattern decreases. Cf. the coloured plates in the Appendix.

corresponding many body state. After half of the hold time, a microwave  $\pi$  pulse is furthermore applied. This spin-echo type pulse is mainly used to cancel unwanted single particle phase shifts e.g. due to inhomogeneities in the trapping potentials. It does not, however, affect the non-trivial and crucial collisional phase shift due to the interactions between the atoms. After such a controlled collision, the atoms are moved back to their original site. Then a final  $\pi/2$  microwave pulse with variable phase is applied and the atom number in state  $|1\rangle$  relative to the total atom number is recorded [13].

For short hold times, where no significant collisional phase shift is acquired, a Ramsey fringe with a high visibility of approx. 50% is recorded (see Fig. 5.5). For longer hold times, we notice a strong reduction in the visibility of the

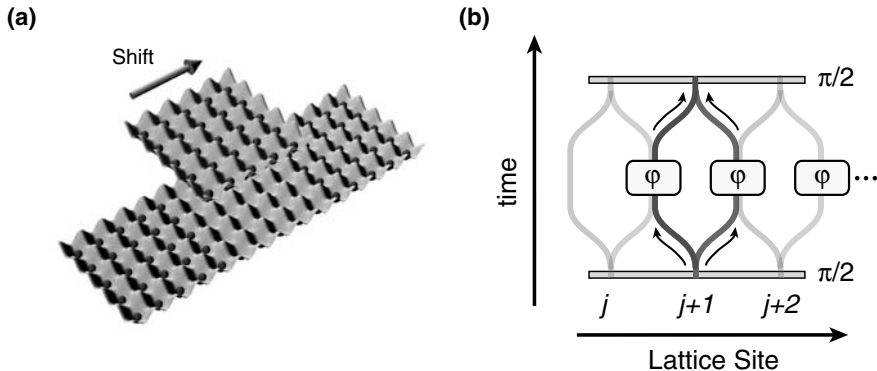


**Fig. 5.4** (a) Controlled interactions between atoms on different lattice sites can be realized with the help of spin-dependent lattice potentials. In such spin dependent potentials, atoms in a, let us say, blue internal state experience a different lattice potential than atoms in a red internal state. These lattices can be moved relative to each other such that two initially separated atoms can be brought into controlled contact with each other. (b) This can be extended to form a massively parallel quantum gate array. Consider a string

of atoms on different lattice sites. First the atoms are placed in a coherent superposition of the two internal states (red and blue). Then spin dependent potentials are used to split each atom such that it simultaneously moves to the right and to the left and is brought into contact with the neighbouring atoms. There both atoms interact and a controlled phase shift  $\varphi$  is introduced. After such a controlled collision the atoms are again moved back to their original lattice sites. Cf. the coloured plates in the Appendix.

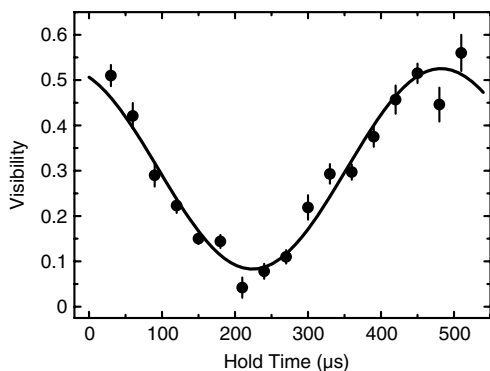


**Fig. 5.5** Visibility of Ramsey fringes vs. hold times on neighbouring lattice sites for the experimental sequence of Fig. 5.4. The solid line is a sinusoidal fit to the data including an offset and a finite amplitude. Such a sinusoidal behaviour of the visibility vs. the collisional phase shift (determined by the hold time  $t_{\text{hold}}$ ) is expected for a Mott insulating state with an occupancy of  $n=1$  atom per lattice site.

Ramsey fringe, with an almost vanishing visibility of approx. 5% for a hold time of 210  $\mu$ s. This hold time corresponds to an acquired collisional phase shift of  $\varphi = \pi$  for which we expect a minimum visibility if the system is

becoming entangled. For a two-particle system this can be understood by observing the resulting Bell state:

$$1/\sqrt{2} \left( |0\rangle_j |+\rangle_{j+1}^\alpha + |1\rangle_j |-\rangle_{j+1}^\alpha \right), \quad (5.2)$$

after the final  $\pi/2$  pulse of the Ramsey sequence has been applied to the atoms. Here  $|+\rangle_{j+1}^\alpha$  and  $|-\rangle_{j+1}^\alpha$  represent two orthogonal superposition states of  $|0\rangle$  and  $|1\rangle$  for which  $|\langle 1|+\rangle^\alpha|^2 + |\langle 1|-\rangle^\alpha|^2 = 0.5$ . A measurement of atoms in state  $|1\rangle$  therefore becomes independent of the phase corresponding to a vanishing Ramsey fringe. This indicates that no single particle operation can place all atoms in either spin-state when a maximally entangled state has been created. The disappearance of the Ramsey fringe has been shown to occur not only for a two-particle system, but is a general feature for an arbitrary  $N$ -particle array of atoms that have been highly entangled with the above experimental sequence [4]. For longer hold times however, the visibility of the Ramsey fringe increases again reaching a maximum of 55% for a hold time of  $450\mu\text{s}$  (see Fig. 5.5). Here the system becomes disentangled again, as the collisional phase shift is close to  $\varphi = 2\pi$  and the Ramsey fringe is restored with maximum visibility. The timescale of the observed collisional phase evolution is in good agreement with the measurements on the Mott insulator transition of the previous section and ab-initio calculations of the onsite matrix element  $U$  [1,2].

## 5.3

### Magnetic Microtraps

Atom chips [14, 15] combine many important features of a scalable architecture for quantum information processing [16]: The long coherence lifetimes of qubits based on hyperfine states of neutral atoms [17], accurate control of the coherent evolution of the atoms in tailored micropotentials [18, 19], and scalability of the technology through microfabrication [20, 21] – which allows the integration of many qubits in parallel on the same device while maintaining individual addressability. Furthermore, atom chips offer the exciting perspective of creating interfaces between the atomic qubits and other QIP systems integrated on the same chip, such as photons in optical fiber cavities or solid-state QIP systems located on the chip surface [22]. However, the experimental demonstration of a fundamental two-qubit quantum gate on an atom chip is an important milestone which still has to be reached.

In [23], a first theoretical proposal for a quantum gate on an atom chip was put forward. In this proposal, the gate operation relies on collisional interactions between two atoms in a state-selective potential on the chip. The

experimental challenge of implementing such a gate can be divided into several steps:

1. A qubit state pair has to be identified which can be manipulated with electromagnetic fields on the atom chip, but still allows for long coherence lifetimes in a realistic experimental situation. In particular, attention has to be paid to decoherence and loss mechanisms induced by the chip surface, which is typically at a distance of only few microns from the atoms.
2. The gate proposed in [23] requires potentials which affect the two qubit states differently in order to achieve conditional logical operations between two atoms. A method to create the required potentials on a chip has to be developed.
3. While Bose-Einstein condensates and thermal ensembles of atoms are routinely manipulated and detected on atom chips, the existing proposals for quantum information processing on atom chips rely on coherent control over single atoms. As a first step towards single atom operation, a single atom detector has to be developed which can be integrated on the atom chip.
4. With a single atom detector available, a method for the deterministic preparation of single neutral atoms in the motional ground state of chip traps with very low occupation probability of excited states has to be found.

In the following, we develop a scenario in which these challenges can be met with atom chips and discuss our experiments towards its realization.

### 5.3.1

#### **Qubit States on the Atom Chip**

Two conflicting requirements have to be met by the qubit states  $\{|0\rangle, |1\rangle\}$  chosen for QIP on an atom chip. On the one hand, both qubit states have to couple to electromagnetic fields which are used for trapping and manipulating the atoms. In all experiments performed so far, at least a part of the trapping potential is provided by static magnetic fields generated by wires or permanent magnet structures on the atom chip. It is therefore desirable that both  $|0\rangle$  and  $|1\rangle$  are magnetically trappable states. On the other hand, gate operations with high fidelity are only possible if the coherence lifetimes of the superposition states  $\alpha|0\rangle + \beta|1\rangle$ , ( $|\alpha|^2 + |\beta|^2 = 1$ ) are sufficiently long. Long coherence lifetimes are possible if qubit basis states are chosen whose energy difference  $h\nu_{10} = E_{|1\rangle} - E_{|0\rangle}$  is robust against noise in realistic experimental situations. In particular, technical fluctuations of magnetic fields are notorious for limiting the coherence lifetime of magnetic-field sensitive qubit states of

atoms or ions to a few milliseconds [24]. On atom chips, magnetic near-field noise due to thermally excited currents in the chip wires is an additional fundamental source of decoherence for magnetic field sensitive qubit states [25]. To achieve long coherence lifetimes on atom chips, it is therefore highly desirable to choose a pair of qubit basis states whose energy difference is insensitive to magnetic field fluctuations.

We choose the  $|F = 1, m_F = -1\rangle \equiv |0\rangle$  and  $|F = 2, m_F = +1\rangle \equiv |1\rangle$  hyperfine levels of the  $5S_{1/2}$  ground state of  $^{87}\text{Rb}$  atoms as qubit basis states. The magnetic moments and the corresponding static Zeeman shifts of the two states are approximately equal, leading to a strong common mode suppression of magnetic field induced decoherence. Furthermore, both states experience nearly identical trapping potentials in magnetic traps, thereby avoiding undesired entanglement between internal and external degrees of freedom of the atoms. At a magnetic field of  $B_0 \sim 3.23\text{G}$ , both states experience the same first-order Zeeman shift and the remaining magnetic field dependence of the transition frequency  $\nu_{10}$  is minimized [26]. In all of our experiments, we therefore adjust the field in the center of the trap to  $B_0$ .

We have studied the coherence properties of the state pair  $\{|0\rangle, |1\rangle\}$  on an atom chip in a series of experiments [17], which we summarize in the following.

The coherence measurements are performed with an ultracold ensemble of atoms, which is prepared in a multi-step sequence involving loading of the microtrap from a mirror-MOT, compression of the trap and evaporative cooling [27]. By the end of this sequence, a thermal atomic ensemble of typically  $N_{\text{at}} = 1.5 \times 10^4$  atoms in state  $|0\rangle$  at a temperature of  $0.6\text{ }\mu\text{K}$  is trapped in a Ioffe-type microtrap. By modulating the currents and offset magnetic fields used to create this trap, the atoms can be placed at distances  $d = 0 - 130\text{ }\mu\text{m}$  from the chip surface with only small changes in the shape of the magnetic potential. It is advantageous to perform the coherence measurements with a small thermal ensemble instead of a Bose-Einstein condensate, since the higher atomic densities in the condensate would lead to a stronger inhomogeneous collisional broadening of the qubit transition [26].

Single-qubit rotations are implemented by coupling the states  $|0\rangle$  and  $|1\rangle$  through a two-photon microwave-rf transition as shown in Fig. 5.6a. The microwave frequency  $\nu_{\text{mw}}$  is detuned by  $\delta/2\pi = 1.2\text{ MHz}$  above the  $|F = 2, m_F = 0\rangle$  intermediate state and radiated from a sawed-off waveguide outside the vacuum chamber. The radio frequency  $\nu_{\text{rf}}$  is either applied to an external coil or to a wire on the chip.  $\nu_{\text{mw}}$  and  $\nu_{\text{rf}}$  are phase locked to a  $10\text{ MHz}$  reference from an ultrastable quartz oscillator.  $\Omega_{\text{mw}}$  and  $\Omega_{\text{rf}}$  are the single-photon Rabi frequencies of the microwave and rf transition, respectively. By applying the two-photon drive for a variable time and detecting the number of atoms  $N_1$  transferred from  $|0\rangle$  to  $|1\rangle$ , we observe Rabi oscillations with a resonant two-

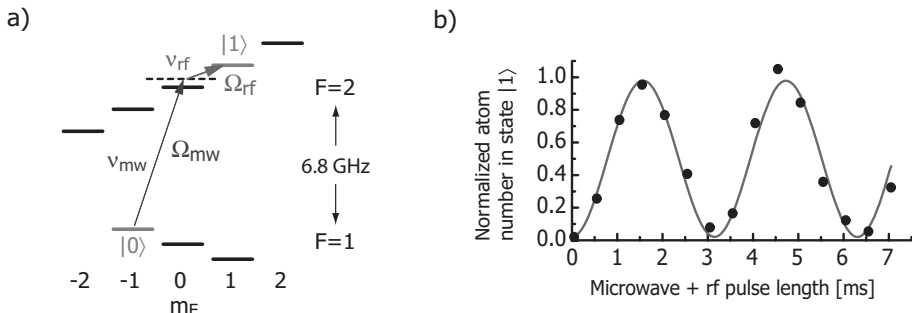


**Fig. 5.6** Single qubit rotations between the states  $|0\rangle$  and  $|1\rangle$ . (a) Ground state hyperfine structure of  $^{87}\text{Rb}$  in a weak magnetic field. The first order Zeeman shift of the states  $|0\rangle$  and  $|1\rangle$  is approximately identical. The two-photon transition  $|0\rangle \leftrightarrow |1\rangle$  is driven by a microwave  $\nu_{\text{mw}}$  and a radio-frequency  $\nu_{\text{rf}}$ .  $\Omega_{\text{mw}}$  and  $\Omega_{\text{rf}}$

are the single-photon Rabi frequencies of the microwave and rf transition, respectively. (b) Two-photon Rabi oscillations recorded as a function of the microwave and rf pulse length. The two-photon Rabi frequency is  $\Omega_{2\text{ph}}/2\pi = 0.32\text{ kHz}$ .

photon Rabi frequency of  $\Omega_{2\text{ph}}/2\pi = 0.32\text{ kHz}$ , see Fig. 5.6b. The maximum transition probability, corresponding to a  $\pi$ -pulse, is  $N_1/N_{\text{at}} = 95 \pm 5\%$ .

The two-photon Rabi frequency is given by  $\Omega_{2\text{ph}} = \Omega_{\text{mw}}\Omega_{\text{rf}}/2\delta$  if  $\Omega_{\text{mw}}^2, \Omega_{\text{rf}}^2 \ll \delta^2$  [28], with  $\Omega_{\text{mw}} \sim \Omega_{\text{rf}} \sim 2\pi \times 25\text{ kHz}$  in our experiment. In the present experiment, the two-photon Rabi-frequency is limited by the available microwave power of typically a few watts. Instead of radiating the microwave and rf from antennas outside the vacuum chamber, they can be applied to the atoms much more efficiently by coupling the microwave and rf signal into wires designed as waveguiding structures on the chip. Consider a waveguide on a chip with a characteristic impedance of  $Z_c = 50\Omega$  carrying a microwave signal of  $P = 1\text{ mW}$ , corresponding to a microwave current of  $I_{\text{mw}} = \sqrt{2P/Z_c} = 6.3\text{ mA}$  on the signal conductor. At a distance of  $d = 10\mu\text{m}$  from the signal conductor, the microwave magnetic field amplitude is approximately  $B_{\text{mw}} \sim \mu_0 I_{\text{mw}}/(2\pi d) = 1.3\text{ G}$ . The microwave induces a coupling with a single-photon Rabi frequency of the order of  $\Omega_{\text{mw}}/2\pi \sim \mu_B B_{\text{mw}}/h = 1.8\text{ MHz}$ . This shows that it is advantageous to couple the atomic transitions with microwave and rf near fields instead of radiation from antennas.

To test for decoherence of the superposition states, we perform Ramsey spectroscopy by applying the following pulse sequence: The atoms in state  $|0\rangle$  are held in the trap before a first  $\pi/2$ -pulse creates a coherent superposition of  $|0\rangle$  and  $|1\rangle$ . After a time delay  $T_R$ , a second  $\pi/2$ -pulse is applied, and the resulting state is probed by detecting the number of atoms transferred to state  $|1\rangle$ . Ramsey fringes are recorded in the time domain by varying  $T_R$  while keeping  $\delta_R = \nu_{\text{mw}} + \nu_{\text{rf}} - \nu_{10}$  fixed ( $\delta_R \ll \nu_{10} \simeq 6.8\text{ GHz}$ ). Alternatively, Ramsey fringes are recorded in the frequency domain by scanning  $\delta_R$  while  $T_R$  remains constant. Loss of coherence of the superposition states can show

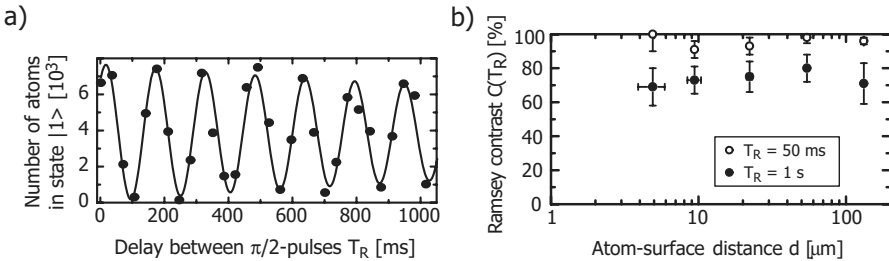


**Fig. 5.7** Coherence lifetime measurements for the qubit state pair. (a) Ramsey spectroscopy of the  $|0\rangle \leftrightarrow |1\rangle$  transition with atoms held at a distance  $d = 9\ \mu\text{m}$  from the chip surface. An exponentially damped sine fit to the Ramsey fringes yields a  $1/e$  coherence lifetime of  $\tau_c = 2.8 \pm 1.6\ \text{s}$ . Each data point corresponds to a single shot of

the experiment. (b) Contrast  $C(T_R)$  of the Ramsey fringes as a function of atom-surface distance  $d$  for two values of the time delay  $T_R$  between the  $\pi/2$ -pulses. For each data point,  $C(T_R) = (N_{\max} - N_{\min}) / (N_{\max} + N_{\min})$  was obtained from a sinusoidal fit to frequency-domain Ramsey fringes.  $N_{\max}$  ( $N_{\min}$ ) is the maximum (minimum) of the oscillation in  $N_1$ .

up in different ways in the Ramsey signal. A spatial variation of  $\nu_{10}$  across the atomic ensemble leads to a decay of the contrast of the Ramsey fringes, while temporal fluctuations of  $\nu_{10}$  lead to increasing phase noise on the Ramsey oscillation as  $T_R$  is increased.

Fig. 5.7a shows Ramsey interference in the time domain. The number of atoms detected in state  $|1\rangle$  oscillates at the frequency difference  $\delta_R = 6.4\ \text{Hz}$ , while the interference contrast decays with a coherence lifetime of  $\tau_c = 2.8 \pm 1.6\ \text{s}$ . The measurement shown in Fig. 5.7a was performed at a distance  $d = 9\ \mu\text{m}$  from the room-temperature chip surface. In [26], similar coherence lifetimes are reported for the same state pair, but with atoms in a macroscopic magnetic trap, far away from any material objects. This suggests that atom-surface interactions indeed do not limit the coherence lifetime in our present experiment.

To further probe for surface effects, we study the decoherence of the Ramsey signal as a function of atom-surface distance. Atomic ensembles are prepared in traps at different distances  $d$  from the surface. In each trap, we record Ramsey oscillations in the frequency domain for several values of  $T_R$  and determine the contrast  $C(T_R)$  of each oscillation. Fig. 5.7b shows the result of these measurements for  $T_R = 50\ \text{ms}$  and  $T_R = 1\ \text{s}$ . Within the experimental error, the contrast does not show a dependence on atom-surface distance for  $d = 5 - 130\ \mu\text{m}$ . Additionally, we have compared the signal-to-noise ratio  $S/N$  of the interference signal in the different traps. We typically observe  $S/N = 6$  for  $T_R = 1\ \text{s}$ , where  $S$  is the peak-to-peak amplitude of the sinusoidal fit to the Ramsey oscillation and  $N$  is the standard deviation of the fit residuals over one oscillation period.  $S/N$  is independent of  $d$  within experimental error, indicating that the processes causing amplitude and phase fluctuations of the interference signal do not depend on atom-surface distance on this time

scale. The observed noise on the Ramsey oscillation is mostly phase noise and can be attributed to ambient magnetic field fluctuations, which are independent of atom-surface distance.

Our experiments show that the robust qubit state pair considered here can be manipulated on the atom chip with coherence lifetimes  $\tau_c > 1$  s at distances down to a few microns from the chip surface. In the proposal for a quantum controlled phase gate on an atom chip [23], a gate operation time of  $\tau_g = 0.4$  ms was estimated. Implementing this gate with our qubit state pair,  $\tau_c/\tau_g \sim 10^3$  gate operations could be performed before decoherence from magnetic noise occurs. In contrast, in the original proposal of [23], the qubit is encoded in two states with a magnetic-field sensitive energy difference. The magnetic field sensitivity is more than a factor of  $10^3$  higher than for our state pair, so that expected coherence lifetimes would be comparable to the gate operation time.

### 5.3.2

#### State-dependent Microwave Potentials

An implementation of the phase gate proposed in [23] with our qubit state pair requires potentials which affect the two qubit states differently. However, a combination of static magnetic and electric fields, as considered in [23, 29], does not provide state-selective potentials for our state pair, whose magnetic moments and electrostatic polarizabilities are equal. Optical potentials created by focussed laser beams with a frequency close to the D1 or D2 transition of  $^{87}\text{Rb}$  are also impractical: if the detuning of the laser from the atomic resonance is much larger than the hyperfine splitting of the  $^{87}\text{Rb}$  ground state, the resulting optical potentials are again nearly identical for the states  $|0\rangle$  and  $|1\rangle$ . If, on the other hand, a detuning comparable to the hyperfine splitting is used, a differential optical potential could be created, but problems with decoherence due to spontaneous scattering of photons would arise.

To generate the state-dependent potential for our qubit, we propose to use microwave potentials in addition to static magnetic potentials on the atom chip [17]. Microwave potentials arise due to the AC Zeeman effect (the magnetic analog of the AC Stark effect) induced by tailored microwave near-fields. In  $^{87}\text{Rb}$ , microwave potentials derive from magnetic dipole transitions with a frequency near  $\omega_0/2\pi = 6.835$  GHz between the  $F = 1$  and  $F = 2$  hyperfine manifolds of the ground state. The magnetic component of a microwave field of frequency  $\omega_{\text{mw}} = \omega_0 + \Delta$  couples the  $|F = 1, m_1\rangle$  to the  $|F = 2, m_2\rangle$  sublevels and leads to energy shifts that depend on  $m_1$  and  $m_2$ . In a spatially varying microwave field, this results in a state-dependent potential landscape.

In Fig. 5.8a, this situation is shown for a  $^{87}\text{Rb}$  atom subject to a static magnetic field  $\mathbf{B}_0(\mathbf{r})$ , which defines the quantization axis, in combination with a

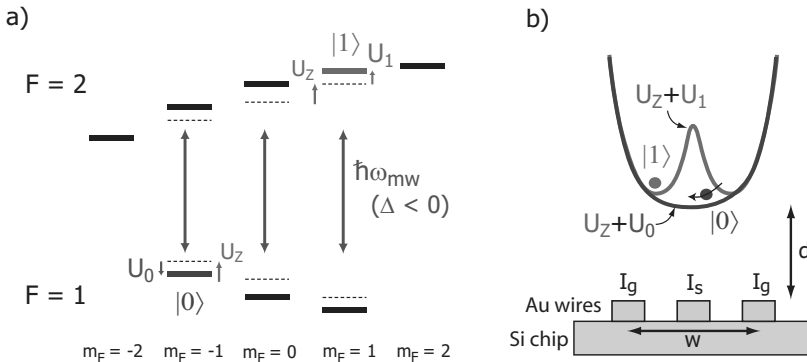


**Fig. 5.8** State-dependent microwave potentials for the qubit states. (a) Energy-level diagram of the hyperfine structure of the  $^{87}\text{Rb}$  ground state in a combined static magnetic and microwave field.  $U_Z$  indicates the energy shift due to the static Zeeman effect, which is identical for  $|0\rangle$  and  $|1\rangle$ . The magnetic field of the microwave couples the levels of  $F = 1$  to the levels of  $F = 2$ , giving rise to energy shifts  $U_1$  ( $U_0$ ) for state  $|1\rangle$  ( $|0\rangle$ ), here shown for pure  $\pi$  polarization and  $\Delta < 0$  (red detuning).

This shift has opposite sign for  $|0\rangle$  and  $|1\rangle$ . (b) Chip layout and state-dependent double well potential for a collisional phase gate on the atom chip. The three gold conductors form a coplanar waveguide of width  $w$  for the microwave.  $I_s$  ( $I_g$ ) are the currents on the signal (ground) wires. The wires carry both stationary and microwave currents, see text. In combination, these currents create the potential  $U_Z + U_1$  for state  $|1\rangle$  and  $U_Z + U_0$  for state  $|0\rangle$  at a distance  $d$  from the chip surface.

microwave magnetic field  $\mathbf{B}_{\text{mw}}(\mathbf{r}) \cos(\omega_{\text{mw}}t)$ . The static field gives rise to the static Zeeman potential  $U_Z(\mathbf{r}) = \mu_B g_F m_F |\mathbf{B}_0(\mathbf{r})|$ , which is identical for the qubit states  $|0\rangle$  and  $|1\rangle$ , since for both states  $g_F m_F = 1/2$ . For simplicity, we assume that  $\mathbf{B}_{\text{mw}}(\mathbf{r})$  is oriented parallel to the static field  $\mathbf{B}_0(\mathbf{r})$ , corresponding to pure  $\pi$  polarization of the microwave. The microwave field thus couples the transitions  $|0\rangle \leftrightarrow |F = 2, m_F = -1\rangle$  and  $|F = 1, m_F = 1\rangle \leftrightarrow |1\rangle$  with identical resonant Rabi frequencies  $\Omega_R(\mathbf{r}) = \sqrt{3/4} \mu_B |\mathbf{B}_{\text{mw}}(\mathbf{r})|/\hbar$ . In the limit of large detuning  $\hbar|\Delta| \gg \hbar\Omega_R$ ,  $U_Z$ , the coupling leads to microwave potentials given by

$$U_1(\mathbf{r}) = -\frac{\hbar|\Omega_R(\mathbf{r})|^2}{4\Delta} \quad \text{and} \quad U_0(\mathbf{r}) = \frac{\hbar|\Omega_R(\mathbf{r})|^2}{4\Delta}$$

for  $|1\rangle$  and  $|0\rangle$ , respectively. Since the qubit state  $|0\rangle$  belongs to  $F = 1$  while  $|1\rangle$  belongs to  $F = 2$ , the microwave potential has opposite sign for the two states, giving rise to the desired state-dependence of the potential.

In a combined static magnetic and microwave trap, in general both  $\mathbf{B}_0(\mathbf{r})$  and  $\mathbf{B}_{\text{mw}}(\mathbf{r})$  vary with position. This leads to a position-dependent microwave coupling with in general all polarization components present. If  $\hbar|\Delta| \gg \hbar\Omega_R$ ,  $U_Z$ , the energy shifts due to the microwave coupling can be evaluated for each transition separately. The overall magnetic microwave potential for the level  $|F, m_F\rangle$  equals the sum of the energy shifts due to the individual transitions connecting to this level. The Zeeman splitting due to the static field (a few

MHz) prevents two-photon transitions between sublevels  $m_F$  belonging to the same  $F$  quantum number.

A trap for neutral atoms based on microwave potentials has been proposed in [30] and experimentally demonstrated in [31]. This trap employs microwave radiation in the far field of the source. Unlike in the case of optical radiation, which can be tightly focussed due to its short wavelength, the centimeter wavelength  $\lambda_{\text{mw}}$  of microwave radiation poses severe limitations on far-field traps: field gradients are very weak [31] and structuring the potential on the micrometer scale is impossible.

On atom chips, there is a natural solution to this problem [17]. The atoms are trapped at distances  $d \ll \lambda_{\text{mw}}$  from the chip surface. Thus, they can be manipulated with microwave near fields, generated by microwave signals in on-chip transmission lines [32]. In the near field of the source currents and voltages, the microwave fields have the same position dependence as the static fields created by equivalent stationary sources. The maximum field gradients depend on the size of the transmission line conductors and on the distance  $d$ , not on  $\lambda_{\text{mw}}$ . In this way, state-dependent microwave potentials varying on the micrometer scale can be realized. In combination with state-independent static magnetic microtraps, the complex potential geometries required for QIP can be realized.

The state-dependent double well potential needed for the phase gate proposed in [23] can be created with a chip layout as shown in Fig. 5.8b. The three wires form a coplanar waveguide for the microwave. They carry both microwave and stationary currents,  $I_s = I_c + I_{\text{mw}} \cos(\omega_{\text{mw}} t)$  and  $I_g = I_o - (I_{\text{mw}}/2) \cos(\omega_{\text{mw}} t)$ . The stationary currents  $I_c$  and  $I_o$  flow in opposite directions and create a static magnetic double well potential at a distance  $d$  from the chip surface, as discussed in [14]. We assume that the atoms are tightly confined in the transverse dimensions by a static magnetic potential created by additional wires not shown in the figure. The microwave currents create a microwave potential which is used to selectively remove the barrier of the double well for state  $|0\rangle$ , while increasing the barrier height for state  $|1\rangle$  (Fig. 5.8b). Note that for  $\Delta < 0$ , as in the figure, the labeling of the states  $|1\rangle$  and  $|0\rangle$  is interchanged compared to [23].

To give a specific example, we consider atoms in a static-field trap at  $d = 1.8 \mu\text{m}$  from a microwave guiding structure of size  $w = d$  carrying a microwave signal of amplitude  $I_{\text{mw}} = 15 \text{ mA}$ . A simulation of the microwave field yields a coupling with  $\Omega_R/2\pi \sim 3.3 \text{ MHz}$  at the position of the static double well barrier, taking into account the magnetic microwave field of the signal wire and both ground wires. For  $\Delta = 10 \Omega_R$ , the change in the static magnetic moment of the qubit states due to the coupling is of the order of  $10^{-3}$ , such that both states still experience approximately the same static magnetic potentials. The microwave, on the other hand, leads to a differential energy

shift of  $U_1 - U_0 = h \cdot 160$  kHz, sufficiently large to remove the barrier for state  $|0\rangle$ . A detailed simulation for a realistic atom chip design shows that an improved version of the quantum phase gate of [23] can be implemented with our robust qubit state pair using microwave potentials on the atom chip. We find an overall gate fidelity of  $F = 0.996$  at a gate operation time of  $\tau_g = 1.1$  ms [33], compatible with the requirements for fault-tolerant quantum computation.

### 5.3.3

#### **Qubit Readout in Microtraps**

The QIP schemes considered here use single atoms as qubit carriers, and thus the final readout requires single-atom detectivity. Again, the ability of atom chips to independently transport the individual qubit atoms is a key advantage: atoms can be brought close together for interaction, but spaced far apart and even transported to a remote detector for readout. This removes the optical resolution limitation that is still an unsolved problem in optical lattices. Thus, the basic requirement on an atom chip qubit detector is single-atom detectivity and compatibility with the presence of the chip. In our experiments, we have focused on optical detectors, where fast progress could be achieved. As an additional feature beyond single-atom detectivity, we have concentrated on detectors that will ultimately allow quantum non-demolition (QND) measurement of the number of atoms. A QND trapped-atom detector would only perturb the phase of the atomic state, but not, in particular, its vibrational energy in the trap. Therefore, such a detector could also be used in qubit preparation, for example in a “feedback loop” that prepares a single-atom state from a larger initial BEC, by combining it with a switchable loss mechanism.

To detect an atom optically, either absorption or dispersion can be used. The collection of fluorescence light from a single trapped atom is possible and has recently enabled remarkable experiments [34, 35]. However, the recoil from the spontaneously emitted fluorescence photons causes heating, ruling out the possibility of a QND measurement. It might seem that single-pass dispersive detection would offer a straightforward solution: the atom trap would be positioned in one arm of an interferometer, operating at a wavelength that is detuned far away from the atomic transitions. However, to reach the high sensitivity required for single-atom detection, a large number of photons must be sent through the interferometer, and it turns out that even this type of detection inevitably leads to spontaneous emission [36, 37]. The situation changes when an optical cavity is used to enhance the interaction of the atom with the optical field. In this case, single-atom detection with high signal-to-noise ratio

is possible with less than one spontaneous emission on average, and improves with high cavity finesse  $\mathcal{F}$  and small mode cross-section  $w^2$ .

This situation is adequately analyzed in the framework of cavity QED (cQED) [38]. The fundamental cavity QED parameters are the coherent atom-photon coupling rate  $g_0$ , the cavity damping rate  $\kappa$  and the linewidth of the atomic transition  $\gamma$ . For single-atom detection, these parameters do not enter independently, but in the combination  $C = g_0^2/2\kappa\gamma$  called the cooperativity parameter. The onset of the QND regime corresponds to  $C > 1$ . Note that this condition is not identical with the strong coupling regime of cQED,  $g_0 > \kappa, \gamma$ . Indeed, QND detection is possible even in the regime of weak coupling.

To translate the cooperativity criterion  $C > 1$  into requirements on the cavity, it is instructive to analyze how  $g_0$  and  $\kappa$  relate to the design parameters of the cavity. For a symmetric Fabry-Perot (FP) cavity, these are the mirror radius of curvature  $R$ , the effective cavity length  $d$ , and the cavity finesse  $\mathcal{F} \approx \pi/(T + \ell)$ , where  $T$  and  $\ell$  are the transmission and losses of a single mirror. One finds

$$\kappa \propto \mathcal{F}^{-1}d^{-1} \quad (5.3)$$

$$g_0 \propto d^{-3/4}R^{-1/4} \quad (5.4)$$

$$C \propto \mathcal{F}(dR)^{-1/2} \quad (5.5)$$

$C$  can be alternatively expressed as

$$C = \frac{3\lambda^2\mathcal{F}}{\pi^3 w^2} \quad (5.6)$$

where  $w$  is the mode waist diameter (and we assume that the atoms are placed in this waist). This latter relation makes it intuitively clear why  $C$  is the relevant parameter for single-atom detection efficiency: it is proportional to  $\mathcal{F}$  (number of round-trips of a cavity photon), and inversely proportional to the mode waist diameter (which is to be compared to the atomic scattering cross-section  $\sigma$ ). These relations hold within the stability range of the cavity, and as long as the mode diameter on the mirrors is small compared to the mirror diameter, so that clipping loss can be neglected.

For the extremely short, small-volume cavities that we consider here,  $\gamma$  is always much smaller than  $\kappa$  and  $g_0$ . Therefore, if the goal is to enter as far as possible into the strong-coupling regime, the cavity should optimize  $g_0/\kappa$ , i.e., increase the mirror distance  $d$  towards the limit of the stability range. Indeed, for a given mirror curvature,  $\kappa$  drops as  $\kappa \propto d^{-1}$ , whereas  $g_0$  only decreases as  $g_0 \propto d^{-3/4}$ , as long as  $d \ll R$ : the ratio  $g_0/\kappa$  increases with growing  $d$  despite the decrease in the absolute value of  $g_0$ . By contrast, a cavity for single-atom detection should be designed to optimize the cooperativity  $C$ . According to the above proportionalities, this means that it should have a short length and small radius of curvature. A high finesse is obviously beneficial in both cases.

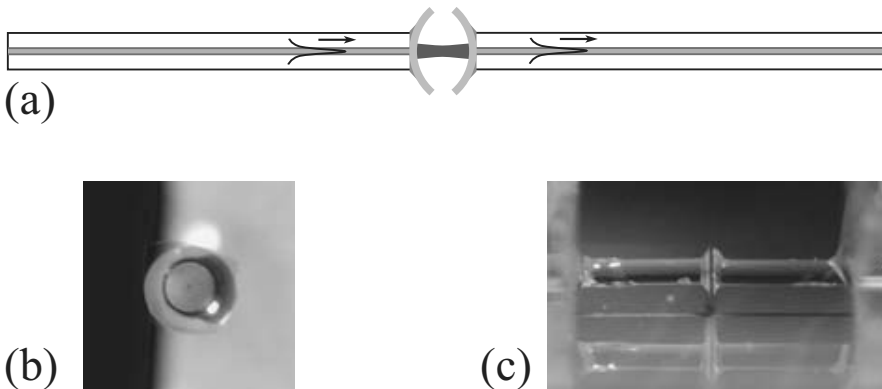


**Fig. 5.9** (a) Concept of the stable FFP cavity. The basic building block is an optical fiber functionalized with a concave dielectric mirror. Two such fibers, brought sufficiently close to each other, result in a stable Fabry-Perot cavity which can be interrogated remotely, either in transmission or in reflection, through the two fibers (b) A single-mode

optical fiber, total diameter 125  $\mu\text{m}$ , processed with a concave mirror. The mirror has radius 1000  $\mu\text{m}$  with a stopband centered at 780 nm. (c) A complete FFP cavity, realizing the configuration (a), mounted on an atom chip used in the detection of cold atoms (Fig. 5.11). Cf. the coloured plates in the Appendix.

### 5.3.3.1 Stable fiber Fabry-Perot Cavities

The “gold standard” for cQED cavities is still being set by macroscopic FP cavities with superpolished, concave mirrors. These mirrors have relatively large radii of curvature ( $R = 20\text{ cm}$  is typical) and achieve record finesse values of  $\mathcal{F} > 2 \times 10^6$  [39]. However, these cavities are not compatible with a chip-based microtrap. The trap-surface distance is  $\lesssim 250\text{ }\mu\text{m}$ , whereas the diameter of existing superpolished FP mirrors is at least  $\sim 1\text{ mm}$ , so that it would be extremely difficult to place the optical axis sufficiently close to the substrate surface and still maintain the tight mirror spacing required for high  $C$ . We have developed stable, fiber-based Fabry-Perot resonators (FFPs) [37] that avoid this problem. They employ concave dielectric mirror coatings with small radius of curvature, realized on the fiber tip. A stable cavity is constructed from two closely spaced fiber tips placed face-to-face (Fig. 5.9(a)). Thus, as an important difference to other microcavities such as microtoroid resonators (see for example [40]), the cavity mode is located in free space between the fibers, thus avoiding the extremely restrictive positioning requirements imposed by evanescent-field coupling.

### 5.3.3.2 FFP Cavity Fabrication and Performance

We have fabricated stable, miniature FFP cavities using two different methods. Method 1 uses a commercially available lift-off coating [41]. The coating is produced on a convex template (we use a commercial ball lens), and then glued onto the fiber tip. After curing the transparent epoxy glue with UV light,

the coating sticks to the fiber and a small force is enough to detach it from the ball lens template. The result is a fiber functionalized with a highly reflecting concave mirror, as shown in Fig. 5.9(b). A complete FFP cavity is shown in Fig. 5.9(c). This method reproducibly leads to cavity finesse values  $\mathcal{F} > 1000$  with modest experimental effort. We have used a cavity of this type to detect magnetically guided and trapped atoms, as described below. Method 2 employs laser surface processing to produce a low-roughness concave depression on the fiber tip, followed by multilayer coating using the ion beam sputtering technique. With this technique, we obtain finesse values  $\mathcal{F} \sim 35000$  [43].

In both cases, because of the small fiber diameter ( $125\text{ }\mu\text{m}$ ), very short cavities ( $< 10\lambda/2$ ) can be realized even when radii of curvature  $R \leq 1\text{ mm}$  are used, still leaving a sufficiently large gap to introduce cold atoms. Let us consider the concrete example of a cavity that we have fabricated using method 1. The mirror curvature is  $R = 1\text{ mm}$  and the distance  $d = 27\text{ }\mu\text{m}$ , leading to a mode volume  $V_m = 600\text{ }\mu\text{m}^3$ , to be compared to  $V_m = 1680\text{ }\mu\text{m}^3$  for the smallest-volume macroscopic FP cavity that has been used with atoms [44]. In terms of cavity QED parameters, the small mode volume results in an exceptionally high coherent atom-photon coupling rate,  $g_0/2\pi = 180\text{ MHz}$  (calculated for the Rb D2 line at  $\lambda = 780\text{ nm}$ ). Therefore, in spite of a comparatively high cavity damping rate  $\kappa/2\pi = 2.65\text{ GHz}$ , which results from the moderate finesse of the transfer coating and short cavity length, the cavity reaches a single-atom cooperativity parameter greater than unity,  $C = g_0^2/2\kappa\gamma = 2.1$  (for the Rb D2 line,  $\gamma/2\pi = 3.0\text{ MHz}$ ), signaling the onset of quantum effects such as enhanced spontaneous emission into the cavity mode [38] and a significant modification of cavity transmission by the presence of a single atom.

Below we present an experiment in which we use the two-fiber cavity to detect an extremely small number of cold atoms magnetically trapped in the cavity using an atom chip. What is still missing is an improved absolute calibration of these results in order to determine whether they already realize, or only come close to single-atom detectivity. In any case, considering that the “method 2” cavities are now available and improve finesse by a factor 30, it seems clear that the problem of qubit detection can be solved using our FFP technology. Beyond QIP, we believe that this cavity type is also attractive for experiments exploiting the strong optical dipoles of semiconductor quantum dots, semiconductor nanocrystals and molecules, and for channel separation in telecommunication.

### 5.3.4

#### On-chip Atom Detection with a FFP Cavity

We have detected magnetically trapped atoms with an FFP cavity on an atom chip [41]. The atoms are trapped on the chip and evaporatively cooled as in

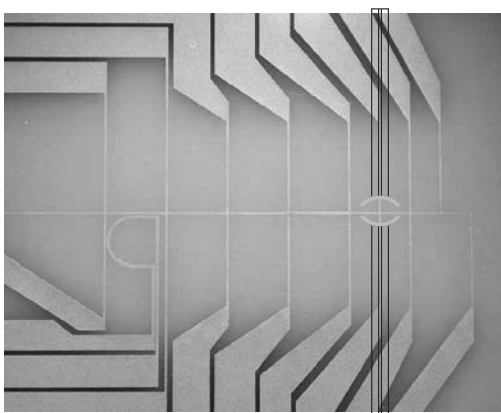


**Fig. 5.10** The chip used for detecting magnetically trapped atoms by their interaction with a single optical mode in a fiber Fabry-Perot (FFP) cavity. The position of the cavity is indicated in exaggerated size for better visibility. Atoms are first trapped in

the structures on the left side of the picture, then transported towards the cavity and evaporatively cooled in a multistep procedure and finally positioned in the resonator mode, where they are detected by the change in cavity transmission.

our previous experiments [17], but on a chip which incorporates the FFP resonator fabricated according to method 1 described above (Fig. 5.10). Trapped and guided atoms could be reproducibly detected in a great variety of experimental parameters and procedures. The cavity transmission signal allowed detection with good signal-to-noise ratio even when the atom number was far too small to be visible by our absorption-imaging camera system. A typical temperature of the atom cloud in the resonator was around  $1\text{ }\mu\text{K}$ , with typical longitudinal and transverse trap frequencies around  $100\text{ Hz}$  and  $1\text{ kHz}$ , respectively. Clouds containing extremely few atoms were prepared using the RF knife, by applying repeated, rapid radiofrequency scans across the “trap bottom” frequency.

Fig. 5.11 shows a cavity transmission spectrum recorded by scanning the probe laser across the D2 atomic transition for a fixed atom-cavity detuning of  $\delta_{\text{cav}} = 0$ . Each point in the spectrum corresponds to a complete experimental sequence of preparation, evaporative cooling, positioning and detection. The atoms are initially trapped in the  $|F = 2, m = 2\rangle$  ground state. The three transmission minima correspond to transitions from this state to the  $F = 1, 2, 3$  sublevels of the  $5p_{3/2}$  excited state. We have recorded such spectra for various  $\delta_{\text{cav}}$  and for different mean atom numbers.

The parameter of interest is the minimum number  $N_{\text{min}}$  of atoms that must interact with the cavity mode in order to produce a detection signal with a good signal-to-noise ratio, say, 4. The actual number of detected atoms is more difficult to extract from the measurements than with a macroscopic resonator.

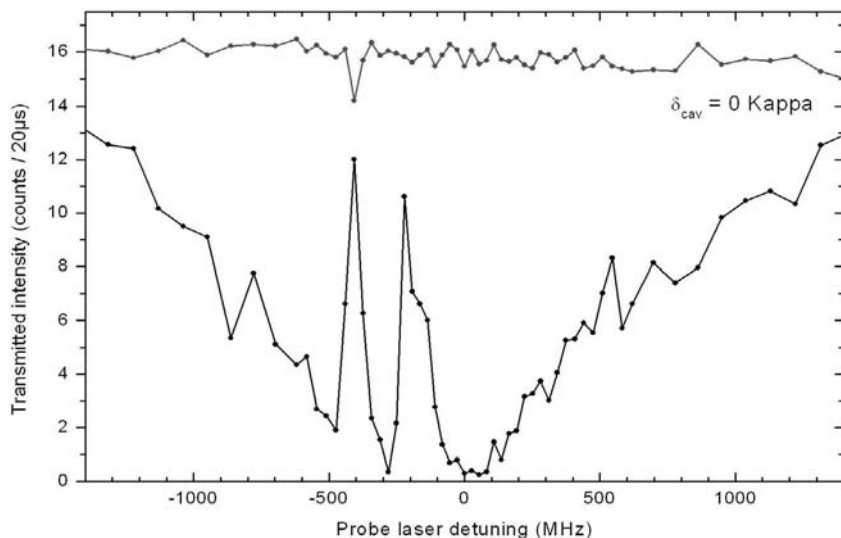


**Fig. 5.11** Cavity transmission spectrum without atoms (upper, red curve) and with atoms magnetically trapped in the on-chip FFP cavity (lower, black curve). The atom-cavity detuning is fixed at  $\delta_{\text{cav}} = 0$ . Each point corresponds to a complete experimental

sequence of preparation, evaporative cooling, positioning and detection, for the atom-laser detuning indicated on the abscissa. Lines are to guide the eye. Zero probe laser detuning corresponds to the  $F = 2 \rightarrow F' = 3$  transition within the D2 multiplett.

This is mainly due to large error bars on the measured on-resonance cavity transmission, which in turn are caused by the fact that incoupling mirror and fiber cannot be separated. For the resonator used in the experiment described here, the on-resonance transmission is in the permille range. This is due to an excessive number of layers in the dielectric mirror stack, applied by the coating manufacturer in an attempt to maximise the reflectivity. This problem no longer occurs with the cavities fabricated later according to method 2. In the experiments described here, however, the low transmission means that for every detected photon, roughly  $10^3$  photons have interacted with the atom without contributing to the signal. They do, however, contribute to heating due to spontaneous-emission, and we therefore expect the detectivity in this experiment to be limited by this spontaneous heating. Nevertheless, we expect  $N_{\min}$  to be close to or below 1.

From atom number measurement by absorption imaging, we can infer an upper limit of  $N_{\min}$  which is of the order of 50 atoms. A much more precise value of  $N_{\min}$  can be obtained from spectra such as in Fig. 5.11. These spectra were obtained with an FFP cavity of relatively low finesse  $\mathcal{F} \sim 260$ . This corresponds to a weak-coupling regime in which the atom-cavity interaction can be understood semiclassically. The spectra depend very strongly on the mean atom number in the cavity. We are now using a semiclassical model to

fit the spectra, which will allow us to determine the actual number of intracavity atoms with good precision without the need to know the absolute cavity transmission. In this way, we will be able to determine the detectivity from the experimental results.

These results demonstrate the suitability of FFP resonators for qubit read-out on atom chips. The combination of this new cavity type with atom chips will enable new applications beyond atom detection. The laser-machined resonators (method 2 described above), which we have now integrated into an atom chip experiment, reach a finesse  $\mathcal{F} \sim 35000$ , combined with an exceptionally small mode volume. For these resonators, with a mirror spacing of  $d = 25 \mu\text{m}$ , one obtains  $g_0 \sim 2\pi \times 400 \text{ MHz}$  and  $g_0/\kappa \sim 4$ , entering the strong-coupling regime of cavity QED. But even in the regime of weak coupling, trapping an ultracold atom cloud in an optical cavity of high cooperativity, as demonstrated here, is a new experimental option which can radically simplify the implementation of high-fidelity atom-photon interfaces, for example in quantum communication [45]. Very recently, we have observed high contrast “telegraph signals”, which demonstrate the single-atom detection capability of these cavities. We have also been able to couple a trapped BEC to the cavity mode [42].

### 5.3.5

#### Single Atom Preparation

With the advent of single-atom detectors on atom chips, it becomes possible to address the problem of deterministic single-atom preparation. For the QIP schemes considered here, each qubit is a single atom *in the ground state of a magnetic potential*. A first, simplistic approach is to start from a BEC and induce losses to reduce the atom number to an average value of 1. With a QND detector, the actual number can be measured, and further reduced if necessary, with negligible excitation and loss. Nevertheless, this “trial-and-error” method becomes impractical for large numbers of qubits. Proposals for deterministic single atom preparation have been put forward in [46, 47]. The key element in these methods is a tightly confining potential, in which states with 1, 2 etc. atoms are energetically resolved due to the collisional interaction. A BEC serves as a reservoir from which single atoms can be repeatedly extracted in a deterministic way. Atom chips appear ideally suited to implement this idea, and we expect it to be experimentally realized within the next two years.

## 5.4

### Conclusion

The fast experimental progress made with atoms in optical lattices and magnetic microtraps underlines the great potential of ultracold quantum gases for applications in QIP. In the experiments with optical lattices described here, a massively parallel quantum gate array was demonstrated for the first time [13], which allows the creation of a highly entangled many-body cluster state. In the future, it is important to explore quantum computing schemes which rely only on single-atom operations and measurements on the entangled many-body state. New theoretical developments show that even without the possibility of performing single-atom manipulations in the optical lattice, a quantum computer based on the controlled collisions demonstrated here could simulate a large class of complex Hamiltonians with translational invariance, which play an important role in condensed-matter physics.

A general quantum computer, however, requires the possibility to perform single-atom operations and measurements. The fiber Fabry-Perot resonators described here are an ideal system for achieving this goal. The detection of very small atom numbers was demonstrated in our experiments with a FFP resonator integrated on the atom chip [41]. It seems clear that the problem of single qubit detection can be solved in the nearest future with the technical improvements of this detector which have been recently implemented [43]. We have furthermore shown that by using a qubit state pair which is robust against magnetic-field fluctuations, coherence lifetimes exceeding one second can be achieved on an atom chip with atoms at distances down to a few microns from the chip surface [17]. Based on these developments, the main experimental challenges for the future are the reproducible preparation of single-atom states and the implementation of a quantum phase gate using microwave potentials on the atom chip. The theoretical fidelity of such a gate is 0.996 [33], compatible with the requirements for fault-tolerant quantum computation.

The success of these future experiments will determine whether QIP with neutral atoms is an advantageous alternative to other systems such as trapped ions, and allows the experimental investigation of even more complex problems such as quantum error correction.

### Acknowledgement

This work has been funded by the Bavarian State Government (Kompetenznetzwerk Quanteninformation “A8”). Y.C. gratefully acknowledges support from the “CONQUEST” network (MRTN-CT-2003-505089).

## References

- 1 D. Jaksch et al., *Phys. Rev. Lett.* **81**, 3108 (1998).
- 2 M. Greiner et al., *Nature* **415**, 39 (2002).
- 3 G. K. Brennen et al., *Phys. Rev. Lett.* **82**, 1060 (1999).
- 4 H.-J. Briegel et al., *J. Mod. Opt.* **47**, 415 (2000).
- 5 R. Raussendorf and H.-J. Briegel, *Phys. Rev. Lett.* **86**, 5188 (2001).
- 6 G. K. Brennen, I. H. Deutsch, and C. J. Williams, *Phys. Rev. A* **65**, 022313 (2002).
- 7 D. Jaksch et al., *Phys. Rev. Lett.* **82**, 1975 (1999).
- 8 H.-J. Briegel and R. Raussendorf, *Phys. Rev. Lett.* **86**, 910 (2001).
- 9 A. Sørensen and K. Mølmer, *Phys. Rev. Lett.* **83**, 2274 (1999).
- 10 W. Dür et al., *Phys. Rev. A* **66**, 052319 (2002).
- 11 E. Jané et al., *Quant. Inf. Comp.* **3**, 15 (2003).
- 12 O. Mandel et al., *Phys. Rev. Lett.* **91**, 010407 (2003).
- 13 O. Mandel et al., *Nature* **425**, 937 (2003).
- 14 J. Reichel, *Appl. Phys. B* **74**, 469 (2002).
- 15 R. Folman, P. Krüger, J. Schmiedmayer, J. Denschlag, and C. Henkel, *Adv. At. Mol. Opt. Phys.* **48**, 263 (2002).
- 16 D. P. DiVincenzo, *Fortschr. Phys.* **48**, 771 (2000).
- 17 P. Treutlein, P. Hommelhoff, T. Steinmetz, T. W. Hänsch, and J. Reichel, *Phys. Rev. Lett.* **92**, 203005 (2004).
- 18 P. Hommelhoff, W. Hänsel, T. Steinmetz, T. W. Hänsch, and J. Reichel, *New J. Phys.* **7**, 3 (2005).
- 19 T. Schumm, S. Hofferberth, L. M. Andersson, S. Wildermuth, S. Groth, I. Bar-Joseph, J. Schmiedmayer, and P. Krüger, *Nature Physics* **1**, 57 (2005).
- 20 B. Lev, *Quant. Inf. Comp.* **3**, 450 (2003).
- 21 S. Groth, P. Krüger, S. Wildermuth, R. Folman, T. Fernholz, J. Schmiedmayer, D. Mahalu, and I. Bar-Joseph, *Appl. Phys. Lett.* **85**, 2980 (2004).
- 22 A. S. Sørensen, C. H. van der Wal, L. I. Childress, and M. D. Lukin, *Phys. Rev. Lett.* **92**, 063601 (2004).
- 23 T. Calarco, E. A. Hinds, D. Jaksch, J. Schmiedmayer, J. I. Cirac, and P. Zoller, *Phys. Rev. A* **61**, 022304 (2000).
- 24 F. Schmidt-Kaler, S. Gulde, M. Riebe, T. Deusdle, A. Kreuter, G. Lancaster, C. Becher, J. Eschner, H. Häffner, and R. Blatt, *J. Phys. B: At. Mol. Phys.* **36**, 623 (2003).
- 25 C. Henkel, P. Krüger, R. Folman, and J. Schmiedmayer, *Appl. Phys. B* **76**, 173 (2003).
- 26 D. M. Harber, H. J. Lewandowski, J. M. McGuirk, and E. A. Cornell, *Phys. Rev. A* **66**, 053616 (2002).
- 27 W. Hänsel, P. Hommelhoff, T. W. Hänsch, and J. Reichel, *Nature* **413**, 498 (2001).
- 28 T. R. Gentile, B. J. Hughey, D. Kleppner, and T. W. Ducas, *Phys. Rev. A* **40**, 5103 (1989).
- 29 P. Krüger, X. Luo, M. W. Klein, A. Brugger, A. Haase, S. Wildermuth, S. Groth, I. Bar-Joseph, R. Folman, and J. Schmiedmayer, *Phys. Rev. Lett.* **91**, 233201 (2003).
- 30 C. C. Agosta et al., *Phys. Rev. Lett.* **62**, 2361 (1989).
- 31 R. J. C. Spreeuw, C. Gerz, L. S. Goldner, W. D. Phillips, S. L. Rolston, and C. I. Westbrook, *Phys. Rev. Lett.* **72**, 3162 (1994).
- 32 R. E. Collin, *Foundations for Microwave Engineering*, 2nd ed. (John Wiley and Sons, Hoboken, 2001).
- 33 P. Treutlein, T. W. Hänsch, J. Reichel, A. Negretti, M. A. Cirone, and T. Calarco, *Phys. Rev. A* **74**, 022312 (2006).
- 34 J. Volz, M. Weber, D. Schlenk, W. Rosenfeld, J. Vrana, K. Saucke, H. Kurtsiefer, and H. Weinfurter, *Phys. Rev. Lett.* **96**, 030404 (2006).
- 35 J. Beugnon, M. P. A. Jones, J. Dingjan, B. Darquié, G. Messin, A. Browaeys, and P. Grangier, *Nature* **440**, 779 (2006).
- 36 J. E. Lye, J. J. Hope, and J. D. Close, *Phys. Rev. A* **67**, 043609 (2003).
- 37 R. Long, T. Steinmetz, P. Hommelhoff, W. Hänsel, T. W. Hänsch, and J. Reichel, *Phil. Trans. R. Soc. Lond. A* **361**, 1375 (2003).
- 38 H. J. Kimble, *Phys. Scr.* **T76**, 127 (1998).
- 39 G. Rempe, R. J. Thompson, H. J. Kimble, and R. Lalezari, *Opt. Lett.* **17**, 363 (1992).

- 40** S. M. Spillane, T. J. Kippenberg, K. J. Vahala, K. W. Goh, E. Wilcut, and H. J. Kimble, *Phys. Rev. A* **71**, 013817 (2005).
- 41** T. Steinmetz, Y. Colombe, D. Hunger, T. W. Hänsch, A. Balocchi, R. J. Warburton, and J. Reichel, *Appl. Phys. Lett.* **89**, 111110 (2006).
- 42** T. Steinmetz, Y. Colombe, G. Dubois, D. Hunger, B. Lev, P. Treutlein, T. W. Hänsch, and J. Reichel, to be published (2006).
- 43** D. Hunger, T. Steinmetz, T. W. Hänsch, and J. Reichel, to be published (2006).
- 44** C. J. Hood, T. W. Lynn, A. C. Doherty, A. S. Parkins, and H. J. Kimble, *Science* **287**, 1447 (2000).
- 45** L.-M. Duan, M. D. Lukin, J. I. Cirac, and P. Zoller, *Nature* **414**, 413 (2001).
- 46** R. B. Diener, B. Wu, M. G. Raizen, and Q. Niu, *Phys. Rev. Lett.* **89**, 070401 (2002).
- 47** B. Mohring, M. Bienert, F. Haug, G. Morigi, W. P. Schleich, and M. G. Raizen, *Phys. Rev. A* **71**, 053601 (2005).

## 6

## Two-dimensional Bose-Einstein Condensates in a CO<sub>2</sub>-laser Optical Lattice

*Giovanni Cennini, Carsten Geckeler, Gunnar Ritt, Tobias Salger, and Martin Weitz*

### 6.1

#### Introduction

Cold atoms in optical lattices provide a very clean testing ground for effects known from solid state physics, such as Bloch oscillations or the Mott-insulator phase transition [1]. In these experiments, “conventional” lattices were used where the spacing between sites is close to half the wavelength of the lowest absorption lines, yielding spacings below half a micron for alkali atoms. For typical parameters of quantum gas experiments, the tunneling time between sites is much lower or comparable with the available coherence times. Much less investigated are lattices with truly independent sites, where the tunneling between sites is negligible. As a loading of quantum degenerate atoms into extremely deep lattices is difficult, this usually requires a spacing between sites clearly above the trapping wavelength. In our experiment, such a lattice is realized by retroreflecting the radiation near a wavelength of 10.6 μm provided by a single-frequency CO<sub>2</sub>-laser, yielding a spacing between sites of 5.3 μm [2]. Other techniques rely on holographic methods [3], the inclination of two closer resonant laser beams under a small angle [4] or optical microstructures [5]. A few of those techniques have also been used with quantum degenerate atomic samples [2, 4]. Interestingly, in anisotropic traps the physics can become one- or two dimensional [6–9]. Optical lattices provide an ideal testing ground for the study of the physics in reduced dimensions. Lattices with negligible coupling between sites also hold fascinating prospects for quantum computing with neutral atoms [10–12] or the generation of arrays of atom lasers [13].

We here describe an experiment realizing an array of disk-shaped  $m_F = 0$  microcondensates in the antinodes of a standing wave near 10.6 μm. The atoms are directly cooled to quantum degeneracy in the independent sites of the mesoscopic lattice. We have studied the far field interference pattern of the independent coherent atom sources. The observed interference con-

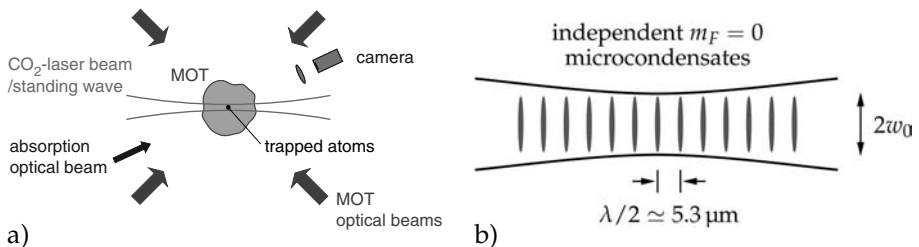


**Fig. 6.1** a) Schematical setup of the experiment. b) Geometry of the mesoscopic optical lattice.

trast decreases with the number of sources. Our results well agree with a random-walk model, predicting a  $1/\sqrt{N}$  scaling of the fringe contrast with the condensate number  $N$ . The time of-flight images of the expanded array also allows us to study the dimensionality of the trapped atom clouds. The results indicate that the axial dimension is frozen out, so that the trapped microclouds are in the two-dimensional regime.

## 6.2

### Experimental Setup and Procedure

A scheme of our experimental setup along with the geometry of the one-dimensional mesoscopic lattice is shown in Fig. 6.1. For a more detailed description of the apparatus, see [2, 14]. Our experiment starts with the trapping and cooling of bosonic atoms in a magneto-optical trap (MOT). Atoms of the isotope <sup>87</sup>Rb are collected and pre-cooled in a magneto-optical trap (MOT), which is loaded from the thermal gas emitted by heated rubidium dispensers placed inside the vacuum chamber. The light for the MOT is generated by two grating stabilized diode lasers.

The optical dipole trap is realized by tightly focussing a CO<sub>2</sub>-laser beam whose wavelength is near 10.6 μm. This mid-infrared light passes an acousto-optic modulator (AOM) which provides optical isolation and allows for a control of the beam intensity. The transmitted beam enters a vacuum chamber and is focused by an adjustable ZnSe lens placed inside the vacuum chamber. By means of a further lens and an external retroreflecting mirror an intense one dimensional standing wave is formed. The longitudinal axis of this mid-infrared standing wave is orthogonal to the gravity axis. The size of the beam waist in the trapping region can be varied with an external telescope within a range of 20–40 μm. This gives us control over the number of populated trapping sites, and on the relative strength of the trap frequencies.

Throughout the MOT loading stage, the CO<sub>2</sub>-laser beam is kept on at full power (30 W). In order to enhance the atom transfer from the MOT into the

purely optical dipole trap, a transient compression of the atomic cloud is achieved with a dark-MOT phase which lasts about 60 ms. During this period, the MOT cooling laser is detuned to the red of the cooling transition by 180 MHz, and the repumping laser intensity is decreased by roughly a factor 100. In this way, atoms are pumped into the lower hyperfine state, reducing light assisted losses and allowing for higher densities, thus improving the overlap between the MOT and the dipole potential.

The CO<sub>2</sub>-laser dipole trapping geometry results in an array of disk-shaped microtraps. If we assume that this beam travels along the  $z$  direction and that is perpendicular to the gravity direction  $x$ , the analytical form of the external potential can be expressed as:

$$U(x, y, z) = \frac{2\alpha_s P}{\pi c \epsilon_0 w_0^2 s(z)^2} e^{-\frac{2(x^2+y^2)}{w_0^2 s(z)^2}} [1 + \cos(2kz)] - mgx \quad (6.1)$$

where  $s(z) = \sqrt{1 + (z/z_0)^2}$ ,  $z_0 = \pi w_0^2 / \lambda$ ,  $m$  is the mass of the atoms and  $g$  the acceleration due to gravity. In this formula, the beam waist of the laser beam is  $w_0$  ( $1/e^2$  radius) and the optical power is  $P$ . We note that adjacent sites are spaced by  $d = \lambda_{\text{CO}_2}/2 \simeq 5.3 \mu\text{m}$ , which is sufficiently far apart that tunneling between sites is completely negligible. The aspect ratio of these microtraps is characterized by the vibrational frequencies  $\nu_r/\nu_z = \sqrt{2}\lambda/2\pi w_0$ . For typical lattice experiments, the beam waist  $w_0$  was chosen to be  $37 \mu\text{m}$ . When a perfect alignment is realized, each microtrap has an aspect ration of nearly 15. Because of the relatively tight longitudinal confinement along the lattice  $z$  axis, the atomic motion along this axis is frozen out and atoms only move in the orthogonal  $x, y$  plane.

Once the atoms are trapped in the antinodes of the CO<sub>2</sub>-laser optical lattice, we apply forced evaporation directly in the dipole potential in order to achieve quantum degeneracy [14–18]. For an efficient evaporation of hot atoms, we initially use a running wave geometry by misadjusting the CO<sub>2</sub>-laser beam backreflection mirror away from a perfect retroreflection. This is achieved by tilting this mirror with the help of an electronically driven piezo. Rubidium atoms from a magneto-optical trap (MOT) are loaded into the running wave geometry. After this transfer, some  $10^6$  atoms, populating the lower hyperfine ground state ( $F = 1, m_F = 0, \pm 1$ ) are left in the optical trap at a temperature near  $100 \mu\text{K}$ . To cool the trapped atomic cloud, the CO<sub>2</sub>-laser beam power is acousto-optically ramped down to induce forced evaporative cooling. The total evaporation stage lasts about 10 seconds, during which the mid-infrared beam power is smoothly reduced from 30 W to a typical final value of 40–50 mW. Throughout the evaporation stage, the MOT quadrupole field with  $10 \text{ G/cm}$  field gradient is left on. This gradient is sufficiently strong to remove atoms in field-sensitive spin projections in this running wave geometry [14]. While the initial phase of this evaporation is performed in the

running wave geometry, cooling to quantum degeneracy is achieved in the lattice geometry. By the end of the evaporative cooling stage, we thus slowly switch to a standing wave geometry by servoing the piezo-mounted mirror correspondingly. The 1D optical lattice geometry is fully aligned at a time of 1–2 seconds before the onset of quantum degeneracy (corresponding to an atomic temperature of a factor 2 above the BEC transition temperature). This ensures that the microcondensates are formed independently. At the end of the evaporation state, an array of  $m_F = 0$  microcondensates is created. The total number of atoms in the optical lattice is about 7000, and the number of condensed lattice sites can be varied from typically 5 to 35 by choosing different beam waists of the lattice beams and – in a smaller range – also by allowing for small misalignments of the lattice beams. For all our measurements, the estimated tunneling time between sites is longer than the age of the universe. The residual sensitivity of the  $m_F = 0$  condensates to stray magnetic fields due to the second order Zeeman shift is near 14 fK/mG<sup>2</sup>. For a typical spatial extension of the lattice of 100 μm, the variation of the condensate phases due to magnetic field inhomogeneities is 0.15 Hz at an estimated field gradient of 50 mG/cm.

### 6.3

#### Experimental Results

For an analysis of the array of microcondensates, we have studied absorption images observed after releasing the atoms (see Figs. 6.2a,b). A few ms after extinguishing the confining lattice potential, the clouds spatially overlap, and an interference pattern of the independent clouds can be observed, as shown in the second image recorded after 15 ms free expansion time. A horizontal profile of this image is shown in Fig. 6.2c. Our experimental imaging resolution only allows us to resolve the fringe pattern arising from the interference of adjacent sites. Notably, the contrast and the phase of the fringe pattern is different for each realization of the experiment. Fig. 6.3a in a polar plot shows the fitted fringe contrast and phase for 130 different measurements. It can be clearly seen that the phase (i. e. position of the fringe pattern) varies from run to run. This can be understood in terms that each of the independently created condensates, despite being initially in a state with undefined phase, upon measurement develops a well-defined relative phase that is random in each of the realizations [19–21]. The expected fringe contrast for an array of  $N$  coherent sources can very elegantly be calculated with a random-walk model in which the number of steps equals the number independent phases, i. e.  $N - 1$  [22]. The calculations predict a  $1/\sqrt{N}$  scaling of the average visibility with the condensate number  $N$ . This reduction of fringe contrast with the number of sources can intuitively be understood as follows. When two independent con-

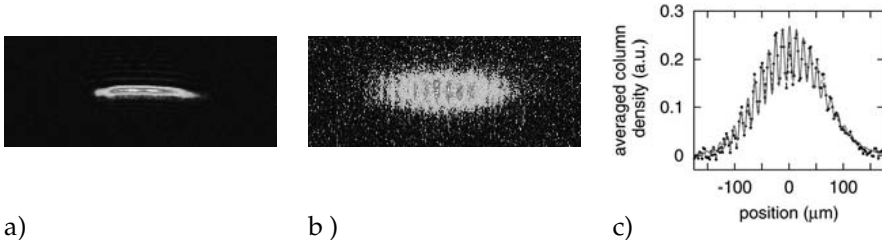


**Fig. 6.2** a) False-color absorption image of 20 microcondensates recorded shortly after switching off the CO<sub>2</sub>-laser trapping potential. b) False-color absorption image of an interference pattern of 20 independently generated  $m_F = 0$  microcondensates released from a CO<sub>2</sub>-laser optical lattice. This image

was recorded after a free expansion time of 15 ms. The field of view is 350 μm × 140 μm. c) Horizontal profile of image b) averaged over a vertical region of 35 μm: Experimental data (dashed line with dots) and fitted fringe pattern (solid line). Cf. the coloured plates in the Appendix.

densates with equal number of atoms interfere, the relative phase varies from run to run, but in all cases a density modulation with 100 % fringe contrast is expected. In the case of three interfering condensates two relative phases come into play. We in general expect that the phase difference between any two of the condensates differs from that between either one of them and the third one. One still expects a fringe pattern, but in general with reduced contrast. For a still larger number of sources, the degree of randomness increases. Interference patterns of condensates released from periodic lattice potentials are commonly investigated [1], but the interference of a larger number of independent condensates was not studied until Hadzibabic et al. [4] recently observed the interference from 30 independent condensates regularly spaced in a one-dimensional lattice and obtained the surprisingly high average fringe contrast of 34 %, which was indeed comparable to the results observed in the early two-condensates interference experiments of [23].

We have experimentally studied the dependence of the interference contrast on the number of condensates [2]. The corresponding results are shown in Fig. 6.3b. The observed average interference contrast decreases with source number  $N$  and agrees well with the result of a theoretical model based on a random walk of the probability amplitude in the complex plane. While the exact result can be given in terms of Klyver's formula, for a large number of condensates a  $1/\sqrt{N}$  scaling of the average fringe contrast is obtained, as given by the central limit theorem [24]. When taking into account the reduction of the contrast due to our experimental imaging resolution, our results agree well with the theoretical predictions.

In subsequent experiments, we have verified whether the produced Bose-Einstein microcondensates are in the two-dimensional regime. For these measurements, the atomic expansion velocity after extinguishing the trapping po-

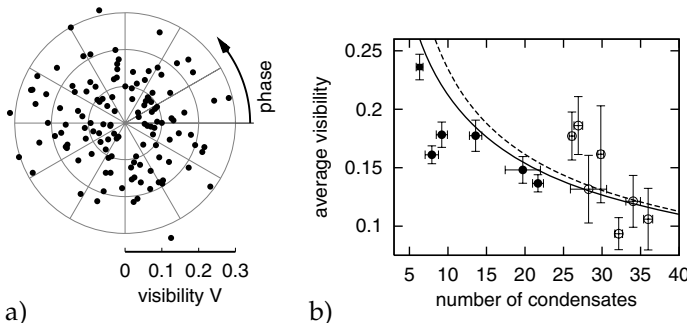


**Fig. 6.3** a) Visibilities and phase angles of fringe patterns arising from the interference of 20 independent Bose-Einstein condensates, as derived from fits as in Fig. 6.2c, have been drawn (dots) in a polar diagram for 130 different realizations of the experiment. b) Average fringe visibilities of far field interference patterns as a function of number of interfering coherent atomic sources. The experimental data sets were recorded with

beam waists: 24.3  $\mu\text{m}$  (squares), 30.0  $\mu\text{m}$  (dots), and 40.2  $\mu\text{m}$  (circles). The data has been fitted with the theoretical calculated fringe contrast multiplied by a constant factor, which is left as a free parameter to account for the finite imaging resolution (solid line). The dashed line gives the corresponding result in the central limit approximation when assuming the same imaging resolution.

tential was analyzed for different number of atoms in the condensates. In Figs. 6.2a,b, typical absorption images of the array of microcondensates before and after free expansion had been shown. From such images of the released array, we have derived the corresponding lengths of the expanded clouds along the longitudinal and the radial axis respectively. Figs. 6.4a and b now show the condensate's expansion during 15 ms of free flight along both directions for different atom numbers. Because the atomic oscillation frequency in the longitudinal direction is much higher than that in the radial plane, one intuitively would expect that the expansion in the longitudinal axis is much faster than that in the radial plane. Experimentally, the measured expansions along both directions however are quite comparable. This is attributed to the issue that the trapped atom clouds are in the two-dimensional regime, i. e. the longitudinal ( $z$ -) axis is frozen out. As a further evidence for the reduced dimensionality, one notices that the observed expansion along the  $z$ -axis is more or less independent on the number of atoms (note that even a small decrease with the number of atoms seems to be present). In contrast, the expansion along the radial axis clearly increases with the number of atoms in the microclouds. This again is an indication for the axial direction being frozen out, with the spatial expansion here being determined only by the momentum uncertainty of the harmonic oscillator ground state, i. e. independent of atom density dependent mean field effects.

The truly two-dimensional regime is expected to occur if both the chemical potential  $\mu$  of each microcondensate and  $k_B T$ , where  $T$  denotes the atomic

temperature, are much smaller than the harmonic oscillator energy along  $z$  direction, namely  $\hbar\omega_z$  [8]. The measured number of atoms in each microcondensate in our experiment is in the range between 100 and 400. For a typical value of the CO<sub>2</sub>-laser beam waist of 37 μm the vibrational frequencies at the end of the evaporation process were measured to be  $\omega_z = 2\pi \times 2160$  Hz and  $\omega_r = 2\pi \times 150$  Hz. Given these parameters, one can derive the maximum allowed number of atoms in each site  $N_s$  of the optical lattice for which the condition  $\mu \ll \hbar\omega_z$  is still fulfilled. One obtains the condition

$$N_s \ll N_{\max} = \sqrt{\frac{32\hbar}{225ma^2}} \sqrt{\frac{\omega_z^3}{\omega_r^4}} \quad (6.2)$$

In our experiment, we estimate  $N_{\max}$  to be  $\simeq 3400$ . Because the atom number in each site is only a few hundreds, we anticipate that the condition  $\mu \ll \hbar\omega_z$  is clearly fulfilled in our lattice.

The second condition for the atoms to be in the fully two-dimensional regime is that  $T \ll \hbar\omega_z/k_B \simeq 104$  nK. As no thermal cloud could be detected in the described experiments, we assume that the atomic temperature is clearly below the BEC transition temperature, i. e.  $T \ll T_c$ . The transition temperature can be calculated from the measured vibrational frequencies and the number of atoms per site  $N_s$  to be  $T_c = 0.94\hbar(\omega_r^2\omega_z)^{1/3}/k_B \cdot N_s^{1/3} \simeq 16$  nK ·  $N_s^{1/3} \simeq 96$  nK for  $N_s = 200$ . That is to say that for small atom numbers and  $T \ll T_c$  the condition  $T \ll \hbar\omega_z/k_B$  is also fulfilled. We conclude that the two-dimensional regime is fully reached in the mesoscopic lattice for the used parameters.

An interesting question is whether phase fluctuations, which are generally more severe in low-dimensional condensates, significantly reduce the coherence of the microcondensates. In a recent interference experiment with a small number of two-dimensional condensates, phase defects were monitored at temperatures slightly below the BEC transition temperature [9]. For the parameters used in our experiments, no signatures for such defects could be observed from the fringe pattern.

## 6.4 Conclusions

To conclude, we have generated an array of Bose-Einstein condensates in a mesoscopic optical lattice. The condensates are formed by atoms in the  $m_F = 0$  spin-projection, with their chemical potential being first-order insensitive to magnetic stray fields. The observed average interference visibility decreases with the condensate number. An analysis of the expansion of the array of microcondensates shows that the microclouds are in the two-dimensional regime. Notably, the lower dimensional regime is entered during the condensa-

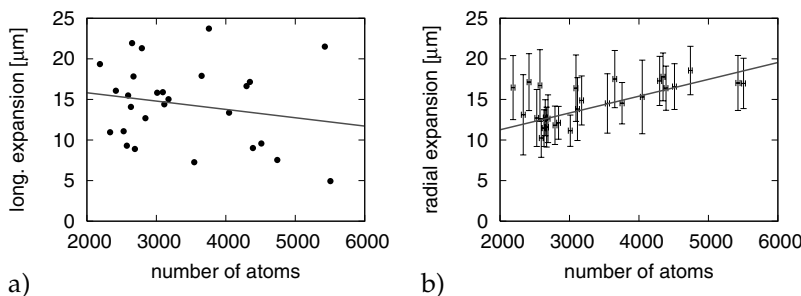


**Fig. 6.4** Measured spatial expansion of the microcondensates in the mesoscopic optical lattice in the longitudinal and radial direction after a free drift time of 15 ms as a function of the number of atoms in all lattice sites.

tion process itself. The experiments here reported give a very direct way for the production of an array of quantum degenerate gases in lower dimensions.

For the future, it is anticipated that mesoscopic optical lattices hold fascinating prospects for the observation of new quantum phases. The described system is e. g. of interest for the study of collective quantum states in rapid rotation traps, as multiparticle states with anyonic statistics of quasiparticles [25]. A different perspective is the possible observation of correlated insulator phases [1], such as the Mott transition, in a system which allows for an optical resolving of individual lattice sites [26]. For extremely low values of the lattice depth, a tunneling between sites can be achieved despite the large lattice spacing, as has been recently demonstrated for a double-well potential [27]. For such weakly confined systems, long scattering lengths are very useful, as can be very elegantly reached with Feshbach tuning in fermionic atoms [28]. The in this way produced strongly interacting periodic systems can have prospects for the observation of solid state effects in the spatial domain. Along different lines, such systems with individual lattice sites being optically addressable, hold fascinating prospects for quantum computing in optical lattices [10, 11, 29].

In a recent remarkable experiment, observation of the Kosterlitz-Thouless transition has been reported in an optical lattice with two-dimensional microtraps [30].

### Acknowledgement

We acknowledge financial support from the Deutsche Forschungsgemeinschaft, the Landesstiftung Baden-Württemberg, and the European Community.

## References

- 1 See e. g., I. Bloch, *Phys. World* **17**, 25 (2004).
- 2 G. Cennini, C. Geckeler, G. Ritt, and M. Weitz, *Phys. Rev. A* **72**, 051601(R) (2005).
- 3 D. Boiron et al., *Phys. Rev. A* **57**, R4106 (1998).
- 4 Z. Hadzibabic et al., *Phys. Rev. Lett.* **93**, 180403 (2004).
- 5 R. Dumke et al., *Phys. Rev. Lett.* **89**, 097903 (2002).
- 6 F. Schreck et al., *Phys. Rev. Lett.* **87**, 080403 (2001).
- 7 A. Görlitz et al., *Phys. Rev. Lett.* **87**, 130402 (2001).
- 8 T. Stöferle, H. Moritz, C. Schori, M. Köhl, and T. Esslinger, *Phys. Rev. Lett.* **92**, 130403 (2004); M. Köhl, H. Moritz, T. Stöferle, C. Schori, and T. Esslinger, *cond-mat/0404338*.
- 9 S. Stock, Z. Hadzibabic, B. Battelier, M. Cheneau, and J. Dalibard, *Phys. Rev. Lett.* **95**, 190403 (2005).
- 10 G. Brennen, C. Caves, P. Jessen, and I. Deutsch, *Phys. Rev. Lett.* **83**, 1060 (1999).
- 11 D. Jaksch, H.-J. Briegel, J. I. Cirac, C. W. Gardiner, and P. Zoller, *Phys. Rev. Lett.* **82**, 1975 (1999).
- 12 O. Mandel et al., *Nature* **425**, 937 (2003).
- 13 G. Cennini, C. Geckeler, G. Ritt, and M. Weitz, *cond-mat/0510629*.
- 14 G. Cennini, G. Ritt, C. Geckeler, and M. Weitz, *Phys. Rev. Lett.* **91**, 240408 (2003).
- 15 M. Barrett, J. Sauer, and M. S. Chapman, *Phys. Rev. Lett.* **87**, 010404 (2001).
- 16 T. Weber et al., *Science* **299**, 232 (2003).
- 17 S. R. Granade, M. E. Gehm, K. M. O'Hara, and J. E. Thomas, *Phys. Rev. Lett.* **88**, 120405 (2002).
- 18 Y. Takasu et al., *Phys. Rev. Lett.* **91**, 040404 (2003).
- 19 J. Javanainen and S. M. Yoo, *Phys. Rev. Lett.* **76**, 161 (1996).
- 20 M. Naraschewski et al., *Phys. Rev. A* **54**, 2185 (1996).
- 21 Y. Castin and J. Dalibard, *Phys. Rev. A* **55**, 4330 (1997).
- 22 S. Ashhab, *Phys. Rev. A* **71**, 063602 (2005).
- 23 M. R. Andrews et al., *Science* **275**, 637 (1997).
- 24 See e. g.: E. Merzbacher, J. M. Feagi, and T.-H. Wu, *Am. J. Phys.* **45**, 964 (1977).
- 25 N. K. Wilkin, and J. M. F. Gunn, *Phys. Rev. Lett.* **84**, 6 (2000); B. Paredes, P. Fedichev, J. I. Cirac, and P. Zoller, *Phys. Rev. Lett.* **87**, 010402 (2001).
- 26 R. Scheunemann, F. S. Cataliotti, T. W. Hänsch, and M. Weitz, *Phys. Rev. A* **62**, 051801 (R) (2000).
- 27 M. Albiez et al., *Phys. Rev. Lett.* **95**, 010402 (2005).
- 28 D. S. Petrov, C. Salomon, and G. V. Shlyapnikov, *Phys. Rev. Lett.* **93**, 090404 (2004).
- 29 S. Friebel, C. D'Andrea, J. Walz, M. Weitz, and T. W. Hänsch, *Phys. Rev. A* **57**, R20 (1998).
- 30 Z. Hadzibabic, P. Krüger, M. Cheneau, B. Battelier, and J. Dalibard, *Nature* **441**, 1118 (2006).



## 7

## Creating and Probing Long-range Order in Atomic Clouds

C. von Cube, S. Slama, M. Kohler, C. Zimmermann, and Ph.W. Courteille

## 7.1

### Introduction

Ideally, a scalable quantum computer consists of registers of globally coupled two-level systems called *qubits*. To match the requirement of individual addressability of the qubits with the necessity of long-range correlations a periodic ordering of the qubits seems desirable. To name only two examples out of a huge number of proposals for quantum computers: Chains of ions confined in Paul-traps [1,2] can be coupled by electrostatic repulsion through a common mode of their center-of-mass oscillation. Arrays of neutral heteronuclear molecules suspended in free space are coupled through long-range dipole-dipole interactions [3].

A proposal which is very similar to the ion chain idea consists in confining neutral atoms in the antinodes of a standing light wave formed by the two counterpropagating modes of a high-finesse ring cavity [4]. The atoms are periodically arranged in a one-dimensional optical lattice. The isolation of single atoms in standing waves and even their controlled shifting has impressively been demonstrated [5]. If several such atoms are confined in different antinodes, they can individually be addressed by probe beams. In fact, optical lattices draw an ever increasing attention, in particular in combination with quantum degenerate gases. E.g. Mott-insulators [6] may constitute good supports for quantum gates [7], and single atom transistors in optical lattices have been proposed [8].

However, ring cavities provide an even more important advantage, because they combine the scalability of optical lattices with a strictly uniform coupling and a coupling strength which *increases* with the number of atoms in contrast to the situation in ion chains: The atoms all couple to the same light fields by scattering photons from one cavity mode into the counterpropagating one and receiving in return twice the photonic recoil. We have provided the proof that a collective dynamics can be driven in high-finesse ring cavities in recent

experiments [9]. However these experiments deal with millions of thermal atoms, which is of course incompatible with individual addressability, and further research is needed to design an operating ring cavity quantum computer.

In this paper we present our research project, which has the goal to experimentally study collective dynamics in high-finesse ring cavities. A priori it is not so clear, that such a dynamics can take place, because perturbative effects known from laser gyroscopes may lock the relative phase of the counterpropagating modes and freeze the essential degree of freedom needed to couple the atomic motions. We found however that under certain circumstances a collective instability leads to self-amplification and exponential gain of a light field on one hand and to atomic bunching on the other. A careful study of our system enabled us to directly relate the observations presented in [9] to a phenomenon called the *collective atomic recoil laser* (CARL) postulated 10 years ago [10].

In the absence of dissipation for the motional degrees of freedom, the gain must remain transient. Consequently, we have observed a burst of light reverse to the pump beam direction. The light frequency decreases in time as its amplitude vanishes. This burst is accompanied by a continuous acceleration of atoms. By introducing dissipation for their kinetic energy, we obtained a steady-state operation of the emitted light at a self-determined frequency. When the energy dissipation (or cooling) mechanism is limited to finite temperatures by some diffusion process, the appearance of a threshold is expected. We report here the observation of such a threshold: A minimum pump power is indeed necessary to start CARL action [11]. The threshold behavior of the cavity fields goes along with a phase transition in the atomic density distribution.

This paper is divided into three parts. In Sect. 7.2, we outline the experimental apparatus and the sequence of our measurements. We emphasize that we have access to all relevant degrees of freedom characterizing our system: We monitor the dynamics of the cavity field by beating the field modes, record pictures of the atomic density distribution and probe the atomic velocity distribution by spectroscopy of recoil-induced resonances (RIR). We present our observations and discuss the signatures of CARL in each of the monitored signals. We show that CARL is a transient phenomenon in the absence of dissipation for the external degrees of freedom. In contrast, in the presence of a friction force (experimentally realized by an optical molasses) a steady state is reached. In Sect. 7.3 we draft a theoretical model that we compare to our observations. An analytic treatment for the ideal case of perfect atomic bunching enables us to find compact solutions for the probe field intensity and frequency. Numerical simulations of Langevin (or alternatively Fokker-Planck) equations at finite temperature show, that dissipation gives rise to

a threshold behavior, which draws an analogy between CARL and conventional lasers. They also reveal that driven by a dissipative force, homogeneous atomic clouds can show collective instabilities spontaneously producing long-range order, atomic bunching and a thermodynamic phase transition reminiscent to self-organization mechanisms in networks of coupled oscillators. Sect. 7.4 focusses on the detection of long-range order via Bragg scattering. This part of the work is obviously motivated by our desire to unveil the most direct signature of CARL, which is atomic bunching. But we will see that the Bragg scattering method has also features, which are interesting in their own rights.

## 7.2

### Collective Coupling

A consequence of the development of new powerful techniques for optical cooling and trapping in the past decades is the ever increasing importance of the role assigned to the center-of-mass degrees of freedom in the interaction of matter with light. Prominent examples of how the motion of atoms can influence the scattering of light are the recoil-induced resonances and the CARL. The RIR are observed [12,13] as Raman transitions between momentum states. Two laser beams having different frequencies and crossing each other under a finite angle give rise to a moving standing light wave. Atoms moving synchronously to this wave can be scattered to other momentum states. The scattering process is monitored via power variations in the Raman beams. The spectroscopy of RIR is today routinely used to characterize the velocity-distribution of atomic samples [14].

The CARL has been conceived as a collection of two-level atoms driven by a single-mode pump field [15]. Under appropriate conditions, atomic density fluctuations (together with excitation and polarization fluctuations) induce a small amount of backscattering which interferes with the pump field and creates a weak traveling modulation wave. This wave, in turn, generates a weak density wave which, for appropriate values of the parameters, radiates and strengthens the backward scattered field in an avalanche process. The signature of CARL (and this distinguishes it from RIR) is thus an *exponential growth* of the backward field. In fact, atomic bunching and probe gain can arise *spontaneously* from fluctuations with no seed field applied [15]. An essential feature of the CARL model is the dynamical role played by the atomic motion. It must be included in the theoretical description to give proper account of recoil effects, which eventually are responsible for producing the organized atomic density modulation, or density grating, which is at the heart of the CARL process.

The CARL effect should emerge most clearly in cold atomic clouds in a collisionless environment [16]. Furthermore, large detunings of the lasers far outside the Doppler-broadened profiles of the atomic resonances are preferable. In this regime, excited states can safely be adiabatically eliminated, and effects from atomic polarization gratings *not* based on density variations, are avoided. Finally, to emphasize the role of exponential gain responsible for self-bunching, i.e. spontaneous formation and growth of a density grating, it is desirable not to seed the probe. The observation of a probe beam is then a clear indication for CARL [9]. Earlier attempts to observe CARL action have been undertaken in hot atomic vapors with near-resonant laser beams [17,18]. They have led to the identification of a reverse field with some of the expected characteristics. However, the gain observed in the reverse field can have other sources [19,20], which are not necessarily related to atomic recoil.

The best way to satisfy the specified conditions is to recycle the probe light in a very high finesse ring cavity. This permits to realize strong atom-field coupling forces very far from atomic resonances, i.e. in a regime where the atomic excitation plays no role. The large power enhancement inside a high-finesse cavity allows to confine the atoms inside the cavity mode-volume and thus to have quasi unlimited interaction times. The atomic cloud can be as cold as 100  $\mu\text{K}$ . The densities are generally low enough to permit only few collisions per second. Far from resonance spontaneous scattering and thus radiation pressure is in most cases negligible.

Apart from ours, other experiments with cold atoms have recently found signatures for collective dynamics. Optical bistability has been observed in a high-finesse ring cavity [22,23]. Spatial self-organization induced by collective friction force has been observed in a linear low-finesse cavity [21]. In both cases the underlying dynamics is however different from CARL [24].

### 7.2.1

#### **Experimental Setup**

Ring cavities are particular in the following sense. The optical dipole force exerted by the light fields on atoms can be understood in terms of momentum transfer by coherent redistribution (via Rayleigh scattering) of photons between optical modes. In multimode configurations, e.g. counterpropagating modes of a ring cavity, the photon pumping can occur between *different* modes having independent photon budgets [25]. As a consequence, the scattering process conserves the total momentum of the atoms and photons, which is not the case for linear cavities, where backscattered photons end up in the same cavity mode. This implies that the atoms exert a noticeable backaction on the optical fields and that the atomic dynamics can be monitored as an intensity [26,27] or a phase imbalance between the modes [9]. Consequently, in a

ring cavity the scattering of a photon between the counterpropagating modes slightly shifts the phase of the standing wave by an amount corresponding to the recoil shift.<sup>1</sup> This shift, being strongly enhanced by a long cavity life time, is sensed by all atoms trapped in the standing wave. Consequently, the simultaneous interaction of the atoms with the two field modes couples the motion of all atoms [4, 28].

### 7.2.1.1 Ring Cavity

The ring cavity which is at the heart of our experiment (see Fig. 7.1) has a round trip length of  $L = 85$  mm and beam waists in horizontal and vertical direction at the location of the MOT of  $w_v = 129$   $\mu\text{m}$  and  $w_h = 124$   $\mu\text{m}$ , respectively [14]. This corresponds to the cavity mode volume  $V_{\text{mode}} = \frac{\pi}{2} L w_v w_h = 2$   $\text{mm}^3$ . For (linear)  $s$ -polarization the two curved high reflecting mirrors have a transmission of  $2 \times 10^{-6}$ , while the plane input coupler has a transmission of  $27 \times 10^{-6}$ . Depositions of rubidium on the mirror surfaces actually reduce the finesse to  $F = 80000$ , measured by cavity ring-down. This corresponds to an amplitude decay rate of  $\kappa = \pi\delta/F = 2\pi \times 22$  kHz, where  $\delta = c/L$  denotes the free spectral range. For  $p$ -polarized light we found  $F = 2500$ .

The optical layout of our experiment is shown in Fig. 7.1. A titanium-sapphire laser is double-passed through an acousto-optic modulator which shifts the laser frequency. The light beam is then mode-matched to one of the two counterpropagating cavity modes. The reflected light bears information about phase deviations between the laser and the intracavity light field. The light reflected from the cavity is fed back via a Pound-Drever-Hall type servo control to phase correcting devices. The phase corrections are made via a piezo transducer mounted to the titanium-sapphire laser cavity and via the acousto-optic modulator. The frequency deviations of the stabilized laser from the ring cavity resonance are much less than the linewidth of the ring cavity. Because the cavity mirrors have very different reflectivities for  $s$ - and  $p$ -polarization, we can switch from high to low finesse by just rotating the linear polarization of the injected laser beam. This tool is useful for tests comparing strong and weak coupling situations.

From the electric field per photon  $\mathcal{E}_1 = \sqrt{\hbar\omega/2\varepsilon_0 V_{\text{mode}}}$  and the dipole moment  $d \approx \sqrt{3\pi\varepsilon_0\hbar\Gamma/k^3}$  [29], we calculate the atom-field coupling constant (or single-photon Rabi frequency) to be  $g_0 = d\mathcal{E}_1/\hbar \approx 2\pi \times 100$  kHz, where  $\Gamma = 2\pi \times 6$  MHz is the natural linewidth of the  $D_2$  line of  $^{85}\text{Rb}$ . Therefore the coupling strength is much larger than the cavity decay rate, but still much smaller than the natural linewidth,  $\kappa \ll g_0 \ll \Gamma$ .

1) In the absence of spatially fixed backscattering objects the phase of the standing wave is free, in contrast to linear cavities where the phase is fixed by boundary conditions at the mirror surfaces.

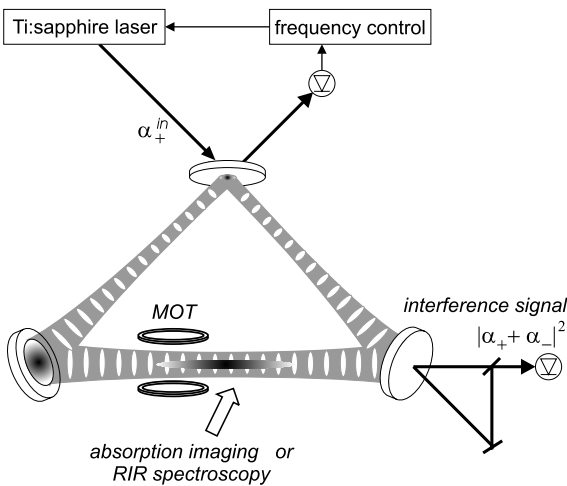


**Fig. 7.1** Scheme of the experimental setup. A titanium-sapphire laser is locked to one of the two counterpropagating modes ( $\alpha_+$ ) of a ring cavity. The atomic cloud is located in the center of the magneto-optical trap (MOT) close to the free-space waist of the cavity mode. We observe the evolution of the interference signal

between the two light fields leaking through one of the cavity mirrors, record the spatial evolution of the atoms via absorption imaging, and measure their velocity distribution by spectroscopy of recoil-induced resonances (RIR).

In the following, we label the modes by their complex field amplitudes scaled to the field per photon, so that  $I_{\pm} = 2\epsilon_0 c \mathcal{E}_1^2 |\alpha_{\pm}|^2$  is the intracavity light intensity in the respective mode  $\alpha_{\pm}$ . The mode  $\alpha_+$  is pumped with the rate  $\eta_+ \equiv \sqrt{\delta\kappa} \alpha_+^{\text{in}}$ , where  $\alpha_+^{\text{in}}$  is the field amplitude of the incoupled laser beam (under the premise of perfect phase and impedance matching). On resonance and in the absence of any losses other than those included in  $\kappa$ , the cavity dramatically enhances the incident light power by  $\alpha_+ = \sqrt{\delta/\kappa} \alpha_+^{\text{in}}$  [23]. The counterpropagating mode  $\alpha_-$  is populated out of  $\alpha_+$  by backscattering from atoms located inside the mode volume or from mirror imperfections. The light power outcoupled through a mirror with reflectivity  $T$  is related to the intracavity power  $P_{\pm} = \frac{\pi}{2} w_h w_v I_{\pm}$  via  $P_{\pm}^{\text{out}} = T P_{\pm} = T \hbar \omega \delta |\alpha_{\pm}|^2$ .

### 7.2.1.2 Dipole Trap for $^{85}\text{Rb}$

The ring cavity is located inside an ultrahigh vacuum recipient. We produce rubidium-85 atoms by a dispenser and collect them with a standard magneto-optical trap before transferring them into a  $\text{TEM}_{00}$  mode of the ring cavity field dipole potential. We typically load several million atoms into the dipole trap at temperatures of a few  $100 \mu\text{K}$  and atomic peak densities of about  $2 \times 10^9 \text{ cm}^{-3}$ . Density and temperature are monitored by time-of-flight absorption imaging.

The dipole force acting on the atoms and allowing for their confinement originates from intensity gradients in the cavity field. Let us assume that the

field frequency  $\omega$  is red-detuned from an atomic resonance  $\omega_a$ ,  $\Delta_a \equiv \omega - \omega_a < 0$ . Radial confinement is then ensured by the transverse Gaussian profile of the TEM<sub>00</sub> mode. Axially, the atoms tend to concentrate around the free space waist of the cavity mode. The optical potential of the dipole force trap is, for a far detuned laser frequency,  $|\Delta_a| \gg \Gamma$ , to a good approximation given by  $\phi(\mathbf{r}) = \hbar\Omega(\mathbf{r})^2/4\Delta_a$ , where  $\Omega^2(\mathbf{r}) = 4g^2(\mathbf{r})|\alpha_+e^{ikz} + \alpha_-e^{-ikz}|^2$  is the local Rabi frequency. Obviously, the atom-field coupling strength  $g(\mathbf{r})$ , also called the cavity mode function, becomes inhomogeneous.  $g_0 = g(0)$  is the one-photon Rabi frequency at the center of the trap, whose expression is given above.

Since rubidium exhibits a fine structure, we must consider the contributions of the  $D_1$  and the  $D_2$  line to the optical potential [29]:

$$\phi(\mathbf{r}) = \hbar U(\mathbf{r})|\alpha_+e^{ikz} + \alpha_-e^{-ikz}|^2, \quad (7.1)$$

$$\text{where } U(\mathbf{r}) \equiv g(\mathbf{r})^2 \left( \frac{1}{\Delta_{D1}} + \frac{2}{\Delta_{D2}} \right).$$

In a running wave laser beam,  $\alpha_- = 0$ , close to the center of the trap (i.e. on the cavity axis,  $r \ll w_0 \equiv \sqrt{w_v w_h}$ , and within the Rayleigh length,  $z \ll \frac{1}{2}kw_0^2$ ) the normalized mode function can be approximated by a harmonic potential  $U(\mathbf{r}) \approx U_0 \left[ 1 - \left( 2z/kw_0^2 \right)^2 - 2(r/w_0)^2 \right]$ . For a typical intracavity light power of  $P = 10$  W and a frequency detuning from the nearest atomic resonance of typically  $\Delta_{D1} = -2\pi \times 1$  THz, we calculate an optical potential depth of  $\phi_0 \approx k_B \times 1.4$  mK. The radial and axial secular frequencies of the trap are  $\omega_r \approx 2\pi \times 1$  kHz and  $\omega_z \approx 2\pi \times 2$  Hz. An important quantity characterizing the coupling strength and used throughout this paper, the *one-photon light shift*, is typically on the order of  $U_0 \equiv U(0) \approx -2\pi \cdot 0.01$  Hz.

Not too close to the resonance, the spontaneous scattering rate out of one beam is well approximated by

$$\gamma_{\text{scat}}(\mathbf{r}) = \gamma(\mathbf{r})|\alpha_+|^2, \quad (7.2)$$

$$\text{where } \gamma(\mathbf{r}) \equiv g(\mathbf{r})^2 \Gamma \left( \frac{1}{\Delta_{D1}^2} + \frac{2}{\Delta_{D2}^2} \right).$$

It decreases faster with detuning than the potential depth, so that for a chosen trap depth it is advantageous to work at higher detunings and higher laser intensities in order to avoid excessive heating by spontaneous scattering processes. For the parameters given above, we expect  $\gamma_0 \approx 6 \times 10^{-8}$  s<sup>-1</sup> and  $\gamma_{\text{scat},0} \approx 600$  s<sup>-1</sup>. In this context the high-finesse optical cavity has the practical advantage that its large intensity enhancement [30] ensures a strong atom-field coupling even at laser detunings as large as 1..10 nm.

Collisions are predicted to hamper the CARL process in buffer gas cells [31, 32], because they remix the atomic distributions faster than bunching through

CARL dynamics. In contrast, for cold atoms the collision rate is generally quite small. At our typical densities and temperatures, we estimate a collision rate of  $\gamma_{coll} = n\sigma\bar{v}/2 \approx 1 \text{ min}^{-1}$ , where  $\bar{v} = \sqrt{k_B T/m}$  the average velocity and  $\sigma \approx 10^{-12} \text{ cm}^2$  the elastic collision cross section [33]. This shows that on the time scale of our experiments (typically ms) the impact of collisions can be discarded.

### 7.2.1.3 Optical Molasses

Some of our experiments are carried out in the presence of a so-called optical molasses. Technically, to create a molasses we use the laser beams of the magneto-optical trap, but without magnetic field gradients. Thus the molasses consists of three orthogonal pairs of counterpropagating  $\sigma^\pm$  polarized laser beams, which are tuned a few natural linewidths  $\Gamma$  below the  $D_2$  resonance. They traverse the dipole trap at angles of either  $45^\circ$  or  $90^\circ$ . The molasses light is linearly polarized at any location with a polarization vector winding about the molasses beam directions. Through these polarization gradients the atomic cloud is cooled well below the Doppler limit. The atomic motion inside an optical molasses is well described as being subject to a velocity-dependent friction force: The atoms are slowed down and move like in a viscous fluid, but there is no restoring force; the atoms are not trapped.

The friction force sensitively depends on the detuning of the molasses beams from resonance. Unfortunately, the dipole trap produces a light shift of the electronic states, which are coupled by the  $D_1$  and  $D_2$  transitions. The light shift increases the effective detuning of the molasses lasers by an amount equivalent to  $U(\mathbf{r})$ . The effective detuning thus gets inhomogeneous.<sup>2</sup>

Another potential problem is the following: In the presence of magnetic fields the atoms are optically pumped towards fully stretched Zeeman states. Once the atoms are doubly spin-polarized, they preferentially interact with *only one* of the counterpropagating molasses beams, which leads to a radiation pressure imbalance. The resulting atomic acceleration interferes with signatures of CARL dynamics (see next sections). In practice, we take care to accurately compensate the magnetic fields.

Our main purpose in using optical molasses is to introduce friction to the system. However, the scattering of light by the molasses also leads to diffusion in momentum space, which limits the temperature to which the atoms are cooled. We will see in Sect. 7.3.2 that the interplay of friction and diffusion has a large impact on the dynamics of the system.

- 2) As long as the dipole trap laser detuning greatly exceeds the hyperfine splittings of the ground and excited states, at least the optical potential is the same for all hyperfine and magnetic sublevels [29].

### 7.2.2

#### Signatures of Collective Atomic Recoil Lasing

A typical experimental sequence goes as follows [9]: After the dipole trap has been filled with atoms, a time of about 100 ms is waited until the atoms have found their thermal equilibrium and form a homogeneous cloud. The CARL process is started by *suddenly switching on the optical molasses*. The molasses beams are extinguished again after some 100 ms.

The observables of our system are the field amplitudes  $\alpha_{\pm}$  and the atomic coordinates  $x$  and  $p$ . In order to clarify the interplay between these degrees of freedom, we measure the response of the coupled atom-cavity system to switching on and off the molasses. Three signals are monitored: First of all, we record the interference signal obtained from a frequency beat of the two counterpropagating ring cavity modes. Second, time-of-flight absorption images allow us to detect spatial displacements of the atomic cloud or to measure its temperature. Finally, we record RIR spectra of the atomic momentum distribution thus obtaining complementary information on the atomic cloud's state of motion.

##### 7.2.2.1 Beat Note of Field Modes

The phase dynamics of two counterpropagating cavity modes is monitored as a beat signal between the two beams, which are outcoupled at one of the high-reflecting cavity mirrors (see Fig. 7.1) and phase-matched on a photodetector. Any frequency difference between pumped mode ( $\omega_+$ ) and reverse (probe) mode ( $\omega_-$ ) gives rise to a propagation of the standing wave inside the ring cavity, which translates into an amplitude variation of the beat signal,

$$P_{\text{beat}} = T\hbar\omega\delta |\alpha_+ + \alpha_-|^2. \quad (7.3)$$

The beat signal oscillates with the frequency  $\Delta\omega \equiv \omega_+ - \omega_-$ .

Fig. 7.2 shows the time evolution of the beat signal. Initially, apart from a certain amount of noise, there is no discernable signal. But as soon as the molasses is irradiated at time  $t = 0$  s, strong oscillations appear with a fixed frequency. They persist for more than 100 ms. The oscillations *do not arise*, when the cavity is set up for low finesse.

To understand this observation, we consider an atomic cloud irradiated by a pump laser. As long as the cloud is homogeneous, the pump light is not coherently backscattered, because the backscattered photons have random phases and interfere destructively. Tiny density fluctuations may however give rise to a small amount of net backscattering. The backscattering atoms are accelerated due to photonic recoil, and the backscattered light is red-detuned because of the Doppler effect. Together with the pump light the backscattered probe generates by interference a weak modulation of the intracavity light intensity, i.e. a standing wave fraction, which propagates in the same direc-

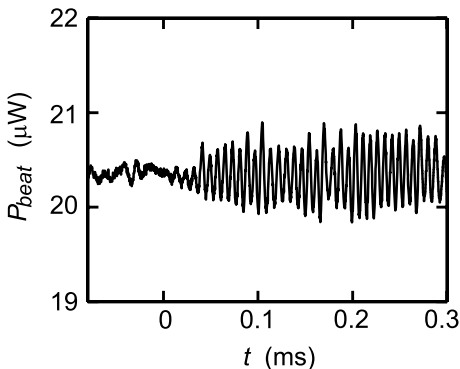


**Fig. 7.2** Recorded time evolution of the beat signal between the two cavity modes [9]. At time  $t = 0$  s the molasses beams have been switched on.

tion as the pump beam. If no other forces are applied, the accelerated atoms spread out in space and merge with the bulk of the homogeneous cloud; the fluctuation disappears and the probe decays. If however an optical molasses is irradiated, the acceleration is balanced by a friction force. The atoms now have time enough to probe the dipole potential of the standing wave and be pulled towards the potential valleys. Therefore they arrange themselves into a periodic pattern, which dramatically increases the backscattering efficiency due to Bragg reflection. The increased standing wave contrast in turn amplifies the tendency of the atoms to self-organize, and so on. Positive feedback results in exponential gain, only limited by the detuning of the probe mode from the cavity resonance (typically a few % of the pump power). The propagating standing wave drags along the atoms, which in turn haul the standing wave. The propagation velocity corresponds to an equilibrium between the acceleration force exerted by the coherent backscattering and the velocity-dependent friction force exerted by the molasses. The atoms behave like *surfing on a self-generated standing light wave*.

As soon as the optical molasses is turned off, the dipole force has no counterbalance. The standing wave and the atoms accelerate each other and start to run without bounds. The frequency difference between the pump and the reverse lasing mode continuously increases. Consequently, the beat signal oscillates faster and faster, and the contrast of the interference fringes gradually fades out, because the frequency of the backscattered light deviates more and more from the cavity resonance (see Fig. 7.3(a)). However fringes are still visible after more than 2 ms, which corresponds to 600 cavity decay times.

A Fourier analysis over consecutive time intervals of the beat signal  $P_{\text{beat}}$  reveals the gradual frequency increase of the oscillations  $\Delta\omega$ , corresponding

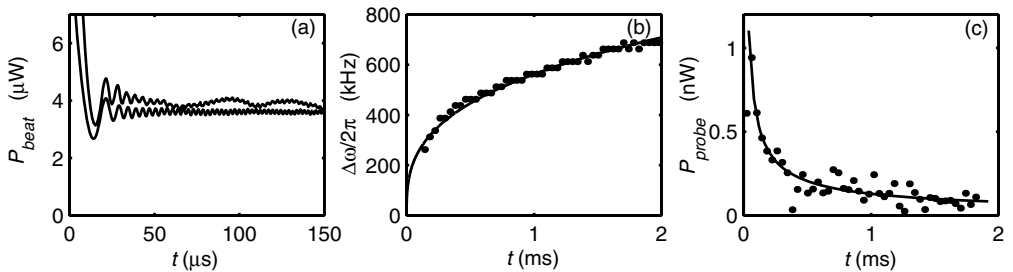


**Fig. 7.3** Acceleration of the standing wave as the molasses beams are interrupted. (a) Measured beat signal (upper curve) together with a numerical simulation (lower curve). The instantaneous frequency difference between pump and probe is plotted in (b) as a function

of time. (c) Instantaneous fringe contrast, which is proportional to the probe beam intensity. The solid lines represent calculations obtained from analytical formulae (Eqs. (7.9) in Sect. 7.3.1) [11].

to an increasingly red-detuned probe beam (see Fig. 7.3(b)). The decrease of the amplitude is visible in Fig. 7.3(c). In practice, we determine the probe beam power,  $P_{\text{probe}} = T\hbar\omega\delta|\alpha_-|^2$ , from the contrast of the beat signal (or the height of the peak in the Fourier spectrum),  $\Delta P_{\text{cont}} \equiv \max P_{\text{beat}} - \min P_{\text{beat}} = 4T\hbar\omega\delta|\alpha_+||\alpha_-|$ ,

$$P_{\text{probe}} = \frac{\Delta P_{\text{cont}}^2}{16P_{\text{pump}}} . \quad (7.4)$$

### 7.2.2.2 Spectra of Recoil-induced Resonances

The above interpretation of the beat signal observation in terms of a propagating intracavity standing wave postulates an acceleration of the atomic cloud in the direction of the pump light. With the aim to provide evidence for an atomic motion, we map the atomic velocity distribution by RIR spectroscopy [14, 34]. Two laser beams in Raman configuration propagating within the ring cavity plane and enclosing a small angle \$\theta = 8^\circ\$ are aligned nearly perpendicularly to the dipole trap. The Raman beams are tuned a few 100 MHz blue to the \$D\_2\$ line.

The RIR spectra are recorded a few ms after the molasses beams have been switched off and immediately after the pump laser has been interrupted, thus suddenly releasing the atoms from the dipole trap. The frequency of one Raman beam is ramped across a detuning range of  $\Delta_{\text{rir}}/2\pi = -200..200$  kHz with respect to the other beam with a scan rate of 2 kHz/\$\mu\text{s}\$. The power transmission of the fixed-frequency Raman beam through the atomic cloud is recorded on a photodetector. Fig. 7.4(a) shows such a RIR spectrum.

As pointed out in [14, 35, 36], the net rate for scattering photons between the Raman beams,  $W_{\text{RIR}}(v)$ , is proportional to the number of atoms  $N$ , to the derivative of their velocity distribution  $\partial\Pi(v)/\partial v$ , and to a constant  $C$  which depends on the intensities of the Raman beams. The velocity class of atoms

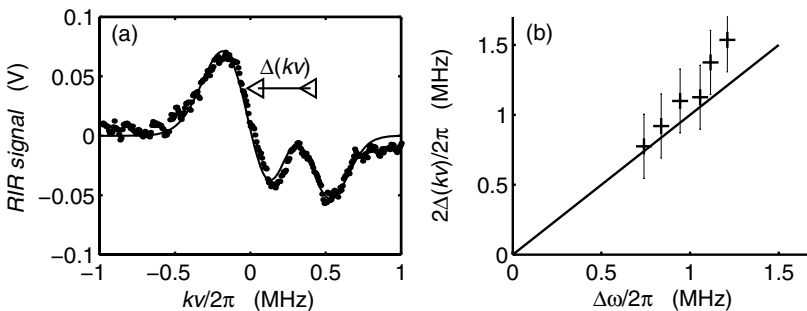


**Fig. 7.4** (a) RIR momentum spectra of a CARL-accelerated atomic cloud. Note that the velocity axis is rescaled in terms of the Doppler shift occurring at the cavity field wavenumber  $k$ . The fitted curve assumes a superposition of two displaced Gaussian

derivatives. (b) Splitting  $\Delta(kv)$  of the two Gaussians shown in (a) for various CARL acceleration times plotted as a function of the beat frequency  $\Delta\omega$  measured shortly before recording the RIR spectrum [35].

contributing to the signal is selected via  $v = \Delta_{\text{rir}}/q$ , where  $q = 2k_{\text{rir}} \sin \frac{\theta}{2}$  and  $k_{\text{rir}}$  is the wavenumber of the RIR beams. The lineshape recorded in Fig. 7.4(a) suggests a bimodal velocity distribution for the CARL-accelerated cloud, which we model by a superposition of *two distinct thermal ensembles* having different atom numbers  $N_j$ , different temperatures  $T_j$ , and different center-of-mass velocities  $v_j$ :

$$W_{\text{RIR}}(v) = \sum_{j=1}^2 \frac{CN_j}{\sigma_j \sqrt{2\pi}} \frac{\partial}{\partial v} e^{-(kv - kv_j)^2/\sigma_j^2}, \quad (7.5)$$

where  $\sigma_j^2 = 2k_B T_j k^2/m$ . From a fit of this formula to the RIR signal exhibited in Fig. 7.4(a), we determine the relative atom number  $N_2/N_1 = 0.9$ , the temperatures  $T_1 = 300 \mu\text{K}$  and  $T_2 = 200 \mu\text{K}$ , and the relative Doppler shift  $\Delta(kv) \equiv kv_2 - kv_1 = 2\pi \times 400 \text{ kHz}$ . The actual values depend on the experimental settings. In particular we find that the relative Doppler shift increases with the time delay between molasses switch-off and RIR scan. By plotting the relative Doppler shift against the instantaneous CARL frequency independently extracted from a simultaneously recorded beat signal (see Fig. 7.3), we obtain the curve in Fig. 7.4(b). The data points correspond to different time delays. The equivalence  $\Delta\omega = 2\Delta(kv)$  nicely demonstrates that atoms are synchronously accelerated with the moving standing wave. On the other hand the bimodal feature of the velocity distribution shows, that a part of the cloud is apparently unaffected by the CARL dynamics.

### 7.2.2.3 Atomic Transport

A Doppler-shift of  $kv = 2\pi \times 500 \text{ kHz}$  corresponds to an atomic velocity of  $40 \text{ cm/s}$  and leads to macroscopic displacements of the atoms on the order of several mm after a few ms. To observe this displacement, we take absorption

pictures of the atomic cloud after a few ms of undamped CARL acceleration followed by a short 1 ms free expansion period.<sup>3</sup> Figs. 7.5(a) and (b) show pictures taken for CARL acceleration times of 0 and 6 ms, respectively. After 6 ms a spatial shift of the cloud is clearly visible.

In order to rule out that the atoms are simply shifted by radiation pressure, we repeat the measurement for weak coupling, i.e. by operating the ring cavity at low finesse and rising the pump power, so that the intracavity power and consequently the radiation pressure are unchanged. Under these conditions we do not observe a shift of the atomic cloud for acceleration times below 10 ms.

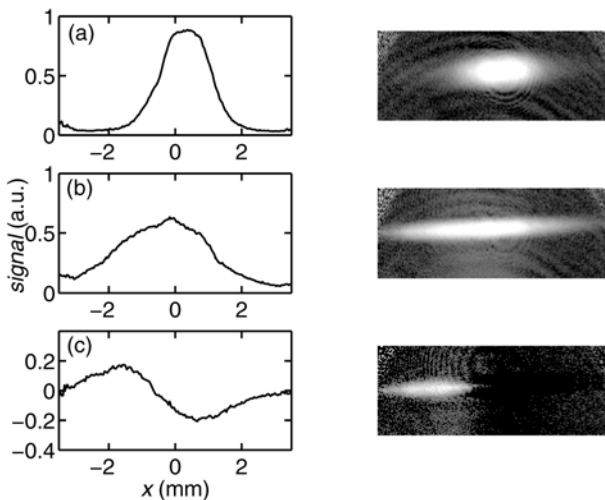


**Fig. 7.5** (a) Absorption images of a cloud of  $6 \times 10^6$  atoms recorded for high cavity finesse after 0 ms and (b) 6 ms of CARL acceleration [9]. Image (c) emphasizes the CARL displacement by subtracting from image (b) an absorption image taken with low cavity finesse after a 6 ms CARL acceleration period. The intracavity power has been adjusted to the same value as in the high-finesse case.

The displacement can be estimated by integrating the formula (9) in Sect. 7.3.1, which describes the time dependence of the Doppler shift:

$$kx = \frac{3}{8} \Delta\omega t . \quad (7.6)$$

This yields  $x \approx 1.8$  mm, which agrees fairly well with the observation in Fig. 7.5. A bimodal structure of the spatial distribution, as observed in the

- 3) For these measurements, the atomic bunching which precedes the CARL acceleration has *not* been realized by an optical molasses. Instead, the atoms were loaded into a standing wave dipole trap obtained by bidirectional pumping of the cavity [9]. This method concentrates the atoms within a smaller segment along the cavity axis and makes the axial displacement due to CARL more visible.

velocity distribution, is not discernible because of the large axial extend for the cloud.

### 7.3

#### Creating Long-range Order

Driven by dissipative forces, certain categories of systems are able to spontaneously develop long-range order all by themselves without the need of periodic force fields. This self-organization is a very general phenomenon. Famous examples are populations of chorusing crickets or blinking fireflies, cardiac pacemaker cells, laser arrays or coupled arrays of Josephson junctions, rhythmic applause or simply Huygens pendulum clocks (see Fig. 7.6(a)), which synchronize their oscillations when attached to the same wall [37]. Self-synchronization is generally driven by the feedback interaction between a macrosystem and microsystems (see Fig. 7.6(b)). A macroscopic order parameter defines the boundary conditions for microscopic processes. On the other hand, these microscopic processes can, if they act collectively, influence the order parameter. This global feedback can give rise to instabilities and to long-range order. In the case of CARL the order parameter is a bunching of atoms, the microscopic processes are light scattering events, and the long-range order shows up as lasing accompanied by a simultaneous formation of an atomic lattice [35].

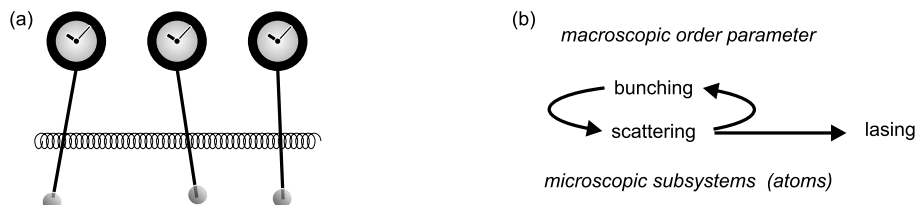


**Fig. 7.6** (a) Scheme of Huygens' coupled pendulum clocks. (b) Sketch of the feedback interaction between macro- and microsystems.

The observations presented in the previous sections support this interpretation and confirm that collective interatomic coupling plays a prominent role in the dynamics of the atoms and the cavity modes. In the following sections we will briefly address some theoretical approaches to describe the dynamics quantitatively.

##### 7.3.1

##### Analytic Treatment for Perfect Bunching

The collective dynamics of atoms simultaneously coupled to light modes with and without the presence of a ring cavity has been studied by Bonifacio et al.

[38], Gangl et al. [28] and Perrin et al. [31]. Our experiments deal with thermal clouds, so that the atomic coordinates may be treated classically.  $x_n$  denotes the position of the  $n^{\text{th}}$  atom and  $p_n$  its momentum. Furthermore, due to its large mode volume, the cavity involves many photons in the dynamics, which allows us to describe the counterpropagating optical fields  $\alpha_{\pm}$  classically as well. The only remaining quantization is that of the internal atomic excitation, whose dynamics essentially follows two-level Bloch equations. However, for the very large detunings used in our experiments the internal degrees of freedom can be adiabatically eliminated [28, 31, 38]: At large detunings the field amplitudes and the atomic coordinates evolve much slower than the atomic excitation. Therefore, the time scales for the external and internal dynamics can be separated, which means that the atomic excitation is always in a (quasi-)stationary state and drops out of the equations of motion.

Furthermore, large detunings allow us to neglect any contribution from radiation pressure,  $\gamma_0 \ll U_0$ . The interaction of the atoms with the ring cavity is then governed by the following set of equations of motion [28],<sup>4</sup>

$$\dot{\alpha}_{\pm} = (-\kappa - iNU_0 + i\Delta_c) \alpha_{\pm} - iU_0 \sum_n e^{\mp 2ikx_n} \alpha_{\mp} + \eta_{\pm}, \quad (7.7a)$$

$$m\ddot{x}_n = 2\hbar k i U_0 \left( \alpha_+^* \alpha_- e^{-2ikx_n} - \alpha_+ \alpha_-^* e^{2ikx_n} \right), \quad (7.7b)$$

with  $\eta_- = 0$ . The equations have the following meaning: The first equation describes the modification of the field amplitudes by decay  $\kappa$ , detuning  $\Delta_c$  of the laser from the cavity resonance, or collective light shift  $NU_0$  (first term), by mutual scattering between the modes (second term) and external pumping (last term). Note that the mutual scattering amplitude is weighted with the location of the atoms modulo  $2\pi/k$ , i.e. the photon scattering balance depends on the atomic locations. The second equation states that the dipole force sensed by the atoms is caused by the scattering of photons between the counterpropagating modes.

Eqs. (7.7) must, in general, be solved numerically. Analytic solutions are only available for special cases. For example, under the assumption of perfect atomic bunching,  $e^{ikx_m} = e^{ikx_n}$  for all  $m, n$ , we can then replace all the individual atomic coordinates by a single pair of variables  $x$  and  $\dot{x}$ .

As discussed by Gangl et al. [25] the dynamics of the CARL system critically depends on the detuning of the pump laser. An important point arising from experimental constraints is now the following: The pump mode  $\alpha_+$  is tightly phase-locked to the cavity. As discussed in [23], the presence of atoms inside the cavity mode volume may shift the cavity resonance, and this shift depends on the atomic bunching. Since the phase-lock continuously works to readjust the detuning  $\Delta_c$  (defined for the empty cavity) to the resonance (of the cavity filled with atoms), the detuning becomes a time-dependent variable, which

4) Friction forces due to optical molasses are not considered here.

follows the dynamics of the system. This fact needs to be considered by theories modeling our experiment, when it is operated in a parameter regime where the shift of the cavity resonances caused by the atoms, which is on the order of  $NU_0$ , exceeds the cavity linewidth  $\kappa$ . A good approach to model the impact of the phase-locking is to simply assume that the *phase* of the pump laser  $\eta_+$  is equal to that of the locked mode  $\alpha_+$ . This assumption is good, because the bandwidth of our servo system largely exceeds all characteristic frequencies of the coupled dynamics. Without loss of generality we may fix these phases to zero, while the phase  $\phi$  of the probe mode remains a dynamic variable,

$$\eta_+ = |\eta_+| \quad , \quad \alpha_+ = |\alpha_+| \quad , \quad \alpha_- = |\alpha_-| e^{i\phi} . \quad (7.8)$$

Eqs. (7.7) can approximately be solved, if we assume that the field amplitudes have no explicit time-dependence,  $\dot{\alpha}_\pm = 0$ . This assumption corresponds to an adiabatic elimination of inertial terms, which means that the standing wave and the atomic grating keep a fixed relative phase. It allows us to derive approximate solutions for the field amplitudes valid at long times,  $t \gg \kappa^{-1}$  [11, 14, 36, 39],

$$\alpha_+ \approx \frac{\eta_+}{\kappa} , \quad (7.9a)$$

$$|\alpha_-|^3 \approx \frac{N^2 U_0 \eta_+}{24 \kappa^2 \epsilon t} , \quad (7.9b)$$

$$(kv)^3 \approx \frac{3\epsilon N U_0^2 \eta_+^2}{\kappa} t , \quad (7.9c)$$

where we introduced the abbreviation  $\epsilon \equiv \hbar k^2 / m$ . These formulae have been fitted to the data in Fig. 7.3(b) and (c).<sup>5</sup>

### 7.3.1.1 Radiation Pressure

Far from atomic resonances,  $\Delta_{D1} \approx -2 \times 10^5 \Gamma$ , the spontaneous scattering rate is many orders of magnitude lower than the coherent scattering rate  $\gamma_0 / U_0 \simeq \Gamma / \Delta_{D1} \approx 5 \times 10^{-6}$ . On the other hand, the photon flux of the pump beam is quite large. When we compare the radiation pressure force to the CARL force resulting from Eq. (7.7b),

$$F_{\text{rp}} = 2\hbar k \gamma_0 |\alpha_+|^2 , \quad (7.10a)$$

$$F_{\text{carl}} < 4\hbar k U_0 |\alpha_+| |\alpha_-| , \quad (7.10b)$$

we find that a power in the probe mode as low as  $P_{\text{probe}} > P_{\text{pump}} (\gamma_0 / 2U_0)^2$  is sufficient to ensure that the CARL force dominates. This shows that the

5) It is interesting to compare the probe power dependence on the atom number  $P_- \propto |\alpha_-|^2 \propto N^{4/3}$  to the dependence expected for superradiance  $P_- \propto N^2$  (see [40]).

radiation pressure can play a substantial role only at very long times, when the CARL acceleration has driven the probe mode very far out of resonance. But it does not take part in the acceleration process observed in Fig. 7.3(c). While the radiation pressure exerts a *constant acceleration* on the atoms, we observe in experiment a *cubic root time-dependence* of the CARL frequency.<sup>6</sup>

### 7.3.1.2 Phase-locking by Imperfect Mirrors

Phase-locking is a known problem of ring laser gyroscopes [41]. Any impurity located on the mirror surfaces, such as small dust particles, may scatter light into the reverse mode. Hence, a standing wave builds up, which adjusts its phase such that the scattering rate and thus the energy transfer into the reverse mode is maximized. The phase of the standing wave thus locks to the impurity.

The dipole force resulting from this standing wave can substantially alter the dynamics of atoms interacting with the cavity. In the worst case, the CARL acceleration is entirely inhibited, because the atoms are trapped in the standing wave caused by the mirror backscattering. In our ring cavity the phase fronts of the light fields hit the mirrors at angles of  $22.5^\circ$  or  $45^\circ$ . Macroscopic dust particles on the mirror surfaces traverse many phase fronts, so that in the average over several standing wave periods the net scattering between the modes should vanish.

However, the high finesse of the cavity amplifies even very small net scattering imbalances induced by microscopic irregularities (spatial noise). To see this, we describe the imbalance as originating from a distribution of  $N_s$  point-like scatterers *fixed* at locations  $x_n$ . With the scattering efficiency  $U_s$  and assuming for simplicity  $\Delta_c = NU_s$ , the stationary solution of Eq. (7.7a) reads

$$\frac{\alpha_-}{\alpha_+} = -i \frac{N_s U_s b_s}{\kappa}. \quad (7.11)$$

where  $b_s \equiv N_s^{-1} \sum_n e^{2ikx_n}$ . This equation shows that, at first sight counterintuitively, the intensity in the reverse mode increases, when the finesse of the mirrors is improved (or  $\kappa$  is reduced). The fraction measured in experiment,  $|\alpha_-|^2/|\alpha_+|^2 \approx 0.35\%$ , corresponds to a collective coupling strength of about  $N_s U_s \approx 0.06\kappa$ , which is smaller but in the same order of magnitude as the atom-field coupling used for observing CARL activity.

Furthermore, inserting the solution (7.11) into the expression for the dipole force (7.7b), we find that the phase of the backscattered light adjusts in such a way that the scatterer sits at half height on the edge of the resulting standing wave. In this configuration the backscattering rate is largest. However, any

6) Note that poor atomic bunching can also reduce the CARL force up to a point where radiation pressure overtakes.

spatial extend of the scatterer's size, expressed by a decrease of the quantity  $b_s$ , will diminish this rate.

### 7.3.2

#### Simulations of Atomic Trajectories with Friction and Diffusion

The CARL equations (7.7) predict unlimited acceleration of the atoms and of the phase of the standing wave formed by the pump mode and the reverse mode. To balance this acceleration, we have introduced in our experiment an optical molasses. As discussed in Sect. 7.2.1.3, at low atomic velocities molasses are well characterized by a velocity-independent friction coefficient [42]. For the theoretical description we may thus supplement Eq. (7.7b) by a friction force  $\gamma_{fr}\dot{x}_n$ .

Through the friction coefficient, the frequency and the amplitude of the probe beam depend on the settings of the molasses. This is verified experimentally [11]. However another prediction of this model is not verified. Simulations of Eqs. (7.7) including friction show a complete synchronization of the atomic trajectories for any set of parameters. After an amount of time, which depends on coupling strength, atom number and pump power, the atomic bunching tends to unity. This is due to the absence of any influence working to counteract the atomic ordering from the model, and contradicts

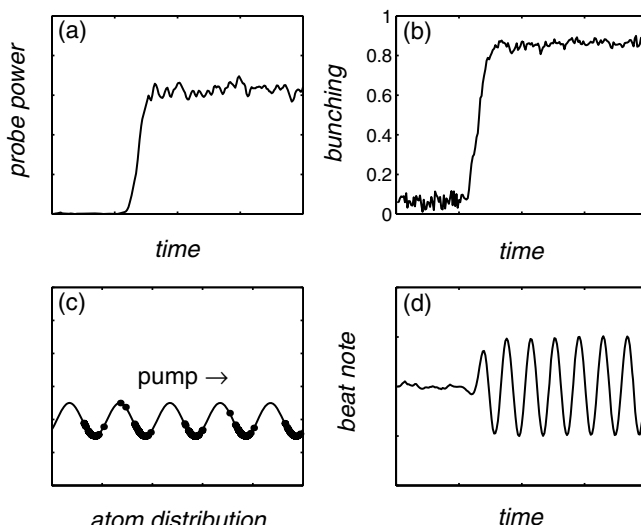


**Fig. 7.7** Simulation of CARL action triggered by suddenly turning on an optical molasses. The figures show (a) the evolution of the probe photon number in the reverse cavity mode, (b) the bunching of the atoms, (c) the spatial distribution of the atoms (filled circles) along the cavity axis at the end of the simulation, and (d) the beat signal between the cavity modes.

the observation of a threshold observed in experiment [11], as we will discuss in the next section.

A heating mechanism which is well-known to occur in optical molasses is momentum-diffusion. Momentum transfer to the atoms due to photonic recoil by scattering of light leads to a random walk of the atoms, which can be described as resulting from a random force [40]. Therefore, we describe the dynamics of our system by a set of Langevin equations. In general these cannot be solved analytically, and we have to numerically iterate them in time. For the sake of computational efficiency, we only calculate the trajectories of 100 atoms. The molasses friction is strong enough to completely overdamp the atomic motion, so that we may adiabatically eliminate the atomic inertia and write [40],

$$\dot{\alpha}_{\pm} = -(\kappa + iNU_0 - i\Delta_c) \alpha_{\pm} - iU_0 \sum_n e^{\mp 2ikx_n} \alpha_{\mp} + \eta_{\pm}, \quad (7.12a)$$

$$0 = 2\hbar k iU_0 \left( \alpha_+^* \alpha_- e^{-2ikx_n} - \alpha_+ \alpha_-^* e^{2ikx_n} \right) - \gamma_{fr} \dot{x}_n + F_{noise}(t). \quad (7.12b)$$

For the simulation, we assume that the atoms are irradiated by a pump laser and that there is initially *one* photon in the probe mode. We start with a homogeneous atomic cloud distributed around the waist of the cavity mode and having a thermal momentum distribution. Fig. 7.7 shows the time evolutions of the backscattered light intensity  $|\alpha_-|^2$ , the bunching parameter<sup>7</sup>  $b \equiv N^{-1} \left| \sum_n e^{2ikx_n} \right|$ , the spatial distribution  $x_n$  of the atoms, and the interference signal  $|\alpha_+ + \alpha_-|^2$ . A short time delay after the optical molasses is switched on, the amplitude of the backscattered beam and the order parameter suddenly start to grow towards macroscopic values. The atoms arrange themselves into a periodic lattice, synchronize their velocities and, together with the standing wave, propagate in the pump beam direction (arrow in Fig. 7.7(c)). In the same time, the beat signal starts to oscillate. The calculated trajectories reproduce quantitatively the experimental observations shown in Figs. 7.2 to 7.5.

### 7.3.2.1 Lasing Threshold

The simulations confirm that, under the influence of an optical molasses and mediated by collective atomic recoil, the coupled atom-cavity system generates laser light. In the same time, the atoms self-organize into a periodic lattice, while breaking translation symmetry. The sudden appearance of a coherent radiation reminds a laser threshold, and the atomic ordering corresponds to a thermodynamic phase transition. To model the phase transition we have chosen an alternative approach. Instead of simulating single-atom trajectories, we derive from Eqs. (7.12) a Fokker-Planck equation for the atomic density

7) The bunching parameter measures the periodic arrangement of the atoms. It is also called the order parameter or Debye-Waller factor.

distribution. The solution of this equation reproduces the time evolution of the density distribution, and a linear stability analysis leads to simple analytic formulae describing the threshold conditions [40, 43].

The calculated threshold behavior is observed in experiment: To trigger the CARL and obtain probe laser emission, a minimum pump laser power is needed. Below this threshold the order parameter disappears, far above threshold it approaches unity. The threshold power should obviously depend on some control parameters. Fig. 7.8 shows that, as expected, the threshold increases when the coupling strength is decreased, i.e. if the pump laser is tuned further away from the atomic resonance [11]. The threshold decreases when the atom number is increased.

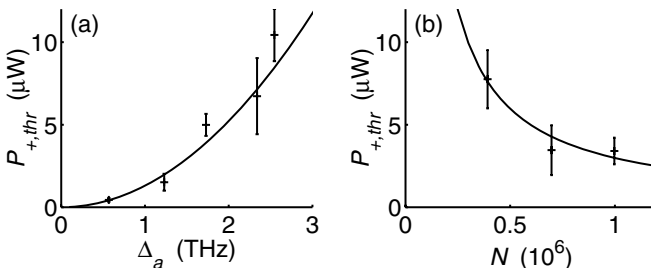


**Fig. 7.8** Behavior of the pump power threshold  $P_{+,thr}$  when (a) the detuning  $\Delta_a$  or (b) the atom number  $N$  is varied. The fits are obtained from a linear stability analysis of a Fokker-Planck equation [11, 40].

The role of the molasses in the CARL dynamics is twofold: On one hand, the dissipation of energy permits to reach a steady-state. On the other hand, atomic momentum-diffusion processes, which are intrinsically connected to optical molasses, limit the equilibrium temperature. The interplay of dissipation and diffusion rules the thermodynamic phase transition, and gives rise to the observed threshold behavior of the CARL radiation.

### 7.3.2.2 Self-synchronization

The simplest model describing synchronization phenomena, known as Kuramoto model [44], considers ensembles of coupled limit cycle oscillators. It predicts the occurrence of spontaneous synchronization, when a critical number of oscillators is put together or when the coupling strength exceeds a critical value [45]. Under certain approximations, the Kuramoto model is also applicable to describe the CARL bunching of atomic trajectories [11]. However in the case of CARL, unlike for the Kuramoto model, the collective oscillation frequency is self-determined. The observed probe mode emits a *new* laser frequency, which only depends on *global* system parameters.

In fact, CARL represents in many respects an ideal system to study self-synchronization phenomena: First of all, free atoms are very simple systems,

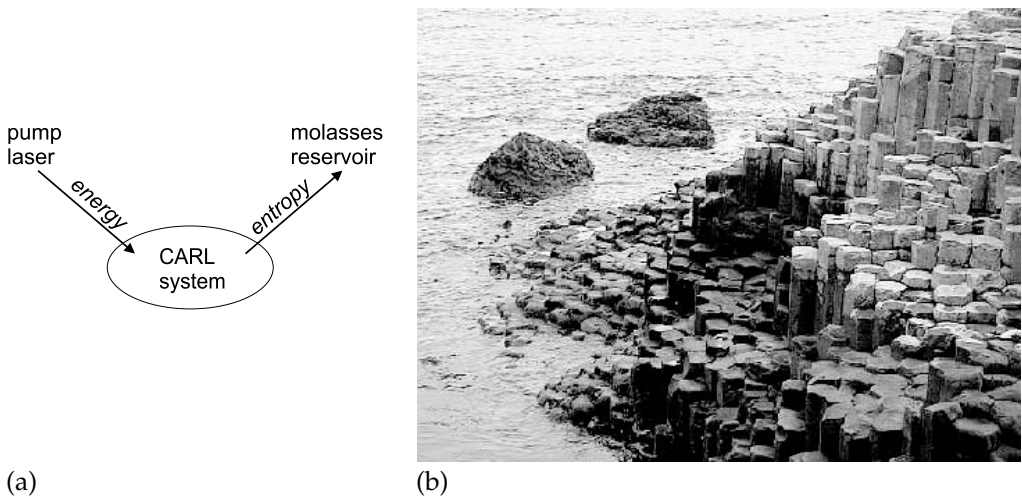


**Fig. 7.9** (a) Scheme of the CARL coupling to the environment.  
 (b) Self-organization at Giant's Causeway in Northern Ireland. The hexagonal rock formations are frozen Bénard convection flow patterns.

the behavior of which is almost completely understood. They are among the smallest entities, which can be handled and controlled with current technologies. Therefore, many of them can be joined together, thus experimentally realizing the thermodynamic limit to a good approximation. Furthermore, a truly universal coupling force (i.e. a force which couples any pair of atoms with the same strength, independently of their distance) is desirable, because the system is much easier to understand if local peculiarities do not affect the global dynamics. The CARL coupling is universal, because it is mediated by a light mode which is completely delocalized within the ring cavity. Finally, the coupling force should be sufficiently strong, so that the subsystems do not evolve independently from each other but execute collective actions. On the other hand, the coupling to the external world, e.g. reservoirs or pumps should be sufficiently weak to allow the system to develop a self-determined behavior.

The atomic self-synchronization corresponds to a thermodynamic phase transition, where the control parameter is time. It is ruled by the competition between the dynamical coupling which generates order, and diffusion which is a source of disorder. It is however important to note that the system is never in thermal equilibrium. To maintain order, one has to constantly inject energy via the pump laser (see Fig. 7.9(a)). The produced entropy is dissipated via the reservoir of the optical molasses. This introduces the irreversibility required in any lasing process. The transition towards a structure with a higher symmetry has certain analogies with the dissipative structures postulated by

Prigogine [46] or with Haken's synergetic systems [47], whose most famous examples are the Bénard structures. Those are regular patterns of convection flow arising in a heated fluid, and can e.g. be observed as frozen geological rock formations (see Fig. 7.9(b)).

## 7.4

### Probing Long-range Order

The hallmark of collective atomic recoil lasing is atomic bunching. The CARL signatures presented in Sect. 7.2.2 are more or less indirect indications for the presence of bunching. There is however a way to probe atomic gratings directly, which is Bragg scattering.

Bragg scattering at three-dimensional near-resonant gaseous atomic gratings (called optical lattices) has been demonstrated 10 years ago by Birkl et al. and Weidmüller et al. [48–50]. In contrast to those experiments, our sample consists of an *one-dimensional* array of atomic clouds confined at the antinodes of a ring cavity standing wave, and the standing wave light is tuned very *far from atomic resonances*, so that the confining lattice potential is conservative and dissipative cooling forces are absent [51].

First attempts to employ the Bragg scattering method to monitor CARL bunching have not been successful. On one hand, this is due to the presence of atomic gratings *not* related to CARL. Spurious mirror backscattering (see Sect. 7.3.1.2) generates a stationary standing wave fraction, which is not generated by CARL dynamics of trapped atoms, but nevertheless forces the atoms into a partial alignment. To solve this problem, having in mind that CARL-bunched atoms always propagate along the cavity axis, we have developed a method of detecting *moving* lattices. On the other hand, the weak Bragg scattering efficiency of typically  $R = 0.1\%$  makes the detection of bunching a challenge. Fortunately, we have been able to show that suitable modifications of the experiment can dramatically increase the Bragg reflection [52] up to a point, where it should clearly be sufficient to detect CARL-bunching in future experiments.

#### 7.4.1

##### Bragg Scattering

The setup for Bragg scattering is shown in Fig. 7.10, with the shutter S closed. We test the setup by generating an atomic lattice by imposing a periodic force field. To this end both counterpropagating modes of the ring cavity are pumped with the same light frequency,  $\omega_+ = \omega_-$ , so that the atoms arrange themselves in an optical grating. To probe the grating, light at 420 nm resonant

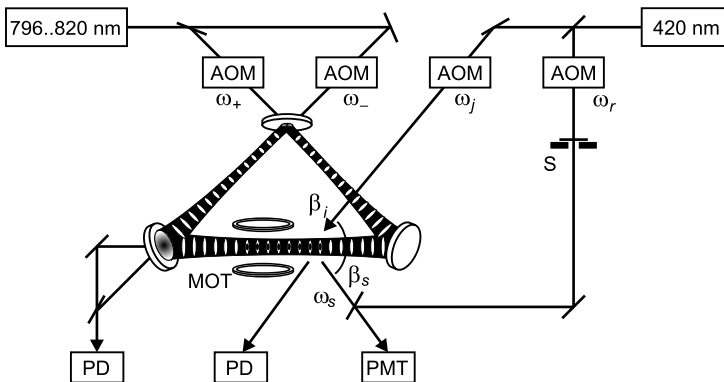


**Fig. 7.10** Modified setup for Bragg spectroscopy. The ring cavity is now pumped in *both* directions with frequencies  $\omega_{\pm}$  tuned by means of acousto-optic modulators (AOM). Probe light,  $\omega_j$ , is shone under the Bragg angle onto the atoms. The transmitted light

is monitored with a photodetector (PD), Bragg reflection is detected with a photomultiplier (PMT). By opening a shutter (S) the Bragg-reflected beam can be heterodyned with a reference frequency  $\omega_r$ .

to the  $5S_{1/2}$ - $6P_{3/2}$  transition is irradiated under the Bragg angle  $58^\circ$ , and the reflected signal is recorded.

There are many obvious signatures of Bragg scattering: First of all, Bragg scattering works only for a well-defined angle of incidence. In fact the observed acceptance angle and the beam divergence of the reflected beam are both on the order of  $0.1^\circ$ . Second, the reflected intensity should scale with the square of the atom number and not linearly, as one would expect for isotropic resonance fluorescence [51]. This is verified in Fig. 7.11(a). Fig. 7.11(b) shows a transmission spectrum of magneto-optically trapped atoms, which serves as a frequency reference. An example of a Bragg reflection spectrum is shown in Fig. 7.11(c). The spectrum is displaced due to the light-shift of the atoms in the dipole trap.

The trapped atoms sense a position-dependent dynamical Stark-shift, which results in inhomogeneous broadening of the atomic transitions. This broadening and also atomic heating induced by the Bragg laser limited the Bragg reflection efficiency in early experiments [51]. Subsequent experiments have shown that the Bragg scattering efficiency can be dramatically improved by tuning the probe laser to the  $D_2$  line at 780 nm. Efficiencies up to  $R = 30\%$  have been reached allowing for studies of subtle effects arising from the one-dimensional geometry of the optical lattice [53]. We have even observed signatures of a tricky interplay between multiple reflections and diffuse scattering in thick lattices [52].

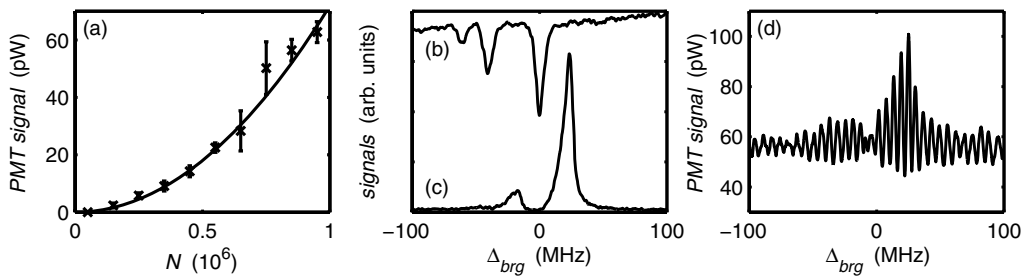


**Fig. 7.11** (a) Dependence of the Bragg scattered peak intensity from the atom number [51]. (b) Absorption spectrum from a cloud confined in a magneto-optical trap (for reference). (c) Bragg reflection spectrum. (d) Spectrum of the beat between the Bragg-reflected light and the incident mode.

#### 7.4.2

##### Heterodyned Bragg Spectra

The Bragg signals have been obtained on atoms confined in a standing wave, i.e. with bidirectional pumping of the ring cavity. The Bragg scattering technique can be refined to be sensitive to *moving* long-range order by heterodyning the Bragg-scattered light with a reference [51]. We test the idea by simulating the CARL behavior, i.e. we create a rotating standing wave inside the ring cavity by supplying *different pump frequencies* for the counterpropagating modes,  $\omega_+ \neq \omega_-$ . The frequencies are shifted by means of two acousto-optic modulators (AOM). The Bragg-reflected beam is phase-matched with a reference laser beam (the shutter (S) in Fig. 7.10 is opened), and the frequency beat is monitored on a photomultiplier (PMT). By means of another AOM the frequency of the reference beam  $\omega_r$  is chosen such that the beat occurs at frequencies low enough to be resolved by our PMT. A fourth AOM ramps the Bragg beam frequency  $\omega_j$  across resonance (see Fig. 7.10).

The observed beat signal between Bragg and reference beam is shown in Fig. 7.11(d). To evaluate the beat frequency, we show in Fig. 7.12 three Fourier spectra: (a) The beat of the counterpropagating cavity modes oscillates at the frequency  $2k_{\text{dip}}v$ ; (b) a reference interferometer (not shown in Fig. 7.10) measures the difference frequency  $\Delta\omega_j = \omega_j - \omega_r$ , and (c) the frequency of the Bragg beat is  $\Delta\omega_s = \omega_s - \omega_r$ . The fact that the Bragg-scattered light is obviously frequency-shifted by an amount corresponding to the Doppler-shift of the moving grating,

$$\Delta\omega_s = \Delta\omega_j - 2k_{\text{dip}}v, \quad (7.13)$$

permits to determine the lattice propagation velocity  $v$  with an accuracy better than 1% by measuring  $\Delta\omega_j$  and  $\Delta\omega_s$ .

Retardation effects resulting from unequal lengths of the interferometer arms lead to shifts in the recorded beat frequencies, as the laser frequency is scanned

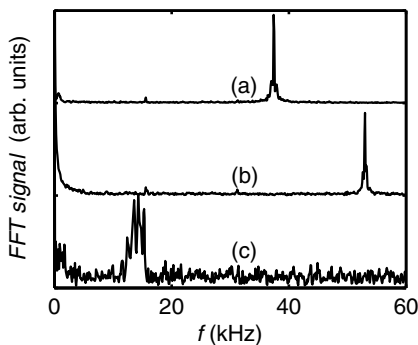


**Fig. 7.12** Detection of moving Bragg lattices. Shown are the Fourier spectra of (a)  $2k_{\text{dip}}v = 37$  kHz, (b)  $\Delta\omega_j = 53$  kHz and (c)  $\Delta\omega_s \approx 16$  kHz.

across resonance. The shifts can be corrected by inverting the scan direction. Furthermore, the Fourier spectrum of the Bragg beat in Fig. 7.12(c) shows asymmetric sidebands. These are artifacts arising from the presence of two hfs-resonances joint to the fact that the signal is amplitude- and phase-modulated by the frequency scan.

#### 7.4.3

#### Measuring the Bragg Scattering Phase

As shown in the previous section, heterodyned Bragg scattering is well-suited not only to probe long-range order, but also to detect its motional dynamics. Hence, it constitutes an interesting tool to study the dynamics of CARL. But there is more information in the heterodyne signal, because it gives access to the scattering phase.

To see this, let us write the global response of the atomic cloud to an incident laser  $E_j = E_{j0}e^{i\omega_j t}$ , as a complex scattering amplitude  $r = Ae^{i\phi}$ . The Bragg-scattered light amplitude is then given by  $E_s = rE_j = E_{j0}A(t)e^{i\omega_j t + i\phi(t)}$ . Heterodyning the Bragg-scattered light with a reference beam,  $E_r = E_{r0}e^{i\omega_r t}$ , yields the signal

$$S \propto |E_r + E_s|^2 \approx E_{j0}^2 + 2rE_{r0}E_{j0} \cos [(\omega_j - \omega_r)t + \phi] , \quad (7.14)$$

if  $rE_{j0} \ll E_{r0}$ . The amplitude and phase information are extracted by de-modulating the beat signal with the reference frequency  $\Delta\omega_j$  using two different phases. From these quadrature components we have determined the amplitude profile  $A(\Delta)$  and the phase profile  $\phi(\Delta)$  of the resonance [51]. The amplitude profile corresponds to the spectrum observed earlier by standard Bragg scattering. But the phase profile represents the first direct measurement of the phase-lag due to elastic scattering of light at an atomic cloud.

Under normal conditions phase measurements are not easy, because in thermal clouds Rayleigh scattering is Doppler-broadened by photonic recoil. In our case, the atoms are not only cold, but strongly confined; the Lamb-Dicke factor is about 100. Thus velocity-dependent recoil shifts are totally absent. Furthermore, Rayleigh scattering is normally weak (too weak to be heterodyned) because the atoms must be pumped at very low powers to avoid inelastic resonance fluorescence. Therefore, we gain a lot by resonantly enhancing the elastic peak by arranging the atoms into a grating and scattering at exactly the Bragg angle. To resume, two conditions are helpful for measurements of Rayleigh scattering phases, *strong atomic confinement* and *atomic ordering*.

## 7.5

### Conclusion

With our work, we have shown that atoms interacting with the counterpropagating modes of a high-finesse ring cavity can exhibit collective dynamics, provided the interatomic coupling constant is sufficiently large as compared to the cavity linewidth. An important prerequisite for the possible use of ring cavities for quantum information processing [4] is thus experimentally verified. The epitome of collective behavior is without doubts the collective atomic recoil laser, the signatures of which we have detected for the first time. Previous attempts to observe CARL [17, 18] were based on a maximization of the coupling strength by tuning the pump laser close to an atomic resonance. In contrast, the use of a high-finesse ring cavity allowed us to obtain strong coupling at huge pump laser detunings, where no noticeable effect is expected from atomic polarization gratings which do not correlate to density gratings and where spontaneous scattering plays no role.

Another important result of our work is the proof that CARL can be made stationary. Optical molasses not only introduce very efficient dissipation forces, but also a coupling to a finite temperature reservoir giving rise to spontaneous self-synchronization beyond a critical pump power or coupling strength. Just like self-synchronization, which is a very common phenomenon known to give rise to macroscopic consequences such as large scale pattern formation, CARL is a purely classical phenomenon. It could in principle be observed with billiard balls, if there was a suitable coupling force at hand [54]. On the other hand, our system consists of atoms, which are microscopic particles. Therefore it ought to exhibit quantum features in some circumstances, in particular at ultra-low temperatures, where quantum statistics come into play. E.g. we may expect effects like quantized acceleration [55], superradiance [56] or quantum entanglement [57, 58].

The study of the quantum regime will be the challenge of our future research efforts. We plan to cool the atoms to very low temperatures, eventually even beyond the limit to quantum degeneracy. It is clear that optical molasses cannot be used to exert friction forces on Bose-Einstein condensates. However there are other dissipation mechanisms working in cavities, such as cavity-cooling [59]. This cooling mechanism is ultimately a consequence of the coupling of the cavity to a zero-temperature reservoir via the finite transmission of the mirrors; vacuum fluctuations couple to the optical cavity, while thermal photons are frozen out, which corresponds to a situation of having dissipation without diffusion. If a threshold behavior is observed under such circumstances, it is an interesting question to ask whether it is linked to a quantum phase transition. In practice, a controllable dissipation mechanism working for Bose-Einstein condensates would be an extremely valuable tool, especially for the study of decoherence mechanisms. Superfluidity makes the condensates insensitive to collisions, and other sources for dissipation are not available.

Regarding quantum information applications, the aptitude of ring cavities is conditioned to a totally coherent evolution of the atomic states and the absence of uncontrolled decoherence. This means that thermal motion must be completely avoided. The sequel of the ring cavity experiment in the ultralow temperature regime thus seems compulsory.

## Acknowledgement

We are grateful for valuable discussions with R. Bonifacio, J. Javaloyes, R. Kaiser, G.-L. Lippi, M. Perrin, N. Piovella, A. Politi, H. Ritsch, and G.R.M. Robb. We acknowledge financial support from the Landesstiftung Baden-Württemberg.

## References

- 1 J. I. Cirac and P. Zoller, *Phys. Rev. Lett.* **74**, 4091 (1995).
- 2 H. C. Nägerl, et al. *Phys. Rev. A* **61**, 23405 (2000).
- 3 D. DeMille, *Phys. Rev. Lett.* **88**, 067901 (2002).
- 4 A. Hemmerich, *Phys. Rev. A* **60**, 943 (1999).
- 5 W. Alt, D. Schrader, S. Kuhr, M. Müller, V. Gomer, and D. Meschede, *Phys. Rev. A* **67**, 033403 (2003).
- 6 M. Greiner, O. Mandel, T. Esslinger, Th. W. Hänsch, and I. Bloch, *Nature* **415**, 39 (2002).
- 7 O. Mandel, M. Greiner, A. Widera, T. Rom, T. W. Hänsch, and I. Bloch, *Nature* **425**, 937 (2003).
- 8 A. Micheli, A. J. Daley, D. Jaksch, and P. Zoller, *Phys. Rev. Lett.* **93**, 140408 (2004).
- 9 D. Kruse, Ch. von Cube, C. Zimmermann, and Ph. W. Courteille, *Phys. Rev. Lett.* **91**, 183601 (2003).

- 10** R. Bonifacio et al., Opt. Commun. **233**, 155 (2004).
- 11** C. von Cube et al., Phys. Rev. Lett. **93**, 083601 (2004).
- 12** J. Guo, P. R. Berman, H. Dubetsky, and G. Grynberg, Phys. Rev. A **46**, 1426 (1992).
- 13** J. Y. Courtois, G. Grynberg, B. Lounis, and P. Verkerk, Phys. Rev. Lett. **72**, 3017 (1994).
- 14** D. Kruse et al., Phys. Rev. A **67**, 051802(R) (2003).
- 15** R. Bonifacio and L. De Salvo, Nucl. Instrum. Methods **341**, 360 (1994).
- 16** P. R. Berman, Phys. Rev. A **59**, 585 (1999).
- 17** G. L. Lippi, G. P. Barozzi, S. Barbay, and J. R. Tredicce, Phys. Rev. Lett. **76**, 2452 (1996).
- 18** P. R. Hemmer et al., Phys. Rev. Lett. **77**, 1996 (1996).
- 19** W. J. Brown, J. R. Gardner, D. J. Gauthier, and R. Vilaseca, Phys. Rev. A **55**, R1601 (1997).
- 20** W. J. Brown, J. R. Gardner, D. J. Gauthier, and R. Vilaseca, Phys. Rev. A **56**, 3255 (1997).
- 21** A. T. Black, H. W. Chan, and V. Vuletic, Phys. Rev. Lett. **91**, 203001 (2003).
- 22** B. Nagorny, Th. Elsässer, and A. Hemmerich, Phys. Rev. Lett. **91**, 153003 (2003).
- 23** Th. Elsässer, B. Nagorny, and A. Hemmerich, Phys. Rev. A **67**, 051401(R) (2003).
- 24** P. Domokos and H. Ritsch, J. Opt. Soc. Am. B **20**, 1098 (2003).
- 25** M. Gangl and H. Ritsch, Eur. Phys. J. D **8**, 29 (2000).
- 26** M. Kozuma, K. Nakagawa, W. Jhe, and M. Ohtsu, Phys. Rev. Lett. **76**, 2428 (1996).
- 27** G. Raithel, W. D. Phillips, and S. L. Rolston, Phys. Rev. Lett. **81**, 3615 (1998).
- 28** M. Gangl and H. Ritsch, Phys. Rev. A **61**, 043405 (2000).
- 29** R. Grimm, M. Weidemüller, and Y. B. Ovchinnikov, Adv. At. Mol. Opt. Phys. **42**, 95 (2000).
- 30** A. Mosk, S. Jochim, H. Moritz, Th. Elsässer, and M. Weidemüller, Opt. Lett. **26**, 1837 (2001).
- 31** M. Perrin, Zongxiong Ye, and L. Narducci, Phys. Rev. A **66**, 043809 (2002).
- 32** J. Javaloyes, G. L. Lippi, and A. Politi, Phys. Rev. A **68**, 033405 (2003).
- 33** J. P. Burke Jr., C. H. Greene, and J. L. Bohn, Phys. Rev. Lett. **81**(16), 3355 (1998).
- 34** D. R. Meacher, D. Boiron, H. Metcalf, C. Salomon, and G. Grynberg, Phys. Rev. A **50**, R1992 (1994).
- 35** Ph. W. Courteille et al., AIP Conf. Proc. (ICAP'04) **770**, 135 (2004).
- 36** D. Kruse, Selbstorganisation und Laseremission in kalten atomaren ensembles, PhD thesis, Universität Tübingen (2004), <http://www.uni-tuebingen.de/ub/elib/tobias.htm>.
- 37** S. H. Strogatz, Nature **410**, 268 (2001).
- 38** R. Bonifacio and L. De Salvo, Appl. Phys. B **60**, S233 (1995).
- 39** C. von Cube, Untersuchungen zum kollektiven atomaren Rückstoß-Laser, PhD thesis, Universität Tübingen (2005), <http://www.uni-tuebingen.de/ub/elib/tobias.htm>.
- 40** G. R. M. Robb et al., Phys. Rev. A **69**, 041403 (2004).
- 41** W. W. Chow et al., Rev. Mod. Phys. **57**, 61 (1985).
- 42** J. Dalibard and C. Cohen-Tannoudji, J. Opt. Soc. Am. B **6**, 2023 (1989).
- 43** J. Javaloyes, M. Perrin, G.-L. Lippi, and A. Politi, Phys. Rev. A **70**, 23405 (2004).
- 44** Y. Kuramoto, Progr. Theor. Phys. Suppl. **79**, 223 (1984).
- 45** S. H. Strogatz, Physica D **143**, 1 (2000).
- 46** G. Nicolis and I. Prigogine, Self-Organization in Non-Equilibrium Systems (Wiley-Interscience, New York, 1977).
- 47** H. Haken, Rev. Mod. Phys. **47**, 67 (1975).
- 48** G. Birkl, M. Gatzke, I. H. Deutsch, S. L. Rolston, and W. D. Phillips, Phys. Rev. Lett. **75**, 2823 (1995).
- 49** M. Weidemüller, A. Hemmerich, A. Görlitz, T. Esslinger, and Th. W. Hänsch, Phys. Rev. Lett. **75**, 4583 (1995).
- 50** M. Weidemüller, A. Görlitz, Th. W. Hänsch, and A. Hemmerich, Phys. Rev. A **58**, 4647 (1998).
- 51** S. Slama et al., Phys. Rev. Lett. **94**, 193901 (2005).
- 52** S. Slama, C. von Cube, M. Kohler, C. Zimmermann, and Ph. W. Courteille, Phys. Rev. A **73**, 023424 (2006).

- 53** S. Slama et al., *Phys. Rev. A* **72**, 031402(R) (2005).
- 54** S. M. Wiggins et al., *Meas. Sci. Technol.* **13**, 263 (2002).
- 55** N. Piovella, M. Gatelli, and R. Bonifacio, *Opt. Commun.* **194**, 167 (2001).
- 56** N. Piovella, R. Bonifacio, B. W. J. McNeil, and G. R. M. Robb, *Opt. Commun.* **187**, 165 (1997).
- 57** M. G. Moore and P. Meystre, *Phys. Rev. A* **59**, 1754 (1999).
- 58** N. Piovella, M. Cola, and R. Bonifacio, *Phys. Rev. A* **67**, 013817 (2003).
- 59** V. Vuletic and S. Chu, *Phys. Rev. Lett.* **84**, 3787 (2000).



**8****Detecting Neutral Atoms on an Atom Chip**

*Marco Wilzbach, Albrecht Haase, Michael Schwarz, Dennis Heine, Kai Wicker, Xiyuan Liu, Karl-Heinz Brenner, Sönke Groth, Thomas Fernholz, Björn Hessmo, and Jörg Schmiedmayer*

**8.1****Introduction**

Detecting single neutral atoms state selectively is one of the essential ingredients for developing atomic physics based quantum technologies, and a prerequisite of most quantum information experiments. The key question to be answered is how to perform such measurements using a robust and scalable technology. Ultra cold atoms can be trapped and manipulated using miniaturized atom chips [1]. So far, atom detection on atom chips is still based on unsophisticated methods. Fluorescence detection and absorption imaging yield detection sensitivities not higher than 10%. The detection is also restricted to ensembles of atoms.

On an atom chip micro fabricated wires and electrodes generate magnetic and electric fields that can be used to trap and manipulate neutral atoms [1,2]. The atoms are trapped a few micrometers above the chip surface with high precision and well defined positions. Many components for integrated matter wave technology have been demonstrated. Examples are atom guides [3], combined magnetic/electrostatic traps of various geometries [4], motors and shift registers [5], atomic beam splitters [6–9], and Bose-Einstein condensation (BEC) in micro traps [10–12].

Integration of the detection optics on the atom chip is a natural development for integrated matter wave manipulation. Using macroscopically sized detectors, state sensitive detection with near unity efficiency has been realized, see for instance [13] and references therein. Miniaturizing and integrating these highly sophisticated and efficient detectors is a difficult challenge.

The scope of this article is to explore how one can use the techniques of integrated miniaturized optics for atom detection as proposed in [14–18] and

how to adapt and implement real world devices to the atom chip and to on-chip atom detection.

## 8.2

### Detecting Single Atoms

Single charged particles can be detected through their direct electric interaction with their environment. Neutral atoms however interact rather weakly with the environment. The coupling of electromagnetic radiation to the atom is characterized by the scattering cross section  $\sigma_{\text{scat}}$

$$\sigma_{\text{scat}} = \frac{\sigma_{\text{abs}}}{1 + 4\Delta^2}, \quad (8.1)$$

where  $\sigma_{\text{abs}} = 3\lambda^2/2\pi$  is the resonant scattering cross section and  $\Delta$  the normalized detuning given by  $\Delta = \frac{\omega - \omega_0}{\Gamma}$ .  $\Gamma$  is the atomic linewidth. The real part of the refractive index results in a phase shift  $\phi$  on the light field. For far off-resonant light fields this becomes

$$\phi = \frac{n_{\text{at}}\sigma_{\text{abs}}}{4\Delta}, \quad (8.2)$$

where  $n_{\text{at}}$  is the atomic column density. Atoms can be detected by monitoring the scattered light in fluorescence, in absorption, or via the imprinted phase shift on the probing light. The efficiency of the detection depends on the coupling strength between the atom and the light, so it is of significant interest to optimize the atom-photon interaction. This requires a high degree of control over the optical fields as well as the dynamics of the atom.

In the following we will restrict ourselves to  $n_{\text{at}}\sigma_{\text{scat}} \ll 1$ . This is the case for detection of small atom numbers and for resonant scattering far below atomic saturation.

#### 8.2.1

##### Measuring the Scattered Light: Fluorescence Detection

One way of detecting an atom is to observe its fluorescence. The basic idea is to drive a transition of the atom to an excited state with an external light field and to detect the spontaneously emitted photons. In principle one scattered photon is sufficient to detect a single atom. The sensitivity of the detection and its fidelity depend on the detection efficiency of the scattered light and the suppression of background noise.

Modern photo detectors have a near unity efficiency, and atom detection is limited by the amount of light collected. Therefore high numerical aperture collection optics is desirable. In a realistic setting the collection efficiency  $\eta_{\text{coll}}$

is much less than unity and it is essential to let each atom scatter many photons. This is best achieved by driving closed transitions. Using a model of a two-level atom with a small number of excitations, the signal to noise ratio for single atom detection is given by:

$$\text{SNR}_{\text{fl}} = \eta_{\text{coll}} \sigma_{\text{abs}} \sqrt{\frac{I_{\text{in}} \tau}{A f_b + \eta_{\text{coll}} \sigma_{\text{abs}}}}, \quad (8.3)$$

where  $I_{\text{in}}$  is the incident photon flux density and  $\tau$  the measurement time. The number of collected fluorescence photons is to be assumed  $n_{\text{coll}} = \eta_{\text{coll}} \sigma_{\text{abs}} j_{\text{in}} \tau \gg 1$ .  $f_b$  is the fraction of incoming light which is scattered by anything else in the beam and collected by the fluorescence detector.  $A$  is the size of the detection region imaged on the detector, with a total background of  $A f_b$ .

In principle, there is no fundamental limit to the efficiency of a fluorescence detector as long as the atom is not lost from the observation region<sup>1</sup>. For trapped ions it is possible to reach very high detection fidelities. See for example [19]. Detection of cold single neutral atoms has been demonstrated in many experiments. For instance, up to 20 atoms trapped in a magneto-optical trap could be counted with a bandwidth of 100 Hz [20]. In Sect. 8.4.1 we discuss the prospects for atom chip based fluorescence detectors.

The disadvantage of fluorescence detection is the destructive nature of the process. The internal state of the detected atom will be altered, and heating of atoms due to spontaneous emission is almost unavoidable.

## 8.2.2

### Measuring the Driving Field

While fluorescence detection uses the spontaneously emitted light, the presence of an atom will also influence the driving field. This is described by the susceptibility of the atom. The imaginary part of the susceptibility describes the absorption, and the real part the phase shift on the driving field. By measurements on the driving field a complete atomic signature can be collected.

#### 8.2.2.1 Absorption on Resonance

The atomic density can be measured by monitoring the attenuation of the driving field. In the unsaturated case, this situation is described by Lambert-

1) As an example: Using a NA 0.5 (F:1) optics  $\eta_{\text{coll}} = 6.25\%$  and driving the D2 line of Rb ( $\sigma_{\text{abs}}^{Rb} = 0.29 \mu\text{m}^2$ ) with about 1/10 saturation intensity ( $\sim 10^7 \text{ photons s}^{-1} \mu\text{m}^{-2}$ ) one collects about 20 fluorescence photons in 100  $\mu\text{s}$ . Imaging a  $10 \mu\text{m}^2$  detection region onto a photo detector one needs a suppression factor  $f_b$  of  $\sim 10^{-3}$  for single atom detection with a  $\text{SNR}_{\text{fl}} \sim 3$ .

Beers law. The transmitted light intensity is given by:

$$\frac{I_{\text{trans}}}{I_{\text{in}}} = \exp(-n_{\text{at}}\sigma_{\text{abs}}) \sim 1 - n_{\text{at}}\sigma_{\text{abs}}. \quad (8.4)$$

The absorption signal of Eq. (8.4) provides a direct measure of the atomic column density<sup>2</sup>. If the mean intensity of the incoming beam is known, the main uncertainty is determined by measuring the transmitted light. The signal-to-noise ratio for an absorption measurement is

$$\text{SNR}_{\text{abs}} = \sqrt{j_{\text{in}}\tau} \frac{1 - \exp(-n_{\text{at}}\sigma_{\text{abs}})}{\sqrt{\exp(-n_{\text{at}}\sigma_{\text{abs}})}} \approx \sqrt{j_{\text{in}}\tau} n_{\text{at}}\sigma_{\text{abs}} \sim \sqrt{N_{\text{abs}} n_{\text{at}}\sigma_{\text{abs}}}, \quad (8.5)$$

where  $N_{\text{abs}} = j_{\text{in}}\tau n_{\text{at}}\sigma_{\text{abs}}$ . The minimum number  $n_{\text{min}}$  of atoms that can be detected with a  $\text{SNR}_{\text{abs}} = 1$  is then given by:

$$n_{\text{min}} = \frac{A}{\sigma_{\text{abs}}} \frac{1}{\sqrt{j_{\text{in}}\tau}} = \frac{1}{\sigma_{\text{abs}}} \sqrt{\frac{A}{I_{\text{in}}\tau}}, \quad (8.6)$$

where we introduced  $j_{\text{in}}$  as the incoming photon flux ( $j_{\text{in}} = A I_{\text{in}}$ ). Driving the D2 of Rubidium with an incoming intensity of  $10^7$  photons  $\text{s}^{-1} \mu\text{m}^{-2}$  (about 1/10 saturation intensity for Rb atoms) and a waist of  $2.5 \mu\text{m}$  ( $A = \frac{\pi}{4} w_0^2 \sim 5 \mu\text{m}^2$ ) one finds  $n_{\text{min}} \sim 2.5 \tau^{-1/2}$  where  $\tau$  is given in  $\mu\text{s}$ .

Equation (8.5) assumes that the mean incident photon flux is known to high precision. In absorption imaging it is common practice to relate the absorption of the atoms to a reference image by dividing the two images. Then the noise of the reference image has to be fully considered. For small absorption, the signal-to-noise ratio of Eq. (8.5) is reduced by a factor  $1/\sqrt{2}$ . This increases the necessary minimum number of detectable atoms by a factor  $\sqrt{2}$ .

To reach unity detection efficiency in absorption imaging it seems natural to reduce the beam waist as much as possible as indicated by Eq. (8.6). This is however not a successful strategy as pointed out by van Enk [21–23]. A strongly focused beam is not optimally overlapped with the radiation pattern of the atoms. The absorption cross section for such a strongly focused beam becomes smaller with a decreased spot size.

Another strategy to improve the sensitivity is to increase the measurement time. The scattered photons will however heat up the atoms and expel them from the observation window. If the atom is held by a dipole trap, the measurement time can be increased significantly (see Sect. 8.4.1). There is no fundamental limit to the detection of a single atoms via its absorption, if it can be kept localized long enough.

- 2) For resonant excitation on the D2 line of Rb a column density of one atom per  $\mu\text{m}^2$  leads to about 30% absorption.

### 8.2.2.2 Refraction

For large detunings ( $\Delta \gg 1$ ) the absorption decreases as  $\propto \Delta^{-2}$  as can be seen from Eq. (8.1). In addition the transmitted beam acquires a phase shift  $\phi_{\text{atom}}$ . This is caused by the refractive index of the atoms. The phase shift decreases only with  $\phi_{\text{atom}} \propto \Delta^{-1}$  as shown by Eq. (8.2). The phase-shift has been used to image clouds of cold atoms and include Mach-Zehnder type interferometers [24], for phase-contrast imaging [25], or in line holography by defocussed imaging [26].

The minimal detectable phase shift  $\Delta\phi$  in an interferometer is given by the number / phase uncertainty relation  $\Delta\phi\Delta N = 1$  resulting in  $\Delta\phi_{\text{min}} = 1/\sqrt{j_{\text{in}}\tau}$  (neglecting absorption). From these scaling laws for the scattered light and the phase shift one finds for the signal-to-noise ratio for dispersive atom detection:

$$\text{SNR}_{\text{disp}} = \frac{\phi}{\Delta\phi} \sim \sqrt{N_{\text{scat}} n_{\text{at}} \sigma_{\text{abs}}} \quad (8.7)$$

with  $N_{\text{scat}} = j_{\text{in}}\tau n_{\text{at}} \sigma_{\text{scat}}$ .  $\text{SNR}_{\text{disp}}$  depends only on the total number of scattered photons  $N_{\text{scat}}$ . In fact it is the same as for on resonant detection, and the optimal achievable SNR for classical light as shown by Hope et al. [27–29]. Going off resonance does not help in obtaining a better measurement compared to plain absorption.

The off-resonant detection of atoms however has significant advantages in combination with cavities to enhance the interaction between photons and the atom [27]. Non-destructive and shot noise limited detection becomes possible.

### 8.2.3

#### Cavities

Cavities enhance the interaction between the light and atoms. The photons are given multiple chances to interact with an atom located in the cavity. The number of interactions is enhanced by increasing the number of round trips. The latter is determined by the cavity finesse  $n_{\text{rt}} = \mathcal{F}/2\pi$ . This can be used to improve the signal-to-noise ratios. Even with moderate finesse cavities single atom detection can be achieved.

##### 8.2.3.1 Absorption on Resonance

The probability for absorption during each round trip is determined by the ratio between the atomic absorption cross section  $\sigma_{\text{abs}} = 3\lambda^2/2\pi$  and the beam cross section inside the cavity  $A = \frac{\pi}{4}w_0^2$ . A natural figure of merit for cavity assisted absorption is therefore

$$C_1 = \frac{\mathcal{F}}{2\pi} \frac{\sigma_{\text{abs}}}{A} = \frac{3\lambda^2}{\pi^3} \frac{\mathcal{F}}{w_0^2}. \quad (8.8)$$

This quantity is identical to the cooperativity parameter  $C_1 = g_0^2/2\kappa\Gamma$  [30], which relates the single photon Rabi frequency of the atom-photon system  $g_0$  to the incoherent decay rates of the cavity field  $\kappa$  and atomic excitation  $\Gamma$ . Interestingly, a reduced cavity mode waist can compensate for a small cavity finesse [14].

When the cooperativity parameter is smaller than unity and the atomic saturation is low, the signal-to-noise ratio for shot-noise limited single atom detection becomes

$$\text{SNR} = \sqrt{j_{\text{in}}\tau} \frac{\kappa_T}{\kappa} C_1 = \frac{3\lambda^2}{\pi^3} \sqrt{j_{\text{in}}\tau} \frac{\kappa_T}{\kappa} \frac{\mathcal{F}}{w_0^2} \sim \sqrt{\frac{\kappa_T}{\kappa} N_{\text{abs}} C_1}, \quad (8.9)$$

where  $N_{\text{abs}} = j_{\text{in}}\tau \frac{\sigma_{\text{abs}}}{A} \frac{\kappa_T}{\kappa} n_{\text{rt}}$ ,  $\kappa_T$  is the mirror transmission rate, and  $\kappa$  the total cavity decay rate [14]. For a fixed measurement time an increased signal-to-noise ratio can be obtained by increasing the cooperativity parameter. This can be done by increasing the cavity finesse, or by decreasing the beam waist.

### 8.2.3.2 Refraction

Similarly, the phase shift induced by the atom in the cavity increases with the each round trip. Accordingly the signal to noise ratio Eq. (8.7) is then increased to

$$\text{SNR} = \sqrt{j_{\text{in}}\tau} \frac{\kappa_T}{\kappa} \frac{C_1}{\Delta} \sim \sqrt{\frac{\kappa_T}{\kappa} N_{\text{scat}} C_1} \sim \sqrt{\frac{\kappa_T}{\kappa} N_{\text{abs}} C_1 / \Delta}, \quad (8.10)$$

where  $N_{\text{scat}} = j_{\text{in}}\tau \frac{\sigma_{\text{scat}}}{A} \frac{\kappa_T}{\kappa} n_{\text{rt}}$ . When the cooperativity parameter is larger than unity, non-destructive detection with low photon scattering becomes possible [27].

### 8.2.3.3 Many Atoms in a Cavity

The above considerations concern the coupling of a single atom to a cavity. This can be extended to the many-atom case by introducing a many-atom cooperativity parameter  $C = N_{\text{eff}} C_1$ , where  $N_{\text{eff}}$  is an effective number of atoms in the cavity mode, which takes into account the spatial dependence of the coupling constant  $g(\vec{r}) = g_0 \psi(\vec{r})$ , given by the cavity mode function  $\psi(\vec{r})$ , and the atomic density distribution  $\rho(\vec{r})$ . The fraction  $N_{\text{eff}}$  of the total atom number  $N$ , which are maximally coupled to the cavity mode, is given by the overlap integral of both functions

$$N_{\text{eff}} = N \int d^3r \rho(\vec{r}) |\psi(\vec{r})|^2. \quad (8.11)$$

The absorptive and dispersive effects of the atoms on the cavity amplitude [14] scale linearly with this effective atom number as long as the atomic saturation is low.

### 8.2.4

#### Concentric Cavity

As seen above, a small mode diameter  $w_0$  is advantageous. Such a small  $w_0$  can be obtained by using a near-concentric cavity. Consider the case when the cavity is formed by two identical mirrors with radius of curvature  $R$  separated by a distance  $L$ . The beam waist  $w_0$  in the cavity center is given by

$$w_0^2 = \frac{\lambda}{2\pi} \sqrt{L(2R - L)}. \quad (8.12)$$

The concentric geometry occurs when the mirror separation  $L$  approaches the value  $2R$ . The waist size  $w_0$  becomes small but the beam size on the cavity mirrors

$$w^2 = \frac{R\lambda}{\pi} \sqrt{\frac{L}{2R - L}}, \quad (8.13)$$

becomes large as one approaches the concentric limit. A large mirror spot size requires very uniform mirrors, as deviations from a spherical mirror shape will lower the optical finesse drastically. Furthermore, as the concentric point is approached, the cavity also becomes extremely sensitive to misalignments and vibrations. For more details on cavities see Siegman [31].

### 8.2.5

#### Miniaturization

The principle advantage of miniaturizing the cavities is that for a fixed geometry, i.e. for a constant ratio of  $R$  and  $L$ , the mode diameter scales with size (see Eqs. (8.12) and (8.13)). This automatically increases the cooperativity parameter. In fact  $C_1$  scales like  $C_1 \propto w_0^{-2}$  and high values for  $C_1$  can be reached even for moderate finesse as illustrated in Table 8.1. Miniaturization allows to build cavities with a very small mode volume  $V_m = \int d^3\vec{r}|\psi(\vec{r})|^2$ . A small cavity volume has the advantage that photons will interact more strongly with atoms localized inside the cavity as the light intensity per photon increases. The interaction between the photon and the atom is described by the atom-photon coupling constant (single photon Rabi frequency)  $g_0 = \sqrt{3\Gamma c\lambda^2/(4\pi V_m)}$ . It determines how much the dressed atomic energy levels inside the cavity are shifted by the presence of a single photon. As  $g_0$  is increased, single atom – single photon coupling becomes feasible if  $g_0 \gg (\kappa, \Gamma)$  can be satisfied.

Since for a fixed finesse, the cavity line width  $\kappa$  becomes larger with decreasing length  $L$  ( $\kappa \propto L^{-1}$ ) the fulfillment of the above condition for strong coupling and CQED does not improve as dramatically as the cooperativity parameter  $C_1 \sim w_0^{-2}$ . One has  $g_0/\Gamma \sim 1/w_0\sqrt{L}$  and  $g_0/\kappa \sim \sqrt{L}/w_0$  so the length must be chosen precisely to achieve strong coupling (see Table 1). It is however always an advantage to choose  $w_0$  small.

**Tab. 8.1** Properties of various cavities as a function of mode geometry and finesse. The cooperativity parameter  $C_1$  stays high if the mode waist is kept small even at moderate cavity finesse. For small mode volumes the single photon Rabi frequency can become very high.

$L$	$w_0$	$\mathcal{F}$	$g_0$	$g_0/\Gamma$	$g_0/\kappa$	$C_1$
[ $\mu\text{m}$ ]	[ $\mu\text{m}$ ]		$2\pi \times [\text{MHz}]$			
200	30	20000	12	4.0	0.65	1.3
50	7.5	5000	97	32	0.32	5.2
20	5	5000	230	77	0.31	11.8
10	2.5	5000	650	217	0.43	47
10	2.5	1250	650	217	0.11	11.8
10	2.5	250	650	217	0.02	2.3
$10^4$	2.5	250	21	6.9	0.68	2.3
$10^5$	2.5	250	6.5	2.2	2.2	2.3
$10^5$	2.5	50	6.5	2.2	0.43	0.47

For detection of atoms the increased cooperativity parameter is the main benefit from miniaturization. Miniaturized cavities with moderate finesse can detect single atoms. Therefore miniaturization is much more beneficial for atom detection than for cavity QED experiments.

### 8.3

#### Properties of Fiber Cavities

The advantage of fibers is that they can be easily handled using well established techniques. For instance, transfer mirror coatings can be directly glued to the fibers. Different fibers can be melted together using commercially available fusion splicers. The fabrication of fiber optical components does usually not require expensive and time consuming lithographic techniques. Fibers also have the advantage that they have very low optical loss, usually less than 3 dB/km.

For miniaturization of optical components for atomic physics several proposals on atom chip integration have been presented [14, 16, 17, 32–34]. In our approach optical fibers are attached to the chip to form fiber-based cavities and to make small dipole traps. For fiber cavity experiments it is interesting to put atoms into the optical resonator. To place the atom inside the cavity it is possible to cut the fiber into two pieces and place the atom in the fiber gap. It is also possible to use a hollow fiber and guide the atom inside it [36]. Because it is quite difficult to load atoms into a hollow fiber, especially if it is mounted on a micro-structured surface, the following section deals with fiber-gap-fiber configurations as the ones outlined in Fig. 8.1.

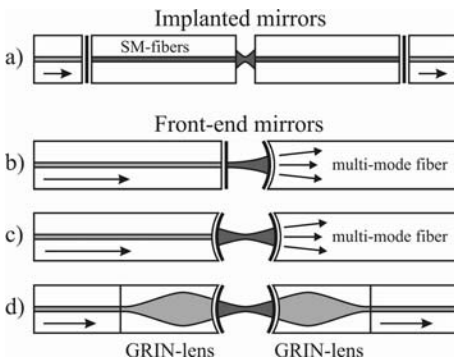


**Fig. 8.1** a) A cavity with implanted mirrors. This cavity requires little alignment of the gap, but the mode volume is large. This configuration can be realized using only single mode fibers. b) A plano-concave cavity. Incoupling from a single mode fiber is efficient, but the mode diameter becomes large at the location of the atom. Outcoupling to a single

mode fiber is not optimal, but a multi-mode fiber can collect the transmitted light well. c) A concave-concave cavity. The mode diameter can be controlled, but coupling to single mode fibers is not optimal. d) Focussing optics can be integrated to optimize the fiber-cavity coupling efficiency. Cavities b)–d) require active alignment of the gap.

One realization of a fiber cavity is to implant mirrors into the fibers, such as Bragg gratings or dielectric coatings inserted between fiber pieces. See Fig. 8.1a). This has the advantage that the interaction volume (the gap where the atoms pass) is defined only by the bare fiber tips. Thus only the fiber itself has to be mounted on the atom chip with little or no need for alignment actuators. Mirrors and tuning actuators can be placed far from the gap. This allows a higher integration of the optics. A disadvantage of this method is that the cavity becomes quite long and that the extra interfaces increase the optical loss of the cavity. Using a long cavity will increase the mode volume and therefore also reduce  $g_0$ . For atom detection the length of the cavity is fortunately not a very important parameter, as indicated by Eq. (8.9).

### 8.3.1

#### Loss Mechanisms for a Cavity

The quality of an optical resonator is described by its finesse. The finesse is related to the losses by:

$$\mathcal{F} = \frac{\pi}{\sum_i \alpha_i}, \quad (8.14)$$

where  $\alpha_i$  are the loss probabilities for the different loss channels. For example, a cavity mirror transmittance of  $T = 0.01$  corresponds to  $\alpha = 0.01$ . As long as  $\sum_i \alpha_i \ll 1$  the cavity finesse is accurately calculated by Eq. (8.14). For further details on resonators we again refer to [31]. For atom detection it is desirable to obtain a high signal-to-noise ratio. This does not automatically mean that

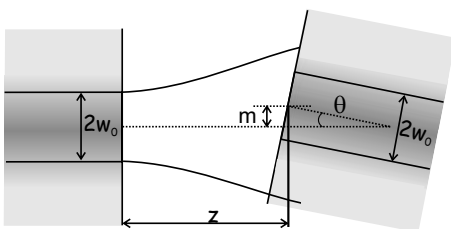


**Fig. 8.2** The fiber light mode diverges, after leaving the fiber on the left with a mode field diameter of  $2w_0$ . The second fiber on the right has a longitudinal displacement of  $z$ , a transversal displacement of  $m$  and an angular misalignment of  $\theta$ .

the finesse should be maximized. The signal-to-noise ratio for atom detection in the weak coupling and low atomic saturation is given by Eq. (8.9), where  $\kappa_T \propto \alpha_T$  describes the mirror transmittance and  $\alpha_{\text{tot}} = \alpha_T + \alpha_{\text{other}}$  is the total cavity loss. This implies that  $\text{SNR} \propto \alpha_T / (\alpha_T + \alpha_{\text{other}})^2$  which is maximized for  $\alpha_T = \alpha_{\text{other}}$ . For each kind of cavity there is an optimal choice for the mirror transmittance.

When the cavity contains a gap (see Fig. 8.1a) the main loss mechanism is related to the reduced coupling efficiency across the gap. This loss depends mainly on three things. (1) It is clear that the mode matching of the two fibers is not optimal and losses will occur as the gap is traversed. This loss increases with the gap size. (2) Also, in the case of transverse misalignment of the two fibers modes are not well-matched at the fiber facets. (3) A tilt between the two fibers also increases the mismatch between the two modes. In this case the loss also increases with the length of the fiber gap.

Fig. 8.2 sketches these misalignments of the gap. The power coupling efficiency  $\eta$  for two fibers can be calculated in the paraxial approximation by the overlap integral of the involved transverse mode functions.

$$\eta = \frac{|\iint_{\mathbf{A}} \Psi_1(\vec{r}) \Psi_2^*(\vec{r}) dA|^2}{\iint_{\mathbf{A}} \Psi_1(\vec{r}) \Psi_1^*(\vec{r}) dA \iint_{\mathbf{A}} \Psi_2(\vec{r}) \Psi_2^*(\vec{r}) dA}, \quad (8.15)$$

where  $\Psi_1(\vec{r})$ ,  $\Psi_2(\vec{r})$  are the fiber optical field modes, and  $\mathbf{A}$  is the plane coinciding with one of the fiber facets. In this text we use this measure to describe cavity losses.

### 8.3.2

#### Losses due to the Gap Length

It is obvious that the losses increase with expanding gap size  $z$ . The light exiting the first fiber at  $z = 0$  diverges until it hits the opposite fiber at a

distance  $z$ . We can describe the light leaving the first fiber as

$$\Psi_1(x, y, z) = \sqrt{\frac{2}{\pi}} \frac{1}{w(z)} \exp\left(-\frac{ik(x^2 + y^2)}{2R(z)}\right) \exp\left(-\frac{x^2 + y^2}{w(z)^2}\right) \times \exp(ikz - i\Phi(z)), \quad (8.16)$$

where  $w_0$  is the Gaussian waist at the first fiber facet,  $R(z) = z + z_0^2/z$  the radius of curvature,  $w(z) = w_0\sqrt{1 + z^2/z_0^2}$  the beam radius,  $z_0 = \pi w_0^2/\lambda$  the Rayleigh length, and  $\Phi(z) = \arctan(z/z_0)$  the Gouy-phase. The wavelength is  $\lambda = \lambda_0/n$  and the wavenumber  $k = k_0 n$  in the medium between the fibers with refractive index  $n$ . The wavelength and the wavenumber in vacuum are  $\lambda_0$  and  $k_0$ , respectively. Assuming that the two fibers are identical, the mode function at the facet of the second fiber is

$$\Psi_2 = \Psi_1(x, y, z = 0) = \sqrt{\frac{2}{\pi}} \frac{1}{w_0} \exp\left(-\frac{x^2 + y^2}{w_0^2}\right). \quad (8.17)$$

The loss  $\alpha_{\text{gap}}$  due to the length of the gap can be calculated from the overlap between functions (8.16) and (8.17).

$$\begin{aligned} \alpha_{\text{gap}}(z) &= 1 - \left| \int_{-\infty}^{\infty} \int_{-\infty}^{\infty} \Psi_1(x, y, z) \Psi_2^*(x, y, 0) dx dy \right|^2 \\ &= \frac{z^2}{4z_0^2 + z^2} \approx \left( \frac{z}{2z_0} \right)^2 = \left( \frac{\lambda^2}{4\pi^2 w_0^4} \right) z^2. \end{aligned} \quad (8.18)$$

Here the transverse and angular misalignments are assumed to be zero. A plot of a finesse measurement with varying gap size  $z$  is shown in Fig. 8.9a. In this case mirrors with a loss of 1% are assumed to be located inside the fibers. This loss is decreased if the gap between the fibers is small and the fiber has a small numerical aperture i.e. a large  $w_0$ . However, to detect atoms  $w_0$  should be small, as indicated by Eq. (8.9).

### 8.3.3

#### Losses due to Transversal Misalignment

If the two fibers are transversally misaligned to each other there will also be a mode mismatch when the light is coupled between the fibers. This loss can easily be calculated from Eq. (8.15). Using normalized Gaussian mode functions for two identical fibers (with  $z = 0$ ) with waist  $w_0$  choosing the gap and angular misalignment to be zero one has

$$\Psi_1(x, y, 0) = \sqrt{\frac{2}{\pi}} \frac{1}{w_0} \exp\left(-\frac{x^2 + y^2}{w_0^2}\right), \quad (8.19)$$

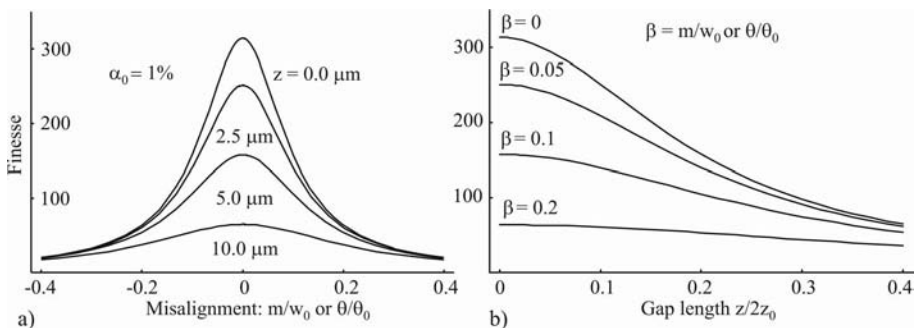


**Fig. 8.3** Theoretical calculations were conducted for an implanted mirror cavity. The fiber mode diameter was  $w_0 = 2.5 \mu\text{m}$  at a wavelength of 780 nm. All losses except the gap losses were set to 1%. Plot a) shows the finesse as a function of  $\theta$  and  $m$ , which were normalized to  $\theta_0$  and  $w_0$ , respectively.  $\theta_0$  is given by  $\lambda/(\pi w_0) = w_0/z_0$ . The different

curves correspond to different gap lengths starting with the highest finesse at  $z = 0 \mu\text{m}$  and ending with the lowest at  $z = 10 \mu\text{m}$ . In b) the finesse is plotted as a function of  $z/2z_0$ . The different curves correspond to different  $\beta$ , where  $\beta$  is either  $\theta/\theta_0$  or  $m/w_0$ .  $\beta$  ranges from 0 to 0.2.

$$\Psi_2(x, y, 0) = \Psi_1(x - m, y, 0) = \sqrt{\frac{2}{\pi}} \frac{1}{w_0} \exp\left(-\frac{(x - m)^2 + y^2}{w_0^2}\right), \quad (8.20)$$

where  $m$  is the transverse misalignment of one of the fibers. This gives a loss due to the transversal misalignment  $\alpha_{\text{tra}}$ :

$$\begin{aligned} \alpha_{\text{tra}}(m) &= 1 - \left| \int_{-\infty}^{\infty} \int_{-\infty}^{\infty} \Psi_1(x, y, 0) \Psi_2^*(x, y, 0) dx dy \right|^2 \\ &= 1 - \exp\left(-\frac{m^2}{w_0^2}\right) \approx \frac{m^2}{w_0^2}, \end{aligned} \quad (8.21)$$

where the last approximation is valid only for  $m \ll w_0$ . A plot of a finesse measurement with varying transversal misalignment is shown in Fig. 8.9b.

### 8.3.4

#### Losses due to Angular Misalignment

Another kind of loss emerges from angular misalignment of the two optical axes of the fibers. This is calculated by performing a basis change of Eq. (8.16) and evaluating the overlap given by Eq. (8.15). The mode leaving the first fiber (see Fig. 8.2) is approximately described by

$$\Psi_1(x, y, z) \approx \sqrt{\frac{2}{\pi}} \frac{1}{w_0} \exp\left(-\frac{x^2 + y^2}{w_0^2}\right) \exp(ikz), \quad (8.22)$$

for small  $z \ll z_0$  neglecting diffraction effects. For a small rotation  $\theta$  around the y-axis is given by

$$\begin{pmatrix} x \\ y \\ z \end{pmatrix} = \begin{pmatrix} \cos \theta & 0 & \sin \theta \\ 0 & 1 & 0 \\ -\sin \theta & 0 & \cos \theta \end{pmatrix} \begin{pmatrix} x' \\ y' \\ z' \end{pmatrix} \approx \begin{pmatrix} 1 & 0 & \theta \\ 0 & 1 & 0 \\ -\theta & 0 & 1 \end{pmatrix} \begin{pmatrix} x' \\ y' \\ z' \end{pmatrix}. \quad (8.23)$$

Transforming  $\Psi_1(x, y, z)$  into the coordinate system  $(x', y', z')$  the mode function for the incident beam at the input plane  $z' = 0$  of the second fiber becomes

$$\Psi_1(x', y', z' = 0) \approx \sqrt{\frac{2}{\pi}} \frac{1}{w_0} \exp\left(-\frac{x'^2 + y'^2}{w_0^2}\right) \exp(ikx'\theta). \quad (8.24)$$

The mode function for the second fiber at the input plane  $z' = 0$  is given by

$$\Psi_2(x', y', z' = 0) = \sqrt{\frac{2}{\pi}} \frac{1}{w_0} \exp\left(-\frac{x'^2 + y'^2}{w_0^2}\right). \quad (8.25)$$

The loss  $\alpha_{\text{ang}}$  due to a pure angle misalignment can be calculated from the overlap between functions (8.24) and (8.25).

$$\begin{aligned} \alpha_{\text{ang}}(\theta) &= 1 - \left| \int_{-\infty}^{\infty} \int_{-\infty}^{\infty} \Psi_1(x', y', 0) \Psi_2^*(x', y', 0) dx' dy' \right|^2 \\ &= 1 - \exp\left(-\frac{\pi^2 w_0^2}{\lambda^2} \theta^2\right) \approx \left(\frac{\theta}{\theta_0}\right)^2, \end{aligned} \quad (8.26)$$

with  $\theta_0 = \lambda/(\pi w_0) = w_0/z_0$ . In general these misalignments are not independent of each other. The combined formula for all the misalignment losses is given by [37]:

$$\begin{aligned} \alpha(\theta, m, z) &= 1 - \eta \approx 1 \\ &- \mu(z) \exp\left[-\mu(z) \left(\frac{m^2}{w_0^2} + \frac{\pi^2 \theta^2 w_0^2}{\lambda^2} + \frac{\theta^2 z^2}{2w_0^2} - \frac{m\theta z}{w_0^2}\right)\right], \end{aligned} \quad (8.27)$$

with  $\mu(z) = 4z_0^2/(4z_0^2 + z^2)$ . A setup with transversal and longitudinal displacement and angle misalignment is plotted in Fig. 8.9. One experimental advantage is that the loss rate depends quadratically on small misalignments.

### 8.3.5

#### Fresnel Reflections

Another effect that has to be taken into account is the reflection of light at the interfaces between the fibers and the introduced gap. It results from the step

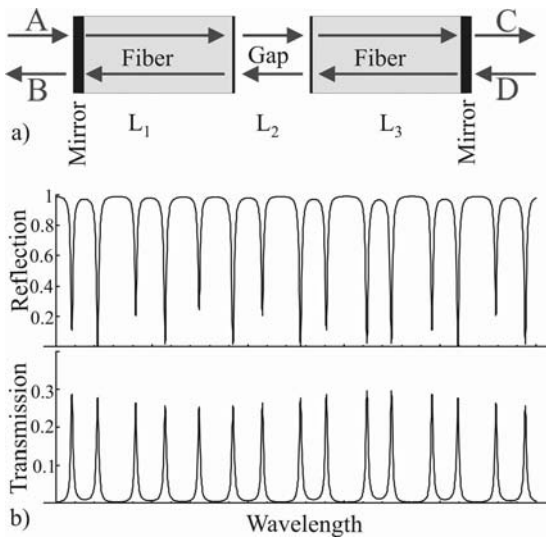


**Fig. 8.4** a) Schematic description of the cavity formed by the three coupled resonators. b) Reflectance and transmittance of a cavity formed by three coupled resonators. The system is constituted by

Mirror-Fiber-Gap-Fiber-Mirror and has  $\alpha = 0.05$ . In addition  $L_1 \neq L_3$  and  $L_2 = \lambda/4$  plus an integer multiple of  $\lambda/2$ . The period of the envelope is given by the length difference of the two fiber pieces.

in the refractive index and is called Fresnel reflection. For a typical fiber ( $n_1 = 1.5$ ) in air or vacuum ( $n_2 = 1$ ) a fraction of  $R_F = (n_2 - n_1)^2 / (n_2 + n_1)^2 = 4\%$  of the incident light is reflected from a polished flat connector. In the case of a fiber gap cavity, these additional reflections lead to a system of three coupled resonators. While for any system of coupled resonators stationary solutions exist, i.e. eigenmodes of the electromagnetic field, they will in general not be equidistantly distributed in the frequency domain.

In a simple one-dimensional model, the coupled cavity system can be treated as a chain of transfer matrices [31]. Fig. 8.4 shows the calculated reflected and transmitted intensities for a model resonator of rather low finesse.

The light intensity inside the gap depends on the specifics of the mode. This changes the overall losses, as can be seen in Fig. 8.4b. Consequently the reflected and transmitted intensities vary from mode to mode. The effect is strongest when the gap length is a multiple of  $\lambda/2$ . In experiments coupling atoms to the light field it has to be considered that the intensity inside the gap depends on the order of the mode and on the exact length of the gap. In absorption experiments only the relative change of transmitted light intensity is measured, which remains mode independent for light intensities well below saturation. Never the less it leads to a mode dependent signal-to noise ratio.

Using fibers with  $n = 1.5$  and intensities below atomic saturation the SNR changes by roughly 15%.

## 8.4

### Other Fiber Optical Components for the Atom Chip

Not only cavities can be mounted on the surface of an atom chip. Miniaturization offers various advantages for a couple of other optical components. Lenses with extremely short focal lengths can be used to focus light to small areas. Such devices can be used to generate very tight dipole traps [38–40], or to collect light from very well-defined volumes [18,35].

#### 8.4.1

##### Fluorescence and Absorption Detectors

A fluorescence detector can be built using a single mode tapered lensed fiber and a multi-mode fiber. In this case, the tapered fiber is used to optically pump the atom. The multi mode fiber is used to collect the fluorescent light. For this configuration one can put the multi mode fiber at any angle with respect to the tapered lensed fiber. At small angles, atoms located in the focus of the tapered lensed fiber will scatter light *away* from the multi mode fiber. This would constitute an absorption detector. Such a device is illustrated in Fig. 7c). If the angle between the two fibers is sufficiently large only the fluorescent emission from the atom will be *collected* by the multi mode fiber. A picture of a 90° fluorescence detector setup is shown in Fig. 8.7b). If no atom is present in the beam focus, very little light is scattered into the fiber. As soon as an atom is present, this signal increases. For single atom detection these two techniques are not sensitive enough, because photon recoils will expel the atom from the detection region and the multi mode fiber only collects a few photons. Therefore one must also trap the atom(s) in the tapered lensed fiber focus. This can be accomplished by a dipole trap.

#### 8.4.2

##### A Single Mode Tapered Lensed Fiber Dipole Trap

To increase the number of detectable photons, the atom can be trapped inside the area where it interacts with the light. One possibility is to hold the atom in place with a dipole trap. An atom with transition frequency  $\omega_0$  is attracted to the intensity maximum of a red-detuned laser beam ( $\omega < \omega_0$ ). A focussed laser beam forms an atom trap in the beam focus. For a far-detuned dipole trap quantities such as trap depth, lifetime and number of scattered photons can be estimated easily. A detailed derivation of dipole trap parameters discussed in

the following paragraph can be found in [41]. The potential depth of a dipole trap is

$$U_{\text{dip}}(\vec{r}) = \frac{\pi c^2 \Gamma}{2\omega_0^3} \left( \frac{2}{\Delta_{D2}} + \frac{1}{\Delta_{D1}} \right) I(\vec{r}), \quad (8.28)$$

and the scattering rate is given by

$$\Gamma_{\text{sc}}(\vec{r}) = \frac{\pi c^2 \Gamma^2}{2\hbar\omega_0^3} \left( \frac{2}{\Delta_{D2}^2} + \frac{1}{\Delta_{D1}^2} \right) I(\vec{r}), \quad (8.29)$$

where  $\Delta_{D2}$  and  $\Delta_{D1}$  are the detunings of the laser with respect to the D2 and D1 lines of the alkali atom. The formulas apply to alkali atoms with a laser detuning much larger than the hyperfine structure splitting and a scattering rate far from saturation. It follows that the scattering rate for a given potential can be decreased by choosing a larger detuning and a higher laser intensity. The potential depth scales as  $\sim \Gamma/\Delta$ , whereas the scattering rate scales as  $\sim \Gamma^2/\Delta^2$ .

The D2 line of Rubidium,  $^2S_{1/2} \rightarrow ^2P_{3/2}$ , has a wavelength of 780 nm, and the D1 line  $^2S_{1/2} \rightarrow ^2P_{1/2}$  has a wavelength of 795 nm. A standard tapered lensed fiber generates a typical waist of  $w_0 = 2.5 \mu\text{m}$  at a wavelength of 780 nm. Far off resonance dipole traps can be realized with easy to use, high power diode lasers at a wavelength of 808 nm. Standard single mode lasers diodes are available with a power up to 150 mW. Assuming a coupling efficiency into the fiber of around 20%, one gets 30 mW of laser power in the dipole trap. These parameters yield a trap depth of 3.9 mK, and a transverse (longitudinal) trap frequency of 80 kHz (6 kHz). The heating rate for the dipole light is almost negligible. Experiments have shown that the lifetime is mainly limited by the background pressure of the vacuum chamber [42].

Using resonant light to detect an atom increases the number of scattered photons as well as the heating rate enormously. In this case the trap lifetime drops to below a millisecond, which yields several thousands scattered photons before the atom is lost.

A multi mode fiber as detector at a distance of 40  $\mu\text{m}$  can collect 2% of the fluorescent emission (see Fig. 8.7b). Assuming a detector efficiency of 60% (APD-based photon counter), including additional losses in the rest of the optical detector setup, it should be possible to detect about 100 photons during the trap lifetime. The signal-to-noise ratio is difficult to calculate without knowing the background noise.

For an absorption detector, such as the one illustrated in Fig. 8.7c, it is possible to use Eq. (8.5) to calculate the expected signal-to-noise ratio. In this case one finds  $\text{SNR} = 4$  for  $\tau = 100 \mu\text{s}$  and  $I_{\text{in}} = 10^7 \text{ photons s}^{-1} \mu\text{m}^{-2}$ .

## 8.5

### Integration of Fibers on the Atom Chip

A method for mounting fibers accurately is needed to integrate the above devices with atom chips. Fibers can be held at the right place with the help of some kind of fiber grippers, aligned and finally glued to the chip. This strategy will not work well for fiber cavities because they need to be actively aligned during operation (see Fig. 8.1b–d). For active alignment of an on-chip cavity an actuator is needed. Useful actuators, such as piezoelectric stacks, are quite large compared to the fibers. Typical dimensions exceed  $2 \times 2 \times 2$  mm. This places restrictions on the level of optical integration one can obtain on the chip. Components that don't need active alignment, such as the cavities with implanted mirrors (see Fig. 8.1a) or tapered fibers for dipole traps, can be directly integrated on the chip. To obtain a high degree of precision in the mounting we have developed a lithographic method where a thick photoresist is patterned to form the mounting structures [34].

#### 8.5.1

##### Building Fiber Cavities

We have so far realized cavities with curved and planar mirrors at the front-end of two fibers, and cavities with implanted mirrors made out of one piece of fiber with a gap for the atoms similar to the ones shown in Fig. 8.1.

The mirror coatings are attached to the fibers using a *transfer technique*. In this process, dielectric mirror coatings with a transmittance of 0.1% to 1% are manufactured on a glass substrate. The substrate is either flat or contains an array of spherical microlenses for curved coatings. The adhesion between the coating and the glass substrate is fairly low. When the coating is glued to an optical fiber it is possible to transfer the coating from the substrate to the fiber [43]. A series of pictures showing this transfer is found in Fig. 8.5.

The transmittance  $T$  is chosen to be around 1% for cavities with implanted mirrors (Fig. 8.1a) because of the higher loss. For the front-end mirrors (Fig. 8.1b–d), the loss is lower therefore it is more suitable to choose a mirror with transmittance around 0.1% to obtain a high SNR for the detection of atoms.

The higher loss for cavities with implanted mirrors has several origins in addition to the ones caused by the gap. For some of our cavities the main intrinsic loss sources are the glue layers holding the mirror coatings to the fibers. These glue layers are typically a few micrometers thick. The transversal confinement of the fiber is absent in the glue layers as well as in the mirror coatings. This leads to losses similar to the ones discussed for the gap length, i.e. Eq. (8.18). Glued mirrors are also sensitive to angular misalignment, which can be treated by Eq. (8.26).

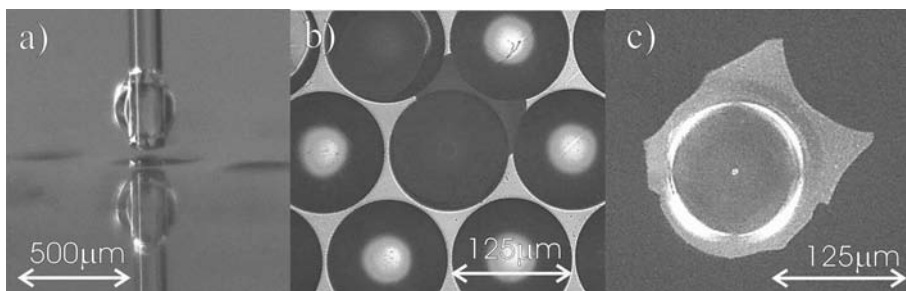


**Fig. 8.5** Picture a) shows a fiber with a drop of glue on the tip. The fiber is hovering 100 microns above a micro lens with dielectric mirror coating. The lower part is a mirror image of the real fiber. Once the fiber is glued to the coating it can be removed by gently pulling the fiber away from the substrate. In

picture b) one can see the micro lens array from above. A closer look reveals that coatings are missing from two of the lenses. One of these is attached to the fiber shown in c). Additionally in c) light was coupled in from the other side of the fiber, so one can see the fiber core in the center of the picture.

Curved coatings may be used to build a concave cavity with front-end mirrors. With this design we reached a finesse of greater than 1000 as shown in Fig. 8.6. Complications due to Fresnel reflections do not exist for the front-end cavity. The quality of the mirrors and their alignment determine how high the finesse may become. The mode profile of the optical fiber does usually not match the cavity mode. This leads to a poor incoupling into the front-end cavity. This problem can be solved by transferring the mirror coatings to a tapered fiber, or a small grin lens to focus the light into the cavity mode. This unfortunately leads to a more complicated and error prone fabrication process. In addition, a cavity with front-end mirrors must be mounted on

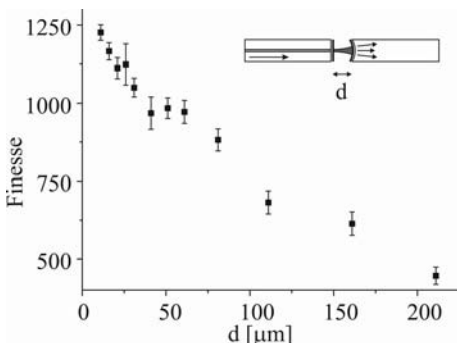


**Fig. 8.6** Finesse measurement of a cavity with a flat mirror on a single mode fiber on the incoupling side and a curved mirror with  $r = 350 \mu\text{m}$  on a multimode fiber on the outcoupling side, as the one illustrated in Fig. 8.1b. Both mirrors have an reflectance of  $R=99.9\%$ . The finesse stays above 400 for fiber separations smaller than  $200 \mu\text{m}$  and has a maximal value of 1200 for small mirror separations.

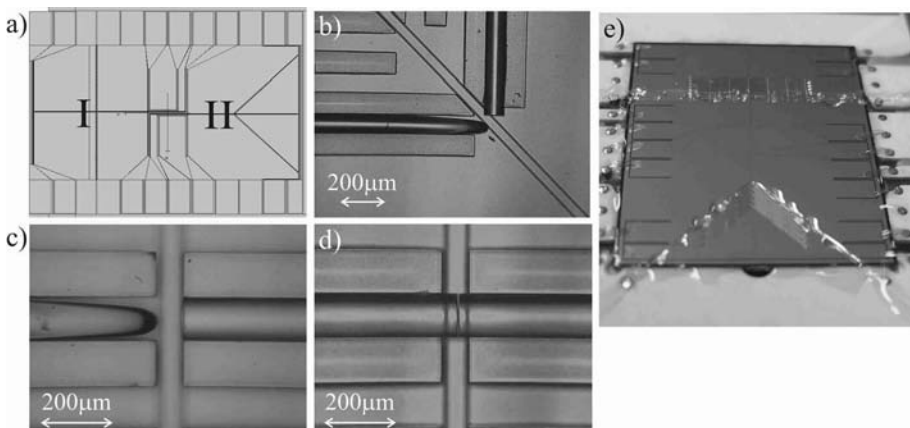


**Fig. 8.7** A drawing of the actual atom chip is shown in a). The pictures b)–d) come from areas I and II. In b) the image shows the 90° fluorescence fiber detector setup. It is built by a tapered fiber (the horizontal fiber) used for a dipole trap and optical pumping. The vertical fiber is a multimode fiber used

to collect scattered light. Picture c) shows a tapered fiber facing a multimode fiber. This setup can be used for absorption detection of a few atoms. Image d) shows a fiber cavity with a gap of a few microns. The actual atom chip containing the structures b)–d) is shown in e).

alignment actuators for efficient tuning of the cavity. This makes miniaturization and integration of multiple cavities harder.

A cavity with the geometry shown in Fig. 8.1a) was built by inserting two planar mirrors into a fiber with length about 10 cm. This fiber cavity is subsequently cut into two halves and the new surfaces are polished. This cavity has the advantage that it is very easy to align and mount. An actual cavity of this kind is shown in Fig. 8.7d) where the cavity is mounted on an atom chip using a SU-8 structure to hold the fibers. The drawback with this cavity geometry is that the finesse is rather low compared to the front-end mirrors, mainly because of the fiber gap and the glue layers as described above. Cavities with inserted mirrors typically reach a finesse of a few hundred instead of a few thousand as for the front-end cavities. The losses due to the glue layers could be reduced by direct coating of the fiber instead of using the transfer technique. The losses due to the gap itself could also be reduced by introducing collimation optics in the gap, such as a small grin lens or a tapered fiber. Such additional optics will however introduce additional Fresnel reflections and may also require active alignment of the gap, as for the front-end cavity.

### 8.5.2

#### The SU-8 Resist

To mount fibers on the atom chip a lithographically patterned photoresist called SU-8 was used. SU-8 is an epoxy based negative resist with high me-

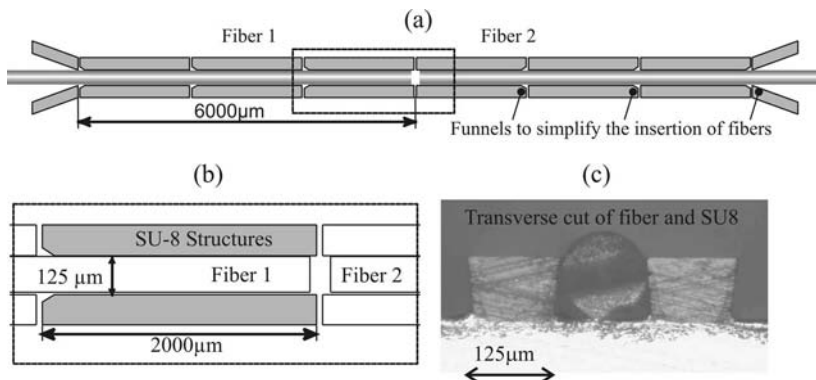


**Fig. 8.8** a) Layout of the alignment structure and a magnified part (dotted rectangle) in b). c) Fiber in a SU-8 structure mounted on a gold coated atom chip. The atom chip and the SU-8 structures have been cut with a wafer saw. The SU-8 maintains structural integrity during the cutting.

chanical, chemical and thermal stability. Its specific properties facilitate the production of thick structures with very smooth, nearly vertical sidewalls [34]. It has been used to fabricate various micro-components. Examples include optical planar waveguides with high thermal stability and controllable optical properties. Mechanical parts such as microgears [44] for engineering applications, and microfluidic systems for chemistry [45] have also been built. The SU-8 is typically patterned with 365-436 nm UV-light.

To assess the quality of the alignment structures, we use the SU-8 structures to hold fiber optical resonators. The finesse of the resonator strongly depends on losses introduced by misalignment as described by Eq. (8.27). The layout of the used alignment structure with fibers is shown in Fig. 8.8. This design includes funnels to simplify assembly. To avoid angular misalignment the total length of the alignment structure is quite long (6000  $\mu\text{m}$ ). The structure is divided into several subsegments to reduce stress induced by thermal expansion.

### 8.5.3

#### Test of the SU-8 Structure

The quality of the SU-8 fiber splice was determined by measuring the finesse of a mounted resonator. The fineses of two intact fiber resonators were found to be  $\mathcal{F}_1 = 110.4 \pm 0.3$  and  $\mathcal{F}_2 = 152.8 \pm 1.1$ . After cutting the fiber and polishing the new surfaces, the two fiber pieces were introduced into the SU-8 structures. We observed the fiber ends under a microscope and minimized the gap size. For these resonators the fineses were found to be  $\mathcal{F}_1 = 101.1 \pm 0.5$  and  $\mathcal{F}_2 = 132.0 \pm 1.3$ . This corresponds to an additional average loss of

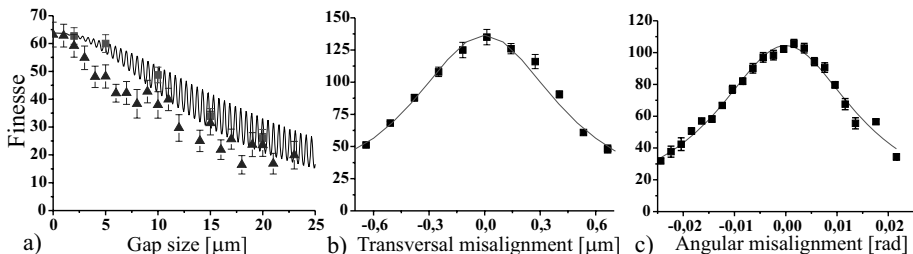


**Fig. 8.9** Measurement of the finesse of a fiber cavity as a function of the gap size is shown in a). The oscillating function shows the theoretical curve for the finesse with varying gap size. The oscillation of the finesse is due to the multiple reflections between the facets and the mirrors. The red squares correspond to the finesse measured for a cavity mounted

inside a SU-8 structure. The blue triangles correspond to a finesse measurement where the cavity is held by precision translation stages. Graph b) shows the finesse of a different cavity measured as a function of transversal misalignment. In c) the finesse is plotted as a function of angular misalignment. Cf. the coloured plates in the Appendix.

$\alpha = (0.29 \pm 0.04)\%$ . Neglecting other additional losses, this corresponds to a transversal misalignment of  $m = 150$  nm or an angular misalignment of  $\theta = 6.3 \times 10^{-3}$  rad  $\approx 0.36^\circ$ . To test thermal stability the temperature of the substrate was varied between 20 °C and 70 °C. The finesse of the inserted fiber resonator showed no change during heating. Another test for the quality of the SU-8 structures was a finesse measurement as a function of gap size. One measurement was done in the SU-8 structures and one outside the structures. The measurement outside was performed with nanopositioning stages, which in principle can be tuned to a few nanometers. With the positioning stages the finesse was optimized. Nevertheless, the finesse obtained inside the SU-8 structures always remained higher than the ones obtained using the positioning stages. The results of these measurements are shown in Fig. 8.9a). The structures have also allowed long-term stability of the cavities in a high-vacuum environment.

## 8.6

### Pilot Test for Atom Detection with Small Waists

To assess the consequences of Eq. (8.9) a test using a macroscopic cavity was performed [46]. The goal was to detect atoms with a cavity with moderate finesse and a very small mode diameter.

#### 8.6.1

##### Dropping Atoms through a Concentric Cavity

To explore atom detection using cavities with small waists, we built a magneto-optical trap (MOT) for  $^{85}\text{Rb}$  atoms approximately 20 mm above the center of

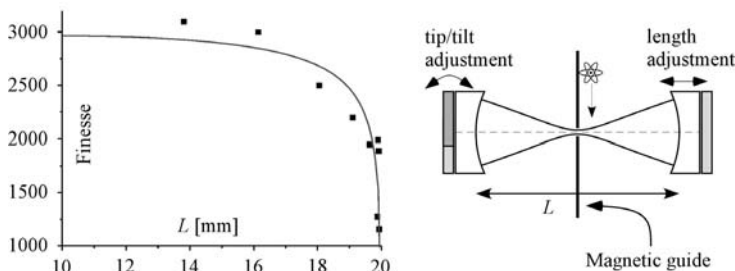


**Fig. 8.10** a) The finesse of the cavity decreases as the concentric point is approached. The curve is calculated from the cavity geometry and mirror specifications. b) Schematic description of the cavity and the magnetic guide mounted next to the cavity.

a near concentric cavity with a finesse of about 1100 formed by normal high-reflectance mirrors. The MOT contained  $\sim 10^7$  atoms at a temperature of 35  $\mu\text{K}$ . In a first experiment, we switched off the trap completely and monitored the atomic cloud as it fell freely through the cavity. This configuration was used to estimate the detection sensitivity of the cavity.

We measured the light intensity transmitted through the cavity with an amplified photodiode for high light intensities or with a photomultiplier tube (PMT) for low light intensities. The PMT provided a near shot-noise limited detection. The low-noise electronic amplification limited the detection bandwidth to 20 kHz. The main source of technical noise in our setup was due to mechanical vibrations of the vacuum chamber that held the cavity.

To minimize the influence of vibrations and long term drifts one of the cavity mirrors was mounted on a piezoelectric tripod that allowed us to keep the  $\text{TEM}_{00}$  mode centered on the cavity axis. The second mirror was mounted on a translating piezoelectric stage for wavelength stabilization. Fig. 8.10 illustrates how the cavity finesse was reduced as the concentric point was approached for our cavity formed by two mirrors with a radius of curvature of  $R = 10$  mm and a transmittance  $T = 10^{-3}$ . For a mirror separation far less than the concentric limit the cavity had a finesse of 3000. The finesse dropped to 1100 when the separation was 70  $\mu\text{m}$  from the concentric point. The cavity mode waist was 12.1  $\mu\text{m}$  for this separation.

The drop in the cavity transmission signal from freely falling atoms is plotted in Fig. 8.11a). The different curves show different pump powers, corresponding to empty cavity transmissions between 1 pW and 600 pW. The atom number in the MOT is  $1.5 \times 10^7$ , the signal drops by 90% as long as the atomic transition is not saturated (Fig. 8.11b). Combining the results of [14] with Eq. 8.11 the effective atom number becomes  $N_{\text{eff}} = 2.5 \pm 0.5$ . This was consistent with an independent atom number measurement based on fluorescence

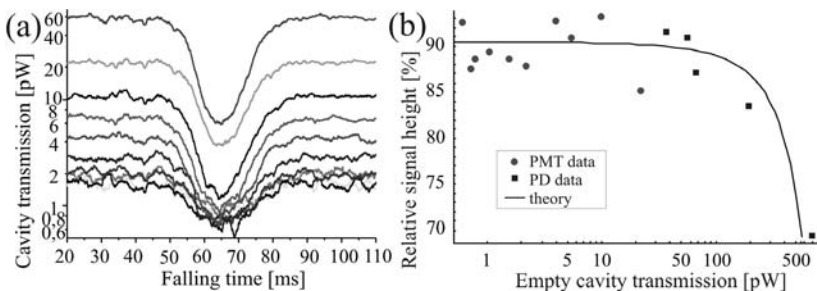


**Fig. 8.11** (a) Cavity transmission signal for atoms dropped from a MOT. Different curves correspond to different cavity pump powers. The signal has been averaged over 2.5ms for better visualization. (b) Relative drop of the signal due to the atoms in (a). The circles (squares) come from measurements with a PMT (photodiode) for different light intensities. The black line is calculated numerically.

imaging. To determine the sensitivity limit of the cavity detector, the number of atoms in the MOT was gradually reduced until the MOT contained  $3.5 \times 10^5$  atoms. This atom number produced a signal drop of approximately 10%. We consider this to be the sensitivity limit. A theoretical fit results in an effective atom number sensitivity of  $N_{\text{eff}} = 0.1 \pm 0.05$ .

### 8.6.2

#### Detecting Magnetically Guided Atoms

As a next step, atoms were magnetically guided to the cavity center using a wire guide [47]. By changing the current in the guiding wire the overlap

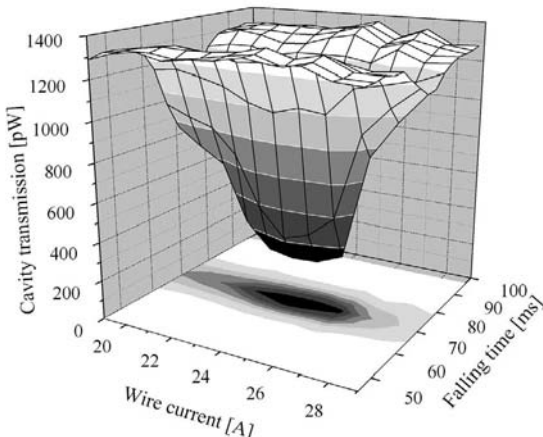


**Fig. 8.12** Cavity transmission signal from atoms being magnetically guided through the cavity mode. The position of the potential minimum is linearly dependent on the wire current.

between the atoms and the cavity mode could be adjusted. In Fig. 8.12 we plot the cavity transmission as the position of the magnetic guide is varied across the cavity mode. As the atomic overlap with the cavity mode was increased, we observed an increased drop in cavity transmission. From the duration of the drop in transmission the temperature of the guided atoms could be determined to be 25  $\mu\text{K}$ . The density distribution for the atoms was much larger than the Rayleigh volume of the cavity. Consequently, it was not possible to distinguish individual atoms in the guide using our cavity. This cavity would show a detectable change in the transmission signal if a single atom crossed the region of maximum coupling as  $N_{\text{eff}}$  can be as small as 0.1. The precision in the positioning can be improved using magnetic microtraps produced by atom chip surface traps [1]. To achieve the same detection sensitivity with a cavity mode diameter of 2  $\mu\text{m}$  a finesse of 40 would be sufficient.

## 8.7

### Conclusion

In this article we have explored and compared various methods of detecting single atoms on an atom chip. Miniaturization brings advantages for such detectors. To detect atoms with a cavity, the requirements on the cavity finesse relaxes quadratically as the mode diameter of the cavity is decreased. This favorable scaling law was tested in a pilot experiment where atoms were detected when magnetically guided through a near-concentric cavity

The simplest way to get to a fully integrated atom detector on an atom chip is to mount optical fibers on to the surface of the chip. Such fiber devices can be used for fluorescence, absorption, and cavity assisted detection of single atoms. To integrate fibers, we have developed a precise lithographic method that allows robust positioning of fibers to within <150 nanometers. The high accuracy allows very reliable fiber-to-fiber coupling, suitable for integration of fiber cavities (Fig. 8.1a). We have built and integrated a fiber cavity on an atom chip which should be able to detect a single atom with a SNR of better than 5 within a measurement time of 10  $\mu\text{s}$ . The same lithographic method has been used to position tapered lenses on the chip. These can be used to combine dipole traps and fluorescence/absorption detectors.

### Acknowledgement

We acknowledge financial support from the Landesstiftung Baden-Württemberg, Forschungsprogramm Quanteninformationsverarbeitung and the European Union, contract numbers IST-2001-38863 (ACQP), MRTN-CT-2003-505032 (Atom Chips), and HPRI-CT-1999-00114 (LSF). The atom chip shown

in this work was fabricated at the The Braun Submicron Center at Weizmann Institute of Science.

## References

- 1 R. Folman, P. Krüger, J. Schmiedmayer, J. Denschlag, and C. Henkel, *Adv. At. Mol. Phys.* **48**, 263 (2002).
- 2 C. Henkel, J. Schmiedmayer, and C. Westbrook (eds.), Special Issue: Atom chips, vol. 35. *Eur. Phys. J. D* (2005).
- 3 R. Folman, P. Krüger, D. Cassettari, B. Hessmo, T. Maier, and J. Schmiedmayer, *Phys. Rev. Lett.* **84**, 4749 (2000).
- 4 P. Krüger, X. Luo, M. W. Klein, K. Brugger, A. Haase, S. Wildermuth, S. Groth, I. Bar-Joseph, R. Folman, and J. Schmiedmayer, *Phys. Rev. Lett.* **91**, 233201 (2003).
- 5 W. Hänsel, J. Reichel, P. Hommelhoff, and T. W. Hänsch, *Phys. Rev. Lett.* **86**, 608 (2001).
- 6 D. Cassettari, B. Hessmo, R. Folman, T. Maier, and J. Schmiedmayer, *Phys. Rev. Lett.* **85**, 5483 (2000).
- 7 D. Müller, E. A. Cornell, M. Prevedelli, P. D. D. Schwindt, A. Zozulya, and D. Z. Anderson, *Opt. Lett.* **25**, 1382 (2000).
- 8 T. Schumm, S. Hofferberth, L. M. Andersson, S. Wildermuth, S. Groth, I. Bar-Joseph, J. Schmiedmayer, and P. Krüger, *Nature Physics* **1**, 57 (2005).
- 9 P. Hommelhoff, W. Hänsel, T. Steinmetz, T. W. Hänsch, and J. Reichel, *New J. Phys.* **7**, 3 (2005).
- 10 H. Ott, J. Fortagh, G. Schlotterbeck, A. Grossmann, and C. Zimmermann, *Phys. Rev. Lett.* **87**, 230401 (2001).
- 11 W. Hänsel, P. Hommelhoff, T. W. Hänsch, and J. Reichel, *Nature* **413**, 498 (2001).
- 12 S. Schneider, A. Kasper, Ch. vom Hagen, M. Bartenstein, B. Engeser, T. Schumm, I. Bar-Joseph, R. Folman, L. Feenstra, and J. Schmiedmayer, *Phys. Rev. A* **89**, 023612 (2003).
- 13 P. W. H. Pinkse, T. Fischer, P. Maunz, and G. Rempe, *Nature* **404**, 365 (2000).
- 14 P. Horak, B. G. Klappauf, A. Haase, R. Folman, J. Schmiedmayer, P. Domokos, and E. A. Hinds, *Phys. Rev. A* **67**, 043806 (2003).
- 15 R. Long, T. Steinmetz, P. Hommelhoff, W. Hänsel, T. W. Hänsch, and J. Reichel, *Phil. Trans. R. Soc. Lond.* **361**, 1375 (2003).
- 16 B. Lev, K. Srinivasan, P. Barclay, O. Painter, and H. Mabuchi, *Nanotechnology* **15**, S556–S561 (2004).
- 17 M. Rosenblit, P. Horak, S. Helsby, and R. Folman, *Phys. Rev. A* **70**, 053808 (2004).
- 18 S. Eriksson, M. Trupke, H. F. Powell, D. Sahagun, C. D. J. Sinclair, E. A. Curtis, B. E. Sauer, E. A. Hinds, Z. Moktadir, C. O. Gollasch, and M. Kraft, *Eur. Phys. J. D* **35**, 135 (2005).
- 19 D. Leibfried, M. D. Barrett, T. Schaetz, J. Britton, J. Chiaverini, W. M. Itano, J. D. Jost, C. Langer, and D. J. Wineland, *Science* **304**, 1476 (2004).
- 20 Y. Miroshnyenko, D. Schrader, S. Kuhr, W. Alt, I. Dotserko, M. Khudaverdyan, A. Rauschenbeutel, and D. Meschede, *Opt. Express* **11**, 3498 (2003).
- 21 S. J. van Enk and H. J. Kimble, *Phys. Rev. A* **61**, 051802 (2000).
- 22 S. J. van Enk and H. J. Kimble, *Phys. Rev. A* **63**, 023809 (2001).
- 23 S. J. van Enk, *Phys. Rev. A* **69**, 043813 (2004).
- 24 S. Kadlecak, J. Sebby, R. Newell, and T. G. Walker, *Opt. Lett.* **26**, 137 (2001).
- 25 M. R. Andrews, M. O. Mewes, N. J. van Druten, D. S. Durfee, D. M. Kurn, and W. Ketterle, *Science* **273**, 84 (1996).
- 26 L. D. Turner, K. P. Weber, D. Paganin, and R. E. Scholten, *Opt. Lett.* **29**, 232 (2004).
- 27 J. J. Hope and J. D. Close, *Phys. Rev. Lett.* **93**, 80402 (2004).
- 28 J. E. Lye, J. J. Hope, and J. D. Close, *Phys. Rev. A* **69**, 023601 (2004).
- 29 J. J. Hope and J. D. Close, *Phys. Rev. A* **71**, 043822 (2004).
- 30 P. R. Berman, *Cavity Quantum Electrodynamics* (Academic Press, San Diego, 1994).

- 31** A. E. Siegman, Lasers (University Science Books, Mill Valley, 1986).
- 32** Z. Moktadir, E. Koukharenka, M. Kraft, D. M. Bagnall, H. Powell, M. Jones, and E. A. Hinds, *J. Micromech. Microeng.* **14**, 82 (2004).
- 33** D. Armani, T. Kippenberg, S. Spillane, and K. Vahala, Ultra-high-Q toroid microcavity on a chip. *Nature* **421**, 925 (2003).
- 34** X. Liu, K. H. Brenner, M. Wilzbach, M. Schwarz, T. Fernholz, and J. Schmiedmayer, Fabrication of alignment structures for a fiber resonator using deep UV-lithography. *Appl. Opt.* **44**, 6857 (2005).
- 35** P. Quinto-Su, M. Tschernek, M. Holmes, and N. P. Bigelow, On-chip detection of laser-cooled atoms. *Opt. Exp.* **12**, 5098 (2004).
- 36** M. Key, I. G. Hughes, W. Rooijakkers, B. E. Sauer, E. A. Hinds, D. J. Richardson, and P. G. Kazansky, *Phys. Rev. Lett.* **84**, 1371 (2000).
- 37** M. Saruwatari and K. Nawate, *Appl. Opt.* **18**, 1847 (1979).
- 38** N. Schlosser, G. Reymond, I. Protsenko, and P. Grangier, *Nature* **411**, 1024 (2001).
- 39** N. Schlosser, G. Reymond, and P. Grangier, *Phys. Rev. Lett.* **89**, 023005 (2002).
- 40** G. Reymond, N. Schlosser, I. Protsenko, and P. Grangier, *Phil. Trans. R. Soc. Lond. A* **361**, 1527 (2003).
- 41** R. Grimm, M. Weidemüller, and Y. Ovchinnikov, *Adv. At., Mol. Opt. Phys.* **42**, 95 (2000).
- 42** J. D. Miller, R. A. Cline, and D. J. Heinzen, *Phys. Rev. A* **47**, 4567 (1993).
- 43** Optische Interferenz Bauelemente GmbH. For further details: <http://www.oib-jena.de>.
- 44** V. Seidemann, J. Rabe, M. Feldmann, and S. Büttgenbach, *Microsyst. Tech.* **8**, 348 (2002).
- 45** D. Duffy, O. Schueller, J. McDonald, and G. Whitesides, *Anal. Chem.* **70**, 4974 (1998).
- 46** A. Haase, B. Hessmo, and J. Schmiedmayer, Detecting magnetically guided atoms with an optical cavity. *Opt. Lett.* **31**, 268–270 (2006).
- 47** J. Denschlag, D. Cassettari, and J. Schmiedmayer, *Phys. Rev. Lett.* **82**, 2014 (1999).

## 9

## High Resolution Rydberg Spectroscopy of Ultracold Rubidium Atoms

*Axel Grabowski, Rolf Heidemann, Robert Löw, Jürgen Stuhler, and Tilman Pfau*

### 9.1

#### Introduction

During the last decades, a lot of studies have been performed on Rydberg atoms [1]. These experiments made use of atomic beams emitted from a thermal source. In the last years, methods of laser cooling [2] of atoms opened new ways to perform experiments on Rydberg states using atom samples at temperatures in the  $100\text{ }\mu\text{K}$  range. Such a system of ultracold Rydberg atoms is known as “frozen Rydberg gas” [3, 4]. The name is correlated to the fact, that there is nearly no thermal motion of the atoms during the time constant of the experiment. Typically, in the time for one experiment of  $\sim 10\text{ }\mu\text{s}$ , an atom moves about  $1\text{ }\mu\text{m}$  which is smaller than the mean interatomic distance. An interesting property of Rydberg atoms are the long-range dipole-dipole and van der Waals interactions. First investigations of the interaction among the atoms in such “frozen Rydberg” systems have started recently [5–9]. In these experiments, the interaction led to an increasing suppression of excitation as a function of increasing Rydberg atom density. This suppression mechanism is called van der Waals blockade, because the van der Waals interaction among the atoms prohibits further excitation by shifting the energy levels of neighboring atoms out of resonance with respect to the excitation lasers.

Rydberg atoms or mesoscopic ensembles of them are discussed in the context of quantum information processing [10, 11] as conditional logic gates based on the strong interaction between the atoms. To use Rydberg atoms in quantum computing, there are several tasks which have to be achieved first. In the proposal given by Jaksch et al. [10], there must be a possibility to arrange the atoms spacially in a defined way. This can either be done in optical [12] or magnetic lattices [13], where ground state atoms are captured. The quantum information is hereby stored in the hyperfine ground state of the atoms.

In this paper, we present experiments on the excitation of cold  $^{87}\text{Rb}$  atoms to Rydberg states. The atoms are first prepared in a magneto-optical trap (MOT)

[2] and then excited in a two-photon two-color excitation step to a Rydberg state. For this purpose, a narrow linewidth cw-laser system for both wavelengths has been set up. Using this system, we investigated Rydberg excitation in the proximity of the  $n = 40$  state. With the high spectroscopic resolution of our laser system, we were able to investigate the Stark splitting of the Rydberg states and could resolve the  $|m_j|$  state dependent Stark splitting for the two 41D finestructure states.

For quantum computing purposes with Rydberg atoms [10] one has to be able to address the atoms individually in space (for example in an optical lattice). Due to the fact that the quantum information is stored in the hyperfine ground states, it is necessary to be able to excite the atoms from a defined ground state (in  $^{87}\text{Rb}$ ,  $F = 1$  and  $F = 2$ ) to the Rydberg state. For every quantum computing scheme, it is essential to conserve coherence during the operations. In case of using Rydberg atoms, this means that a coherent excitation of the atom to Rydberg states is needed. To get to know the time constants of the experimental cycle, we measured the Rabi frequency of the lower transition of the two photon excitation process. For this purpose, we investigated the Autler Townes splitting of the  $5\text{S}_{1/2}(F = 2) \rightarrow 5\text{P}_{3/2}(F = 3)$  transition coupled to the light field. This is done by probing the splitting of this splitted state with a narrow band excitation to a Rydberg state [14].

This paper is organized as follows: In Sect. 2, we describe the experimental setup, especially the laser system for the Rydberg excitation and the detection of the atoms. In Sect. 3, we give an example for the spectroscopic resolution and the overall stability of the system by measuring a Stark map in the vicinity of the  $n = 40$  manifold. Sect. 4 presents experiments on the state- and spatially selective excitation. Beyond this, we report in Sect. 5 on the measurements of the Rabi frequency on the  $5\text{S}_{1/2}(F = 2) \rightarrow 5\text{P}_{3/2}(F = 3)$  transition by observing the Autler-Townes splitting of this transition coupled to the light field.

## 9.2

### Experimental Setup and Cold Atom Preparation

#### 9.2.1

##### Vacuum System and Magneto Optical Trap (MOT)

The experiments presented here are performed inside a vacuum-chamber as shown in Fig. 9.1. The chamber consists of a steel tube with an inner diameter of 10 cm. In the radial direction, optical access is provided on three axes ( $4 \times \text{CF-36}$  flanges with windows and  $2 \times \text{CF-16}$  flanges with windows). The bottom of the chamber is sealed with a large glass window of 175 mm in diameter. The MOT is built up as a reflection MOT [15] where two of the MOT beams are reflected from a reflective surface inside the vacuum chamber. The other MOT

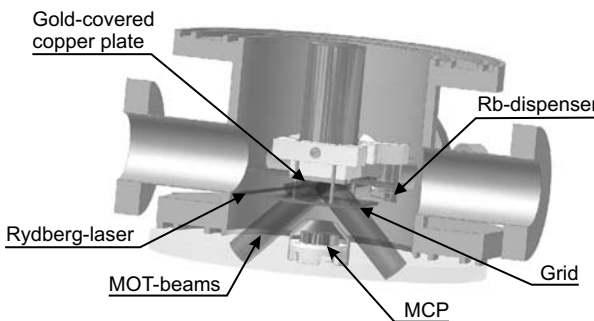


**Fig. 9.1** Setup of the vacuum system with field plates and micro channel plate (MCP). Furthermore the laser beams for both MOT (red) and Rydberg excitation are drawn (blue beam in front). The gold covered copper plate and the copper grid are 10 mm apart from

each other (middle of the picture) surrounding the MOT. The dispenser in the background is shielded by a cage. The MCP is situated in the middle of the vacuum chamber on the lower window.

beams use one of the accessible axes of the chamber. One other axis of the chamber is used for fluorescence imaging of the atomic cloud. The magnetic quadrupole field for the MOT is produced by the current through a wire behind the gold covered copper plate inside the vacuum chamber superimposed with a homogeneous magnetic field produced by Helmholtz coils outside the chamber (U-type quadrupole) [16].

The rubidium for the MOT is provided by a dispenser (SEAS Getters) situated close to the atomic cloud and well shielded by a mesh cage to prohibit any disturbances in the electrical field inside the vacuum chamber. The pressure inside the vacuum chamber which is pumped by both a titanium sublimation pump and an ion pump is in the range of  $10^{-10}$  mbar.

Due to the fact, that Rydberg atoms are very sensitive to electrical fields [1], all sources for electrical stray fields inside the vacuum have to be shielded as good as possible. To control the electrical field, we placed field plates inside the vacuum chamber around the MOT region. Here, we used the gold covered Cu plate which is likewise used for the reflection MOT as one field plate. A copper mesh (SPI Fine Grid Mesh, 02199C-AG), sitting 1 cm below the copper plate forms the second field plate. The mesh has a high optical transmission of 85 % and the size of the holes in the grid is only 234  $\mu\text{m}$ . These field plates enable us to apply a homogeneous electrical field and shield the MOT region from electric field gradients. By applying a voltage to these plates, we can generate an electrical field and are able to investigate the Stark interaction of the Rydberg atoms with it.

For the magneto optical trap, we use grating stabilized diode lasers in the Littrow configuration [17]. The MOT-laser is quasi-resonant to the  $5S_{1/2}(F=2) \rightarrow 5P_{3/2}(F=3)$  transition ( $\lambda=780.248$  nm, see Fig. 9.2). It is stabilized via polarization spectroscopy on a crossover transition in the Rubidium spectrum [18],

133 MHz below the MOT transition. The laser light is afterwards amplified in a “slave” diode and then frequency shifted by an accusto-optical modulator (AOM). The frequency is usually detuned by  $-2\Gamma$  with respect to the  $5S_{1/2}(F=2) \rightarrow 5P_{3/2}(F=3)$  transition. We end up with a total power of about 30 mW in the 3 MOT beams (all of them are retro-reflected). A second laser for the MOT, another grating stabilized diode laser is also locked on a crossover signal. This laser is shifted with an AOM in single pass to resonance with the  $5S_{1/2}(F=1) \rightarrow 5P_{3/2}(F=2)$  transition ( $\lambda=780.231$  nm, see Fig. 9.2). This second so-called repumper laser is needed because MOT atoms can be pumped to the lower hyperfine ground state by off-resonant excitation and are yet lost out of the MOT cycle. The repumper pumps these otherwise lost atoms back. It is superimposed with all the beams of the MOT laser. The AOMs in both of the beams can also be used for fast switching.

For the detection of the MOT atoms, a CCD camera outside the vacuum chamber is used to record both fluorescence and absorption images. The cloud is imaged with a 1:1 telescope to the camera. For the experiments presented here, only fluorescence pictures are taken. The number of atoms in the MOT can be calculated from these fluorescence pictures. The temperature of the atoms in the MOT can be determined by the time-of-flight expansion of the cloud.

We usually operate the Rubidium dispenser at low currents of 4–4.5 A to prevent contamination of the vacuum chamber during the experiments. This leads to atom numbers in the MOT of  $10^6$  atoms at a density of  $10^{10}$  atoms/cm<sup>3</sup>. The temperature of the MOT is about 100–400  $\mu$ K.

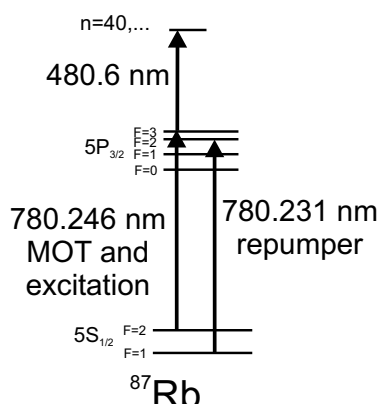


**Fig. 9.2** Level scheme of  $^{87}\text{Rb}$  for cooling, trapping and Rydberg excitation.

### 9.2.2

#### Rydberg Laser System and Rydberg Excitation

As shown in Fig. 9.2, two lasers with wavelengths of 780 nm and 480 nm are needed for the two-photon Rydberg excitation. For this purpose, we built up a laser system consisting of three diode lasers. For the 480 nm laser system the problem arises, that one wants to be able to stabilize the laser to every possible optical Rydberg transition between  $n = 30$  and the ionization threshold. For this reason, we decided to stabilize a master laser to a reference resonator. This 30 cm long reference cavity is stabilized in length by means of a highly stable laser system. With this setup we gain the possibility to lock the laser on every resonator fringe, with a separation of 125 MHz. The fringe to lock on is first found with a wavemeter (Advantest TQ 8325, 100 MHz resolution) and afterwards by scanning the laser around the Rydberg resonance with an AOM. The laser system is built up as a master-slave diode laser system at a wavelength around 960 nm. The master laser is as described before a cavity stabilized diode laser, which is locked to the reference cavity. The laser beam is afterwards frequency shifted with a 400 MHz AOM in double pass configuration, which allows us to vary the frequency more than 250 MHz. After passing the AOM the beam seeds a 300 mW slave diode. If the master laser is locked onto the reference cavity it is possible to change the slave frequency by shifting the frequency of this AOM. With this set up, it is possible to generate every frequency in between two resonator fringes. Afterwards this 960 nm laser is frequency doubled in a home built doubling resonator by second harmonic generation in a KNbO<sub>3</sub> crystal, which yields a laser power of up to 20 mW at 480 nm after the cavity. This blue beam passes afterwards a 200 MHz AOM in single pass, which is used to regulate the power and to switch the beam.

With our laser system it is possible to scan the master-slave system unlocked to the cavity mode hop free about 6 GHz continuously (respectively frequency doubled 12 GHz). This scan range is limited by the available voltage range we apply to the piezo actuator in the master laser. By locking the laser to the reference cavity, the laser frequency is basically fixed, but the frequency of the slave laser can be adjusted using the AOM between master and slave laser. This way, we can scan the blue laser frequency about 500 MHz with high stability and small linewidth.

For the 780 nm wavelength, an external cavity stabilized diode laser is used, locked to a rubidium cell via polarization spectroscopy. This laser has two applications. It is both used as a reference for stabilizing the length of our reference cavity and as first laser of the two-photon transition. This laser beam passes a 200 MHz double pass AOM which enables us to switch the laser fast, attenuate the beam and vary the laser frequency by more than 100 MHz. Depending on the line in the polarization spectroscopy spectrum we lock the

laser to, we are able to work on the  $5S_{1/2}(F=2) \rightarrow 5P_{3/2}(F=3)$  resonance or up to 500 MHz blue detuned with respect to this transition.

Both of the laser beams are guided to the experiment by two singlemode optical fibers. After the optical fiber, we have typically 2.5 mW for the blue 480 nm beam and for the red 780 nm a power of about 7 mW. The red laser is collimated ( $1/e^2$  diameter of 0.95 mm) and shown onto the atomic cloud. The beam diameter is therefore larger than the MOT diameter. The blue laser is focused into the MOT cloud, and has a  $1/e^2$  diameter of 20  $\mu\text{m}$  with a Rayleigh range of 650  $\mu\text{m}$ . The overlapped pair of beams is irradiated inside the chamber. The beams are slightly tilted with an angle of about 10° with respect to the main axes of the chamber.

Due to the selection rules for the two-photon excitation of atoms from the  $5S_{1/2}$  via the  $5P_{3/2}$  state to a Rydberg state only excitations to nS and nD states are dipole allowed transitions. However, even for small electrical fields the selection rules are no longer strict. Excitations to usually dipole transition forbidden states become possible because the target Rydberg states are no longer pure states but a mixture of different unperturbed states. Therefore, it is possible to excite atoms to P or even  $l > 3$  states in a non-vanishing electrical field. The  $l > 3$  states are called hydrogen-like states because the quantum defect for these states is negligible and they can be seen as pure hydrogen states showing a linear Stark effect with a permanent dipole moment. In contrast, the states with  $l < 3$  sustain for small electrical fields a quadratic Stark effect.

### 9.2.3

#### Detection of the Rydberg Atoms

For the detection of the Rydberg atoms, we use the way of field-ionizing the Rydberg atoms by an electrical field pulse and subsequent detection of the emerging ions with a micro channel plate (MCP). For the field ionization, the electrical field is switched on by a high speed, high voltage MOSFET switch (Type: Behlke HTS-6103 GSM). The typical rise time of this switch is 60 ns. We slow down the switching by a 2<sup>nd</sup> order low pass filter. This yields a rise time of the electrical field of 55  $\mu\text{s}$ , which allows us to probe both ions and field-ionized Rydberg atoms selectively at different times. The ions are accelerated towards the MCP by the electrical field and are detected. The MCP signal is amplified in a home built current to voltage converter circuit. The readout of the data is done by a computer with a digitizer card. The maximum sampling rate of the analog electronics and the digitizer card is 50 ns.

For the calibration of the MCP, we directly photo-ionize the atoms from the MOT in an electrical field above the ionization threshold. This leads to a loss of atoms in the MOT due to ionization. After 100 ms the MOT atom number is decreased to a new steady state population which is related to the loading rate

of the MOT and the loss rates. Measuring the reduced steady-state MOT atom number with the CCD-camera and recording simultaneously the number of produced ions with the MCP, we can calibrate the MCP efficiency. With this calibration, we are now able to calculate atom numbers from the MCP signal.

#### 9.2.4

#### Excitation Sequence

During the Rydberg excitation all the MOT and repumper beams are switched off with the AOMs. After 100  $\mu$ s expansion time, the two collinear beams for Rydberg excitation are switched on simultaneously for a variable time between 100 ns and 1 ms. With a variable delay after the excitation pulse a voltage of 300 V is applied to the gold covered copper plate for field ionization of the Rydberg atoms. At the same time the copper grid is at ground potential, which yields an electrical field of 300 V/cm.

In Fig. 9.3 an example for the excitation sequence is shown. Here the excitation pulse is 100  $\mu$ s long. Already during the excitation pulse without an electrical field a signal on the MCP is seen (a). This signal is attributed to Rydberg-Rydberg collisions which lead to an ionization process among the Rydberg atoms [19]. Immediately after the excitation pulse is switched off, the electrical field is ramped up. At the beginning of this ramp a first bunch of ions is detected by the MCP (b). We assign this to ions that first remained in the atom cloud and are now pulled out by the rising electrical field of the ionization pulse. About 40  $\mu$ s later, a broad peak appears on the MCP signal (c), which is due to the field-ionized Rydberg atoms. The time until they reach the MCP is determined by the rising time of the electrical field. Only when the electrical field is high enough, the atoms are ionized and the ions are

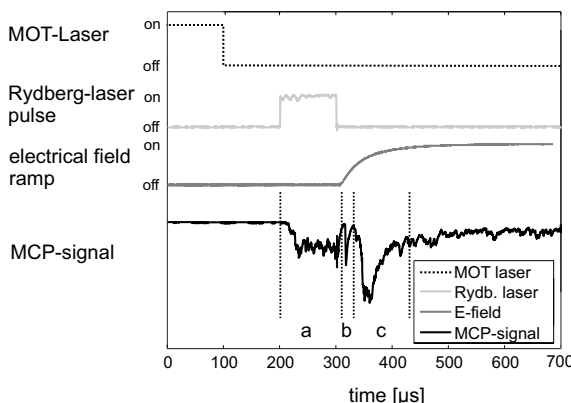


**Fig. 9.3** Excitation sequence of the Rydberg atoms, field ionization pulse and corresponding MCP signal (see text).

then accelerated towards the MCP. This peak is broadened due to l-changing collisions [20]. In the data shown in the next sections (see e.g. Fig. 9.4), every data point consists of such a measurement as in Fig. 9.3. All the data of the single measurements are collected and stored. Afterwards the ion signal is integrated to get together with the calibration factor an absolute Rydberg atom number. The typical repetition rate of the experiment is 30 Hz.

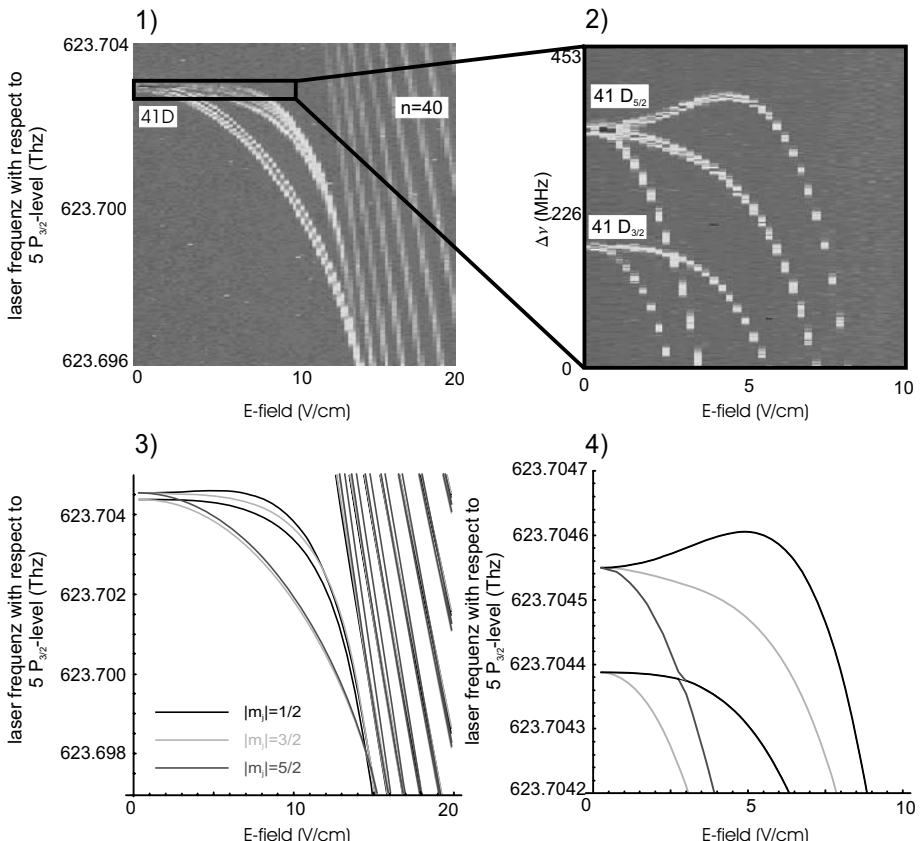


**Fig. 9.4** Example for the spectroscopic resolution of the laser system. On the upper left hand side (1) a Stark map scan is shown where the electrical field and the blue laser frequency is changed. On the upper right side a measurement of a smaller region with a higher resolution is shown, revealing the  $|m_l|$ -Splitting of the Rydberg states in the electrical

field. The two lower pictures (3,4) show the result of a numerical calculation with no free parameters. Only the atomic properties of  $^{87}\text{Rb}$  are used. The different observed states can be assigned to the different  $|m_l|$  states. The color of the pictures indicates the signal strength (blue-low to red-high signal). Cf. the coloured plates in the Appendix.

## 9.3

**Spectroscopy of Rydberg States,  $|m_j|$  Splitting of the Rydberg States**

Fig. 9.4 shows a high resolution spectrum of the 41D doublet. For this experiment, we held the frequency of the red laser constant on resonance of the of the  $5S_{1/2}(F=2) \rightarrow 5P_{3/2}(F=3)$  transition and changed both the frequency of the blue laser and the electrical field during excitation. In Fig. 9.4 a) the spectrum is taken with the unstabilized blue laser while in b) a spectrum obtained by scanning the locked laser system is shown. The electrical field applied across the interaction region during the excitation sequence is changed between 0 V/cm and 20 V/cm (a), respectively 10 V/cm (b). The color of the pictures indicates the signal strength (dark-low to bright-high signal).

On the right hand side in Fig. 9.4 1) both the 41 D doublet and the manifold of the  $n = 40$  states can be found. As expected the signal strength of the  $n = 40$  lines is much weaker than the one of the D-lines, because these are  $l > 3$  states. Because some shift in the Rydberg lines cannot be excluded, we improved the stability by locking the laser onto the reference cavity. In Fig. 9.4 2) the measurement is done by changing the frequency of the AOM between master and slave laser. Thus we were able to scan the laser frequency with a stability of better than 1 MHz.

As can be seen in Fig. 9.4 1,2) one of the two D-lines splits up into 2, the other in 3 different states in dependence of the electrical field. To explain these data and to identify the different states a numerical calculation according to [21] has been performed. The results of this calculation are shown in Fig. 9.4 3,4). In this calculation, there are no free parameters, but only the atomic properties of  $^{87}\text{Rb}$  are used. With this calculation, which shows an excellent agreement with the experimental data, the splitting of the states can be indentified with the different  $|m_j|$ -substates. The  $41D_{5/2}$ -level has the magnetic substates  $|m_j| = 1/2, 3/2$  and  $5/2$ , the  $41D_{3/2}$  the magnetic substates  $|m_j| = 1/2$  and  $3/2$ . These finestructure states are furthermore hyperfine splitted. This splitting is included in the calculation, but is much smaller than the spectroscopic resolution of our laser system and can therefore not be seen. The additional stark shift of the  $5S_{1/2}$  and  $5P_{3/2}$  states is omitted, because the polarizability of  $^{87}\text{Rb}$  in these low lying states is negligible.

Beyond this, we measured the  $n = 40$  manifold in the environment of the zero field crossing. From these data we could estimate the residual electrical field components to be less than 1 V/cm. The accuracy of the measurement was only limited by the small zero field excitation rate.

For small detunings and on resonance of the red transition, the linewidths of the entire transition we observe are basically determined by the linewidth of the lower transition. For large detunings from the  $5P_{3/2}$  state, the linewidth becomes smaller, because the intermediate state is adiabatically eliminated. The smallest linewidth we have measured so far was 3.7 MHz, although the

laser linewidth is well below 1 MHz, determined from the laser stabilization signal. We attribute the residual line broadening to remaining magnetic fields of the MOT. The MOT has a magnetic field gradient of about 16 G/cm. The shift of the atoms in the  $S_{1/2}$  states is 0.7 MHz/G between two neighboring  $m_F$  substates ( $m_F = -2, \dots, 2$ ). At an  $1/e^2$  MOT diameter of 680  $\mu\text{m}$  this yields a linewidth due to magnetic field broadening of 3 MHz which is in excellent agreement with our measurements.

## 9.4

### Spatial and State Selective Addressing of Rydberg States

#### 9.4.1

#### Spatial Selective Rydberg Excitation

For quantum computing approaches with Rydberg atoms according to the proposal of D. Jaksch et al. [10] it is necessary to address the atoms individually at different positions in space. One possibility to do this is addressing via the Stark shift in electrical field gradients which links the resonance frequency of the atoms to their position. Here we present a demonstration experiment with Rydberg atoms in an electrical field gradient. For this purpose, we applied an electrical field gradient across our MOT and varied the position of the excitation lasers along this gradient. In Fig. 9.5 the  $41D_{3/2}$  and  $41D_{5/2}$  resonance lines are shown. The shift of the excitation beams by the diameter of the MOT cloud yields a line shift of 98 MHz and 75 MHz which is already larger than the linewidth of the broadened transitions. This broadening is due to electrical field gradient across the MOT. This is because the gradient we applied is not homogeneous in one direction, but also varies in the orthogonal direction. So each individual atom along the Rydberg excitation beam in the MOT is exposed to a different electrical field which leads to an inhomogeneous broadening. The measured linewidth of the two lines is 81 MHz, respectively 57 MHz which is much larger than the linewidth of the  $5S_{1/2}(F=2) \rightarrow 5P_{3/2}(F=3)$  transition.

The origin for the different linewidths and shifts of the two transitions is the different slope of the two transitions in the electrical field as can be seen in Fig. 9.4. From the slope of this state in an electrical field and from the size of the cloud, the gradient of the electrical field in the direction of the movement of the laser can be estimated to be 18.8 V/cm<sup>2</sup>. In future experiments, we will be able to apply a homogeneous electric field gradient which will shift the lines without the line broadening.

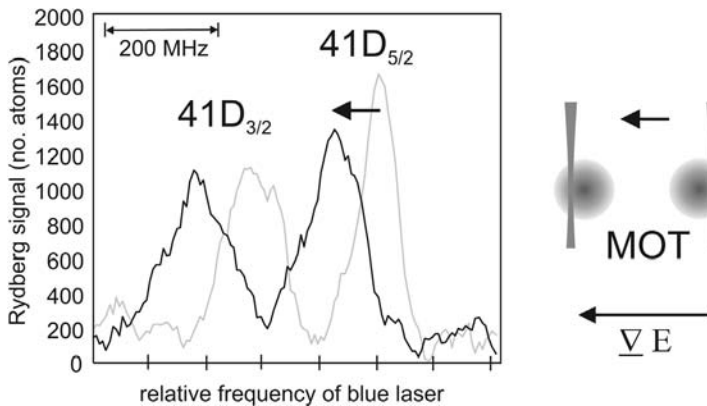


**Fig. 9.5** Spatial dependent addressing of atoms of the cold cloud by using an electrical field gradient. The spacial addressing was done by moving the laser across the MOT. The frequency of the Rydberg lines is shifted according to the electrical field gradient.

#### 9.4.2

#### Hyperfine Selective Rydberg Excitation

In the quantum computing scheme with rubidium Rydberg atoms, the quantum information is stored in both of the hyperfine ground states ( $5S_{1/2}$   $F=1$ ,  $F=2$ ). For this reason, state selectivity of the ground states in the excitation scheme should be assured. This means that one of the  $5S_{1/2}$  ground states has to be accessible for the excitation to the Rydberg state, in a way that during the excitation, the other state is not affected. To test this, we excited from both hyperfine ground states to Rydberg states. In the experiment, we scanned the frequency of the blue laser across the resonance  $5P_{3/2} \rightarrow 41D$  and excited the atoms on the  $5S_{1/2} \rightarrow 5P_{3/2}$  transition with the MOT and the repumper laser as red laser system. The repumper light was resonant with the  $5S_{1/2}(F=1) \rightarrow 5P_{3/2}(F=1)$  transition. We did the excitation with and without optical pumping of the atoms to the  $F=1$  state before the Rydberg excitation. In an experiment where no atoms are actively pumped to the  $F=1$  state, an excitation is only possible from  $F=2$  state to the Rydberg state (Fig. 9.6, (3)). No atoms can be excited from the  $F=1$  state to a Rydberg state (Fig. 9.6, (1)). An excitation from the  $F=1$  state is only possible by actively pumping the atoms prior to the excitation process in the  $F=1$  state. This was done by switching off the repumper laser 300  $\mu$ s earlier than the MOT laser before the Rydberg excitation. As shown in Fig. 9.6 (2) and (4) the number of atoms excited from  $F=2$  to the  $n = 41D$  shrinks (4) and an excitation from  $F=1$  to the  $n = 40D$  states becomes possible (2). Since we could not completely switch off the AOM, we were not able to pump all the atoms in the  $F=1$  and it was not possible to fully deflate the  $F=2$  state. The measured frequency shift between the lines is about

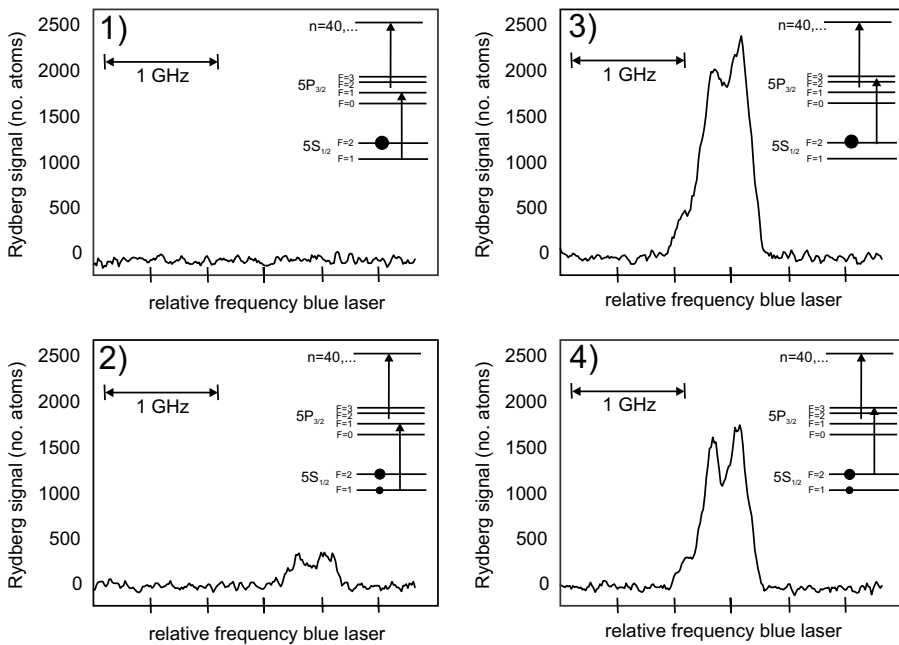


**Fig. 9.6** State selective excitation of the Rydberg atoms from both the  $5S_{1/2}$  ( $F = 1$ ) (1 and 2) and ( $F = 2$ ) (3 and 4) states to the 41D doublet. Without optical pumping of the atoms to the  $F = 1$  state no Rydberg excitation is possible (1). With optical pumping before

Rydberg excitation, atoms can be excited to a Rydberg state (2). Rydberg atom signal without optical pumping before Rydberg excitation (3) and with optical pumping of the atoms from the  $F = 2$  to the  $F = 1$  state (4).

460 MHz which is in a reasonable agreement with the theoretical prediction (423 MHz). The spectroscopic lines in this experiment are rather broad because of an electrical field gradient across the atom cloud. To improve the transfer efficiency, we will use in future experiments a Raman laser system to transfer the atoms between the hyperfine ground states.

## 9.5

### Autler-Townes Splitting

In an atomic ensemble that strongly interacts with a coherent light field, a new set of basis states for the coupled system can be found [22]. One consequence of this coupling is the well known Autler-Townes splitting [23]. The magnitude of the splitting is given by the Rabi Frequency of the transition. In a three level system, it is possible to probe the Autler-Townes splitting of one state with a transition to an other state and therefore measure directly the Rabi frequency of the two-state system [14]. The knowledge of the Rabi frequency of our Rydberg system (for the red and for the blue transition) is necessary

because for coherent excitation to Rydberg states, the Rabi frequency has to be larger than the inverse timescale of decoherence processes. To efficiently excite atoms in a two-photon process to Rydberg state coherently, the Rabi frequencies of the two transition have to be known and both Rabi frequencies have to match. We used this method to measure the Rabi Frequency of the red laser by probing the  $5S_{1/2}(F=2) \rightarrow 5P_{3/2}(F=3)$  transition with the transition to the  $43S_{1/2}$  state (see Fig. 9.7).

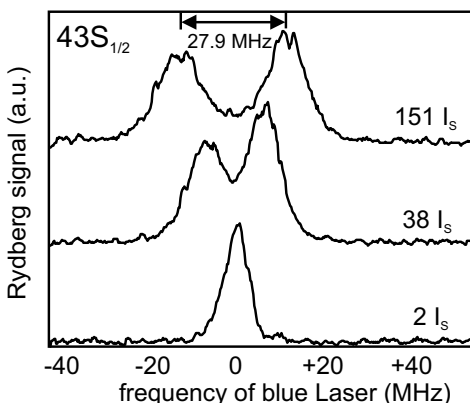


**Fig. 9.7** Autler-Townes splitting of the  $5S_{1/2} \rightarrow 5P_{3/2}$  transition probed with a Rydberg transition to the  $43S_{1/2}$  state. For an intensity of  $151 I_s$  we get an Autler-Townes splitting of 27.9 MHz.

Increasing the red laser intensity, the  $5S_{1/2}(F=2) \rightarrow 5P_{3/2}(F=3)$  transition coupled to the light field splits up into two lines, where the splitting of the two lines is given by the Rabi frequency  $\Omega_r = \Gamma \sqrt{\frac{I}{2I_s}}$ . Here  $\Gamma$  is the linewidth of the transition,  $I$  the intensity of the laser and  $I_s$  the saturation intensity of the transition. The measured splitting of the two new states is 27.9 MHz. In Fig. 9.7 can be seen, that the signal height of the two lines is not identical. The reason for this is the fact, that the excitation laser was slightly detuned from resonance with the transition, resulting in a different signal strength. The ratio between the height of the two signal is 0.79, which corresponds to a detuning of 7.83 MHz. Taking this into account the corrected Rabi frequency is 26.6 MHz. In the theoretical calculation of the Rabi frequency, one has to take into account, that we excite the atoms from a MOT, where the atoms are at the beginning of the excitation randomly distributed over the different  $m_F$  substates of the  $5S_{1/2}(F=2)$  states. Exciting this system with a linear polarized beam pumps the atoms after a few cycles mainly to the  $m_F = 0, \pm 1$  states. So for the calculation of the transition these 3 starting states have to be taken into account and the saturation intensity in the Rabi frequency calculation has to be corrected correspondingly. This leads to correction of the Rabi frequency according to  $\Omega \approx 0.49\Omega_r$ . The calculated Rabi frequency for an laser intensity

of  $151 I_s$  is  $0.49 \cdot 52.2 \text{ MHz} = 25.6 \text{ MHz}$ , what is in good agreement with the measurement of 26.6 MHz.

## 9.6

### Conclusion and Outlook

In this paper, we described a high resolution system for the excitation and investigation of  $^{87}\text{Rb}$  atoms in Rydberg states. All presented experiments were performed on an ensemble of ultracold atoms in a MOT. With this system, studies in the regime of a “frozen Rydberg gas” are possible. As first experiments, we tested the resolution and frequency stability of the system by the investigation of the Stark effect in the vicinity of the  $n = 40$  Rydberg states. We could resolve the Stark effect of these states and even the field dependent splitting of the  $|m_j|$  states of both the  $43\text{D}_{3/2}$  and  $43\text{D}_{5/2}$  finestructure states. The smallest Rydberg lines we measured had a linewidth of 3.7 MHz which was limited by the broadening due to the MOT magnetic field.

To test the usability for quantum computing approaches, we excited both atoms spatial and state selectively to Rydberg states. We furthermore investigated the Autler-Townes splitting of the  $5\text{S}_{1/2} \rightarrow 5\text{P}_{3/2}$  transition which could be observed by probing this transition with an excitation to a Rydberg state.

In the next future, we will be able to start Rydberg excitation experiments on our  $^{87}\text{Rb}$  Bose-Einstein condensate. Furthermore an optical lattice is currently set up. So experiments on Rydberg excitation from atoms trapped inside an optical lattice will be possible, too.

### Acknowledgement

We acknowledge financial support by the ‘A8 Quantum Information Highway’ programme of the Landesstiftung Baden-Württemberg.

### References

- 1 T. F. Gallagher, *Rydberg Atoms* (Cambridge University Press, Cambridge 1994).
- 2 H. J. Metcalf and P. van der Straten, *Laser Cooling and Trapping* (Springer Verlag, New York, 1999).
- 3 W. R. Anderson, J. R. Veale, and T. F. Gallagher, *Phys. Rev. Lett.* **80**, 249 (1998).
- 4 I. Mourachko, D. Comparat, F. de Tomasi, A. Fioretti, P. Nosbaum, V. M. Akulin, and P. Pillet, *Phys. Rev. Lett.* **80**, 253 (1998).
- 5 K. Singer, M. Reetz-Lamour, T. Amthor, L. G. Marcassa, and M. Weidemüller, *Phys. Rev. Lett.* **93**, 163001 (2004).
- 6 D. Tong, S. M. Farooqi, J. Stanojevic, S. Krishnan, Y. P. Zhang, R. Côté, E. E. Ylyer, and P. L. Gould, *Phys. Rev. Lett.* **93**, 063001 (2004).

- 7** T. J. Carroll, K. Claringbould, A. Goodsell, M. J. Lim, and M. W. Noel, *Phys. Rev. Lett.* **93**, 153001 (2004).
- 8** K. Afrousheh, P. Bohlouli-Zanjani, D. Vagale, A. Mugford, M. Fedorov, and J. D. D. Martin, *Phys. Rev. Lett.* **93**, 233001 (2004).
- 9** Wenhui Li, P. J. Tanner, and T. F. Gallagher, *Phys. Rev. Lett.* **94**, 173001 (2005).
- 10** D. Jaksch, J. I. Cirac, P. Zoller, S. L. Rolston, R. Côté, and M. D. Lukin, *Phys. Rev. Lett.* **85**, 2208 (2000).
- 11** M. D. Lukin, M. Fleischauer, R. Côté, L. M. Duan, D. Jaksch, J. I. Cirac, and P. Zoller, *Phys. Rev. Lett.* **87**, 037901 (2001).
- 12** See, for example, R. Grimm, M. Weidemüller, and Y. B. Ovchinnikov, *Adv. At. Mol. Opt. Phys.* **42**, 95 (2000).
- 13** A. Grabowski and T. Pfau, *Eur. Phys. J. D* **22**, 347–354 (2003).
- 14** B. K. Teo, D. Feldbaum, T. Cubel, J. R. Guest, P. R. Berman, and G. Raithel, *Phys. Rev. A* **68**, 053407 (2003).
- 15** J. Reichel, W. Hänsel, and T. W. Hänsch, *Phys. Rev. Lett.* **83**, 3398 (1999).
- 16** J. Reichel, W. Hänsel, P. Hommelhoff, and T. W. Hänsch, *Appl. Phys. B* **72**, 81 (2001).
- 17** L. Riccib, M. Weidemüller, T. Esslinger, A. Hemmerich, C. Zimmermann, V. Vuletic, W. König, and T. W. Hänsch, *Opt. Commun.* **117**, 541 (1995).
- 18** W. Demtröder, *Laser Spectroscopy* (Springer Verlag, Berlin, 2002).
- 19** M. P. Robinson, B. Laburthe Tolra, M. W. Noel, T. F. Gallagher, and P. Pillet, *Phys. Rev. Lett.* **85**, 4466 (2000).
- 20** A. Walz-Flanigan, J. R. Guest, J.-H. Chio, and G. Raithel, *Phys. Rev. A* **69**, 063405 (2004).
- 21** M. L. Zimmermann, M. G. Littman, M. M. Kash, and D. Kleppner, *Phys. Rev. A* **20**, 2251 (1979).
- 22** C. Cohen-Tannoudji, J. Dupont-Roc, and G. Grynberg *Atom-Photon Interactions* (Wiley-Interscience Publications, New York, 1992).
- 23** S. H. Autler and C. H. Townes, *Phys. Rev.* **100**, 703 (1955).



## 10

# Prospects of Ultracold Rydberg Gases for Quantum Information Processing

*Markus Reetz-Lamour, Thomas Amthor, Johannes Deiglmayr, Sebastian Westermann,  
Kilian Singer, André Luiz de Oliveira, Luis Gustavo Marcassa, and  
Matthias Weidemüller*

### 10.1

#### Introduction

During the past ten years, we have witnessed a tremendous progress towards the physical realization of quantum computers. Among the most promising concepts are trapped ions, atoms interacting with photons in high-Q cavities, and nuclear spins in combination with NMR methods [1,2]. The essential feature of these systems is the ability to create entanglement via controlled interactions. Besides these systems, neutral atoms are particularly attractive candidates for quantum information processing because of their relatively weak coupling to dissipative processes of the environment, the ability to precisely manipulate internal and motional degrees of freedom and the possibility to achieve long coherence times [3,4]. Therefore, several schemes were proposed to entangle neutral atoms for the realization of quantum gates with considerable fidelity [5]. However, entanglement between neutral atoms is hard to achieve due to the weakness of their mutual interactions, in contrast to, *e.g.*, the long-range Coulomb force acting between charged particles. Proposed mechanisms for obtaining entanglement between neutral atoms leading to the realization of quantum gates employ cold collisions [6], optically controlled ground-state interactions [7] and dipole-dipole interactions [8,9].

Rydberg atoms appear to be particularly well suited for quantum information processing [8,9]. They exhibit extremely long-range dipolar forces due to the strong polarizability of the weakly bound outer electron, which scales as  $n^7$  ( $n$  denotes the principal quantum number of the atom). The relevant qubits are either two ground states of a single atom [8], or collective states of the multi-particle ensemble [9]. The many-body approach also solves the ubiquitous problem of addressability. Instead of addressing single atoms, which requires very high optical resolution and detection efficiency, single Rydberg

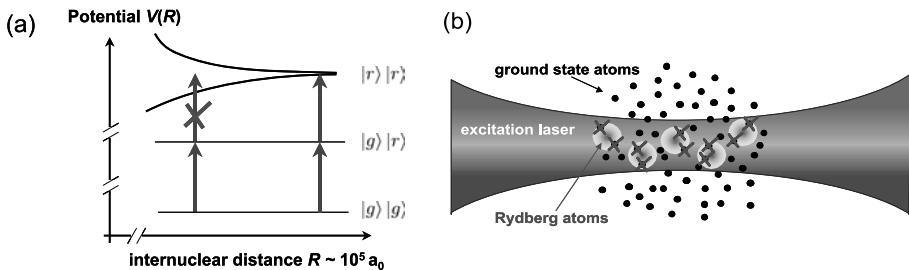


**Fig. 10.1** Explanation of the dipole blockade. (a) Simplified presentation of the dipole blockade with only one pair of atoms being involved.  $|g\rangle$  and  $|r\rangle$  denote the ground and Rydberg state, respectively. The ultralong range dipole interaction splits the Rydberg pair state and thus suppresses excitation of a Rydberg pair by a resonant laser field,

as indicated by the vertical arrows. (b) Local dipole blockade. An excitation laser beam is overlapped with a cloud of cold atoms. Rydberg excitation out of the gas is suppressed in the vicinity of a Rydberg atom by the interaction, resulting in the local dipole blockade.

excitation in a mesoscopic ensemble is enforced by the so-called “dipole blockade”, i.e. the suppression of many-body states with more than a single excitation through the strong dipole-dipole interaction between Rydberg atoms. Employing the dipole blockade, several mesoscopic systems may be used to perform gate operations, by either transferring qubits between distant systems or by direct dipole-dipole interaction of two closely spaced systems.

A simplified picture of the blockade effect is shown in Fig. 10.1. At large internuclear separations, Rydberg atoms are resonantly excited by a laser field indicated by the arrows in Fig. 10.1(a). When the internuclear distance is decreased, the dipole interaction between pairs of Rydberg atoms splits the energy levels, thus shifting the Rydberg pair out of resonance with the laser and impeding the excitation of a Rydberg pair. As indicated in Fig. 10.1(b), each Rydberg atom in a gas defines a volume in which no further Rydberg states can be excited. The size of the volume is given by the condition that the interaction energy is larger than the linewidth of the single-Rydberg excitation line. As a consequence, further Rydberg excitation is locally blocked around each Rydberg atom resulting in optically addressable domains with a well defined excitation (local dipole blockade).

To realize fast phase gates for quantum computation involving Rydberg atoms, the atoms are either entangled by the interaction of the permanent dipole moments of Rydberg states in a static electric field, or by the dipole interaction (van-der-Waals interactions or Förster resonant energy exchange). The Förster process has recently been experimentally demonstrated in a frozen Rydberg gas [10,11]. In order to use this process for gate operations, the atomic center-of-mass has to be stationary in order to avoid entanglement between internal and motional degrees of freedom. Therefore, ultracold samples of atoms have to be used. To realize quantum logic operations with Rydberg atoms, it

is mandatory to enter a regime in which the dipole-dipole interaction governs the internal dynamics of the system. However, it has been shown that cold Rydberg gases at high densities tend to spontaneously evolve into ultracold plasmas [12] or may undergo strong  $\ell$ -mixing processes thus forming high-angular-momentum states [13]. Both effects destroy the entanglement since the interaction between the Rydberg atoms is strongly modified. In particular, free charges igniting the evolution into a plasma have to be excluded.

In this article we describe our experiments towards the implementation of quantum information processing with Rydberg atoms. We have explored the prospects of three different scenarios for the creation of strong interparticle forces as a prerequisite for fast quantum gates: van-der-Waals interactions, interactions of permanent dipoles, and Förster resonances (resonant dipole-dipole interactions). Signatures of these interactions are discussed in Sects. 10.3, 10.4, and 10.5, respectively. Sect. 10.2 gives an overview over the experimental setup. A short summary and outlook is given in section 10.6.

## 10.2

### Excitation of Rydberg Atoms from an Ultracold Gas

The experimental setup is described in detail in [14]. Grating stabilized diode lasers are used to trap a cloud of cold  $^{87}\text{Rb}$  atoms in a magneto-optical trap (MOT) as schematically shown at the center of Fig. 10.2(a). The MOT is placed between two metal grids (1.5cm apart) with high optical transmission which are used to apply electric fields during excitation and to field-ionize the Rydberg atoms. The resulting ions and electrons are accelerated by electric fields and detected by micro-channel plates (MCP). Between  $10^7$  and  $10^8$   $^{87}\text{Rb}$  atoms are typically trapped at a peak density of about  $10^{10}\text{cm}^{-3}$  with loading times of roughly 5 s. The steady state temperature of the MOT is about  $200\text{ }\mu\text{K}$ . The temperature can be reduced in pulsed operation down to  $4.5\text{ }\mu\text{K}$  using optical molasses or below  $1\text{ }\mu\text{K}$  with 3D degenerate Raman sideband cooling [15, 16].

The cold atoms are prepared in Rydberg states by a two-photon excitation scheme shown in Fig. 10.2(b). The first photon is provided by a commercial high-power diode laser with a line width  $\lesssim 1\text{MHz}$  (Toptica, DLX 110), while the second photon is generated by a commercial cw laser system consisting of a frequency-doubled semiconductor laser source with a line width  $<2\text{MHz}$  (Toptica, TA-SHG 110). The wavelength of this laser can be tuned to address Rydberg levels starting from  $n \simeq 30$  up to the ionization threshold. All lasers can be independently switched by acousto-optical modulators with switching times in the 100-ns range.

In a typical experimental cycle (repeated every 70 ms) the MOT lasers are switched off 3ms after the quadrupole magnetic field used for trapping is

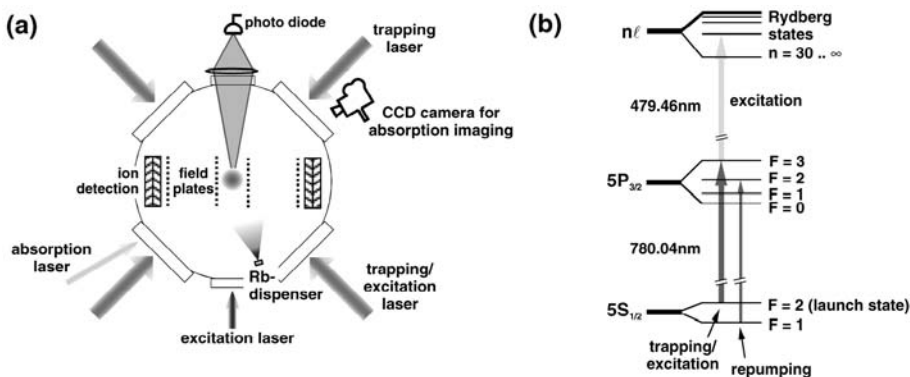


**Fig. 10.2** (a) Experimental setup for the preparation of a frozen Rydberg gas from a magneto-optical trap. (b) Relevant energy levels for the two-photon excitation of  $^{87}\text{Rb}$  Rydberg atoms. The population of the launch state  $5\text{S}_{1/2}(F=2)$  can be controlled by depumping atoms to the dark  $5\text{S}_{1/2}(F=1)$  state.

turned off. The red and blue excitation lasers are switched on for a variable time period. The cycle is completed by ionizing the Rydberg atoms with either an electric field pulse or ramp and detecting the resulting ions and electrons on two opposite MCPs. The MCP signals are calibrated by comparison with the loss in MOT fluorescence. The density of Rydberg atoms can be controlled by varying the population in the  $5\text{S}_{1/2}(F=2)$  launch state through optical pumping into the  $5\text{S}_{1/2}(F=1)$  state.

A recent improvement to the experiment is an active frequency stabilization for the blue excitation laser. While all other lasers are stabilized via Doppler-free Rb spectroscopy, no such reference is available for the blue laser which has to be stabilized over a wide range of optical frequencies. We use an ultrastable cavity made of ZERODUR® as a reference. A monitor beam of the fundamental laser is tuned by a wide-range acousto-optical frequency shifter onto a cavity mode and stabilized by frequency modulation techniques (see Fig. 10.3). The optical power at the photodiode is as low as 100 nW while the amplification stage of the photodiode still provides a bandwidth of 10 MHz. With this scheme, the excitation laser at 480 nm can be stabilized with an absolute frequency stability better than 1 MHz over a period of one hour.

### 10.3

#### Van-der-Waals Interaction

Van-der-Waals (vdW) interaction is the weakest interaction between neutral atoms and typically depends on the interatomic distance  $R$  as  $C_6/R^6$ . However, due to the high polarizability of Rydberg atoms the interaction strength

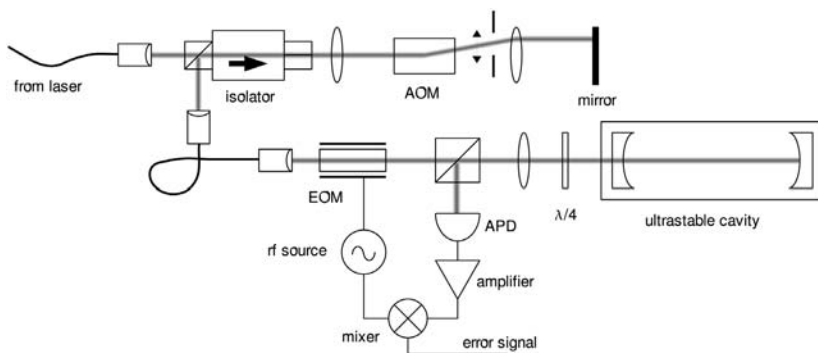


**Fig. 10.3** Simplified sketch of the frequency stabilization of the Rydberg excitation laser at 480 nm. The laser passes through an optical isolator and an acousto-optical modulator (AOM) in double-pass configuration. The frequency-shifted reflected beam is guided through another fiber, modulated by an

electro-optical modulator (EOM) and coupled into the ultrastable cavity. An avalanche photo diode (APD) picks up the reflected beam. The output is amplified and mixed with the modulating signal to obtain an error signal for locking the laser.

increases drastically ( $C_6 \propto n^{11}$ ) with the principal quantum number  $n$  [17, 18]. Van-der-Waals interaction therefore provides strong interaction for high- $n$  states and seems promising for demonstrating an excitation blockade.

### 10.3.1

#### Blockade of Excitation

Clear evidence of a local blockade due to van-der-Waals interaction has recently been reported by a group at the University of Connecticut [19] and by our group [20]. In the Connecticut experiment, Rydberg atoms are excited by a single-photon, pulsed laser excitation. Saturation of Rydberg excitation was observed with increasing laser power for highly-excited Rydberg states ( $n \simeq 70$ ) while no saturation was present for states with low quantum numbers ( $n \simeq 30$ ). Care was taken to exclude that the saturation was induced by power saturation or saturation of the MCP detectors. The observed suppression of Rydberg excitation could quantitatively be described by a theoretical mean-field model which is based on a solution of the optical Bloch equations for an atom interacting with nearby Rydberg atoms. Besides a suppression of Rydberg excitation with increasing laser intensity, the dipole blockade was also observed by increasing the density of launch state atoms.

Equivalent to this approach for the investigation of the dipole blockade, we have recorded excitation spectra of the  $82S_{1/2}$  state at different Rydberg densities [20]. The density is changed by either varying the power of the excitation laser or by changing the density of atoms in the  $5S_{1/2}(F=2)$  launch state. We observe a significant broadening of the S line with increasing density.

The line broadening is accompanied by suppression of excitation on resonance as shown in Fig. 10.4. If no interaction is present, the peak density of Rydberg atoms  $\hat{n}_{\text{Ryd}}$  scales linearly with the launch state density  $\hat{n}_g$ . This is indeed realized in the “low intensity” regime as a fit to the data yields  $\hat{n}_{\text{Ryd}} = p_{82,\text{low}} \hat{n}_g^{0.99(2)}$ , with  $p_{82,\text{low}}$  being the excitation probability at low laser intensities. In the “high intensity” regime, however, the increase of Rydberg density scales less than linearly with  $\hat{n}_g$  clearly showing the onset of an excitation blockade as schematically depicted in Fig. 10.1. At high excitation rate and density, we detect only  $10^4$  Rydberg atoms, which is a factor of  $\sim 2.7$  less than expected from simple linear density scaling indicated by the dashed line in Fig. 10.4. It is important to note that power saturation cannot explain the *density-dependent* saturation of the Rydberg excitation since it would still lead to a linear dependence of the Rydberg density on the launch state density.

We have also compared the saturation for different principal quantum numbers. The vdW interaction potential between two Rydberg atoms strongly increases with the principal quantum number. Therefore, one expects weaker suppression of Rydberg excitation for lines with lower principal quantum number, although the transition strength of these lines is much higher. Indeed we observed that the  $82S_{1/2}$  line saturates at significantly smaller launch state densities than the  $62S_{1/2}$  line. Additionally, the asymptotic Rydberg saturation density for  $62S_{1/2}$  excitation relative to  $82S_{1/2}$  excitation is larger by factor of 3.4.

### 10.3.2

#### Ionization

Interactions in cold Rydberg gases can also be induced by ions present in the sample. These ion-Rydberg atom interactions strongly perturb the Rydberg excitation spectra and impede the use of Rydberg atoms for quantum information processing. It is therefore crucial to understand how ions are formed out of a gas of Rydberg atoms (see also [21]).

To this aim we have investigated the dynamics of ion formation. After excitation with a variable duration of the laser pulse we detect Rydberg atoms with state-selective field ionization. In this way, different Rydberg states and ions can be distinguished. Fig. 10.5 shows the electron signal for different excitation times monitored while the field is ramped up for ionization. For short excitation pulses, only Rydberg atoms are detected (see signals (b) and (c) in Fig. 10.5). The two peaks in the signal represent atoms in the initially excited  $82S_{1/2}$  state. As the electric field is ramped up for ionization, atoms in the  $82S$  state are diabatically transferred to states with higher angular momentum. As these states are ionized at higher fields, the characteristic electron signal of S states is a double peak structure.

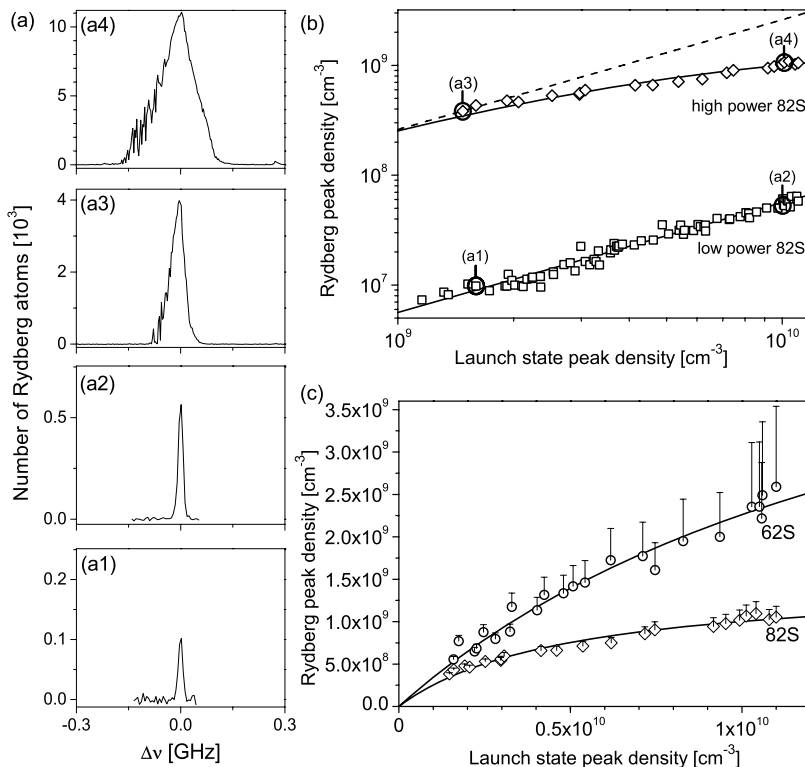


**Fig. 10.4** (a) Excitation spectra of the  $82S_{1/2}$  state at different intensities of the blue excitation laser [ $6 \text{ W/cm}^2$  for (a1) and (a2),  $500 \text{ W/cm}^2$  for (a3) and (a4)] and launch state densities [(a1)  $1.6 \times 10^9 \text{ cm}^{-3}$ , (a2)  $1.0 \times 10^{10} \text{ cm}^{-3}$ , (a3)  $1.5 \times 10^9 \text{ cm}^{-3}$ , (a4)  $1.0 \times 10^{10} \text{ cm}^{-3}$ ]. (b) Rydberg peak densities on the  $82S_{1/2}$  resonance versus launch state density for  $6 \text{ W/cm}^2$  (□) and  $500 \text{ W/cm}^2$  (◊). The dashed line is a linear extrapolation from the origin through the first data point.

Data points corresponding to the spectra (a1) to (a4) are marked. (c) Comparison of the density-dependent suppression of Rydberg excitation for the  $82S_{1/2}$  (same data as in (b)) and  $62S_{1/2}$  (○) resonances. The  $62S_{1/2}$  data were taken at  $350 \text{ W/cm}^2$ . The solid lines in (b) and (c) show fitted saturation functions. The upper error bars are caused by assuming that the maximum measured signals fully saturate the MCP. We see that the MCP saturation hardly affects the 82S data.

When the excitation time is increased a small electron signal is detected during laser excitation (see signal (d) in Fig. 10.5). The origin of the electrons is discussed in the next paragraph. As these electrons leave the cloud, the much heavier cold ion cores remain, forming an electrostatic potential well for subsequently produced electrons [12]. Electrons are trapped in the potential of these ion cores, thus forming a neutral plasma with the ions. In an avalanche process, these trapped electrons ionize more Rydberg atoms through electron impact. When the electric field is ramped up, plasma electrons are released from the Coulomb trough and appear at much lower fields

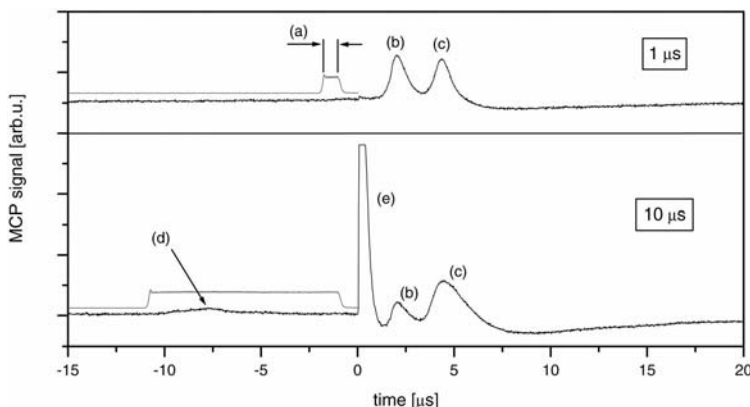


**Fig. 10.5** Electron signals of the  $82S_{1/2}$  state excited with two different excitation times of  $1\text{ }\mu\text{s}$  (upper graph) and  $10\text{ }\mu\text{s}$  (lower graph). The gray line depicts the time and duration of the blue excitation laser (a). At zero time a rising electric field ramp is applied. This leads to the detection of electrons obtained by field ionization of the initially excited Rydberg

state (b) and (c). For excitation times of  $10\text{ }\mu\text{s}$  two additional features occur: Approximately  $2\text{ }\mu\text{s}$  after starting the excitation pulse free electrons from spontaneously generated ions are visible (d) and right after starting the field ramp trapped electrons from the neutral plasma are detected (e). See text.

(signal (e) in Fig. 10.5) than the electrons produced by the ionization of bound Rydberg states.

While the avalanche-like formation of the cold plasma by electron impact ionization is well understood, the initial ionization process producing free electrons remained obscure. Collisions with hot background atoms occur at a rate of  $200\text{ Hz}$  while blackbody radiation leads to an ionization rate below  $3\text{ kHz}$  [22]. Both processes can therefore not account for the initial electrons triggering the plasma formation. Recently, Li et al. [23] pointed out that the initially frozen gas can pick up kinetic energy due to the interaction of Rydberg atoms. We are currently performing further measurements on this initial ionization process.

In order to suppress effects of motion and/or ionization one has to work at timescales that are shorter than typical timescales for ionization. As the excitation rate scales with  $1/n^3$  lower  $n$  states are needed for short excitation times [22]. However, since van-der-Waals interaction ( $\propto n^{11}$ ) is smaller for lower  $n$ , stronger interactions are required, *e.g.* dipole-dipole interactions.

## 10.4

### States with Permanent Electric Dipole Moments

In the previous section induced electric dipole interactions (van-der-Waals interactions) were discussed. The interaction energy of induced dipoles scales

as  $1/R^6$  with interatomic distance  $R$ . Permanent dipole-dipole interactions exhibit a  $1/R^3$  scaling law and is therefore dominating the vdW-interaction at large interatomic distances  $R$ . It can thus be detected even at lower principal quantum number  $n$ .

Permanent dipole moments can be produced by applying an electric field to the atom sample mixing states with different orbital momentum projection. The dipole moment can be determined by the electric field dependence (i.e. the Stark shift) of the resonance lines. As the energy of an electric dipole  $\mu$  in an electric field  $\mathcal{E}$  scales as  $\mu \cdot \mathcal{E}$  the dipole moment can be directly measured as the slope of the lines in a Stark map (see Fig. 10.6).

The dipole interaction energy for a pair of atoms is given by

$$V_{dd} = \frac{1}{4\pi\epsilon_0} \frac{\mu^2}{R^3}. \quad (10.1)$$

When exciting with a laser linewidth of a few MHz, an interaction energy corresponding to a frequency of  $V_{dd}/h \sim 10$  MHz is needed at the typical distance of atoms in an ultracold sample of about  $10 \mu\text{m}$  in order to achieve a blockade effect. This gives a necessary dipole moment of  $\mu = 3200ea_0 = 4.1 \text{ GHz}/(\text{V}/\text{cm})$ . For instance the  $46\text{D}_{5/2}$  state in Rb has such a dipole moment at a very moderate electric field of  $10.5 \text{ V}/\text{cm}$ .

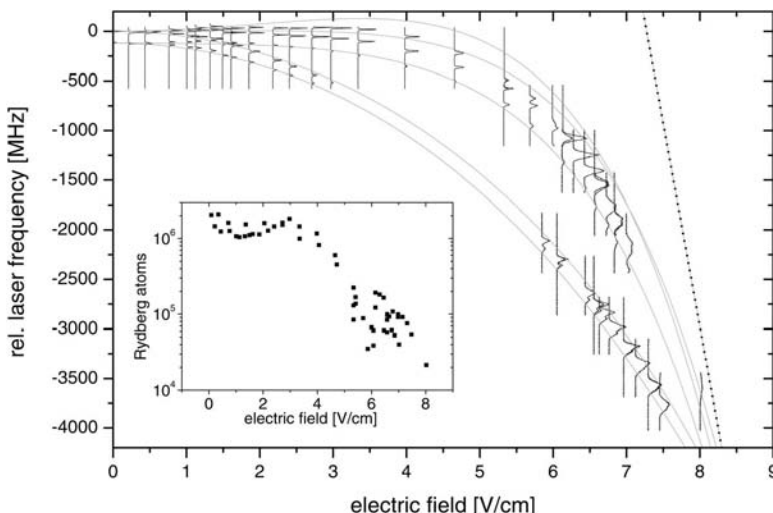


**Fig. 10.6** Electric field dependence (Stark map) of the  $46\text{D}_{5/2}$  and  $46\text{D}_{3/2}$  states. The electric field lifts the degeneracy of the  $m_J$  sublevels. Resonances that shift with the electric field belong to states with a permanent dipole moment. The solid grey lines are calculated. The measured spectra are enlarged at high electric fields because

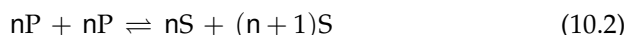
of the decreasing excitation rate. The desired dipole moment of  $4.1 \text{ GHz}/(\text{V}/\text{cm})$  (see text) is indicated as a dotted line at the right hand side. The inset shows the maximum number of Rydberg atoms detected at each electric field. At  $8 \text{ V}/\text{cm}$  the excitation rate has already decreased by two orders of magnitude.

We have measured the corresponding Stark map which is shown in Fig. 10.6. The measured spectra at different electric fields are overlayed by calculated positions of the spectral lines in an electric field [24]. Note that the excitation rate drops drastically as the electric field is increased. The inset of Fig. 10.6 shows the maximum number of detected Rydberg atoms at different electric fields. At 8 V/cm, their number has already decreased by two orders of magnitude. So while the dipole moment is sufficient, the low excitation rate makes it difficult to excite a high enough density in order to observe a dipole blockade. There are three possible ways to overcome this problem and to make interactions between permanent dipole moments amendable for quantum information processing. One possibility consists in an increase of the density by state-of-the-art techniques for quantum gases. An alternative way consists of exciting the states at small fields and to transiently switch the field to the desired higher value. Other states with comparable dipole moments are hydrogen-like states. These, however, cannot be excited to high enough densities with our current laser setup but one can use an additional excitation step in order to obey the selection rules for optical excitation.

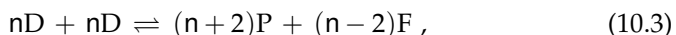
## 10.5

### Förster Resonances

Besides using permanent dipoles one can also resonantly enhance the interaction strength using two-particle resonances. Resonant energy transfer collisions occur when one collisional partner loses as much internal energy as the other one gains. While molecules offer many close-lying levels for such resonant collisions, atoms rely on coincidentally resonant states. Rydberg states however can easily be shifted by electric fields and therefore constitute a perfect tool to study these resonant energy transfer collisions [25]. The exact electric field value needed to tune in to these so-called Förster resonances depend on the quantum defects of the atom used. Rubidium offers two possible processes, namely



and



which can be tuned to resonance at reasonable electric fields due to the different Stark shifts of the involved states.

Förster resonances are of interest because a simple change in the electric field turns the interaction from off-resonant van-der-Waals ( $V_{dd} = (\sqrt{2}\mu\mu')^2/(\Delta R^6)$  in a.u.) to on-resonant dipole-dipole ( $V_{dd} = \sqrt{2}\mu\mu'/R^3$ ) interaction. Fig. 10.7 compares the interaction potentials of two atoms in the 46D state for these cases. The strength changes by more than one order of magnitude at the

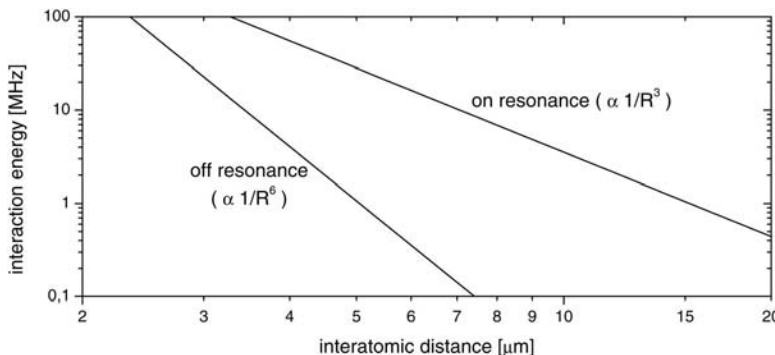


**Fig. 10.7** Comparison of the on-resonant and off-resonant interaction for the Förster process (10.3) at  $n=46$ . The dipole moments  $\mu = \langle 46D | er | 48P \rangle$  and  $\mu' = \langle 46D | er | 44F \rangle$  are both  $\simeq 1600$  a.u. Note that the potentials are simplified not taking all possible molecular symmetries into account (see text).

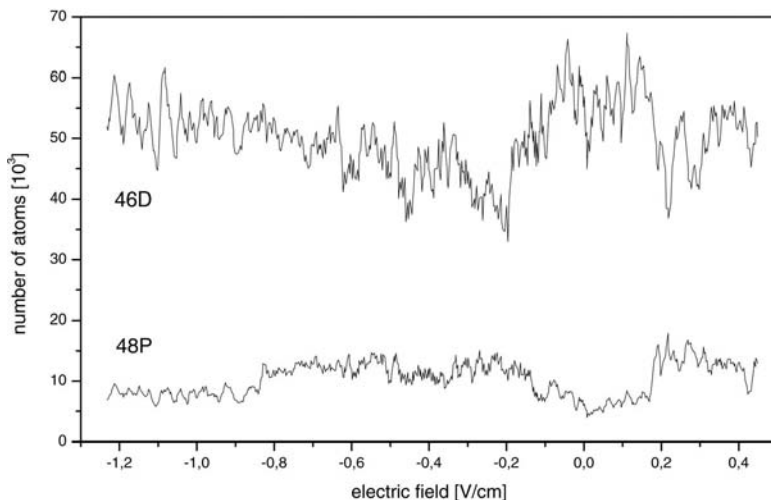


**Fig. 10.8** When setting the excitation laser to the 46D resonance, also 48P atoms are detected due to the energy transfer process (10.3). The upper trace shows the 46D atoms initially excited, the lower trace shows the 48P atoms due to redistribution. The atom numbers for the different states depend on the electric field as this transfer process is resonant at a field of  $\pm 0.25$  V/cm.

typical interatomic spacing of  $5\text{ }\mu\text{m}$  underlining the great amount of control Förster resonances offer.

We have experimentally explored this resonance: We excite the atom cloud to the  $46D_{5/2}$  state and then switch the electric field to a variable value  $\mathcal{E}$  for  $1\text{ }\mu\text{s}$  after which the atom cloud is ionized by applying a field ramp. Since 46D and 48P ionize at different electric fields they can be distinguished by their

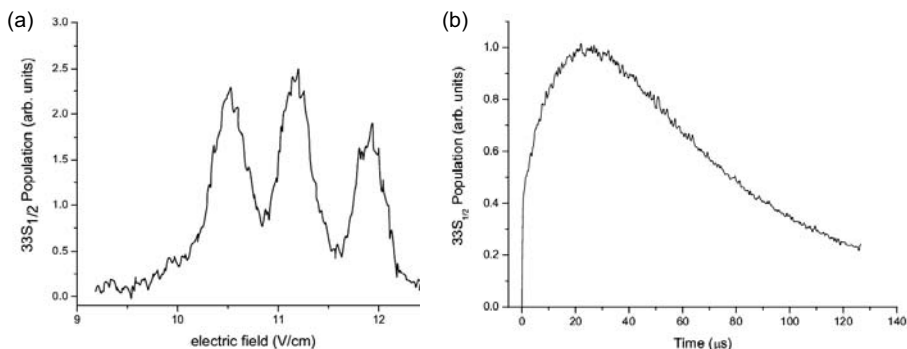


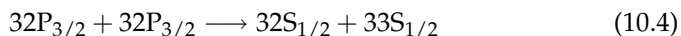
**Fig. 10.9** (a) Population of the  $33S_{1/2}$  when exciting to the  $32P_{3/2}$  state and scanning the electric field over the Förster resonance. Three resonances appear which correspond to the different combinations of involved  $|m_J|$  levels. In a setup with a narrowband laser, different  $|m_J|$  values are spectroscopically resolved

and only one resonance would appear. (b) Evolution of the  $33S_{1/2}$  signal at an electric field of 10.4 V/cm. The initial increase up to 20  $\mu$ s has been attributed to atomic motion while the slow decay is due to the finite lifetime of the  $33S_{1/2}$  state.

arrival time on the detector. Fig. 10.8 shows the number of  $48P$  atoms depending on the chosen electric field. The resonance can be seen as an increase of  $48P$  atoms at electric fields  $|\mathcal{E}| \simeq 0.25$  V/cm. It broadens to the high-field side, which we attribute to the fact that the  $44F$  state can mix with higher angular momentum states which are energetically almost degenerate.

Walker and Saffman [26] pointed out that the simple picture of Fig. 10.7 is not valid. In fact molecular symmetries have to be considered, which can lead to negligible interaction strengths for some symmetries even in the on-resonant case. This shows the importance of control over the excitation process. For example, excitation to specific sublevels can reduce the number of involved molecular states. In particular our narrow-bandwidth laser system allows to distinguish different  $|m_J|$  levels when exciting in electric fields and can therefore show complementary results to setups with broadband pulsed lasers.

As a first step, in a joined experiment carried out in São Carlos, we have therefore studied the following collisional process in rubidium:



In this case the excitation of the Rydberg level was done with a pulsed dye laser resonant to the  $5P_{3/2} \rightarrow 32P_{3/2}$  transition in the presence of a DC electric field. Note that in the excitation scheme transitions to  $nP$  states are actually dipole forbidden and are only possible (with limited excitation rates) while deliberately applying electric fields. The  $33S_{1/2}$  population, produced by collisions between the atoms in the  $32P_{3/2}$  state, was detected through the field-

ramp ionization technique  $5\mu\text{s}$  after the excitation. More details about our experimental setup and detection technique are described in [27]. In Fig. 10.9(a), the  $33\text{S}_{1/2}$  population is shown as a function of the DC electric field. Three resonances are distinguishable corresponding to different combinations of the initial states  $32\text{P}_{3/2,|m|=3/2}$  and  $32\text{P}_{3/2,|m|=1/2}$  which cannot be resolved by the pulsed laser. The position of the peaks differ from the calculated values by  $0.4\text{ V/cm}$ , which we attribute to residual stray electric fields.

We have studied the  $33\text{S}_{1/2}$  population as a function of time between excitation and detection, which is shown in Fig. 10.9(b) for an electric field of  $10.4\text{ V/cm}$ . Over the first  $20\mu\text{s}$  population in the  $33\text{S}_{1/2}$  state builds up, until decay of this state by spontaneous emission results in an exponential decay of the population. The question arises, how the population from  $32\text{P}_{3/2}$  is transferred into the  $33\text{S}_{1/2}$  state. In one possible scenario, the dynamics is explained based on a frozen gas picture with many-body diffusion of excitation [10,11]. Alternatively, the buildup of population may also be explained in a picture where center-of-mass motion of the Rydberg atoms takes place due to large internuclear forces resulting in state-changing collisions [27]. Evidence of such interaction-induced motion was recently pointed out by Li et al. [23].

We are currently conducting experiments to disentangle collisionally induced population transfer from Förster resonant energy transfer, as any motion due to interatomic interactions will play an important role for future application of cold Rydberg atoms in the field of quantum computation as has already been pointed out in Sect 3. The same holds for a dephasing of the resonant energy transfer which has been seen by Anderson et al. [28]. In a recent series of experiments we have investigated how the dynamics of resonant energy transfer processes depends on the Rydberg density and found good agreement with a Monte-Carlo model describing the coherent evolution of many-body systems [29]. So, while Förster resonances promise large control over the interaction strength they come along with a number of important effects that need further investigation.

## 10.6 Conclusion

Quantum information processing in Rydberg systems relies on the strong interaction between Rydberg atoms to realize fast quantum gates. One favorable approach uses this interaction also for an excitation blockade, i.e. a suppression of excitation due to strong (long-range) interactions. Three approaches to control the interaction and produce an excitation blockade have been described and their advantages and disadvantages have been discussed with regard to experimental results.

*Induced dipole (van der Waals) interactions* appear to be a possible candidate for the blockade effect and a suppression of excitation has already been observed. The vdW interaction is a very weak interaction, but due to its  $n^{11}$  scaling reasonable interaction strengths can be reached for high principal quantum numbers. However, the need for high- $n$  states also causes an important drawback of this method. The excitation rate, scaling as  $n^{-3}$ , becomes very low, and thus long excitation times are necessary. Dynamic processes, such as acceleration of Rydberg atoms and ionization, can then take place during the excitation, which influences the atomic interactions and the blockade behaviour.

Using Rydberg states with *permanent dipole moments* represents a possible alternative requiring excitation in an electric field. Interaction energies of several MHz at a distance of a few microns can be achieved at small electric fields. This method is limited by the fact that large dipole moments are found only in combination with small excitation rates. Therefore, samples of higher ground state atom density have to be achieved, *e.g.* by magnetic trapping in combination with evaporative cooling, in order to overcome the limitations of the small excitation rate.

The third method is based on *Förster resonances* (resonant energy transfer collisions) to turn a strong dipole-dipole interaction on and off by switching (small) electric fields. This controllable interaction seems to be the most promising approach for the implementation of quantum information processing with Rydberg atoms due to the resonant character of the interaction process. High densities can be achieved by using states with a dipole-allowed excitation (*e.g.* D states). Different effects caused by Förster resonances, such as diffusion of excitation, dephasing of the resonant energy transfer, and interaction-induced motion have already been studied with broadband excitation schemes [10, 11, 27, 28]. We will investigate these resonances and their applicability to quantum information in more detail. The high spectral resolution of our Rydberg excitation scheme will allow for a detailed spectroscopic analysis and for the selective excitation of interacting pairs.

We will further study the autoionization of Rydberg gases mentioned in section 10.3, since the presence of ions influences the interaction potentials and the behavior of the system strongly. A detailed understanding of the processes leading to ionization is important in order to control Rydberg interactions. Demonstrating the dipole blockade is only the first step towards quantum information processing with Rydberg atoms. As quantum information relies on the coherent superposition of atomic states one has to demonstrate the coherent excitation into Rydberg states as a precursor step to encode qubits. We present investigations of rapid adiabatic passage and coherent two-photon excitation to Rydberg states in another work [30]. In order to observe Rabi oscillations in Rydberg excitation we are currently setting up dedicated optical

beam shaping systems for the coherent excitation of Rydberg states and for spatially structuring mesoscopic Rydberg ensembles.

## Acknowledgement

The project is supported in part by the Landesstiftung Baden-Württemberg in the framework of the "Quantum Information Processing" program, and a grant from the Ministry of Science, Research and Arts of Baden-Württemberg (Az: 24-7532.23-11-11/1). Exchange with the University of São Paulo is financed by the bilateral PROBRAL program of DAAD and CAPES. We thank G. Raithel, R. Côté, P. Gould and E. Eyler for many valuable discussions and suggestions.

## References

- 1 D. Bouwmeester, A. Ekert, and A. Zeilinger (eds.), *The physics of quantum information* (Springer-Verlag, Berlin, 2000).
- 2 M. A. Nielsen and I. L. Chuang, *Quantum computation and quantum information* (Cambridge University Press, Cambridge, 2000).
- 3 P. Treutlein, P. Hommelhoff, T. Steinmetz, T. W. Hänsch, and J. Reichel, *Phys. Rev. Lett.* **92**, 203005 (2004).
- 4 D. Schrader, I. Dotsenko, M. Khudaverdyan, Y. Miroshnychenko, A. Rauschenbeutel, and D. Meschede, *Phys. Rev. Lett.* **93**, 150501 (2004).
- 5 T. Calarco, H.-J. Briegel, D. Jaksch, J. I. Cirac, and P. Zoller, *J. Mod. Opt.* **2137**, 415 (2000).
- 6 D. Jaksch, H.-J. Briegel, J. I. Cirac, C. W. Gardiner, and P. Zoller, *Phys. Rev. Lett.* **82**, 1975 (1999).
- 7 M. D. Lukin and P. R. Hemmer, *Phys. Rev. Lett.* **84**, 2818 (2000).
- 8 D. Jaksch, J. I. Cirac, P. Zoller, S. L. Rolston, R. Côté, and M. D. Lukin, *Phys. Rev. Lett.* **85**, 2208 (2000).
- 9 M. D. Lukin, M. Fleischhauer, R. Côté, L. M. Duan, D. Jaksch, J. I. Cirac, and P. Zoller, *Phys. Rev. Lett.* **87**, 037901 (2001).
- 10 W. R. Anderson, J. R. Veale, and T. F. Gallagher, *Phys. Rev. Lett.* **80**, 249 (1998).
- 11 I. Mourachko, D. Comparat, F. de Tomasi, A. Fioretti, P. Nosbaum, V. M. Akulin, and P. Pillet, *Phys. Rev. Lett.* **80**, 253 (1998).
- 12 M. P. Robinson, R. L. Tolra, M. W. Noel, T. F. Gallagher, and P. Pillet, *Phys. Rev. Lett.* **85**, 4466 (2000).
- 13 S. K. Dutta, D. Feldbaum, A. Walz-Flannigan, J. R. Guest, and G. Raithel, *Phys. Rev. Lett.* **86**, 3993 (2001).
- 14 K. Singer, M. Reetz-Lamour, T. Amthor, S. Fölling, M. Tscherneck, and M. Weidemüller, *J. Phys. B: At. Mol. Opt. Phys.* **38**, 321 (2005).
- 15 A. J. Kerman, V. Vuletić, C. Chin, and S. Chu, *Phys. Rev. Lett.* **84**, 439 (2000).
- 16 M. Weidemüller, M. Reetz-Lamour, T. Amthor, J. Deiglmayr, and K. Singer, *Laser Spectroscopy XVII*, edited by E. A. Hinds, A. Ferguson, and E. Riis (World Scientific, New Jersey, 2005), p. 264.
- 17 C. Boisseau, I. Simbotin, and R. Côté, *Phys. Rev. Lett.* **88**, 133004 (2002).
- 18 K. Singer, J. Stanojevic, M. Weidemüller, and R. Côté, *J. Phys. B: At. Mol. Opt. Phys.* **38**, S295 (2005).
- 19 D. Tong, S. M. Farooqi, J. Stanojevic, S. Krishnan, Y. P. Zhang, R. Côté, E. E. Eyler, and P. L. Gould, *Phys. Rev. Lett.* **93**, 063001 (2004).

- 20** K. Singer, M. Reetz-Lamour, T. Amthor, L. G. Marcassa, and M. Weidemüller, Phys. Rev. Lett. **93**, 163001 (2004).
- 21** T. F. Gallagher, P. Pillet, M. P. Robinson, B. Laburthe-Tolra, and M. W. Noel, J. Opt. Soc. Am. B **20**, 1091 (2003).
- 22** T. F. Gallagher, Rydberg atoms (Cambridge University Press, Cambridge, 1994).
- 23** W. Li, P. J. Tanner, and T. F. Gallagher, Phys. Rev. Lett. **94**, 173001 (2005).
- 24** M. L. Zimmerman, M. G. Littman, M. M. Kash, and D. Kleppner, Phys. Rev. A **20**, 2251 (1979).
- 25** K. A. Safinya, J. F. Delpech, F. Gounand, W. Sandner, and T. F. Gallagher, Phys. Rev. Lett. **47**, 405 (1981).
- 26** T. G. Walker and M. Saffman, J. Phys. B **38**, S309 (2005).
- 27** A. L. De Oliveira, M. W. Mancini, V. S. Bagnato, and L.G. Marcassa, Phys. Rev. Lett. **90**, 143002 (2003).
- 28** W. R. Anderson, M. P. Robinson, J. D. D. Martin, and T.F. Gallagher, Phys. Rev. A **65**, 063404 (2002).
- 29** S. Westermann, T. Amthor, A. L. de Oliveira, J. Deiglmayr, M. Reetz-Lamour, and M. Weidemüller, Eur. Phys. J. D **40**, 37 (2006).
- 30** J. Deiglmayr, M. Reetz-Lamour, T. Amthor, S. Westermann, A. L. de Oliveira, and M. Weidemüller, Opt. Comm. **264**, 293 (2006).

## 11

# Quantum State Engineering with Spins

Andreas Heidebrecht, Jens Mende, and Michael Mehring

### 11.1

#### Introduction

Since the invention of the first quantum algorithm by Deutsch [1], great theoretical advancements have been made in the field of quantum computing and quantum cryptography. There now exist a number of algorithms for problems which can be solved exponentially faster on a quantum computer than on a classical computer. Schemes for error correction and protocols for quantum cryptography have been devised and substantial progress has been made in understanding the phenomenon of entanglement which lies at the heart of quantum information.

Extensive efforts have also been made to implement these theoretical concepts experimentally. The first technique to demonstrate *quantum computing* (QC) was Nuclear Magnetic Resonance (NMR) [2,3]. Other key concepts of QC demonstrated with high resolution NMR in liquid state are most notably the implementation of different QC algorithms such as Deutsch [2, 4–7], Grover [8–10] and Shor [11] algorithms. Preparation of *pseudo-pure states* and error correction protocols have also been demonstrated.

The objects of theoretical discussion of QC are *qubits* and *quantum gates*. A qubit is the unit of quantum information and can in practice be represented by any two-level quantum system. Gates are operations performed by the experimentalist on the qubits to modify their state. The required set of available gates must be complete in the sense that any arbitrary operation on the system must be constructible from this basic set. [12] Further considerations place additional requirements on the properties of a suitable quantum system such as degree of decoherence as compared to the achievable speed of gates, scalability and so on [13].

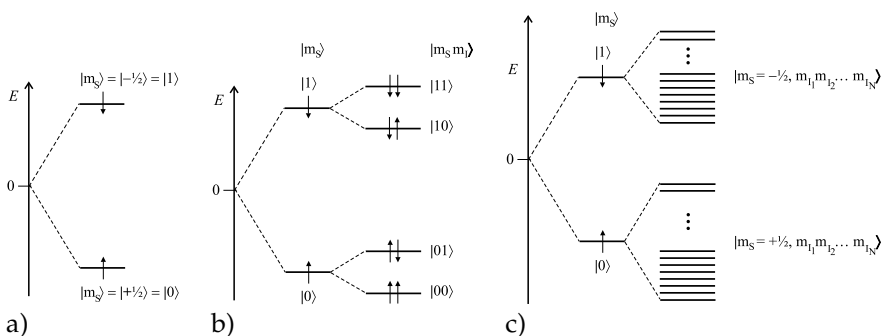


**Fig. 11.1** Energy level diagram of a) a single electron spin- $\frac{1}{2}$ ; b) electron spin- $\frac{1}{2}$  coupled to a nuclear spin or alternatively two different nuclear spins; c) system consisting of  $N$  nuclear spins coupled to an electron spin.

### 11.1.1

#### Quantum States of Spins

The archetypical representative of a two-level system is the spin- $\frac{1}{2}$  in a constant magnetic field. When a particle with the spin- $\frac{1}{2}$  is placed in an external magnetic field  $B_0$  along the  $z$ -axis, its Hamiltonian is given by

$$\mathcal{H} = -\mu_s \vec{B}_0 = -\gamma \hbar \vec{S} \vec{B} = -\gamma \hbar S_z B_0 \quad (11.1)$$

where  $\gamma$  is the *gyromagnetic ratio* whose sign is negative for the electron spin and positive for the nuclear spin. The eigenstates of this Hamiltonian correspond to the parallel and anti-parallel orientation of the spin with respect to the external field with the spin quantum number  $m_S = \pm \frac{1}{2}$ . These basis states are called “up” and “down”. Other commonly used notations are  $|\uparrow\rangle$  and  $|\downarrow\rangle$ , and  $|+\frac{1}{2}\rangle$  and  $|-\frac{1}{2}\rangle$ . For the purposes of quantum computing, where usually only two-level systems are discussed, the notation  $|0\rangle$  and  $|1\rangle$  is more convenient.

Fig. 11.1 a) shows the energy level diagram for a spin whose gyromagnetic ratio is negative (typical for electron spins). The splitting of the energy levels is called the *Zeeman splitting*. For nuclear spins the gyromagnetic ratio is in most cases positive, such that the order of the energy levels is reversed. A quantum system consisting of two qubits has four energy levels as shown in Fig. 11.1 b). The different base states are labeled according to the spin quantum number of the constituent spins.

Generally, a system comprised of  $N$  spin- $\frac{1}{2}$  particles has  $2^N$  energy levels spanning the basis of the Hilbert space. Fig. 11.1 c) shows an example of an electron spin coupled to  $N$  nuclear spins- $\frac{1}{2}$ .

The notation using state vectors as above is suitable for description of isolated *pure quantum systems*. In magnetic resonance, one predominantly deals with large ensembles of spins, thus the need arises for a formalism capable of dealing with pure as well as mixed states. The standard framework used for this purpose is the *density matrix* formalism.

A general state of a two-level system described by the state vector

$$|\psi\rangle = c_0 |0\rangle + c_1 |1\rangle \quad (11.2)$$

is represented by the  $4 \times 4$  density matrix

$$\rho_\psi = |\psi\rangle \langle \psi| = \begin{pmatrix} c_0 c_0^\dagger & c_0 c_1^\dagger \\ c_1 c_0^\dagger & c_1 c_1^\dagger \end{pmatrix} \quad (11.3)$$

The basis states  $|0\rangle$  and  $|1\rangle$  commonly used in describing quantum algorithms are expressed as

$$|0\rangle : \rho_0 = \begin{pmatrix} 1 & 0 \\ 0 & 0 \end{pmatrix} \quad \text{and} \quad |1\rangle : \rho_1 = \begin{pmatrix} 0 & 0 \\ 0 & 1 \end{pmatrix} \quad (11.4)$$

In magnetic resonance, it is most natural to also use the basis consisting of the spin component operators expressed in units of  $\hbar$  with the Pauli matrices and the unity matrix:

$$\begin{aligned} I_0 &= \begin{pmatrix} 1 & 0 \\ 0 & 1 \end{pmatrix}, & I_x &= \frac{1}{2} \begin{pmatrix} 0 & 1 \\ 1 & 0 \end{pmatrix}, \\ I_y &= \frac{1}{2} \begin{pmatrix} 0 & -i \\ i & 0 \end{pmatrix}, & I_z &= \frac{1}{2} \begin{pmatrix} 1 & 0 \\ 0 & -1 \end{pmatrix} \end{aligned} \quad (11.5)$$

In systems consisting of more than one spin, this basis is extended to include spin product operators by taking the direct product of the single spin operators:

$$I_{y_1} I_{z_2} = I_y \otimes I_z = \frac{1}{4} \begin{pmatrix} 0 & 0 & -i & 0 \\ 0 & 0 & 0 & i \\ i & 0 & 0 & 0 \\ 0 & -i & 0 & 0 \end{pmatrix} \quad (11.6)$$

A general pure state of a single spin (qubit) is then given by

$$\rho = \frac{1}{2} I_0 + a_x I_x + a_y I_y + a_z I_z \quad (11.7)$$

Magnetic resonance experiments are usually performed at temperatures where the spin ensembles are close to the maximally mixed state. This has led to the question, to what extent such experiments actually involve entanglement and can consequently be considered valid implementations of quantum algorithms [14, 15]. The realization of proper entanglement at the available temperatures is problematic<sup>1</sup>. However, it is possible to rewrite the density matrix such that it has the same operator structure as that of a pure state:

$$\rho = (1 - \epsilon) \frac{1}{2} I_0 + \epsilon \left( \frac{1}{2} I_0 + a_x I_x + a_y I_y + a_z I_z \right) \quad (11.8)$$

where  $\epsilon$  is, in typical experiments, at most in the order of  $10^{-4}$ . The dominating term  $(1 - \epsilon) \frac{1}{2} I_0$  is invariant under unitary transformations and cannot be observed in magnetic resonance. Thus, all quantum algorithms take on the same form as in the case of pure states. In particular, the unitary transforms and pulse sequences can be constructed and studied in detail.

## 11.2

### Deutsch-Josza Algorithm

#### 11.2.1

##### The Deutsch-Josza Algorithm

Peter Deutsch was the first to formulate a problem which can be solved exponentially faster when a quantum computer is used as opposed to classical computer [1, 19]. Formally, the problem consists in determining a property of certain functions with as few evaluations of these functions as possible. The functions in question map an input consisting of  $N$  bits to a single output bit. Only two types of functions are considered: *constant* functions, i.e., those returning the same output for all possible inputs; and *balanced* functions, which produce 1 as often as 0 over the entire range of inputs. A unitary transform  $U_f$  which implements the evaluation of a tested function  $f$  for any given input is called an *oracle* for  $f$ . The Deutsch-Josza algorithm allows the distinction between constant and balanced functions with exponentially fewer applications of  $U$  when a quantum superposition of all possible inputs is used.

The original algorithm proposed by Deutsch and Josza [1] has later been significantly simplified [20, 21]. In its modern form, the block diagram of the DJ algorithm is shown in Fig. 11.2. In the first step, all the qubits of the input

1) It is, in principle, possible to reach the so called *quantum limit* [16, 17] by using low temperatures or polarizing the spin ensemble by other means such as polarization transfer from optically excited triplet states. Under such conditions, it is possible to achieve  $\epsilon$  on the order of magnitude of 1 [18].

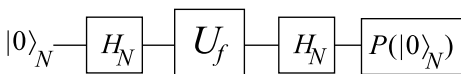


**Fig. 11.2** Block diagram of the optimized version of the Deutsch-Josza algorithm.

state  $|0\rangle_N = |0\dots 0\rangle$  are brought into coherent superposition of their basis states by the  $N$ -qubit *Hadamard transform*  $H_N = H \otimes H \otimes \dots \otimes H \otimes H$ . The application of  $U_f$  then encodes the global property of the tested function in the phases of the qubits. The final Hadamard transform produces an interference of the phase factors of the single qubits as is seen in the following equation

$$\begin{aligned}
 |0\rangle_N &\xrightarrow{H_N} \frac{1}{\sqrt{2^N}} \sum_{k=0}^{2^N-1} |k\rangle_N \\
 &\xrightarrow{U_f} \frac{1}{\sqrt{2^N}} \sum_{k=0}^{2^N-1} (-1)^{f(k)} |k\rangle_N \\
 &\xrightarrow{H_N} \frac{1}{2^N} \sum_{k=0}^{2^N-1} (-1)^{f(k)} \sum_{m=0}^{2^N-1} (-1)^{\sum_{j=0}^{N-1} m_j k_j} |m\rangle_N
 \end{aligned} \tag{11.9}$$

The decision criterion is given by the amplitude of the input state  $|0\rangle_N$  in the output state:

$$P(|0\rangle_N) = \frac{1}{2^N} \left| \sum_{k=0}^{2^N-1} (-1)^{f(k)} \right| = \begin{cases} 1 & \text{if } f \text{ constant} \\ 0 & \text{if } f \text{ balanced} \end{cases} \tag{11.10}$$

## 11.2.2

### Implementation of the 3-qubit Deutsch-Josza Algorithm Using Liquid State NMR

#### 11.2.2.1 2,3,4-Trifluoroaniline

The Deutsch-Josza algorithm has become a standard procedure for demonstrating the techniques and approaches to implementing quantum computing by means of magnetic resonance. The works more closely related to our contribution are [5–7, 22].

We used 100% 2,3,4-Trifluoroaniline in liquid state at room temperature in a home-built 300 MHz NMR spectrometer. The structure and spectrum of this molecule are shown in Fig. 11.3.

The lines of the  $3^{19}\text{F}$ -spins are separated by approximately 6.5 ppm and the  $J$ -couplings are  $J_{12} \approx J_{23} \approx 20$  Hz whereas  $J_{13} \approx 1.5$  Hz. The Hamiltonian is approximately given by

$$H = \omega_1 \mathbf{I}_{z_1} + \omega_2 \mathbf{I}_{z_2} + \omega_3 \mathbf{I}_{z_3} + 2\pi J (\mathbf{I}_{z_1} \mathbf{I}_{z_2} + \mathbf{I}_{z_2} \mathbf{I}_{z_3}) \tag{11.11}$$

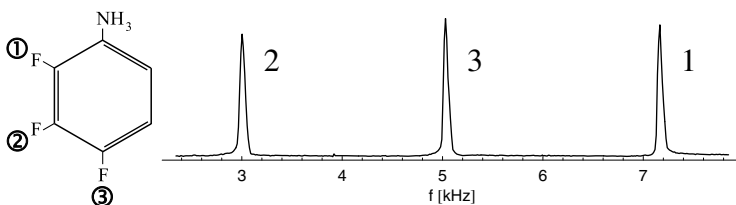


**Fig. 11.3** a) Molecular structure of 2,3,4-Trifluoroaniline. b) NMR spectrum.

and has the same structure as in experiments described in [6]. The missing coupling  $J_{13}$  requires additional effort when preparing the pseudo-pure states and implementing some of the Deutsch-Josza oracles as will be explained below.

#### 11.2.2.2 Preparation of Pseudo-pure States

As mentioned in Sect. 11.1.1, the first step to implementing the Deutsch-Josza algorithm is the preparation of the 3-qubit pseudo-pure input state

$$\rho_{000} = \frac{1}{8}I_0 + \frac{1}{4}I_{z_1} + \frac{1}{4}I_{z_2} + \frac{1}{4}I_{z_3} + \frac{1}{2}I_{z_1}I_{z_2} + \frac{1}{2}I_{z_1}I_{z_3} + \frac{1}{2}I_{z_2}I_{z_3} + I_{z_1}I_{z_2}I_{z_3} \quad (11.12)$$

from the Boltzmann state

$$\rho_B = I_0 + \epsilon (I_{z_1} + I_{z_2} + I_{z_3}) \quad (11.13)$$

This is an essentially non-unitary transformation and therefore requires dissipative operations in addition to the unitary rf-pulses. Gradient pulses followed by a period of free diffusion were used to implement these steps. The multi-qubit terms not present in the Boltzmann state are created utilizing the  $J$ -coupling between spins in times of free evolution. The pulse sequence deployed to obtain  $\rho_{000}$  is shown in Fig. 11.4. This rather complex procedure is necessary because of the missing direct coupling between the qubits 1 and 3. Interestingly, the term  $I_{z_1}I_{z_2}I_{z_3}$  is more readily obtained than  $I_{z_1}I_{z_3}$ . The latter must be prepared from the former by additional periods of free evolution. The procedure depicted in Fig. 11.4 can be used with small modifications to obtain the other seven pseudo-pure states [23]. With proper adjustment of some of the pulse rotation angles to account for pulse imperfections and relaxation effects, we were able to prepare pseudo-pure states with *fiducial* close to unity. This has been measured by full tomography of the  $8 \times 8$  density matrix. The resulting tomogram as given in Fig. 11.5 shows the quality of preparation of the input state  $\rho_{000}$ .

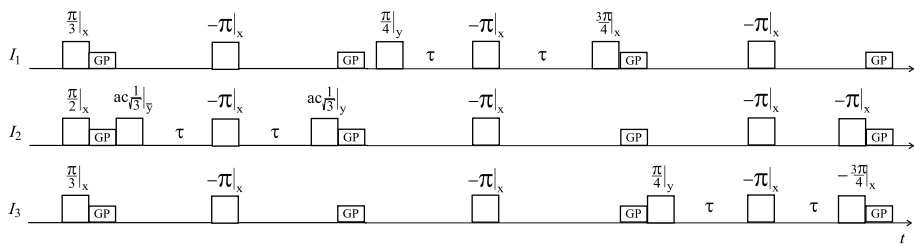


**Fig. 11.4** Pulse sequence used for the preparation of the pseudo-pure state  $\rho_{000}$ .

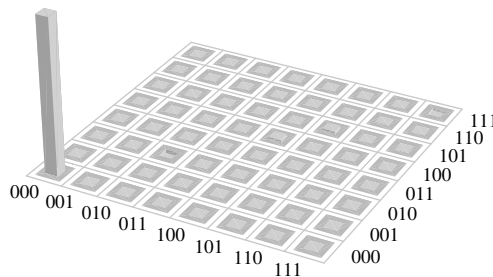


**Fig. 11.5** Tomogram of the density matrix of an experimentally prepared pseudo-pure state  $\rho_{000}$ .

### 11.2.2.3 Results on the 3-qubit DJ-algorithm

Starting with the pseudo pure state  $\rho_{000}$  described in the previous section, we implemented a number of oracles for a selected set of test functions. There is a total of 2 constant and 70 balanced functions in the 3-qubit DJ problem. The unitary transformation corresponding to a given function is trivially obtained from its inputs and outputs. The set of operations, required to implement such a transformation, however, is closely connected to the operator structure of the corresponding matrix and the coupling network between spins [6].

According to the combination of one-, two-, and three-qubit gates needed to implement the transformation, we have divided the oracles in seven sets. Within each set, the transformations are equivalent under exchange of the qubits and the labeling of the basis states. The oracles requiring two-qubit gates can be further subdivided into those utilizing direct qubit-qubit couplings and those that require successive application of two- and three-qubit gates to compensate for the missing interaction. For instance, a straight forward implementation of the oracle for the function  $f_7$  with the output sequence  $\{0, 0, 1, 1, 0, 1, 1, 0\}$

$$U_7 = I_{z_2} + 2I_{z_1}I_{z_3} + 2I_{z_2}I_{z_3} - 4I_{z_1}I_{z_2}I_{z_3} \quad (11.14)$$

employs a two-qubit gate between qubits 1 and 3 which is not present in the coupling network.

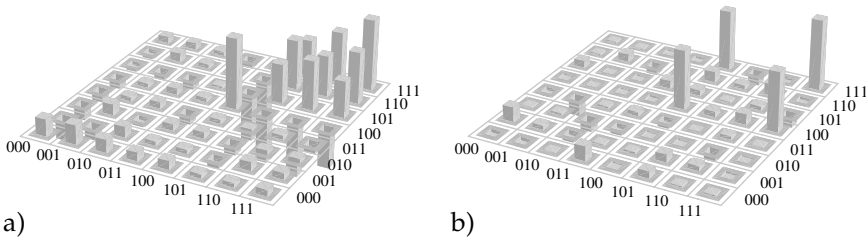


**Fig. 11.6** a) Output density matrix of the oracle for the function  $f_6$ . b) The same density matrix after a local transformation showing the Bell state  $\Phi^+$  for the qubits 2 and 3.

We have implemented nine different oracle transformations and evaluated the decision criterion Eq. (11.10). Fig. 11.6 a) shows the tomogram of the output state for the oracle of the balanced function  $f_6$  with the output sequence  $\{0, 0, 0, 1, 1, 1, 1, 0\}$ . In all cases, the decision parameter was within 0.2 of the expected value.

In addition to the evaluation of the decision criterion, it is instructive to analyze the output state of the DJ algorithm in more detail. It has been shown previously [21] that the 2-qubit version of the DJ algorithm does not involve entanglement. In the 3-qubit case, intermediate entanglement is necessary for some but not all tested functions. This is most readily seen by subjecting the output state of the algorithm to a series of *local* transformations. E.g., the output  $\rho_6$  of  $U_6$  can be partially separated into the state  $\rho_1$  of the qubit 1 and the Bell state  $\Phi^+$  in the subspace of qubits 2 and 3:

$$P_{x_3}(\pi)P_{y_2}(-\frac{\pi}{2})\rho_6 = \left(\frac{1}{2}\mathbf{I}_0 - \mathbf{I}_{z_1}\right) \left(\frac{1}{4}\mathbf{I}_0 + \mathbf{I}_{x_2}\mathbf{I}_{x_3} + \mathbf{I}_{y_2}\mathbf{I}_{y_3} + \mathbf{I}_{z_2}\mathbf{I}_{z_3}\right) = \\ \begin{pmatrix} 0 & 0 \\ 0 & 1 \end{pmatrix} \otimes \begin{pmatrix} \frac{1}{2} & 0 & 0 & \frac{1}{2} \\ 0 & 0 & 0 & 0 \\ 0 & 0 & 0 & 0 \\ \frac{1}{2} & 0 & 0 & \frac{1}{2} \end{pmatrix} \quad (11.15)$$

where  $P_{\phi_j}(\beta)$  means an rf pulse with the phase  $\phi$  and rotation angle  $\beta$ , applied to the spin  $j$ . Thus transformed experimental result is shown in Fig. 11.6 b). The maximally entangled *Greenberger-Horne-Zeilinger* state  $1/\sqrt{2}(|000\rangle + |111\rangle)$  also appears as the output of the 3-qubit DJ algorithm. For further details see [23].

Some of the experiments described above involve in excess of 50 single operations and have execution times over 100 ms. No other experimental technique has so far been able to provide this combination of accurate control of the quantum state and long time preservation of coherence. This shows that,

although quantum computing with liquid state high resolution NMR has its limitations, it is a very useful testbed for theoretical and experimental concepts and an excellent technique for problems involving a limited number of qubits.

### 11.3

#### Entanglement of an Electron and Nuclear Spin in $^{15}\text{N}@\text{C}_{60}$

There have been several proposals for the use of the endohedral fullerene  $^{15}\text{N}@\text{C}_{60}$  as basic building block of a quantum computer [24–26]. In this section we summarize some of the aspects of the use of this molecule for the purposes of quantum information.

The fullerene molecule  $\text{C}_{60}$  presents the  $^{15}\text{N}$  enclosed within it with an almost spherical environment as shown in Fig. 11.7 a). We used samples prepared according to [27] which contained  $^{15}\text{N}@\text{C}_{60}$  embedded in a solid  $\text{C}_{60}$  matrix at a concentration of approximately  $10^{-4}$ . The measurements were performed in an Electron Paramagnetic Resonance (EPR) spectrometer at  $T = 50$  K at X-band frequency (9.5 GHz). The manipulation of the nuclear spins was done by means of an Electron Nuclear Double Resonance (ENDOR) probe at rf frequencies in the range of 12 MHz to 35 MHz. In this setup, the state of the nuclear spin is not directly observable. Its readout is therefore performed indirectly via the EPR signal by encoding the desired information with special phase modulation procedures [28].

The trapped nitrogen atom carries a nuclear spin  $I = 1/2$  and an electron spin  $S = 3/2$ . The corresponding Hamiltonian in first order and its eigenvalues are given by

$$\mathcal{H} = \hbar (\omega_S S_z + \omega_I I_z + a S_z I_z) \quad (11.16)$$

$$E(m_S, m_I) = \hbar (\omega_S m_S + \omega_I m_I + a m_S m_I) \quad (11.17)$$

Where  $\omega_S$  and  $\omega_I$  are the Larmor frequencies of the electron and nuclear spin respectively and  $a$  is the hyperfine coupling strength. The corresponding energy level diagram is displayed in Fig. 11.7 b). Due to the high local symmetry, all EPR transitions ( $\Delta m_S = \pm 1$ ) are degenerate and lead to two EPR lines corresponding to the nuclear quantum numbers  $m_I = \pm 1/2$  [27, 29]. There are four ENDOR lines ( $\Delta m_I = \pm 1$ ) for the four electron spin states  $m_S \in \{3/2, 1/2, -1/2, -3/2\}$ . The Nitrogen atom is well shielded from the environment leading to very long relaxation times and narrow EPR lines, such that selective excitation of the electron spin transitions is viable.

Most quantum algorithms operate with qubits, i.e., 2-level systems. The electron spin in  $^{15}\text{N}@\text{C}_{60}$  has four energy levels and is, therefore, not strictly speaking a qubit. It is, however, possible to confine the treatment to a subset of the  $S$ -spin states. The presence of the other energy levels is still relevant

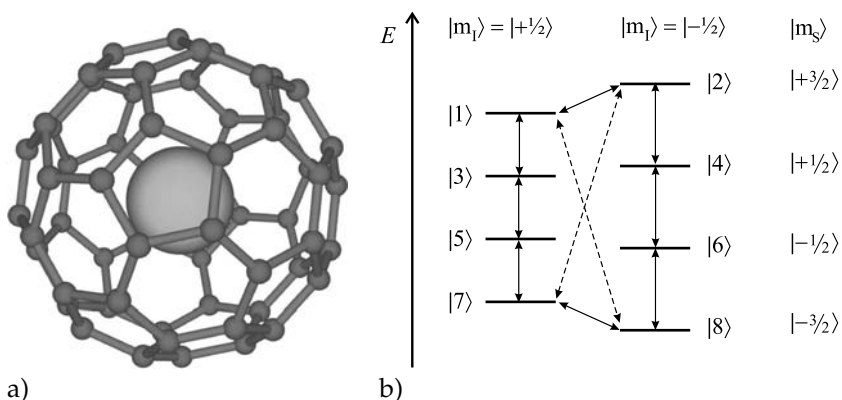


**Fig. 11.7** a) Molecular structure of the endohedral  $^{15}\text{N}@\text{C}_{60}$  fullerene molecule. b) Energy level diagram. The vertical lines indicate transitions at the EPR frequency ( $\Delta m_S = \pm 1$ ). The horizontal lines correspond to ENDOR transitions ( $\Delta m_I = \pm 1$ ). The dashed lines indicate the levels involved in the prepared entangled states.

and must be carefully considered in calculations and experiment. We have confined ourselves to using the levels  $+3/2$  and  $-3/2$  as a single fictitious qubit for the electron and the nuclear spin states  $m_I = \pm 1/2$  as a second qubit. In the following, we refer to these states by the signs of the spin quantum numbers  $|\pm \frac{3}{2} \pm \frac{1}{2}\rangle$ .

In this system we were able to generate the 2-qubit pseudo-pure state  $\rho_7$  (cf. Fig. 11.7) by applying appropriate pulses at the relevant selective EPR and ENDOR transitions. The density matrix  $\rho_7$  is an  $8 \times 8$  diagonal matrix which contains the 2-qubit submatrix with elements  $\{r_1, r_2, r_7, r_8\}$  where the 2-qubit pseudo-pure state  $\rho_7$  is expected to be  $\{0, 0, 1, 0\}$ . The tomogram of the corresponding density matrix as given in Fig. 11.8 a) clearly shows the high fidelity of the preparation.

Starting with this state we created the pseudo-entangled states corresponding to the Bell states  $\Psi_{27}^\pm$  and  $\Phi_{18}^\pm$ . The entangled state shown in Fig. 11.8 b) corresponds to the subsystem  $\{m_S = \pm 3/2; m_I = \pm 1/2\}$ . Its preparation was achieved by a selective  $\pi/2$ -pulse at the ENDOR transition immediately followed by a selective  $\pi$ -pulse at the appropriate EPR transition. In order to perform a tomography on the resulting density matrix a phase encoded inverse sequence was applied to determine the relevant parts of the density matrix. For more details consult [28, 42].

These findings demonstrate that atoms trapped in endohedral fullerenes, indeed, constitute a viable platform for more advanced quantum processors and quantum memories involving some sort of switchable interaction between the basic units. Even for small ensembles or isolated systems or at tempera-

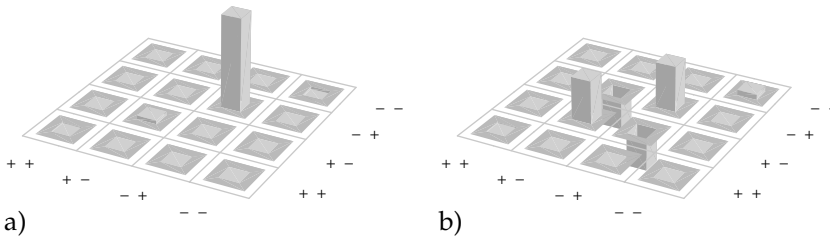


**Fig. 11.8** Density matrices of the quantum states prepared in  $^{15}\text{N}@\text{C}_60$ :  
a) Pseudo-pure state  $\rho_7$ ; b) Pseudo-entangled Bell state  $\Psi^-$ .

tures below the quantum limit, we expect that the behavior of such systems will be comparable to the one observed close to the maximally mixed state. In fact it was pointed out that the current system could reach the quantum limit at an EPR frequency of 95 GHz at 7K [28].

## 11.4

### Spin Quantum Computing in the Solid State: S-bus

The early experiments on quantum information with magnetic resonance were preformed using NMR in the liquid state at room temperature. The advantages of this approach are highly developed experimental techniques, narrow transition lines, simple and well understood interactions.

The disadvantages are spectral crowding, relatively weak coupling between the qubits and the scalability problems due to the large ensemble size. Magnetic resonance in highly ordered solid state systems promises to alleviate these shortcomings because it offers much stronger interactions and other intriguing possibilities for coupling isolated quantum computers with each other. There have been many proposals of different schemes to implement quantum computing in solid state systems. We pursue an arrangement called the *S-bus*.

#### 11.4.1

##### The S-bus Concept

The S-bus concepts derives from the early experiments on Multiple Quantum ENDOR (MQE) [30] which were detailed in [31]. In the S-bus concept [32–34] sketched in Fig. 11.9 the constituent qubits are implemented through nuclear spins- $\frac{1}{2}$  (*I*-spins) strongly coupled to a “central” electron spin (the *S*-spin) via the hyperfine interaction. The *S*-spin thus plays the role of a “quantum-bus” connecting to the *I*-spins. In addition to this connection, the *I*-spins may directly interact with each other through dipole-dipole coupling. A similar sit-

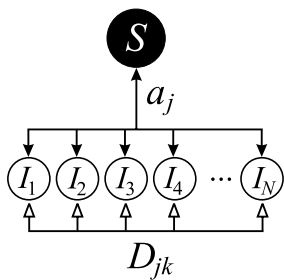


**Fig. 11.9** In the *S*-bus concept, a “central” electron spins (*S*-spin) is used to serve as a *quantum-bus* connecting the nuclear spins (*I*-spins) serving as qubits.

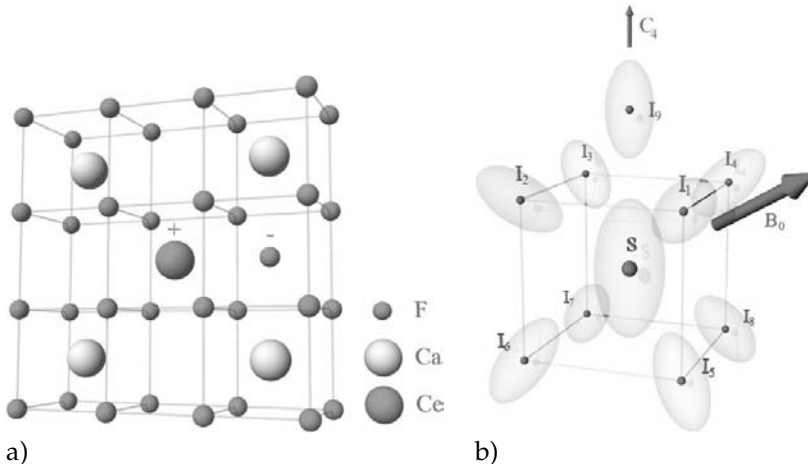


**Fig. 11.10** a) Crystal structure of  $\text{CaF}_2 : \text{Ce}^{3+}$ . b) Structure of the  $\text{Ce}^{3+}$  paramagnetic center with the next neighbor  $^{19}\text{F}^-$  nuclear spins. The strongly anisotropic interaction tensors are indicated.

uation arises in hetero-nuclear multiple quantum spectroscopy. See the earlier work [35] and a more recent contribution [36].

The main advantages of this concept are that the electrons by virtue of their  $10^3$  larger gyromagnetic ratio are much more strongly polarized than the nuclei and provide greater detection sensitivity. In solids with shallow donors (or acceptors), the electron spin may be delocalized over many nuclear spins leading to a huge quantum register of nuclear spins. Additionally, in many solids, the hyperfine couplings of nuclear spins are very large and strongly anisotropic such that the position of the ENDOR lines can be tuned over a large region depending on the orientation of the sample.

## 11.4.2

**Single Crystal  $\text{CaF}_2 : \text{Ce}^{3+}$  as an S-bus system**

For the implementation of the S-bus concept, we use a single crystal  $\text{CaF}_2$  doped with  $\text{Ce}^{3+}$  at a concentration of  $10^{-4}$  [32, 34]. The EPR and ENDOR properties of rare earth ions implanted in  $\text{CaF}_2$  have been studied extensively [37].

The crystal structure of  $\text{CaF}_2$  is shown in Fig. 11.10 a). The  $\text{Ce}^{3+}$ -ion substitutes for a  $\text{Ca}^{2+}$ -ion. The excessive charge is compensated by an additional interstitial  $\text{F}^-$ .<sup>2</sup> The configuration of the  $\text{Ce}^{3+}$ -center is shown in Fig. 11.10 b). The charge compensating  $\text{F}^-$  reduces the  $O_5^h$  symmetry of the host lattice to  $C_4$  by displacing the  $\text{Ce}^{3+}$ -ion and the fluorines in the neighboring plane. This results in a strongly anisotropic  $g$ -tensor of the electron and the hyperfine tensors of the nine adjacent  $^{19}\text{F}$  nuclei.

The magnetic Hamiltonian in this system is given by

$$\mathcal{H} = \frac{\mu_B}{\hbar} \mathbf{S} \cdot \mathbf{g} \cdot \mathbf{B}_0 + \frac{\mu_n}{\hbar} B_0 \sum_{j=1}^N g_{n_j} I_{z_j} + \mathbf{S} \cdot \sum_{j=1}^N \mathbf{A}_j \cdot \mathbf{I}_j + \sum_{j < k} \mathbf{I}_j \cdot \mathbf{D}_{jk} \cdot \mathbf{I}_k \quad (11.18)$$

where  $\mathbf{B}_0$  is the external magnetic field,  $\mathbf{g}$  is the electron  $g$ -tensor,  $g_{n_j}$  and  $\mathbf{A}_j$  the  $g$ -factor and the hyperfine tensor of the  $j$ -th nuclear spin, and  $\mathbf{D}_{jk}$  the dipole-dipole coupling between the  $j$ -th and  $k$ -th nuclear spins. This Hamiltonian can be approximated to first order by

$$\mathcal{H} = \omega_0 S_z + \sum_j \omega_0 I_{z_j} + S_z \sum_j a_{zzj} I_{z_j} + \sum_{j < k} D_{jk} I_{z_j} I_{z_k} \quad (11.19)$$

Different parts of this Hamiltonian are manipulated with microwave and rf pulses in the manner described in Sect. 11.3. Due to the strong anisotropy of the hyperfine coupling tensors, there exists a broad range of orientations of the external field where the ENDOR-spectrum is fully resolved. As an example, Fig. 11.11 shows the two sets of nuclear spin transitions corresponding to the two states of the electron spin  $m_S = \pm \frac{1}{2}$ . Since we are dealing with an ensemble, this indicates that we have, in principle, 18 independently accessible qubits.

In order to demonstrate the very high degree of correlations possible in this system, we performed *multi-quantum ENDOR* (MQE) [31] measurements. Fig. 11.12 a) shows the non-selective correlation of up to 20 nuclear spins. As shown in Fig. 11.12 b) it is also possible to create correlations between a

2) The charge compensating  $\text{F}^-$  can be situated locally at the  $\text{Ce}^{3+}$  or in the bulk material. The concentration of the former configuration can be boosted by the proper choice of the crystal growth parameters.

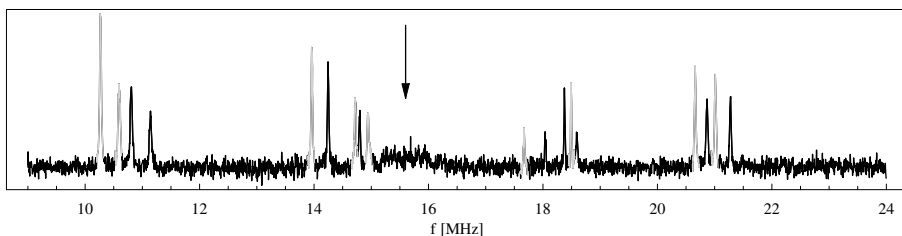


**Fig. 11.11** ENDOR spectrum of  $\text{CaF}_2 : \text{Ce}^{3+}$  showing the two sets of nuclear transitions corresponding to the two electron states  $m_S = \pm \frac{1}{2}$ . The arrow indicates the Larmor frequency of free  $^{19}\text{F}$  nuclei.

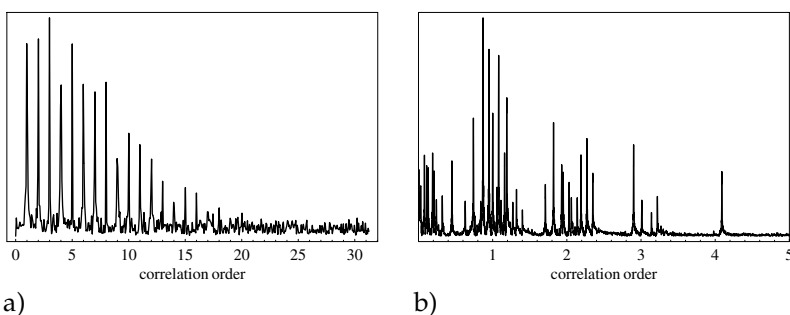


**Fig. 11.12** Multi-quantum ENDOR on  $\text{CaF}_2 : \text{Ce}^{3+}$ . a) Non-selective correlation of a large number of nuclear spins. Correlations of more than 20 qubits are readily obtainable. b) Correlation of four qubits by selective rf pulses.

chosen set of qubits by applying rf pulses selectively at their ENDOR resonance frequencies. These experiments demonstrate the favorable properties of  $\text{CaF}_2 : \text{Ce}^{3+}$  as an *S*-bus system.

#### 11.4.3

#### Experimental Details

A typical experiment begins with the preparation of a highly correlated nuclear spin state by a couple of  $\frac{\pi}{2}$  EPR pulses separated by the evolution time  $\tau_S$ . After the decay of the transient components due to  $T_2$  processes, the actual quantum computing pulse sequence is applied to the nuclear spins. After another decay period, the state of the qubits is encoded onto the electron spin by a detection sequence identical to the preparation sequence. For experimental reasons, the resulting state of the electron spin is observed by means of a remote echo detection sequence as shown in Fig. 11.13.

The operator part of the density matrix (truncated density matrix) of the spin system after the preparation sequence and the decay of  $x$ - and  $y$ -comp-

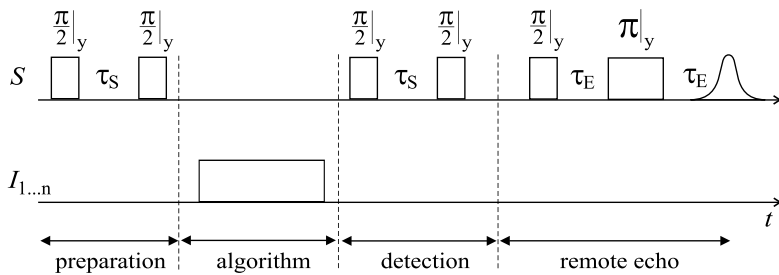


**Fig. 11.13** General pulse sequence used in the S-bus experiments consisting of the preparation, manipulation, and detection of the nuclear spin states.

onents has the form

$$\rho_p = S_z \left( \sum_j^N p_j I_{z_j} + \sum_{j < k}^N p_{jk} I_{z_j} I_{z_k} + \dots + p_{12\dots N} I_{z_1} \dots I_{z_N} \right) \quad (11.20)$$

Since we are only going to consider a small number of spins here (up to three), it is convenient to absorb the contributions of all other  $I$ -spins into pre-factors [32]. In the case of two  $I$ -spins, the truncated density matrix may be written as

$$\rho = S_z (p_1 I_{z_1} + p_2 I_{z_2} + p_{12} I_{z_1} I_{z_2}) \quad (11.21)$$

where  $p_i$  contain sums of products of the  $I_{z_k}$  with  $k \neq 1, 2$ . When all these contributions are traced out,  $p_i$  provide the coefficients of the components of the remaining 2-spin density matrix.

As already mentioned, direct detection of the state of the nuclear spins is not feasible. In order to obtain such information, a method based on MQE is employed. The pulse sequence is shown in Fig. 11.14. It consists of applying a  $\pi/2$ -pulse to each spin, followed by an inverse  $\pi/2$ -pulse whose phase is rotated according to  $\phi_i = 2\pi\nu_i t_{\text{MQE}}$  with the fictitious time  $t_{\text{MQE}}$ . The density

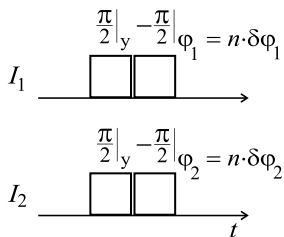


**Fig. 11.14** Pulse sequence for tomography of the nuclear part of the density matrix.

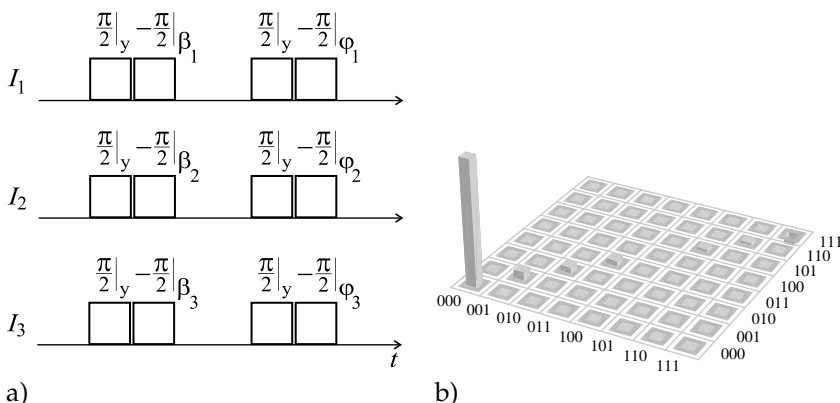


**Fig. 11.15** a) Pulse sequence used to prepare and detect the pseudo-pure states  $\rho_{ijk}$  of three nuclear spins in  $\text{CaF}_2 : \text{Ce}$ . b) Density matrix tomogram of  $\rho_{000}$ .

matrix after such a sequence is given by

$$\begin{aligned} \rho &= S_z (p_1 \cos \phi_1 I_{z_1} + p_2 \cos \phi_2 I_{z_2} + p_{12} \cos \phi_1 \cos \phi_2 I_{z_1} I_{z_2}) \\ &= S_z (q_1 I_{z_1} + q_2 I_{z_2} + q_{12} I_{z_1} I_{z_2}) \end{aligned} \quad (11.22)$$

The application of the detection sequence combined with the remote echo detection leads to the following amplitude of the detected electron spin echo

$$\begin{aligned} S &= 1 + p_1 q_1 + p_2 q_2 + p_{12} q_{12} \\ &= 1 + p_1^2 \cos \phi_1 + p_2^2 \cos \phi_2 + p_{12}^2 \cos \phi_1 \cos \phi_2 \end{aligned} \quad (11.23)$$

The Fourier transform of the echo amplitude with respect to  $t_{\text{MQE}}$  thus yields the amplitudes of the different terms of the density matrix. For an example see Fig. 11.17. Employing variations on this basic concept, tomography of the different states generated by the quantum algorithms is possible.

#### 11.4.4

##### 3-qubit Pseudo-pure States

Using these techniques, we have prepared pseudo-pure states  $\rho_{ijk}$  of three nuclear qubits in  $\text{CaF}_2 : \text{Ce}^{3+}$ . The pulse sequence used is given in Fig. 11.15 a). The decay of the off-diagonal components due to spin diffusion after the first set of pulses plays the role of dissipative operation mentioned in Sect. 11.2.2.2. The resulting density matrix is shown in Fig. 11.15 b) for the case of  $\rho_{000}$ . The fidelity of the preparation as defined by

$$F = 1 - \text{tr} \left\{ \left( \rho^{(\text{exp})} - \rho^{(\text{theo})} \right)^2 \right\} \quad (11.24)$$

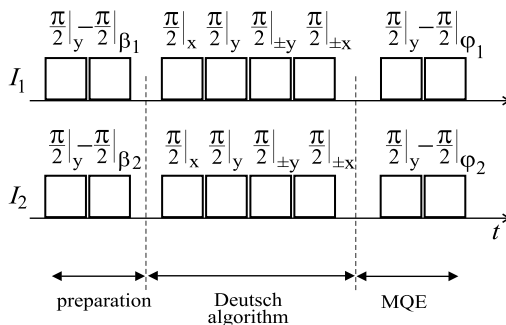


**Fig. 11.16** The pulse sequence for the 2-qubit Deutsch-Josza algorithm in the *S*-bus system including the preparation of the 2-qubit pseudo-pure state, the implementation of the Deutsch-Josza algorithm and the MQE-detection of the output state.

in this particular case is 0.96. We routinely generate pseudo-pure states with fidelities within 0.02 of unity.

#### 11.4.5

#### 2-qubit Deutsch-Josza Algorithm

The Deutsch-Josza algorithm with two qubits does not involve any entanglement [21] and is readily implemented in our *S*-bus system by the pulse sequence in Fig. 11.16. The sequence shown includes the pulses required for the preparation of the 2-qubit pseudo-pure state  $\rho_{00}$  the implementation of the Deutsch-Josza algorithm and the MQE-sequence used to encode the output state in the amplitude of the remote electron spin echo. The Deutsch-Josza algorithm is essentially implemented by applying separately to each of the two spins two consecutive  $\pi/2$ -pulses acting as the two Hadamard transforms. Various phase shifts of the two pulses with respect to each other implement the different oracle functions. The actual sequence we used utilizes composite pulses to correct for excitation inhomogeneities.

Four different functions were tested. The oracle transformations implementing these functions are diagonal matrices with diagonal elements

$$U_{0000} : \{+1, +1, +1, +1\} = I_0 \quad (11.25)$$

$$U_{0101} : \{+1, -1, +1, -1\} = -ie^{i\pi I_{z2}} \quad (11.26)$$

$$U_{0011} : \{+1, +1, -1, -1\} = -ie^{i\pi I_{z1}} \quad (11.27)$$

$$U_{0110} : \{+1, -1, -1, +1\} = e^{i\pi(I_{z1} + I_{z2})} \quad (11.28)$$

where the oracles only differ by different phase shifts of  $\pi$ .

The resulting MQE-spectra for the four possible test functions are shown in Fig. 11.17. The constant function is clearly recognized by the fact that its

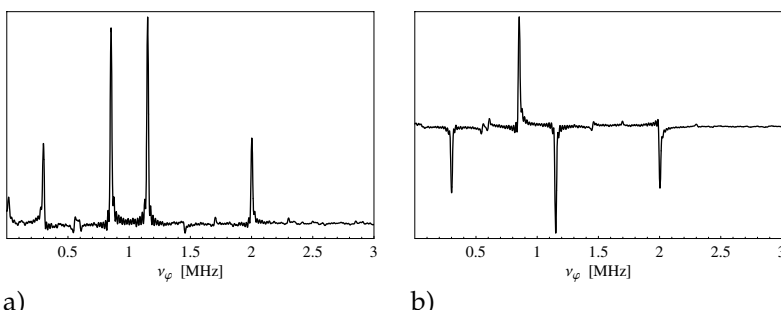


**Fig. 11.17** MQE-tomography of the four output states of the 2-qubit Deutsch-Jozsa algorithm in the *S*-bus system after application of the four oracle transforms for the tested functions: (a)  $f_{0000}$ , (b)  $f_{0101}$ .

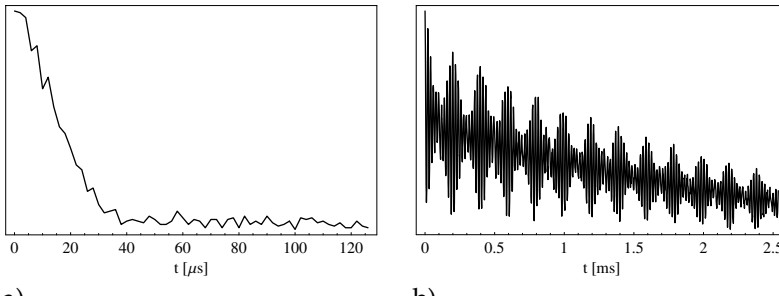
output state is  $\rho_{00}$ . The balanced functions produce the other pseudo-pure states which are orthogonal to  $\rho_{00}$  thus satisfying the decision criterion.

#### 11.4.5.1 Controlling Nuclear Spin Decoherence in $\text{CaF}_2 : \text{Ce}$

The experiments on the *S*-bus system described above demonstrate the feasibility of the *S*-bus concept and the  $\text{CaF}_2 : \text{Ce}^{3+}$  as a suitable implementation platform. However, they did not involve any coherence transfer between linear and quadratic terms in  $I_{z_j}$ . Such a transfer is required for the implementation of the fundamental  $C_{\text{NOT}}$  operation and must utilize the spin-spin coupling between the  $I$ -spins.

Since the dipolar couplings between the nuclear spins in  $\text{CaF}_2 : \text{Ce}^{3+}$  lie in the range of 1 kHz – 10 kHz, typical gate times are on the order of 100  $\mu\text{s}$ . During this free evolution time, the spin system is subject to strong decoherence processes. This is due to the fact that the  $^{19}\text{F}$ -spins are abundant in the sample and form an extended spin network leading to fast spin diffusion away from the paramagnetic center caused by  $I_{+j}I_{-k} + I_{-j}I_{+k}$  flip-flop terms of the full Hamiltonian. Our first attempts at implementing the  $C_{\text{NOT}}$  gate indicate that the realization of multi-qubit algorithms will require suppression of such decoherence effects. We have deployed a series of established and novel pulse sequences in order to ascertain the feasibility of such decoherence suppression schemes.

The *free induction decay* (FID) of the nuclear spin magnetization which is dominated by  $T_2$ -processes indicates a  $T_2 = 30 \mu\text{s}$ . The simplest refocusing pulse sequence for a single spin, the *Hahn echo* sequence already yields a decay time on the order of  $T_2 \approx 400 \mu\text{s}$ . The more advanced single-spin sequences such as *spin locking* and *rotary echo* sequence indicate, however, that the coherence can be kept in the spin system for much longer periods of time of up to several milliseconds. Fig. 11.18 juxtaposes the FID and rotary echo decays to demonstrate this.



a)

b)

**Fig. 11.18** a) Free induction decay of a single nuclear spin in  $\text{CaF}_2$  : Ce. b) Coherence decay under the 1-spin rotary echo sequence.

The sequences mentioned in the previous paragraph, are designed to decouple a single spin from the environment as effectively as possible. In order to be able to utilize the coupling between a pair of spins, their interaction must be recoupled while maintaining the decoupling of all other interactions. The internuclear dipolar Hamiltonian is given approximately by

$$\mathcal{H}_D = \sum_{j < k} D_{jk} I_{z_j} I_{z_k} \quad (11.29)$$

which includes the couplings of all nuclei present. The effective Hamiltonian desired for the implementation of 2-qubit gate should have the form

$$\tilde{\mathcal{H}}_D = D_{jk} I_{z_j} I_{z_k} \quad (11.30)$$

We have experimentally evaluated a number of sequences commonly deployed in this situation.

The simplest sequence yielding the desired Hamiltonian in Eq. (11.30) is the *Spin Echo Double Resonance* (SEDR) sequence [38, 39] shown in Fig. 11.19. The average evolution is governed by the first order average Hamiltonian

$$\tilde{\mathcal{H}}_D^{(\text{SEDR})} = D_{jk} I_{z_j} I_{z_k}. \quad (11.31)$$

It effectively refocuses the inhomogeneity of the external field  $B_0$  and partially decouples the other nuclear spins. However, for long free evolution times  $\tau$  the suppression of the flip-flop terms during the free evolution becomes less and less effective, leading to a fast decay which is reflected in the linewidth of 2.2 kHz.

The *Carr-Purcell-Meiboom-Gill* (CPMG) sequence [40] which extends on the SEDR by employing multiple  $\pi$ -pulses provides better decoupling due to the shorter free evolution times and has the same average Hamiltonian. However it suffers from finite pulse width effects. In the limiting case of  $\tau = 0$

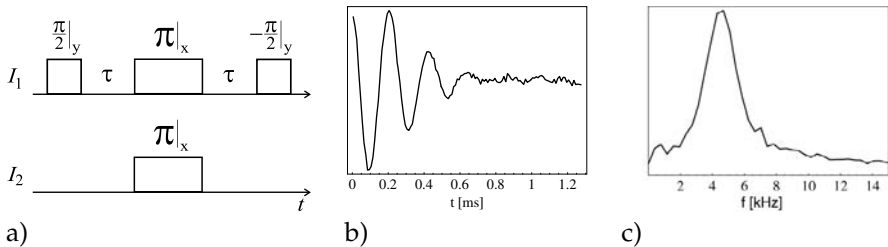


**Fig. 11.19** a) The SEDOR sequence for selective recoupling of two spins. b) Time trace of an oscillation under the SEDOR sequence. c) Fourier transform.

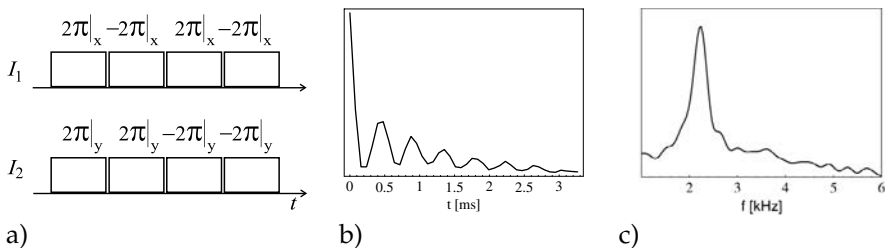


**Fig. 11.20** a) The  $8\pi$  pulse sequence for selective recoupling of a 2-spin dipolar interaction. b) Time evolution. c) Fourier transform

the CPMG sequence results in the *simultaneous spin locking* sequence which amounts to constant decoupling of all unwanted interactions. However, the effective Hamiltonian of the spin locking sequence has a tilted quantization axis:

$$\tilde{\mathcal{H}}_D^{(\text{SPIN LOCK})} = \frac{1}{2} D_{jk} (I_{z_j} I_{z_k} + I_{y_j} I_{y_k}) \quad (11.32)$$

Additionally, the constant rf irradiation aggravates the effect of the inhomogeneity of the rf field.

We have devised a pulse sequence [41], which combines the advantages of constant rf irradiation and avoids the problem of  $B_2$  inhomogeneity and a tilted quantization axis at the cost of scaling the interaction strength by a factor of 1/2. The average Hamiltonian under this pulse sequence is given by

$$\tilde{\mathcal{H}}_D^{(8\pi)} = \frac{1}{2} D_{jk} I_{z_j} I_{z_k} \quad (11.33)$$

The sequence is sketched in Fig. 11.20 a). The time trace and its Fourier transform in Fig. 11.20 b,c) demonstrate the resulting evolution. A detailed comparison with the other schemes shows that the current experimental implementation of this sequence does not realize the full potential which is due to pulse imperfections and the non-linearity of our rf amplifier.

## 11.5

### Summary and Outlook

We have demonstrated that quantum states of electron and nuclear spins in liquids and solids can be controlled at will to prepare appropriate initial states for quantum computing and implement complex unitary transformations as quantum algorithms. The advancement in coherent control of microwave and radio-frequency irradiations allows to tailor unitary transformations for the special need which differs significantly for liquids and solids and also for electron and nuclear spins.

In this contribution, we have presented several examples where the specific engineering of phase encoding of the irradiations allows to prepare and tomograph entangled states. Although these were pseudo-entangled states, the systems discussed here can be polarized either by going to a lower temperature or increasing the magnetic field in order to reach the quantum limit. Experimentally this is well in reach of current technology and will certainly be done.

### Acknowledgement

The authors would like to thank the Landesstiftung Baden-Württemberg and the BMBF for financial support.

### References

- 1 D. Deutsch and R. Jozsa, Proc. R. Soc. Lond. A **439**, 553–558 (1992).
- 2 J. A. Jones and M. Mosca, J. Chem. Phys. **109**, 1648–1653 (1998).
- 3 D. G. Cory, M. D. Price, and T. F. Havel, Physica D **120**, 82 (1998).
- 4 N. A. Gershenfeld and I. L. Chuang, Science **275**, 350–356 (1997).
- 5 K. Dorai, Arvind, and A. Kumar, Phys. Rev. A **41**, 042306/1–7 (2000).
- 6 D. Collins, K. W. Kim, W. C. Holton, H. Sierzputowska-Gracz, and E. O. Stejskal, Phys. Rev. A **62**, 022304 (2000).
- 7 Jaehyun Kim, Jae-Seung Lee, and Soonchil Lee, Phys. Rev. A **62**, 022312 (2000).
- 8 I. L. Chuang, N. A. Gershenfeld, and M. Kubinec, Phys. Rev. Lett. **80**, 3408–3411 (1998).
- 9 J. A. Jones, M. Mosca, and R. H. Hansen, Nature **393**, 344–6 (1998).
- 10 J. Kim, J. Seung, and S. Lee, Phys. Rev. A **65**, 054301–054304 (2002).
- 11 L. M. K. Vandersypen, M. Steffen, G. Breyta, C. S. Yannoni, M. H. Sherwood, and I. L. Chuang, Nature **414**, 883 (2001).
- 12 A. Barenco, C. H. Bennett, R. Cleve, D. P. DiVincenzo, N. Margolus, P. Shor, T. Sleator, J. A. Smolin, and H. Weinfurter, Phys. Rev. A **52**, 3457 (1995).
- 13 W. S. Warren, N. Gershenfeld, and I. Chuang, Science **277**, 1688 (1997).
- 14 S. L. Braunstein, C. M. Caves, R. Josza, N. Linden, S. Popescu, and R. Schack, Phys. Rev. Lett. **83**, 1054–1057 (1999).
- 15 R. Schack and C. M. Caves, Phys. Rev. A **60**, 4354–4362 (1999).
- 16 D. Bruss, J. Math. Phys. **43**, 4237 (2002), quant-ph/0110078.
- 17 K. Eckert, O. Gühne, F. Hulpke, P. Hyllus, J. Korbicz, D. Bruß, J. Mompart,

- M. Lewenstein, and A. Sanpera, *Quantum Information Processing*, chapter Entanglement properties of composite quantum systems (Wiley-VCH, 2003).
- 18** N. Gershenfeld and I. L. Chuang, *Science* **277**, 1689 (1997).
- 19** D. Deutsch, *Proc. R. Soc. Lond. A* **400**, 97–117 (1985).
- 20** R. Cleve, A. Ekert, C. Macchiavello, and M. Mosca, *Proc. R. Soc. Lond. A* **454**, 339–354 (1998).
- 21** D. Collins, K. W. Kim, and W. C. Holton, *Phys. Rev. A* **58**, R1633–R1636 (1998).
- 22** Arvind, Kavita Dorai, and Anil Kumar, *Pramana* **56**, L705–L713 (2001).
- 23** O. Mangold, A. Heidebrecht, and M. Mehring, *Phys. Rev. A* **70**, 042307 (2004).
- 24** W. Harneit, *Phys. Rev. A* **65**, 032322 (2002).
- 25** D. Suter and K. Lim, *Phys. Rev. A* **65**, 052309 (2002).
- 26** J. Twamley, *Phys. Rev. A* **67**, 052318 (2003).
- 27** T. Almeida Murphy, Th. Pawlik, A. Weidinger, M. Hoehne, R. Alcala, and J. M. Spaeth, *Phys. Rev. Lett.* **77**, 1075–1078 (1996).
- 28** M. Mehring, W. Scherer, and A. Weidinger, *Phys. Rev. Lett.* **93**, 206603 (2004).
- 29** N. Weiden, H. Käß, and K. P. Dinse, *J. Phys. Chem. B* **103**, 9826 (1999).
- 30** M. Mehring, P. Höfer, H. Käß, and A. Grupp, *Europhys. Lett.* **6**, 463 (1988).
- 31** M. Mehring and V. A. Weberruß, *Object Oriented Magnetic Resonance* (Academic Press, London, 2001).
- 32** M. Mehring and J. Mende, *Phys. Rev. A* **73**, 052303 (2006).
- 33** J. Mende, *Festkörper-Spin-Quantencomputing nach dem S-Bus-Konzept in CaF<sub>2</sub> : Ce*. PhD thesis, Universität Stuttgart (2005).
- 34** J. Mende and M. Mehring, The qubyte+1 S-bus system Ce:CaF<sub>2</sub>. In preparation (2006).
- 35** D. P. Weitekamp, J. R. Garbow, and A. Pines, *J. Chem. Phys.* **77**, 2870 (1982).
- 36** K. Saalwächter and H. W. Spiess, *J. Chem. Phys.* **114**, 5707 (2001).
- 37** J. M. Baker, E. R. Davies, and J. P. Hurrel, *Proc. Roy. Soc. A* **308**, 403 (1968).
- 38** M. Emschwiller, E. L. Hahn, and D. Kaplan, *Phys. Rev.* **118**, 414 (1960).
- 39** H. Thomann and M. Bernardo, *J. Am. Chem. Soc.* **118**, 5806 (1996).
- 40** S. Meiboom and D. Gill, *Rev. Sci. Inst.* **29**, 688 (1958).
- 41** A. Heidebrecht, M. Mehring, and J. Mende, *Solid State Nucl. Magn. Reson.* **29**, 90–94 (2006).
- 42** W. Scherrer and M. Mehring, Density matrix tomography of entangled electron and nuclear spin states in <sup>15</sup>Na@C<sub>60</sub>. [arXiv e-print: quant-ph/0602201] (2006).

## 12

# Improving the Purity of One- and Two-qubit Gates

*Sigmund Kohler and Peter Hänggi*

### 12.1

#### Introduction

The experimental realization of one-qubit gates in solid state setups [1–3] and two-qubit gates in ion traps [4, 5] and Josephson junctions [6] has demonstrated that these systems provide remarkable coherence properties although the goal of  $10^{-5}$  errors per gate operation [7] has not yet been accomplished experimentally. The unavoidable coupling to external degrees of freedom and the thereby caused decoherence still presents a main obstacle for the realization of a quantum computer. Several proposals to overcome the ensuing decoherence have been put forward, such as the use of decoherence free subspaces [8–12], coherence-preserving qubits [13], quantum Zeno subspaces [14], optimized pulse sequences [15, 16], dynamical decoupling [17–21], and coherent destruction of tunneling [22, 23]. Theoretical studies of decoherence of two-level systems have been extended to gate operations in the presence of an environment in [24–29].

A variety of suggestions towards coherence stabilization relies on the influence of external fields. One of the most prominent examples is the application of a sequence of  $\pi$ -pulses that flip the sign of the qubit-bath coupling operator resulting in a so-called dynamical decoupling (DD) of the qubit from the bath [17–21, 23]. A drawback of this scheme is the fact that it eliminates only noise sources with a frequency below the repetition rate of the pulses. This clearly causes practical limitations. However, these limitations may be circumvented by using a related scheme based on continuous-wave driving, i.e. one with a harmonic time-dependence, which allows higher driving frequencies.

A different proposal for coherence stabilization is to employ the physics of the so-called coherent destruction of tunneling (CDT). CDT has originally been discovered in the context of tunneling in a driven bistable potential [30–34]. There, it has been found that a particle which is initially in the, say, left well of a symmetric bistable potential, can be prevented from tunneling by

the purely coherent influence of an oscillating driving field. This effect is stable against dissipation in the sense that the AC field also decelerates the dissipative transitions from the left to the right well [35–37]. Moreover, if each well of the bistable potential is contacted to a respective electron reservoir, CDT becomes visible in current measurements [38, 39].

A less frequently studied problem is the extension of coherence stabilization protocols to systems that consist of two or more interacting qubits. Such an interaction is essential for two-qubit operations which represent an indispensable part of all quantum algorithms [40–42]. For a CNOT gate based on an isotropic Heisenberg interaction [24, 43], it has been proposed to stabilize coherence by applying a control field to one of the qubits and thereby obtain an effective Ising interaction which is less sensitive to the influence of environmental degrees of freedom [44]. This scheme possesses the beneficial properties that (i) it involves only intermediately large driving frequencies that can lie well below the bath cutoff and (ii) it does not increase the gate operation time. Moreover, since the driving field couples to the same coordinate as the quantum noise, this coherence stabilization is distinctly different from the recently measured dynamical decoupling of a spin pair from surrounding spin pairs [45].

In this work, we extend our previous studies on coherence stabilization of one- [23] and two-qubit operations [44] and, moreover, detail some technical aspects. In Sect. 12.2, we introduce a model for two qubits coupled to a heat bath and derive a Bloch-Redfield master equation to describe quantum dissipation and decoherence. This formalism is applied in Sects. 12.3 and 12.4, respectively, to the single qubit dynamics and to a two-qubit gate operation. In each case, we derive within a rotating-wave approximation (RWA) analytical results for the decay of the gate purity. Thereby, the proper treatment of the qubit-bath coupling is of crucial importance. The computation of averages for the ensemble of all pure states is deferred to the appendix.

## 12.2

### Quantum Gate with Bit-flip Noise

We consider a pair of qubits described by the Hamiltonian [24, 40–43]

$$H_{\text{qubits}} = \frac{1}{2} \sum_{j=1,2} \left( \Delta_j \sigma_j^z + \epsilon_j \sigma_j^x \right) + J \vec{\sigma}_1 \cdot \vec{\sigma}_2, \quad (12.1)$$

with a qubit-qubit coupling of the Heisenberg type, where  $j$  labels the qubits. In order to construct a quantum gate, the tunnel splittings  $\Delta_j$ , the biases  $\epsilon_j$ , and the qubit-qubit coupling  $J$  have to be controllable in the sense that they can be turned off and that their signs can be changed.

The bit-flip noise is specified by the system-bath Hamiltonian [46, 47]

$$H = H_{\text{qubits}} + H_{\text{coupl}} + H_{\text{bath}} \quad (12.2)$$

where

$$H_{\text{coupl}} = \frac{1}{2} \sum_{j=1,2} \sigma_j^x \sum_{\nu} \hbar \omega_{\nu} (a_{j\nu}^{\dagger} + a_{j\nu}) \quad (12.3)$$

denotes the coupling of qubit  $j$  to a bath of harmonic oscillators with frequencies  $\omega_{\nu}$  described by the Hamiltonian  $H_{\text{bath}} = \sum_{j\nu} \hbar \omega_{\nu} a_{j\nu}^{\dagger} a_{j\nu}$  and the spectral density  $I(\omega) = \pi \sum_{\nu} c_{\nu}^2 \delta(\omega - \omega_{\nu})$ . This coupling of each qubit to an individual bath represents a proper model for sufficiently distant qubits [29]. Within the present work, we consider the so-called ohmic spectral density

$$I(\omega) = 2\pi\alpha\omega e^{-\omega/\omega_c} \quad (12.4)$$

with the dimensionless coupling strength  $\alpha$  and the cutoff frequency  $\omega_c$ . In order to complete the model, we specify the initial condition of the Feynman-Vernon type, i.e., initially, the bath is in thermal equilibrium and uncorrelated with the system,  $\rho_{\text{tot}}(t_0) = \rho(t_0) \otimes R_{\text{bath,eq}}$ , where  $\rho$  denotes the reduced density operator of the two qubits and  $R_{\text{bath,eq}} \propto \exp(-H_{\text{bath}}/k_B T)$  is the canonical ensemble of the bath.

### 12.2.1

#### Bloch-Redfield Master Equation

If  $\alpha k_B T$  is smaller than the typical system energy and if the dissipation strength is sufficiently small,  $\alpha \ll 1$ , the dissipative system dynamics is well described within a Bloch-Redfield approach, which is also referred to as Born-Markov approach. There, one starts from the Liouville-von Neumann equation  $i\hbar\dot{\rho}_{\text{tot}} = [H, \rho_{\text{tot}}]$  for the total density operator and obtains by standard techniques the master equation [48]

$$\dot{\rho} = -\frac{i}{\hbar} [H_{\text{qubits}}, \rho] - \sum_j [\sigma_j^x, [Q_j(t), \rho]] - \sum_j [\sigma_j^x, \{P_j(t), \rho\}] \quad (12.5)$$

$$\equiv -\frac{i}{\hbar} [H_{\text{qubits}}, \rho] - \Lambda(t) \rho \quad (12.6)$$

with the anti-commutator  $\{A, B\} = AB + BA$  and

$$Q_j(t) = \frac{1}{4\pi} \int_0^{\infty} d\tau \int_0^{\infty} d\omega \mathcal{S}(\omega) \cos(\omega\tau) \tilde{\sigma}_j^x(t - \tau, t), \quad (12.7)$$

$$P_j(t) = \frac{1}{4\pi} \int_0^{\infty} d\tau \int_0^{\infty} d\omega I(\omega) \sin(\omega\tau) \tilde{\sigma}_j^x(t - \tau, t). \quad (12.8)$$

Thus, the influence of the bath is determined by the Heisenberg operators of the system, the spectral density  $I(\omega)$  of the heat baths, and the Fourier transformed

$$\mathcal{S}(\omega) = I(\omega) \coth(\hbar\omega/2k_B T) \quad (12.9)$$

of the symmetrically-ordered equilibrium auto-correlation function  $\frac{1}{2}\langle\{\xi_j(\tau), \xi_j(0)\}\rangle_{\text{eq}}$  of the collective bath coordinate  $\xi_j = \sum_\nu c_\nu (a_{j\nu}^\dagger + a_{j\nu})$ . The notation  $\tilde{X}(t, t')$  is a shorthand for the Heisenberg operator  $U^\dagger(t, t') X U(t, t')$  with  $U$  being the propagator of the coherent system dynamics. Note that  $\mathcal{S}(\omega)$  and  $I(\omega)$  are independent of  $j$  due to the assumption of two identical environments. We emphasize that the particular form (12.5) of the master equation is valid also for an explicitly time-dependent qubit Hamiltonian.

### 12.2.2

#### Purity Decay

The heat baths, whose influence is described by the second and third term of the master equation (12.5), lead to decoherence, i.e., the evolution from a pure state to an incoherent mixture. This process can be measured by the decay of the purity  $\text{tr}(\rho^2)$  from the ideal value 1. The gate purity (frequently also referred to as “purity”)  $\mathcal{P}(t) = \overline{\text{tr}(\rho^2(t))}$ , which characterizes the gate independently of the specific input, results from the ensemble average over all pure initial states [49]. For weak dissipation, the purity is determined by its decay rate at initial time,

$$\Gamma \equiv -\frac{d}{dt} \ln \mathcal{P}(t) \Big|_{t=0} = 2 \overline{\text{tr}(\rho \Delta \rho)} = \frac{4}{N(N+1)} \sum_j \text{tr}(\sigma_j^x Q_j(0)). \quad (12.10)$$

In order to obtain the last expression, we have used the cyclic property of the trace and performed the ensemble average over all pure states as described in Appendix A. Here,  $N$  is the dimension of the system Hilbert space. The purity loss rate  $\Gamma$  represents a figure of merit for the coherence of the quantum gate – ideally, it vanishes. Interestingly enough, only the second term on the right-hand side of the master equation (12.5) contributes to the purity decay. This relates to the interpretation that the first term of the master equation is responsible for the coherent dynamics, while the second and third term correspond to decoherence and relaxation, respectively.

The average over all pure states, which underlies the rate (12.10), may differ from the average over a discrete set of initial states by a factor of the order unity, due to the particular choice of a discrete ensemble: There, one commonly chooses ensembles which are unsymmetric on the Bloch sphere [27, 28] or which do not include entangled states [27–29].

## 12.2.3

**Numerical Solution**

The purity decay rate (12.10) by construction accounts only for the behavior at initial time  $t = 0$ . Thus, for a more complete picture, it is desirable to have the exact numerical solution of the master equation (12.5) at hand. For studying the influence of an external AC field, such a solution must properly capture the case of a  $T$ -periodic system Hamiltonian. An efficient scheme for that purpose is a modified Bloch-Redfield formalism whose cornerstone is a decomposition into the Floquet basis of the driven system [48]: According to the Floquet theorem, the Schrödinger equation of a driven quantum system with a Hamiltonian of the form  $H(t) = H(t + T)$  possesses a complete set of solutions of the form  $|\psi_\alpha(t)\rangle = \exp(-i\epsilon_\alpha t/\hbar)|\phi_\alpha(t)\rangle$ . The so-called Floquet states  $|\phi_\alpha(t)\rangle$  obey the time-periodicity of the Hamiltonian and  $\epsilon_\alpha$  denotes the so-called quasienergy. The Floquet states are elements of an Hilbert space extended by a  $T$ -periodic time coordinate and are computed from the eigenvalue equation

$$\left(H(t) - i\hbar \frac{d}{dt}\right)|\phi_\alpha(t)\rangle = \epsilon_\alpha|\phi_\alpha(t)\rangle. \quad (12.11)$$

In the Floquet basis  $\{|\phi_\alpha(t)\rangle\}$ , the master equation (12.5) assumes the form

$$\dot{\rho}_{\alpha\beta} = -\frac{i}{\hbar}(\epsilon_\alpha - \epsilon_\beta)\rho_{\alpha\beta} - \sum_{\alpha'\beta'} \Lambda_{\alpha\beta,\alpha'\beta'}(t) \rho_{\alpha'\beta'}. \quad (12.12)$$

Besides computational advantages, using the Floquet basis has the benefit that it implies the numerically exact treatment of the coherent system dynamics. Thereby, one avoids artefacts like the violation of equilibrium properties in the undriven limit [50–54].

For weak dissipation, we can replace within a rotating-wave approximation  $\Lambda(t)$  by its time average [48]. Finally, we integrate the master equation to obtain the dissipative propagator  $\mathcal{W}_{\alpha\beta,\alpha'\beta'}$  which provides the final state  $\rho_{\text{out},\alpha\beta} = \sum_{\alpha'\beta'} \mathcal{W}_{\alpha\beta,\alpha'\beta'} \rho_{\text{in},\alpha'\beta'}$  and, thus, allows one to evaluate all quantities of interest. In particular, it is possible to compute for a pure initial state  $|\psi\rangle = \sum_\alpha c_\alpha |\phi_\alpha\rangle$ , i.e. for  $\rho_{\text{in},\alpha\beta} = c_\alpha c_\beta^*$ , the final state  $\rho_{\text{out}}$  which possesses the purity

$$\text{tr} \rho_{\text{out}}^2 = \sum_{\alpha\beta} \rho_{\text{out},\alpha\beta} \rho_{\text{out},\beta\alpha} = \sum_{\alpha\beta\alpha'\beta'\alpha''\beta''} \mathcal{W}_{\alpha\beta,\alpha'\beta'} \mathcal{W}_{\beta\alpha,\beta''\alpha''} c_\alpha c_{\beta'}^* c_{\beta''} c_{\alpha''}^*. \quad (12.13)$$

In order to average over all pure initial states, we employ Eq. (A.5) derived in the Appendix to obtain the gate purity

$$\mathcal{P}_{\text{out}} = \frac{1}{N(N+1)} \sum_{\alpha\beta\alpha'\beta'} \left( \mathcal{W}_{\alpha\beta,\alpha'\beta'} \mathcal{W}_{\beta\alpha,\beta'\alpha'} + \mathcal{W}_{\alpha\beta,\alpha'\alpha'} \mathcal{W}_{\beta\alpha,\beta'\beta'} \right). \quad (12.14)$$

We emphasize that this result is independent of the particular choice of the basis.

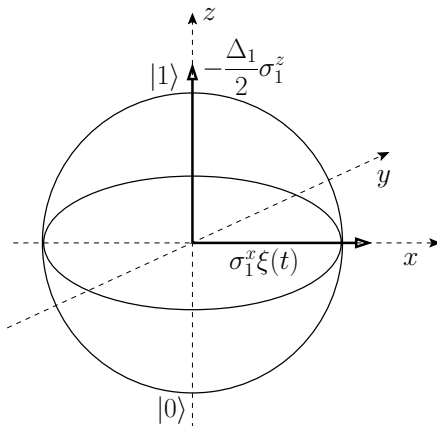


**Fig. 12.1** Bloch sphere representation of the single-qubit Hamiltonian (12.15) and the bath coupling studied in Sect. 12.3.

### 12.3

#### Coherence Stabilization for Single Qubits

During the stage of single qubit operations, i.e., for  $J = 0$ , both qubits together with the respective bath evolve independently of each other. Thus, it is sufficient to focus on qubit 1 with the Hilbert space dimension  $N = 2$ . We restrict ourselves to an operation with  $\epsilon_1 = 0$  and the fixed tunnel splitting  $\Delta_1 > 0$ , i.e. to the Hamiltonian

$$H_{\text{qubit1}} = \frac{\Delta_1}{2} \sigma_1^z. \quad (12.15)$$

This situation is characterized by the fact that the bath couples to a system operator which is different from the qubit Hamiltonian. In the Bloch sphere representation sketched in Fig. 12.1, the qubit Hamiltonian (12.15) and the bath coupling correspond to orthogonal vectors. We start out by bringing the master equation (12.5) into a more explicit form by inserting the Heisenberg operator

$$\tilde{\sigma}_1^x(t - \tau, t) = \sigma_1^x \cos \frac{\Delta_1 \tau}{\hbar} + \sigma_1^y \sin \frac{\Delta_1 \tau}{\hbar}, \quad (12.16)$$

which is readily derived from its definition together with the qubit Hamiltonian (12.1). Performing the integration over  $\tau$  and  $\omega$  and neglecting renormalization effects, which are small provided that  $\alpha \ln(\omega_c/\Delta_1) \ll 1$ , yields for  $\Delta_1 \ll \omega_c$ , the Markovian master equation

$$\dot{\rho} = -\frac{i}{\hbar} [H_{\text{qubit1}}, \rho] - \frac{\mathcal{S}(\Delta_1/\hbar)}{8} [\sigma_1^x, [\sigma_1^x, \rho]] + i \frac{\pi \alpha \Delta_1}{4} [\sigma_1^x, \{\sigma_1^y, \rho\}]. \quad (12.17)$$

Then the purity decay (12.10) is readily evaluated to read

$$\Gamma_0 = \frac{1}{6} \mathcal{S}(\Delta_1/\hbar), \quad (12.18)$$

where the subscript “0” refers to the absence of any AC field.

A possible coupling to an external driving field might have any “direction”  $\vec{n}$  on the Bloch sphere (cf. Fig. 12.1), i.e. be proportional to  $\vec{n} \cdot \vec{\sigma}_1$ . Herein, we restrict ourselves to the cases parallel to the bath coupling and parallel to the static Hamiltonian, i.e., to a field that couples to  $\sigma_1^z$  and  $\sigma_1^x$ , respectively.

### 12.3.1

#### Dynamical Decoupling by Harmonic Driving

The first option is to act on the qubit with a driving of the form

$$H_{\parallel} = \frac{A}{2} \sigma_1^z \cos(\Omega t) \quad (12.19)$$

“parallel” to the static Hamiltonian. This relates to a recently proposed mechanism for coherence stabilization, namely the so-called dynamical decoupling (DD) [17–21]. This scheme employs sequences of  $\pi$ -pulses that flip the sign of the operator  $\sigma_1^x$  which couples the qubit to the bath. The basic idea dates back to the suppression of spin diffusion in nuclear magnetic resonance experiments [55, 56] and by now is an established technique in that area [57]. In the present case where the bath couples to the operator  $\sigma_1^x$  [cf. Eq. (12.3)], such a transformation is e.g. induced by the Hamiltonian  $\hbar\omega_R \sigma_1^z$  for a pulse duration  $\pi/\omega_R$ . Since the corresponding propagator is a function of the qubit Hamiltonian, the coherent dynamics is not altered. Besides the prospective benefits of such a control scheme, there is also a number of possible drawbacks that the application of  $\pi$ -pulses might cause: For a driven system, there is always the possibility of unwanted off-resonant transitions [58], especially in the case of ideal rectangular pulses. A more practical limitation is the fact that only noise with frequencies below the pulse repetition rate can be eliminated in such a way. These disadvantages can be overcome partially by applying a continuous wave version of the dynamical decoupling scheme, i.e. a driving of the form (12.19) for which the available frequency range is larger.

For the computation of the coherence properties, we use the fact that  $H_{\parallel}(t)$  commutes with the static qubit Hamiltonian (12.15) and, consequently, the propagator for the driven qubit can be computed exactly reading

$$U(t, t') = \exp \left( -i \frac{A}{2\hbar\Omega} [\sin(\Omega t) - \sin(\Omega t')] \sigma_1^z \right) \exp \left( -\frac{i}{\hbar} \Delta_1 \sigma_1^z (t - t') \right). \quad (12.20)$$

We have written the propagator in a form that is suitable for simplifying the master equation (12.5). Inserting this into the expression (12.7) results for  $\Delta_1 \ll \Omega$  in the effective coupling operator

$$Q_{\text{DD}} = \frac{1}{8} \left( J_0^2 (A/\hbar\Omega) \mathcal{S}(\Delta_1/\hbar) + 2 \sum_{n=1}^{\infty} J_n^2 (A/\hbar\Omega) \mathcal{S}(n\Omega) \right) \sigma_1^x. \quad (12.21)$$

In order to derive this expression, we have decomposed the exponentials of the trigonometric functions into a Fourier series using the identity  $\exp[ix \sin(\Omega t)] = \sum_k J_k(x) \exp(ik\Omega t)$ , where  $J_k$  is the  $k$ th order Bessel function of the first kind [59]. The effective coupling operator  $Q_{\text{DD}}$  is proportional to  $\sigma_1^x$  and, thus, the master equation is again of the form (12.5). The only difference is that the dissipative terms have acquired the prefactor

$$\eta_{\text{DD}} = J_0^2(A/\hbar\Omega) + 2 \sum_{n=1}^{\infty} \frac{n\hbar\Omega}{\Delta_1} \frac{\tanh(\Delta_1/2k_B T)}{\tanh(n\hbar\Omega/2k_B T)} e^{-n\Omega/\omega_c} J_n^2(A/\hbar\Omega) \quad (12.22)$$

which modifies the purity decay rate accordingly,  $\Gamma_{\text{DD}} = \eta_{\text{DD}}\Gamma_0$ . Equation (12.22) allows for the interpretation that now the decoherence rate depends on the spectral density of the bath at multiples of the driving frequency  $\Omega$  which may be larger than the cutoff frequency  $\omega_c$ . The  $\pi$ -pulses applied in the original version [17] of dynamical decoupling, correspond for a continuous driving to a field amplitude that is adjusted such that  $A/\hbar\Omega$  equals the first zero of the Bessel function  $J_0$ , i.e. it assumes a value 2.404825 . . . Then only the sum in Eq. (12.22) contributes to the decoherence rate  $\Gamma_{\text{DD}}$ . If now the driving frequency is larger than the cutoff of the spectral density,  $\Omega > \omega_c$ , decoherence is considerably reduced: For low temperatures,  $k_B T \ll \Delta_1$ , the hyperbolic tangent in the factor (12.22) becomes unity and each contribution is weighted by a possibly large factor  $n\hbar\Omega/\Delta_1$ . In the high-temperature limit  $k_B T \gg \hbar\Omega$ , we use  $\tanh(x) \approx x$  and find that the dependence of the prefactor on  $n\Omega$  cancels. This means that the dynamical decoupling scheme is especially useful for high temperatures. The physical reason for this is that the driving shifts the qubit dynamics towards high frequencies where the thermal occupation of the bath modes is negligible.

Fig. 12.2 compares the coherence stabilization  $\eta_{\text{DD}}$  as a function of the driving frequency for  $A/\hbar\Omega = 2.4$ , i.e. close to a zero of the Bessel function  $J_0$ . It reveals that for driving frequencies well below the cutoff, the driving rather spoils the coherence. This improves with increasing driving frequency and, finally, for a high-frequency driving,  $\eta_{\text{DD}}$  becomes much smaller than unity corresponding to a significant coherence stabilization. The data demonstrate the particular usefulness of dynamical decoupling at high temperatures.

### 12.3.2

#### Coherent Destruction of Tunneling

Our second example under consideration is a driving field

$$H_{\perp}(t) = f(t)\sigma_1^x, \quad (12.23)$$

where the energy  $f(t)$  is a  $2\pi/\Omega$ -periodic function of time with zero mean. The field couples to the qubit by the same operator  $\sigma_1^x$  as the bath, i.e., “perpen-

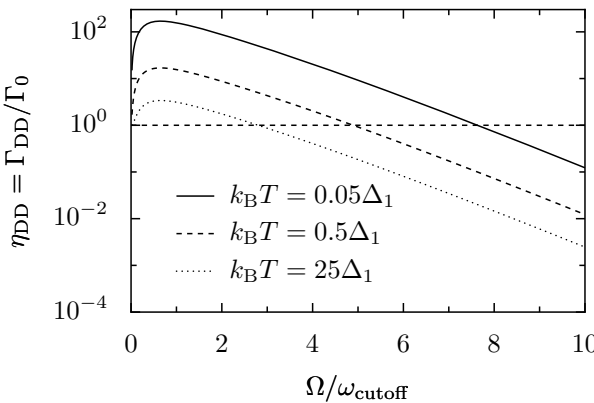


**Fig. 12.2** Decoherence reduction by dynamical decoupling,  $\eta_{DD}$ , as a function of the driving frequency for various temperatures. The cutoff frequency is  $\omega_c = 500\Delta_1/\hbar$ ,  $A/\hbar\Omega = 2.4$ , and the dissipation strength is  $\alpha = 0.01$ . The horizontal line marks the value 1 below decoherence is lower than in the static case.

icular" to the static Hamiltonian (12.15). Thus, it commutes with the qubit-bath coupling but not with the static Hamiltonian. Such a time-dependent field causes already interesting effects for the coherent qubit dynamics that we will briefly review before discussing decoherence.

For that purpose, we derive within a rotating-wave approximation (RWA) analytical expressions for both the coherent propagator  $U(t, t')$  and the purity decay (12.10). We start out by transforming the total Hamiltonian into a rotating frame with respect to the driving via the unitary transformation

$$U_{AC}(t) = e^{-i\phi(t)\sigma_1^x}, \quad \phi(t) = \frac{1}{\hbar} \int_0^t dt' f(t'). \quad (12.24)$$

This yields the likewise  $2\pi/\Omega$ -periodic interaction-picture Hamiltonian

$$\tilde{H}_{\text{qubit1}}(t) = U_{AC}^\dagger(t) H_{\text{qubit1}} U_{AC}(t) \quad (12.25)$$

$$= \frac{\Delta_1}{2} \left\{ \sigma_1^z \cos \left( \frac{A}{\hbar\Omega} \sin(\Omega t) \right) + \sigma_1^y \sin \left( \frac{A}{\hbar\Omega} \sin(\Omega t) \right) \right\} \quad (12.26)$$

and the S-matrix  $S(t, t') = U_{AC}^\dagger(t) U(t, t') U_{AC}(t')$ . The corresponding Schrödinger equation cannot be integrated exactly since  $\tilde{H}_{\text{qubit1}}(t)$  does not commute with itself at different times and, thus, time-ordering has to be taken into account. We restrict ourselves to an approximate solution and neglect corrections of the order  $\Delta_1^2$ . Within this approximation, the propagator is simply given by the exponential of the integral of the time-dependent interaction-picture Hamiltonian. This is equivalent to replacing (12.26) by its time-average

$$\bar{H}_{\text{qubit1}} \equiv \langle \tilde{H}_{\text{qubit1}}(t) \rangle_{2\pi/\Omega} = \frac{\Delta_{\text{eff}}}{2} \sigma_1^z, \quad (12.27)$$

where  $\langle \dots \rangle_{2\pi/\Omega}$  denotes the time-average over the driving period. This RWA approximation to the driven qubit Hamiltonian is of the same form as the original static Hamiltonian (12.1), but with the tunneling matrix element being renormalized according to

$$\Delta_1 \rightarrow \Delta_{\text{eff}} = \langle \cos[2\phi(t)] \rangle_{2\pi/\Omega} \Delta_1, \quad (12.28)$$

Consequently, we find  $S(t, t') = \exp\{-i\bar{H}_{\text{qubit1}}(t - t')/\hbar\}$ , such that within RWA, the entire propagator for the qubit in the Schrödinger picture reads

$$U(t, t') = e^{-i\phi(t)\sigma_1^x} e^{-i\bar{H}_{\text{qubit1}}(t-t')/\hbar} e^{i\phi(t')\sigma_1^x}. \quad (12.29)$$

Of particular interest are now driving parameters for which the effective tunnel splitting (12.28) and, thus,  $\bar{H}_{\text{qubit1}}$  vanish. Then, the one-period propagator  $U(t + T, t)$  becomes the identity [recall that  $U_{\text{AC}}$  is  $2\pi/\Omega$ -periodic and, thus,  $U_{\text{AC}}(2\pi/\Omega) = U_{\text{AC}}(0) = \mathbf{1}$ ]. This implies that the long-time dynamics is suppressed. The dynamics within the driving period requires a closer look at the  $2\pi/\Omega$ -periodic contribution  $U_{\text{AC}}(t)$ : For an initial preparation in an eigenstate of  $\sigma_1^x$ , it provides only a global phase, such that the dynamics as a whole is suppressed also within the driving period. This effect of suppressing the time-evolution by the purely coherent influence of an external field has been investigated first in the context of driven tunneling [30, 31] and is named “coherent destruction of tunneling” (CDT). Therefore, we will refer to a driving of the form (12.23) as “CDT driving” despite the fact that we also consider working points at which the coherent dynamics is not completely suppressed. Note that for a preparation other than an eigenstate of  $\sigma_1^x$ , the periodic propagator  $U_{\text{AC}}(t)$  will still cause a non-trivial dynamics within the driving period.

Let us now turn to the influence of the CDT driving (12.23) on quantum dissipation and decoherence. For that purpose, we have to evaluate the operator  $Q_j$  contained in the master equation (12.5). Inserting the RWA propagator (12.29) into (12.7), we obtain after some algebra the result

$$Q_{\text{CDT}} = \frac{1}{8} \mathcal{S}(\Delta_{\text{eff}}/\hbar) \sigma_1^x. \quad (12.30)$$

Thus, the master equation again is of the same form as in the undriven case, Eq. (12.5), but the generator of the dissipative dynamics is modified by the factor

$$\eta_{\text{CDT}} = \frac{\mathcal{S}(\Delta_{\text{eff}}/\hbar)}{\mathcal{S}(\Delta_1/\hbar)} = \frac{\coth(\Delta_{\text{eff}}/2k_B T)}{\coth(\Delta_1/2k_B T)} \langle \cos[2\phi(t)] \rangle_{2\pi/\Omega}. \quad (12.31)$$

Consequently, the purity decay becomes  $\Gamma_{\text{CDT}} = \eta_{\text{CDT}} \Gamma_0$ . Since the spectral density  $\mathcal{S}(\omega)$  increases monotonically with the frequency  $\omega$  and, moreover,

the Bessel function  $J_0(x) \leq 1$ , the CDT driving – in clear contrast to the dynamical decoupling – never enhances dissipation and decoherence.

In the high-temperature limit  $k_B T \gg \Delta_{\text{eff}}$ , we employ the approximation  $\coth(x) \approx 1/x$  which implies that for an ohmic bath,  $\mathcal{S}(\Delta/\hbar) \approx 4\pi\alpha k_B T/\hbar$  is independent of the tunnel splitting. Consequently,  $\eta_{\text{CDT}} \approx 1$ , i.e., the purity decay is essentially unchanged.

In the opposite limit of low temperatures,  $k_B T \ll \Delta_{\text{eff}}$ , the argument of the hyperbolic cotangent is large such that  $\coth(x) \approx 1$ . Then  $\eta_{\text{CDT}} = \Delta_{\text{eff}}/\Delta_1 = \langle \cos[2\phi(t)] \rangle_{2\pi\Omega} \leq 1$ . This reduction of decoherence is brought about by the fact that the driving (12.23) decelerates the long time dynamics of the qubit. Thereby, the frequencies which are relevant for the decoherence are shifted to a range where the spectral density of the bath is lower. Consequently, the influence of the bath is diminished.

An important special case is that of a harmonically time-dependent driving field,  $f(t) = \frac{1}{2}A \cos(\Omega t)$ . Then, the time-average in the effective matrix element (12.28) can be expressed by a zeroth-order Bessel function of the first kind such that  $\Delta_{\text{eff}} = J_0(A/\hbar\Omega)\Delta_1$ . Consequently, we find that at sufficiently low temperatures decoherence is reduced by a factor  $\eta_{\text{CDT}} = J_0(A/\hbar\Omega)$ . These results imply that for an ohmic bath, the coherent dynamics is slowed down by the same factor as the decoherence, cf. Eqs. (12.28) and (12.31) in the low-temperature limit. Thus, if for a specific application, the figure of merit is the number of coherent oscillations, the present coherence stabilization scheme may therefore not prove very useful.

## 12.4

### Coherence Stabilization for a CNOT Gate

Logic operations in both quantum and classical computers require that the time evolution of a qubit (or a bit, respectively) depends on the state of another qubit. The physics behind such processes is a non-linear interaction between two qubits which in many implementations is of the Heisenberg type [24, 43]

$$H_{\text{Heisenberg}} = J\vec{\sigma}_1 \cdot \vec{\sigma}_2 \quad (12.32)$$

as assumed in our model Hamiltonian (12.1). In the context of decoherence, the question arises whether it is possible to stabilize coherence by a proper AC field while maintaining the desired non-linear time evolution.

The qubit Hamiltonian (12.1) together with the bath coupling (12.2), allows one to implement the CNOT operation sketched in Fig. 12.3a [24, 27, 40–42, 60]. Apart from single qubit operations, it consists of the propagator

$$U_{\text{H}}(\varphi) = \exp(-i\varphi \vec{\sigma}_1 \cdot \vec{\sigma}_2) \quad (12.33)$$

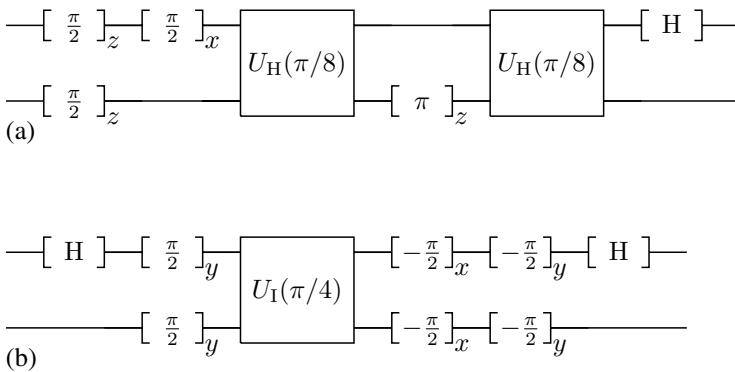


**Fig. 12.3** Realizations of a CNOT operation for different types of qubit-qubit interaction [40–42]. (a) Heisenberg interaction providing the transformation (12.33) and (b) Ising coupling along the  $x$ -direction corresponding to (12.42). The symbol  $[H]$  denotes the Hadamard operation and  $[\phi]_n$  the rotation of the respective qubit around the axis  $n$  by an angle  $\phi$ .

for the Heisenberg qubit-qubit interaction (12.32) which in total acts for a time  $t_J = \pi\hbar/4J$  such that  $\varphi = \pi/4$ . For single qubit operations, we have discussed in Sect. 12.3 that pulse sequences [17–21] and harmonic driving fields [23] can suppress decoherence. Therefore, we focus here on decoherence during the stage of the qubit-qubit interaction and, thus, take as a working hypothesis that the coherence of one-qubit operations can be stabilized ideally. Then the remaining decoherence takes place during the qubit-qubit interaction time  $t_J$ .

#### 12.4.1

##### Heisenberg vs. Ising Coupling

Before discussing the influence of a driving field, we provide for later reference the results for the purity decay in the static situation. Therefore, we need to evaluate  $\text{tr}(\sigma_j^x Q_j)$  where

$$Q_j = \frac{1}{4\pi} \int_0^\infty dt \int_0^\infty d\omega \mathcal{S}(\omega) \cos(\omega\tau) e^{iH_{\text{Heisenberg}}\tau/\hbar} \sigma_j^x e^{-iH_{\text{Heisenberg}}\tau/\hbar}. \quad (12.34)$$

This calculation is most conveniently performed in the basis of the total (pseudo) spin  $\vec{L} = \frac{1}{2}(\vec{\sigma}_1 + \vec{\sigma}_2)$  because  $H_{\text{Heisenberg}} = J(2\vec{L}^2 - 3)$ , where  $\vec{L}^2$  possesses the eigenvalues  $\ell(\ell+1)$ ,  $\ell = 0, 1$ . For  $\ell = 0$ , the corresponding eigenstate is the singlet state  $(|01\rangle - |10\rangle)/\sqrt{2}$  with energy  $\epsilon_0 = -3J$ , while for  $\ell = 1$ , one finds the triplet  $|00\rangle$ ,  $(|01\rangle + |10\rangle)/\sqrt{2}$ ,  $|11\rangle$  with  $\epsilon_1 = J$ . After evaluating the matrix elements of  $\sigma_j^x$  and  $Q_j$ , we finally arrive at the purity decay rate

$$\Gamma_{\text{Heisenberg}} = \frac{2}{5} \{ \mathcal{S}(0) + \mathcal{S}(4J/\hbar) \}. \quad (12.35)$$

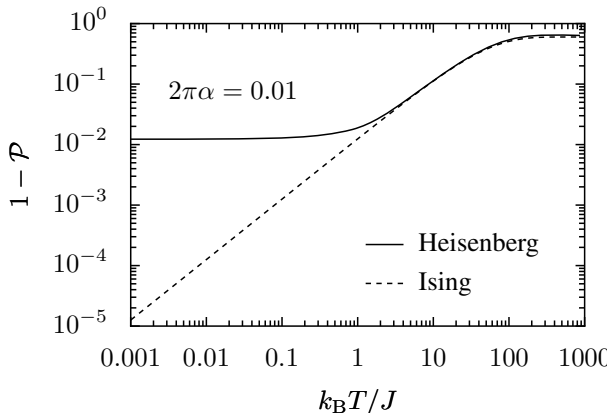


**Fig. 12.4** Purity loss ( $1 - \mathcal{P}$ ) of two qubits interacting for a time  $t_I = \pi\hbar/4J$  comparing Heisenberg (solid) and Ising (dashed) coupling. The dimensionless dissipation strength is  $\alpha = 0.01/2\pi$ .

The corresponding purity loss is sketched in Fig. 12.4. In the derivation, we have ignored Lamb shifts and defined

$$\mathcal{S}(0) \equiv \lim_{\omega \rightarrow 0} \mathcal{S}(\omega) = \frac{4\pi}{\hbar} \alpha k_B T. \quad (12.36)$$

In particular, we find that for low temperatures,  $k_B T \lesssim J$ , decoherence is dominated by the term  $\mathcal{S}(4J/\hbar)$  such that  $\Gamma \approx 16\pi\alpha J/5\hbar$ . This part reflects the influence of the so-called quantum noise which is temperature-independent and, thus, cannot be reduced by cooling the environment.

It is intriguing to compare the result (12.35) with the purity decay of a similar system, namely a pair of qubits interacting with the Ising interaction

$$H_{\text{Ising}} = J\sigma_1^x\sigma_2^x. \quad (12.37)$$

Such an interaction can also be employed for the construction of quantum gates like the CNOT gate in Fig. 12.3b. (Note, however, that for several physical realizations of a quantum computer [24,43], the natural interaction is of the Heisenberg type). The main difference to the Heisenberg interaction (12.32), is the fact that  $H_{\text{Ising}}$  commutes with the bath coupling (12.3), i.e., the bath couples to a good quantum number. Carrying out the same calculation as above yields the purity decay

$$\Gamma_{\text{Ising}} = \frac{4}{5} \mathcal{S}(0) = \frac{16}{5\hbar} \pi \alpha k_B T \quad (12.38)$$

which exhibits a significantly different low-temperature behavior: Instead of saturating, it remains proportional to the temperature, cf. Fig. 12.4.

## 12.4.2

**Coherence Stabilization by an AC Field**

In Sects. 12.3.2 and 12.4.1 we presented two results that lead to the central idea for coherence stabilization of a qubit pair under the influence of a Heisenberg coupling: First, an AC field can suppress the dynamics “transverse” to the driving, i.e., it can effectively eliminate the parts of the Hamiltonian that depend on spin matrices other than  $\sigma_1^x$ . Second, qubits with Ising interaction are less sensitive to decoherence than qubits with Heisenberg interaction. Thus, the question arises whether one can act with an AC field on the system (12.1) in such a way that precisely the part of the Hamiltonian (12.32) that causes the quantum noise becomes suppressed. This is indeed the case and can be performed by driving qubit 1 with the AC field (12.23). Note that qubit 2 remains undriven.

For the computation of the coherence properties, we proceed as in Sect. 12.3.2: We first derive an effective static qubit Hamiltonian by transforming the time-dependent Hamiltonian  $H_{\text{Heisenberg}} + H_{\perp}(t)$  via (12.24) into rotating frame and subsequently replace it by its time average. After some algebra along the lines of Sect. 12.3.2, we obtain the Hamiltonian

$$\bar{H}_{\text{qubits}} = J\sigma_1^x\sigma_2^x + J_{\perp}(\sigma_1^y\sigma_2^y + \sigma_1^z\sigma_2^z), \quad (12.39)$$

where the constant

$$J_{\perp} = J\langle \cos[2\phi(t)] \rangle_{2\pi/\Omega} \quad (12.40)$$

denotes an effective interaction “transverse” to the driving and  $\langle \dots \rangle_{2\pi/\Omega}$  the time average over the driving period. Consequently, we find the S-matrix  $S(t, t') = \exp\{-i\bar{H}_{\text{qubits}}(t - t')/\hbar\}$ , such that the propagator of the *driven* system again assumes the form (12.29) with  $\bar{H}_{\text{qubit1}}$  replaced by  $\bar{H}_{\text{qubits}}$ . Having this propagator at hand, we are in the position to derive explicit expressions for the operators  $\sigma_j^x(t - \tau, t)$  and  $Q_j$ . Again, the calculation is conveniently done in the basis of the total spin  $\vec{L}$  and  $L_x$  which, owing to the relation  $\sigma_1^x\sigma_2^x = \frac{1}{2}(\sigma_1^x + \sigma_2^x)^2 - 1$ , is an eigenbasis of the Hamiltonian (12.39). We evaluate the purity decay rate (12.10) in this basis and finally obtain

$$\Gamma_{\text{Heisenberg, driven}} = \frac{2}{5}\{\mathcal{S}(0) + \mathcal{S}(4J_{\perp}/\hbar)\}, \quad (12.41)$$

i.e., the result (12.35) but with  $J$  replaced by  $J_{\perp}$ . For  $f(t) \equiv 0$ , we find  $J_{\perp} = J$  such that the static result is reproduced; otherwise, the inequality  $|J_{\perp}| < J$  holds and, thus, the bath correlation function  $\mathcal{S}$  in Eq. (12.41) has to be evaluated at a lower frequency. For an ohmic or a super-ohmic bath,  $\mathcal{S}(\omega)$  is a monotonously increasing function and, consequently, the AC field reduces purity decay (unless  $J > \omega_{\text{cutoff}}$ ).

The purity decay assumes its minimum for  $J_{\perp} = 0$ . This condition marks the working points on which we shall focus henceforth. For an ohmic spectral

density  $I(\omega) = 2\pi\alpha\omega$ , the purity decay at the working points becomes  $\Gamma = \frac{4}{5}\mathcal{S}(0) = 16\pi\alpha k_B T/5\hbar$ . This value has to be compared to the purity decay in the absence of driving: An analysis reveals that for  $k_B T > J$ , decoherence is essentially driving independent. By contrast for low temperatures,  $k_B T < J$ , the driving reduces the decoherence rate by a factor  $k_B T/J$ . This low-temperature behavior results from the fact that for  $J_\perp = 0$ , the effective Hamiltonian (12.39) is identical with the Ising Hamiltonian (12.37) and, thus, commutes with the qubit-bath coupling operators  $\sigma_j^x$ . Note that the latter are not affected by the transformation (12.24). This means that the driving modifies the effective qubit Hamiltonian such that the bath acts as pure phase noise whose influence is proportional to the temperature. The fact that the driving field couples to the same coordinate as the bath distinguishes the present coherence stabilization from dynamical decoupling. In that respect, the present scheme is complementary to coherence-preserving qubits [13]. For the latter, heating errors are the only source of decoherence.

For a rectangular driving for which  $f(t)$  switches between the values  $\pm A/2$ , the condition  $J_\perp = 0$  is equivalent to  $A = \hbar\Omega$  and corresponds to two  $\pi$ -pulses per period. For a harmonic driving,  $f(t) = A \cos(\Omega t)/2$ , one obtains  $J_\perp = J J_0(A/\hbar\Omega)$ , where  $J_0$  denotes the zeroth-order Bessel function of the first kind. Then, at the working points  $J_\perp = 0$ , the ratio  $A/\hbar\Omega$  assumes a zero of  $J_0$ , i.e., one of the values  $2.405\ldots, 5.520\ldots, 8.654\ldots, \dots$ .

So far, we ignored that the driving also affects the coherent dynamics and, thus, the pulse sequence of the CNOT operation needs a modification: At the working points of the driven system, the propagator becomes  $U_{\text{eff}}(t, t') = U_I(J(t - t')/\hbar)$  where

$$U_I(\varphi) = \exp(-i\varphi\sigma_1^x\sigma_2^x) \quad (12.42)$$

is the propagator corresponding to the ideal Ising interaction (12.37). This allows one to implement the alternative CNOT operation depicted in Fig. 12.3b [41, 42, 61]. Note that the interaction time  $t_J = \pi\hbar/4J$  is the same as for the original gate operation in Fig. 12.3a. Since  $U_{\text{AC}}(2\pi/\Omega)$  is the identity [cf. Eq. (12.24)], we assume for convenience that  $t_J$  is an integer multiple of the driving period  $2\pi/\Omega$ , i.e.,  $\Omega = 8kJ/\hbar$  with integer  $k$ .

#### 12.4.3

#### Numerical Solution

In order to confirm our analytical results, we compute the dissipative propagator as described in Sect. 12.2.3. Thereby, we restrict ourselves to purely harmonic driving  $f(t) = A \cos(\Omega t)/2$ . The resulting purity loss during the interaction time  $t_J$  is depicted in Fig. 12.5. We find that for large temperatures,  $k_B T > J$ , decoherence is fairly independent of the driving. This behavior changes as the temperature is lowered: Once  $k_B T < J$ , the purity loss

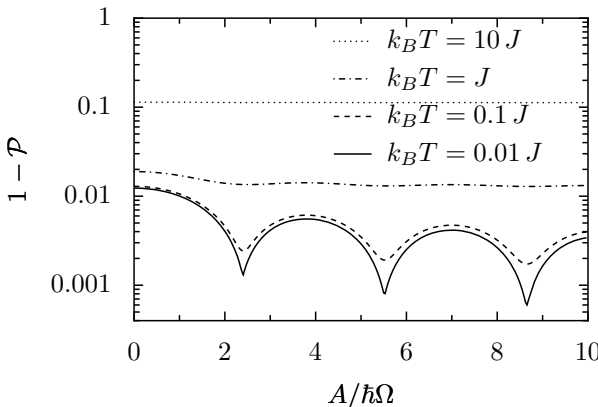


**Fig. 12.5** Purity loss during the interaction time  $t_I$  as a function of the driving amplitude. The driving frequency is  $\Omega = 32J/\hbar$  and the dissipation strength  $2\pi\alpha = 0.01$ . For  $A = 0$ , the undriven situation is reproduced.

is significantly reduced whenever the ratio  $A/\hbar\Omega$  is close to a zero of the Bessel function  $J_0$ . Both observations confirm the preceding analytical estimates. The behavior at the first working point  $A \approx 2.4\hbar\Omega$  is depicted in Fig. 12.6a. For relatively low driving frequencies, we find the purity loss being proportional to  $J/\Omega$ . This significant deviation from the analytical result for small  $\Omega$  relates to the fact that the low-frequency regime is not within the scope of our rotating-wave approximation which assumes  $\Omega$  to be the largest frequency scale. With increasing driving frequency, the discrepancy decreases until finally decoherence is dominated by thermal noise  $\propto T$  and the numerical solution confirms the analytical results. Fig. 12.7 reveals that the accuracy of our analytical estimates increases with the driving frequency: While for the relatively low frequency  $\Omega = 16J/\hbar$ , the purity loss is still close to the one of the undriven Heisenberg gate, it converges in the limit  $\Omega \rightarrow \infty$  to the value obtained for Ising interaction (cf. the dashed line in Fig. 12.4).

Still, there remains one caveat: The gate operation in Fig. 12.3b relies on the fact that the static effective Hamiltonian  $\bar{H}_{\text{qubits}}$  describes the dynamics of the driven system sufficiently well – any discrepancy results in a coherent error. Therefore, we still have to justify that such coherent errors are sufficiently small. As a measure, we employ the so-called fidelity [49]

$$\mathcal{F} = \overline{\text{tr}[\rho_{\text{ideal}}\rho(t_I)]}, \quad (12.43)$$

which is defined as the overlap between the real outcome of the operation,  $\rho(t_I)$ , and the desired final state  $\rho_{\text{ideal}} = U_I(\pi/4)\rho_{\text{in}}U_I^\dagger(\pi/4)$  in the average over all pure initial states. The time-evolution (12.42) of the ideal Ising qubit-qubit interaction is characterized by  $\mathcal{F} = 1$ . Fig. 12.6b demonstrates that the

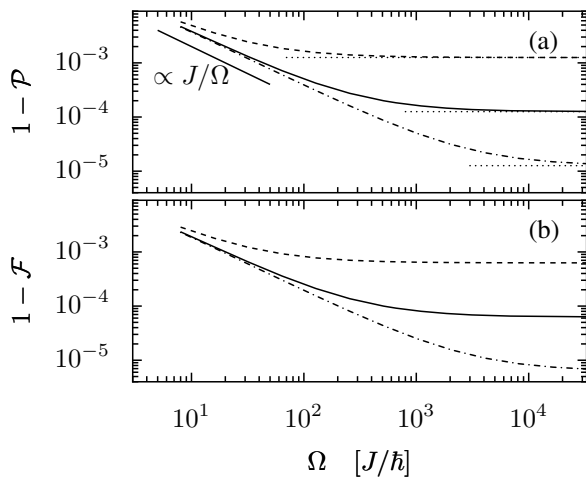


**Fig. 12.6** (a) Purity loss ( $1 - \mathcal{P}$ ) for a pair of qubits with Heisenberg interaction as a function of the driving frequency for the temperatures  $k_B T = 0.1J$  (dashed),  $0.01J$  (solid), and  $0.001J$  (dash-dotted). The dotted lines mark the analytical estimate  $1 - \mathcal{P}(t_f) \approx \Gamma_{\text{Ising}} t_f$ . (b) Corresponding fidelity defect  $1 - \mathcal{F}$ .

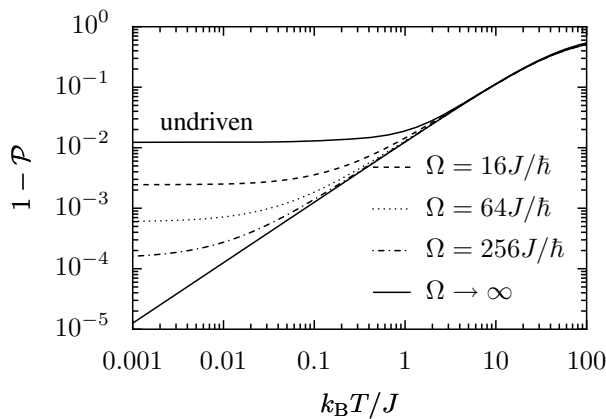


**Fig. 12.7** Purity loss shown in Fig. 12.6 as a function of the temperature. The driving amplitude  $A \approx 2.4\hbar\Omega$  is adjusted such that  $1 - \mathcal{P}$  assumes its first minimum; cf. Fig. 12.5. All other parameters are as in Fig. 12.6.

fidelity defect  $1 - \mathcal{F}$  at the first working point is even smaller than the purity loss. Thus, we can conclude that coherent errors are not of a hindrance.

### 12.4.4

#### Implementation with Quantum Dots

Fig. 12.7 indicates that the benefits of a “preferably infinitely” large driving frequency and amplitude. Thus, a crucial question is whether sufficiently large values are experimentally within reach. For spin qubits in quantum dots [24] a typical exchange coupling is  $J = 0.1$  meV which for a temperature  $T = 10$  mK corresponds to the solid lines in Figs. 12.5 and 12.6. These results demonstrate that driving with the feasible frequency  $\Omega = 2\pi \times 100 J/\hbar \approx 10^{12}$  Hz and amplitude  $A = 10$  meV already reduces the purity loss by two orders of magnitude while the fidelity loss stays at a tolerable level.

### 12.5

#### Conclusions

We have investigated the influence of oscillating fields on the coherence properties of one- and two-qubit gate operations for three different cases for which it is beneficial. The first case constitutes a continuous-wave version of dynamical decoupling of a single qubit from its environment. It is characterized by a driving Hamiltonian that does not commute with the bath coupling. There, we have found that a low-frequency driving is rather destructive because it generally even enforces decoherence. However, once the frequency exceeds the bath cutoff, the coherence properties recover and are finally significantly improved, especially at high temperatures. Since such a dynamical decoupling by a harmonic driving allows higher driving frequencies than the pulsed version, this form of coherence stabilization bears interesting perspectives for applications.

A second possibility for manipulating the decoherence of a single qubit is provided by the physics of coherent destruction of tunneling. For such a driving, we have found that the coherence stabilization results from the fact that the driving shifts the coherent long-time dynamics of the qubit towards lower frequencies. There, the spectral density of an ohmic bath is lower and, consequently, the effective dissipation is weaker. This implies that decoherence is generally reduced – most significantly at low temperatures. For high temperatures, however, the lower spectral density is counterbalanced by an increasing thermal noise, such that in this regime decoherence is essentially not influenced the driving.

For two qubits interacting via a Heisenberg exchange coupling, a suited AC field turns the interaction into an effective Ising interaction, which is much less sensitive to decoherence. For qubits with such a Heisenberg interaction, like e.g. spin qubits, this suggests the following coherence stabilization protocol: Use for the CNOT operation a pulse sequence that is suitable for Ising inter-

action with the latter being realized by a Heisenberg interaction with a proper additional AC field. This coherence stabilization scheme differs from previous proposals in two respects: First, it is different from dynamical decoupling because the driving commutes with the bath coupling. By contrast, the central idea of our scheme is to suppress rather the coherent system dynamics “transverse” to this sensitive system coordinate. Consequently, the bit-flip noise acts as pure phase noise, which is proportional to the temperature. Cooling, thus, enables a further coherence gain. The second difference is that the proposed scheme eliminates also the noise stemming from the spectral range above the driving frequency and, thus, is particularly valuable for ohmic noise spectra with large cutoff frequencies. Moreover, the driven system still allows one to perform the desired CNOT operation with high fidelity and within the same operation time as in the absence of the control field. Hence, the gained coherence time fully contributes to the number of feasible gate operations.

### Acknowledgement

We acknowledge helpful discussions with K. M. Fonseca-Romero, C. M. Wubs, R. Doll, F. K. Wilhelm, M. J. Storcz, and U. Hartmann. This work has been supported by the Freistaat Bayern via the network “Quanteninformation längs der A8” and by the Deutsche Forschungsgemeinschaft through SFB 631.

### A Average over all Pure States

In this appendix, we derive formulas for the evaluation of expressions of the type  $\text{tr}(\rho A)$  and  $\text{tr}(\rho A \rho B)$  in an ensemble average over all pure states  $\rho = |\psi\rangle\langle\psi|$ . The state  $|\psi\rangle$  is an element of an  $N$ -dimensional Hilbert space. Decomposed into an arbitrary orthonormal basis set  $\{|n\rangle\}_{n=1\dots N}$ , it reads

$$|\psi\rangle = \sum_{n=1}^N c_n |n\rangle, \quad (\text{A.1})$$

where the only restriction imposed on the coefficients  $c_n$  is the normalization  $\langle\psi|\psi\rangle = \sum_n |c_n|^2 = 1$ . Hence the ensemble of all pure states is described by the distribution

$$P(c_1, \dots, c_N) = \frac{2\pi^N}{(N-1)!} \delta\left(1 - \sum_{n=1}^N |c_n|^2\right). \quad (\text{A.2})$$

The prefactor on the right-hand side of Eq. (A.2) has been determined from the normalization

$$\int d^2c_1 \dots d^2c_N P(c_1, \dots, c_N) = 1 \quad (\text{A.3})$$

of the distribution and  $\int d^2c$  denotes integration over the real and the imaginary part of  $c$ . We emphasize that  $P(c_1, \dots, c_N)$  is invariant under unitary transformations of the state  $|\psi\rangle$ . The computation of the ensemble averages of the coefficients with the distribution (A.2) is straightforward and yields

$$\overline{c_m c_n^*} = \frac{1}{N} \delta_{mn}, \quad (\text{A.4})$$

$$\overline{c_m c_n^* c_{m'} c_{n'}^*} = \frac{1}{N(N+1)} (\delta_{mn} \delta_{m'n'} + \delta_{mn'} \delta_{nm'}). \quad (\text{A.5})$$

Using these expressions, we find for the ensemble averages of the expressions  $\text{tr}(\rho A)$  and  $\text{tr}(\rho A \rho B)$  the results

$$\overline{\text{tr}(\rho A)} = \overline{\langle \psi | A | \psi \rangle} = \frac{\text{tr}(A)}{N}, \quad (\text{A.6})$$

$$\overline{\text{tr}(\rho A \rho B)} = \overline{\langle \psi | A | \psi \rangle \langle \psi | B | \psi \rangle} = \frac{\text{tr}(A) \text{tr}(B) + \text{tr}(AB)}{N(N+1)}, \quad (\text{A.7})$$

which have been used to obtain the purity decay rate (12.10).

## References

- 1 Y. Nakamura, Y. A. Pashkin, and J. S. Tsai, *Nature* **398**, 786 (1999).
- 2 D. Vion, A. Aassime, A. Cottet, P. Joyez, H. Pothier, C. Urbina, D. Esteve, and M. H. Devoret, *Science* **296**, 886 (2002).
- 3 I. Chiorescu, Y. Nakamura, C. J. P. Harmans, and J. E. Mooij, *Science* **299**, 1869 (2003).
- 4 D. Leibfried, B. DeMarco, V. Meyer, D. Lucas, M. Barrett, J. Britton, W. M. Itano, B. Jelenković, C. Langer, T. Rosenband, and D. J. Wineland, *Nature* **422**, 412 (2003).
- 5 F. Schmidt-Kaler, H. Häffner, M. Riebe, S. Gulde, G. P. T. Lancaster, T. Deusched, C. Becher, C. F. Roos, J. Eschner, and R. Blatt, *Nature* **422**, 408 (2003).
- 6 Y. A. Pashkin, T. Yamamoto, O. Astafiev, Y. Nakamura, D. V. Averin, and J. S. Tsai, *Nature* **421**, 823 (2003).
- 7 A. M. Steane, *Fortschr. Phys.* **46**, 443 (1998).
- 8 G. M. Palma, K.-A. Suominen, and A. K. Ekert, *Proc. R. Soc. London, Ser. A* **452**, 567 (1996).
- 9 L.-M. Duan and G.-C. Guo, *Phys. Rev. Lett.* **79**, 1953 (1997).
- 10 P. Zanardi and M. Rasetti, *Phys. Rev. Lett.* **79**, 3306 (1997).
- 11 D. A. Lidar, I. L. Chuang, and K. B. Whaley, *Phys. Rev. Lett.* **81**, 2594 (1998).
- 12 A. Beige, D. Braun, B. Tregenna, and P. L. Knight, *Phys. Rev. Lett.* **85**, 1762 (2000).
- 13 D. Bacon, K. R. Brown, and K. B. Whaley, *Phys. Rev. Lett.* **87**, 247902 (2001).
- 14 P. Facchi and S. Pascazio, *Phys. Rev. Lett.* **89**, 080401 (2002).
- 15 H. Jirari and W. Pötz, *Phys. Rev. A* **72**, 013409 (2005).
- 16 A. K. Spoerl, T. Schulte-Herbrueggen, S. J. Glaser, V. Bergholm, M. J. Storcz, J. Ferber, and F. K. Wilhelm, *quant-ph/0504202*.
- 17 L. Viola and S. Lloyd, *Phys. Rev. A* **58**, 2733 (1998).
- 18 L. Viola, E. Knill, and S. Lloyd, *Phys. Rev. Lett.* **82**, 2417 (1999).
- 19 D. Vitali and P. Tombesi, *Phys. Rev. A* **65**, 012305 (2002).

- 20** H. Gutmann, F. K. Wilhelm, W. M. Kaminsky, and S. Lloyd, *Phys. Rev. A* **71**, 020302(R) (2005).
- 21** G. Falci, A. D'Arrigo, A. Mastellone, and E. Paladino, *Phys. Rev. A* **70**, 040101(R) (2004).
- 22** M. Thorwart, L. Hartmann, I. Goychuk, and P. Hänggi, *J. Mod. Opt.* **47**, 2905 (2000).
- 23** K. M. Fonseca-Romero, S. Kohler, and P. Hänggi, *Chem. Phys.* **296**, 307 (2004).
- 24** D. Loss and D. P. DiVincenzo, *Phys. Rev. A* **57**, 120 (1998).
- 25** M. Grifoni, E. Paladino, and U. Weiss, *Eur. Phys. J. B* **10**, 719 (1999).
- 26** M. Governale, M. Grifoni, and G. Schön, *Chem. Phys.* **268**, 273 (2001).
- 27** M. Thorwart and P. Hänggi, *Phys. Rev. A* **65**, 012309 (2002).
- 28** M. J. Storcz and F. K. Wilhelm, *Phys. Rev. A* **67**, 042319 (2003).
- 29** M. J. Storcz, U. Hartmann, S. Kohler, and F. K. Wilhelm, *Phys. Rev. B* **72**, 235321 (2005).
- 30** F. Grossmann, T. Dittrich, P. Jung, and P. Hänggi, *Phys. Rev. Lett.* **67**, 516 (1991).
- 31** F. Großmann, P. Jung, T. Dittrich, and P. Hänggi, *Z. Phys. B* **84**, 315 (1991).
- 32** F. Großmann and P. Hänggi, *Europhys. Lett.* **18**, 571 (1992).
- 33** Y. Kayanuma, *Phys. Rev. A* **50**, 843 (1994).
- 34** M. Grifoni and P. Hänggi, *Phys. Rep.* **304**, 229 (1998).
- 35** T. Dittrich, B. Oelschlägel, and P. Hänggi, *Europhys. Lett.* **22**, 5 (1993).
- 36** M. Grifoni, M. Sassetti, P. Hänggi, and U. Weiss, *Phys. Rev. E* **52**, 3596 (1995).
- 37** L. Hartmann, I. Goychuk, M. Grifoni, and P. Hänggi, *Phys. Rev. E* **61**, R4687 (2000).
- 38** J. Lehmann, S. Camalet, S. Kohler, and P. Hänggi, *Chem. Phys. Lett.* **368**, 282 (2003).
- 39** S. Kohler, S. Camalet, M. Strass, J. Lehmann, G.-L. Ingold, and P. Hänggi, *Chem. Phys.* **296**, 243 (2004).
- 40** M. A. Nielsen and I. L. Chuang, *Quantum Computing and Quantum Information* (Cambridge University Press, Cambridge, 2000).
- 41** Y. Makhlin, G. Schön, and A. Shnirman, *Rev. Mod. Phys.* **73**, 357 (2001).
- 42** A. Galindo and M. A. Martín-Delgado, *Rev. Mod. Phys.* **74**, 347 (2002).
- 43** B. Kane, *Nature (London)* **393**, 133 (1998).
- 44** K. M. Fonseca-Romero, S. Kohler, and P. Hänggi, *Phys. Rev. Lett.* **95**, 140502 (2005).
- 45** C. Ramanathan, S. Sinha, J. Baugh, T. F. Havel, and D. G. Cory, *Phys. Rev. A* **71**, 020303(R) (2005).
- 46** P. Hänggi, P. Talkner, and M. Borkovec, *Rev. Mod. Phys.* **62**, 251 (1990).
- 47** A. J. Leggett, S. Chakravarty, A. T. Dorsey, M. P. A. Fisher, A. Garg, and W. Zwerger, *Rev. Mod. Phys.* **59**, 1 (1987).
- 48** S. Kohler, T. Dittrich, and P. Hänggi, *Phys. Rev. E* **55**, 300 (1997).
- 49** J. F. Poyatos, J. I. Cirac, and P. Zoller, *Phys. Rev. Lett.* **78**, 390 (1997).
- 50** E. G. Petrov, I. A. Goychuk, and V. May, *Phys. Rev. E* **54**, 4726 (1996).
- 51** E. G. Petrov, I. A. Goychuk, and V. May, *Chem. Phys. Lett.* **253**, 428 (1996).
- 52** T. Novotný, *Europhys. Lett.* **59**, 648 (2002).
- 53** V. May and O. Kühn, *Charge and Energy Transfer Dynamics in Molecular Systems*, 2nd ed. (Wiley-VCH, Weinheim, 2003).
- 54** S. Kohler, J. Lehmann, and P. Hänggi, *Phys. Rep.* **406**, 379 (2005).
- 55** H. Y. Carr and E. M. Purcell, *Phys. Rev.* **94**, 630 (1954).
- 56** U. Haeberlen and J. S. Waugh, *Phys. Rev.* **175**, 453 (1968).
- 57** C. P. Slichter, *Principles of Magnetic Resonance*, Springer Series in Solid State Sciences, Vol. 1, 3rd ed. (Springer, Berlin, 1990).
- 58** L. Tian and S. Lloyd, *Phys. Rev. A* **62**, 050301 (2000).
- 59** I. M. Gradshteyn and I. S. Ryzhik, *Table of Integrals, Series, and Products*, 5th ed. (Academic Press, San Diego, 1994).
- 60** N. Schuch and J. Siewert, *Phys. Rev. A* **67**, 032301 (2003).
- 61** N. Gershenfeld and I. L. Chuang, *Science* **275**, 350 (1997).



## 13

# How to Distill Entanglement from a Finite Amount of Qubits?

*Stefan Probst-Schendzielorz, Thorsten Bschorr, and Matthias Freyberger*

### 13.1

#### Introduction

Quantum physics has undoubtedly strongly influenced the fields of communication and information processing [1]. It has become clear that information itself is a physical quantity that cannot solely be defined in classical terms. Fundamental aspects of quantum mechanics, which for a long time have been treated on the level of gedanken experiments [2], are now considered as promising pillars of a new quantum information technology.

The concept of entanglement is the most intriguing feature that allows to establish new paradigms in information processing without any classical counterpart. Corresponding examples like teleportation [3], quantum dense coding [4] or quantum cryptography [5] are now widely known. If we want to take advantage of these non-classical protocols, we have to invest a certain degree of entanglement as a quantum resource [6]. Consequently we have to understand how entanglement can be processed and how it can be measured [7,8].

In this respect the typical situation is that several communicating parties share components of an entangled system. Processing of entanglement then means that they can perform local unitary operations and local measurements on their respective parts of the complete system. Under these conditions it has been shown [9–11] that two parties, sharing a supply of non-maximally entangled qubit pairs, can extract a sample of stronger entangled pairs. This process of entanglement distillation is a particularly useful tool to improve communication based on entanglement that has been lowered by dissipative effects. Explicit examples of distillation protocols [9–12] are known, but so far no general approach to optimal distillation exists. However, in order to improve the fidelity, modifications of the original versions have been proposed [13–15]. Lower bounds for the fidelity of entanglement distillation based on faulty local operations have been studied [16]. Moreover, the concept of quantum repeaters [18] for long distance communication in the presence of errors needs

the distillation idea. On the other hand, entanglement distillation has led to the discovery of entangled states that cannot be distilled<sup>1</sup>, so called bound entangled states [19–21].

In the present work we investigate the entanglement distillation protocol described in [10] for the case that only a finite sample of entangled qubit pairs is available. In particular, we propose an iterative distillation scheme that starts from a finite number of identical pairs and delivers a single distilled pair applicable for further communication tasks. The corresponding mean fidelity can be formulated recursively in closed form. Its behavior turns out to be particularly interesting for small initial samples of entangled qubit pairs.

The article is organized as follows: We first state basic requirements of entanglement distillation in Sect. 2 and then review a specific protocol [10]. In Sect. 3 we analyze the general limitations of this distillation protocol under the constraint of finite samples of qubit pairs. In particular, we present an explicit iterative scheme to extract a single highly distilled pair from finite resources. Sect. 4 is finally devoted to an example of this iterative method showing its generic behavior. We conclude with Sect. 5.

## 13.2

### Entanglement Distillation

For any non-classical communication entangled systems first have to be distributed between a sender (Alice) and a receiver (Bob). In the course of this distribution the systems are influenced by various noise sources, which usually diminish the amount of entanglement. Any distillation process for such distributed systems is restricted to local operations and classical communication (LOCC). Moreover, realistic entanglement distillation schemes have to take into account errors [16] and the fact that Alice and Bob share only a finite amount of mixed entangled systems. In the present paper we focus on this last important restriction regarding resources.

We describe the entanglement distillation scheme [10] for the case that Alice and Bob share a finite ensemble of  $N$  entangled qubit pairs, see Fig. 13.1. Furthermore we restrict the state of these pairs to density operators

$$\hat{\rho} = A \hat{\Phi}^+ + B \hat{\Psi}^- + C \hat{\Psi}^+ + D \hat{\Phi}^-, \quad (13.1)$$

which are diagonal in the Bell-basis [1]. Here we have introduced a convenient abbreviation for projectors  $\hat{\Phi}^\pm \equiv |\phi^\pm\rangle\langle\phi^\pm|$  and  $\hat{\Psi}^\pm \equiv |\psi^\pm\rangle\langle\psi^\pm|$  on the Bell-states. The coefficients  $A, B, C$  and  $D$  describe the normalized probabilities to measure  $\hat{\Phi}^+, \hat{\Psi}^-, \hat{\Psi}^+$  or  $\hat{\Phi}^-$  on a system described by  $\hat{\rho}$ , Eq. (13.1). We assume

1) Note however, that entangled qubit pairs can always be distilled towards a maximally entangled system, see also [21].

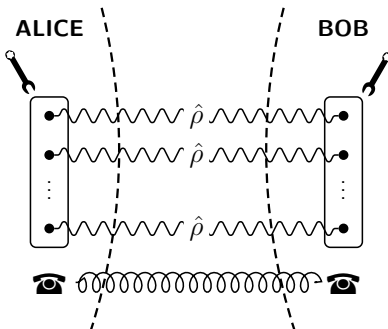


**Fig. 13.1** General setup for entanglement distillation. Alice and Bob share a finite set of  $N$  entangled systems, each described by the density operator  $\hat{\rho}$ . They try to enhance the amount of entanglement as much as possible for at least one system. Because of spatial separation, Alice and Bob are restricted to local operations, local measurements and classical communication (LOCC).

that  $A$  is the largest coefficient in this mixture with  $A > 0.5$  since only in this case  $\hat{\rho}$  is non-separable [21]. We emphasize that for the other coefficients  $B$ ,  $C$ , and  $D$  no further assumptions are needed for the method presented in this paper.

To quantify the quality of a distillation scheme, one needs a corresponding measure. A frequently used quantity is the fidelity

$$F_{|\psi\rangle}(\hat{\rho}) = \text{tr}(\hat{\rho} |\psi\rangle\langle\psi|) \quad (13.2)$$

of a state  $\hat{\rho}$  with respect to a maximally entangled reference state  $|\psi\rangle$ . The reference state  $|\psi\rangle$  should be reached asymptotically by the distillation protocol. For an entanglement distillation scheme the aim is to gain asymptotically entangled systems described by a pure state. In the case of two qubits this is typically one of the Bell-states. In our case this means for  $A > 0.5$ , that the fidelity  $F_{|\phi^+\rangle}(\hat{\rho})$ , which quantifies the amount of entanglement, has to be maximized.

### 13.2.1

#### The Protocol

The explicit distillation protocol we refer to was introduced in [9, 10]. The process increases the fidelity  $F(\hat{\rho}) \equiv F_{|\phi^+\rangle}(\hat{\rho})$ , whereby  $\hat{\rho}$ , Eq. (13.1), is only restricted by  $A > 0.5$ . Its central element is a CNOT transformation [1] and hence we denote it as CNOT distillation. We review the scheme [10] and then analyze its behavior for finite quantum resources.

The CNOT distillation processes two qubit pairs in one step. Alice and Bob arrange the corresponding locally accessible qubits of the pairs 1 and 2 as shown in Fig. 13.2.

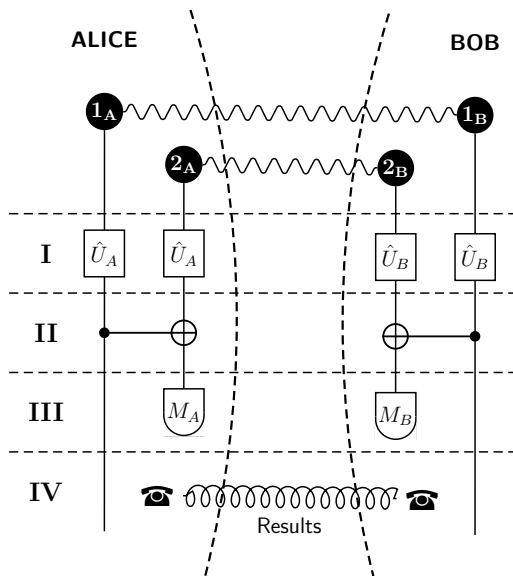


**Fig. 13.2** Single step of CNOT distillation [10] for two entangled qubit pairs. Alice and Bob share the qubit pairs 1 (qubits  $1_A$  and  $1_B$ ) and 2 (qubits  $2_A$  and  $2_B$ ). With their locally accessible qubits they perform four operations:

(I) single qubit rotations, (II) CNOT with the locally accessible qubits, (III) measurement of the target qubits and (IV) classical exchange of the measurement results to select the distilled system.

Alice holds the qubits  $1_A$  and  $2_A$  and Bob holds the qubits  $1_B$  and  $2_B$ . These qubits can now be treated locally using the following operations:

- I. Alice and Bob perform a unitary operation on all locally accessible qubits. Alice rotates her qubits using  $\hat{U}_A = \frac{1}{\sqrt{2}}(\hat{1} - i\hat{\sigma}_x)$ , whereas Bob applies the rotation  $\hat{U}_B = \frac{1}{\sqrt{2}}(\hat{1} + i\hat{\sigma}_x)$ , with the corresponding Pauli-operators  $\hat{\sigma}_x$  [1]. After these unitary transformations the initially Bell-diagonal state  $\hat{\rho}$  of qubit pair 1, Eq. (13.1), reads

$$\hat{U}_A \otimes \hat{U}_B \hat{\rho} \hat{U}_B^\dagger \otimes \hat{U}_A^\dagger = A \hat{\Phi}^+ + D \hat{\Psi}^- + C \hat{\Psi}^+ + B \hat{\Phi}^- \quad (13.3)$$

and analogously for the state of qubit pair 2. Hence in total these rotations simply exchange the  $\hat{\Psi}^-$  contribution with the  $\hat{\Phi}^-$  contribution of the initial state  $\hat{\rho}$ , Eq. (13.1).

- II. Alice and Bob then perform CNOT operations on their respective qubits. The qubits of pair 1 act as control qubits (qubits  $1_A$  and  $1_B$ , see Fig. 13.2) and the other pair as target qubits (qubits  $2_A$  and  $2_B$ ) of the CNOTs. operation see appendix A, in which we also present an explicit expression, Eq. (A.1), for the resulting state  $\hat{R}$  of the two pairs.
- III. Both measure their target qubits (qubits  $2_A$  and  $2_B$ ) in the computational basis  $\{|0\rangle, |1\rangle\}$ . They obtain either the result “0” or “1”.

IV. Alice and Bob exchange classically their measurement results. The distillation was successful if the combined result reads “00” or “11”. Then they keep pair 1. Using the complete state  $\hat{R}$ , Eq. (A.1), we arrive at the conditioned density operator

$$\begin{aligned}\hat{\rho}^{(s)} &= \frac{1}{p^{(s)}/2} {}_2\langle 00|\hat{R}|00\rangle_2 = \frac{1}{p^{(s)}/2} {}_2\langle 11|\hat{R}|11\rangle_2 \\ &= \frac{1}{p^{(s)}} \left[ (A^2 + B^2) \hat{\Phi}^+ + 2CD \hat{\Psi}^- + (C^2 + D^2) \hat{\Psi}^+ + 2AB \hat{\Phi}^- \right],\end{aligned}\quad (13.4)$$

which is normalized by the success probability

$$p^{(s)} \equiv (A + B)^2 + (C + D)^2 \quad (13.5)$$

to find the result “00” or “11”.

If Alice and Bob read off the results “01” or “10”, the reduced density operator of pair 1 reads

$$\begin{aligned}\hat{\rho}^{(u)} &= \frac{1}{1 - p^{(s)}} \left[ (AC + BD)\hat{\Phi}^+ + (AD + BC)\hat{\Psi}^- \right. \\ &\quad \left. + (AC + BD)\hat{\Psi}^+ + (AD + BC)\hat{\Phi}^- \right].\end{aligned}\quad (13.6)$$

One can immediately see that the coefficients of the  $\hat{\Phi}^+$  and the  $\hat{\Psi}^+$  components are equal. Hence if we start from a dominant  $\hat{\Phi}^+$  component, that is  $A > 0.5$ , we can never achieve  $F(\hat{\rho}^{(u)}) > \frac{1}{2}$ . Consequently, in this unsuccessful case Alice and Bob discard pair 1.

In the successful case pair 1 is mapped from a Bell-diagonal state  $\hat{\rho}$ , Eq. (13.1), to the Bell-diagonal state  $\hat{\rho}^{(s)}$ , Eq. (13.4). The corresponding new fidelity is given by

$$\begin{aligned}F(\hat{\rho}^{(s)}) &= \text{tr}(\hat{\rho}^{(s)}\hat{\Phi}^+) \\ &= \frac{A^2 + B^2}{(A + B)^2 + (C + D)^2} = \frac{A^2 + B^2}{(A + B)^2 + (1 - A - B)^2}.\end{aligned}\quad (13.7)$$

We show this fidelity as a function of the initial fidelity  $F(\hat{\rho}) = A$  for different values of  $B$  in Fig. 13.3.

Analyzing Eq. (13.7) shows that for  $B < B_{\text{crit}} = \sqrt{A} - A$  the fidelity increases, that is  $F(\hat{\rho}^{(s)}) > A$ . However, this fidelity does not completely describe the single step process. A complete description also has to take into account the unsuccessful case (discarding qubit pair 1 in step IV of the distillation protocol). Therefore we have to average between the successfull cases,

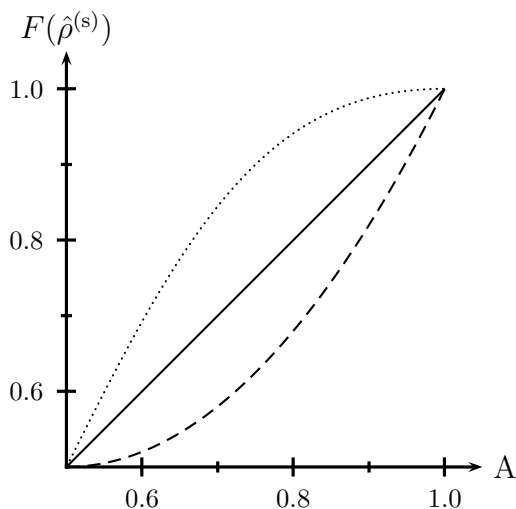


**Fig. 13.3** Fidelity  $F(\hat{\rho}^{(s)})$ , Eq. (13.7), for a successful distillation step as a function of the initial fidelity  $A$ . All possible curves lie in between the extreme curves for  $B = 0$  (dotted line) and for  $B = 1 - A$  (dashed line). The straight line obtained for  $B_{\text{crit}} \equiv \sqrt{A} - A$  separates the domain  $B < B_{\text{crit}}$  for which the fidelity increases in a single distillation step from the domain  $B > B_{\text{crit}}$  for which it decreases.

$F(\hat{\rho}^{(s)})$  Eq. (13.7), and the unsuccessful case<sup>2</sup>,  $F(\hat{\rho}^{(u)}) \leq \frac{1}{2}$ , Eq. (13.6). Hence we define the average fidelity

$$\begin{aligned}\langle F \rangle &\equiv p^{(s)}F(\hat{\rho}^{(s)}) + (1 - p^{(s)})F(\hat{\rho}^{(u)}) \\ &= A^2 + B^2 + AC + BD \\ &= A^2 + A(C - B) + B(1 - C).\end{aligned}\tag{13.8}$$

For all possible values of  $B$  and  $C$  the average fidelity  $\langle F \rangle$  turns out to be equal to or less than the original fidelity  $A$ . This can be seen by analyzing the parabola of the average fidelity, Eq. (13.8), for the boundary values  $A = 1/2$ , where we obtain

$$\begin{aligned} \langle F \rangle \Big|_{A=1/2} &= \left(\frac{1}{2}\right)^2 + \frac{1}{2}(C - B) + B(1 - C) \\ &= \frac{1}{2} \left(\frac{1}{2} + C + B\right) - BC \leq \frac{1}{2}, \end{aligned} \quad (13.9)$$

- 2) Note that if the unsuccessful case occurs the parties are able to prepare with further local operations and classical communication two qubits with a fidelity of  $\frac{1}{2}$ . However, we are studying the distillation process by itself, for further information see [17].

and  $A = 1$ , which results in  $\langle F \rangle = 1$  and hence we always have  $\langle F \rangle \leq A$ . This is consistent with the fact that the total *amount* of entanglement cannot increase under a LOCC process [9].

However, we emphasize that so far we have just discussed a single distillation step performed on two entangled qubit pairs. The situation becomes different and more interesting when we now consider a finite ensemble with  $N > 2$  pairs.

### 13.3

#### CNOT Distillation for a Finite Set of Entangled Systems

Alice and Bob now perform the scheme of Fig. 13.2 with an even number  $N$  of pairs<sup>3</sup>. After one distillation step they have  $m \leq N/2$  pairs left with probability

$$p(N, m) = \binom{N/2}{m} [p^{(s)}]^m [1 - p^{(s)}]^{N/2-m}, \quad (13.10)$$

which contains the success probability  $p^{(s)}$  according to Eq. (13.5).

For more than two pairs of entangled qubits the unsuccessful case occurs when all these pairs have to be discarded in a single distillation step. Hence starting from  $N$  pairs we can define the average fidelity

$$\langle F \rangle(N) \equiv p(N, 0) F(\hat{\rho}^{(u)}) + [1 - p(N, 0)] F(\hat{\rho}^{(s)}) \quad (13.11)$$

using the density operators  $\hat{\rho}^{(s)}$ , Eq. (13.4), and  $\hat{\rho}^{(u)}$ , Eq. (13.6). With an increasing amount  $N$  of pairs the average fidelity  $\langle F \rangle(N)$  also increases, because of the decreasing probability  $p(N, 0)$  to lose all qubit pairs. Using Eq. (13.11) one finds that

$$N_{\min} = 2 \frac{\ln \left[ \frac{A - F(\hat{\rho}^{(s)})}{F(\hat{\rho}^{(u)}) - F(\hat{\rho}^{(s)})} \right]}{\ln(1 - p^{(s)})} \quad (13.12)$$

pairs are needed to obtain an average fidelity  $\langle F \rangle(N_{\min}) = A$ . Fig. 13.4 shows the minimal size  $N_{\min}$  for a finite ensemble described by Werner-states ( $B = C = D = (1 - A)/3$ ) [22] which leads to a successful distillation in a single step of the protocol. In the plot one can clearly identify the region where on average the fidelity increases, that is  $\langle F \rangle(N) > A$ .

Moreover, if  $m \geq 2$  pairs are left after such a first step we can continue with the distillation. We consider such an iteration in the following paragraph.

- 3) Due to the fact that the entangled qubit pairs are being processed pairwise in the protocol, we assume an even number of pairs. For a single application of the protocol this assumption is without loss of generality.

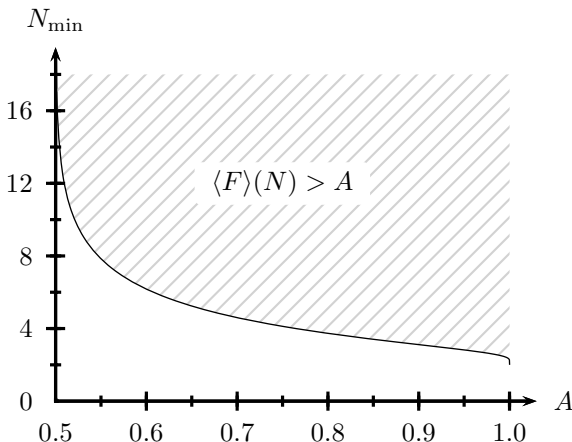


**Fig. 13.4** Minimal size  $N_{\min}$ , Eq. (13.12), of the finite sample of entangled qubits to obtain an average fidelity  $\langle F \rangle(N_{\min}) = A$ . The plot has been calculated for Bell-diagonal states with  $B = C = D = (1 - A)/3$ . For small initial fidelities, that is  $A \rightarrow 1/2$ , the

amount of necessary qubit pairs grows very fast according to  $2 \ln \left( \frac{4}{5}(A - 1/2) \right) / \ln \left( \frac{4}{9} \right)$ . For  $A \rightarrow 1$  the minimal size  $N_{\min}$  behaves like  $2 - \ln(9) / \ln \left( \frac{4}{3}(1 - A) \right)$  with  $\lim_{A \rightarrow 1} N_{\min} = 2$ .

### 13.3.1

#### Iterative Distillation

The resulting state  $\hat{\rho}^{(s)}$ , Eq. (13.4), of a successful distillation step is again Bell-diagonal and hence the complete process can be applied iteratively, as long as qubit pairs are left to use. Starting from an initial density operator  $\hat{\rho}_0^{(s)} \equiv \hat{\rho}$ , Eq. (13.1), the density operator  $\hat{\rho}_{i-1}^{(s)}$  is mapped on a density operator  $\hat{\rho}_i^{(s)}$  if the  $i^{\text{th}}$  distillation step was successful. The corresponding coefficients of the Bell-projectors, see Eq. (13.4), transform as

$$\begin{pmatrix} A_i^{(s)} \\ B_i^{(s)} \\ C_i^{(s)} \\ D_i^{(s)} \end{pmatrix} = \frac{1}{p_i^{(s)}} \begin{pmatrix} (A_{i-1}^{(s)})^2 + (B_{i-1}^{(s)})^2 \\ 2 C_{i-1}^{(s)} D_{i-1}^{(s)} \\ (C_{i-1}^{(s)})^2 + (D_{i-1}^{(s)})^2 \\ 2 A_{i-1}^{(s)} B_{i-1}^{(s)} \end{pmatrix} \quad (13.13)$$

with the success probability, Eq. (13.5),

$$p_i^{(s)} \equiv \left( A_{i-1}^{(s)} + B_{i-1}^{(s)} \right)^2 + \left( C_{i-1}^{(s)} + D_{i-1}^{(s)} \right)^2. \quad (13.14)$$

This mapping was studied in detail in [23] and we just show an example in Fig. 13.5. The decrease in the first step of this example could be avoided with a modified protocol like [15]. However, for such modifications one needs more specified knowledge about the parameters of  $\hat{\rho}$ , Eq. (13.1). Our only

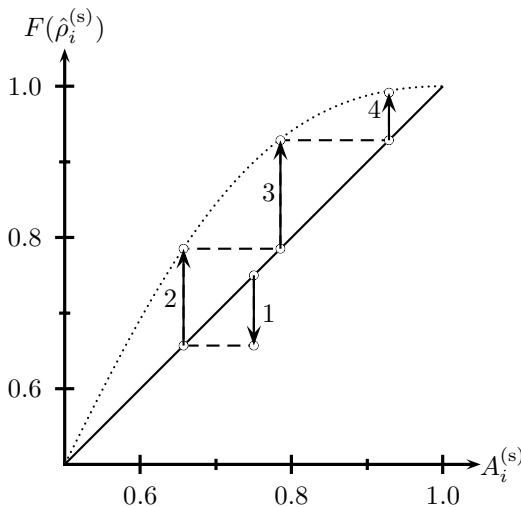


**Fig. 13.5** Behavior of the fidelity  $F(\hat{\rho}_i^{(s)})$ , Eq. (13.7), for four successful iterations according to the mapping Eq. (13.13). As starting point we have chosen a state  $\hat{\rho}_0^{(s)}$  parameterized by  $(A_0^{(s)} = 0.75, B_0^{(s)} = 0.21, C_0^{(s)} = 0.02, D_0^{(s)} = 0.02)$ . One can clearly see, that in the first step the fidelity

decreases to  $F(\hat{\rho}_1^{(s)}) \approx 0.66$ . However, for the following iterations the coefficients  $B_i^{(s)}$  become very small ( $B_i^{(s)} = 0$  parameterizes the dotted line, see also Fig. 13.3) leading to a rapid increase of the fidelity. After just four successful iterations the fidelity reaches a value  $F(\hat{\rho}_1^{(s)}) > 0.99$ .

assumption about  $\hat{\rho}$  is that  $A > 0.5$ . Note that for an iteration of the operations  $\hat{U}_A$  and  $\hat{U}_B$  of Alice and Bob in step I are very important, otherwise the process would converge towards  $(A_\infty^{(s)} = 0.5, B_\infty^{(s)} = 0, C_\infty^{(s)} = 0, D_\infty^{(s)} = 0.5)$ .

If, however, the  $i^{\text{th}}$  step was unsuccessful we have a mapping from  $\hat{p}_{i-1}^{(s)}$  to  $\hat{p}_i^{(u)}$  according to

$$\begin{pmatrix} A_i^{(u)} \\ B_i^{(u)} \\ C_i^{(u)} \\ D_i^{(u)} \end{pmatrix} = \frac{1}{1 - p_i^{(s)}} \begin{pmatrix} A_{i-1}^{(s)} C_{i-1}^{(s)} + B_{i-1}^{(s)} D_{i-1}^{(s)} \\ A_{i-1}^{(s)} D_{i-1}^{(s)} + B_{i-1}^{(s)} C_{i-1}^{(s)} \\ A_{i-1}^{(s)} C_{i-1}^{(s)} + B_{i-1}^{(s)} D_{i-1}^{(s)} \\ A_{i-1}^{(s)} D_{i-1}^{(s)} + B_{i-1}^{(s)} C_{i-1}^{(s)} \end{pmatrix}. \quad (13.15)$$

A full iteration of the entanglement distillation for finite quantum resources has to take into account all possible combinations of such successful and unsuccessful steps. Our aim then is to obtain at the end one entangled qubit pair with an average fidelity as high as possible.

In order to find an expression for the average fidelity of the complete iterative process, we first regard one specific step of the iteration. For the  $i^{\text{th}}$  step of the protocol at most  $n_{\max} = N/2^{i-1}$  pairs are left to use. In general, we have  $n \leq n_{\max}$  pairs left for the  $i^{\text{th}}$  step and we obtain  $j \leq n/2$  distilled pairs with

the probability

$$p_i(n, j) = \binom{\lfloor n/2 \rfloor}{j} \left( p_i^{(s)} \right)^j \left( 1 - p_i^{(s)} \right)^{\lfloor n/2 \rfloor - j}, \quad (13.16)$$

where we have defined the symbol

$$\left\lfloor \frac{n}{2} \right\rfloor := \begin{cases} \frac{n}{2} & \text{for even } n \\ \frac{n-1}{2} & \text{for odd } n. \end{cases} \quad (13.17)$$

In fact this means that we do not yet consider the left over pair if  $n$  is odd. This restriction will be removed later.

The corresponding average fidelity of the  $i^{\text{th}}$  step therefore reads

$$\langle F \rangle_i(n) = p_i(n, 0)F(\hat{\rho}_i^{(u)}) + p_i(n, 1)F(\hat{\rho}_i^{(s)}) + \sum_{j=2}^{\lfloor n/2 \rfloor} p_i(n, j)F(\hat{\rho}_i^{(s)}). \quad (13.18)$$

Here we average over the fidelities for discarding all pairs, for having exactly one qubit pair left (end of iteration) and for obtaining more than one distilled pair. In the last case we can iteratively repeat the distillation. This corresponds to replacing the fidelity  $F(\hat{\rho}_i^{(s)})$  by the average fidelity  $\langle \mathcal{F} \rangle_{i+1}(j)$ . We therefore arrive at a recursive definition for the average fidelity

$$\langle \mathcal{F} \rangle_i(n) = p_i(n, 0)F(\hat{\rho}_i^{(u)}) + p_i(n, 1)F(\hat{\rho}_i^{(s)}) + \sum_{j=2}^{\lfloor n/2 \rfloor} p_i(n, j)\langle \mathcal{F} \rangle_{i+1}(j) \quad (13.19)$$

for distilling until either no pair is left or until one highly distilled pair is delivered after we have started from  $n$  pairs in step  $i$ . Hence the average fidelity for a complete distillation process of  $N$  entangled qubit pairs is given by  $\langle \mathcal{F} \rangle_1(N)$ .

An important improvement can be achieved in the case of an odd number of pairs. In each distillation step we may obtain an odd number  $n$  of pairs and hence we can store the additional pair as a backup [24]. In this case we still can use the last backup pair  $\hat{\rho}^{(b)}$ , if we would have to discard all pairs in a further distillation step. In Eq. (13.19) this corresponds to replacing the fidelity  $F(\hat{\rho}_i^{(u)})$  by the fidelity  $F(\hat{\rho}^{(b)})$  of the backup pair. The complete process is shown in Fig. 13.6. In the following example we will see that such a backup procedure strongly enhances the average fidelity.

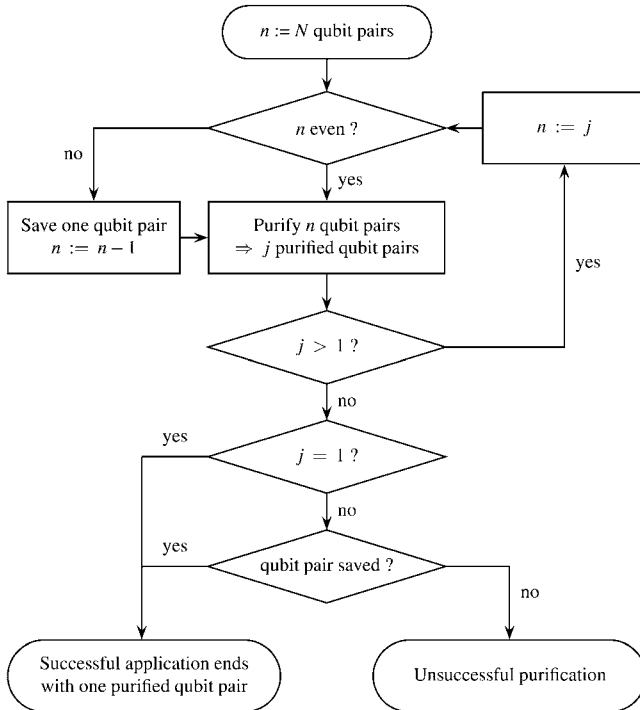


**Fig. 13.6** Flow chart for the iterative CNOT distillation scheme with finite quantum resources. Starting from  $N$  entangled qubit pairs we extract a single highly distilled pair. In every step  $\lfloor n/2 \rfloor$  measurements are performed and some pairs have to be

discarded. To increase the average fidelity one pair is saved in every iteration step for an odd number  $n$  [24]. Rarely the distillation may still fail if no pair was saved and all pairs in the last step have to be dismissed.

### 13.4

#### Example of the Iterative Distillation for Small Finite Sets

We demonstrate the behavior of the iterative distillation with an example. For this we have chosen a state  $\hat{\rho}_0^{(s)} \equiv \hat{\rho}$  which is initially parameterized by  $(A_0^{(s)}, B_0^{(s)} = (1 - A_0^{(s)})/5, C_0^{(s)} = (1 - A_0^{(s)} - B_0^{(s)})/2, D_0^{(s)} = (1 - A_0^{(s)} - B_0^{(s)})/2)$ .

First we compare in Fig. 13.7 the relative average fidelity  $\langle \mathcal{F} \rangle_1(N) / A_0^{(s)}$  for different resources of qubit pairs. In accordance with the previous paragraph we have calculated the final average fidelity  $\langle \mathcal{F} \rangle_1(N)$  with backup as a function of the initial fidelity  $A_0^{(s)}$  for  $N = 4$  (dotted line),  $N = 5$  (solid line) and  $N = 6$  (dashed line) pairs. We see that  $N = 5$  pairs are always superior to the nearby even cases, because for an odd  $N$  already in the first step of the distillation a backup pair is stored. For even numbers  $N$  there is a minimal initial fidelity  $A_{\min}(N)$  which is needed to have a successful iterative distillation. Clearly one can also start from initial states  $\hat{\rho}_0^{(s)}$  that show such a minimal

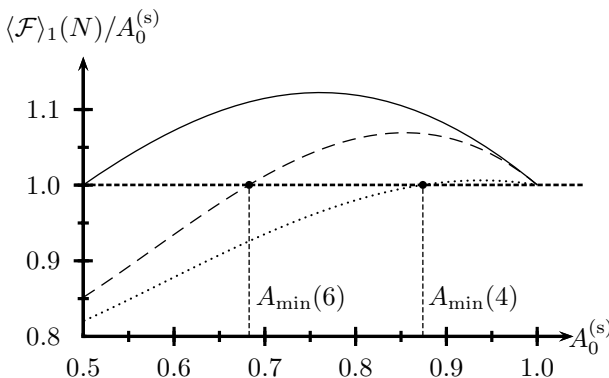


**Fig. 13.7** Relative average fidelity  $\langle \mathcal{F} \rangle_1(N)/A_0^{(s)}$  with backup step as a function of the initial fidelity  $A_0^{(s)}$  for different amounts  $N$  of qubit pairs. The initial states are described by the parameters  $(A_0^{(s)}, B_0^{(s)} = (1 - A_0^{(s)})/5, C_0^{(s)} = (1 - A_0^{(s)} - B_0^{(s)})/2, D_0^{(s)} = (1 - A_0^{(s)} - B_0^{(s)})/2)$ . For  $N = 5$

qubit pairs (solid line) one can see clearly that in our example we always get an improvement. Whereas for  $N = 4$  qubit pairs (dotted line) we only get an improvement if  $A_0^{(s)} > A_{\min}(4) \approx 0.87$ . For  $N = 6$  qubit pairs (dashed line) we need at least an initial fidelity of  $A_{\min}(6) \gtrsim 0.68$  to succeed.

initial fidelity for odd numbers  $N$ . However, due to the missing backup pair at the beginning of the iteration, this effect is much more pronounced for even numbers  $N$ .

For even numbers of entangled qubit pairs the behavior of this minimal fidelity  $A_{\min}(N)$  is therefore demonstrated in Fig. 13.8. As expected the minimal fidelity decreases towards  $A_{\min}(N) \rightarrow 1/2$  for an increasing amount of pairs. However, this decrease is relatively slow for larger resources of pairs.

Finally, we show in Fig. 13.9 the generic behavior of the average fidelity  $\langle \mathcal{F} \rangle_1(N)$  depending on the available amount  $N$  of pairs. We compare the iterative results without and with backup for a fixed initial fidelity  $A_0^{(s)} = 0.75$  to the completely successful mapping, Eq. (13.13). Storing a backup pair in the case of an odd amount clearly leads to a higher average fidelity. The zigzag in the curves reveals the difference between odd and even numbers  $N$  of pairs. If the iteration starts with an odd number of entangled qubit pairs, at least one pair is saved. One can even see that for even numbers it is on average better to drop one pair before performing the first distillation step. Although this means to start with one pair less, the average fidelity is higher. This is most obvious for small finite ensembles.

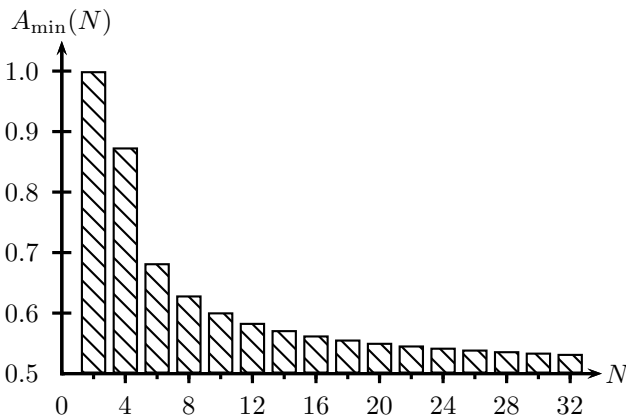


**Fig. 13.8** Minimal fidelity  $A_{\min}(N)$  for even numbers  $N$  of entangled qubit pairs. For initial fidelities larger than  $A_{\min}(N)$  we obtain an increased average fidelity in the iterative CNOT distillation with backup, see also Fig. 13.6. We have used the same initial

state as in Fig. 13.7. Only for  $N = 2$  pairs the minimal fidelity  $A_{\min}(2)$  is equal to 1. For larger finite ensembles of pairs the necessary minimal fidelity converges rather slowly towards 0.5.

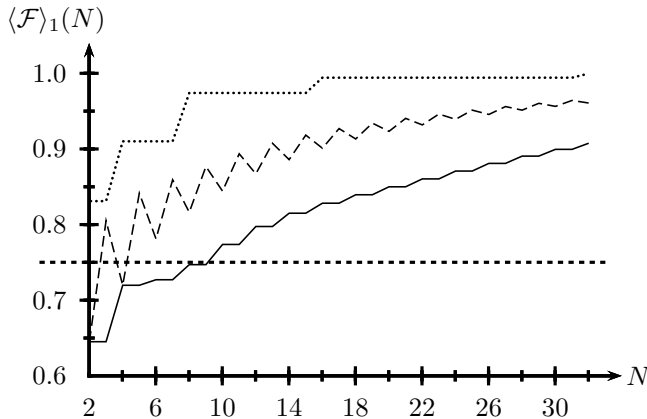


**Fig. 13.9** Comparison of the average fidelities depending on the amount  $N$  of initially accessible qubit pairs. The plot shows the average fidelities of iterative schemes based on the CNOT protocol without backup (solid curve), with backup (dashed curve) and the mapping of the completely successful case (dotted curve), Eq. (13.13). We show their

behavior for the example state with an initial fidelity  $A_0^{(s)} = 0.75$ . The plot again shows the advantage of storing one pair in the case of odd numbers  $N$ . It turns out that for even numbers  $N$  it is on average advantageous to drop one pair and to start the distillation with one pair less.

## 13.5 Conclusions

Entanglement is a fundamental resource to perform non-classical information processing. It is therefore essential to understand its prospects as well as its limitations. Entanglement distillation is a tool of central interest for such ques-

tions. It is a process that clearly shows how a quantum resource can be treated by local operations and how sensitive it is.

In the present article we have presented a method how to distill entanglement from a finite amount of qubits. We have analyzed an iterative scheme for a known distillation protocol. This protocol is especially useful for the implementation of an iteration since it puts very low restrictions on the density operators of the processed systems. In particular, we have emphasized the application to finite quantum resources. In this respect it was possible to demonstrate the limitations on the needed number of entangled qubit pairs as well as on their initial entanglement for a successful distillation. Stronger entanglement can be obtained iteratively already for small initial numbers of pairs, even though many pairs have to be sacrificed in order to obtain one distilled pair. We have partially lowered this loss by introducing backup pairs in our algorithmic description.

Clearly this is not the only possibility to achieve iterative entanglement distillation. First, one can think of recycling backup systems in the distillation process. This, however, works only in a rather narrow regime in which the fidelities of the recycled pairs are close. Second, it is also possible to iterate completely different distillation methods, like quantum hashing [9] for finite resources.

Finally, it would be important to simulate distillation for an experimental system, which offers a way to control a finite number of qubit pairs. A possible candidate for this would be an optical lattice filled with atoms, which can be controlled by collisions [25–27].

## Acknowledgement

We acknowledge financial support by the Deutsche Forschungsgemeinschaft within the *Schwerpunktprogramm Quanten-Informationsverarbeitung* (SPP1078).

## A CNOT operations on two entangled qubit pairs

This operation consists of two spatially separated CNOT operations, see also Fig. 13.2. It is applied to two qubit pairs, where the qubits of the first pair are used as control qubits and the qubits of the second pair are acting as target qubits. The operation acts on the Bell-projectors as shown in Table 13.1.

After step II of the distillation protocol we obtain the state  $\hat{R}$  of two qubit pairs. The state results from the application of the local rotations  $\hat{U}_A$  and  $\hat{U}_B$ , Eq. (13.3), and the CNOT operations on the state  $\hat{\rho}_1 \otimes \hat{\rho}_2$  of the Bell-diagonal

**Tab. 13.1** Two-qubit-pair CNOT operation on Bell-state projectors of control pair 1 and target pair 2.

C T \ \diagdown	$\hat{\Phi}_1^+$	$\hat{\Phi}_1^-$	$\hat{\Psi}_1^+$	$\hat{\Psi}_1^-$
$\hat{\Phi}_2^+$	$\hat{\Phi}_1^+ \hat{\Phi}_2^+$	$\hat{\Phi}_1^- \hat{\Phi}_2^+$	$\hat{\Psi}_1^+ \hat{\Psi}_2^+$	$\hat{\Psi}_1^- \hat{\Psi}_2^+$
$\hat{\Phi}_2^-$	$\hat{\Phi}_1^- \hat{\Phi}_2^-$	$\hat{\Phi}_1^+ \hat{\Phi}_2^-$	$\hat{\Psi}_1^- \hat{\Psi}_2^-$	$\hat{\Psi}_1^+ \hat{\Psi}_2^-$
$\hat{\Psi}_2^+$	$\hat{\Phi}_1^+ \hat{\Psi}_2^+$	$\hat{\Phi}_1^- \hat{\Psi}_2^+$	$\hat{\Psi}_1^+ \hat{\Phi}_2^+$	$\hat{\Psi}_1^- \hat{\Phi}_2^+$
$\hat{\Psi}_2^-$	$\hat{\Phi}_1^- \hat{\Psi}_2^-$	$\hat{\Phi}_1^+ \hat{\Psi}_2^-$	$\hat{\Psi}_1^- \hat{\Phi}_2^-$	$\hat{\Psi}_1^+ \hat{\Phi}_2^-$

qubit pairs 1 and 2, Eq. (13.1). Using Table 13.1 this state then reads

$$\begin{aligned} \hat{R} = & (A^2 \hat{\Phi}_1^+ + CD \hat{\Psi}_1^- + C^2 \hat{\Psi}_1^+ + AB \hat{\Phi}_1^-) \otimes \hat{\Phi}_2^+ \\ & + (B^2 \hat{\Phi}_1^+ + CD \hat{\Psi}_1^- + D^2 \hat{\Psi}_1^+ + AB \hat{\Phi}_1^-) \otimes \hat{\Phi}_2^- \\ & + (BD \hat{\Phi}_1^+ + BC \hat{\Psi}_1^- + BD \hat{\Psi}_1^+ + AD \hat{\Phi}_1^-) \otimes \hat{\Psi}_2^- \\ & + (AC \hat{\Phi}_1^+ + AD \hat{\Psi}_1^- + AC \hat{\Psi}_1^+ + BC \hat{\Phi}_1^-) \otimes \hat{\Psi}_2^+ . \end{aligned} \quad (A.1)$$

## References

- 1 For recent books on the subject, see H.-K. Lo, T. Spiller, and S. Popescu (eds.), *Introduction to Quantum Computation and Information* (World Scientific Publishing, Singapore, 1998); J. Gruska, *Quantum Computing* (McGraw Hill, London, 1999); D. Bouwmeester, A. Ekert, and A. Zeilinger (eds.), *The Physics of Quantum Information* (Springer-Verlag, Berlin, 2000); M. A. Nielsen and I. L. Chuang, *Quantum Computation and Quantum Information* (Cambridge University Press, Cambridge, 2000); G. Alber, T. Beth, M. Horodecki, P. Horodecki, R. Horodecki, M. Rötteler, H. Weinfurter, R. Werner, and A. Zeilinger, *Quantum Information: An Introduction to Basic Theoretical Concepts and Experiments* (Springer-Verlag, Berlin, 2001).
- 2 See, for example, G. Auletta, *Foundations and interpretations of Quantum Mechanics* (World Scientific, Singapore, 2000).
- 3 C. H. Bennett, G. Brassard, C. Crépeau, R. Jozsa, A. Peres, and W. K. Wootters, *Phys. Rev. Lett.* **70**, 1895 (1993).
- 4 C. H. Bennett and S. J. Wiesner, *Phys. Rev. Lett.* **69**, 2881 (1992); K. Mattle, H. Weinfurter, P. G. Kwiat, and A. Zeilinger, *Phys. Rev. Lett.* **76**, 4656 (1996).
- 5 A. K. Ekert, *Phys. Rev. Lett.* **67**, 661 (1991).
- 6 C. H. Bennett, *Phys. Scr.* **T76**, 210 (1998).
- 7 V. Vedral and M. B. Plenio, *Phys. Rev. A* **57**, 1619 (1998).
- 8 M. Horodecki, *Quantum Inf. Comput.* **1**(1), 3 (2001).
- 9 C. H. Bennett, G. Brassard, S. Popescu, B. Schumacher, J. A. Smolin, and W. K. Wootters, *Phys. Rev. Lett.* **76**, 722 (1996); C. H. Bennett, D. P. DiVincenzo, J. A. Smolin, and W. K. Wootters, *Phys. Rev. A* **54**, 3824 (1996).
- 10 D. Deutsch, A. Ekert, R. Jozsa, C. Macchiavello, S. Popescu, and A. Sanpera, *Phys. Rev. Lett.* **77**, 2818 (1996).

- 11 N. Gisin, Phys. Lett. A **210**, 151 (1996).
- 12 J. Dehaene, M. Van den Nest, B. De Moor, and F. Verstraete, Phys. Rev. A **67**, 022310 (2003).
- 13 T. Opatrný and G. Kurizki, Phys. Rev. A **60**, 167 (1999).
- 14 E. Maneva and J. A. Smolin, in: AMS Contemporary Mathematics Series, vol. 30, 5; S. J. Lomonaco and H. E. Brandt (eds.), AMS (2002), pp. 203–212.
- 15 N. Metwally, Phys. Rev. A **66**, 054302 (2002).
- 16 G. Giedke, H. J. Briegel, J. I. Cirac, and P. Zoller, Phys. Rev. A **59**, 2641 (1999).
- 17 S. Probst-Schendzielorz, T. Bschorr, and M. Freyberger, to be published in FNL **5** (2005).
- 18 H. J. Briegel, W. Dür, J. I. Cirac, and P. Zoller, Phys. Rev. Lett. **81**, 5932 (1998).
- 19 For a review on distillation and bound entanglement see, P. Horodecki and R. Horodecki, Quantum Inf. Comput. **1**(1), 45 (2001).
- 20 M. Horodecki, P. Horodecki, and R. Horodecki, Phys. Rev. Lett. **80**, 5239 (1998); M. Horodecki, P. Horodecki, and R. Horodecki, Phys. Rev. Lett. **82**, 1056 (1999).
- 21 M. Horodecki, P. Horodecki, and R. Horodecki, Phys. Rev. Lett. **78**, 574 (1997).
- 22 R. F. Werner, Phys. Rev. A **40**, 4277 (1989).
- 23 C. Macchiavello, Phys. Lett. A **246**, 385 (1998).
- 24 D. G. Fischer, H. Mack, and M. Freyberger, Phys. Rev. A **63**, 042305 (2001).
- 25 G. K. Brennen, C. M. Caves, P. S. Jessen, and I. H. Deutsch, Phys. Rev. Lett. **82**, 1060 (1999).
- 26 D. Jaksch, H. J. Briegel, J. I. Cirac, C. W. Gardiner, and P. Zoller, Phys. Rev. Lett. **82**, 1975 (1999).
- 27 O. Mandel, M. Greiner, A. Widera, T. Rom, T. W. Hänsch, and I. Bloch, Nature **425**, 937 (2003).

## 14

# Experimental Quantum Secret Sharing

Christian Schmid, Pavel Trojek, Sascha Gaertner, Mohamed Bourennane,  
Christian Kurtsiefer, Marek Zukowski, and Harald Weinfurter

### 14.1

#### Introduction

Quantum communication offers methods to securely exchange sensitive information between separated parties by using fundamental principles of quantum mechanics. Quantum key distribution schemes are well known, and for two parties already close to an application in everyday life. They can be naturally extended to more than two parties. However, the protocols for more-than-two-party communication known up to now, due to the technical effort required for their implementation, are in general still far from a real life application. Still the following represents a trailblazing step towards the feasibility of a real life application even in multiparty quantum communication.

We present two different protocols for the solution of a particular secure multiparty communication task, the so called secret sharing, and their proof-of-principle experimental realization. Let us start with sketching the idea behind the term secret sharing. As can be already gathered from the name, its main goal is splitting a secret in such a way that neither a single person, nor any unauthorized subset of partners, is able to reconstruct it. This is a common task in information processing, and especially in high security applications. Suppose, for example, that the launch sequence of a nuclear missile is protected by a secret code. Yet, it should be ensured that not a single person alone, but at least *two* persons are required to activate it. Solutions for this problem, and its generalization and variations, are studied in classical cryptography [1]. The aim here is to split information, using some mathematical algorithms, and to distribute the resulting pieces to two or more legitimate parties. However classical communication is susceptible to eavesdropping attacks. As the usage of quantum resources can lead to unconditionally secure communication (e.g. [2,3]), a protocol applying quantum cryptography ideas to secret sharing was proposed [4–7]. In this protocol a shared GHZ-state allows the information

splitting, and the protection against eavesdropping simultaneously. But, due to lack of efficient multi-photon sources an experimental demonstration of a working quantum secret sharing (QSS) was missing for a long time. Solely the in-principle feasibility of an experimental realization using pseudo-GHZ states was shown [8], and only very recently, a GHZ-protocol for three parties was implemented [9].

Here we consider two protocols: The first is applicable to four parties and uses a particular four-qubit entangled state, denoted as  $|\Psi_4^-\rangle$ , as resource [10]. The advantage of this scheme compared to the GHZ-protocol is, that the state it uses can be directly observed in the process of spontaneous parametric down conversion (SPDC), needs no beam overlap to obtain it, and is thus easier to implement [11–13]. The second works in general for  $N$  participants and does not need GHZ- or any other multi-qubit entangled states, as it employs only sequential single qubit communication between the parties [14]. Due to this fact, the latter scheme is very easily realizable with current state-of-the-art technology, and above all, scalable with respect to the number of participating parties. These traits made the experimental demonstration of that protocol for six parties possible.

## 14.2

### Theory

#### 14.2.1

##### The GHZ-protocol

Before describing the two new protocols, we first shortly recapitulate the entanglement based protocol for secret sharing, which utilizes a multi-qubit GHZ state [5]. Consider  $N$  persons, each having a particle from the maximally entangled  $N$  particle GHZ-state

$$|\text{GHZ}\rangle = \frac{1}{\sqrt{2}} \left( \underbrace{|00\ldots 0\rangle}_N + \underbrace{|11\ldots 1\rangle}_N \right). \quad (14.1)$$

The partners randomly and independently choose the value of a parameter  $\phi_j = 0$  or  $\pi/2$  and perform measurement on the local particle of the observable

$$\hat{\sigma}_j(\phi_j) = \sum_{k_j=\pm 1} k_j |k_j, \phi_j\rangle \langle k_j, \phi_j|. \quad (14.2)$$

The eigenstates  $|k_j, \phi_j\rangle = 1/\sqrt{2}(|0\rangle + k_j \exp(i\phi_j)|1\rangle)$  ( $j = 1, 2, \dots, N$ ) are associated with eigenvalues  $k_j = \pm 1$ . The correlation function for a  $N$ -particle GHZ state, defined as the expectation value of the product of  $N$  local results,

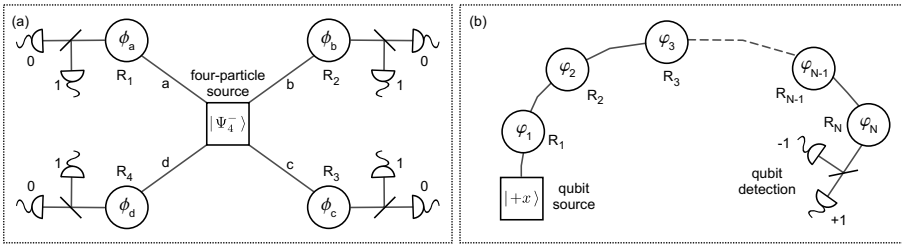


**Fig. 14.1** (a) Scheme for four party quantum secret sharing via four qubit entanglement. Each of the four parties  $R_1, \dots, R_4$  receives a qubit of the entangled state  $|\Psi_4^-\rangle$  and performs a local measurement characterized by a randomly chosen parameter  $\phi_j, j = a, \dots, d$ ; for particular choices of  $\phi_j$  the detection events associated with bit values of 0 and 1 are perfectly correlated and can be used to establish a shared secret key. (b) Scheme for  $N$  party single qubit secret

sharing. A qubit is prepared in an initial state and sequentially communicated from party to party, each acting on it with a phase operator  $\hat{U}(\varphi_j)$ , Eq. (14.7), applying a randomly chosen phase  $\varphi_j$ . The last recipient performs a measurement on the qubit leading to the result  $\pm 1$ . In half of the cases the phases add up such that the measurement result is deterministic. These instances can be used to achieve the aim of secret sharing.

is given by

$$E(\phi_1, \dots, \phi_N) = \langle \prod_{j=1}^N \hat{\sigma}_j(\phi_j) \rangle = \cos \left( \sum_{j=1}^N \phi_j \right). \quad (14.3)$$

After the measurement each partner publicly announces her/his choice of  $\phi_j$ , but keeps the result  $k_j$  secret. Then, all of them know whether this procedure leads to perfect correlations, i.e. whether  $|\cos(\sum_j^N \phi_j)| = 1$ . This happens in half of the runs. In these instances, on the basis of the perfect correlations, any subset of  $N - 1$  partners, whom we shall call hereafter recipients, is able to infer the measurement result of the remaining person,  $P_R$ , if, and only if, all the recipients collaborate. Thereby, they achieve the principal task of secret sharing.

#### 14.2.2

#### The $|\Psi_4^-\rangle$ -protocol

In the following, we want to consider an entanglement based quantum secret sharing protocol for four participants ( $N = 4$ ) [10], which is similar to the scheme described above, but uses another multi-particle entangled state. The state is called  $|\Psi_4^-\rangle$ ,

$$|\Psi_4^-\rangle = \frac{1}{\sqrt{3}} (|0011\rangle + |1100\rangle - \frac{1}{2} (|0101\rangle + |0110\rangle + |1001\rangle + |1010\rangle))_{abcd}, \quad (14.4)$$

and is shared between the parties (see Fig. 14.1(a)) [13]. It is invariant under joint identical unitary transformations and shows perfect four-particle corre-

lations. The four-qubit correlation function for  $|\Psi_4^-\rangle$  is given by [11–13]:

$$E(\phi_a, \phi_b, \phi_c, \phi_d) = \frac{2}{3} \cos(\phi_a + \phi_b - \phi_c - \phi_d) + \frac{1}{3} \cos(\phi_a - \phi_b) \cos(\phi_c - \phi_d). \quad (14.5)$$

The correlations contained in the entangled state can be exploited to establish a shared secret among the parties. To this end the partners proceed as follows: They randomly choose one out of two values of the parameter  $\phi_j$  representing an arbitrary complementary basis set and perform the corresponding local projection measurement on their qubit. Then they announce publicly the choice of  $\phi_j$ , but keep the result  $k_j$  secret. Using Eq. (14.5) it can be decided which choices of the values  $\phi_j$  lead to correlated results. In general in these instances three parties have to collaborate in order to infer the measurement results of the last party.

#### 14.2.3

#### The Single Qubit Protocol

An  $N$  party scheme (see Fig. 14.1(b)) for the *same* task, where only the sequential communication of a single qubit is used runs as follows [14]. The qubit is initially prepared in the state

$$|+x\rangle = \frac{1}{\sqrt{2}}(|0\rangle + |1\rangle). \quad (14.6)$$

During the protocol the qubit is sequentially communicated from partner to partner, each acting on it with the unitary phase operator

$$\hat{U}_j(\varphi_j) = \begin{cases} |0\rangle \rightarrow |0\rangle \\ |1\rangle \rightarrow e^{i\varphi_j}|1\rangle, \end{cases} \quad (14.7)$$

with a randomly chosen value of  $\varphi_j \in \{0, \pi, \pi/2, 3\pi/2\}$ . Therefore, having passed all parties, the qubit will end up in the state

$$|\chi_N\rangle = \frac{1}{\sqrt{2}}\left(|0\rangle + e^{i(\sum_j^N \varphi_j)}|1\rangle\right). \quad (14.8)$$

The last party performs a measurement on the qubit in the basis  $|\pm x\rangle = \frac{1}{\sqrt{2}}(|0\rangle \pm |1\rangle)$  leading to the result  $\pm 1$ . For her/him it suffices to choose only between  $\varphi_N = 0$  or  $\varphi_N = \pi/2$ . The probability that she/he detects the state  $|\pm x\rangle$  reads

$$p_{\pm}(\varphi_1, \dots, \varphi_N) = \frac{1}{2} \left( 1 \pm \cos \left( \sum_j^N \varphi_j \right) \right). \quad (14.9)$$

The expectation value of the measurement is

$$E'(\varphi_1, \dots, \varphi_N) = p_+(\varphi_1, \dots, \varphi_N) - p_-(\varphi_1, \dots, \varphi_N) = \cos \left( \sum_j^N \varphi_j \right). \quad (14.10)$$

Note that this expectation value (Eq. (14.10)) has the same structure like the correlation function (Eq. (14.3)), and therefore can also be used to obtain a shared secret. For this purpose each participant divides his action for every run into two classes: a class X corresponding to the choice of  $\varphi_j \in \{0, \pi\}$  and a class Y corresponding to  $\varphi_j \in \{\pi/2, 3\pi/2\}$ . Following this classification they broadcast the class of their action for each run, but keep the particular value of  $\varphi_j$  secret. This corresponds in the GHZ scheme to the announcement of  $\phi_j$  while keeping  $k_j$  secret. The order in which they announce the classification is the reversed order of the sequential qubit communication [15]. From that procedure they can determine which runs lead to a deterministic measurement result, i.e. whether  $\cos(\sum_j^N \varphi_j)$  equals to either 1 or -1 or equivalently whether  $p_+ = 1$  or  $p_- = 1$ . Such sets of  $\varphi$ 's occur on average in half of the runs. These are valid runs of the protocol. In such cases any subset of  $N - 1$  parties is able to infer the choice of  $\varphi_R$  of the remaining partner, if and only if, all the recipients collaborate and reveal among themselves their values of  $\varphi_j$ . If this subset contains the last partner, he/she must reveal the measurement result. Thus, the collaboration of all recipients is necessary. The task of secret sharing is now achieved via local manipulation of phases on a single qubit, communicated sequentially by the partners, and no multiparticle entangled GHZ state is required anymore.

#### 14.2.4

#### Security of the Protocols

As security considerations for the  $|\Psi_4^-\rangle$ -protocol are basically an analogue to those for the GHZ-protocol [5, 16], we describe for that protocol the eavesdropping check procedure just very briefly, pointing out the significant differences, and focus on the security analysis of the single-qubit protocol.

In order to check for eavesdropping in the  $|\Psi_4^-\rangle$ -protocol, the partners can compare a subset of their measurement results, which should be perfectly correlated. From the obtained quantum bit error rate they can estimate an upper bound on the information which an eavesdropper might have on the raw key. If this is low enough to distill a secure key, they can keep their results, if not, they have to discard their bits and start a new key exchange.

One difference in the use of the  $|\Psi_4^-\rangle$ - instead of the GHZ-state, which should be noted, is the fact that there can occur instances where the collaboration of only two parties is already sufficient for the reconstruction of one shared secret bit. As can be seen from the structure of the state itself, this

happens for  $\phi_j = 0$  if the measurement results of the first two or respectively the last two parties are equal. However for a complete bit sequence this means only partial information and in general the collaboration of three out of four parties is still required for the reconstruction of the full sequence, especially if the final key is transposed by hash functions.

In order to ensure the security of the single-qubit protocol against eavesdropping or cheating (by eavesdropping we refer to an attack from a person which is not participating in the protocol, whereas by cheating we refer to an attack from a participant) the partner  $P_R$  arbitrarily selects a certain subset of valid runs. The size of this subset depends on the degree of security requirements. For these runs the value of  $\varphi_R$  is compared with the one inferred by the recipients. To this end each of the recipients sends in a random order the value of his/her phase  $\varphi_j$ . The comparison reveals any eavesdropping or cheating strategy. This can be easily seen by discussing the following intercept/resend eavesdropping attacks.

Imagine, for instance, the first recipient  $R_j$ , who follows directly after  $P_R$ , tries to infer the secret without the help of the remaining participants by measuring the qubit, *before* acting on it with  $\hat{U}_j(\varphi_j)$  and sending it to the next recipient  $R_{j+1}$ . For convenience, let us assume  $R_j$  chooses for this measurement one of the two protocol bases  $|\pm x\rangle$  or  $|\pm y\rangle = \frac{1}{\sqrt{2}}(|0\rangle \pm i|1\rangle)$ . The choice of these bases is natural, because at any stage of the protocol the qubit is in one of these four states. As  $P_R$  applies randomly one of four different phase shifts, the probability that the qubit is an eigenstate of the measurement chosen by  $R_j$  is  $1/2$  and thus in half of the cases the measurement result of  $R_j$  will be completely bitwise random, because  $|\langle \pm y | \pm x \rangle|^2 = 1/2$ . Thus, recipient  $R_j$  gets no information about the secret. Furthermore, such cheating causes an overall error of 25% in the final measurement results. Simply, if  $R_j$  chooses the wrong basis, the final state of the qubit after all the introduced phase shifts will not always be of the form (14.8).

An eavesdropper following such a strategy faces a similar situation. The usage of the bases  $x$  and  $y$  for an intercept/resend attack is the optimal one concerning the information gain on the valid runs. One might also consider using the intermediate (or so-called Breidbart) basis  $|\pm b\rangle = \frac{1}{\sqrt{2+\sqrt{2}}}(|\pm x\rangle + |\pm y\rangle) = \frac{1}{\sqrt{2}}(|0\rangle \pm e^{i\pi/4}|1\rangle)$  which gives the eavesdropper maximum information on all exchanged bits [17]. But even here the error rate goes necessarily up to 25 %. The security of the presented protocol against a general eavesdropping attack follows from the proven security of the well known BB84 protocol [1, 2]. Each communication step between two successive parties can be regarded as a BB84 protocol using the bases  $x$  and  $y$ . Any set of dishonest parties in our scheme can be viewed as an eavesdropper in BB84 protocol.

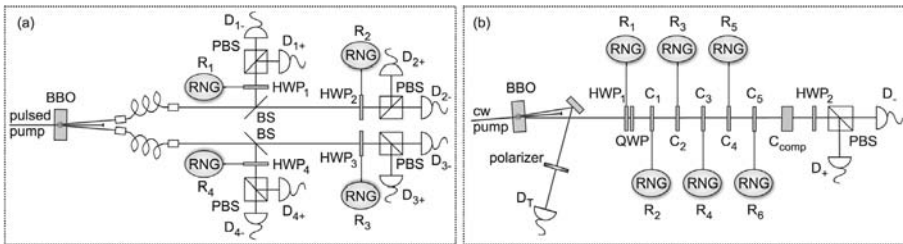


**Fig. 14.2** (a) Setup for four qubit secret sharing. Four photons are generated in the second order emission of a pulsed, type II SPDC process in a BBO crystal and split up in four spatial modes by two beam splitters (BS). Under the condition that one photon is detected in each output mode, the four-photon entangled state  $|\Psi_4^-\rangle$  is observed. In order to establish a shared key each photon is measured randomly by the recipients  $R_1, \dots, R_4$  in one of two complementary bases. The analysis direction is set using a half-wave plate (HWP) driven by motor according to the output of a pseudo-random number generator (RNG). (b) Setup for single qubit secret sharing. Pairs of orthogonally

polarized photons are generated via a type II SPDC process in a BBO crystal. The detection of one photon from the pair by  $D_T$  heralds the existence of the other one used in the protocol. The initial polarization state is prepared by placing a polarizer in front of the trigger detector. Each of the recipients ( $R_1 \dots R_6$ ) introduces one out of four phase shifts, according to the output of a pseudo-random number generator (RNG), using half- and quarter wave plate (HWP<sub>1</sub>, QWP) or YVO<sub>4</sub> crystals (C<sub>1</sub>...C<sub>5</sub>), respectively. The last party analyzes additionally the final polarization state of the photon by detecting it behind a half-wave plate (HWP<sub>2</sub>) and a polarizing beam splitter.

## 14.3 Experiment

### 14.3.1

#### The $|\Psi_4^-\rangle$ -protocol

The state  $|\Psi_4^-\rangle$ , in the polarization degree of freedom of four photons, required for the four-party quantum secret sharing protocol can be obtained from the two pair emission of a non-collinear type II spontaneous parametric down conversion process (SPDC) (see Fig. 5.2(a)). That means the basis states  $|0\rangle$  and  $|1\rangle$  are represented by the polarization states  $|H\rangle$  and  $|V\rangle$ , respectively (horizontal (H) and vertical (V) linear polarization).

In the experiment we used a solid state laser, with a pump power of  $P = 10$  W and a wavelength of  $\lambda = 532$  nm, to pump a mode locked Ti:Sa laser. The Ti:Sa laser emits pulses of a length of about 120 fs, at a repetition rate of 82 MHz. The pulses are frequency doubled in a lithium-triborate (LBO) crystal to  $\lambda = 390$  nm, and are used to pump a 2 mm thick beta-barium-borate (BBO) crystal. The photons emitted from the crystal via pulsed SPDC, provided that they split up to four distinct spatial modes a, b, c, d at two beam splitters (BS), are in the polarization state given by Eq. (14.4). Thus, once each of the recipients  $R_i$ , ( $i = 1, \dots, 4$ ) obtains one of the four photons, they can be directly used to accomplish the secret sharing protocol. The recipients  $R_i$  measure

randomly in one of two different complementary bases. A pseudo-random number generator (RNG) is used to set the analysis direction of a lambda half-wave plate ( $HWP_i$ ) in front of a polarizing beam splitter (PBS). The detection of a photon at  $D_{i-}$  in the transmitted output mode of the PBS corresponds to a bit value of 0, while the detection of a photon at  $D_{i+}$  in the reflected output mode is associated with 1. The detectors were silicon avalanche photodiodes with a photon detection efficiency of about 40%. For the registration of all 16 relevant four-photon coincidences we employed an eightchannel multiphoton coincidence unit [19]. In order to establish a common key, we used for each randomly chosen analyzer setting a data acquisition time of 1 second. In situations in which more than one four-photon coincidence event was registered during that time, only the first one was chosen.

We performed a key exchange according to the protocol described in Sect. 14.2.2. We observed bit rates of about 100 bits per hour, with an average quantum bit error rate of about 5% [10]. This value is comparable with values usually obtained in quantum key distribution experiments for two parties. Moreover, it is well below several known security thresholds and should therefore be low enough to ensure secure quantum communication [2].

### 14.3.2

#### The Single-qubit Protocol

The single-qubit protocol was experimentally implemented for six parties. This clearly shows the practicality and user-friendliness of the scheme.

We encoded the protocol qubit in the polarization of a single photon. The single photons were provided by a heralded single photon source. The setup is shown in Fig. 5.2(b). A pair of polarization entangled photons is created via a spontaneous parametric down conversion (SPDC) process. As the photons of a pair are strongly correlated in time, the detection of one photon in  $D_T$  heralds the existence of the other one which is used for the protocol. A coincidence detection between  $D_T$  and  $D_+/D_-$ , within a chosen time window of 4 ns, implies communication of only a single photon. For this coincidence time window, and single-count rates of about  $35000\text{ s}^{-1}$  both in  $D_+$  and  $D_-$  and about 5000 in  $D_T$ , we obtained a coincidence rate of  $1200\text{ s}^{-1}$ . Accidental coincidences, or multi-coincidences, were thus negligible. The SPDC process was run by pumping a 2 mm long  $\beta$ -barium borate (BBO) crystal with a blue single mode laser diode (402.5 nm), at an optical output power of 10 mW. Type-II phase matching was used, at the degenerate case, leading to pairs of orthogonally polarized photons at a wavelength of  $\lambda = 805\text{ nm}$  ( $\Delta\lambda \approx 6\text{ nm}$ ).

In order to prepare the initial polarization state a polarizer transmitting vertically polarized photons was put in front of the trigger detector  $D_T$ . Thus only (initially) horizontally polarized photons can lead to a coincidence detection.

The first partner was equipped with a motorized half-wave plate ( $HWP_1$ ) followed by quarter-wave plate (QWP) at an angle of  $45^\circ$ . By rotation of  $HWP_1$  to the angles  $0^\circ, 45^\circ$  and  $22.5^\circ, -22.5^\circ$  one could transform the horizontally polarized photons coming from the source to  $|\pm y\rangle$  and  $|\pm x\rangle$ . This corresponds to applying the phase-shifts  $\varphi \in \{\pi/2, 3\pi/2\}$  and  $\varphi \in \{0, \pi\}$  respectively. As the phase-shifts of the other partners had to be applied independently from the incoming polarization state, the usage of standard wave plates was not possible. Therefore the unitary phase operator was implemented using birefringent uniaxial  $200\text{ }\mu\text{m}$  thick Yttrium Vanadate ( $YVO_4$ ) crystals ( $C_i$ ). The crystals were cut such that their optic axis lies parallel to the surface, and is aligned in such a way that H and V polarization states correspond to their normal modes. Therefore by rotating the crystals along the optic axis by a certain angle a specific relative phase shift was applied independently of the incoming polarization state. An additional  $YVO_4$  crystal ( $C_{\text{comp}}$ ,  $1000\text{ }\mu\text{m}$  thick) was used to compensate dispersion effects. The last party performed the measurement behind a half-wave plate ( $HWP_2$ ) at an angle of  $22.5^\circ$ , followed by polarizing beam-splitter (PBS). The photons were detected at  $D_+/D_-$  and  $D_T$  by passively quenched silicon avalanche photo diodes (Si-APD), with an efficiency of about 35 %.

The protocol was repeated  $z_{\text{total}} = 25000$  times. One run consisted of choosing pseudo-random variables, rotating the crystals and opening the detectors for a collection time window  $\tau = 200\text{ }\mu\text{s}$ , what took together about 1 s. Due to the requirement of communicating a single photon only those runs were included into the protocol in which just one coincidence between  $D_T$  and either  $D_+$  or  $D_-$  (coincidence gate time  $\tau_c \approx 4\text{ ns}$ ) was detected during  $\tau$ . In these runs a single coincidence detection happened  $z_{\text{raw}} = 2107$  times. This provided us with the raw key. From this we extracted  $z_{\text{val}} = 982$  valid runs for which  $|\cos(\sum_j^N \varphi_j)| = 1$  (506 times  $\cos(\sum_j^N \varphi_j) = 1$  and 476 times  $\cos(\sum_j^N \varphi_j) = -1$ ), with a quantum bit error rate (QBER) of  $2.34 \pm 0.48\text{ %}$ . Note that error correction protocols (like e.g. parity check) could be used to further reduce the errors, exactly like in conventional quantum cryptography.

**Tab. 14.1** Results of the simulation of an intercept/resend eavesdropping strategy, and intermediate basis strategy. The attack was done by inserting a polarizer between the distributor and the first recipient. In each case the quantum bit error rate (QBER) rises up to more than 25 % and by this blows the eavesdropper's cover.

	$z_{\text{total}}$	$z_{\text{raw}}$	$z_{\text{val}}$	QBER [%]
$ \pm x\rangle$	27501	883	452	$25.22 \pm 2.04$
$ \pm y\rangle$	24993	784	409	$30.32 \pm 2.27$
$ \pm b\rangle$	38174	1137	588	$30.27 \pm 1.89$

In order to show that the QBER increases significantly in case of an eavesdropping attack, we simulated an intercept/resend strategy by inserting a polarizer between the first two partners. The attack was done in the protocol bases  $|\pm x\rangle$ ,  $|\pm y\rangle$ , as well as in the intermediate basis  $|\pm b\rangle$ . For the latter two the polarizer was additionally sandwiched by two quarter-wave plates. The angular settings (1st QWP, polarizer, 2nd QWP) were  $\{45^\circ, 0^\circ, -45^\circ\}$  and  $\{-45^\circ, 22.5^\circ, 45^\circ\}$ . For every choice of the basis the QBER went up to at least 25 % (or even higher due to other experimental imperfections). The results are summarized in Table 14.1.

A different eavesdropping/cheating strategy could be of a Trojan Horse type. One of the partners could pass a pulse of polarized light through the devices of the other partners and attempt to gain information on local phase shifts. However, such action may be easily discovered by the partners by checking from time to time the nature of light passing through their devices. Also the excess photons coming from our source, by which we mean those not in coincidence with the trigger, cannot be utilized for eavesdropping/cheating as they do not have a defined polarization. This is because the initial polarization of the heralded photons is fixed in the experiment by putting the polarization filter in the path to the trigger detector, Fig. 2. Since the photons form polarization entangled EPR pairs, detection of a trigger photon behind a polarization filter collapses the initially undefined polarization state of the heralded one to the required  $|+x\rangle$ . All other photons, since no trigger event accompanies them, remain unpolarized. Only higher-order emissions, i.e. two pairs emitted within the coherence time ( $\approx 360$  fs), are useful for beam-splitting attacks [20]. The probability for such an opportunity, however, for our parameters is as low as  $7.6 \times 10^{-7}$  per run .

#### 14.4 Conclusion

In summary, we experimentally implemented two schemes for solving the multiparty communication task of secret sharing. The first one uses as resource multi-particle entanglement, while the second requires just single qubits. In the entanglement based protocol the usage of a particular multi-qubit state, which can be obtained from a simple and stable experimental setup, shows the feasibility of secure multi-party quantum communication via multi-photon entanglement. Especially promising, with respect to real life applications, is the second scheme using only the sequential communication of a single qubit. As single qubit operations using linear optical elements and the analysis of photon polarization states are quite well accomplishable with present day technology, we were therefore able to present the first experimental demonstration of that protocol for as many as six parties. This

is, to our knowledge, the highest number of actively performing parties in a quantum protocol ever implemented. In principle we see no experimental barrier to extend that performed protocol to even significantly higher number of participants.

We also simulated an eavesdropping intercept/resend attack and by this showed the resistance of the single-qubit protocol against such kind of attacks, because of the significantly increasing error rate. Since eavesdropper might have an access to input and output ports of the partners, particularly Trojan Horse attacks might be a potential security danger for our new single-qubit scheme. Yet they can be precluded by the partners with a reasonable technological effort like e.g. recently discussed in [21]. One could argue that the use of weak coherent pulses of light containing much less than one photon on average, instead of a heralded single photon source, could further reduce the required experimental resources. However, this would be against the concept of communicating strictly one qubit, and can be also disadvantageous for the practical performance of the protocol [22, 23]. While we have realized our single-qubit secret sharing protocol using photons and polarization encoding, alternative schemes, like proposed or realized in BB84-type protocols can be adopted as well. Finally, by showing that a single qubit approach can be effectively used for solving the secret sharing task, instead of methods involving many qubit GHZ states, we conjecture that this approach may be a practical solution for many other multiparty communication tasks. Recently, for example, it was possible to successfully apply that approach in quantum communication complexity (separated parties performing local computations exchange information in order to accomplish a globally defined task, which is impossible to solve singlehandedly, see [24]).

## Acknowledgement

This work was supported by the Bavarian Forschungsstiftung, the German DFG and the European Commission through the IST FET QIPC RamboQ and QAP. MZ is supported by Wenner-Gren Foundation and MNiL Grant IP03B 04927, and our collaboration is supported by a DAAD/MNiL programme.

## References

- 1 B. Schneier, *Applied Cryptography*, 2nd edition (John Wiley & Sons, Inc., New York, 1996).
- 2 N. Gisin, G. Ribordy, W. Tittel, and H. Zbinden, *Rev. Mod. Phys.* **74**, 145 (2002).
- 3 A. K. Ekert, *Phys. Rev. Lett.* **67**, 661 (1991).
- 4 M. Żukowski, A. Zeilinger, M. A. Horne, and H. Weinfurter, *Acta Phys. Pol.* **93**, 187 (1998).
- 5 M. Hillery, V. Bužek, and A. Berthiaume, *Phys. Rev. A* **59**, 1829 (1999).
- 6 R. Cleve, D. Gottesmann, and H.-K. Lo, *Phys. Rev. Lett.* **83**, 648 (1999).
- 7 A. Karlsson, M. Koashi, and N. Imoto, *Phys. Rev. A* **59**, 162 (1998).
- 8 W. Tittel, H. Zbinden, and N. Gisin, *Phys. Rev. A* **63**, 042301 (2001).
- 9 Y. A. Chen et al., *Phys. Rev. Lett.* **95**, 200502 (2005).
- 10 S. Gaertner, C. Kurtsiefer, M. Bourennane, and H. Weinfurter, *quant-ph/0610112* (2006).
- 11 H. Weinfurter and M. Zukowski, *Phys. Rev. A* **64**, 010102 (2001).
- 12 M. Eibl, S. Gaertner, M. Bourennane, Ch. Kurtsiefer, M. Zukowski, and H. Weinfurter, *Phys. Rev. Lett.* **90**, 200403 (2003).
- 13 S. Gaertner et al., *Appl. Phys. B* **77**, 803 (2003).
- 14 C. Schmid, P. Trojek, M. Bourennane, C. Kurtsiefer, M. Zukowski, and H. Weinfurter, *Phys. Rev. Lett.* **95**, 230505 (2005).
- 15 G. P. He, *Phys. Rev. Lett.*, to be published; Ch. Schmid et al., *Phys. Rev. Lett.*, to be published.
- 16 V. Scarani and N. Gisin, *Phys. Rev. A* **65**, 012311 (2001).
- 17 B. Huttner and A. K. Ekert, *J. Mod. Opt.* **41**, 2455 (1994).
- 18 C. Bennett and G. Brassard, *Proc. of IEEE International Conference on Computer, Systems & Signal Processing*, Bangalore, India (1984).
- 19 S. Gaertner, Ch. Kurtsiefer, and H. Weinfurter, *Rev. Scient. Inst.* **76**, 123108 (2005).
- 20 This is just the same as in entanglement-based quantum cryptography, see T. Jennewein, Ch. Simon, G. Weihs, H. Weinfurter, and A. Zeilinger, *Phys. Rev. Lett.* **84**, 4729 (2000); D. S. Naik, C. G. Peterson, A. G. White, A. J. Berglund, and P. G. Kwiat, *Phys. Rev. Lett.* **84**, 4733 (2000); W. Tittel, J. Brendel, H. Zbinden, and N. Gisin, *Phys. Rev. Lett.* **84**, 4737 (2000); A. Poppe et al., *Optics Express* **12**, 3865 (2004).
- 21 N. Gisin, S. Fasel, B. Kraus, H. Zbinden, and G. Ribordy, *quant-ph/0507063*.
- 22 G. Brassard, N. Lütkenhaus, T. Mor, and B. C. Sanders, *Phys. Rev. Lett.* **85**, 1330 (2000).
- 23 N. Lütkenhaus, *Phys. Rev. A* **61**, 052304 (2000).
- 24 P. Trojek, Ch. Schmid, M. Bourennane, C. Brukner, M. Zukowski, and H. Weinfurter, *Phys. Rev. A* **72**, 050305(R) (2005).

## 15

# Free Space Quantum Key Distribution: Towards a Real Life Application

*Henning Weier, Tobias Schmitt-Manderbach, Nadja Regner, Christian Kurtsiefer, and Harald Weinfurter*

### 15.1

#### Introduction

Whenever sensitive information has to be exchanged between two parties, cryptography is employed to ensure that no unauthorised third party can get access to the content. Classical cryptographic methods like the one-time pad have been shown to be provably secure, if and only if the key has been deployed securely. Yet, this task cannot be provably accomplished by classical means.

Quantum cryptography, also known as quantum key distribution (QKD) [1], makes use of fundamental principles of quantum mechanics to ensure the security of secret key generation. The system subject to this report employs the so-called BB84 protocol [2], encoding qubits in the polarisation of faint laser pulses. Ideally, one party (Alice) prepares a sequence of single photons, their polarisations being chosen randomly from four possible non-orthogonal states (e.g. horizontal, vertical and  $\pm 45^\circ$ ). She sends the photons to the second party (Bob), who analyses the polarisation of each detected photon in a randomly and independently chosen basis (e.g. either H/V or  $\pm 45^\circ$ ). Afterwards both parties compare publicly their basis choices and discard those events where they had used different bases. This process is called sifting.

Due to fundamental laws of quantum mechanics, an eavesdropper (Eve) cannot determine the polarisation of a single photon if the polarisation states are non-orthogonal. Even worse, she will introduce errors during the polarisation measurement, so that the quantum bit error rate (QBER) of the sifted key gives an upper bound on the information an eavesdropper might have gained. The QBER is calculated during the classical error correction procedure and is used to infer the shrinking ratio that is needed to make sure that the information of a potential eavesdropper on the key is negligible. The key is then hashed to this secure length during privacy amplification.

The scope of this particular experiment is to show the feasibility of autonomous free space quantum key distribution systems, generating symmetric keys, for example between two buildings within a city. Once it has been set up, it is supposed to be working continuously without human interaction. There have already been some free space experiments over relatively large distances, for example a 10 km link in the group of Richard Hughes [3] and a 23 km link from Zugspitze to Karwendelspitze in our group in collaboration with the group of John Rarity [4]. The results of those free space trials show the possibility to build global quantum key exchange systems based on quantum communication satellites [5]. The experience gathered during the latter experiment was used as a starting point for building a stable quantum cryptography system for urban areas.

## 15.2

### Setup

The system can be divided into three parts: The transmitter contains a weak coherent pulse source, which sends out pulses of polarised light with a Poissonian distribution characterised by a mean photon number  $\mu$ . The quantum channel is an optical free space link which is formed by two telescopes plus spatial and spectral filter on the receiver end. Finally, there is the receiver unit, which analyses the polarisation and detects the single photons. The three parts will be described in detail in the following sections.

#### 15.2.1

##### Transmitter Unit

The transmitter unit basically consists of four laser diodes plus a conical mirror and a spatial filter to combine the four beams. Ideally, the sender unit would produce a stream of single polarised photons according to the choice of basis and bit value. Since currently no single photon source is competitive, we use weak coherent pulses with a mean photon number  $\mu$ , which are produced as follows: The light of laser diodes has a high intrinsic polarisation (typically better than 1:1000) and they can be oriented so that there is one laser diode for sending out photons in each desired polarisation. The advantage of this method is that no active polarisation manipulations are needed. Four such laser diodes emitting at wavelength 850 nm are arranged around a conical mirror (see Fig. 15.1) in such a way that the four beams are reflected and combined into one direction. After the beams have been reflected by the conical mirror, they pass a spatial filter, which consists of two pinholes designed to restrict the beam to only a single spatial mode. This is vital, because it must be

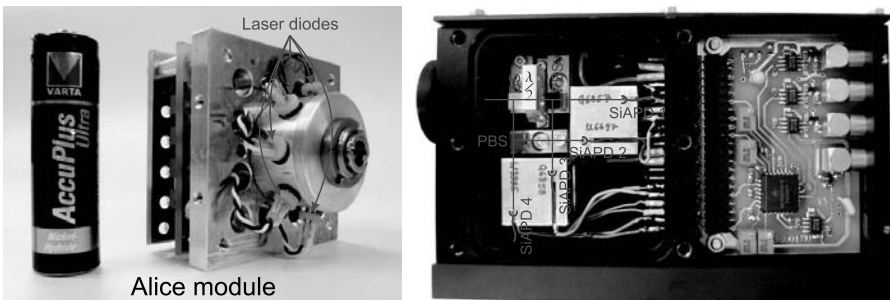


**Fig. 15.1** Transmitter (left) and receiver unit (right). In the Alice module, the pulses of four differently polarised laser diodes are combined on a conical mirror. The Bob module uses a non-polarising beam splitter, a half wave plate, two polarising beam splitters and four single photon detectors to analyse incident photons in the H/V or  $+/45$  basis.

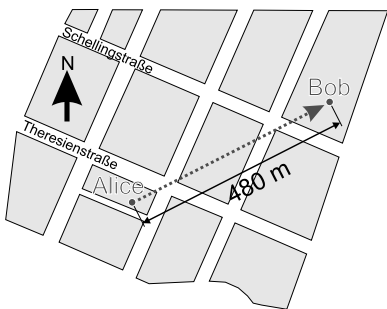


**Fig. 15.2** Left: Location of the test bed in Munich. Right: Photograph of the receiver telescope with the Bob module attached.

ensured that no information on the polarisation of the photons can be gathered by measuring their momentum or position.

### 15.2.2

#### Free Space Link

To ensure that as many photons from Alice as possible are detected by Bob, two telescopes are employed, one at each end. Both telescopes have the same front lens ( $f = 310$  mm, open aperture  $a = 75$  mm), but the rest of the system is chosen to match the different requirements of transmitter and receiver.

On the transmitter side, two pinholes forming the spatial filter define the initial beam parameters.

To ensure that as little stray light as possible is collected by the receiver, a pinhole was inserted into the receiver telescope. Because of their narrow field of view (the receiver sees a region of approximately  $14\text{ cm} \times 17\text{ cm}$  at a distance of 480 m), the orientation of the telescopes has to be aligned very

precisely. Thus, stable mounts are necessary which permit the required pointing accuracy. To allow for automatic alignment control, each tip-tilt stage is equipped with two stepper motors, which drive micrometer screws to adjust the two possible angles.

The experiment is situated in downtown Munich, sender and receiver are located on the roof tops of two university buildings (see Fig. 15.2). There are no solid obstacles in the line of sight, so that transmission values of up to 90% can be reached.

### 15.2.3

#### Receiver Unit

The receiver unit consists of

- the so-called Bob module (containing the optics and detectors for polarisation analysis of the incoming photons),
- the timestamp card, which assigns a time to every click of a detector, and
- the software in Bob's computer, which is responsible for the extraction of synchronisation information to enable successful key-sifting.

The Bob module is directly attached to the end of the receiver telescope. A non-polarising beam splitter (BS), a set of two polarising beam splitters (PBS) and a half-wave plate are used to perform the polarisation analysis of the incoming photons. An incident photon first sees the 50/50 beam splitter; depending whether the photon is reflected or transmitted, the polarisation is analysed in the H/V basis or in the  $\pm 45^\circ$  basis. The choice of bases is therefore random, but completely passive. This made it possible to shrink the module to as small dimensions as just 130 mm  $\times$  80 mm  $\times$  55 mm.

The single photons are detected by silicon avalanche photo diodes (APDs) which are peltier-cooled to about  $-20^\circ$  C in order to keep the dark count rate at a tolerable level. The module already contains all the electronics needed for stabilising the temperature of the detectors, for biasing of the APDs and for signal recovery. For each of the four detector channels, a corresponding electronic pulse is output with a timing accuracy of about 1 ns. Attached to the outputs of the Bob module is the timestamp unit, that records the time of arrival of each detection event. This circuitry works with a timing resolution of better than 1 ns. The timing data are transferred to the PC via a digital I/O card and analysed by the synchronisation software.

### 15.2.4

#### **Synchronisation and Automatic Alignment Control**

The basic idea for synchronisation is to take advantage of the known 10 MHz repetition rate of the transmitter. As soon as this pattern has been identified in the stream of received clicks, good events can be discriminated from bad ones, so that a large fraction of dark and background counts can be filtered out. Since the local oscillators are not necessarily as stable as required, the calculated frequency and phase of the good events has to be adjusted continuously. Thanks to this technique, cheap standard crystal oscillators are sufficient for both sender and receiver.

In a next step, known patterns in the photon stream which have been inserted by Alice, are used to find out the number of each detected photon. Thus, Alice and Bob do not have to communicate classically during synchronisation. The advantage of this fact is that a temporarily unavailable or slow classical channel will not hinder the synchronisation routine and the sifting procedure can be performed later, when classical communication is again available. In other words, a time-stable classical channel is not required.

Thermal drifts of the setup required an active pointing control mechanism for both tip-tilt stages. In order to keep the hardware complexity as low as possible, the actual single photon signal itself is used to control the alignment. The extra advantage of this is, that one does not have to align additional equipment with respect to the telescopes. Two digital control loops similar to the lock-in technique with different frequencies allow us to separate the influence of the sender's and of the receiver's misalignment. The automatic alignment control is capable of compensating slow temperature-induced drifts of the setup and its mounts. It has been running for more than four days non-stop without human interaction, tracking on a bright cw laser source. When the single photon signal is used for alignment, the setup is to date operating in darkness only.

### 15.2.5

#### **Sifting, Error Correction and Privacy Amplification**

Once the synchronisation task has been accomplished, Alice and Bob can start the key sifting process. Whenever Bob has detected a photon, he will tell Alice its number and the basis in which he has analysed it. If Alice has sent the photon in the same basis, they will use the assigned bit value for the sifted key. If not, they have to discard the bit. At the end of this process, they will both have a so-called sifted key. Ideally, both sifted keys would be perfectly correlated. With experimental imperfections and/or an eavesdropper present, however, the key will contain errors. For security reasons all errors are accredited to the presence of an eavesdropper. In order to make the key usable, the errors have

to be corrected and the amount of information that has potentially leaked to the eavesdropper has to be made negligibly small.

We have implemented an error correction scheme based on the CASCADE algorithm [6]. This is a purely classical method to reveal and eliminate errors that have been introduced while being sent over a “noisy channel”. According to Shannon’s noisy coding theorem, a minimum of information has to be transmitted between the two communicating parties in order to correct those errors. Unfortunately, such an optimal algorithm has not been found so far. Using suitable parameters, CASCADE gets close to the optimum. It does so by exchanging parity bits of subsets of the key in multiple passes. If the parity of a pair of chosen subsets of bits is not equal, there has to be an odd number of errors in that subset. The algorithm locates an error by exchanging parity bits of first and second half of the subset and so on. After the first pass has left an even number of errors in all subsets, new subsets (reorganised and of different length) are chosen and the procedure is repeated.

When the parameters are chosen correctly, the probability of a remaining error can be neglected. Of course, the disposal of errors does not come for free. Each publicly transmitted parity bit increases the eavesdropper’s knowledge of the key. Hence, these announced bits are counted and have to be taken into account during privacy amplification [7].

### 15.2.6

#### Experimental Results

To test the system, a free space link has been set up between two buildings of the University. The transmitter is separated from the receiver by about 480 m, both are located on the roof tops of the respective buildings. A 10 Mbit/s internet connection provides the classical channel that is needed for the automatic alignment of the telescopes as well as synchronisation tasks and the key sifting procedure. The results of some more test runs are shown in Table 15.1.

A set of data has been chosen to show the performance of the system in more detail (see Fig. 15.3). It was taken starting November 27th, 2004 under good conditions. The sifted key rate was limited by the bandwidth of the classical channel, a problem that is being tackled at the moment. Error correction and privacy amplification results can be found below:

Initial key length (bits)	Discarded bits	Disclosed bits	Corrected bits	Final key length (bits)	QBER (%)	Priv. Amp. factor
2968502272	8077312	661681477	81432331	1636520736	2.8	0.55

The mean photon number was set to be on the order  $\mu \sim 0.1$ . Table 15.1 summarises several runs over three months and shows a varying, on average

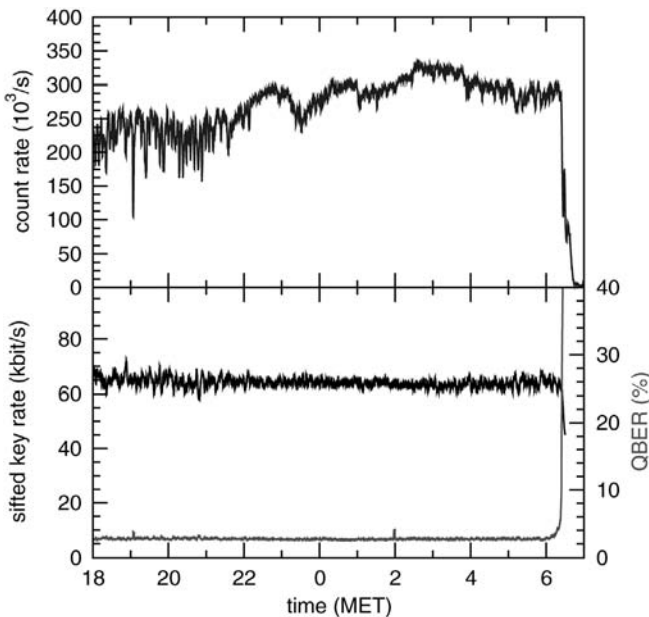


**Fig. 15.3** Counting rate, sifted key rate and quantum bit error rate of the measurement run starting November 27th. The increase of the QBER and the decrease of the counting rate in the morning is due to stray light hitting the detectors after sunrise, saturating them. Cf. the coloured plates in the Appendix.

**Tab. 15.1** Exemplary experimental data taken at the test site over a distance of 480 m. The sifted key rate varies due to different transmission values which are themselves strongly influenced by the weather conditions.

Date	Start	Time Stop	Total	Key length (MB)	Sifted Key rate avg. (kbit/s)	QBER (%)
27.11.04	18:22	08:00	14:38	354	56,42	2,8
21.12.04	18:19	07:00	12:42	250	44,80	4,5
11.01.05	18:59	07:00	12:01	331	62,66	3,2
12.01.05	17:03	07:00	13:58	206	33,57	3,6
20.01.05	21:10	07:00	09:50	96	22,22	3,1
01.02.05	21:37	07:00	09:23	39	9,46	4,3
03.02.05	18:11	07:00	12:49	149	26,44	5,0
25.02.05	17:41	10:00	16:20	277	38,61	4,3

increasing quantum bit error rate, that seems to originate from mechanical rotational instability. The setup has not been realigned between different measurement runs concerning the polarisation, but there seem to have been drifts in both directions. We will tackle this problem by using more rugged mechanics.

Weather conditions do, of course, affect the attenuation of the free space link. However, we found that only fog, heavy rain or snowfall limit the transmission severely so that the sifted key rate drops dramatically. In previous cw transmission measurements we saw that a more significant problem is caused by strong turbulence above sun heated roofs close to the optical path.

### 15.3

#### **Conclusion**

We have reported on the progress of our mid range free space quantum key distribution system which is designed to work continuously without human interaction. Currently the system works unattended during nights over a distance of 480 m, producing average sifted key rates of more than 50 kbit/s on average over a period of more than 12 hours. Essential additional subroutines like error correction and privacy amplification have been implemented into the software. They collaborate well with the previously developed parts like automatic alignment, synchronisation and sifting.

We have identified extra requirements that will have to be fulfilled to allow for daylight operation of the setup. These include temperature control of the transmitter module (currently in progress) and insertion of narrow spectral filters. The introduction of a monitoring APD into the transmitter unit is also scheduled for the near future. An additional task is the implementation of authentication of the public channel and the use of a decoy state protocol to increase the secure key rate.

#### **Acknowledgement**

The project is supported by the A8 Quantum Information Highway project and the EU project SECOQC.

## References

- 1** N. Gisin et al., *Rev. Mod. Phys.* **74**, 145–195 (2002).
- 2** C. H. Bennett et al., *Proceedings of IEEE International Conference on Computers, Systems and Signal Processing*, Bangalore, India (1984).
- 3** R. J. Hughes et al., *New J. Phys.* **4**(43), 1–14 (2002).
- 4** C. Kurtsiefer et al., *Nature* **419**, 450 (2002).
- 5** M. Pfennigbauer et al., *J. Opt. Netw.* **4**, 549–560 (2005).
- 6** G. Brassard et al., *Advances in Cryptology – Proceedings of Eurocrypt '93, Lecture Notes in Computer Science* 765, 410–423, Springer (1994).
- 7** N. Lütkenhaus, *Phys. Rev. A*, **61**, 052304 (2000).



## 16

# Continuous Variable Entanglement Between Frequency Modes

*Oliver Glöckl, Ullrik L. Andersen, and Gerd Leuchs*

### 16.1

#### Introduction

Entanglement is one of the most intriguing features of quantum mechanics. During the last decade we have witnessed that the concept of entanglement has undergone a profound transition from being a pure academically interesting concept to being one of the most useful features of quantum mechanics in terms of practical applications. For example entanglement may enable the unconditional secure communication between two distant parties [1] and it allows for ultra-precise sub-shot noise position measurements [2].

In some specific applications, entanglement between variables with a continuous spectrum is used. This is for example the case for unconditional quantum teleportation [3–6] and unconditional quantum dense coding [7–9]. The standard way to generate continuous variable entanglement is either by using a non-degenerate (e.g. in polarisation or direction) optical parametric amplifier [10–12] or to interfere two squeezed beams generated from two independent squeezing sources (like degenerate parametric amplifier or nonlinear optical fibre setup) on a 50/50 beam splitter [13–17].

The individually squeezed beams generated in either of the two sources are, however, intrinsically quantum correlated themselves: Frequency components or side bands symmetrically located around the center frequency  $\omega$  are quantum correlated. This can be seen from the idealized output state of a two-photon process (generated either in a second- or a third order nonlinear medium) given by

$$|\Phi\rangle \propto \int_{\Omega} d\Omega G \delta\hat{a}_+^\dagger(\omega + \Omega) \delta\hat{a}_-^\dagger(\omega - \Omega) |0\rangle \quad (16.1)$$

Here the function  $G$  represents the effective nonlinearity of the process. As a result of the nonlinearity, two photons at the side band frequencies  $\omega + \Omega$  and  $\omega - \Omega$  and represented by the creation operators  $\delta\hat{a}_+^\dagger$  and  $\delta\hat{a}_-^\dagger$ , are generated simultaneously (see Fig. 16.1). Due to the simultaneity in their production,

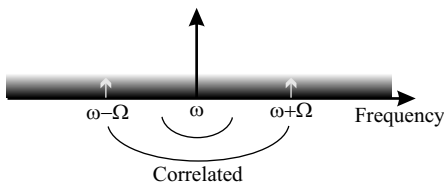


**Fig. 16.1** The pairwise production of photons in nonlinear optical processes ensures quantum correlations to occur between two photons symmetric with respect to the degenerate downconverted mode (for the parametric downconversion) or to the

pump (for the Kerr effect). This is illustrated here where the large frequency mode in the middle symbolises the classical carrier mode surrounded by a sea of tiny quantum frequency modes, all of which are pairwise correlated.

the two photons are correlated in many degrees of freedom. In particular the symmetrically located frequency modes are quantum correlated in the field quadrature components, such as the conjugate amplitude  $\delta\hat{X} = \delta\hat{a} + \delta\hat{a}^\dagger$  and phase quadratures  $\delta\hat{Y} = i(\delta\hat{a}^\dagger - \delta\hat{a})$ . The joint action of these correlations lead to the observation of quadrature squeezing if the local oscillator (or carrier of the beam itself) used for probing the noise is centered in between the correlated modes as shown in Fig. 16.1. In a measurement, the local oscillator (or carrier) beats simultaneously with the upper and lower sideband modes. Since the local oscillator has a different frequency to the sideband modes, these modes are heterodyned and thus a simultaneous measurement of the amplitude and phase quadrature of each of the sideband modes is performed. This yields the following composition of quadratures:

$$\delta\hat{X}(\Omega t) = \delta\hat{a}_+ e^{i\Omega t} + \delta\hat{a}_- e^{-i\Omega t} + \delta\hat{a}_+^\dagger e^{-i\Omega t} + \delta\hat{a}_-^\dagger e^{i\Omega t} \quad (16.2)$$

$$= (\delta\hat{X}_+ + \delta\hat{X}_-) \cos(\Omega t) + (\delta\hat{Y}_- - \delta\hat{Y}_+) \sin(\Omega t) \quad (16.3)$$

From this combination of quadratures, it is straightforwardly seen that squeezing, which means  $V(\delta\hat{X}) < 1$ , is equivalent to simultaneous amplitude quadrature anti-correlations ( $V(\delta\hat{X}_+ + \delta\hat{X}_-) < 1$ ) and phase quadrature correlations ( $V(\delta\hat{Y}_- - \delta\hat{Y}_+) < 1$ ) between the upper and lower sideband modes. *Thus, single-mode squeezing is a direct result of entanglement between sideband modes [21–23].*

Already in the the first ever observation of squeezing this intrinsic quadrature entanglement between sideband modes was demonstrated to be the nature of noise reduction below the vacuum noise level [24]. The entangled sideband modes have been also employed to demonstrate a new excitation regime in atomic spectroscopy [25]. For some applications in quantum information science (such as for teleportation and key distribution), entanglement must be present between two spatially distinct modes. Therefore, for these applications, the frequency modes must be transformed into spatially separated modes . This can likewise be done by using a cavity as experimentally

realised in [19]: The cavity is detuned from the center frequency so that a sideband frequency mode is resonant, and thus transmitted through the cavity, whereas the adjacent sideband mode will be reflected. In [19] the two frequency modes were homodyned with two frequency shifted (740 MHz) local oscillators, thereby probing the upper and lower sideband modes. In that experiment the degree of entanglement was measured to  $-3.8\text{dB}$  ( $4.1\text{dB}$  after electronic noise subtraction).

While the observation of quantum correlations between different cavity modes defines the starting point of the experimental squeezed light era, the corresponding correlations within a single cavity mode are less obvious. One reason being that inside the cavity a photon in a single cavity mode covers the full spectral width of the mode. Huntington and Ralph [18] proposed to use the cavity filtering set-up to check for sideband correlations within a singly peaked squeezed light spectrum, and Zhang [20] elaborated further on this topic.

As an alternative to the cavity, one can use an asymmetric interferometer for the separation of the frequency modes into distinct spatial modes. This approach is preferable when ultra-short squeezed pulses are used, since in that case the cavity approach is technically demanding due to the multi-mode structure of the pulses and the dispersion properties of the cavity. The work presented here was originally proposed and experimentally demonstrated in [26]. In this article we elaborate on this work by describing the theory and experiment in greater details.

## 16.2

### Sideband Separation

A schematic diagram of the asymmetric Mach-Zehnder interferometer is shown in Fig. 16.2. The basic idea behind the function of the interferometer is that the carrier wave of the input state with frequency  $\omega$  as well as the two sideband modes with frequencies  $\omega + \Omega$  and  $\omega - \Omega$  will experience different phase shifts during propagation. Owing to the different relative phase shifts of the upper and lower sideband modes for the two spatial modes inside the interferometer, the original sidebands of the input modes can be separated into two distinct spatial modes through interference at the second beam splitter.

First we present the theory for the quantum operation of the interferometer and later we interpret its function using a pictorial representation.

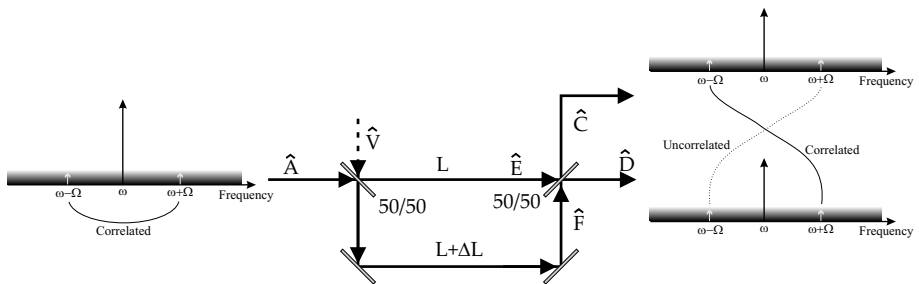


**Fig. 16.2** Schematic diagram of the asymmetric Mach-Zehnder interferometer for separating entangled sidebands. The signal input is quadrature squeezed as a result of correlated sidebands. These sidebands are transferred into two different spatial modes at the output of the interferometer, resulting in quadrature entanglement between spatially separated modes.

### 16.2.1

#### Theory

The bright input field  $\hat{A}$  and the vacuum field  $\hat{V}$  are described in a three-mode picture:

$$\hat{A}(t) = \alpha e^{i\omega t} + \delta\hat{a}_- e^{i(\omega - \Omega)t} + \delta\hat{a}_+ e^{i(\omega + \Omega)t}, \quad (16.4)$$

$$\hat{V}(t) = \delta\hat{v}_- e^{i(\omega - \Omega)t} + \delta\hat{v}_+ e^{i(\omega + \Omega)t}. \quad (16.5)$$

where  $\alpha$  is the classical amplitude of the input field and  $\delta\hat{a}_+$  and  $\delta\hat{a}_-$  are the annihilation operators for the upper and lower sidebands of the input field. Likewise  $\delta\hat{v}_+$  and  $\delta\hat{v}_-$  are the annihilation operators for the upper and lower sidebands of the vacuum field. At the first beam splitter in the interferometer the input field under investigation is combined with the vacuum field which yields the intra-interferometer modes (see Fig. 16.2),

$$\begin{aligned} \hat{E}(t) &= \frac{1}{\sqrt{2}}(\hat{A}(t) + \hat{V}(t)) \\ &= \alpha \exp(i\omega t) + (\delta\hat{a}_+ + \delta\hat{v}_+) \exp(i(\omega + \Omega)t) \\ &\quad + (\delta\hat{a}_- + \delta\hat{v}_-) \exp(i(\omega - \Omega)t), \end{aligned} \quad (16.6)$$

$$\begin{aligned} \hat{F}(t) &= \frac{1}{\sqrt{2}}(\hat{A}(t) - \hat{V}(t)) \\ &= \alpha \exp(i\omega t) + (\delta\hat{a}_+ - \delta\hat{v}_+) \exp(i(\omega + \Omega)t) \\ &\quad + (\delta\hat{a}_- - \delta\hat{v}_-) \exp(i(\omega - \Omega)t). \end{aligned} \quad (16.7)$$

Due to the path length difference, given by  $\Delta L$ , mode  $\hat{F}$  is time delayed by  $\tau = \Delta L/c$  relative to mode  $\hat{E}$ . After propagation, the two modes interfere and

the output modes of the interferometer can be described by

$$\begin{aligned}\hat{C}(t) &= \frac{1}{\sqrt{2}} [\hat{E}(t) + \hat{F}(t - \tau)] \\ &= \frac{1}{2} [(\alpha + \alpha \exp(-i\omega\tau)) \exp(i\omega t) \\ &\quad + \{\delta\hat{a}_+ + \delta\hat{v}_+ + (\delta\hat{a}_+ - \delta\hat{v}_+) \exp(-i\Omega\tau - i\omega\tau)\} \exp(i(\omega + \Omega)t) \\ &\quad + \{\delta\hat{a}_- + \delta\hat{v}_- + (\delta\hat{a}_- - \delta\hat{v}_-) \exp(i\Omega\tau - i\omega\tau)\} \exp(i(\omega - \Omega)t)],\end{aligned}\quad (16.8)$$

$$\begin{aligned}\hat{D}(t) &= \frac{1}{\sqrt{2}} [-\hat{E}(t) + \hat{F}(t - \tau)] \\ &= \frac{1}{2} [(-\alpha + \alpha \exp(-i\omega\tau)) \exp(i\omega t) \\ &\quad + \{-\delta\hat{a}_+ - \delta\hat{v}_+ + (\delta\hat{a}_+ - \delta\hat{v}_+) \exp(-i\Omega\tau - i\omega\tau)\} \exp(i(\omega + \Omega)t) \\ &\quad + \{-\delta\hat{a}_- - \delta\hat{v}_- + (\delta\hat{a}_- - \delta\hat{v}_-) \exp(i\Omega\tau - i\omega\tau)\} \exp(i(\omega - \Omega)t)].\end{aligned}\quad (16.9)$$

The relative optical phase  $\varphi = \omega\tau$  between  $\hat{E}$  and  $\hat{F}$  can be set by fine tuning the path length difference. Furthermore, the phase shift at the radio-frequency  $\theta = \Omega\tau$  is chosen through the coarse adjustment of the relative path length difference. Note that the effect of adjustments of the relative optical phase on the radio frequency phase can be neglected, as the two wavelengths  $\omega$  and  $\Omega$  differ by about  $\sim 10^7$ . Now by choosing  $\Omega\tau = \pi/2$  and  $\omega\tau = \pi/2$  the output modes read

$$\begin{aligned}\hat{C}(t) &= \frac{1}{2} \alpha (1 - i) \exp(i\omega t) + v_+ \exp(i(\omega + \Omega)t) \\ &\quad + a_- \exp(i(\omega - \Omega)t),\end{aligned}\quad (16.10)$$

$$\begin{aligned}\hat{D}(t) &= \frac{1}{2} \alpha (-1 - i) \exp(i\omega t) - a_+ \exp(i(\omega + \Omega)t) \\ &\quad - v_- \exp(i(\omega - \Omega)t).\end{aligned}\quad (16.11)$$

Each of the two output modes consists of three contributions: A carrier term at frequency  $\omega$  and the upper and lower sidebands at frequencies  $\omega + \Omega$  and  $\omega - \Omega$ , respectively. However, in contrast to the input field, the upper and lower sideband modes have been split into two spatially separated modes,  $\hat{C}$  and  $\hat{D}$ . The reason is simply destructive and constructive interference of the two adjacent sidebands when they merge at the second beam splitter: in one output the upper side bands interfere constructively, while the lower sidebands interfere destructively to form mode  $\hat{D}$  and vice versa in the other output port. As a result the correlated sideband modes of the input field have been separated into two spatially distinct modes. Note that if one instead sets,  $\varphi = \pi/2$  and  $\theta = \pi$ , a phase quadrature measurement can be performed [32].

Direct detection of the output modes yield amplitude quadrature fluctuations (for arbitrary  $\varphi$  and  $\theta$ ):

$$\begin{aligned}\delta\hat{X}_{c,d}(\Omega t) = & \frac{1}{2\sqrt{2}}[\delta\hat{X}_a(\Omega t) + \delta\hat{X}_a(\Omega t - \theta) \pm \delta\hat{X}_a^{-\varphi}(\Omega t) \pm \delta\hat{X}_a^{\varphi}(\Omega t - \theta) \\ & + \delta\hat{X}_v(\Omega t) - \delta\hat{X}_v(\Omega t - \theta) \pm \delta\hat{X}_v^{-\varphi}(\Omega t) \\ & \mp \delta\hat{X}_v^{\varphi}(\Omega t - \theta)],\end{aligned}\quad (16.12)$$

where the upper and lower signs correspond to mode  $\hat{C}$  and  $\hat{D}$ , respectively, and  $\delta\hat{X}^{\varphi} = \cos\varphi\delta\hat{X} + \sin\varphi\delta\hat{Y}$ . The phase quadrature fluctuations are given by

$$\begin{aligned}\delta\hat{Y}_{c,d}(\Omega t) = & \frac{1}{2\sqrt{2}}[\delta\hat{Y}_a(\Omega t) + \delta\hat{Y}_a(\Omega t - \theta) \\ & \pm \delta\hat{X}_a^{-\varphi+\pi/2}(\Omega t) \pm \delta\hat{X}_a^{\varphi+\pi/2}(\Omega t - \theta) + \delta\hat{Y}_v(\Omega t) + \delta\hat{Y}_v(\Omega t - \theta) \\ & \pm \delta\hat{X}_v^{-\varphi+\pi/2}(\Omega t) \mp \delta\hat{X}_v^{\varphi+\pi/2}(\Omega t - \theta)].\end{aligned}\quad (16.13)$$

The variances of the output fields (normalised to the shot noise) for the amplitude and phase quadratures in case of  $\varphi = \pi/2$  and  $\Theta = \pi/2$  are then easily found to

$$V(\delta\hat{X}_c) = V(\delta\hat{X}_d) = \frac{1}{4}[V(\delta\hat{X}_a) + V(\delta\hat{Y}_a) + 2], \quad (16.14)$$

$$V(\delta\hat{Y}_c) = V(\delta\hat{Y}_d) = \frac{1}{4}[V(\delta\hat{X}_a) + V(\delta\hat{Y}_a) + 2]. \quad (16.15)$$

where we have used that  $V(\delta\hat{X}_v) = V(\delta\hat{Y}_v) = 1$  and  $V(\delta\hat{X}_a(\Omega t - \pi/2) + \delta\hat{X}_a(\Omega t)) = 2V(\delta\hat{X}_a(\Omega t)) = 2V(\delta\hat{X}_a)$ . If the input field is squeezed, the two output modes are strongly correlated: the sum and difference of the amplitude quadratures of these two modes are (normalised to the shot noise level)

$$V(\delta\hat{X}_c + \delta\hat{X}_d) = \frac{1}{2}[V(\delta\hat{X}_a) + 1], \quad (16.16)$$

$$V(\delta\hat{X}_c - \delta\hat{X}_d) = \frac{1}{2}[V(\delta\hat{Y}_a) + 1], \quad (16.17)$$

Therefore if the amplitude quadratures of the two beams are anti-correlated, the sum variance goes below the shot noise level. The sum and difference variance of the phase quadratures are likewise

$$V(\delta\hat{Y}_c + \delta\hat{Y}_d) = \frac{1}{2}[V(\delta\hat{Y}_a) + 1], \quad (16.18)$$

$$V(\delta\hat{Y}_c - \delta\hat{Y}_d) = \frac{1}{2}[V(\delta\hat{X}_a) + 1], \quad (16.19)$$

and so correlated phase quadrature fluctuations result in sub-shot noise behaviour of the difference signal. If both the amplitude sum variance  $V(\delta\hat{X}_c + \delta\hat{X}_d)$  and the phase quadrature difference variance  $V(\delta\hat{Y}_c - \delta\hat{Y}_d)$  are below the shot noise level, entanglement is witnessed according to the criteria of Duan et al. [27] and Simon [28].

### 16.2.2

#### Pictorial Description

The operation of the interferometer can be understood easily using a pictorial diagram, as shown in Fig. 16.3. We now describe each point shown in the figure:

1. We consider an input signal composed of three modes; the carrier and the two sidebands. This signal mode interferes with a vacuum mode at a 50/50 beam splitter. Upon reflection of the input signal, a  $\pi$  phase shift occurs both to the sidebands and the carrier, and thus these modes are rotated by  $\pi$ .
2. Through propagation in the long arm of the interferometer, the sideband modes are phase shifted by  $\pi/2$  relative to the carrier mode. This results in rotations of the two sideband modes by  $\pi/2$  in opposite directions relative to the carrier mode. Note that the relative phase shift between the three modes is in fact the feature that at the end enables the sideband separation. Furthermore, the optical phase of the field in the long arm is shifted by  $\pi/2$ , by which all three modes are rotated by  $\pi/2$ .
3. The two fields in the interferometer finally merge and interfere at the second beam splitter. Again, the phase shift of  $\pi$  upon reflection of one of the fields must be included. It is now evident that through the interference, the upper sideband mode of the input signal leaves one output port while the lower sideband mode leaves the other output port. It is also clear that the carrier mode is divided equally between the two output modes, and thus they are equally intense.

### 16.3

#### Experiment and Results

As was shown in the previous section, the output modes of the unbalanced Mach-Zehnder interferometer are entangled, i. e. they exhibit sub shot noise correlations in the phase and the amplitude quadrature as described by eqns. (16.16) and (16.19). Our goal here is to experimentally verify these quantum correlations. We chose an interferometric scheme to determine the common quantum state of the two modes: We bring the two potentially entangled

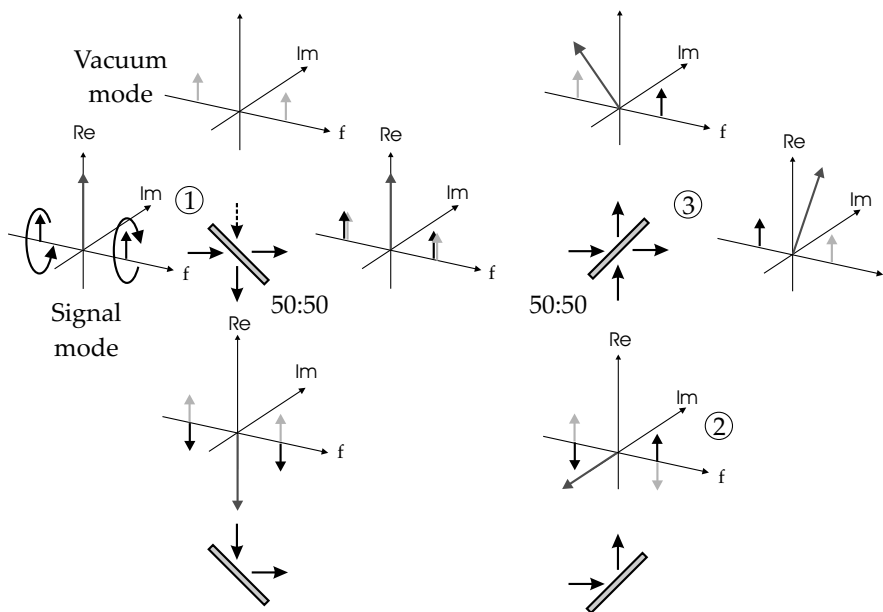


**Fig. 16.3** Pictorial diagram illustrating the function of the asymmetric interferometer in the sideband picture. Cf. the coloured plates in the Appendix.

beams to interference at yet another beam splitter and detect the sum and the difference fluctuations of the resulting photocurrents (see Fig. 16.4) [29–31]. Calculating the resulting fluctuations of the photocurrent after the interference shows that the sum and the difference signals deliver the desired correlation results:

$$\begin{aligned}\delta\hat{n}_1 + \delta\hat{n}_2 &= \frac{\alpha}{\sqrt{2}}(\delta\hat{X}_c + \delta\hat{X}_d) \\ &= \frac{1}{2}\alpha[\delta\hat{X}_a(\Omega t - \theta) + \delta\hat{X}_a(\Omega t) - \delta\hat{X}_v(\Omega t - \theta) \\ &\quad + \delta\hat{X}_v(\Omega t)],\end{aligned}\tag{16.20}$$

$$\begin{aligned}\delta\hat{n}_1 - \delta\hat{n}_2 &= \frac{\alpha}{\sqrt{2}}(\delta\hat{Y}_c - \delta\hat{Y}_d) \\ &= \frac{1}{2}\alpha[-\delta\hat{X}_a(\Omega t - \theta) + \delta\hat{X}_a(\Omega t) \\ &\quad + \delta\hat{X}_v(\Omega t - \theta) + \delta\hat{X}_v(\Omega t)].\end{aligned}\tag{16.21}$$

The identical result is obtained by adding and subtracting the fluctuations of the amplitude and the phase quadrature given in eqns. (16.12) and (16.13). This corresponds to a measurement of the amplitude or phase quadrature

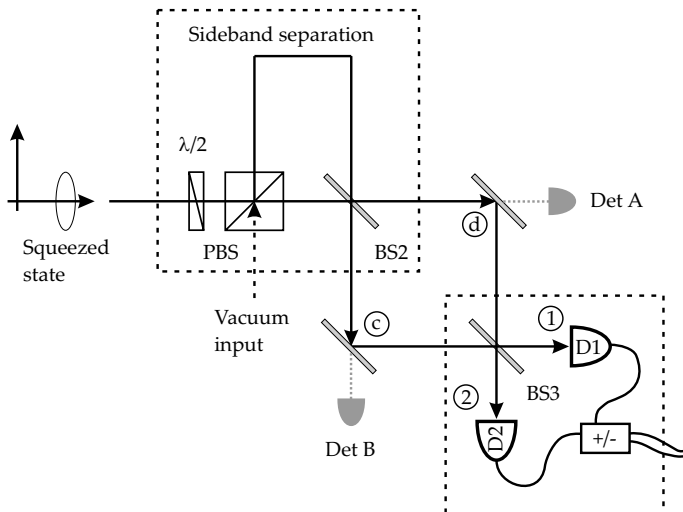


**Fig. 16.4** The experimental setup for the demonstration of sideband separation. PBS: Polarizing beam splitter; BS1 and BS2: 50/50 beam splitter. Detectors Det A and Det B are used to phase lock the asymmetric Mach-

Zehnder interferometer by collecting the light leaking through the high reflecting mirrors. The signals from the detectors D1 and D2 are used to lock the interference phase in the second interferometer.

fluctuations in the two output ports separately and subsequent addition or subtraction of the photocurrents. However, the interferometric scheme has the advantage of not needing an additional phase measurement, furthermore, both correlation signals for the amplitude and phase quadrature can be obtained in a single measurement.

Let us look at the experimental setup in more detail (see Fig. 16.4). For the experimental demonstration of the sideband separation, we use intense Fourier limited light pulses (pulse length  $\sim 120\text{fs}$ , wavelength 1530nm) which are squeezed using an asymmetric fibre Sagnac interferometer where the third order Kerr non linearity is exploited [33,34]. These squeezed states are coupled into the asymmetric Mach-Zehnder interferometer where a delay of  $\pi/2$  needs to be introduced for a given sideband frequency. The measurement frequency is determined by the arm length difference between the two interferometer arms: For  $\Omega = 10.25\text{MHz}$ , a delay of  $\Delta L = 7.32\text{m}$  between the two interferometer arms is required to achieve the  $\pi/2$  phase shift. As we have a pulsed source of squeezed light, we note that the actual delay and accessible measurement frequencies are determined by the repetition rate of the system, as interference between subsequent pulses is required at the beam splitter. After that, the modes  $\hat{c}$  and  $\hat{d}$  interfere at beam splitter BS3, before the output modes 1 and 2 are detected directly.

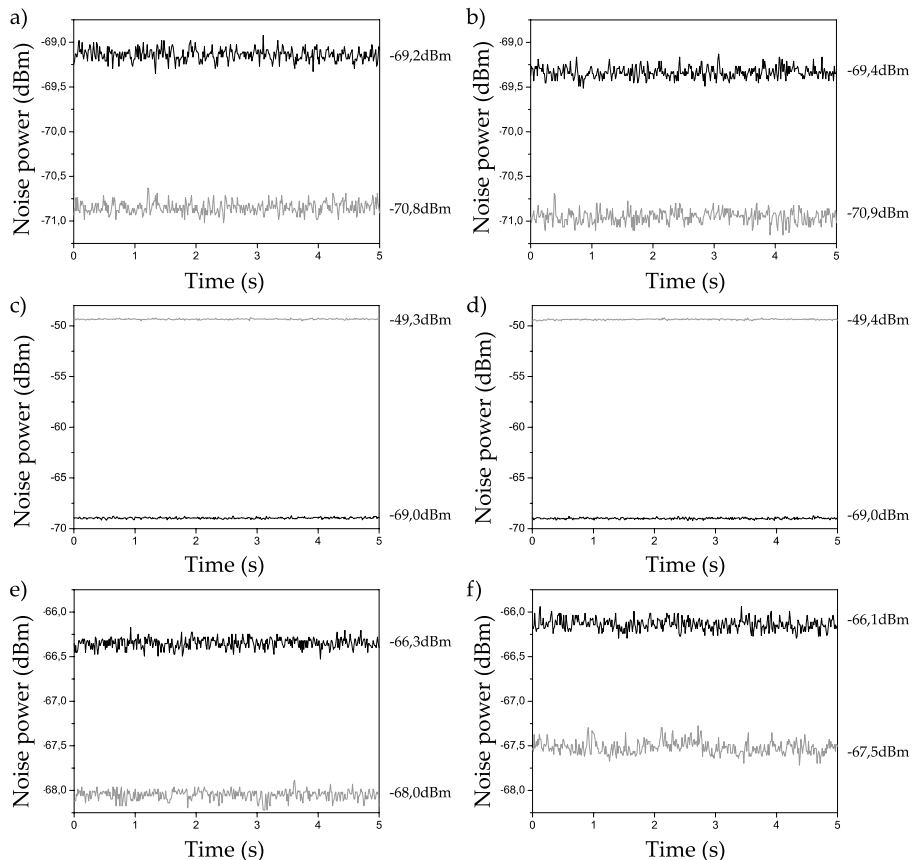


**Fig. 16.5** Experimental results of the sideband separation experiment. (a) and (b) show the noise power of the squeezed input (grey) state together with the shot noise level (black). Note that these traces correspond to squeezed states after 50% attenuation, as it is measured after BS2. The amplitude noise of the two entangled beams  $\hat{c}$  and  $\hat{d}$  after

sideband separation is presented in (c) and (d) clearly showing the large excess phase noise in each beam. The correlation signals for the amplitude and the phase quadrature are plotted in (e) and (f). The measurement frequency was at 10.25MHz, the resolution bandwidth 300kHz and the video bandwidth 30Hz. [Parts c)-f)] are taken from [26]]

The results of the characterization of the side band separation are shown in Fig. 16.5. In a first step, we characterized the initial squeezing of the input state. Therefore, the  $\lambda/2$ -plate in front of the first polarising beamsplitter (PBS) was adjusted such that all light propagates through one arm. At the second beam splitter BS2, the squeezed state is then split into two parts. Blocking one of the modes  $\hat{c}$  or  $\hat{d}$ , the noise power of the 50% attenuated squeezed states are detected using the balanced detection scheme comprised of BS3 and the detectors D1 and D2. The results are shown in 16.5 a) and b) respectively for arm c and d blocked respectively. From the observed noise reduction of  $1.6 \pm$

0.1dB and  $1.5 \pm 0.1$ dB for the two ‘halves’ of the squeezed input, a squeezing level of approximately 4dB is inferred.

In the next step, the input squeezed state is split equally at the PBS by adjusting the wave plate. The separation of the side bands and hence entanglement generation is achieved by the interference at BS2. The visibility was 95%, and the interference phase was chosen such that the two output ports had equal intensity corresponding to  $\varphi = \pi/2$ . Figs. 16.5 c) and d) show the amplitude noise of the single modes c and d. Again, one of the modes was blocked inside the second interferometer, and BS3 and the detectors D1 and D2 are used as a balanced detection scheme. The amplitude noise of both beams is more than 20dB above the shot noise level, as is expected from equation (16.14) as the large excess phase noise typically present in our fibre sources [14,32] is transferred onto modes  $\hat{c}$  and  $\hat{d}$ . This measurement indicated that the unbalanced Mach-Zehnder interferometer does not act as an ordinary beamsplitter, but the uncertainties of the conjugate quadrature components are completely redistributed.

The interferometric verification of sub shot noise correlations of modes  $\hat{c}$  and  $\hat{d}$  is plotted in Fig. 16.5 e) and f). Now the noisy modes (their noise being displayed in 16.5c and d) interfere at BS3 and the visibility was measured to be higher than 90%. The noise power for the sum and the difference of the photocurrents were measured to be  $1.6 \pm 0.1$ dB and  $1.4 \pm 0.1$ dB below the respective shot noise level. These correlations show that the quantum correlated sideband modes of the squeezed input have been transferred successfully into two spatial separate modes. The degree of the observed correlations agrees nicely with the prediction of equations (16.16) and (16.19).

## 16.4

### Conclusion and Discussion

It is known that degenerate nonlinear processes, such as degenerate optical parametric amplification and the Kerr effect, do not produce correlated photons in spatially separable modes. However, in the quantum domain, the simultaneously produced photons are always nondegenerate in frequency in order to ensure energy conservation, and thus entanglement is present between frequency modes inside a single spatial mode. This intrinsic entanglement can be thoroughly measured by separating the correlated frequency modes into spatially distinct modes followed by standard detection techniques.

In this article this has been done by using an asymmetric Mach-Zehnder interferometer and a balanced homodyne detection setup. We used an amplitude quadrature squeezed beam with a squeezing degree of about 4dB. In principle this results in a quadrature amplitude correlation between the sideband modes of 4dB in conjugate quadratures. However due to the imper-

fect measurement method in which the local oscillator was probing not only the correlated frequency modes but also the uncorrelated vacuum modes, less than 2dB correlation was observed experimentally.

The full correlation of 4dB can be measured using frequency shifted local oscillators [19]: The frequency shifted local oscillators probe simultaneously the modes which are symmetrically located around the them, and since the two upper sidebands are correlated with the two lower sidebands (as indicated in the figure) the full quadrature entanglement can be extracted. This approach was successfully employed by Schori et al. [19] to probe the quadrature entanglement between different cavity modes generated by an optical parametric oscillator below threshold.

The asymmetric interferometer can be also used to manipulate sidebands of single photon states (or very weak coherent states). E.g. in [35] a quantum key distribution protocol where information was encoded into weak adjacent sideband modes and manipulated using the interferometer was proposed and experimentally realised, and in [36] it was suggested to use the interferometer for enabling a basic linear operations onto a qubit encoded by single photon onto adjacent frequency modes.

## Acknowledgement

The authors acknowledge valuable discussions with Tim Ralph, Elenor Huntington and Stefan Lorenz. This work was supported by the network of competence QIP of the State of Bavaria (A8) and the EU project COVAQIAL (Project No. FP6-511004).

## References

- 1 C. H. Bennett and G. Brassard, in: Proceedings of IEEE International Conference on Computers, Systems and Signal Processing, Bangalore, India (IEEE, New York, 1984), p. 175
- 2 V. Giovannetti, S. Lloyd, and L. Maccone, *Nature* **412**, 417 (2001).
- 3 L. Vaidman, *Phys. Rev. A* **49**, 1473 (1994)
- 4 S. L. Braunstein and H. J. Kimble, *Phys. Rev. Lett.* **80**, 869 (1998);
- 5 T. C. Ralph and P. K. Lam, *Phys. Rev. Lett.* **81**, 5668 (1998).
- 6 A. Furusawa, J. L. Sørensen, S. L. Braunstein, C. A. Fuchs, H. J. Kimble, and E. S. Polzik, *Science* **282**, 706 (1998).
- 7 M. Ban, *J. Opt. B: Quantum Semiclass. Opt.* **1**, L9 (1999).
- 8 S. L. Braunstein and H. J. Kimble, *Phys. Rev. A* **61**, 042302 (2000).
- 9 X. Li et al. *Phys. Rev. Lett.* **88**, 047904 (2002).
- 10 Z. Y. Ou, S. F. Pereira, H. J. Kimble, and K. C. Peng, *Phys. Rev. Lett.* **68**, 3663 (1992).
- 11 Y. Zhang, H. Wang, X. Li, J. Jing, C. Xie, and K. Peng, *Phys. Rev. A* **62**, 023813 (2000).
- 12 J. Laurat, T. Coudreau, G. Keller, N. Treps, and C. Fabre, *Phys. Rev. A* **70**, 042315 (2004).

- 13** A. Furusawa, J. L. Sørensen, S. L. Braunstein, C. A. Fuchs, H. J. Kimble, and E. Polzik, *Science* **282**, 706 (1998).
- 14** C. Silberhorn, P. K. Lam, O. Weiss, F. König, N. Korolkova, and G. Leuchs, *Phys. Rev. Lett.* **86**, 4267 (2001).
- 15** W. P. Bowen, R. Schnabel, P. K. Lam, and T. C. Ralph, *Phys. Rev. Lett.* **90**, 043601 (2004).
- 16** T. Aoki, N. Takei, H. Yonezawa, K. Wakui, T. Hiraoka, and A. Furusawa, *Phys. Rev. Lett.* **91**, 080404 (2003).
- 17** J. Wenger, A. Ourjoumtsev, R. Tualle-Brouri, and Ph. Grangier, *Eur. Phys. J. D* **32**, 391 (2004).
- 18** E. H. Huntington and T. C. Ralph, *J. Opt. B: Quantum Semiclass. Opt.* **4**, 123 (2002).
- 19** C. Schori, J. L. Sørensen, and E. Polzik, *Phys. Rev. A* **66**, 033802 (2002).
- 20** J. Zhang, *Phys. Rev. A* **67**, 054302 (2003).
- 21** C. M. Caves, *Phys. Rev. D* **26**, 1817 (1982).
- 22** C. M. Caves and B. L. Schumaker, *Phys. Rev. A* **31**, 3068 (1985).
- 23** J. Gea-Banacloche and G. Leuchs, *J. Mod. Opt.* **34**, 793 (1987).
- 24** R. E. Slusher, L. W. Hollberg, B. Yurke, J. C. Mertz, and J. F. Valley, *Phys. Rev. Lett.* **55**, 2409 (1985).
- 25** N. Ph. Georgiades, E. S. Polzik, K. Edamatsu, and H. J. Kimble, *Phys. Rev. Lett.* **75**, 3426 (1995).
- 26** E. Huntington, G. N. Milford, C. Robilliard, T. C. Ralph, O. Glöckl, U. L. Andersen, S. Lorenz, and G. Leuchs, *Phys. Rev. A* **71**, 041802 (2005).
- 27** L.-M. Duan, G. Giedke, J. I. Cirac, and P. Zoller, *Phys. Rev. Lett.* **84**, 4002 (2000).
- 28** R. Simon, *Phys. Rev. Lett.* **84**, 2726 (2000).
- 29** S. M. Tan, *Phys. Rev. A* **60**, 2752 (1999).
- 30** G. Leuchs et al., *J. Mod. Opt.* **46**, 1927 (1999).
- 31** J. Zhang and K. Peng, *Phys. Rev. A* **62**, 064302 (2000).
- 32** O. Glöckl, U. L. Andersen, S. Lorenz, C. Silberhorn, N. Korolkova, and G. Leuchs, *Opt. Lett.* **29**, 1936 (2004).
- 33** S. Schmitt, J. Ficker, M. Wolff, F. König, A. Sizmann, and G. Leuchs, *Phys. Rev. Lett.* **81**, 2446 (1998).
- 34** D. Krylov and K. Bergman, *Opt. Lett.* **23**, 1390 (1998).
- 35** J.-M. Merolla, L. Duraffourg, J.-P. Goedebuer, A. Soujaeff, F. Patois, and W. T. Rhodes, *Eur. Phys. J. D* **18**, 141 (2002).
- 36** E. H. Huntington and T. C. Ralph, *Phys. Rev. A* **69**, 042318 (2005).



## 17

**Factorization of Numbers with Physical Systems**

*Wolfgang Merkel, Ilya Sh. Averbukh, Bertrand Girard, Michael Mehring, Gerhard G. Paulus, and Wolfgang P. Schleich*

**17.1****Introduction**

Chirped pulses with a quadratic phase dependence are characterized by a linearly varying instantaneous frequency [1]. A Gauss sum is the sum over quadratic phase factors [2, 3]. Due to their intrinsic properties Gauss sums allow for the factorization of numbers [4]. These three thoughts were the unifying theme of a series of papers [4–6] in which we have analyzed the potential of Gauss sums to factor numbers. In particular we have proposed three physical systems to implement this factorization scheme. In the present paper we summarize the main ideas of these papers without going into the details.

The central idea of our method rests on the observation [7, 8] that the generalized Gauss sum

$$\mathcal{S}_N(\xi) \equiv \sum_{m=-\infty}^{\infty} w_m \exp \left[ 2\pi i \left( m + \frac{m^2}{N} \right) \xi \right] \quad (17.1)$$

for real valued arguments  $\xi$  displays a pronounced maximum at an integer  $\xi = \ell$  when

$$\ell = q \frac{N}{r} \quad (17.2)$$

with  $q$  and  $r$  coprime. Since  $\ell$  is an integer, Eq. (17.2) implies that  $r$  must be a factor of  $N$  and hence  $\ell$  is a multiple integer  $q$  of this factor  $N/r$ . For  $q = 1$  we find the prime factors of  $N$  as well as 1 and  $N$ . We emphasize that this argument only holds true when the weight factors  $w_m$  are slowly varying and  $N$  is odd. Needless to say in the present context we are only interested in odd numbers  $N$  since powers of 2 can always be removed. This correspondence between maxima of  $\mathcal{S}_N$  and factors of  $N$  is a consequence [4, 9] of the periodicity properties of Gauss sums [2, 3].

In physics Gauss sums arise from the interference of multiple quantum paths which are weighted by quadratic phase factors. We pursue this key idea in the present paper by discussing three physical realizations leading to Gauss sums.

The use of quadratic phases to factor numbers has also been proposed in [10, 11]. However, these techniques differ from our approach. For a more detailed comparison we refer to [4, 9].

Our article is organized as follows: In Sect. 17.2 we consider a two-photon transition in a specific ladder system which is driven by a weak chirped pulse [6]. Then we study in Sect. 17.3 two realizations of laser-driven one-photon transitions [5]. In each system we deal with multiple competing excitation paths which involve quadratic phase factors. The resulting total excitation probability is experimentally accessible via a detection of the fluorescence signal of the excited state. We illustrate this factorization scheme in Sect. 17.4 by various examples.

## 17.2

### Chirping a Two-photon Transition

We now consider the interaction of the multi-state ladder system shown in Fig. 17.1 with a weak chirped laser pulse. The resulting excitation probability amplitude in second order perturbation theory is of the form of the generalized Gauss sum, Eq. (17.1). The deeper reason for this emergence for the Gauss sum is the interference of quantum paths which are weighted by quadratic phase factors. We demonstrate that the dependence of the excitation probability as a function of the dimensionless chirp reveals the factors of an integer encoded in the ladder system. Experimentally the population in the excited state is accessible via an acquisition of the fluorescence signal as a function of the rescaled chirp.

#### 17.2.1

##### Chirped Laser Pulses

We start with a brief summary of the description of chirped pulses which are the major prerequisite for the present paper. For a more detailed discussion of the widespread applications we refer to [1, 12–15]. The electric field

$$E_c(t) = \mathcal{E}_0 \left[ e^{-i\omega_L t} f(t) + \text{c.c.} \right], \quad (17.3)$$

of a chirped laser pulse with amplitude  $\mathcal{E}_0$  and carrier frequency  $\omega_L$  contains the pulse shape

$$f(t) = f_0 \exp \left[ -\frac{1}{2} (\Delta\omega f_0)^2 t^2 \right]. \quad (17.4)$$

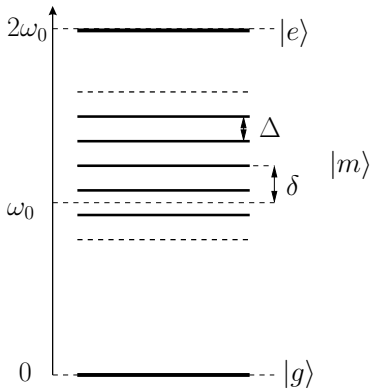


**Fig. 17.1** Ladder system leading to an excitation probability amplitude in the form of a Gauss sum when driven by a weak chirped pulse. A two-photon transition connects the ground state  $|g\rangle$  to the excited state  $|e\rangle$ . We include a harmonic manifold of  $D$  intermediate

states  $|m\rangle$  which are shifted by the offset  $\delta_m = \delta + m \Delta$  with respect to the central frequency  $\omega_0$ . The offset of the central state  $|m = 0\rangle$  is  $\delta$  whereas  $\Delta$  denotes the separation of the states in the harmonic manifold

Here we have introduced the complex-valued factor

$$f_0 = f_0(\phi'') \equiv \sqrt{\frac{1 + i \Delta \omega^2 \phi''}{1 + \Delta \omega^4 \phi''^2}}, \quad (17.5)$$

together with the bandwidth  $\Delta\omega$  and the quadratic phase dispersion  $\phi''$  which is a measure for the quadratic frequency dependence of the spectral phase of the pulse giving rise to a linear variation of the instantaneous frequency with time.

### 17.2.2

#### Excitation Probability Amplitude

The ladder system of Fig. 17.1 consists of a ground state  $|g\rangle$ , an excited state  $|e\rangle$  separated by an energy  $2\hbar\omega_0$  and  $D$  intermediate states  $|m\rangle$  with quantum numbers  $M' \leq m \leq M$ . These intermediate states are displaced by the offset

$$\delta_m = \delta + m \Delta. \quad (17.6)$$

with respect to the central frequency  $\omega_0$ . The harmonic manifold is characterized by the offset  $\delta$  of a central state  $|0\rangle$  and separation  $\Delta$  of adjacent states.

In the interaction picture the Hamiltonian describing the interaction between the electric field of the chirped pulse, Eq. (17.3), with envelope, Eq. (17.4), and our ladder system reads

$$V(t) = -\hbar \sum_{m=M'}^M \left[ \Omega_{mg} e^{i \delta_m t} f(t) |m\rangle \langle g| + \Omega_{em} e^{-i \delta_m t} f(t) |e\rangle \langle m| + \text{c.c.} \right] \quad (17.7)$$

where we have introduced the Rabi frequencies as  $\Omega_{ij}$  associated with the transition  $|i\rangle \rightarrow |j\rangle$ .

When we assume that the duration of the laser pulse is shorter than the time scale of spontaneous emission the Schrödinger equation is the adequate tool to describe the time evolution of our system. For a weak chirped pulse second order perturbation theory is sufficient to find the excitation probability amplitude

$$c_e = -\frac{1}{2\hbar^2} \int_{-\infty}^{\infty} dt' \int_{-\infty}^{t'} dt'' \langle e|V(t')V(t'')|g\rangle. \quad (17.8)$$

after the action of the chirped pulse. Here we have assumed that the ladder system is prepared initially in the ground state.

As shown in [6] we arrive at the explicit form

$$c_e = \mathcal{N} \sum_{m=M'}^M w_m \exp \left[ 2\pi i \left( m + \frac{m^2}{N} \right) \xi \right] \equiv \mathcal{N} S_N(\xi). \quad (17.9)$$

where we have introduced the number

$$N = \frac{2\delta}{\Delta} \quad (17.10)$$

to be factorized and the dimensionless chirp

$$\xi = \frac{\delta\Delta}{\pi} \phi''. \quad (17.11)$$

Here  $\mathcal{N}$  denotes a prefactor which covers all quantities which are not relevant in the context of factorization. The weight factors [6]

$$w_m \equiv -\frac{\pi}{2} \frac{\Omega_{em}\Omega_{mg}}{\Delta\omega^2} \operatorname{erfc} \left( i \frac{\delta_m}{\Delta\omega} \sqrt{1 - i \Delta\omega^2 \phi''} \right) \exp \left[ - \left( \frac{m + N/2}{\Delta m} \right)^2 \right] \quad (17.12)$$

contain the complementary error function [16] and are approximately constant [6] for negative values of the rescaled chirp  $\xi \propto \phi''$  and for an appropriately chosen width  $\Delta m \equiv \Delta\omega/\Delta$ . The fact that we are restricted to negative chirps arises from the various excitation mechanisms in the present system [1,17].

### 17.2.3

#### Example for Factorization

Now we demonstrate that the population  $|S_N(\xi)|^2$  in the excited state contains the factors of  $N$ . The numerical results obtained in the present section are

generated on the basis of an ladder system that contains  $D$  intermediate states in the harmonic manifold.

We adapt the dimension  $D$  to the number  $N$  to be factorized. In order to factorize  $N$  we require  $D = N \dots 2N$  intermediate states where the lowest quantum number is bound by  $M' > N/2$ . Furthermore, we assume that the product  $\Omega_{gm}\Omega_{me}$  of Rabi frequencies is independent of  $m$ .

In Fig. 17.2 we show the signal  $|S_N(\xi)|^2$  for the number  $N = 21$  as a function of the continuous argument  $\xi$ . In addition, we provide magnified insets of the signal in the vicinity of integer arguments  $\xi$ . Only if  $\xi$  corresponds to a factor of  $N$  the signal displays a pronounced maximum. No peculiarities arise at non-factors [4].

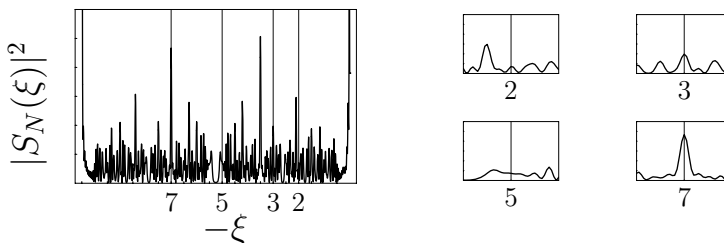


**Fig. 17.2** Factorization of  $N = 21 = 3 \cdot 7$  with the help of the ladder system of Fig. 17.1 using  $D = 21$  intermediate states. On the left we provide an overview over the complete signal  $|S_N(\xi)|^2$ , Eq. (17.9), as a function of the dimensionless chirp  $\xi$ . On the right we show the magnified signal in the vicinity of candidate

prime factors. Pronounced maxima at the prime factors  $-\xi = 3$  and  $7$  are clearly visible. In contrast, at non-factors  $-\xi = 2$  and  $5$  the signal does not exhibit any peculiarities. in this simulation we have assumed identical Rabi frequencies for all quantum paths and have chosen  $\Delta m = 50.83$ .

## 17.3

### Driving a One-photon Transition

In the preceding Sect. we have shown that the excitation probability of a driven ladder system leads to the generalized Gauss sum  $S_N$  which allows us to factor numbers. In [6] we have analyzed various systems such as Rydberg atoms, diatomic molecules, quantum dots and trapped cold atoms with respect to the possibility of meeting the constraint of a harmonic manifold. The outcome of these investigation was that such a ladder system is difficult to realize in an experiment. Fortunately, this problem can be overcome by using one-photon transitions in appropriately modulated systems as we show in the present section.

## 17.3.1

**Model**

In particular, we study a two-level system with ground state  $|g\rangle$  and excited state  $|e\rangle$  separated by an energy  $\hbar\omega_0$ . This system is driven by two electric fields: The permanent dipole moment  $\wp_{ee}$  associated with the excited state interacts with the electric field  $E_m(t)$  which modulates  $|e\rangle$ . We consider two cases of  $E_m(t)$ : (i) a sinusoidal time dependence manifesting itself in a periodic modulation of the excited state and (ii) a linear sweep reflecting itself in a linear shift of the excited state energy as a function of time. The driving field  $E_d(t)$  leads to weak-field excitation in the two-level system.

Depending on the two cases (i) and (ii) the field

$$E_d(t) = \mathcal{E}_0 \left[ e^{-i\omega_L t} f(t) + \text{c.c.} \right], \quad (17.13)$$

with pulse shape  $f(t)$  is either (i) a chirped pulse or (ii) a train of sharp pulses. Here the amplitude of the pulse is  $\mathcal{E}_0$  and  $\omega_L$  denotes the optical carrier frequency.

This arrangement results in the interaction Hamiltonian

$$V = -\wp_{ee} E_m(t) |e\rangle\langle e| - [\wp_{ge} E_d(t) |e\rangle\langle g| + \text{c.c.}] \quad (17.14)$$

where we denote the dipole moments by  $\wp_{ij}$ .

We assume that the frequencies of both fields are clearly separated resulting in the fact that the modulating field  $E_m(t)$  only acts on the excited state and the driving field  $E_d(t)$  only on the transition. Again we neglect spontaneous emission since the interaction time with the laser field  $E_d(t)$  is much shorter compared to the decay time of the atomic level. Hence, the Schrödinger equation is adequate to describe the time evolution of the present system.

We recall that the strong field  $E_m(t)$  responsible for the modulation of the excited state appears in the diagonal of Eq. (17.14). Only the weak driving field  $E_d(t)$  couples the off-diagonal elements leading to transitions. Thus it suffices to apply perturbation theory of first order.

We start with a two-level system which is initially prepared in the ground state. Then the probability amplitude  $c_e$  to be in the excited state reads in rotating wave approximation

$$c_e(t) = i \Omega_{ge} e^{i\beta(t)} \int_{t_0}^t dt' e^{-i\beta(t')} e^{i\delta t'} f(t'), \quad (17.15)$$

where we have introduced the phase

$$\beta(t) \equiv \frac{\wp_{ee}}{\hbar} \int_{t_0}^t dt' E_m(t'). \quad (17.16)$$

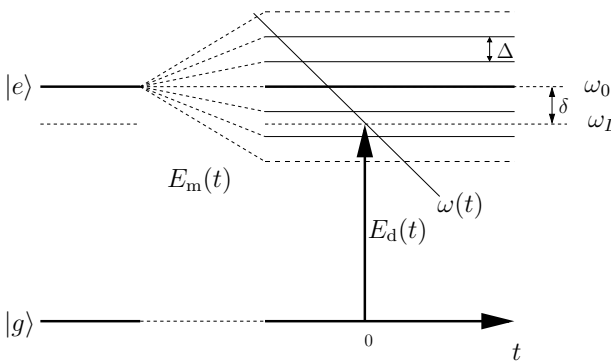


**Fig. 17.3** Engineering the Floquet ladder. We consider a two-level system with the ground state  $|g\rangle$  and the excited state  $|e\rangle$  separated by the energy  $\hbar\omega_0$ . The excited state is modulated by a strong sinusoidal field  $E_m(t)$ , Eq. (17.17) giving rise to equidistant

sidebands separated by  $\hbar\Delta$ . The one-photon transition is driven by a chirped laser pulse  $E_d(t)$ , Eq. (17.3), which is characterized by a linear variation of the instantaneous frequency  $\omega(t)$ .

together with the time-independent Rabi-frequency  $\Omega_{ge} \equiv \varphi_{ge}\mathcal{E}_0/\hbar$  associated with the electric field of the transfer pulse, Eq. (17.13), and the detuning  $\delta \equiv \omega_0 - \omega_L$  between atomic and carrier frequency.

### 17.3.2

#### Floquet Ladder

The key idea of the first approach (*i*) is the periodic modulation of the excited state  $|e\rangle$  induced by a strong laser field. As a result  $|e\rangle$  splits up into equidistant sidebands whose weights are determined by the Bessel function  $J_n$ .

We now specify the electric fields. The modulating field

$$E_m(t) = \mathcal{F}_0 \sin(\Delta t), \quad (17.17)$$

has the period  $2\pi/\Delta$  and amplitude  $\mathcal{F}_0$ . As in Sect. 17.2 a chirped pulse with envelope, Eq. (17.4), acts as the driving field  $E_d(t)$ .

When we substitute the electric fields  $E_m$  and  $E_d$  defined in Eq. (17.17) and Eq. (17.3) into the expression for the probability amplitude Eq. (17.15) we obtain in the long-time limit that is, after the action of the chirped pulse

$$c_e = \mathcal{N} \sum_n w_n \exp \left[ -2\pi i \left( n - \frac{n^2}{N} \right) \xi \right] \equiv \mathcal{N} S_N(\xi). \quad (17.18)$$

Hence, the excitation probability amplitude is again determined by the generalized Gauss sum  $S_N$ .

We express the number

$$N = \frac{2\delta}{\Delta} \quad (17.19)$$

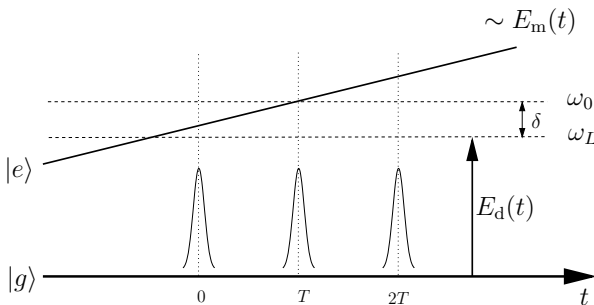


**Fig. 17.4** Excitation by a pulse train. We consider a two-level system with ground state  $|g\rangle$  and excited state  $|e\rangle$ . The modulation field  $E_m(t)$ , Eq. (17.22), causes a linear variation of the excited state energy. Simultaneously a pulse sequence of  $M + 1$  delta-shaped laser pulses  $E_d(t)$ , Eq. (17.23) with carrier frequency  $\omega_L = \omega_0 - \delta$  induces transfer in the weak field limit. Consecutive pulses are separated by  $T$ .

to be factorized in terms of parameters characterizing the laser fields. The dimensionless argument

$$\xi = \frac{\delta\Delta}{2\pi} \phi'' \quad (17.20)$$

is proportional to the chirp of the transfer pulse.

The weight factors

$$w_n \equiv \frac{1}{\sqrt{2\pi\Delta n}} \exp \left[ -\frac{1}{2} \left( \frac{n - N/2}{\Delta n} \right)^2 \right] J_n(\kappa). \quad (17.21)$$

depend on a Gaussian with width  $\Delta n \equiv \Delta\omega/\Delta$  and the Bessel function  $J_n(\kappa)$  with argument  $\kappa = \varrho_{ee}\mathcal{F}_0/(\hbar\Delta) = \Omega_{ee}/\Delta$ . The width  $\Delta n$  can be controlled by adjusting the parameters of the laser fields, Eq. (17.3) and Eq. (17.17).

Although the constant  $\mathcal{N}$  in Eq. (17.18) connecting the probability amplitude  $c_e$  with the signal  $S_N$  is different from the one appearing in Eq. (17.9) we still use the same letter to bring out the close analogy between the formulas Eq. (17.9) and Eq. (17.18). For this reason we also use the argument  $\xi$  despite the fact that in Eq. (17.9) it is different by a factor of 2 from the one defined in Eq. (17.18). It is obvious that the weight factors  $w_n$  in the ladder system are different from the ones in the Floquet system. The same notation applies to the system discussed in the next subsection.

### 17.3.3

#### Pulse Train

Before we turn to the factorization scheme using the modulated one-photon transition we discuss the alternative approach (ii) to generate a Gauss sum in the excitation probability amplitude of a two-level system. In contrast to the

previous schemes the quadratic phase factors are not due to chirped pulses, but arise from the combination of a temporal variation of the resonance condition and a sequence of equidistant delta-shaped laser pulses. We find that the excitation probability amplitude induced by this sequence is the sum over contributions arising from each individual pulse.

In our second approach towards factorization of numbers with laser pulses we modulate the energy of the excited state by an electric field

$$E_m(t) = \mathcal{F}_0 \frac{t}{T}, \quad (17.22)$$

with amplitude  $\mathcal{F}_0$  and time scale  $T$ .

The one-photon transition is driven by the field  $E_d(t)$  consisting of a train of  $M + 1$  delta-shaped pulses

$$f(t) = \sum_{m=0}^M \delta(t - mT) \quad (17.23)$$

where the  $m$ -th pulse arrives at the time  $mT$ . The temporal width of each individual pulse is smaller than the separation  $T$  of adjacent pulses.

When we substitute the fields  $E_m$  and  $E_d$ , Eq. (17.22) and Eq. (17.23), into Eq. (17.15) and perform the integrals the excitation probability amplitude in the long-time limit reads

$$c_e = \mathcal{N} \sum_{m=0}^M \exp \left[ -2\pi i m^2 \frac{N}{\xi} \right] = \mathcal{N} \mathcal{A}_N^{(M)}(\xi) \quad (17.24)$$

where we encode the number

$$N \equiv \frac{\delta T}{2\pi}. \quad (17.25)$$

to be factorized in terms of parameters of the pulse sequence. The dimensionless argument

$$\xi \equiv \frac{2\delta}{\Omega_{ee}} \quad (17.26)$$

is expressed in terms of the Rabi frequency  $\Omega_{ee} = \varphi_{ee} \mathcal{F}_0 / \hbar$ .

## 17.4

### Factorization

We now use the expressions, Eq. (17.18) and Eq. (17.24), for the excitation probabilities to demonstrate the potential for factorization. For this purpose we first simplify the expressions and analyze them at integer values of the argument.

## 17.4.1

## Factorization with Floquet Ladder

In the approach of the Floquet ladder (*i*) we collect the fluorescence signal for integer values  $\ell$  of the dimensionless chirp  $\xi \equiv \ell$ . As a consequence the term linear in the summation index in the phase factor drops out. In this case the probability amplitude  $c_\ell$  is proportional to the signal

$$S_N(\ell) = \sum_n w_n \exp \left[ 2\pi i n^2 \frac{\ell}{N} \right]. \quad (17.27)$$

For a special choice of the argument  $\kappa$  of the Bessel function and  $\kappa \gg n$  we find [5] that all weight factors  $w_n$  with odd index  $n$  vanish. The only  $n$ -dependence left is given by the Gaussian in Eq. (17.21). For an appropriate choice of  $\Delta n$  the weight factors can be adjusted to vary slowly as a function of the summation index  $n$ .

In Fig. 17.5 we present numerical results for the factorization of  $N = 105$  employing a truncated Floquet basis of 306 harmonics. In contrast to Fig. 17.2 the signal  $|S_N(\xi)|^2$  is depicted only for integer values of the rescaled chirp  $\xi = \ell$ . The positions of prime factors of  $N$  and their products are indicated by vertical lines. The signal exhibits pronounced maxima at the factors  $\ell = 3, 5, 7, 15, 21$ , and  $35$  whereas at non-factors it is considerably weaker. Moreover, we recognize that the values of the signal at the factors of  $N$  lie on a straight line through the origin. In [4] we provide an analytical argument for this fact.

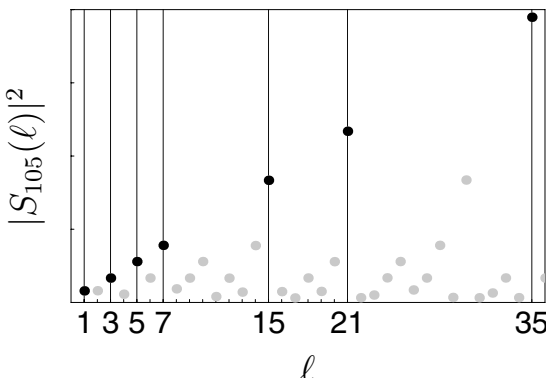


**Fig. 17.5** Factorization of  $N = 105 = 3 \cdot 5 \cdot 7$  in the Floquet ladder approach. We show the signal  $|S_N(\xi)|^2$ , Eq. (17.18), for integer values  $\xi = \ell$  of the rescaled chirp. In order to satisfy the criterion of slowly varying weight factors we have chosen the parameters  $\Delta n = 50.83$  and  $\kappa = 10000$ . The positions of the prime

factors and products of them are indicated by vertical lines. At the prime factors  $\ell = 3, 5$  and  $7$  and products  $\ell = 15, 21, 35$  the signal displays a maximum (black dots). At non-factors the signal is weaker (gray dots). For this simulation we have employed 306 harmonics.

## 17.4.2

**Factorization with a Pulse Train**

We now turn to the factorization method based on a train of pulses (ii). In order to reveal the prime factors of the number  $N$  we analyze the modulus of

$$\mathcal{A}_N^{(M)}(\ell) \equiv \sum_{m=0}^M \exp \left[ -2\pi i m^2 \frac{N}{\ell} \right]. \quad (17.28)$$

as a function of the integer argument  $\ell$ . Since the Rabi frequency  $\Omega_{ee}$  is a free parameter we can adjust  $\ell$  to any integer.

When we compare the two Gauss sums, Eq. (17.18) and Eq. (17.24), we note that the role of the argument  $\ell$  and the number  $N$  to be factorized in the exponential are interchanged. Nevertheless, Eq. (17.28) is also a Gauss sum and can be cast into the familiar form using the reciprocity law [3].

We now demonstrate that  $\mathcal{A}_N$  is even more suited to factor numbers than the generalized Gauss sum, Eq. (17.1). Whenever the integer argument  $\ell$  is a factor of  $N$  the phase is an integer multiple of  $2\pi$ . As a consequence each term in the sum is unity. Since the sum contains  $M + 1$  terms the signal takes on the maximum value of

$$|\mathcal{A}_N^{(M)}(\ell)| = M + 1. \quad (17.29)$$

In Fig. 17.6 we illustrate the power of this read-out formalism using the example  $N = 1911$ . We find that a pulse sequence with a relatively small number  $M + 1 \ll N$  of pulses provides a clear identification of the factors of  $N$ .

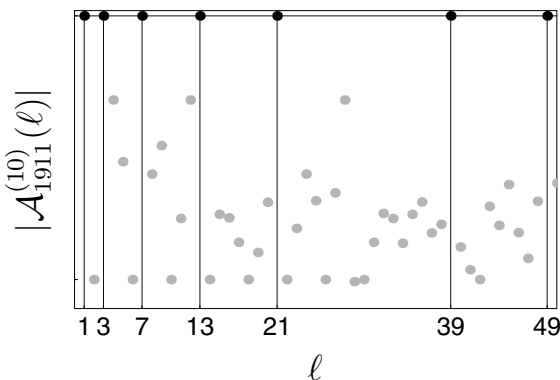


**Fig. 17.6** Factorization of  $N = 1911 = 3 \cdot 7^2 \cdot 13$  using a pulse train. The modulus  $|\mathcal{A}_N^{(M)}(\ell)|$  of the signal, Eq. (17.28), exhibits clear maxima indicated by black dots at integer arguments  $\ell$  corresponding to factors of  $N$ . The value of the signal at these points is proportional to the number  $M + 1$  of laser pulses in the train Eq. (17.23). In the present example we have used  $M+1=11$  delta-shaped pulses.

## 17.5

## NMR-experiment

We now turn to an experimental realization [18] of a Gauss sum closely related to  $\mathcal{A}_N^{(M)}$  defined by Eq. (17.28). In the implementation of Section 17.3.3 the Gauss sum arises through the time evolution of a two-level atom whose transition frequency increases linearly in time and which is driven by a train of laser pulses. In our NMR-experiment we subject an ensemble of spins  $I = 1/2$  to a specific sequence of RF pulses as depicted in Fig. 17.7. This sequence induces a series of signals which when summed represent a Gauss sum of the type of Eq. (17.28).

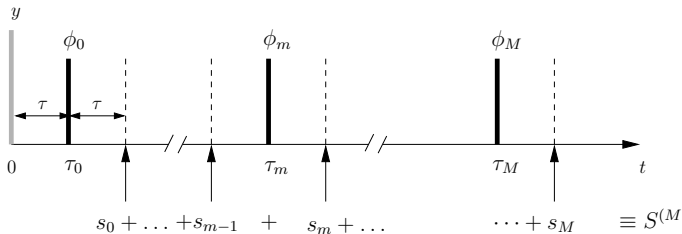


**Fig. 17.7** NMR implementation of our factorization scheme using Gauss sums. The  $y$ -pulse which prepares the initial density matrix  $\rho_{\text{in}}$  is followed after a time  $\tau$  by a pulse which imprints the phase  $\phi_0$  on the spins. This pulse is the first of a sequence of  $M + 1$  pulses each imprinting a different phase  $\phi_m$ . At times  $\tau_m + \tau \equiv (2m + 1)\tau + \tau$  we measure the echo,

that is the polarization  $s_m$  in  $x$ -direction and sum the echos  $s_m$  over all  $m$  to obtain  $S^{(M)}$ . In order to implement a Gauss sum the phases  $\phi_m$  need to be proportional to the number  $N$  to be factored and have to increase linearly as a function of  $m$  since the spin dynamics expressed by  $s_m$  depends on the sum over all phases of the previous pulses.

We use  $\text{H}_2\text{O}$  as an ensemble of protons with nuclear spin  $1/2$  in Boltzmann equilibrium at room temperature. Radio frequency pulses are applied at the Larmor frequency of the protons. The pulse sequence depicted in Fig. 17.7 is chosen such that the time evolution of the proton spins resulting from the Hamiltonian

$$H = \hbar\Delta\omega I_z + \pi\hbar \sum_{k=0}^M \delta(t - \tau_k) (\cos \phi_k I_x + \sin \phi_k I_y) \quad (17.30)$$

gives rise to a sequence of echos which leads to the desired Gauss sum. Here  $\Delta\omega$  denotes the frequency of the spins in the rotating frame and the spin operators  $I_i \equiv \sigma_i/2$  are proportional to the well-known Pauli spin matrices  $\sigma_i$ . The  $k$ -th radio frequency pulse with phase  $\phi_k$  arrives at the time  $\tau_k \equiv (2k + 1)\tau$ .

After an initiating  $\pi/2$ -pulse in  $y$ -direction which creates  $\rho_{\text{in}}$  the pulse sequence consists of  $M + 1$   $\pi$ -pulses with separation  $2\tau$  which are individually

phase shifted with respect to the  $x$ -axis of the rotating frame by an angle

$$\phi_k \equiv \begin{cases} (-1)^k(2k-1)\pi \frac{N}{\ell} & \text{for } k \geq 1 \\ 0 & \text{for } k = 0. \end{cases} \quad (17.31)$$

At times  $\tau_m + \tau$  we measure the polarization

$$s_m \equiv \frac{\text{Tr}(\sigma_x \rho_m)}{\text{Tr}(\sigma_x \rho_{\text{in}})} \quad (17.32)$$

in  $x$ -direction with  $\rho_m \equiv \rho(\tau_m + \tau)$  and the sum

$$\mathcal{C}_N^{(M)}(\ell) = \sum_{m=0}^M s_m \quad (17.33)$$

over the signals  $s_m$  of Eq. (17.32) reads

$$\mathcal{C}_N^{(M)}(\ell) = \sum_{m=0}^M \cos \left( \sum_{k=0}^m (-1)^k 2\phi_k \right) = \sum_{m=0}^M \cos \left( 2\pi m^2 \frac{N}{\ell} \right). \quad (17.34)$$

Hence, the spin dynamics expressed by the signal  $s_m$  depends on its complete history, that is the phases of all previous pulses. When we compare  $\mathcal{C}_N^{(M)}$  to the Gauss sum  $\mathcal{A}_N^{(M)}$  of Eq. (17.28) we find the relation

$$\mathcal{C}_N^{(M)} = \text{Re } \mathcal{A}_N^{(M)}. \quad (17.35)$$

In Fig. 17.8 we display the results of our NMR implementation of our factor-

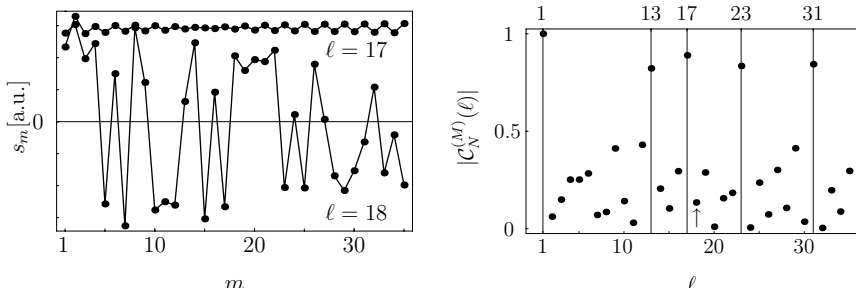


**Fig. 17.8** Experimental realization of factoring  $N = 157573 = 13 \cdot 17 \cdot 23 \cdot 31$  using the NMR implementation of the Gauss sum  $\mathcal{C}_N^{(M)}$  of Eq. (17.34). On the left and right we depict the echo height  $s_m$  measured at times  $\tau_m + \tau$  and the resulting average  $\mathcal{C}_N^{(M)}$  for different trial factors  $\ell$ , respectively. For

factors such as  $\ell = 17$  the signals  $s_m$  are approximately constant as a function of  $m$  with an average value  $\mathcal{C}_N^{(M)}(17)$  close to unity. In contrast, for a non-factor such as  $\ell = 18$   $s_m$  oscillates around zero and when summed over  $m$  almost averages out as indicated by the arrow.

ization scheme based on Gauss sums for  $N = 157573 = 13 \cdot 17 \cdot 23 \cdot 31$ . On the left we show the time evolution of the spin under the influence of the particular sequence of pulses with phases  $\phi_k$  defined by Eq. (17.31). As a measure of the dynamics we display the echo signal  $s_m$  following from Eq. (17.32). For factors of  $N$  such as  $\ell = 17$  the signal is constant. Consequently we find for the average  $\mathcal{C}_N^{(M)}(\ell = 17)$  a value close to  $M + 1$  as indicated on the right. However, for non-factors such as  $\ell = 18$  the echo signal oscillates around zero and leads to a rather small average value  $\mathcal{C}_N^{(M)}(\ell = 18)$ , as indicated by the arrow. We emphasize that due to the quasi-random interference of Gauss sums  $M = 11$  terms are sufficient to discriminate factors from non-factors.

## 17.6 Conclusions

In summary, we have presented the key results of the factorization of numbers with laser-driven one- or two-photon transitions. For each system we have presented analytical expressions for the excitation probability amplitude induced by weak field excitation. In all cases they are given by a Gauss sum, that is the sum over quadratic phases. The periodicity property of the Gauss sum is the essential ingredient to factorize numbers. For each of the proposed systems we have demonstrated the potential to factorize numbers by numerical examples. Moreover, we have reported on an experimental realization of our factorization scheme by means of NMR.

## Acknowledgement

We thank M. Bienert, O. Crasser, M. Freyberger, D. Haase, E. Lutz, H. Meier, M. Stefanak, S. Stenholm and F. S. Straub for many fruitful and stimulating discussions. In particular we are grateful to K. Müller (Physikalische Chemie, Universität Stuttgart) for making the Varian NMR spectrometer available. W. M., M. M. and W. P. S. acknowledge financial support by the Landesstiftung Baden-Württemberg. In addition, this work was supported by a grant from the Ministry of Science, Research and the Arts of Baden-Württemberg in the framework of the Center of Quantum Engineering. Moreover, W. P. S. also would like to thank the Alexander von Humboldt Stiftung and the Max-Planck-Gesellschaft for receiving the Max-Planck-Forschungspreis. I. Sh. A. thanks the Israel Science Foundation for supporting this work.

## References

- 1 See for example: B. Chatel, J. Degert, S. Stock, and B. Girard, *Phys. Rev. A*, **68**, 041402(R) (2003).
- 2 S. Lang, *Algebraic Number Theory* (Addison Wesley, New York, 1970).
- 3 H. Davenport, *Multiplicative Number Theory* (Springer, New York, 1980).
- 4 W. Merkel, I. Sh. Averbukh, B. Girard, and W. P. Schleich, Factorization of numbers with Gauss sums and laser pulses: I. Mathematical background. In preparation for *Phys. Rev. A* (2006).
- 5 W. Merkel, I. Sh. Averbukh, G. G. Paulus, and W. P. Schleich, Factorization of numbers with Gauss sums and laser pulses: II. Implementations. In preparation for *Phys. Rev. A* (2006).
- 6 W. Merkel, H. Mack, E. Lutz, G. G. Paulus, B. Girard, and W. P. Schleich, Chirping a two-photon transition in a multistate ladder. In preparation for *Phys. Rev. A* (2006).
- 7 H. Mack, M. Bienert, F. Haug, M. Freyberger, and W. P. Schleich, *phys. stat. sol. (b)* **233**, No. 3, 408–415 (2002).
- 8 H. Mack, M. Bienert, F. Haug, F. S. Straub, M. Freyberger, and W. P. Schleich, Wave packet dynamics and factorization of numbers, in: *Proceedings of the Enrico Fermi Summer School, Course CXLVIII: Experimental Quantum Computation*, edited by P. Mataloni and F. De Martini (Elsevier, Amsterdam, 2002), pp. 369–383.
- 9 W. Merkel, O. Crasser, F. Haug, E. Lutz, H. Mack, M. Freyberger, W. P. Schleich, I. Sh. Averbukh, M. Bienert, B. Girard, H. Maier, and G. G. Paulus, Chirped pulses, Gauss sums and the factorization of numbers. *Int. J. Mod. Phys. B* **20**, 1893–1916 (2006).
- 10 J. F. Clauser and J. P. Dowling, *Phys. Rev. A* **53**, 4587 (1996).
- 11 W. G. Harter, *Phys. Rev. A* **64**, 012312 (2001).
- 12 B. Broers, H. B. van Linden van den Heuvell, and L. D. Noordam, *Phys. Rev. Lett.* **69**, 2062 (1992).
- 13 P. Balling, D. J. Maas, and L. D. Noordam, *Phys. Rev. A* **50**, 4276 (1994).
- 14 D. J. Maas, C. W. Rella, P. Antoine, E. S. Toma, and L. D. Noordam, *Phys. Rev. A* **59**, 1474 (1999).
- 15 A. Assion, T. Baumert, J. Helbing, V. Seyfried, and G. Gerber, *Chem. Phys. Lett.* **259**, 488 (1996).
- 16 M. Abramowitz and I. A. Stegun, *Handbook of mathematical functions* (Dover Publications, New York, 1972).
- 17 B. Chatel, J. Degert, and B. Girard, *Phys. Rev. A* **70**, 053414 (2004).
- 18 M. Mehring, K. Müller, I. Sh. Averbukh, W. Merkel, and W. P. Schleich, NMR experiment factors numbers with Gauss sums, submitted to *Phys. Rev. Lett.* (2006), e-print: quant-ph/0609174.



**18****Quantum Algorithms for Number Fields***Daniel Haase and Helmut Maier***18.1****Introduction****18.1.1****Outline of the Survey**

Shor's factoring algorithm [10] was the first quantum algorithm to solve a famous number theoretic problem, the computation of the unique prime factorization of a rational integer, by reducing it to a period finding problem. It is natural to ask for quantum algorithms which generalize this concept. While factorization of integer numbers is still classically impractical, number theory has already provided the natural generalization of the fact that any integer can be uniquely decomposed into prime numbers. It appears that integer factorization complexity remains hidden when viewed over  $\mathbb{Z}$  only. Most mechanisms controlling the factorization of numbers into prime numbers become visible on larger domains of numbers. Such domains, called number fields, come with a set of invariants measuring certain aspects of their structure. In this survey we discuss recently developed quantum algorithms which compute these invariants. The next section introduces the concept of number fields and their geometry. Sect. 18.3 describes the theory of reduced ideals, a technique used to classically deal with number theoretic objects of infinite nature in number fields. Sect. 18.4 introduces  $\zeta$ -functions, the central objects of analytic number theory, which encode information about the invariants we want to compute. Sect. 18.5 contains examples and diagrams to illustrate the invariants defined in the previous sections. Sect. 18.6 describes the period finding algorithm of Hallgren which can be used to compute the regulator in case of real quadratic number fields, and its generalization to arbitrary number fields by Schmidt and Vollmer. Sect. 18.7 briefly describes modifications of these algorithms to compute other invariants like the class number.

## 18.1.2

**Why Number Fields?**

No efficient classical algorithm to compute the factorization of a rational integer is known, even for the simple case of a composite  $n = pq$  of two distinct prime numbers. This is somewhat unexpected, since the inverse problem, the computation of the product of two numbers, is very easy and can be performed efficiently for very large numbers. Some aspects of factorization are hidden if we restrict ourselves to rational integers, the problem becomes much more complicated if we pass to larger domains of numbers. Modern factoring algorithms, namely the number field sieve, view the given problem in such a domain. Therefore it is necessary to measure the growth of factorization complexity outside  $\mathbb{Z}$ . This is done by defining so called invariants, numbers which measure the complexity of certain structural aspects of a number field. It is astonishing that the computation of such invariants, i.e. the question how complex such a field is, becomes at least as difficult as the original factoring problem, even if we fix the dimension of the field. If we can compute these invariants, we can efficiently factor integers in  $\mathbb{Z}$ . Apart from this practical approach, complexity theory naturally asks for quantum algorithms that solve problems which are more difficult than factorization. While most hard problems of computer science (which are related to the famous NP=P problem of theoretical computer science) are not believed to be efficiently solvable on quantum computers, the generalizations of integer factoring are not believed to belong to these hard classes of problems, and therefore are natural candidates for quantum algorithms.

## 18.1.3

**Some History of the Subject**

The first classical algorithm to compute the factorization of an integer is of course the naive approach, which checks if a given  $n$  is divisible by the primes  $p \leq \sqrt{n}$ . Its complexity is therefore  $\sqrt{n}$  (not taking into account the computational task of singling out prime numbers of  $\mathbb{Z}$ ), which is exponential in the input length of  $n$ , which is usually given by the binary representation of  $n$  using  $\lfloor \log_2(n) \rfloor + 1$  bits. Improved classical methods, which still stick to the trivial number field  $\mathbb{Q}$ , admit complexity  $\sqrt[4]{n}$ . Modern factoring algorithms, using the structure of higher number fields, provide much better complexities like  $\exp(\sqrt[3]{\log(n)} \log(\log(n)))$ . The first computations of invariants were performed by Gauß 1801 in his work *Disquisitiones Arithmeticae*. He was the first to calculate class numbers, the most important invariant of a number field. The concept of number field invariants was not known at that time, Gauß calculated class numbers of so called quadratic forms, which are known today to be equal to the class numbers of certain quadratic fields. Gauß invented the

theory of reduction of forms as his principal tool to compute class numbers, which is similar to the reduction theory for ideals. The task of computing class numbers appeared to be quite hard, and was feasible for small number fields only. Shanks constructed in 1972 an algorithmic reduction from factorization to computation of class numbers, which, in terms of complexity theory, implies that the computation of these invariants is at least as difficult as factorization of integers. The concept of reduction first applied by Gauß to quadratic forms was generalized by Buchmann and his group to the context of number fields to compute class numbers and regulators. This finally led to a subexponential algorithm (known today as Buchmann-McCurley-Algorithm) which computes both class number and regulator of an arbitrary number field. This algorithm uses a still unproven conjecture, the Generalized Riemann Hypothesis. Also other important number theoretic algorithms, especially deterministic prime number tests, assume the truth of this conjecture. Shor invented his famous quantum factorization algorithm in 1994, the first polynomial algorithm for factoring integers. Shor's idea was to transform the algebraic situation to a period problem, and this idea was soon generalized to compute the structure of more general algebraic groups on a quantum computer. Most invariants of number fields are based on group structures. However, these structures have particular shortcomings which prohibit the direct application of Shor's algorithm: the ideal class group (base structure for the class number) admits no canonical representatives for its elements (which are infinite sets of numbers), the unit group (base structure for the regulator) is infinite itself. So it was necessary to invent variants of Shor's algorithm to deal with these special groups. This was accomplished first by Hallgren [7] in 2002 by adapting the quantum fourier transform to the concept of weak periodicity in quadratic number fields. Schmidt and Vollmer published a further generalization [9] to number fields of higher dimension in 2005. These quantum algorithms rely on efficient classical algorithms to do the necessary computations in number fields, which were given by Thiel 1995 in his doctoral thesis [11], using an approximation method to compute elements of number fields. A simplified variant using only ideal theoretic computations is given in [6].

## 18.2

### Geometry of Numbers

#### 18.2.1

#### Number Fields

In this section we summarize some facts from basic algebraic number theory (see [8] or [4] for a thorough introduction). A number field is a field extension

$F$  of the rational numbers  $\mathbb{Q}$  of finite degree  $n$ . As a vector space over  $\mathbb{Q}$  it is generated by the powers of an algebraic number  $\theta \in \mathbb{C}$ :  $F = \mathbb{Q}(\theta) = \{a_0\theta^0 + a_1\theta^1 + \dots + a_{n-1}\theta^{n-1} \mid a_0, \dots, a_{n-1} \in \mathbb{Q}\}$ . Number fields of degree  $n = 2$  are called quadratic number fields. They are generated by square roots  $\theta = \sqrt{d}$  of squarefree integers  $d \in \mathbb{Z}$ . These fields are called imaginary quadratic if  $d < 0$  and real quadratic if  $d > 0$ . Computations in number fields usually employ the isomorphism  $F = \mathbb{Q}(\theta) \cong \mathbb{Q}[X] / f(X)\mathbb{Q}[X]$  of  $\mathbb{Q}$ -algebras valid for any root  $\theta$  of a monic and irreducible rational polynomial  $f(X)$ . The input of an algorithm dealing with  $F$  are the coefficients of  $f(X)$ , which can always be chosen to be integral, so its input length is of magnitude  $O(n \cdot \log_2(\max |c_j|))$ . A number field of degree  $n$  admits embeddings  $\sigma_1, \dots, \sigma_n$  of  $F$  into the field  $\mathbb{C}$  of complex numbers, which arise from mapping the generator  $\theta$  to one of the  $n$  roots  $f(X)$ . The signature of  $F$  (or  $f(X)$  respectively) is  $(r, s)$  with  $r$  being the number of real roots of  $f(X)$  and  $s$  being the number of conjugate pairs of complex roots. We sort the  $\sigma_j$  such that  $\sigma_1, \dots, \sigma_r$  actually map  $F$  to  $\mathbb{R}$  and the remaining complex embeddings  $\sigma_r + 1, \dots, \sigma_n$  are grouped to pairs,  $\sigma_{r+2} = \bar{\sigma}_{r+1}$ ,  $\sigma_{r+4} = \bar{\sigma}_{r+3}$  etc. Each assignment of  $\theta$  to one of the  $n$  zeros of  $f(X)$  defines an embedding  $\sigma$  which maps  $F$  to  $\mathbb{R}$  if  $\sigma(\theta)$  is a real zero of  $f(X)$  or to  $\mathbb{C}$  if  $\sigma(\theta)$  is a complex zero. The tuple of all embeddings maps  $F$  to  $\mathbb{R}^r + \mathbb{C}^s \cong \mathbb{R}^n$  ( $n = r + 2s$ ). This space is called the (number theoretic) Minkowski-space of  $F$ , and is used to geometrically interpret number theoretical objects. We define  $r + s$  distinct absolute values  $|\alpha|_j = |\sigma_j(\alpha)|^c$ ,  $c = 1$  if  $\sigma_j$  is real and  $c = 2$  if  $\sigma_j$  is complex. This allows us to embed the unit group  $F^\times = F \setminus \{0\}$  into  $\mathbb{R}^{r+s}$  via the logarithmic homomorphism  $L(\alpha) = (\log |\alpha|_1, \dots, \log |\alpha|_{r+s})$ . The space  $\mathbb{R}^{r+s}$  is called logarithmic Minkowski-space of  $F$ .

### 18.2.2

#### Lattices

Lattices play an important role in algebraic number theory. Minkowski first used embeddings of number fields into lattices to deduce algebraic results, a technique known as Geometry of Numbers (the title of his book which introduced the concept). By a lattice we mean a  $\mathbb{Z}$ -submodule  $L$  of  $\mathbb{R}^m$  or, equivalently, a discrete subgroup of  $\mathbb{R}^n$ . Lattices are of the form  $L = \mathbb{R}\vec{v}_1 + \dots + \mathbb{R}\vec{v}_m$  with independent vectors  $\vec{v}_1, \dots, \vec{v}_m$ . The number  $m$  is called the rank of  $L$ .  $L \subset \mathbb{R}^n$  has full rank if  $m = n$ . We associate these invariants to a lattice:

**Definition 18.2.1** A fundamental epipede of a lattice is a set  $[0, 1)\vec{v}_1 \times \dots \times [0, 1)\vec{v}_m$  (depending on the basis  $\{\vec{v}_j\}$ ). Its volume is independent of the choice of basis, and is called the determinant or the volume  $\det(L)$  of the lattice  $L$ . The volume of  $L$  is zero if and only if  $L$  has rank  $m < n$ . The first minimum of  $L$  is

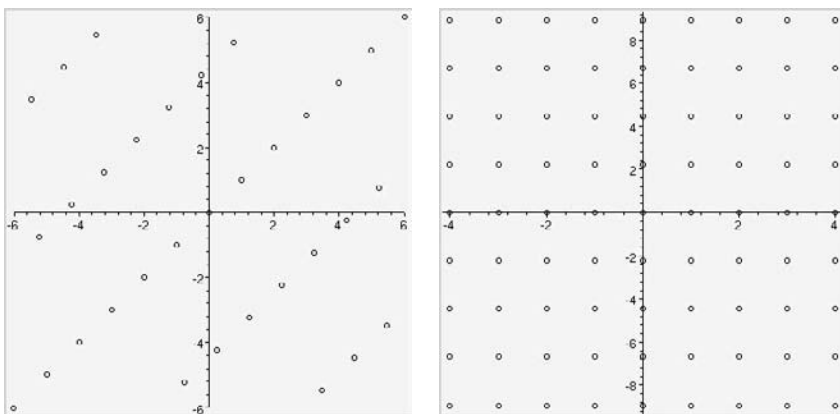


**Fig. 18.1** The ring  $\mathcal{O}$  of a real quadratic and an imaginary quadratic number field as a lattice in Minkowski-space.

the length of a shortest vector of  $L$ :

$$\lambda_1(L) = \min \left\{ \|\vec{x}\| \mid \vec{x} \in L \setminus \{0\} \right\}.$$

### 18.2.3

#### Integral Elements

The ring of integral elements of  $F$  is  $\mathcal{O} = \{\alpha \in F \mid g(\alpha) = 0 \text{ for some monic } g(X) \in \mathbb{Z}[X] \setminus \{0\}\}$ . It is the integral closure of  $\mathbb{Z}$  in  $F$ , or equivalently the maximal order of  $F$ .  $F$  itself is the quotient field of  $\mathcal{O}$ , and the ring  $\mathcal{O}_{\mathbb{Q}}$  is of course the most simple maximal order  $\mathbb{Z}$ .  $\mathcal{O}$  forms a lattice in Minkowski-space. Note that  $F$  itself is a dense subspace of  $\mathbb{R}^n$  via the embeddings  $(\sigma_j)$ .

A set of generators  $\omega_1, \dots, \omega_n \in \mathcal{O}$  of  $\mathcal{O}$  (or the lattice respectively) is called an integral basis of  $F$ . The square

$$\Delta = \det \begin{pmatrix} \sigma_1(\omega_1) & \sigma_1(\omega_2) & \cdots & \sigma_1(\omega_n) \\ \sigma_2(\omega_1) & \sigma_2(\omega_2) & \cdots & \sigma_2(\omega_n) \\ \vdots & \vdots & \ddots & \vdots \\ \sigma_n(\omega_1) & \sigma_n(\omega_2) & \cdots & \sigma_n(\omega_n) \end{pmatrix}^2$$

is independent of the choice of the integral basis  $\omega_1, \dots, \omega_n$  and the ordering of the embeddings  $\sigma_j$ . It can be shown that  $\Delta$  is always a rational integer, called the discriminant of  $F$ . It is a custom in algorithmic number theory to relate the complexity of number field algorithms to this value. This is based on

**Proposition 18.2.2**  $\log |\Delta|$  is polynomial in the input length  $O(n \cdot \log_2(\max |c_j|))$  if  $F$  is given by a monic and irreducible polynomial  $f(X) = \sum c_j X^j$ .

This allows us to use  $\Delta$  as a complexity measure which is independent of the representation used for  $F$ . We will always express the running time of number theoretic algorithms in terms of  $|\Delta|$ . Such an algorithm has polynomial time complexity, if its time complexity is polynomial in  $\log |\Delta|$ .

#### 18.2.4

##### The Class Number

The fundamental theorem of arithmetics states that factorizations of natural numbers  $n = p_1 \cdots p_k$  into prime numbers are unique. This theorem is no longer true for integral elements of number fields, an easy counterexample being  $21 = 3 \cdot 7 = (1 + 2\sqrt{-5}) \cdot (1 - 2\sqrt{-5})$  in the maximal order  $\mathcal{O}$  of  $\mathbb{Q}(\sqrt{-5}) = \{a + b\sqrt{-5} \mid a, b \in \mathbb{Q}\}$ . We pass from algebraic numbers to ideals to eliminate this problem, an ideal  $\mathfrak{a}$  being a subgroup of  $\mathcal{O}$  with the additional property  $ra \in \mathfrak{a}$  for all  $r \in \mathcal{O}$  and  $a \in \mathfrak{a}$ . Arithmetic operations on ideals are

$$\mathfrak{a} + \mathfrak{b} = \{a + b \mid a \in \mathfrak{a}, b \in \mathfrak{b}\} , \quad \mathfrak{a} \cdot \mathfrak{b} = \{\sum a_i b_i \mid a_i \in \mathfrak{a}, b_i \in \mathfrak{b}\} .$$

The ideals of  $\mathcal{O}$  form a commutative monoid<sup>1</sup>, denoted by  $\mathcal{I}$ . Introduction of denominators gives a commutative group

$$\mathcal{J} = \left\{ \frac{1}{d} \mathfrak{a} \mid \mathfrak{a} \in \mathcal{I}, d \in \mathbb{N} \right\}$$

with respect to multiplication. Algebraic numbers  $a \in F$  are transformed to ideals via  $\mathfrak{a} = (a) = a\mathcal{O} = \{ar \mid r \in \mathcal{O}\}$ . These ideals are called principal, and form a subgroup  $\mathcal{P} \subseteq \mathcal{J}$ . Note that multiplication of ideals is a generalization of ordinary multiplication:  $(\alpha) \cdot (\beta) = (\alpha\beta)$ . The division relation  $\alpha|\beta \Leftrightarrow \beta = \alpha \cdot \gamma$  in  $\mathcal{O}$  reads  $\mathfrak{a}|\mathfrak{b} \Leftrightarrow \mathfrak{a} \supseteq \mathfrak{b}$  if we pass to ideals. The fundamental theorem is now valid for ideals in number fields, i.e.  $\mathfrak{a} \in \mathcal{I}$  admits a unique decomposition  $\mathfrak{a} = \mathfrak{p}_1 \cdots \mathfrak{p}_k$  into prime ideals, an ideal being prime if  $\mathfrak{p}|\mathfrak{ab}$  implies  $\mathfrak{p}|\mathfrak{a}$  or  $\mathfrak{p}|\mathfrak{b}$ . The loss of unique factorization in  $\mathcal{O}$  is therefore compensated by the growth of  $\mathcal{J}$  with respect to  $\mathcal{P}$ . The factor group  $\text{Cl} = \mathcal{J}/\mathcal{P}$  is called the class group of  $F$ . One of the most important results of algebraic number theory is

**Proposition 18.2.3** *The class group of a number field is always finite.*

Its order  $h = |\text{Cl}|$  is called the class number of  $F$ . It measures the loss of unique prime factorization in  $\mathcal{O}$ : class number  $h = 1$  is equivalent to  $\mathcal{J} = \mathcal{P}$ , i.e. unique factorization of numbers as in  $\mathbb{Z}$ , while  $h > 1$  implies multiple factorizations of numbers and, simultaneously, the existence of ideals which are not principal. Given any fractional ideal  $\mathfrak{a}$ , its  $h$ -th power is always principal. Proposition 18.2.3 states that if loss of unique factorization happens in a number field, this loss is bound by a finite degree.

<sup>1</sup>) The zero ideal  $(0) = \{0\}$  is always excluded from the sets  $\mathcal{I}, \mathcal{J}, \mathcal{P}, \text{Cl}$ .

## 18.2.5

**The Regulator**

Principal ideals may be viewed as elements of  $F$  modulo units. The kernel of the surjective homomorphism  $F^\times \rightarrow \mathcal{P}$ ,  $\alpha \mapsto (\alpha)$  is precisely the unit group  $\mathcal{O}^\times = \{\alpha \in \mathcal{O} \setminus \{0\} \mid \alpha^{-1} \in \mathcal{O}\}$  of  $\mathcal{O}$ , therefore  $\mathcal{P} \cong F^\times / \mathcal{O}^\times$ . The structure of  $\mathcal{O}^\times$  is given by the well known unit theorem of Dirichlet:  $\mathcal{O}^\times = \mu(F) \times \langle \epsilon_1, \dots, \epsilon_{r+s-1} \rangle$ ,  $\mu(F)$  being the (finite and cyclic) group of roots of unity in  $F$  and  $\epsilon_1, \dots, \epsilon_{r+s-1}$  being a so called set of fundamental units. This is equivalent to say that  $L(\mathcal{O}^\times)$  is a lattice of rank  $r+s-1$  in logarithmic Minkowski-space. Therefore the structure of  $\mathcal{O}^\times$  is  $\mathbb{Z}/m\mathbb{Z} \times \mathbb{Z}^{r+s-1}$ , it depends only on the signature and the roots of unity lying in  $F$ . Unfortunately we cannot compute the generators  $\epsilon_1, \dots, \epsilon_{r+s-1}$ , for it is even impossible to write them down using a polynomial amount of memory. Already in the real quadratic case  $F = \mathbb{Q}(\sqrt{d})$  with  $d > 0$  and  $(r, s) = (2, 0)$ , the logarithm  $\mathfrak{R} = \log |\epsilon|$  of a fundamental unit is known to grow like  $\sqrt{\Delta}$ . So we try to compute the quantity  $\mathfrak{R}$  instead. Its generalization is  $\mathfrak{R} = |\det(U')|$ ,  $U'$  resulting from the conjugate matrix

$$U = \begin{pmatrix} \log |\epsilon_1|_1 & \log |\epsilon_2|_1 & \cdots & \log |\epsilon_{r+s-1}|_1 \\ \log |\epsilon_1|_2 & \log |\epsilon_2|_2 & \cdots & \log |\epsilon_{r+s-1}|_2 \\ \vdots & \vdots & \ddots & \vdots \\ \log |\epsilon_1|_{r+s} & \log |\epsilon_2|_{r+s} & \cdots & \log |\epsilon_{r+s-1}|_{r+s} \end{pmatrix}$$

by deleting one row.

**Definition 18.2.4** The value  $\mathfrak{R} \in \mathbb{R}$  is independent of the deleted row and the choice of generators  $\epsilon_j$ , it is called the regulator of  $F$ .

Note that  $\mathfrak{R}$  is not the volume of the unit lattice of  $F$  (which is always zero since it does not have full rank). We will see that  $\mathfrak{R}$  is the volume of the image of a so called distance function, which is a modification of the logarithmic map.

## 18.2.6

**Complexity Results**

The first step in defining an algorithm to compute  $h$  and  $\mathfrak{R}$  is to show that these numbers cannot become too large:

**Proposition 18.2.5** *Let  $F$  be any number field of discriminant  $\Delta$  and signature  $(r, s)$ . Then*

$$h \leq d \cdot \frac{(n-1 + \log(d))^{n-1}}{(n-1)!}, \quad h \cdot \mathfrak{R} \leq d \cdot \frac{(\log(d))^{r+s-1} \cdot (n-1 + \log(d))^s}{(n-1)!},$$

$$\mathfrak{R} > c$$

where  $d = (2/\pi)^s \cdot \sqrt{|\Delta|}$  and  $c > 0$  is a universal constant independent of  $F$ .

This implies that we can write down  $h$  and a suitable approximation of  $\mathfrak{R}$  using a polynomial amount of space if  $n$  is fixed. There are still no classical polynomial algorithms to do this, the best known algorithm (Buchmann & McCurly 1990) admits subexponential complexity. Already in the most simple case of an imaginary quadratic field we have

**Proposition 18.2.6** *There is a probabilistic polynomial reduction from computation of  $h$  to  $\mathbb{Z}$ -factorization.*

This was proved by Shanks in 1972 and states that any polynomial algorithm computing the class number of imaginary quadratic fields could be used to efficiently factor rational integers, therefore computation of class numbers is at least as difficult as factorization in  $\mathbb{Z}$ .

## 18.3

### Reduction

#### 18.3.1

#### Reduced Ideals

The concept of reduction was invented by Gauß in his work on quadratic forms. There are several ways to characterize reduced ideals. We use a geometric approach using the lattice structure of ideals in Minkowski-space:

**Definition 18.3.1** Let  $\mathfrak{a}$  be a fractional ideal. An element  $\mu \in \mathfrak{a}$  is called a minimum of  $\mathfrak{a}$ , if there is no  $\alpha \in \mathfrak{a} \setminus \{0\}$  with  $\forall j : |\alpha|_j < |\mu|_j$ . The set of minima of  $\mathfrak{a}$  is denoted by  $\text{MIN}(\mathfrak{a})$ .

This definition is equivalent to the condition  $Q(\mu) \cap \mathfrak{a} = \{0\}$ ,  $Q(\mu) = \{\alpha \in \mathbb{R}^n \mid |\alpha|_j < |\mu|_j\}$  in Minkowski-space.

Let  $\mathfrak{a} \in \mathcal{J}$  be arbitrary and  $\mu \in \mathfrak{a}$  any element whose point in Minkowski-space is a shortest nonzero vector of the lattice  $\mathfrak{a}$ , then  $\mu$  is a minimum of  $\mathfrak{a}$ . The lattice of  $\mathfrak{a}$  is a discrete subgroup of  $\mathbb{R}^n$ , so we always have shortest vectors, and every ideal admits at least one minimum. The unit group  $\mathcal{O}^\times$  operates on the set of minima of any ideal by multiplication, therefore we have (with the exception of imaginary quadratic fields) infinitely many minima in each ideal. However the number of orbits in  $\text{MIN}(\mathfrak{a})$  under the operation of  $\mathcal{O}^\times$  is always finite (see [1]). This enables us to select representatives in each ideal class:

**Definition 18.3.2** A fractional ideal  $\mathfrak{a}$  is called reduced, if  $1 \in \text{MIN}(\mathfrak{a})$ . The set of reduced ideals is denoted by  $\mathbf{R}$ .

We obtain a reduced ideal from any ideal  $\mathfrak{a}$  by moving one of its minima to the position of 1, i.e. by multiplying  $\mathfrak{a}$  with  $\mu^{-1}$ ,  $\mu$  being any minimum of  $\mathfrak{a}$ . We call this operation reduction of  $\mathfrak{a}$ . For each ideal  $\mathfrak{a}$  reduction is a one-to-one

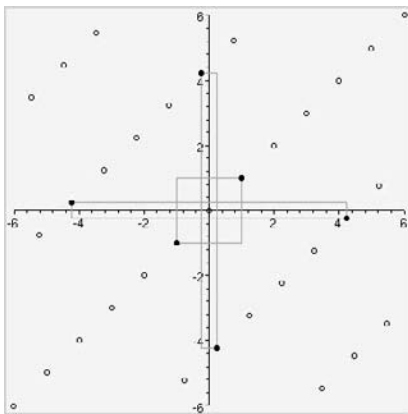


Fig. 18.2 Some minima of an ideal in Minkowski-space.

mapping

$$\text{MIN}(\mathfrak{a}) / \mathcal{O}^\times \leftrightarrow \{\text{reduced ideals equivalent to } \mathfrak{a}\} , \quad \mu \mapsto \mu^{-1}\mathfrak{a}$$

proving

**Proposition 18.3.3** *Each ideal class  $\bar{\mathfrak{a}} \in \text{Cl}$  contains only finitely many reduced ideals, but at least one.*

We can efficiently represent ideal classes by using reduced representatives, and applying reduction after arithmetical operations. However, we are faced with the problem of deciding whether two classes  $\bar{\mathfrak{a}}, \bar{\mathfrak{b}} \in \text{Cl}$  given by a reduced ideals  $\mathfrak{a}, \mathfrak{b}$  are equal. This amounts to the decision if  $\mathfrak{a}^{-1}\mathfrak{b}$  is a principal ideal. With exception of imaginary quadratic fields there is still no efficient algorithm to decide principality because the number of reduced ideals in a ideal class grows like  $\sqrt{\Delta}$ , and is therefore exponential. We cannot compute all reduced ideals in a class.

### 18.3.2

#### Infrastructure

The set of reduced ideals of a number field admits a canonical graph structure, first noted by Shanks in 1968, called the infrastructure of  $F$ . We impose such a structure on the set of minima of an ideal:

**Definition 18.3.4** Let  $\mathfrak{a}$  be a fractional ideal.  $\mu, \nu \in \text{MIN}(\mathfrak{a})$  are called neighbors, if there is no  $\alpha \neq 0$  in  $\mathfrak{a}$  with  $|\alpha|_j < \max(|\mu|_j, |\nu|_j)$  for all  $j$ .

Again this definition is equivalent to a geometric condition  $Q(\mu, \nu) \cap \mathfrak{a} = \{0\}$ ,  $Q(\mu, \nu) = \{\alpha \in \mathbb{R}^n \mid |\alpha_j| < \max(|\mu|_j, |\nu|_j)\}$  in Minkowski-space.

**Definition 18.3.5** Reduced ideals  $\mathfrak{a}, \mathfrak{b}$  are called neighbors, if  $\mathfrak{a} = \mu^{-1}\mathfrak{b}$  with  $\mu$  being a minimum of  $\mathfrak{b}$  which is a neighbor of  $1 \in \text{MIN}(\mathfrak{b})$ .

The infrastructure of a number field  $F$  is the finite graph  $\mathbf{G} = \mathbf{G}(F)$ , its vertices being the reduced ideals of  $F$ . The edges are defined by 18.3.5. The central property of this graph is

**Proposition 18.3.6** *Let  $\mathbf{G}$  be the infrastructure of any number field  $F$ . The number of connected components of  $\mathbf{G}$  is precisely the class number of  $F$ .*

It is clear that ideals of distinct ideal classes cannot share an edge, but it is quite difficult to show that there is always a path between ideals of the same ideal class. We refer to [1] for the details.

### 18.3.3

#### Geometric Interpretation of $\mathbf{G}$

**Definition 18.3.7** The distance function of  $F$  is given by  $\delta : F^\times \longrightarrow H$ ,  $\delta(\alpha) = P(L(\alpha))$ ,  $L$  being the logarithmic embedding of  $F$  into  $\mathbb{R}^{r+s}$  and  $P$  the orthogonal projection onto the hyperplane  $H = \{x \in \mathbb{R}^{r+s} \mid x_1 + \dots + x_n = 0\}$ .

The distance function is a homomorphism, but neither surjective nor injective. Its kernel is the set  $\{\alpha \in F^\times \mid |\alpha|_1 = |\alpha|_2 = \dots = |\alpha|_n\}$ . Passing from algebraic numbers to principal ideals we obtain a function  $\delta : \mathcal{P} \longrightarrow H/\Gamma$ ,  $\Gamma$  being the image of the unit group  $\mathcal{O}^\times$  in logarithmic Minkowski-space.  $\Gamma$  is a lattice of rank  $r+s-1$  by the unit theorem, which admits full rank in the hyperplane  $H$  (note that  $\delta(\epsilon) = L(\epsilon) \in H$  for any unit  $\epsilon \in \mathcal{O}^\times$ ). Therefore  $T = H/\Gamma$  is a compact  $n$ -dimensional torus. The connected component of principal ideals is mapped to  $T$  by the distance function. Now we are able to relate the regulator  $\mathfrak{R}$  of  $F$  to the infrastructure of  $F$ :

**Proposition 18.3.8**  $\mathfrak{R}$  is the surface volume of  $T$ .

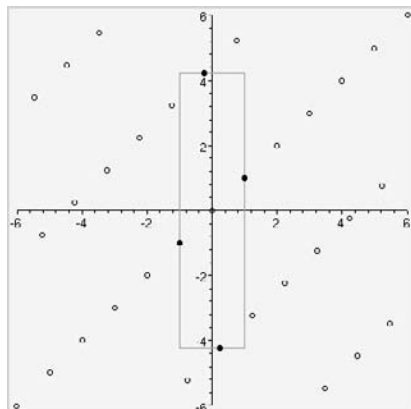


**Fig. 18.3** Neighbors of an ideal in a quadratic number field.

This is straightforward from the definition of  $\mathfrak{R}$  and  $T$ . Note that this geometric interpretation imposes an antiproportional connection between  $h$  and  $\mathfrak{R}$ , which we will make precise in Sect. 18.4: Since there is only a finite number of reduced ideals (which are the vertices of  $\mathbf{G}$ ), a large class number forces these ideals to be distributed between many tori corresponding to the connected components of  $\mathbf{G}$ , so these tori cannot be too large (i.e. their surface volume is small). The geometric interpretation of  $\mathbf{G}$  is also used to derive an algorithm which computes a reduced ideal admitting a given distance vector, i.e. a point on  $T$ . This is the central ingredient used to define the quantum algorithms in Sect. 18.6:

**Proposition 18.3.9** *There is a polynomial classical algorithm which, given any  $x \in T$ , computes a reduced principal ideal  $\mathfrak{a}$  close to  $x$ , i.e.  $\|\delta(\mathfrak{a}) - x\| < p(\log |\Delta|)$ ,  $p$  being a fixed polynomial depending only on  $(r, s)$ .*

This is one of the results of [11]. A simplified proof for totally real number fields using the geometric interpretation to enhance the navigation in the graph  $\mathbf{G}$  is given in [6]. We refer to this work for the details.

We conclude this section with some examples: Let  $F = \mathbb{Q}(\sqrt{d})$ ,  $d < 0$ , be an imaginary quadratic field. The two embeddings of  $F$  into  $\mathbb{C}$  are  $\sigma_1 = \text{id}$  and  $\sigma_2 = \bar{\sigma}_1$  which maps  $\alpha$  to  $\bar{\alpha}$ , and the only absolute value  $|\cdot|_1$  defined by the equality  $|\alpha| = |\bar{\alpha}|$ . Definition 18.3.1 now consists of just one inequality  $|\alpha| < |\mu|$ , so all minima in  $\text{MIN}(\mathfrak{a})$  must share the same absolute value. Definition 18.3.2 implies that  $\text{MIN}(\mathfrak{a})$  is the (finite) set of roots of unity lying in  $F$  if  $\mathfrak{a}$  is reduced. But the reduction map  $\mu \mapsto \mu^{-1}\mathfrak{a}$  does not depend on units or roots of unity, which proves

**Proposition 18.3.10** *Let  $F$  be imaginary quadratic. There is exactly one reduced ideal in each ideal class, and the number of reduced ideals equals  $h$ . Each ideal class corresponds to one vertex of the graph  $\mathbf{G}$ , i.e. the tori  $T = \{0\}$  are trivial.*

So calculating the class number of imaginary quadratic fields amounts to counting reduced ideals, and the graph  $\mathbf{G}$  consists of  $h$  isolated vertices. Due to the absence of fundamental units and no surface on  $T$ ,  $\mathfrak{R}$  is defined to be 1 in this case.

The situation is somewhat different for  $F = \mathbb{Q}(\sqrt{d})$ ,  $d > 0$ . The embeddings of  $F$  into  $\mathbb{C}$  are given by  $\sigma_1 = \text{id}$  and  $\sigma_2(a + b\sqrt{d}) = a - b\sqrt{d}$  (which is also called conjugation), which define different absolute values  $|\alpha|_1 = |\alpha|$  and  $|\alpha|_2 = |\sigma_2(\alpha)|$ . By the unit theorem  $\mathcal{O}^\times \cong \{\pm 1\} \times \mathbb{Z}$  is infinite, so ideals contain infinitely many minima. Reduced ideals are mapped to  $T$  by  $\delta$ , but in this case  $H \cong \mathbb{R}^1$  and  $\Gamma = L(\{\pm 1\} \times \{e^k \mid k \in \mathbb{Z}\}) = \mathfrak{R}\mathbb{Z}$  is a lattice of rank one, so  $T = H/\Gamma$  is a circle of circumference  $\mathfrak{R}$ , forcing the principal component of  $\mathbf{G}$  to be cyclic. In this case  $\delta(\alpha)$  is the actual distance of vectors from  $\alpha$  to 1 in logarithmic Minkowski-space, hence the name distance function.

Consider number fields of signatures  $(1, 1)$  and  $(0, 2)$ . The distance function maps the principal component of  $\mathbf{G}$  into a  $(r + s - 1)$ -dimensional torus, but  $r + s - 1 = 1$ . Thus infrastructures of such number fields behave exactly like those of real quadratic fields: the reduced ideals admit a cyclic ordering, which is mapped by  $\delta$  to circles of circumference  $\mathfrak{R}$ .

## 18.4

### Results from Analytic Number Theory

#### 18.4.1

#### Distribution of Prime Numbers

One of the most prominent results of analytic number theory is the prime number theorem, which reveals the asymptotic distribution of prime numbers among natural numbers:

**Proposition 18.4.1** (Prime number theorem) *Let  $\pi(x) = |\{p \leq x \text{ prime}\}|$  be the number of natural prime numbers not greater than  $x$ . Then*

$$\lim_{x \rightarrow \infty} \frac{\pi(x)}{x \cdot \log(x)^{-1}} = 1.$$

So if we want to find a large prime number (say  $\geq n$ ) by checking the values  $n, n + 1, n + 2, \dots$ , the number of checks should be approximately  $\log(n)$  for large  $n$ . But the prime number theorem does not tell us how large  $n$  should be for the limit to be effective. Riemann noted first that this question of convergence is related to the behavior of the Riemann  $\zeta$ -function

$$\zeta(s) = \sum_{k=1}^{\infty} \frac{1}{k^s}.$$

Explicitly, if and only if the zeros of  $\zeta(s)$  obey a certain rule, the limit in 18.4.1 converges fast enough for computational purposes. Today it is known that  $\zeta(s)$  provides even more information, it somehow encodes the arithmetic data of the field  $\mathbb{Q}$ , a concept which generalizes to arbitrary number fields:

**Definition 18.4.2** The Dedekind  $\zeta$ -function of a number field  $F$  is given by

$$\zeta_F(s) = \sum_{\mathfrak{a} \trianglelefteq \mathcal{O}} \mathcal{N}(\mathfrak{a})^{-s},$$

the sum taken over all integral ideals of  $F$ .

Since  $\mathbb{Q}$  has class number one (there is a bijection from  $\mathbb{N}$  to the set of ideals of  $\mathbb{Z}$  given by  $n \mapsto n\mathbb{Z} = \{0, \pm n, \pm 2n, \pm 3n, \dots\}$ ) the function  $\zeta_{\mathbb{Q}}(s) = \zeta(s)$  is the usual Riemann  $\zeta$ -function. The function  $\zeta_F(s)$  converges if  $\text{Re}(s) > 1$ . There is a meromorphic continuation to the plane  $\mathbb{C}$  admitting a pole of order

1 at  $s = 1$ . The well known Riemann Hypothesis claims that zeros  $\varrho$  of  $\zeta_{\mathbb{Q}}(s)$  in the critical strip  $\operatorname{Re}(\varrho) \in [0, 1]$  of this continuation are located on the line  $\operatorname{Re}(\varrho) = \frac{1}{2}$ . This can be generalized to

**Definition 18.4.3** The Generalized Riemann Hypothesis (GRH) states: For all number fields  $F$ , all zeros of  $\zeta_F(s)$  which lie in the strip  $0 \leq \operatorname{Re}(s) \leq 1$  are actually located on the abscissa  $\operatorname{Re}(s) = \frac{1}{2}$ .

This hypothesis is still unproved. It is deeply related to the distribution of prime ideals in the integral ring  $\mathcal{O}$  of  $F$  by the Euler product formula

$$\zeta_F(s) = \prod_{\mathfrak{p} \trianglelefteq \mathcal{O} \text{ prime}} \frac{1}{1 - \mathcal{N}(\mathfrak{p})^{-s}}$$

which specializes to the original product formula

$$\zeta(s) = \zeta_{\mathbb{Q}}(s) = \prod_{p \in \mathbb{N} \text{ prime}} \frac{1}{1 - p^{-s}}$$

for the Riemann  $\zeta$ -function. The original Riemann Hypothesis implies that the asymptotic statement of the prime number theorem is sufficiently well attained for small (i.e. polynomial)  $x$ . For number fields, GRH implies such a bound for the distribution of prime ideals among integral ideals. This distribution is used frequently in algorithmic number theory, requiring most algorithms which compute class numbers and regulators to assume GRH. One of the applications of GRH in this area is

**Proposition 18.4.4** *If GRH is true, then for any number field  $F$  the set*

$$\left\{ \mathfrak{p} \trianglelefteq \mathcal{O} \text{ prime} \mid \mathcal{N}(\mathfrak{p}) \leq 12(\log |\Delta|)^2 \right\}$$

*generates the class group of  $F$ .*

Note that this set can be calculated easily by first computing all natural prime numbers  $p \leq 12(\log |\Delta|)^2$  and computing all prime ideals which satisfy  $\mathfrak{p} \cap \mathbb{Z} = p\mathbb{Z}$ . Important algorithmic results, for example Buchmanns subexponential method [2], Millers deterministic prime number test and Thiel's complexity results (see [4] and [12]), assume the truth of 18.4.3 for this reason. However, GRH and its weaker predecessor, the Riemann Hypothesis, resisted all efforts of verification (of falsification). It has been proved that infinitely many zeros lie on  $\operatorname{Re}(s) = \frac{1}{2}$ , that at least a third of all zeros lie on  $\operatorname{Re}(s) = \frac{1}{2}$ , and all zeros which have been computed numerically (up to a billion by now) lie on  $\operatorname{Re}(s) = \frac{1}{2}$ . Unfortunately none of these results prove the hypothesis.

## 18.4.2

### Class Number Formulas

Modern algorithms for the computation of  $h$  and  $\mathfrak{R}$  are known to compute both values at once, and there is no gain in running time if we want just one

of those values. The reason for this is a deep connection between the class number and the regulator, which was exposed geometrically in Sect. 18.3. The exact relationship is given by the class number formula. One of the marvels of  $\zeta$ -functions is the fact that most values attached to  $F$ , which are by definition of a pure algebraic nature, can be retrieved analytically by looking at  $\zeta(s)$  in the right way. The following formula shows for example that  $h \cdot \mathfrak{R}$  is determined by the behavior of  $\zeta_F$  near its pole at  $s = 1$ :

**Proposition 18.4.5** (Analytic class number formula) *Let  $F$  be a number field of discriminant  $\Delta$ , class number  $h$ , Regulator  $\mathfrak{R}$  and  $\zeta$ -function  $\zeta_F(s)$ . Let  $m$  be the number of roots of unity lying in  $F$ , then*

$$h \cdot \mathfrak{R} \cdot g = \text{res}_{s=1}(\zeta_F), \quad g = \frac{2^r \cdot (2\pi)^s}{m \cdot \sqrt{|\Delta|}}.$$

This is equivalent to the Laurent-expansion of  $\zeta_F$  at  $s = 1$  being

$$\zeta_F(s) = \frac{h \cdot \mathfrak{R} \cdot g}{s - 1} + \sum_{k=0}^{\infty} a_k (s - 1)^k.$$

The (additive) series defining  $\zeta_F(s)$  converges too slow for any computational purpose, so we use a modification of the Euler product to extract an approximation of  $\text{res}(\zeta_F)$ . Again, the convergence of the product is connected to the truth of GRH:

**Proposition 18.4.6** *Let  $r$  be the real number*

$$r = g^{-1} \cdot \prod_{p \leq x \text{ prime}} (1 - p^{-1}) \prod_{\mathfrak{p} \cap \mathbb{Z} = p\mathbb{Z}} \left(1 - p^{-f(\mathfrak{p})}\right)^{-1}$$

for some  $x > 0$ . There is a constant  $c$  (independent of  $F$ ), such that  $2^{-\frac{1}{2}} \leq \frac{h \cdot \mathfrak{R}}{r} \leq 2^{\frac{1}{2}}$  if  $x \geq c \cdot \sqrt{|\Delta|}$ . If GRH is true,  $x \geq c \cdot (\log |\Delta|)^2$  is sufficient.

The value  $f(\mathfrak{p})$  is called inertia degree of the prime ideal  $\mathfrak{p}$ , and is a natural number  $\leq \deg(F)$  which describes the relation of the prime ideal  $\mathfrak{p} \trianglelefteq \mathcal{O}$  to the prime number  $p \in \mathbb{N}$ . It is defined by  $\mathcal{N}(\mathfrak{p}) = p^f$  (norms of prime ideals are always powers of a single prime number). This enables us to check class numbers and regulators classically (see [12] for details), a fact used intrinsically in all quantum algorithms on number fields, which are by nature probabilistic.

## 18.5

### Examples of Minima Distributions

We give some examples of number fields which are simple enough to effectively calculate their invariants:

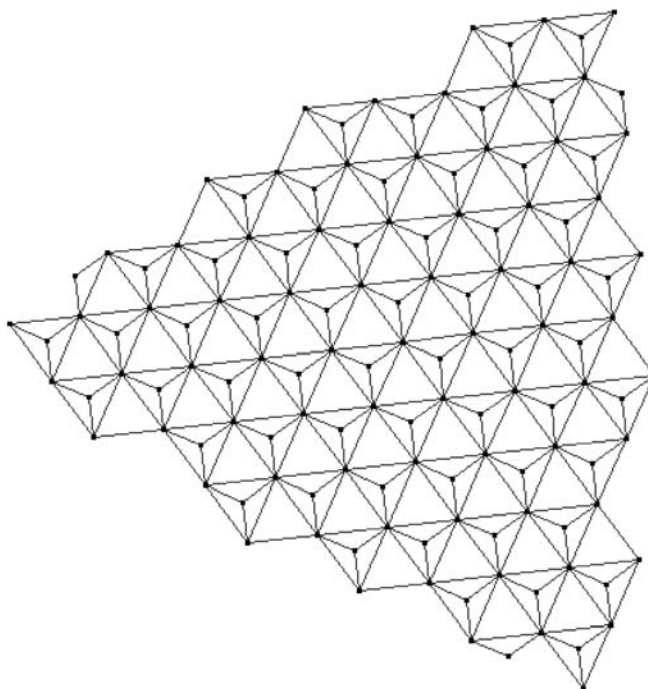


**Fig. 18.4** Part of the lattice  $L(\mathcal{O}^\times)$  (black), minima and neighbor edges of the number field  $K^+$ .

**Example 18.5.1**  $K = \mathbb{Q}(\zeta_9)$  with  $\zeta_9 = \exp\left(\frac{2\pi i}{9}\right)$  is the so called cyclotomic field of order 9 and degree 6. Its real subfield  $K^+ = K \cap \mathbb{R}$  is a number field of degree 3 and signature  $(r, s) = (3, 0)$ . Its unit lattice  $L(\mathcal{O}^\times)$  has rank two. The class number of  $K^+$  is one (all ideals are principal). There are two reduced ideals:  $(1) = \mathcal{O}$  and  $\mu^{-1}\mathcal{O}$  for any  $\mu \in \text{MIN}(\mathcal{O})$  which is not a unit.  $K^+$  is a Galois extension of  $\mathbb{Q}$  with Galois group  $G(K^+/\mathbb{Q}) = \{\text{id}, \sigma, \sigma^2\} \cong \mathbb{Z}/3\mathbb{Z}$ . The automorphism  $\sigma$  induces a rotation by  $\frac{2}{3}\pi$  on  $L(\mathcal{O}^\times)$ , hence the hexagonal symmetry. Note that vertices can have more than three neighbors.

**Example 18.5.2** Let  $L = \mathbb{Q}(\varrho)$  be generated by a root of  $f(x) = x^3 + 7x^2 - x - 1$ . It is also a number field of degree 3 and signature  $(r, s) = (3, 0)$ . It is not a Galois extension of  $\mathbb{Q}$ , so  $L(\mathcal{O}^\times)$  has no symmetries except reflection at the origin. This symmetry applies to units only, its minima are scattered freely inside the fundamental epipede, but are of course affected by unit translations.

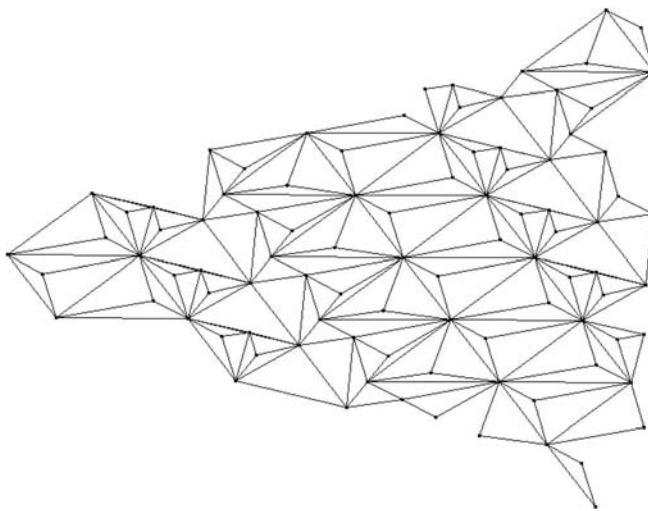


**Fig. 18.5** Part of the lattice  $L(\mathcal{O}^\times)$  and minima of the number field  $L$ .

## 18.6

### Computing the Regulator

#### 18.6.1

##### Real Quadratic Case

We use the model of a quantum computer having two registers, basic measurement and the quantum fourier transform. We refer to [5] for the details on these standard techniques. Let  $F = \mathbb{Q}(\sqrt{d}) = \{a + b\sqrt{d} \mid a, b \in \mathbb{Q}\}$ ,  $d > 0$ , be a real quadratic number field. There are just two embeddings of  $F$  into the real numbers given by the identity map  $\sigma_1 = \text{id}$  and the conjugation map  $\sigma_2 : a + b\sqrt{d} \mapsto a - b\sqrt{d}$ . The pair  $(\sigma_1, \sigma_2)$  maps  $F$  to a dense subset of  $\mathbb{R}^2$ . The integral ring of  $F$  is  $\mathcal{O} = \{a + b\omega \mid a, b \in \mathbb{Z}\}$ , generated by the elements 1 and  $\omega = \frac{1}{2}(d + \sqrt{d})$ . Since  $\{\pm 1\}$  are the only roots of unity in a subfield of  $\mathbb{R}$  and  $r + s - 1 = 1$ , the unit group is given by  $\mathcal{O}^\times = \{\pm 1\} \times \{\epsilon_1^k \mid k \in \mathbb{Z}\}$ . It is generated by a single fundamental unit  $\epsilon_1$ , which can be chosen to satisfy  $\epsilon_1 > 1$  ( $F \subset \mathbb{R}$  implies a canonical ordering of  $F$ ). Definition 18.2.4 now reads  $\mathfrak{R} = \ln |\epsilon_1|$ . The hyperplane  $H = \{x_1 + x_2 = 0\}$  is the diagonal line through the origin, the distance function  $\delta$  is

$$\begin{aligned} \delta(\alpha) &= P_H(L(\alpha)) = P_H \begin{pmatrix} \ln |\sigma_1(\alpha)| \\ \ln |\sigma_2(\alpha)| \end{pmatrix} = \begin{pmatrix} \ln |\sigma_1(\alpha)| \\ \ln |\sigma_2(\alpha)| \end{pmatrix} \\ &\quad - \frac{1}{2}(\ln |\sigma_1(\alpha)| + \ln |\sigma_2(\alpha)|) \begin{pmatrix} 1 \\ 1 \end{pmatrix}. \end{aligned}$$

By identification of  $(x, -x)^T \in H$  and the real number  $x$  we get a real valued function

$$\delta(\alpha) = \frac{1}{2} (\ln |\sigma_1(\alpha)| - \ln |\sigma_2(\alpha)|) = \frac{1}{2} \ln \left| \frac{\alpha}{\bar{\alpha}} \right|$$

where  $\bar{\alpha} = \sigma_2(\alpha)$  denotes the (real quadratic) conjugation in  $F$  (this operation does change the absolute value of a real quadratic number, in contrast to complex conjugation). The inverse function is

$$f : \mathbb{R} \rightarrow \mathbb{R}^1 \times \mathbb{R} , \quad x \mapsto (\alpha(x), \delta(\alpha(x)) - x) ,$$

mapping a real number to the optimal ideal near  $x$  and the distance error  $\delta - x$ . Its period is precisely  $\mathfrak{R}$ , since  $(\alpha) = (\beta)$  is equivalent to  $\alpha^{-1}\beta \in \mathcal{O}^\times$  and  $\delta(\mathcal{O}^\times) = L(\mathcal{O}^\times) = l(\{e^k \mid k \in \mathbb{Z}\}) = \mathfrak{R}\mathbb{Z}$ . The second component ensures injectivity inside a period interval.

### 18.6.2

#### Hallgren's Algorithm

We adopt Hallgren's formalism to describe the periodicity condition used in the quantum algorithm:

**Definition 18.6.1** A function  $\hat{f} : \mathbb{Z} \rightarrow M$  into an arbitrary set  $M$  is called weakly periodic with respect to  $D$  and period  $S$ , if there is a polynomial  $P(x)$  such that the set

$$K = \left\{ k = 0, 1, \dots, \lfloor S \rfloor \mid \forall j \in \mathbb{N}_0 : f(k + \lfloor jS \rfloor) = f(k) \text{ or } f(k + \lceil jS \rceil) = f(k) \right\}$$

contains at least  $(\lfloor S \rfloor + 1) \cdot (1 - \frac{1}{P(D)})$  elements.

This definition states that  $\hat{f}$  is periodic with period  $S$  up to a sufficiently small fraction of  $k$ 's. Hallgren showed that such a period, despite being irrational and defined on the infinite continuum  $\mathbb{R}$ , can be found by a polynomial quantum algorithm. He proposes an approximation of  $f$  by  $\tilde{f}(j) = f(\frac{j}{N})$ ,  $j \in \mathbb{Z}$ , for a sufficiently large  $N \in \mathbb{N}$ :

**Proposition 18.6.2** *If we choose  $N \geq n\sqrt{d}$ , the approximation function  $\tilde{f}$  is weakly periodic with respect to  $\ln |\Delta|$  and period  $S = N \cdot \mathfrak{R}$ .*

The key idea of Hallgren's quantum algorithm is the computation of an irrational value, which is given by a weakly periodic function. We shortly describe his quantum algorithm first published in [7], which needs two registers, measurements on single registers and the quantum fourier transform

$$\text{QFT}_q \sum_{j=0}^{q-1} a_j |j\rangle = \sum_{k=0}^{q-1} e^{\frac{2\pi i k j}{q}} |k\rangle .$$

First we initialize the system to

$$\psi_0 = \sum_{j=0}^{q-1} |j\rangle |\tilde{f}(j)\rangle$$

and perform a measurement of the second register, discarding the measured value, giving

$$\psi_1 = \sum_{i=0}^{p-1} |k + \lfloor iS \rfloor\rangle.$$

Application of the quantum fourier transform leaves the system in the state

$$\psi_2 = \text{QFT}_p \psi_1 = \sum_{j=0}^{p-1} \alpha_j |j\rangle, \quad \alpha_j = \frac{1}{pq} \sum_{i=0}^{p-1} \omega_q^{j \lfloor iS \rfloor}.$$

We have

$$\left| \frac{1}{pq} \sum_{i=0}^{p-1} \omega_q^{j \lfloor iS \rfloor} \right|^2 \geq \frac{1}{pq} c p^2 \geq \frac{c}{S}$$

(this is claim 3.2 of [7]) with a constant  $c > 0$  independent of the number field or the register size. Since  $\alpha_j$  does not depend on  $j$ , we have obtained a equidistributed state. The number of  $j$  satisfying

$$(*) \quad j = \left\lfloor k \frac{q}{S} \right\rfloor, \quad 0 \leq k \leq S, \quad j < \frac{q}{\log(S)}$$

is at least  $\lfloor S / \log(S) \rfloor$ , so we measure  $|j\rangle$  satisfying  $(*)$  with probability at least  $\frac{c}{\log(S)}$ . Since  $\log(S) \leq \log(N\mathfrak{R})$  we get (on average) such  $j$  after a polynomial number of iterations of these steps. We repeat the process until we obtain two such values

$$a = \left\lfloor k \frac{q}{S} \right\rfloor, \quad b = \left\lfloor k' \frac{q}{S} \right\rfloor$$

with  $\gcd(k, k') = 1$ . Note that there are sufficiently many pairs of such numbers by the prime number theorem (see [4]).

**Proposition 18.6.3** *For any  $d \in \mathbb{N}$  (squarefree) there is a quantum algorithm with running time bounded from above by a polynomial in  $P(\log(d), n)$  in  $\log(d)$  and  $n$  computing a rational number  $r$  with  $|\mathfrak{R} - r| < 10^{-n}$  with probability bounded from below by  $P(\log(d), n)^{-1}$ .*

### 18.6.3

#### Generalization of the Weak Periodicity Condition

Schmidt and Vollmer generalized Hallgren's algorithm in [9] to compute irrational period lattices of multidimensional functions. Let  $\|\vec{x}\|_\infty = \max |x_j|$  denote the maximum of the absolute component values.

**Definition 18.6.4** Let  $B(X)$  be a fixed polynomial and  $B = B_F = B(\log(\Delta))$  for any number field  $F$ . A function  $f : \mathbb{Z}^m \rightarrow S$  ( $S$  an arbitrary set) is called loosely periodic with period lattice  $L = \mathbb{R}\vec{v}_1 + \dots + \mathbb{R}\vec{v}_m \subset \mathbb{R}^m$  with respect to  $B$ , if at least one  $\vec{v} \in \mathbb{Z}^r$  with  $\|\vec{v}\|_\infty \leq B$  exists such that

1. There is a period  $\vec{p} \in L$  and an error vector  $\vec{d} \in \mathbb{R}^m$  with  $\vec{v} + \vec{p} + \vec{d} \in \mathbb{Z}^m$  and  $f(\vec{v}) = f(\vec{v} + \vec{p} + \vec{d})$ ,
2.  $\|\vec{d}\|_\infty < 2$ ,
3. any  $\vec{v}' \in \mathbb{Z}^m$  with  $f(\vec{v}) = f(\vec{v}')$  satisfies  $\vec{v} - \vec{v}' = \vec{p} + \vec{d}$  with  $\vec{p} \in L$  and  $\|\vec{d}\|_\infty < 2$ .

Schmidt and Vollmer prove

**Proposition 18.6.5** *For a fixed  $m$ , there is a quantum algorithm which computes for given  $f : \mathbb{Z}^m \rightarrow S$  loosely periodic with period lattice  $L \subset \mathbb{R}^m$  a set  $\{\vec{b}'_1, \dots, \vec{b}'_m\}$  of vectors. There is a constant probability  $P > 0$  depending only on  $m$ , such that there is basis  $\{\vec{b}_1, \dots, \vec{b}_m\}$  of  $L$  with  $\|\vec{b}'_j - \vec{b}_j\|_\infty < 1$  for  $j = 1 \dots m$ . The algorithm evaluates  $f$  on arguments of size bounded by  $O(\log(\det(L))/\lambda_1(L))$ , and uses  $O((\log(\det(L))/\lambda_1(L))^3)$  quantum steps.*

Again their algorithm does not depend on the number theoretic problem we want to solve. Before we describe this algorithm we briefly show how it is applied to compute the regulator of an arbitrary number field. We may assume  $\deg(F) \geq 2$ : the case  $(r, s) = (2, 0)$  is already solved and  $(r, s) = (0, 1)$  implies  $\mathfrak{R} = 1$  by definition of the regulator (as the determinant of an empty matrix). The distance function  $\delta$  maps  $F^\times$  to  $\mathbb{R}^{r+s-1}$ , and principal ideals of  $F$  to  $\mathbb{R}^{r+s-1}/L$  respectively with  $L = \delta(\mathcal{O}^\times)$  being the unit lattice of  $F$ . It is a lattice of full rank having determinant  $\mathfrak{R}$ . We define the loosely periodic function

$$\tilde{f} : \mathbb{Z}^m \longrightarrow \mathbf{R} \times \mathbb{R}_r, \quad v \longmapsto (\mu(v)^{-1}\mathcal{O}, \frac{1}{N}(\lceil N(v - \delta(\mu(v))) \rceil))$$

arising from the inversion  $f$  of the distance function (described in [6] in detail), where  $\lceil x \rceil$  is the vector  $(\lceil x_1 \rceil, \dots, \lceil x_m \rceil)$ . Note that the second component of  $f$  is actually an element of  $\frac{1}{N}\mathbb{Z}^m$ . This function is loosely periodic with period lattice  $N \cdot L$ ,  $L = \delta(\mathcal{O}^\times)$ , because  $\mu(x + v) = \mu(x) \cdot \epsilon$  for a unit  $\epsilon \in \mathcal{O}^\times$  (equivalent to  $\mu(x + v)^{-1}\mathcal{O} = \mu(x)\mathcal{O}$  for any  $v \in \delta(\mathcal{O}^\times)$ ). Errors due to approximation fulfill conditions (2) and (3) of Definition 18.6.4 (Proposition 3 [9] gives the technical details). The number of steps necessary to (classically) evaluate  $\tilde{f}$  is polynomial in  $\log |\Delta|$  and its input length by Proposition 18.3.9. Again, and in contrast to most classical algorithms, this result does not depend on the Generalized Riemann Hypothesis. We briefly describe the generalization of the algorithm of Hallgren used by Schmidt and Vollmer to prove Proposition 18.6.5. First choose  $q = 2^k \in \mathbb{N}$  such that  $q > \mathfrak{R}$

(there is a known upper bound for  $\mathfrak{R}$  which can be computed classically). The quantum computer used consists of  $m = r + s - 1$  registers of size  $2mq$  and a result register to store the values  $\tilde{f}(\vec{v})$ . It is initialized in the state

$$\psi_0 = \frac{1}{(q-1)^{r/2}} \sum_{v_1=0}^{q-2} \cdots \sum_{v_m=0}^{q-2} |v_1\rangle \cdots |v_m\rangle |\tilde{f}(\vec{v})\rangle.$$

The algorithm consists of a measurement of the last register and the application of the quantum fourier transform to the first  $m$  registers. The measurement gives a state

$$\psi_1 = \frac{1}{\sqrt{p}} \sum_{\vec{x} \in L'} |\vec{y} + \vec{x} + \vec{d}(\vec{x})\rangle |\tilde{f}(\vec{y})\rangle$$

with a random  $\vec{y}$  and an error vector  $\vec{d}$  depending on  $\vec{x}$ .  $L' \subset L$  satisfies  $\vec{y} + \vec{x} + \vec{d}(\vec{x}) \in \{\vec{v} \in \mathbb{R}^m \mid 0 \leq v_j \leq q-2\}$  for all  $\vec{x} \in L'$  and  $p = |L'| \approx \frac{q^m}{\mathfrak{R}}$ . Application of the quantum fourier transform to the first  $m$  registers gives

$$\psi_2 = \frac{1}{\sqrt{(2mq)^m p}} \sum_{z_1, \dots, z_r=0}^{2mq-1} e^{2\pi i \cdot \frac{(\vec{y} + \vec{x} + \vec{d}(\vec{x})) \cdot \vec{z}}{2mq}} \cdot |z_1\rangle \cdots |z_m\rangle |f(\vec{y})\rangle.$$

As in Hallgren's algorithm the translation invariance of fourier transforms allows us to assume  $\vec{y} = 0$  and  $\|\vec{x}\|_\infty < q$ . Some calculations show that with a fixed probability we measure  $\vec{z}$  on the first  $m$  registers such that  $\|\frac{1}{2mq}\vec{z} - \vec{x}^*\|_\infty \leq \frac{1}{4mq}$  for a vector  $\vec{x}^* \in L^*$ ,  $L^*$  being the dual lattice of  $L$ . Note that the concept of dual lattices was not needed in Hallgren's algorithm because the unit lattice is of rank 1 in the real quadratic case. There are classical techniques to compute a basis of  $L$  from a given basis of  $L^*$ , so it is enough to measure enough vectors  $\vec{z}$  close to the dual lattice  $L^*$ . We leave the numerous technical details (influence of the error  $\vec{d}(\vec{x})$ , propagation of this errors to the dual lattice, bounds for the probability of a correct measurement) to [9]. Finally note that it is easy to compute the determinant  $\mathfrak{R} = \det(L)$  once a basis of  $L$  is known.

## 18.7

### Computation of Other Invariants

#### 18.7.1

##### The Principal Ideal Problem

It is not difficult to compute other invariants of a number field once the regulator is at hand. We describe the concept for real quadratic fields (see [7]) for simplicity. First we are able to compute the distance of a principal ideal

$\mathfrak{a} = (\alpha)$  using a modification of the period finding algorithm. There is still no algorithm of polynomial complexity to do this classically. Given  $\mathfrak{a}$ , the operation  $(a, b) \mapsto \mu(a) \cdot \mathfrak{a}^b$  of  $\mathbb{Z} \times \mathbb{Z}$  on  $\mathfrak{a}$  reads  $(a, b) \mapsto a + bx \bmod \mathfrak{R}\mathbb{Z}$  on the circle  $T = \mathbb{R}/\mathfrak{R}\mathbb{Z}$ , where  $x \in T$  is the (unknown) distance of  $\mathfrak{a}$ . Since we can compute  $\mathfrak{R}$  it is straightforward to find a (weak) period  $(a_0, b_0)$  of this operation using a slight modification of the period finding algorithm of Hallgren, from which the value  $x$  can be computed. We refer to [7] for the technical details of this algorithm. This enables us to check if any ideal  $\mathfrak{a}$  is principal and compute a generator  $\alpha$  if it is: Given  $\mathfrak{a}$  we compute the value  $x$  as explained and use Proposition 18.3.9 to compute a principal ideal  $\mathfrak{b} = (\beta)$  with  $\delta(\mathfrak{b}) = x$ . Then  $\mathfrak{a}$  is principal if and only if  $\mathfrak{a} = \mathfrak{b} = (\beta)$ , which can be checked easily.

### 18.7.2

#### Computing the Class Number

The class number is defined to be the order of  $\text{Cl} = \mathcal{J}/\mathcal{P}$ , the class group of  $F$ . This group is finite and abelian. Note that Proposition 18.4.4 allows us to compute a generating system for  $\text{Cl}$  classically if GRH is true. If  $F$  is imaginary quadratic, classes  $\bar{\mathfrak{a}}$  contain exactly one reduced ideal, so computation in  $\text{Cl}$  can be done by multiplying and reducing ideals. Computation of  $h$  is now an instance of the hidden subgroup problem for finite abelian groups, a standard technique in quantum computing (see [5]). However we cannot transform this setting to an instance of known structure algorithms if  $F$  is not imaginary quadratic: there are several distinct reduced ideals in each ideal class in general, and there is no canonical way to select one as a representative. The tuplet of all reduced ideals would be a unique representative of a class, however the number of reduced ideals is exponential in  $\log |\Delta|$ , so we cannot write down such a tuplet. The solution is not to compute a tuplet, but the superposition of these ideals, and use such a superposition as a representative in a quantum algorithm. Thus given any ideal  $\mathfrak{a}$ , we wish to represent its ideal class  $\bar{\mathfrak{a}}$  by the state

$$(*) \quad \sum_{\substack{\mathfrak{b} \in \bar{\mathfrak{a}} \\ \text{reduced}}} |\mathfrak{b}\rangle.$$

We cannot compute  $\mathfrak{b} \in \bar{\mathfrak{a}}$  directly, so we apply the operation used in the distance computation algorithm to compute ideals  $\mu(x) \cdot \mathfrak{a}$  where  $x = \frac{j}{N}$  with  $j = 0 \dots r$  and  $N$  sufficiently large. We have already seen how to choose  $N$  for the errors resulting from this approximation to be small enough. Note that we need the regulator  $\mathfrak{R}$  to choose  $r = \lfloor N \cdot \mathfrak{R} \rfloor$ . Thus the points  $\frac{j}{N}$  are equidistributed on the circle  $T = \mathbb{R}/\mathfrak{R}\mathbb{Z}$ , and we can apply the same techniques as in the case of imaginary quadratic fields to compute the class

number by using the approximation

$$\sum_{j=0}^{r-1} |\mu(j/N) \cdot \mathfrak{a}\rangle$$

of  $(*)$  as a representative for the class  $\bar{\mathfrak{a}}$ . Note that this quantum algorithm does need the assumption of GRH, which is used to compute a small generating system of  $\text{Cl}$ .

## Acknowledgement

We acknowledge financial support by the Landesstiftung Baden-Württemberg.

## References

- 1 J. Buchmann, *J. Number Theory* **26**, 8–30 (1987).
- 2 J. Buchmann, *Math. Comput.* **53**, 679–688 (1989).
- 3 J. Buchmann, M. Maurer, and B. Müller, Cryptography based on number fields with large regulator, Technical report TI-5/00, TU Darmstadt, 2000.
- 4 H. Cohen, *A Course in Computational Algebraic Number Theory* (Springer-Verlag, 1993).
- 5 J. Gruska, *Quantum Computing* (McGraw-Hill, 1999).
- 6 D. Haase, Polynomiale Inversion der Distanzfunktion total reeller Zahlkörper, Diplomarbeit, Universität Karlsruhe (TH), 2003.
- 7 S. Hallgren, Polynomial time quantum algorithms for Pell's equation and the principal ideal problem, *Symposium on the theory of computation STOC*, May 2002.
- 8 J. Neukirch, *Algebraische Zahlentheorie* (Springer-Verlag, 1992).
- 9 A. Schmidt and U. Vollmer, Polynomial time quantum algorithm for the computation of the unit group of a number field, *Proceedings of the 37th Annual ACM Symposium on Theory of Computing STOC'05*.
- 10 P. Shor, Algorithms for Quantum Computation: Discrete Logarithm and Factoring, *Proc. 35th Annual Symposium on Foundations of Computer Science* (1994) pp. 124–134 and *SIAM J. Comput.* **26**, 1484–1509 (1997).
- 11 C. Thiel, On the complexity of some problems in algorithmic algebraic number theory, *Dissertation, Universität des Saarlands, Saarbrücken* 1995.
- 12 C. Thiel, Verifying the class number belongs to  $\text{NP} \cap \text{CoNP}$ , *Proceedings of the 1994 Algorithmic Number Theory Symposium* (Springer-Verlag).

## 19

## Implementation Complexity of Physical Processes as a Natural Extension of Computational Complexity

*Dominik Janzing*

## 19.1

### Introduction

After Shor invented an algorithm [1] that factorizes large numbers into primes in polynomial time it seems likely that quantum and classical complexity of solving computational problems differ substantially. This insight lead to a quantum complexity theory [2, 3].

Usual approaches to quantum complexity theory are either based on the quantum Turing machine [2] or on quantum circuits consisting of elementary gates [3]. In the sequel we will focus on the latter approach which we will refer to as the standard model of a quantum computer [4]. Its  $n$  qubit register is described by the state space  $(\mathbb{C}^2)^n$  spanned by the computational basis vectors  $|b\rangle$  with  $b \in \{0, 1\}^n$ . A circuit is a sequence of gates which are unitary transformations that act on a few number of qubits only. It is common to restrict the elementary gates to two-qubit operations. Usually one assumes<sup>1</sup> that a computation starts by initializing the register to the state  $|0 \dots 0\rangle$ . The readout of the register is restricted to measurements of some or all qubits in the computational basis. Important complexity measures for circuits are the number of gates and the depth:

**Definition 19.1.1 (Depth of a Quantum Circuit)** Assume that one- and two-qubit gates that act on disjoint sets of qubits can be implemented simultaneously in one time step. Then the depth is the number of time steps.

In quantum complexity an algorithm is said to be efficient if not only the number of required gates increases only polynomially in the input size but also that the running time of the *classical* precomputation, designing the circuit for registers of increasing size, does. We will later mention control problems where our results indicate that they cannot be solved efficiently. Therefore it is

1) Note that this is not possible in usual NMR experiments. Therefore one can ask whether this is really an implementation of a quantum computer [5, 6].

important to mention that the reason for non-efficiency can also be that there is no efficient generation of the required circuits and not necessarily that the circuit itself would consist of a large number of gates.

It is clear that the elementary operations of a reasonable model for quantum computation must correspond to operations which are (at least in principle) physically feasible and are also in a physical sense not too complex to implement. Of course, also in classical computation models the elementary steps must correspond to operations which are sufficiently basic for real hardware. However, there is an interesting sense in which quantum gates are more elementary than classical gates. The idea is that the gates of a quantum computer can only work correctly if they avoid that there is a copy of the processed information somewhere in the world, i.e., the ideal quantum computer is closed in the sense that there exists no information, no entropy and no heat exchange with its environment. In Sect. 19.5 we will present a model of quantum computation which is a closed physical system even with respect to energy.

After having accepted the point of view that the basic operations of quantum computing are not only basic *computing* operations but simply basic physical processes, one may ask for the complexity of other processes than computations. Among others, one could have algorithms for the following tasks.

### 1. State Preparation:

An entangled state can be a resource for a whole computation [7]. Entanglement may also be a useful for improved Ramsey spectroscopy [8]. To prepare large scale entanglement would also be interesting from the perspective of pure research in order to challenge *macrorealism* [9, 10]. A rather general algorithmic approach to state preparation has been presented in [11].

### 2. Algorithmic Cooling:

In the context of NMR quantum computing, algorithms have been proposed that transfer the entropy of one part of the register to the other in order to lower the temperature of the former [12].

### 3. Algorithmic Heat Engines:

In [13] we have considered toy models of future heat engines where the hot and the cold bath are given by quantum systems and the heat engine is a unitary process that extracts energy. In such a setting there is a close connection between logical operations and operations that extract work. Complex logical operations are required when the extracted work should be optimal or when work is extracted from two reservoirs with small temperature differences.

#### 4. Von-Neumann Measurements:

The measurement of important physical observables like the energy of an interacting many-particle system can already be a non-trivial algorithmic problem [14, 15]. Standard tools of quantum algorithmic like phase estimation can be used for this task.

#### 5. Generalized Measurements (POVMs)

The implementation of generalized measurements can in principle be reduced to von-Neumann measurements on an extended system. However, the required measurement or the required unitary transforms can be hard to implement. Algorithms for the implementation of some interesting symmetric positive-operator valued measures are presented in [16–18]. As in Shor’s algorithm, the quantum Fourier transform turns out to be a useful building block.

The idea of this article is to show that a complexity theory for this kind of control problems can be developed along the same lines as the theory of computational complexity. In Sect. 19.2 we will explain how a simple technical lemma provides lower bounds on the implementation complexity for rather different problems. In Sect. 19.3 we will show that hard computational problems can be reduced to some natural control problems which are therefore likely to be complex. In Sect. 19.4 we describe some approaches to extend the definition of complexity to systems which do not consist of qubits. These ideas should suggest that implementation complexity is not only an *extension* of computational complexity but also its *foundation*. In Sect. 19.5 we show that even a relatively simple Hamiltonian generates a time evolution that allows for universal computation. The time and space resources for an implementation in such a model would therefore be a physically motivated complexity measure.

## 19.2

### Similar Complexity Bounds for Different Tasks

The intention of this section is to show that the same mathematical observation may lead to complexity bounds for quite different control problems. As an example, we consider the following simple observation [10] that will be used several times below. It describes how a quantum circuit of given depth changes observables when the operations are considered in the Heisenberg picture.

**Lemma 19.2.1 (Increase of Observable Cluster Size)** *Let  $A$  be a  $k$ -cluster observable on an  $n$  qubit quantum register, i.e.,  $A$  acts like the identity on  $n - k$  qubits. Let  $U$  be a unitary on  $\mathcal{H} := (\mathbb{C}^2)^{\otimes n}$  implemented by a quantum circuit of depth  $d$  consisting of two-qubit gates. Then  $U^\dagger A U$  is a  $2^d k$  cluster observable.*

The proof is given by induction: each step can at most double the cluster size.

We will below also make use of an implication of Lemma 19.2.1 which was derived in [10] in order to prove lower bounds on the “complexity of violating macrorealism” in the following sense. A one-qubit observable  $a$  defines for large  $n$  a “macroscopic” observable<sup>2</sup>  $\bar{a}$  by

$$\bar{a} := \frac{1}{n} \sum_{j=0}^n a_j, \quad (19.1)$$

where  $a_j$  denotes the 1-qubit observable  $a$  acting on qubit  $j$ . In [9] we have argued why a mixed state  $\rho$  violates macrorealism if the trace norm of  $[\bar{a}, \rho]$  is closer to 1 than to  $1/\sqrt{n}$  for  $\|a\| = 1$ . The idea is that for pure states we have

$$\|[\bar{a}, \rho]\|_1 = 2\Delta\bar{a} \quad (19.2)$$

where  $\Delta\bar{a}$  denotes the standard deviation of  $\bar{a}$  measurements applied to the state  $\rho$ . For mixed states we have concluded by convexity arguments that a large trace norm of the commutator implies that there is no decomposition into pure states with low uncertainty, i.e., the uncertainty of  $\bar{a}$  is then mainly caused by quantum fluctuations. Even though one should consider  $\bar{a}$  only as macroscopic for extremely large  $n$  we can use the mathematical way of reasoning also for small  $n$ . In order to obtain states where the trace norm is close to 1 one needs circuits whose depth is close to  $\log_2(n)$ :

**Theorem 19.2.2 (Quantum Uncertainty of “Macroscopic” Observables)**  
*An  $n$ -qubit state  $\rho$  which has been prepared by a quantum circuit with depth  $d$  starting in a product state satisfies*

$$\|[\bar{a}, \rho]\|_1 \leq \sqrt{\frac{2}{n}} 2^d,$$

where  $\bar{a}$  is defined by  $a$  as in Eq. (19.1) with  $\|a\| = 1$ .

The proof can be found in [10] and uses the Heisenberg picture. The idea is that the circuit  $U$ , when applied to the observable  $\bar{a}$ , generates a sum of observables whose cluster sizes are bounded by Lemma 19.2.1. The variance of  $U^\dagger \bar{a} U$  in a product state can therefore be bounded by elementary arguments. The bound of the trace norm still holds when mixtures of low-complexity states are considered.

We can use Theorem 19.2.2 in order to derive a lower bound on the complexity of preparing the kind of entanglement that has been considered for improving frequency standards in Ramsey spectroscopy [8]. In order to simplify the discussion we restrict ourselves to a situation without decoherence and to so-called single shot measurements. Furthermore we discuss the idea

2) For further justification of this term see [9, 10, 19].

in the abstract setting of a quantum register. The idea is that a pure state  $\rho$  of  $n$  qubits is evolving according to the Hamiltonian  $\omega_0 H$  with an appropriate frequency  $\omega_0$ , where  $H$  is defined by

$$H := \sum_{j=0}^{n-1} \sigma_z^{(j)}, \quad (19.3)$$

where  $\sigma_z^{(j)}$  is the Pauli matrix  $\sigma_z$  acting on qubit  $j$ . Now we assume that we measure (on the joint system) the observable

$$A_t := e^{-i\omega t H} A e^{i\omega t H}$$

after the time  $t$ , where  $\omega$  is some frequency close to  $\omega_0$ . In other word, we measure  $A$  with respect to a frame that rotates with frequency  $\omega$ . The expectation value of  $A_t$  in the state

$$\rho_t := e^{-i\omega_0 t H} \rho e^{i\omega_0 t H}$$

is given by

$$\langle A_t \rangle = \text{tr}(A_t \rho_t) = \text{tr}(A_0 e^{i\Omega t H} \rho e^{-i\Omega t H})$$

where  $\Omega := \omega - \omega_0$  is the “detuning” between both frequencies. Without going into the details, we mention that a single shot measurement of  $A_t$  allows to estimate  $\Omega$  up to an error  $\delta\Omega$  given by

$$\delta\Omega = \frac{\Delta A_t}{\left| \frac{d}{d\omega} \langle A_t \rangle \right|}, \quad (19.4)$$

where  $\Delta A_t := \sqrt{\text{tr}(\rho_t A_t^2) - (\text{tr}(\rho_t A_t))^2}$ . One can show that entangled states  $\rho$  can decrease  $\delta\Omega$  [8]. Whereas unentangled states allow for an estimation error of the order  $1/\sqrt{n}$  one could in principle achieve the order  $1/n$  with large-scale entanglement. We are now prepared to derive bounds for preparing the appropriate entanglement.

**Theorem 19.2.3 (Complexity of Improving Frequency Standards)** *Let  $\rho$  be a pure state obtained by a circuit of depth  $d$  from a product state. Then  $\delta\Omega$  in Eq. (19.4) satisfies*

$$\delta\Omega \geq \frac{1}{\sqrt{2n} t 2^d}$$

This shows that a depth of the order  $\log_2 n$  is needed in order to prepare entanglement that enables a decrease of the error with  $O(1/n)$ .

*Proof.* The results [20] (see also [21]) imply that for pure states the minimum of Eq. (19.4) over all observables  $A$  is given by  $1/(2t \Delta E)$  where  $\Delta E$  is the standard deviation of the energy corresponding to the Hamiltonian  $H$ . Observing

that  $H/n$  is an observable of the type in Theorem 19.2.4 we conclude

$$\Delta E \leq \sqrt{\frac{n}{2}} 2^d,$$

and the Theorem follows.  $\square$

Within the philosophical context of [10] we have asked for the complexity of von-Neumann measurements that are strongly incompatible with the macroscopic observables above. The observable  $A := \sigma_x^{\otimes n}$  is an interesting example since it detects the difference between the coherent superposition

$$\frac{1}{\sqrt{2}}(|0\dots0\rangle + |1\dots1\rangle)$$

and the corresponding mixture of basis states. The obvious method to measure  $A$  by a  $\sigma_x$ -measurement on each qubit is not a measurement in the sense of Lüders' postulate [22] since it does not *project* onto the eigenspaces of  $A$ . The projections onto the eigenspaces of  $A$  are given by

$$P_{\pm} := \frac{1}{2}(\mathbf{1} \pm A).$$

Applied to the state  $|0\dots0\rangle$  they generate the highly entangled states

$$\frac{1}{\sqrt{2}}(|0\dots0\rangle \pm |1\dots1\rangle).$$

We assume that the elementary measurements on our quantum register are given by reading out  $k \leq n$  qubits. If we assume that the first  $k$  qubits are measured, we have

$$P_j = |b_j\rangle\langle b_j| \otimes \mathbf{1}^{\otimes(n-k)}, \quad (19.5)$$

where each  $b_j$  is some binary word with  $k$  digits. Since  $A$  has only two eigenvalues we must only measure one qubit and can therefore conclude with Lemma 19.2.1 that a circuit of depth  $\log_2 n$  is necessary. We can find similar complexity bounds for a more general class of observables including  $A$ , namely those which are strongly incompatible with the macroscopic ones in an appropriate sense:

**Theorem 19.2.4 (Commutator with Low Complexity Observables)** *Let  $U$  be a unitary implemented in a circuit of depth  $d$  and each  $P_j$  be as in Eq. (19.5). Then we have*

$$\|[\bar{a}, U^\dagger P_j U]\| \leq \frac{1}{\sqrt{2n}} 2^d.$$

The proof in [10] does not directly use Lemma 19.2.1 but uses estimations on the number of pairs  $i, j$  for which  $Ua_i U^\dagger$  and  $Ua_j U^\dagger$  act on disjoint regions.

This shows that estimations on cluster sizes of observables enter into the proof, too.

Now we will show that Lemma 19.2.1 can also be used for deriving bounds on the complexity of a computational problem which will first be stated formally.

**Definition 19.2.5 (Computing MAJORITY without ancillas)** Given  $2n + 1$  qubits. Let  $U$  be a unitary such that for every binary word  $b$  the basis state  $|b\rangle$  satisfies

$$U|b\rangle = |\psi_b\rangle \otimes |M(b)\rangle,$$

where  $M$  is the MAJORITY function which is 1 if and only if  $b$  contains more symbols 1 than symbols 0.

Note that MAJORITY is used as an interesting example in [23] where it is shown that no classical circuit of constant depth is able to compute it. It is possible that the constraint that no ancilla qubits are allowed increases the complexity substantially. We derive a weak bound which is likely not to be tight in this case but checking the proof makes it clear that the bound of Theorem 19.2.6 holds even for circuits that use ancillas.

**Theorem 19.2.6 (Complexity of Computing MAJORITY)** *The depth of a circuit  $U$  that computes the boolean function MAJORITY in the sense of Definition 19.2.5 is at least*

$$d \geq \log_2(2n + 1)$$

*Proof.* The observable which measures whether the suffix of a binary word is 1 or 0 is  $A := 1^{\otimes 2n} \otimes \sigma_z$ . The observable  $UAU^\dagger$  which measures whether the majority of qubits are 1 is a proper  $2n + 1$ -qubit observable because the logical states of all qubits are relevant. Then the theorem follows with Lemma 19.2.1.  $\square$

Formally the same problem appears in the context of thermodynamic machines. We start by defining a particular instance of algorithmic cooling where the entropy of one of  $2n + 1$  two-level systems is transferred to the  $2n$  other qubits such that the temperature of the former is reduced.

**Definition 19.2.7 (Optimal Algorithmic Cooling)** Given  $2n + 1$  two level systems being in their Gibbs state

$$\rho = p_0|0\rangle\langle 0| + p_1|1\rangle\langle 1|$$

with  $p_1/p_0 = \exp(-E/(kT))$  for some temperature  $T \notin \{0, \infty\}$ . Then optimal algorithmic cooling of the last qubit is to implement a unitary  $U$  which lowers the probability for its upper state as much as possible.

The following theorem is actually only a simple observation:

**Theorem 19.2.8 (Optimal Cooling Computes MAJORITY)** *A circuit  $U$  implements optimal cooling in the sense of Definition 19.2.7 if and only if it computes MAJORITY in the sense of Definition 19.2.5.*

*Proof.* The Hamiltonian  $H$  in Eq. (19.3) can (up to a common shift of all eigenvalues) be rewritten as

$$H := \sum_b wgt(b) |b\rangle\langle b|,$$

where  $wgt(b)$  denotes the Hamming weight of  $b$ , i.e., the sum of all digits. The probability of a basis state  $|b\rangle$  is in a temperature state proportional to  $\exp(-wgt(b)/(kT))$ .  $U$  is optimal if it maps the  $2^{2n}$  least likely half of basis states  $|b\rangle$  on states  $|\psi_b\rangle \otimes |1\rangle$  and the others on states  $|\psi_b\rangle \otimes |0\rangle$ . The least likely states are exactly those with Hamming weight at least  $n + 1$ .  $\square$

We can also treat the reverse thermodynamic machine, namely a heat engine, with the same methods. First we define a heat engine formally.

**Definition 19.2.9 (Unitary Heat Engine)** A heat engine is a unitary transformation  $U$  on a bipartite system with Hamiltonian  $H := H_A \otimes \mathbf{1} + \mathbf{1} \otimes H_B$ . It is initially in the state  $\rho = \rho_A \otimes \rho_B$  where  $\rho_A, \rho_B$  are equilibrium states with different temperatures  $T_A, T_B$ , respectively and  $U$  extracts energy in the sense that  $E_{gain} > 0$  with

$$E_{gain} := \text{tr}((\rho_A \otimes \rho_B)H) - \text{tr}(U(\rho_A \otimes \rho_B)U^\dagger H)$$

A unitary  $U$  is an optimal heat engine if it maximizes  $E_{gain}$ .

A specific instance of this engine is inverse to the refrigerator in Definition 19.2.7:

**Theorem 19.2.10 (Optimal Heat Engine is Inverse to MAJORITY)** *Let  $U$  be an optimal heat engine on  $2n$  two-level systems with temperature  $T_A \neq 0$  and one two-level system with  $T_B = 0$  where all  $2n + 1$  systems have the same energy gap. Then  $U^{-1}$  computes MAJORITY in the sense of Definition 19.2.5.*

*Proof.* Let the suffix of each of this binary words indicate the state of the cold two-level system. Then all binary words with suffix 0 have non-zero probability and words with suffix 1 have probability 0. Every optimal heat engine  $U$  has to map the subspace spanned by the former  $2^n$  words onto the subspace corresponding to the  $2^n$  smallest eigenvalues of  $H$  [13]. It is the space spanned by all words with Hamming weight at least  $n + 1$ . Therefore the inverse of the heat engine, i.e.,  $U^{-1}$  computes the boolean function MAJORITY in the sense that the rightmost qubit in the state

$$U^{-1}|b\rangle$$

is 1 if and only if  $wgt(b) > n$ , i.e., the majority of the qubits are in the 1 state.  $\square$

We conclude that the bound in Theorem 19.2.6 applies to the optimal refrigerator and to the optimal heat engine since the depth of  $U$  and  $U^{-1}$  coincide.

The connections between computational complexity and implementation complexity presented so far were basically a simple exercise and the bounds derived in this section were rather weak. Now we want to develop a theory on hard control problems by relating them to hard computational problems.

### 19.3

#### Relating Control Problems to Hard Computational Problems

In this section we want to show that there are natural quantum control problems which are at least as hard to solve as some very hard computational problems. Our kind of reasoning is in strong analogy to reducing computational problems onto each other in usual complexity theory.

First we describe an instance of heat engines, which could solve NP-complete computational problems if the former existed. Second we describe a measurement apparatus which could be used to solve PSPACE-complete problems if it existed. Note that the claim here is not that the *construction* of these machines requires to solve hard computational problems. This would be hardly worth mentioning since it is standard that hard computational problems arise from optimal design of machines. The statement is rather that the machines themselves, i.e., the heat engines and the measurement apparatus, would be powerful computers if they existed.

First we recall a popular example of a problem that is complete for the complexity class NP:

**Definition 19.3.1 (KNAPSACK)** Given the natural numbers  $E_1, \dots, E_n, K, V$  with  $K \leq V$ . Is there a subset of the values  $E_1, \dots, E_n$  such that their sum  $S$  satisfies  $K \leq S \leq V$ ?

It is commonly believed in computer science that no algorithm can exist that computes the answer of this question such that the running time increases only polynomially in the number of bits specifying the input values  $E_1, \dots, E_n, K, V$  [24]. Therefore it is remarkable that the following instance of an optimal heat engine would solve KNAPSACK. Consider  $n$  two-level systems with temperature  $T_A$  and energy gaps  $E_1, \dots, E_n$  and one hot two-level system with gap  $E_A := V - 1$ . Here the energy values can be given with respect to an arbitrary unit (therefore the physical energy gaps do not necessarily increase with increasing numbers of  $E_j$  and  $K$ ). Let the temperature of the hot two-level system be given by  $T_A = (K - 1)T_B/E_A$ . Then we have :

**Theorem 19.3.2 (Optimal Heat Engine Solves NP)** Let  $E_A, E_1, E_2, \dots, E_n$  be the energy gaps of  $n + 1$  two-level systems. Let  $T_A$  be the temperature of the 0th system and  $T$  of the remaining  $n$ . Let the values be such that there is no  $b \in \{0, 1\}^n$

such that

$$\sum_{j=1}^n b_j E_j = \frac{E_A T_B}{T_A}.$$

Let  $U$  acting on  $\mathbb{C}^2 \otimes (\mathbb{C}^2)^{\otimes n}$  be an optimal unitary heat engine for this system. Let  $b \in \{0, 1\}^n$  be a possible result obtained by reading out the  $n$  rightmost qubits being in the state

$$U(|1\rangle \otimes 0 \dots 0\rangle).$$

Then  $b$  satisfies

$$E_A > \sum_j b_j E_j > E_A \frac{T_B}{T_A} \quad (19.6)$$

if and only if such a binary word  $b$  exists.

A detailed proof can be found in [13]. The message of this result should be discussed carefully. In complexity theory it is a standard conjecture that there is no algorithm that solves NP-complete problems such that the running time increases only polynomially in the *input length*. Here the input length is the number of bits that specify the energy levels. This means that the optimal heat engine which solves NP problems would even take into account exponentially small changes in the level spacing when choosing the optimal “strategy” for work extraction. It is, of course, not physically reasonable to assume that we can adjust the level spacing with an arbitrary precision.

In order to consider the relevance of the result from another perspective, assume there existed a classical algorithm which generates the optimal circuit  $U$  after it has received a description of the level spacing as input. Then we would not need to adjust the level spacing of real physical two-level systems in order to solve NP-complete problems. We could apply  $U$  to an arbitrary  $n + 1$ -qubit register. Therefore we conjecture that no efficient algorithmic generation of a circuit with polynomial length exists which implements the optimal  $U$ . This suggests that there is some trade-off between complexity and efficiency even though the amount of energy wasted by suboptimal heat engines may be negligible from a practical perspective.

Now we mention a theorem that shows that the implementation of exact von-Neumann measurements may even be hard for quite natural classes of joint observables. First we introduce a definition of exactness where the theorem below refers to:

### Postulate 1 (Measurement Accuracy)

Let  $A$  be a self-adjoint operator on a finite dimensional Hilbert space and  $\sum_j \lambda_j P_j$  its spectral resolution where  $\lambda_j$  are the eigenvalues and  $P_j$  are the corresponding spectral projections.

A measurement of  $A$  with accuracy  $\Delta\lambda$  has the following property: For all density matrices  $\rho$  the probability to obtain an outcome in the interval  $I := [\lambda_j - \Delta\lambda, \lambda_j + \Delta\lambda]$  is at least  $(3/4) \text{tr}(\rho P_j)$ .

Applying the measurement instrument to an eigenstate with eigenvalue  $\lambda_j$  this implies that the probability that the result differs by more than  $\Delta\lambda$  from the correct result  $\lambda_j$  is at most  $1/4$ . The results described below are not sensitive to the particular definition of accuracy. However, it is convenient to work with the formulation above. Then we obtain:

**Theorem 19.3.3 (Measuring 4-Local Observables is PSPACE-Hard)** *Let  $M$  be a hypothetical machine with the following properties:*

1.  *$M$  receives a classical description of a 4-local  $n$ -qubit observable  $A$ , i.e., an operator that is a sum of 4-qubit observables.*
2.  *$M$  receives a state  $|\psi\rangle$  on a quantum register with state space  $(\mathbb{C}^2)^{\otimes n}$ .*
3.  *$M$  implements an  $A$ -measurement on  $|\psi\rangle$  and gives the result as output*
4. *The accuracy of the output is sufficient to distinguish all different eigenvalues of  $A$ .*

*Then  $M$  can be used to solve any decision problem in the complexity class PSPACE in polynomial time.*

For the proof (which is quite lengthy) we refer to [15]. We will only rephrase the idea. First we can construct a quantum circuit  $U$  which would solve a PSPACE complete problem in exponential running time in the following sense. Let

$$f : \{0, 1\}^n \rightarrow \{0, 1\}$$

be a boolean function which is PSPACE complete to compute. Then

$$U^m(|0 \dots 0\rangle \otimes |x\rangle \otimes |y\rangle) = |0 \dots 0\rangle \otimes |x\rangle \otimes |y \oplus f(1)\rangle,$$

where  $m$  is some exponentially large number. In words, the  $m$ -fold concatenation of  $U$  inverts the output bit on the right if and only if  $f(x) = 1$ . Furthermore, the circuit is constructed in such a way that one knows  $m$  and that for all  $m' < m$  the  $m'$ -fold application of  $U$  leads to a state that is orthogonal to the initial state. It follows that the spectrum of the restriction of  $U$  to the orbit of the initial state is  $\exp(-ij/m)$  with  $j = 0, \dots, m-1$  if  $f(x) = 0$  and  $\exp(-ij/(2m))$  if  $f(x) = 1$ . Then we construct a 4-local observable  $A$  whose spectrum on the orbit above consists of the values  $\cos(-ij/m)$  and  $\cos(-ij/(2m))$  depending on  $f(x)$ . A small number of precise  $A$ -measurements, applied to the initial state, can then distinguish between both cases since the initial state is almost an equally weighted superposition of all  $m$  or  $2m$  eigenstates of the restriction of  $A$ .

## 19.4

### The Need for a Control-theoretic Foundation of Complexity

In the preceding section we have addressed the complexity of physical processes by restricting the attention to processes that act on a collection of two-level systems. For these systems we could interpret the physical two-level systems as qubits of a quantum register and their initial state as the input of a computation. In such a context we can refer to those operations as elementary which are considered as elementary in the standard model of quantum computation.

However, we may also be interested in defining complexity for systems which are not a collection of qubits. Therefore we would also need assumptions on the set of elementary operations that can, for instance, be applied to a Schrödinger wave function. Let us consider such a continuous variable quantum system. If the particle is confined to one dimension, its Hilbert space is given by  $L^2(\mathbb{R})$ , the space of square-integrable functions on the real line. This space is isomorphic to  $L^2(\mathbb{N}_0)$ , the set of square summable sequences. When referring to oscillators, one will prefer the latter representation. On infinite-dimensional systems the definition of a reasonable sense of complexity is much less clear than for qubit registers.

An example where interesting complexity issues arise in infinite systems like oscillator modes is the problem of implementing an optimal heat engine on two modes (in the sense of Definition 19.2.9) being in a thermal state with different temperatures. In Fig. 19.1 we have illustrated how the optimal heat engine acts on two modes with appropriately chosen temperatures and frequencies.

One may state that the map in Fig. 19.1 is rather complex to implement, but “complex” is here rather understood in an intuitive sense: the arrows seem to be quite irregular. To show that it is also complex in a computer scientific sense could be a hard task.

It would be desirable to connect complexity of operations on continuous systems with complexity on qubit systems. A natural way for doing so is to construct an interface between both types of systems. Therefore we have considered [25] the complexity of implementing an analogue to digital and of implementing a digital to analogue converter for quantum information. We give a not too formal definition of A/D conversion :

**Definition 19.4.1 (A/D conversion)** A family of unitaries  $U_n$  acting on the Hilbert space

$$L^2(\mathbb{R}) \otimes (\mathbb{C}^2)^{\otimes n}$$

is an analogue to digital converter if for every sufficiently smooth wave function  $\psi$  essentially supported by an interval  $[a, b]$  the restriction of the state

$$U_n(|\psi\rangle \otimes |0\dots0\rangle)$$

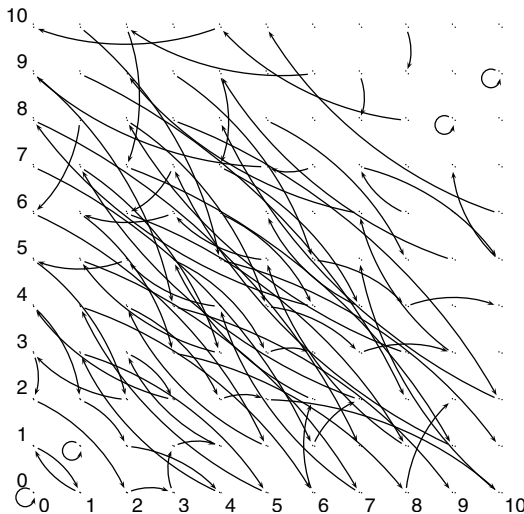


**Fig. 19.1** (Taken from [13]) Optimal heat engine of two harmonic oscillators with frequency ratio  $\omega_A/\omega_B = \sqrt{2}$  and temperature ratio  $T_B/T_A = \omega_B/(\sqrt{3}\omega_A)$ . A point in row  $n$  and column  $m$  is a basis state with  $n$  quanta in mode A and  $m$  in mode B. An arrow

$(n, m) \rightarrow (\tilde{n}, \tilde{m})$  indicates that a state with  $n$  quanta in mode A and  $m$  in mode B has to be converted into a state with  $\tilde{n}, \tilde{m}$  quanta, respectively. Points which have their image or pre-image outside the depicted area obtain no arrow.

to the digital system coincides with the pure state

$$c \sum_{j=0}^{2^n-1} \psi\left(a + \frac{(b-a)j}{2^n}\right) |j\rangle,$$

for appropriate  $c \in \mathbb{C}$  up to an error  $\epsilon_n$  which tends to zero for  $n \rightarrow \infty$ .

[25] shows in a control theoretic setting that a conversion is possible that is efficient in the number  $N = 2^n$  of points. It is also efficient in  $n$  if squeezing operations are available. Clearly such a statement depends strongly on the assumptions of the interface between the analogue and the digital part.

We found the following model reasonable. Given the Jaynes-Cummings Hamiltonian

$$H := a \otimes (\sigma^+ \otimes \mathbf{1}^{\otimes n-1}) + a^\dagger \otimes (\sigma^- \otimes \mathbf{1}^{\otimes n-1}),$$

(where  $\sigma^\pm := \sigma_x \pm i\sigma_y$  and  $a$  is the usual lowering operator) which connects the continuous degree of freedom with the first qubit. Assume that we have the possibility of bang-bang control on the first qubit, i.e., we can implement one-qubit unitaries on a negligible time scale compared to the time scale of the dynamics generated by  $H$ . Assume furthermore that we have universal quantum computation capability on the  $n$  qubit register. Then there is an algorithm for A/D conversion using the following resources:

1. Several periods of free evolution according to  $H$ ,
2. interspersed by bang-bang operations on the first qubit and
3. universal quantum computation capability on the digital register.

The total interaction time for (1) and the number of gates are both polynomial in  $N$ .

The algorithm can be found in [25]. It uses the interaction Hamiltonian once for intervals of length

$$1, 2, 4, \dots, 2^{n-1}.$$

The total length is less than  $2^n = N$ . Apart from this we need only the Fourier transform on  $n$  qubits which is even efficient in  $n$  [4].

Conversion between analogue and digital quantum degrees of freedom would at least allow for indirect implementations on continuous systems using a standard quantum computer. Direct operations on continuous systems have been considered for instance in [26, 27]. A further understanding of analogue complexity has to be left to the future. We will now come back to qubit systems. In order to relate physical understanding and computer science definition of complexity even stronger to each other, we would like to explain discrete complexity by analyzing the set of physical interactions and evaluating which unitary operations and gates they can easily implement.

Taking into account that a physical process is always given by a continuous time evolution, we should not be restricted to the idea that an algorithm is a sequence of discrete steps. In [28] we have therefore defined an algorithm as a map

$$t \mapsto H(t),$$

where  $H(t)$  with  $t \in [0, T]$  is some physically reasonable set  $S$  of available Hamiltonians acting on  $n$  qubits and  $T$  is the running time. One should add the remark that the map must have an efficient description.

In [28] we have tried to find a complexity measure for continuous algorithms which is as close to gate complexity as possible. For doing so, we modify the complexity measure *depth* (see Definition 19.1.1) such that it better meets the continuity of physical processes: in order to take into account that gates which are close to the identity can possibly be implemented more quickly, we introduced the concept *weighted depth*. First we defined the *angle* of a unitary  $U$  as the minimal norm over all self-adjoint  $A$  with  $\exp(iA) = U$ . Then we define (see Fig. 19.2 for an illustration):

**Definition 19.4.2 (Weighted Depth of a Circuit)** The weighted depth  $w$  of a quantum circuit of depth  $d$  is the sum

$$w := \sum_{j=1}^d w_j$$

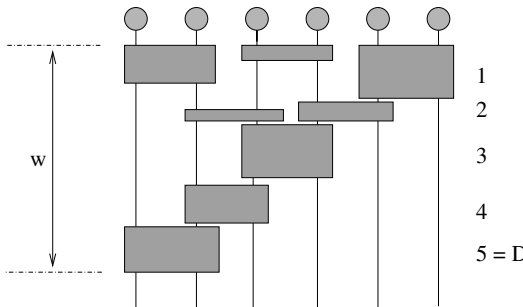


**Fig. 19.2** Depth ( $D$ ) and weighted depth ( $w$ ) of a circuit:  $D$  counts only the number of layers (time steps) while  $w$  takes also into account their weights.

where the weight  $w_j$  is the maximal angle of all gates implemented in step  $j$ .

In order to define complexity of continuous algorithms we define first the complexity of an interaction. We will restrict ourselves to pair-interactions partly for physical reasons and partly because this fits well with the discrete model with two-qubit gates. Let  $H$  on  $n$  qubits be given by

$$H := \sum_{1 \leq j, k \leq n} H_{jk},$$

where each  $H_{jk}$  acts on the qubit pair  $jk$ . Our following definition of complexity is lead by the intuition that  $H$  is more complex if many  $H_{jk}$  are non-zero for overlapping qubit pairs and is not complex if it acts only on mutually disjoint pairs. Furthermore, due to the remarks above, we call an interaction more complex if the norms of  $H_{jk}$  are large. A complexity measure which takes both aspects into account is given as follows. First define a weighted graph with the qubit numbers  $1, \dots, n$  as vertices and  $c_{jk} := \|H_{jk}\|$  as weights. Two vertices  $j, k$  are connected if and only if  $H_{jk} \neq 0$ . As a generalization of the chromatic index of a graph<sup>3</sup> we define [28]:

**Definition 19.4.3 (Weighted Chromatic Index)** The weighted chromatic index  $W$  of a weighted graph with weights  $c_{jk} \geq 0$  is given as follows. Let  $n_r$  be the chromatic index of the graph which consists of all edges  $(j, k)$  for which  $c_{jk} > r$ . Then

$$W := \int_0^\infty n_r dr.$$

Note that in this definition the set  $S$  of available interactions is a vector space of all pair-interactions. Therefore, every reasonable sense of complexity must

3) The chromatic index is the least number of colors needed to color the edges such that no two edges which have a vertex in common have the same color.

take into account the interaction strength because the required running time in a continuous algorithms is not bounded from below in this case.

Now we can straightforwardly define the complexity of a continuous algorithm as the time integral of the complexity of the interaction over the whole running time:

**Definition 19.4.4 (Continuous Complexity)** Let  $t \mapsto H(t)$  with  $t \in [0, T]$  a continuous algorithm and  $W(t)$  its weighted chromatic index at time  $t$ . Then its complexity is

$$C := \int_0^T W(t) dt.$$

In [28] we have shown that this continuous complexity measure coincides with the weighted depth, i.e., we have:

**Theorem 19.4.5 (Continuous Complexity Equals Weighted Depth)** *There is a continuous algorithm with complexity  $C$  which implements  $U$  if and only if there is a sequence of discrete algorithms implementing unitaries  $U_n$  converging to  $U$  such that their weighted depth converges to  $C$ .*

The motivation for defining the integrated chromatic index as a complexity measure was two-fold. First it helped to relate continuous with discrete complexity. Second it meets some intuitive understanding of complexity to consider an interaction as complex when many interaction terms overlap. Nevertheless, this is insufficient as a physical foundation of complexity. Interesting physical foundations are rather given by the theory of mutual simulation of Hamiltonians.

We rephrase only one briefly the setting since there exists meanwhile a large number of articles on this approach (e.g. [29–31]). We considered  $n$ -qubit interactions of the form

$$H := \sum_{1 \leq k < l \leq n} \sum_{\alpha, \beta=x, y, z} J_{kl; \alpha \beta} \sigma_{\alpha}^{(k)} \sigma_{\beta}^{(l)},$$

with a symmetric  $3n \times 3n$  matrix  $J$ . Then we assume that the natural time evolution of the system can be interspersed by independent unitaries on each qubit, i.e., one has transformations of the form

$$U := u_1 \otimes u_2 \otimes \cdots \otimes u_n. \quad (19.7)$$

It is assumed that the implementation time of the 1-qubit unitaries is negligible compared to the time scale of the free evolution. This model is a strongly idealized version of real NMR-physics (e.g. [32, 33]). Remarkably our theory of simulation of Hamiltonians justifies the point of view that interactions with low weighted chromatic index are easy to simulate by an Ising-interaction where all pairs interact with the same strength:

**Theorem 19.4.6 (Relevance of Weighted Chromatic Index)** *The time overhead to simulate an arbitrary pair-interaction  $\tilde{H}$  on  $n$  qubits by the Hamiltonian*

$$H := \sum_{1 \leq k < l \leq n} \sigma_z^{(k)} \sigma_z^{(l)}$$

*is at most the weighted chromatic index of  $\tilde{H}$ .*

The proof can be found in [30]. One should mention that the above setting fits to our Definition of a continuous algorithm above. First one could consider bang-bang operations as the limit of an infinitely strong control field, hence the set  $S$  of available Hamiltonians consists of the two-qubit interaction and the vector space spanned by all Pauli operators  $\sigma_\alpha^{(j)}$ . One could also define the set  $S$  as the set of interactions obtained by conjugating the natural interaction  $H$  with unitaries of the form (19.7) of the two-quit interactions and add the remark that there is possibly an additional operation (19.7) at the end.

## 19.5

### Hamiltonians that Compute Autonomously

When investigating the complexity of physical processes it may also be questionable to consider the bang-bang operations as elementary since they require sophisticated experimental setup. The most radical approach to physical complexity would be to demand that there must be a natural Hamiltonian which can implement the required transformation simply by its autonomous time evolution. In [34] we have therefore constructed a model where a computation is reduced to (1) initializing the qubits to appropriate basis states (this state encodes the input of the computation as well as its program), (2) let the system evolve according to its free Hamiltonian evolution, and (3) read the result out at a random time instant. The fact that the result is also present in the time average state formalizes the fact that no external clock is needed. Our Hamiltonian is lattice symmetric with finite interaction length as in real physical crystals. However, it consists of 10-qubit terms which is unlikely to find in real physical systems.

Therefore we have constructed a Hamiltonian that consists only of nearest neighbor interactions of spin-1/2 particles moving on a 2D lattice [35]. Even though it is not clear in which physical systems one should find such a Hamiltonian, the model is not too far from physics since it involves only pair-interactions. We briefly describe the second model presented in [35] since its dynamical evolution is solvable. We start by explaining how its clock works. Consider particles which are located on a 2-dimensional lattice as follows. The lattice sites are the black fields of a “diagonal chess board” as depicted in Fig. 19.3.

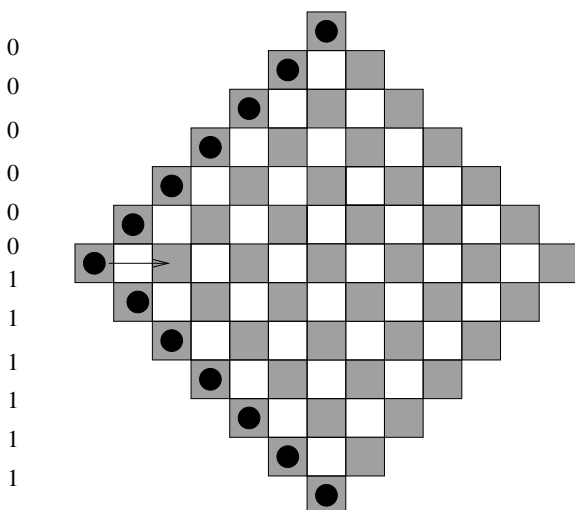


**Fig. 19.3** Initial particle configuration. The arrow shows the only possible motion. The digits at the left indicate the corresponding binary string which is explained in the text.

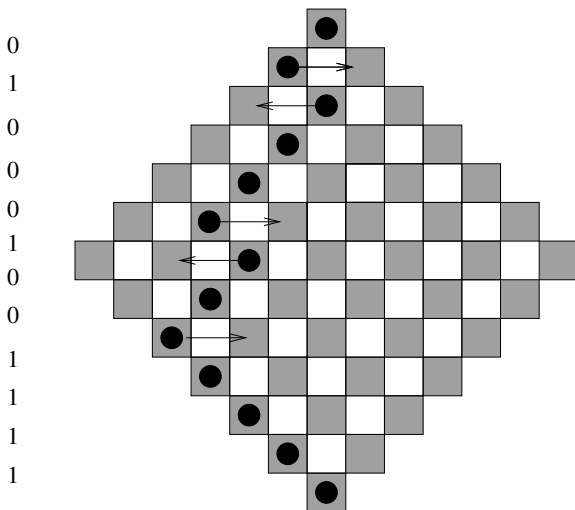


**Fig. 19.4** Possible particle configuration and the possible motions. The corresponding binary string is shown on the left.

The figure shows furthermore how the particles are initially positioned. Now we assume (1) that hopping terms allow tunnelling to the next of the preceding black field in the same row and (2) that attractive nearest neighbor interactions between the particles prevents that the chain of particles tears off. Another possible particle configuration is seen in Fig. 19.4.

For every particle we have only the two possibilities, either that it has already propagated one step further than its upper neighbor or that it is still one step behind it. Accordingly, we can describe the whole configuration by a  $2n$  digit binary word if there are  $2n + 1$  rows. Therefore the clock is described on the Hilbert space  $(\mathbb{C}^2)^{\otimes 2n}$  and we have argued [35] that its effective dynamics generated by the hopping terms and the attractive interactions coincides with the dynamics of a Heisenberg XY-Hamiltonian. The latter is isomorphic to the quasi-free evolution of fermions. The initial binary word is  $0\dots01\dots1$  and the Hamming weight is conserved by the dynamics. This clock triggers the implementation of gates as follows. The qubits are represented by an inner degree of freedom of the particles. We assume, for instance, that the latter is the spin of a spin-1/2 system. Assume that on the left half of the diagonal square there is an interaction region which is enclosed in the first  $k \ll n$  rows. In this region, there is a spatially inhomogeneous spin-spin interaction between adjacent particles such that the qubits are subjected to a time-dependent Hamiltonian while the particles are propagating along the rows. When checking the particle configuration at some random time instant after the system has freely evolved it is likely that all particles have passed the interaction region. We have assumed [35] that the inhomogeneous interactions change slowly along the rows such that they implement in the adiabatic limit holonomic quantum computing [36] on the degenerate subspaces of the interactions. This method ensures that the unitary implemented on the qubits does not depend on the time required by the particles to pass the interaction region. We have constructed nearest neighbor interactions which are universal for holonomic quantum computing.

From the perspective of quantum computing there may be little motivation to find simple interactions that are able to compute autonomously. In this context the goal is more to make it work at all, no matter whether external control operations are needed or not. However, there are other reasons why it would be useful to understand to what extent a simple Hamiltonian is able to drive a complex process: for a molecular heat engine it would not be acceptable that it is driven by control operations that require more energy than the engine extracts from the molecules. We would rather demand that an interaction between the hot and the cold reservoir and the energy sink implements autonomously a transformation that extracts work from the two reservoirs and transfers them to the energy sink. In [13] we have shown that molecular computing and molecular heat engines are closely connected to each other. Hence it is justified to explore in a more general sense which complex transformation can be implemented by a simple interaction. A computation is only an extreme example of a complex physical process and the autonomous quantum computers in [34, 35] are only extreme examples of Hamiltonians that show complex behavior. From a quantum computing perspective it would certainly

be interesting to know which Hamiltonians need only a few control operations in order to show complex dynamics. For the model [34] we have shown that there is only a small time and space overhead for simulating a usual quantum circuit. For the slightly more physical model in [35] this issue has to be left to the future.

In the context of these models one could also ask for the complexity of initializing the system and of reading out the result. Since measurements and state initializations can be a difficult experimental problem one may really doubt to consider them as elementary. However, then the problem of physical complexity would become circular as it would include the interaction between the initializing controller and the system as a new system.

### Acknowledgement

Thanks to Peng Xue for helpful discussions about the use of entanglement for improving frequency standards. This work was funded by the Landesstiftung Baden-Württemberg, Project "Kontinuierliche Modelle der Quanteninformationsverarbeitung", AZ1.1422.01.

### References

- 1 P. Shor, SIAM J. Comput. **26**(5), 1484–1509 (1997).
- 2 E. Bernstein and U. Vazirani, SIAM Journal on Computing **26**(5), 1411–1473 (1997).
- 3 A. Kitaev, A. Shen, and M. Vyalyi, Classical and Quantum Computation, volume 47 (Am. Math. Soc., Providence, Rhode Island, 2002).
- 4 M. Nielsen and I. Chuang, Quantum Computation and Quantum Information (Cambridge University Press, Cambridge (U.K.), 2000).
- 5 S. Braunstein, C. Caves, R. Josza, N. Linden, S. Popescu, and R. Schack, Phys. Rev. Lett. **83**, 1054–1057 (1999).
- 6 R. Schack and C. Caves, Phys. Rev. A **60**, 4354–4363 (1999).
- 7 R. Raussendorf and H. Briegel, Phys. Rev. Lett. **86**, 5188 (2000).
- 8 S. Huelga, C. Machiavello, T. Pellizzari, A. Ekert, M. Plenio, and I. Cirac, Phys. Rev. Lett. **79**, 3865 (1997).
- 9 D. Janzing and T. Beth, Phys. Rev. A **61**, 052308 (2000).
- 10 D. Janzing and Th. Beth, Remark on multi-particle states and observables with constant complexity. <http://xxx.lanl.gov/abs/quant-ph/0003117>.
- 11 A. Soklakov and R. Schack, Efficient state preparation for a register of quantum bits. <http://xxx.lanl.gov/abs/quant-ph/0408045>.
- 12 L. Schulman and U. Vazirani, Scalable NMR Quantum Computers. <http://xxx.lanl.gov/abs/quant-ph/9804060> (1998).
- 13 D. Janzing, On the computational power of molecular heat engines. J. Stat. Phys. **122**(3), 531–556 (2006); see also <http://xxx.lanl.gov/abs/quant-ph/0502019>.
- 14 D. Janzing, Quantum Inf. Comput. **2**(3), 198–207 (2002).
- 15 P. Wocjan, D. Janzing, Th. Decker, and Th. Beth, Measuring 4-local n-qubit observables could probabilistically solve

- PSPACE. Proceedings of the WISICT conference, Cancun 2004. See also <http://xxx.lanl.gov/abs/quant-ph/0308011>.
- 16** T. Decker, D. Janzing, and T. Beth, *Int. J. Quant. Inform.* **2**(3), 353–377 (2004).
- 17** T. Decker, D. Janzing, and M. Rötteler, *J. Math. Phys.* **46**, 012104 (2005).
- 18** T. Decker and D. Janzing, Minimal disturbing implementation of symmetric generalized measurements for quantum registers and Schrödinger waves. <http://xxx.lanl.gov/abs/quant-ph/0507097>.
- 19** D. Poulin, *Phys. Rev. A* **71**, 022102 (2005).
- 20** B. Braunstein, C. Caves, and G. Milburn, *Ann. Phys. (New York)* **247**, 135–173 (1996).
- 21** D. Janzing and T. Beth, *IEEE Trans. Inf. Theory* **49**(1), 230–240 (2003).
- 22** Lüders, *G. Ann. Phys. (Leipzig)* **8**, 322 (1951).
- 23** J. Håstad, *Computational Limitations for Small-Depth Circuits* (MIT Press, Cambridge, Massachusetts, 1987).
- 24** J. van Leeuwen (ed.), *Algorithms and Complexity* (Elsevier, Cambridge, MA, 1990).
- 25** F. Schmüser and D. Janzing, On quantum analogue-to-digital and digital-to-analogue conversion, *Phys. Rev. A* **72**, 042324 (2005), <http://xxx.lanl.gov/abs/quant-ph/0505008>.
- 26** B. Sanders, S. Bartlett, and H. de Guise, From qubits to continuous-variable quantum computation. *CLEO/Europe Focus 2000*, Munich 2001. See also <http://xxx.lanl.gov/abs/quant-ph/0208008>.
- 27** S. Lloyd and S. Braunstein, *Phys. Rev. Lett.* **82**(8), 0031–9007 (1999).
- 28** D. Janzing and Th. Beth, *Phys. Rev. A* **64**(2), 022301 (2001).
- 29** C. Bennett, J. Cirac, M. Leifer, D. Leung, N. Linden, S. Popescu, and G. Vidal, *Phys. Rev. A* **66**, 012305 (2002).
- 30** P. Wocjan, D. Janzing, and Th. Beth, *Quantum Inf. Comput.* **2**(2), 117–132 (2002).
- 31** P. Wocjan, M. Rötteler, D. Janzing, and Th. Beth, *Phys. Rev. A* **65**, 042309 (2002).
- 32** C. P. Slichter, *Principles of Magnetic Resonance* (Springer-Verlag, Berlin, 1990).
- 33** W. K. Rhim, A. Pines, and J. S. Waugh, *Phys. Rev. Lett.* **25**, 218–220 (1970).
- 34** D. Janzing and P. Wocjan, *Quant. Inf. Process.* **4**(2), 129–158 (2005).
- 35** D. Janzing, Spin-1/2 particles moving on a 2D lattice with nearest-neighbor interactions can realize an autonomous quantum computer. <http://xxx.lanl.gov/abs/quant-ph/0506270>.
- 36** P. Zanardi and M. Rasetti, *Phys. Lett. A* **264**, 94–99 (1999).



**20****Implementation of Generalized Measurements  
with Minimal Disturbance on a Quantum Computer***Thomas Decker and Markus Grassl***20.1****Introduction**

A central problem in quantum computing and quantum information theory is to find efficient methods to obtain information about the state of a quantum system. In order to gain maximal knowledge about a quantum state, one should not only consider orthogonal von Neumann measurements, but also positive operator-valued measures (POVMs). Hence we are aiming at efficient implementations of POVMs. In order to allow for a sequence of measurements that refines our knowledge about the quantum state, we are also interested in an implementation of the POVM that minimizes the disturbance of the state of the system.

In the context of quantum computing, a quantum algorithm is composed of the following three steps: the initialization of the quantum registers, a sequence of unitary transformations, and finally a measurement. For orthogonal measurements, the complexity of the measurement can be reduced to the complexity of the unitary and a “standard measurement” since the distinction between the unitary transform and the measurement is not strict. This is clear if we consider the Heisenberg picture where the unitary transform operates on the measurement. Hence this unitary can be arbitrarily shifted between the second and third step of the computation. As an extremal case, the result of the computation can directly be obtained by a measurement of the initialized system. Then the complexity of the computation is determined by the complexity of the measurement alone. To define a complexity measure, the other extremal case is usually preferred: The measurements are restricted to orthogonal measurements in the computational basis with the consequence that the complexity lies completely in the unitary transform. The advantage of this approach is that we can use the quantum circuit model to define a convenient measure of complexity. This is for example the case for Shor’s

factorization algorithm where the measurement at the end is a measurement in the computational basis.

There are algorithms where the measurement at the end is a POVM and not an orthogonal measurement. Some algorithms for the solution of hidden subgroup problems are of this type. The algorithm of Bacon et al. [1] for the solution of dihedral hidden-subgroup problems, for example, consists of the preparation of a special state and a symmetric POVM where an efficient implementation of the POVM is unknown. This example shows that the implementation complexity of symmetric POVMs has to be taken into account for the complexity of algorithms and that efficient implementations can lead to new efficient quantum algorithms. As for orthogonal measurements, the complexity of the implementation of a POVM can be reduced to the complexity of a unitary. Then we can use the quantum circuit model as complexity measure, too.

The implementation of POVMs is likewise of interest for quantum information theory. It is a basic problem to obtain as much knowledge about an unknown quantum state as possible. Using quantum systems, one can not only transfer classical information, but also time information [3] or spin directions [4]. It has been shown that in some cases a POVM yields more information about a quantum state than an orthogonal measurement [5, 6]. Additionally, the convex set of POVMs allows to compute optimized measurements, whereas this is more difficult for orthogonal measurements.

A general scheme for the implementation of symmetric POVMs is described in [2]. However, this implementation is destructive, i.e., the quantum state is destroyed during the measurement process. Although the result is the most important constituent of a measurement the state after the measurement can be relevant, too. Then we want to implement the POVM with minimal disturbance.

It is known that any POVM can be implemented using a unitary transform on the system and an ancilla, followed by an orthogonal measurement of the ancilla [7]. However, this general implementation scheme is not necessarily efficient. This is clear since even for orthogonal measurements, we cannot hope to obtain efficient general implementation schemes [8]. To avoid this basic problem we restrict our attention to the class of symmetric POVMs which, e.g., can be used in the context of quantum cryptography or discretized time evolutions where the states and optimal POVMs possess some symmetry. We take advantage of the symmetry by the application of basic results of representation theory. We construct efficient quantum circuits and implementation schemes for POVMs on a qubit with cyclic symmetry and POVMs with Heisenberg-Weyl symmetry, respectively. The latter are particularly interesting as there are so-called SIC-POVMs which can be used for quantum state tomography. It has been shown that such SIC-POVMs exist for many small

dimensions, including non prime-power dimensions [9]. Furthermore, it is conjectured that they exist for all dimensions [10].

In the first two sections the basic concepts and notations of the theory of generalized measurements and from representation theory, resp., are presented. The application to the implementation of symmetric POVMs is derived in Sect. 20.4, followed by two examples. Further details and e.g. the extension to infinite dimensional quantum systems can be found in [11].

## 20.2

### Minimal-disturbing Implementations of POVMs

In this section we outline the model of generalized measurements that encompasses the computation of the probabilities of the results and the state after the measurement. A simplified description of generalized measurements leads to the notion of POVMs with the important special case of orthogonal measurements. Orthogonal measurements are relevant since they are considered to be the physically implementable measurements. The measurements of some standard models of quantum computers working e.g. with ion traps are orthogonal measurements [7]. Therefore, the reduction of a POVM to an orthogonal measurement is necessary for the experimental implementation and the definition of a useful complexity model. Furthermore, we define the disturbance of a measurement and resume the general implementation scheme with minimal disturbance.

#### 20.2.1

##### Generalized Measurements of Quantum Systems

A measurement of a quantum system is performed by a measurement device. We insert a state, which is described by the density matrix  $\rho$ , into the measurement device and obtain a result. During the measurement process the state of the quantum system changes depending on the result. We assume that the number of different measurement results is finite. Hence we can enumerate the results, i.e., we identify the set of results with the set  $\{0, \dots, m-1\}$ . The behavior of the measurement device is completely described by a family of operators. This means that the probabilities of the results and the state after the measurement are specified by these operators for each possible input state [7, 12, 13].

**Definition 20.2.1** (Generalized Measurement) A generalized measurement with results  $\{0, \dots, m-1\}$  is described by a family  $(A_{bj})_{b,j}$  of linear operators.

To each result  $b$  we associate the operators  $A_{b1}, \dots, A_{bn_b}$  with

$$\sum_{j=1}^{n_b} A_{bj}^\dagger A_{bj} = \Pi_b$$

for a semi-positive operator  $\Pi_b$ . Furthermore, the equation  $\sum_b \Pi_b = I_d$  holds with the identity matrix  $I_d$ .

The probabilities of the results are defined by the operators  $\Pi_b$  and the density matrix [12, 13].

**Definition 20.2.2** (Probability of a result) Let  $\rho$  be the state of the quantum system and  $\Pi_b$  the operator corresponding to result  $b$ . Then the probability of this result is  $\text{tr}(\Pi_b \rho)$ .

The equation  $\sum_b \Pi_b = I_d$  corresponds to the condition that the sum of probabilities of the results equals one for each possible state. The semi-positivity of the  $\Pi_b$  means that the probabilities are non-negative. The state after the measurement process is defined by the operators  $A_{bj}$ . They are called Kraus operators [12–14]. In general, the state transition of the measurement process is non-unitary. Therefore, the measurement process gives rise to a second type of state transform besides the evolution of an isolated quantum system which is described by Schrödinger's equation [7, 12, 13].

**Definition 20.2.3** (State after measurement) A generalized measurement  $(A_{bj})_{b,j}$  changes the state according to

$$\rho \mapsto \rho_b := \frac{1}{p(b)} \sum_j A_{bj} \rho A_{bj}^\dagger \quad \text{with} \quad p(b) := \text{tr}(\rho \Pi_b) \quad (20.1)$$

if the result is  $b$ .

This transition can be interpreted as follows [12, 13]: The measurement device determines internally the results  $(b, j)$  with corresponding state transitions

$$\rho \mapsto \frac{1}{\text{tr}(A_{bj}^\dagger A_{bj} \rho)} A_{bj} \rho A_{bj}^\dagger.$$

We obtain the mixture of Eq. (20.1) if the measurement device merely outputs  $b$ .

## 20.2.2

### Positive-operator Valued Measures

If a measurement is the last step of a computation then the state after the measurement is of no relevance. This is the case for many of the known quantum algorithms [7] where the only important information is the measurement result. Hence the only relevant operators for the description of the measurement are the operators  $\Pi_b$  which determine the probabilities of the results. If

we restrict our attention to these operators we obtain a definition of measurements that is much simpler than the general definition.

**Definition 20.2.4 (POVM)** A positive operator-valued measure (POVM) is a family  $\{\Pi_0, \dots, \Pi_{n-1}\}$  of semi-positive operators with  $\sum_b \Pi_b = I_d$ .

**Example 20.2.5** The operators

$$\Pi_0 = \frac{1}{3} \begin{pmatrix} 1 & 1 \\ 1 & 1 \end{pmatrix}, \quad \Pi_1 = \frac{1}{3} \begin{pmatrix} 1 & \omega_3^2 \\ \omega_3 & 1 \end{pmatrix}, \quad \text{and} \quad \Pi_2 = \frac{1}{3} \begin{pmatrix} 1 & \omega_3 \\ \omega_3^2 & 1 \end{pmatrix}$$

with the third root of unity  $\omega_3 := e^{-2\pi i/3}$  constitute a POVM.

Each generalized measurement with operators  $(A_{bj})_{b,j}$  and  $\Pi_b$  is a unique POVM. Conversely, the construction of a generalized measurement for a POVM is not unique since there are many possible operators  $A_{bj}$  for given operators  $\Pi_b$ . However, with plausible assumptions for the measurement device we can define essentially unique operators  $A_{bj}$ : We assume that for each result  $b$  there is only a single operator  $A_{b1}$  with  $A_{b1}^\dagger A_{b1} = \Pi_b$ . Following the interpretation of Sect. 20.2.1 this means that the measurement device does not conceal internally available results. With the polar decomposition [7]  $A_{b1} = U_{b1}P_{b1}$  where  $U_{b1}$  is unitary and  $P_{b1}$  is semi-positive we obtain the equality  $A_{b1}^\dagger A_{b1} = P_{b1}^2 = \Pi_b$ , i.e., we have  $P_{b1} = \sqrt{\Pi_b}$  and the unitary  $U_{b1}$  is not specified by  $\Pi_b$ . If we write the state transition of a measurement with result  $b$  as

$$\rho \mapsto \frac{1}{\text{tr}(\Pi_b \rho)} P_{b1} \rho P_{b1} \mapsto \frac{1}{\text{tr}(\Pi_b \rho)} U_{b1} P_{b1} \rho P_{b1} U_{b1}^\dagger = \frac{1}{\text{tr}(\Pi_b \rho)} A_{b1} \rho A_{b1}^\dagger$$

the second transition can be interpreted as a unitary which is performed by the device after the actual measurement process. If we assume that the measurement device does not perform such a transform we can assign the unique positive semi-definite operator  $A_{b1} := \sqrt{\Pi_b}$  to each result of a POVM.

### 20.2.3

#### Orthogonal Measurements

Orthogonal measurements (also called von Neumann or projective measurements [7]) constitute a special class of POVMs. The results of an orthogonal measurement are mutually exclusive, i.e., immediate repetition of the same measurement yields the same result. This exclusiveness corresponds to the orthogonality of the POVM operators [7].

**Definition 20.2.6 (Orthogonal measurements)** An orthogonal measurement is a POVM with orthogonal projectors  $\Pi_b$ , i.e.,  $\Pi_b^2 = \Pi_b$  for all  $b$  and  $\Pi_b \Pi_c = 0$  for  $b \neq c$ .

If we assign to each result  $b$  of an orthogonal measurement the operator  $A_{b1} = \sqrt{\Pi_b} = \Pi_b$  we obtain the usual projection formula

$$\rho \mapsto \frac{1}{\text{tr}(\Pi_b \rho)} \Pi_b \rho \Pi_b$$

corresponding to the result  $b$  of an orthogonal measurement. A special orthogonal measurement is the measurement in the computational basis, i.e., we have the operators  $\Pi_b = |b\rangle\langle b|$ . In the standard model of quantum computers, this is the only possible measurement. In the following, we will reduce POVMs to this type of measurement.

#### 20.2.4

#### Disturbance of a Generalized Measurement

In general, a measurement changes a quantum state, i.e., the states before and after the measurement differ. The difference between two states  $\rho$  and  $\tilde{\rho}$  can be quantified via the fidelity [7, 12, 13], which is given by

$$F(\rho, \tilde{\rho}) := \left( \text{tr} \sqrt{\rho^{1/2} \tilde{\rho} \rho^{1/2}} \right)^2.$$

Using this definition, the disturbance is defined as follows [12, 13].

**Definition 20.2.7** (Disturbance) The disturbance of a generalized measurement  $(A_{bj})_{b,j}$  is given by

$$1 - \int d\Omega_\Psi \sum_b F(\rho'_b, |\Psi\rangle\langle\Psi|).$$

Here  $\Omega_\Psi$  is a unitarily invariant normalized measure on the set of all states and  $\rho'_b$  denotes the non-normalized state after the measurement with result  $b$ , i.e.  $\rho'_b := \sum_j A_{bj} |\Psi\rangle\langle\Psi| A_{bj}^\dagger$ .

For this definition, we assume that we have no prior knowledge about the input state  $|\Psi\rangle\langle\Psi|$  and hence assume that the pure input states  $|\Psi\rangle$  are uniformly distributed. Then we average over all possible input states and all possible measurement results.

As discussed in Sect. 20.2.2 a POVM can be implemented by many different measurements. The problem considered here is to find a measurement with minimal disturbance. It can be shown [12, 13] that for a measurement with minimal disturbance the state transition for result  $b$  has to be

$$\rho \mapsto \frac{1}{\text{tr}(\Pi_b \rho)} \sqrt{\Pi_b} \rho \sqrt{\Pi_b}. \quad (20.2)$$

Therefore, for each operator  $\Pi_b$  there is only the single operator  $A_{b1} := \sqrt{\Pi_b}$ . Following the interpretation of Sect. 20.2.2 it is clear that there is only a single

operator since a device that obtains internally more information than necessary cannot have less disturbance.

### 20.2.5

#### Minimal-disturbing Implementation of a POVM

As discussed in Sect. 20.2.4 a minimal disturbing implementation of a POVM with operators  $\Pi_b$  corresponds to the state transition of Eq. (20.2) during the measurement process. We now outline how this state transition can be implemented with a unitary and an orthogonal measurement [7]. Since the standard model only allows orthogonal measurements we add an ancilla with Hilbert space  $\mathbb{C}^n$ , i.e., to each possible result we assign a basis vector. We denote the elements of the computational basis by  $|0\rangle, \dots, |n-1\rangle$  and initialize the ancilla with  $|0\rangle = (1, 0, \dots, 0)^T$ . Assume that we have a unitary  $U \in \mathcal{U}(dn)$  which respects the equation

$$U(|0\rangle \otimes |\Psi\rangle) = \sum_{b=0}^{n-1} |b\rangle \otimes \sqrt{\Pi_b} |\Psi\rangle \quad (20.3)$$

for all possible states  $|\Psi\rangle$  of the system. After the implementation of  $U$  we implement the orthogonal measurement of the ancilla in the computational basis. If this measurement yields the result  $b$ , we discard the ancilla system and obtain the state of Eq. (20.2).

The unitary  $U$  we want to implement is not uniquely defined by Eq. (20.3). It is only defined for the ancilla state  $|0\rangle$  whereas for other states we can implement an arbitrary transform because these states never occur. Therefore, the POVM only defines the first  $d$  columns of  $U$ . These columns can be combined to the matrix

$$M := \sum_{b=0}^{n-1} |b\rangle \otimes \sqrt{\Pi_b} \in \mathbb{C}^{dn \times d}. \quad (20.4)$$

The extension of  $M$  to a unitary  $U$  is always possible [7] since the columns of  $M$  are orthonormal as the Gram matrix

$$M^\dagger M = \sum_{b=0}^{n-1} \sqrt{\Pi_b} \sqrt{\Pi_b} = \sum_{b=0}^{n-1} \Pi_b = I_d$$

of the columns shows.

**Example 20.2.8** For the POVM with the operators  $\Pi_0, \Pi_1$ , and  $\Pi_2$  from Ex. 20.2.5 we have

$$M = \sqrt{\frac{1}{6}} \begin{pmatrix} 1 & 1 \\ 1 & 1 \\ 1 & \omega_3^2 \\ \omega_3 & 1 \\ 1 & \omega_3 \\ \omega_3^2 & 1 \end{pmatrix}.$$

$$\text{The matrix } U = \sqrt{\frac{1}{6}} \begin{pmatrix} 1 & 1 & -1 & -1 & 1 & -1 \\ 1 & 1 & 1 & 1 & 1 & 1 \\ 1 & \omega_3^2 & -1 & -\omega_3^2 & \omega_3 & -\omega_3 \\ \omega_3 & 1 & \omega_3 & 1 & \omega_3^2 & \omega_3^2 \\ 1 & \omega_3 & -1 & -\omega_3 & \omega_3^2 & -\omega_3^2 \\ \omega_3^2 & 1 & \omega_3^2 & 1 & \omega_3 & \omega_3 \end{pmatrix}$$

is a possible unitary extension of  $M$ . This extension can be obtained systematically with the methods we describe in the following.

## 20.3

### Symmetric Matrices and their Structure

The implementation of a POVM can be reduced to an orthogonal measurement in the computational basis, preceded by a unitary transform. General schemes for the decomposition of unitary matrices into elementary operations [15–17] do not necessarily yield efficient implementations. The example of the Fourier transform, however, shows that there are non-trivial unitaries which can be implemented efficiently. This efficiency can be obtained by a decomposition [18–20] which is based on the symmetry of the Fourier transform. Hence our target is to obtain a unitary with symmetry for the implementation of a POVM, too. In this section we outline basic definitions and properties of group representations which are the basis of the symmetry of POVMs and matrices. Using elementary results of representation theory we can reach our target as we will show in Sect. 20.4.

## 20.3.1

**Representations of Finite Groups**

A matrix representation assigns to each element of a group an invertible matrix [21]. This assignment respects the group operation, i.e., the group operation corresponds to the multiplication of the matrices.

**Definition 20.3.1** (Representation) Let  $G$  be a finite group. Then a homomorphism  $\sigma : G \rightarrow \mathrm{GL}_d(\mathbb{C})$  is a matrix representation, i.e.,  $\sigma(g)\sigma(h) = \sigma(gh)$  for  $g, h \in G$ . The degree of  $\sigma$ , written  $\deg(\sigma)$ , is  $d$ . A unitary representation assigns to each  $g \in G$  a unitary matrix  $\sigma(g)$ .

We refer to the set of unitary matrices of dimension  $d$  as  $\mathrm{U}(d)$ . In the following we only consider unitary representations since unitary matrices preserve the length of state vectors. As example we consider two representations of the cyclic group  $C_3 = \langle r : r^3 = 1 \rangle = \{1, r, r^2\}$ .

**Example 20.3.2** The assignments

$$r^j \mapsto \begin{pmatrix} 1 & 0 & 0 \\ 0 & \omega_3 & 0 \\ 0 & 0 & \omega_3^2 \end{pmatrix}^j \quad \text{and} \quad r^j \mapsto \begin{pmatrix} 0 & 0 & 1 \\ 1 & 0 & 0 \\ 0 & 1 & 0 \end{pmatrix}^j$$

are both unitary representations of  $C_3$ . Here,  $\omega_3 := e^{-2\pi i/3}$  is a third root of unity.

Both representations of this example are in a certain sense the same representation. More precisely, we can conjugate the second matrix for  $j \in \{0, 1, 2\}$  with the Fourier transform

$$F_3 := \sqrt{\frac{1}{3}} \begin{pmatrix} 1 & 1 & 1 \\ 1 & \omega_3 & \omega_3^2 \\ 1 & \omega_3^2 & \omega_3 \end{pmatrix}$$

and obtain the diagonal matrices of the first assignment. Therefore, using this basis transform both representations become equal. In general, this equivalence of representations is defined as follows [21].

**Definition 20.3.3** (Equivalence) Two unitary representations  $\sigma, \tau : G \rightarrow \mathrm{U}(d)$  are equivalent if there is a unitary  $A \in \mathrm{U}(d)$  with  $\sigma(g) = A\tau(g)A^\dagger$  for all  $g \in G$ .

The most important representations of a group are the irreducible representations. A finite group only has a finite number of inequivalent irreducible representations [22]. In the following, we identify each set of equivalent irreducible representations with a representative  $\kappa_j$ , i.e., the group has the irreducible representations  $\kappa_1, \dots, \kappa_z$ . An irreducible representation is defined by the action of the representation on vectors [22].

**Definition 20.3.4** (Irreducibility) A representation  $\sigma : G \rightarrow \mathrm{U}(d)$  is irreducible if for all subspaces  $V \leq \mathbb{C}^d$  with  $\sigma(g)V \subseteq V$  for all  $g \in G$  the equation  $V = \{0\}$  or  $V = \mathbb{C}^d$  holds.

The importance of the irreducible representations is based on the fact that all representations of a group can be decomposed into a direct sum of irreducible representations [22]. The analysis of representations can be simplified by this decomposition in many cases.

**Lemma 20.3.5** *Let  $\sigma : G \rightarrow \mathrm{U}(d)$  be a representation and  $\kappa_1, \dots, \kappa_z$  the irreducible unitary representations of  $G$ . Then there is a unitary  $A \in \mathrm{U}(d)$  with*

$$A\sigma A^\dagger = \bigoplus_j \left( I_{m_j} \otimes \kappa_j \right).$$

The numbers  $m_j$  are the multiplicities [23] of the irreducible representations  $\kappa_j$  in  $\sigma$ , i.e., there are  $m_j$  copies of  $\kappa_j$  in  $A\sigma A^\dagger$ .

**Example 20.3.6** The group  $C_3 = \langle r : r^3 = 1 \rangle$  has three irreducible representations. They are defined by

$$\kappa_1(r) = (1), \quad \kappa_2(r) = (\omega_3), \quad \text{and} \quad \kappa_3(r) = (\omega_3^2).$$

Both representations of Ex. 20.3.2 are equivalent to  $\kappa_1 \oplus \kappa_2 \oplus \kappa_3$ .

### 20.3.2

#### Projective Representations

A generalization of unitary representations are projective representations which are sometimes used in the context of quantum systems. This generalization is motivated by the irrelevance of phase factors for quantum systems, i.e., the state vectors  $|\Psi\rangle$  and  $e^{i\phi}|\Psi\rangle$  describe the same state for all  $\phi \in \mathbb{R}$ . For a projective representation the condition  $\sigma(g)\sigma(h) = \sigma(gh)$  of Definition 20.3.1 is replaced by a weaker condition [21].

**Definition 20.3.7** (Projective representation) A projective representation is an assignment  $\sigma : G \rightarrow \mathrm{U}(d)$  with

$$\sigma(g)\sigma(h) = \gamma_{g,h}\sigma(gh),$$

where  $\gamma_{g,h} \in \mathbb{C}$  with  $|\gamma_{g,h}| = 1$  for all  $g$  and  $h$ . The set  $\{\gamma_{g,h} : g, h \in G\}$  is called factor set.

**Example 20.3.8** The assignment  $\sigma : C_2 \times C_2 \rightarrow \mathrm{U}(2)$  which is defined by

$$\sigma((1,1)) = \begin{pmatrix} 1 & 0 \\ 0 & 1 \end{pmatrix}, \quad \sigma((1,s)) = \begin{pmatrix} 1 & 0 \\ 0 & -1 \end{pmatrix},$$

$$\sigma((r,1)) = \begin{pmatrix} 0 & 1 \\ 1 & 0 \end{pmatrix}, \text{ and } \sigma((r,s)) = \begin{pmatrix} 0 & 1 \\ -1 & 0 \end{pmatrix}$$

is a projective representation of  $C_2 \times C_2 = \{(1,1), (r,1), (1,s), (r,s)\}$  where  $r^2 = s^2 = 1$ .

Projective representations can be transformed into non-projective representations [21]. For this construction we consider the group  $H := \langle \gamma_{g,h} : g, h \in G \rangle$  which is generated by the factor set. Together with  $G$  this group allows to define an extension  $\hat{G}$  of  $G$  and a non-projective representation  $\hat{\sigma} : \hat{G} \rightarrow \mathrm{U}(d)$ .

**Lemma 20.3.9** *Let  $\sigma : G \rightarrow \mathrm{U}(d)$  be a projective representation with the factor set  $\gamma_{g,h}$  generating the group  $H = \langle \gamma_{g,h} : g, h \in G \rangle$ . Define the group  $\hat{G} := \{(g, h) : g \in G, h \in H\}$  with the multiplication*

$$(g, h)(g', h') = (gg', \gamma_{g,g'}hh').$$

*Then  $\hat{\sigma}((g, h)) := h\sigma(g)$  is a representation of  $\hat{G}$ .*

The representation  $\hat{\sigma}$  is an extension of  $\sigma$  since we have  $\hat{\sigma}((g,1)) = \sigma(g)$  for all  $g \in G$ . The set  $\{\sigma(g) : g \in G\}$  is extended to the group  $\langle \sigma(g) | g \in G \rangle$ . From Def. 20.3.7 it follows that all matrices in this group are scalar multiples of the matrices  $\sigma(g)$ .

**Example 20.3.10** Consider the representation  $\sigma$  of Ex. 20.3.8. We have  $H = \{1, -1\}$  and  $\hat{G}$  is isomorphic to the dihedral group with eight elements. The extension  $\hat{\sigma}$  of  $\sigma$  is defined by

$$\begin{aligned} \hat{\sigma}(((1,1),1)) &= \begin{pmatrix} 1 & 0 \\ 0 & 1 \end{pmatrix}, & \hat{\sigma}(((1,s),1)) &= \begin{pmatrix} 1 & 0 \\ 0 & -1 \end{pmatrix}, \\ \hat{\sigma}(((r,1),1)) &= \begin{pmatrix} 0 & 1 \\ 1 & 0 \end{pmatrix}, & \hat{\sigma}(((r,s),1)) &= \begin{pmatrix} 0 & 1 \\ -1 & 0 \end{pmatrix}, \\ \hat{\sigma}(((1,1),-1)) &= \begin{pmatrix} -1 & 0 \\ 0 & -1 \end{pmatrix}, & \hat{\sigma}(((1,s),-1)) &= \begin{pmatrix} -1 & 0 \\ 0 & 1 \end{pmatrix}, \\ \hat{\sigma}(((r,1),-1)) &= \begin{pmatrix} 0 & -1 \\ -1 & 0 \end{pmatrix}, & \hat{\sigma}(((r,s),-1)) &= \begin{pmatrix} 0 & -1 \\ 1 & 0 \end{pmatrix}. \end{aligned}$$

Using the extension of Lemma 20.3.9, we can assume in the following that all representations are non-projective. This allows to circumvent some problems when computing with projective representations, e.g., it is not trivial to define the direct sum of two projective representation of the same group when the factor sets differ [24].

## 20.3.3

**Symmetry of a Matrix and Schur's Lemma**

The symmetry of an object is defined by its invariance under the action of a group. In the case of matrices the action of the group is defined by two matrix representations [18].

**Definition 20.3.11** (Matrix symmetry) Let  $\sigma : G \rightarrow \mathrm{U}(m)$  and  $\tau : G \rightarrow \mathrm{U}(n)$  be two representations of the group  $G$ . Then the matrix  $M \in \mathbb{C}^{m \times n}$  has the symmetry  $(G, \sigma, \tau)$  if  $\sigma(g)M = M\tau(g)$  holds for all  $g \in G$ . We write  $\sigma M = M\tau$  for short.

The symmetry is completely defined if it is specified for the generators of the group. In the following we use this fact to obtain a concise notation of matrix symmetries.

**Example 20.3.12** Let  $\alpha, \beta, \gamma \in \mathbb{C}$ . Then the equation

$$\begin{pmatrix} 1 & 0 & 0 \\ 0 & \omega_3 & 0 \\ 0 & 0 & \omega_3^2 \end{pmatrix} \begin{pmatrix} \alpha & \alpha & \alpha \\ \beta & \beta\omega_3 & \beta\omega_3^2 \\ \gamma & \gamma\omega_3^2 & \gamma\omega_3 \end{pmatrix} = \begin{pmatrix} \alpha & \alpha & \alpha \\ \beta & \beta\omega_3 & \beta\omega_3^2 \\ \gamma & \gamma\omega_3^2 & \gamma\omega_3 \end{pmatrix} \begin{pmatrix} 0 & 0 & 1 \\ 1 & 0 & 0 \\ 0 & 1 & 0 \end{pmatrix}$$

defines a symmetry of the matrix containing the parameters  $\alpha, \beta$ , and  $\gamma$ . The corresponding symmetry group is  $C_3$  and both representation are defined in Ex. 20.3.2.

The example suggests that a matrix with symmetry has a special structure. In order to characterize the structure of matrices with symmetry we analyze the intertwining space [18] of two representations  $\sigma$  and  $\tau$ . This is the set of all matrices  $M$  with  $\sigma M = M\tau$ . Obviously, this set is a linear space.

**Definition 20.3.13** (Intertwining space) The intertwining space  $\mathrm{Int}(\sigma, \tau)$  of two representations  $\sigma : G \rightarrow \mathrm{U}(m)$  and  $\tau : G \rightarrow \mathrm{U}(n)$  is the linear space

$$\mathrm{Int}(\sigma, \tau) := \{M \in \mathbb{C}^{m \times n} : \sigma M = M\tau\}.$$

A matrix  $M$  has the symmetry  $(G, \sigma, \tau)$  if and only if  $M \in \mathrm{Int}(\sigma, \tau)$ . Hence the structure of a matrix with symmetry  $(G, \sigma, \tau)$  is specified by the structure of the intertwining space  $\mathrm{Int}(\sigma, \tau)$ . The latter can be easily characterized if we assume that  $\sigma$  and  $\tau$  are decomposed into direct sums of the  $\kappa_j$  with respect to the standard basis, i.e.,

$$\sigma = \bigoplus_{j=1}^z (I_{m_j} \otimes \kappa_j) \quad \text{and} \quad \tau = \bigoplus_{j=1}^z (I_{n_j} \otimes \kappa_j), \quad (20.5)$$

where  $z$  is the number of inequivalent irreducible representations of  $G$ . Furthermore,  $m_j$  and  $n_j$  are the multiplicities of the irreducible representation  $\kappa_j$  in  $\sigma$  and  $\tau$ , respectively. (Note that the multiplicities might be zero.) Using

Schur's lemma [22] we obtain the following simple structure of the intertwining space [20]:

**Theorem 20.3.14** *Let  $\sigma : G \rightarrow \mathrm{U}(m)$  and  $\tau : G \rightarrow \mathrm{U}(n)$  be two representations of  $G$  as defined in Eq. (20.5). Then the equation*

$$\mathrm{Int}(\sigma, \tau) = (\mathbb{C}^{m_1 \times n_1} \otimes I_{\deg(\kappa_1)}) \oplus \dots \oplus (\mathbb{C}^{m_z \times n_z} \otimes I_{\deg(\kappa_z)}) \quad (20.6)$$

holds.

Note that for  $m_j = 0$  and  $n_j \neq 0$  we have a matrix of size  $0 \times n_j$ , i.e., the direct sum of this component corresponds to  $n_j \deg(\kappa_j)$  zero columns. For  $m_j \neq 0$  we analogously insert  $m_j \deg(\kappa_j)$  zero rows.

**Example 20.3.15** With the representations of Ex. 20.3.6 let  $\sigma = \kappa_1 \oplus \kappa_3$  and  $\tau = \kappa_1 \oplus \kappa_2 \oplus \kappa_3$ . Then

$$\mathrm{Int}(\sigma, \tau) = \left\{ \begin{pmatrix} \alpha & 0 & 0 \\ 0 & 0 & \beta \end{pmatrix} : \alpha, \beta \in \mathbb{C} \right\}.$$

The unitarity of a matrix with symmetry restricts the set of possible representations for the symmetry. Assume that  $M$  is a unitary matrix with the symmetry  $(G, \sigma, \tau)$ . Let  $\sigma$  and  $\tau$  be decomposed into a direct sum of irreducible representations as defined in Eq. (20.5). Then  $M = \bigoplus_j (M_j \otimes I_{\deg(\kappa_j)})$  with unitary matrices  $M_j$  of size  $m_j \times n_j$ . For  $m_j \neq n_j$  the matrix  $M_j$  is not a square matrix and cannot be unitary. Hence for a unitary matrix with symmetry  $\sigma M = M\tau$  we have  $m_j = n_j$ , i.e., the representations  $\sigma$  and  $\tau$  are equivalent. This observation is the guideline for the construction in Sect. 20.4.

### 20.3.4

#### Symmetric POVMs Define Matrices with Symmetry

The symmetry of a POVM is defined by the invariance of the set of its operators  $\Pi_b$  under the action of a group which is given by a group representation. As discussed in Sect. 20.3.2 we can assume that the representation is non-projective since the set of POVM operators is not affected by the extension of the group in order to obtain a non-projective representation.

**Definition 20.3.16** (Symmetric POVM) The POVM  $P = \{\Pi_0, \dots, \Pi_{n-1}\}$  with  $\Pi_b \neq \Pi_c$  for  $b \neq c$  is symmetric with respect to the group  $G$  and the representation  $\sigma : G \rightarrow \mathrm{U}(d)$  if  $\sigma(g)\Pi_b\sigma(g)^\dagger \in P$  for all  $b$  and all  $g \in G$ .

Symmetric POVMs are also referred to as group-covariant POVMs [25, 26].

**Example 20.3.17** Consider the POVM  $P = \{\Pi_0, \Pi_1, \Pi_2\}$  with the operators of Ex. 20.2.5. This POVM is symmetric with respect to the group  $C_3$  and the representation  $\sigma : C_3 \rightarrow \mathrm{U}(2)$  with  $\sigma(r) = \mathrm{diag}(1, \omega_3)$ .

The invariance of the set of operators  $\Pi_b$  under the action of the group implies that for each  $g \in G$  the set of operators is permuted. Hence the representation  $\sigma$  of a POVM symmetry gives rise to a permutation representation  $\pi : G \rightarrow S_n$  where  $S_n$  denotes the symmetric group on  $n$  letters. The representation  $\pi$  is defined by the equation

$$\sigma(g)\Pi_b\sigma(g)^\dagger = \Pi_{\pi(g)b}.$$

Here  $\pi$  is well-defined because all operators  $\Pi_b$  are distinct. To see that  $\pi$  is a representation one checks that

$$\begin{aligned}\Pi_{\pi(gh)b} &= \sigma(gh)\Pi_b\sigma(gh)^\dagger = \sigma(g)\sigma(h)\Pi_b\sigma(h)^\dagger\sigma(g)^\dagger \\ &= \sigma(g)\Pi_{\pi(h)b}\sigma(g)^\dagger = \Pi_{\pi(g)\pi(h)b}.\end{aligned}$$

We have  $\pi(gh)b = \pi(g)\pi(h)b$  for all  $g, h \in G$  and  $b$  since the  $\Pi_b$  are distinct. This shows the equation  $\pi(gh) = \pi(g)\pi(h)$ .

We now analyze the consequences of the POVM symmetry for the implementation scheme of Sect. 20.2.5. The basic idea of this scheme is to extend the matrix  $M$  of Eq. (20.4) to a unitary matrix  $U$ . The matrix  $M$  consists of the square roots of the operators  $\Pi_b$ . These square roots have the same symmetry as the operators  $\Pi_b$ . Consequently, the matrix  $M$  has a symmetry as we show in the following. Define for  $\pi$  the permutation matrix representation  $\sigma_\pi : G \rightarrow U(n)$  by  $\sigma_\pi(g)|j\rangle := |\pi(g)j\rangle$ . Then the POVM symmetry implies the symmetry  $(\sigma_\pi \otimes \sigma)M = M\sigma$  of the matrix  $M$ :

$$\begin{aligned}(\sigma_\pi(g) \otimes \sigma(g)) \left( \sum_{b=0}^{n-1} |b\rangle \otimes \sqrt{\Pi_b} \right) \sigma(g)^\dagger &= \sum_{b=0}^{n-1} \sigma_\pi(g)|b\rangle \otimes \sigma(g)\sqrt{\Pi_b}\sigma(g)^\dagger \\ &= \sum_{b=0}^{n-1} |\pi(g)b\rangle \otimes \sqrt{\Pi_{\pi(g)b}}\end{aligned}$$

The last expression differs from the definition in Eq. (20.4) only by a permutation of the summation order.

**Example 20.3.18** The matrix  $M$  of Ex. 20.2.8 with the POVM symmetry of Ex. 20.3.17 has the symmetry  $(C_3, \sigma_\pi \otimes \sigma, \sigma)$  where

$$(\sigma_\pi \otimes \sigma)(r) = \begin{pmatrix} 0 & 0 & 1 \\ 1 & 0 & 0 \\ 0 & 1 & 0 \end{pmatrix} \otimes \begin{pmatrix} 1 & 0 \\ 0 & \omega_3 \end{pmatrix} \quad \text{and} \quad \sigma(r) = \begin{pmatrix} 1 & 0 \\ 0 & \omega_3 \end{pmatrix}.$$

## 20.4

### Implementation of Symmetric POVMs

For the implementation of a POVM we extend the matrix  $M$  of Eq. (20.4) to a unitary  $U$ . As mentioned in Sect. 20.3.4, the matrix  $M$  has the symmetry  $(G, \sigma_\pi \otimes \sigma, \sigma)$  when the POVM has the symmetry group  $G$  with representation  $\sigma$ . Our goal is to construct a unitary  $U$  which possesses a symmetry, too. This can be attained with a procedure consisting of two extension steps. In the first step the symmetry of  $M$  is extended to the symmetry

$$(G, \sigma_\pi \otimes \sigma, \sigma \oplus \tilde{\sigma}) \quad (20.7)$$

with a suitable representation  $\tilde{\sigma}$ . In the second step we choose an extension  $U$  of  $M$  in the corresponding intertwining space  $\text{Int}(\sigma_\pi \otimes \sigma, \sigma \oplus \tilde{\sigma})$ . As noted at the end of Sect. 20.3.3 our guideline is to construct a representation  $\tilde{\sigma}$  such that  $\sigma_\pi \otimes \sigma$  and  $\sigma \oplus \tilde{\sigma}$  are equivalent. We show that this extension is always possible and how we can construct a symmetric matrix  $U$ .

We decompose both representations of the symmetry of  $M$  into irreducible components. For the extension procedure it is necessary to take the unitary matrices of Lemma 20.3.5 for the conjugation into account. We have  $A \in \text{U}(dn)$  and  $B \in \text{U}(d)$  which decompose  $\sigma_\pi \otimes \sigma$  and  $\sigma$ :

$$A(\sigma_\pi \otimes \sigma)A^\dagger = \bigoplus_{j=1}^z (I_{m_j} \otimes \kappa_j) \quad \text{and} \quad B\sigma B^\dagger = \bigoplus_{j=1}^z (I_{n_j} \otimes \kappa_j). \quad (20.8)$$

**Example 20.4.1** For Ex. 20.2.8 we obtain  $A = X_6(F_3 \otimes I_2)$  and  $B = I_2$  where  $X_6 = \sum_{j=0}^5 |j+1 \bmod 6\rangle\langle j|$  is the cyclic shift matrix of size  $6 \times 6$ . The decompositions are

$$A(\sigma_\pi \otimes \sigma)A^\dagger = (I_2 \otimes \kappa_1) \oplus (I_2 \otimes \kappa_2) \oplus (I_2 \otimes \kappa_3) \quad \text{and} \quad B\sigma B^\dagger = \kappa_1 \oplus \kappa_2$$

with  $\kappa_1, \kappa_2$ , and  $\kappa_3$  from Ex. 20.3.6.

Using Eq. (20.8) the symmetry  $(\sigma_\pi \otimes \sigma)M = M\sigma$  can be rewritten as

$$\bigoplus_{j=1}^z (I_{m_j} \otimes \kappa_j)N = N \bigoplus_{j=1}^z (I_{n_j} \otimes \kappa_j) \quad (20.9)$$

where we set  $N := AMB^\dagger \in \mathbb{C}^{dn \times d}$ . The multiplication with unitaries from the left and the right preserves the column orthogonality of a matrix. Consequently, both  $M$  and  $N$  have orthogonal columns.

**Example 20.4.2** For the example we obtain

$$N = \sqrt{\frac{1}{2}} \begin{pmatrix} 1 & 1 & 0 & 0 & 0 & 0 \\ 0 & 0 & 1 & 1 & 0 & 0 \end{pmatrix}^T.$$

The symmetry we want to obtain for an extended matrix  $W$  is described by the equation

$$\bigoplus_{j=1}^z (I_{m_j} \otimes \kappa_j) W = W \left( \bigoplus_{j=1}^z (I_{n_j} \otimes \kappa_j) \oplus \bigoplus_{j=1}^z (I_{m_j - n_j} \otimes \kappa_j) \right), \quad (20.10)$$

i.e., we complement the representation on the right side of Eq. (20.9). This is only possible if  $m_j \geq n_j$  holds for all  $j$ . For symmetric POVMs these inequalities always hold: The permutation matrix representation  $\sigma_\pi$  contains the trivial representation  $g \mapsto (1)$  of rank one at least once because the vector  $(1, \dots, 1)^T$  is invariant under all permutations of the positions. Hence the decomposition  $C(\sigma_\pi \otimes \sigma)C^\dagger = \sigma \oplus \sigma'$  holds for an appropriate unitary  $C \in U(dn)$  and an appropriate representation  $\sigma'$ . This shows that  $m_j \geq n_j$  for all  $j$  and that the first step of the extension procedure is always possible.

In the second step we extend the matrix  $N$  to a symmetric unitary  $W = (N|\tilde{N})$  with  $\tilde{N} \in \mathbb{C}^{dn \times d(n-1)}$  by appending appropriate orthogonal columns. We can directly choose the matrix  $W$  in the intertwining space of the symmetry which is defined in Eq. (20.10).

**Example 20.4.3** All possible extensions of  $N$  from Ex. 20.4.2 are specified by

$$W = \sqrt{\frac{1}{2}} \begin{pmatrix} 1 & 0 & * & 0 & 0 & 0 \\ 1 & 0 & * & 0 & 0 & 0 \\ 0 & 1 & 0 & * & 0 & 0 \\ 0 & 1 & 0 & * & 0 & 0 \\ 0 & 0 & 0 & 0 & * & * \\ 0 & 0 & 0 & 0 & * & * \end{pmatrix}$$

where  $*$  denotes the entries we can choose under the condition that  $W$  is unitary. The representations in Eq. (20.10) are  $(I_2 \otimes \kappa_1) \oplus (I_2 \otimes \kappa_2) \oplus (I_2 \otimes \kappa_3)$  and  $(\kappa_1 \oplus \kappa_2) \oplus \kappa_1 \oplus \kappa_2 \oplus (I_2 \otimes \kappa_3)$ .

We have to prove that it is always possible to construct the unitary  $W$  in the intertwining space. This proof can be simplified if we modify the representation on the right hand side of Eq. (20.10) in such a way that the irreducible representations have the same order on both sides. To accomplish this we permute the columns of  $W$  by a right multiplication with an appropriate permutation matrix  $P$ . The resulting symmetry is defined by

$$\bigoplus_{j=1}^z (I_{m_j} \otimes \kappa_j) WP = WP \bigoplus_{j=1}^z (I_{m_j} \otimes \kappa_j).$$

The matrix  $N$  defines  $d$  columns of  $WP$ . We can construct the other  $d(n-1)$  orthogonal columns arbitrarily under the condition that we take the structure

of the intertwining space into account. With Lemma 20.3.14 we can write  $WP = \bigoplus_j (M_j \otimes I_{\deg(\kappa_j)})$  with square matrices  $M_j$ . Since all  $M_j$  are square matrices and the columns defined by  $N$  are orthogonal the extension to unitary  $M_j$  is always possible. We can optimize the implementation of the POVM if we use the degrees of freedom of this extension.

**Example 20.4.4** With the permutation

$$P := \begin{pmatrix} 1 & 0 & 0 & 0 & 0 & 0 \\ 0 & 0 & 1 & 0 & 0 & 0 \\ 0 & 1 & 0 & 0 & 0 & 0 \\ 0 & 0 & 0 & 1 & 0 & 0 \\ 0 & 0 & 0 & 0 & 1 & 0 \\ 0 & 0 & 0 & 0 & 0 & 1 \end{pmatrix} \quad \text{we obtain } WP = \sqrt{\frac{1}{2}} \begin{pmatrix} 1 & * & 0 & 0 & 0 & 0 \\ 1 & * & 0 & 0 & 0 & 0 \\ 0 & 0 & 1 & * & 0 & 0 \\ 0 & 0 & 1 & * & 0 & 0 \\ 0 & 0 & 0 & 0 & * & * \\ 0 & 0 & 0 & 0 & * & * \end{pmatrix}$$

for the matrix  $W$  of Ex. 20.4.3. Hence we can exemplarily choose  $WP = I_3 \otimes F_2$ .

The matrix  $W$  is a symmetric extension of  $N$  and can be obtained from  $WP$  by undoing the permutation of the columns. However, to complete the second step we need an extension of  $M$ , and not of  $N$ . The transition from  $M$  to  $N$  is defined by  $M = A^\dagger N B$  and we want to extend this equation to an equation describing the transition from  $U$  to  $W$ . This extension is not uniquely defined because only the multiplicities of the  $\kappa_j$  in  $\tilde{\sigma}$  of Eq. (20.7) are specified. In the following, we characterize all possible extensions.

By using Eq. (20.8) we can rewrite the symmetry of  $W$  in Eq. (20.10) as follows:

$$A(\sigma_\pi \otimes \sigma)A^\dagger W = W \left( B\sigma B^\dagger \oplus \bigoplus_{j=1}^z (I_{m_j-n_j} \otimes \kappa_j) \right).$$

Using the representation

$$\tilde{\sigma} := \tilde{B}^\dagger \left( \bigoplus_{j=1}^z I_{m_j-n_j} \otimes \kappa_j \right) \tilde{B},$$

where  $\tilde{B}$  is an arbitrary unitary matrix, we obtain

$$A(\sigma_\pi \otimes \sigma)A^\dagger W = W(B \oplus \tilde{B})(\sigma \oplus \tilde{\sigma})(B \oplus \tilde{B})^\dagger. \quad (20.11)$$

We rearrange the matrices of Eq. (20.11) and obtain  $(\sigma_\pi \otimes \sigma)U = U(\sigma \oplus \tilde{\sigma})$  with

$$U := A^\dagger W(B \oplus \tilde{B}) = A^\dagger(AMB^\dagger|\tilde{N})(B \oplus \tilde{B}) = (M|A^\dagger\tilde{N}\tilde{B}). \quad (20.12)$$

Consequently, the matrix  $U$  is a unitary extension of  $M$  with appropriate symmetry. This completes the second step of the extension procedure. By varying

the matrix  $\tilde{B}$  we obtain all possible representations  $\tilde{\sigma}$  which lead to equivalent representations on both sides of Eq. (20.11). From Eq. (20.12) it follows that the matrix  $\tilde{B}$  has no effect on the prescribed part  $M$  of the unitary matrix  $U$ . Hence the matrix  $\tilde{B}$  can be used to optimize the implementation.

**Example 20.4.5** For the POVM of Ex. 20.2.5 with  $W$  of Ex. 20.4.4, we choose  $\tilde{B} = I_4$  and obtain the unitary  $U$  of Ex. 20.2.8.

## 20.5

### Cyclic and Heisenberg-Weyl Groups

We apply the general implementation scheme of Sect. 20.4 to two physically relevant families of POVMs: We obtain efficient quantum circuits for POVMs on a qubit with cyclic symmetry and efficient implementation schemes for POVMs with Heisenberg-Weyl symmetry on systems of arbitrary finite dimension.

We use the following notations: For  $d \geq 2$  we define the cyclic shift and phase matrices

$$X_d := \sum_{j=0}^{d-1} |(j+1) \bmod d\rangle \langle j| \quad \text{and} \quad Z_d := \sum_{j=0}^{d-1} \omega_d^j |j\rangle \langle j|$$

with the root  $\omega_d := e^{-2\pi i/d}$  of unity. The matrix

$$F_d := \sqrt{\frac{1}{d}} \left( \omega_d^{kl} \right)_{k,l=0}^{d-1}$$

is the discrete Fourier transform [27].

#### 20.5.1

##### Cyclic Groups

Quantum states on a great circle of the Bloch sphere with cyclic symmetry constitute a very simple yet important class of ensembles. We can assume without loss of generality that the states are on the plane which is perpendicular to the  $z$ -axis, i.e., the states can be described by the state vectors

$$|\phi_t\rangle := \sqrt{\frac{1}{2}} \left( |0\rangle + e^{it} |1\rangle \right)$$

for certain  $t$ . These states are the orbit of the time evolution with Hamiltonian  $\sigma_z$ . For example, the measurement of these states can be used to estimate the time, i.e., these systems can be used as simple models of quantum clocks. A finite ensemble is obtained by discretization of time. For some optimality criteria of measurements, e.g., the mutual information [5,28] or detection error

probability [29,30], there exists an optimal POVM with cyclic symmetry. Consequently, the implementation of POVMs with this symmetry is of physical relevance for the estimation of time using this clock model.

Let  $n \geq 2$  be a natural number and  $C_n := \langle r : r^n = 1 \rangle$  the cyclic group with  $n$  elements and generator  $r$ . The rotation of order  $n$  about the  $z$ -axis of the Bloch sphere corresponds to the representation  $\sigma : C_n \rightarrow \mathrm{U}(2)$  with  $\sigma(r^j) = R_n^j$  for  $R_n := \mathrm{diag}(1, \omega_n)$ . The orbit of the vector  $\sqrt{1/n}(1, 1)^T$  leads to the POVM operators

$$\Pi_b := \frac{1}{n} \begin{pmatrix} 1 & 0 \\ 0 & \omega_n^b \end{pmatrix} \begin{pmatrix} 1 & 1 \\ 1 & 1 \end{pmatrix} \begin{pmatrix} 1 & 0 \\ 0 & \omega_n^{-b} \end{pmatrix} = \frac{1}{n} \begin{pmatrix} 1 & \omega_n^{-b} \\ \omega_n^b & 1 \end{pmatrix}$$

for  $b \in \{0, \dots, n-1\}$ . With the appropriate trace normalization these operators are density matrices which correspond to states with the cyclic symmetry in the Bloch sphere. The square root of the operator  $\Pi_b$  is

$$\sqrt{\Pi_b} = \sqrt{\frac{1}{2n}} \begin{pmatrix} 1 & \omega_n^{-b} \\ \omega_n^b & 1 \end{pmatrix}.$$

Following the implementation scheme of Sect. 20.4 we write these square roots as matrix  $M$  and obtain

$$M = \sum_{b=0}^{n-1} |b\rangle \otimes \sqrt{\Pi_b} \in \mathbb{C}^{2n \times 2}.$$

This matrix has the symmetry group  $C_n$ . The symmetry is defined by the equation

$$(X_n \otimes R_n)M = MR_n \quad (20.13)$$

because  $R_n \sqrt{\Pi_b} R_n^\dagger = \sqrt{\Pi_{b+1 \bmod n}}$  and the equations

$$\begin{aligned} (X_n \otimes R_n)MR_n^\dagger &= (X_n \otimes R_n) \left( \sum_{b=0}^{n-1} |b\rangle \otimes \sqrt{\Pi_b} \right) R_n^\dagger \\ &= \sum_{b=0}^{n-1} |(b+1) \bmod n\rangle \otimes \sqrt{\Pi_{b+1 \bmod n}} = M \end{aligned}$$

hold. We decompose the representation  $r^j \mapsto (X_n \otimes R_n)^j$  on the left hand side of Eq. (20.13) in two steps. In the first step we diagonalize  $X_n$  to  $Z_n$  because then the second step of the decomposition merely consists of a reordering of the irreducible components. We use the equation  $F_n X_n F_n^\dagger = Z_n$  and rewrite the symmetry of Eq. (20.13) as

$$(Z_n \otimes R_n)(F_n \otimes I_2)M = (F_n \otimes I_2)MR_n. \quad (20.14)$$

The cyclic shift  $X_{2n}$  accords to the necessary reordering of the second step: The right hand side of

$$X_{2n}(Z_n \otimes R_n)X_{2n}^\dagger = Z_n \otimes I_2 \quad (20.15)$$

corresponds to the decomposition  $\bigoplus_{\ell=0}^{n-1} (I_2 \otimes \kappa_\ell)$  of  $\sigma_\pi \otimes \sigma$  into a direct sum of the irreducible representations  $\kappa_\ell : j \mapsto (\omega_n^{j\ell})$ . We insert Eq. (20.15) into Eq. (20.14) and obtain

$$(Z_n \otimes I_2)X_{2n}(F_n \otimes I_2)M = X_{2n}(F_n \otimes I_2)MR_n.$$

Hence the resulting matrix symmetry is  $(Z_n \otimes I_2)N = NR_n$  where we have

$$N := X_{2n}(F_n \otimes I_2)M = \sqrt{\frac{1}{2}} \begin{pmatrix} 1 & 0 \\ 1 & 0 \\ 0 & 1 \\ 0 & 1 \\ 0 & 0 \\ \vdots & \vdots \\ 0 & 0 \end{pmatrix} \in \mathbb{C}^{2n \times 2}.$$

The matrices  $A$  and  $B$  of Sect. 20.4 are  $A = X_{2n}(F_n \otimes I_2)$  and  $B = I_2$ . The extended symmetry of the matrix  $W \in \mathrm{U}(2n)$  we want to construct is  $(Z_n \otimes I_2)W = W(I_2 \otimes Z_n)$ . The order of the representations on the right hand side of this equation differs from the order described in Eq. (20.10). This modification of the construction of Sect. 20.4 allows some simplifications. We choose  $W := (I_n \otimes F_2)K^\dagger$  as intertwining matrix where  $K \in \mathrm{U}(2n)$  is the permutation matrix that can be written as

$$K|2j\rangle = |j\rangle \quad \text{and} \quad K|2j+1\rangle = |n+j\rangle$$

for  $j \in \{0, \dots, n-1\}$ . With the matrix  $W$  we have all crucial matrices for the construction. The resulting unitary for the implementation of the POVM is

$$U := A^\dagger W(B \oplus \tilde{B}) = (F_n^\dagger \otimes I_2)X_{2n}^\dagger(I_n \otimes F_2)K^\dagger \in \mathrm{U}(2n).$$

Here we extend the matrix  $B = I_2$  with  $\tilde{B} = I_{2n-2}$  to  $B \oplus \tilde{B} = I_{2n}$  because this is obviously the simplest extension which can be implemented.

In the case  $n = 2^m$  with  $m \geq 1$  the ancilla is a register of qubits, i.e., we can decompose the unitary  $U$  directly into elementary gates. The ancilla consists of  $m$  qubits and the total system of  $m+1$  qubits. The Fourier transform  $F_{2^m}$  can be implemented efficiently on a quantum register [27, 31] for all  $m$ . The unitary  $K$  corresponds to a cyclic shift  $|x_1 x_2 \dots x_m x_{m+1}\rangle \mapsto |x_{m+1} x_1 x_2 \dots x_m\rangle$

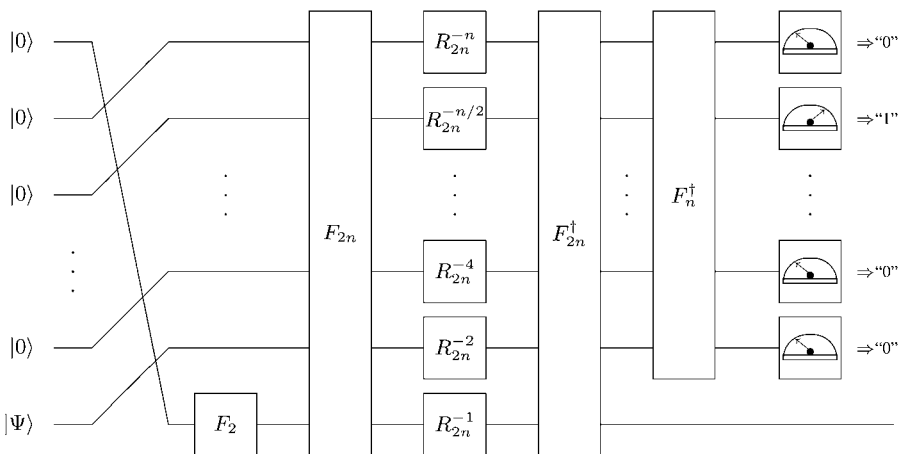


**Fig. 20.1** Quantum circuit for the implementation of the POVM on a qubit with cyclic symmetry.

of qubits. The shift  $X_{2n}$  can be implemented efficiently on a quantum register, too: We use the conjugation  $X_{2n}^\dagger = F_{2n}^\dagger Z_{2n}^\dagger F_{2n}$  and the decomposition

$$Z_{2n}^\dagger = R_{2n}^{-n} \otimes R_{2n}^{-n/2} \otimes \dots \otimes R_{2n}^{-1}.$$

In summary, for  $n = 2^m$  the unitary  $U$  can be written as

$$U = (F_n^\dagger \otimes I_2) F_{2n}^\dagger Z_{2n}^\dagger F_{2n} (I_n \otimes F_2) K^\dagger.$$

The corresponding quantum circuit is shown in Fig. 20.1.

### 20.5.2

#### Heisenberg-Weyl Groups

Heisenberg's uncertainty principle states that it is not possible to determine the position and momentum of a particle precisely at the same time. However, we can measure both values simultaneously if we content ourselves with approximations. The idea of this measurement [32] is to use a POVM with operators  $\Pi_{j,k}$  which are defined by appropriate shifts in the position and momentum spaces of an initial operator  $\Pi$ . Then the measurement result  $(j, k)$  can be interpreted as position  $j$  and momentum  $k$  of the particle. To obtain useful results the operator  $\Pi$  has to be localized both in position and momentum space. We only consider finite-dimensional systems where such a measurement is described by operators with Heisenberg-Weyl symmetry [33], i.e., the symmetry group is generated by the shifts  $X_d$  and phases  $Z_d$ .

We consider a quantum system of dimension  $d \geq 2$ . The Heisenberg-Weyl group  $G = \langle X_d, Z_d \rangle$  is a group with  $d^3$  elements [9]. For the initial positive

operator  $\Pi$  with trace normalization  $\text{tr}(\Pi) = 1/d$  we consider the POVM with  $d^2$  operators

$$Z_d^k X_d^j \Pi X_d^{-j} Z_d^{-k} \text{ for } j, k = 0, \dots, d-1.$$

The representation of the POVM symmetry, the Heisenberg-Weyl group, is given as a matrix group. Hence we consider the representation  $\sigma(X_d) = X_d$  and  $\sigma(Z_d) = Z_d$  with the notation of Def. 20.3.16. Elementary computations with the character of this representation show that  $\sigma$  is an irreducible representation.

For the Heisenberg-Weyl symmetric POVM with initial operator  $\Pi$  the matrix  $M$  of Sect. 20.4 is

$$M = \sum_{j,k=0}^{d-1} |jd+k\rangle \otimes Z_d^k X_d^j \sqrt{\Pi} X_d^{-j} Z_d^{-k} \in \mathbb{C}^{d^3 \times d} \quad (20.16)$$

and the symmetry is determined by the equations

$$(I_d \otimes X_d \otimes Z_d) M = M Z_d \quad \text{and} \quad (X_d \otimes I_d \otimes X_d) M = M X_d.$$

We decompose the left representation of this matrix symmetry in two steps. In the first step we apply the Fourier transform to the left hand side in order to diagonalize both shifts  $X_d$ . The resulting equations are

$$(I_d \otimes Z_d \otimes Z_d) (F_d \otimes F_d \otimes I_d) M = (F_d \otimes F_d \otimes I_d) M Z_d$$

and

$$(Z_d \otimes I_d \otimes X_d) (F_d \otimes F_d \otimes I_d) M = (F_d \otimes F_d \otimes I_d) M X_d.$$

The representation on the left hand side can be written as

$$(I_d \otimes Z_d \otimes Z_d) = \bigoplus_{j=0}^{d^2-1} \omega_d^{j \bmod d} Z_d \quad \text{and} \quad (Z_d \otimes I_d \otimes X_d) = \bigoplus_{j=0}^{d^2-1} \omega_d^{j \div d} X_d. \quad (20.17)$$

This shows that all components of the direct sum equal  $\sigma$  up to phase factors. Therefore, the second step of the decomposition of the representation is the elimination of these phase factors. This elimination can be conveniently accomplished if we define the unitaries

$$X_{\text{mod}} := \bigoplus_{j=0}^{d^2-1} X_d^{j \bmod d} \quad \text{and} \quad Z_{\text{div}} := \bigoplus_{j=0}^{d^2-1} Z_d^{j \div d}.$$

Using the commutation relations  $Z_d^\dagger X_d Z_d = \omega_d^{-1} X_d$  and  $X_d Z_d X_d^\dagger = \omega_d^{-1} Z_d$  for  $X_d$  and  $Z_d$  we obtain

$$\begin{aligned}
X_{\text{mod}} \left( \bigoplus_{j=0}^{d^2-1} \omega_d^{j \bmod d} Z_d \right) X_{\text{mod}}^\dagger &= \bigoplus_{j=0}^{d^2-1} Z_d \quad \text{and} \quad Z_{\text{div}}^\dagger \left( \bigoplus_{j=0}^{d^2-1} \omega_d^{j \bmod d} X_d \right) Z_{\text{div}} \\
&= \bigoplus_{j=0}^{d^2-1} X_d.
\end{aligned}$$

With both equations we can write the representation as

$$X_{\text{mod}} Z_{\text{div}}^\dagger (I_d \otimes Z_d \otimes Z_d) Z_{\text{div}} X_{\text{mod}}^\dagger = (I_d \otimes I_d \otimes Z_d)$$

and

$$X_{\text{mod}} Z_{\text{div}}^\dagger (Z_d \otimes I_d \otimes X_d) Z_{\text{div}} X_{\text{mod}}^\dagger = (I_d \otimes I_d \otimes X_d).$$

Hence we have eliminated the phase factors with these conjugations. With Eq. (20.17) the symmetry of  $M$  can be written as

$$(I_d \otimes I_d \otimes Z_d) X_{\text{mod}} Z_{\text{div}}^\dagger (F_d \otimes F_d \otimes I_d) M = X_{\text{mod}} Z_{\text{div}}^\dagger (F_d \otimes F_d \otimes I_d) M Z_d$$

and

$$(I_d \otimes I_d \otimes X_d) X_{\text{mod}} Z_{\text{div}}^\dagger (F_d \otimes F_d \otimes I_d) M = X_{\text{mod}} Z_{\text{div}}^\dagger (F_d \otimes F_d \otimes I_d) M X_d.$$

The representation on the left hand side is  $I_d \otimes I_d \otimes \sigma$  and is the decomposition we need for the construction of Sect. 20.4. We have the matrix  $N := X_{\text{mod}} Z_{\text{div}}^\dagger (F_d \otimes F_d \otimes I_d) M$  which has the symmetry

$$(I_d \otimes I_d \otimes \sigma) N = N \sigma. \quad (20.18)$$

The matrices  $A$  and  $B$  of Sect. 20.4 for the decomposition of the representations are

$$A := X_{\text{mod}} Z_{\text{div}}^\dagger (F_d \otimes F_d \otimes I_d) \quad \text{and} \quad B = I_d. \quad (20.19)$$

The intertwining space of the decomposed representations is  $\text{Int}(I_d \otimes I_d \otimes \sigma, \sigma)$ , and the matrix  $N$  lies in this space. Following Eq. (20.6) of Lemma 20.3.14 we have for an appropriate vector  $|\Phi_0\rangle \in \mathbb{C}^{d^2}$  the decomposition  $N = |\Phi_0\rangle \otimes I_d \in \mathbb{C}^{d^3 \times d}$ . Elementary computations show

$$|\Phi_0\rangle := (F_d^\dagger \otimes I_d) \left( \sum_{q=0}^{d-1} |q\rangle \langle q| \otimes X_d^{-q} \right) \left( \sqrt{d} \sum_{j,k=0}^{d-1} \sqrt{\Pi}_{jk} |j\rangle \otimes |k\rangle \right). \quad (20.20)$$

Here  $\sqrt{\Pi}_{jk}$  denotes the entry of  $\sqrt{\Pi}$  in the  $j$ th row and  $k$ th column.

Following the construction of Sect. 20.4 we want to extend the symmetry in the first step and the matrix  $N$  in the second step. More precisely, the first step is the extension of  $\sigma$  on the right hand side of Eq. (20.18) to the representation  $I_d \otimes I_d \otimes \sigma$  consisting of  $d^2$  copies of  $\sigma$ . This extension is very simple because all

representations are equal and hence there is no need to care about their order. In the second step we extend the matrix  $N$  to a unitary  $W$  in the corresponding intertwining space. Lemma 20.3.14 states that we have the decomposition  $W = C \otimes I_d$  with  $C \in U(d^2)$ . We write  $C$  as collection of column vectors to simplify the implementation scheme of the POVM in the following: Consider  $|\Phi_0\rangle$  given by Eq. (20.20) of  $N$  as vector and extend it to an orthonormal basis  $\{|\Phi_0\rangle, |\Phi_1\rangle, \dots, |\Phi_{d^2-1}\rangle\}$  of  $\mathbb{C}^{d^2}$ . Then define the unitary matrix

$$U := A^\dagger W (B \oplus \tilde{B}) = A^\dagger \left( \sum_{\ell=0}^{d^2-1} |\Phi_\ell\rangle\langle\ell| \otimes I_d \right)$$

according to the construction of Sect. 20.4. This expression is particularly simple as we can choose  $\tilde{B} := I_{(d-1)d}$  and obtain  $B \oplus \tilde{B} = I_{d^2}$ .

Next we exploit the tensor structure of  $U$  to obtain the same unitary for all initial operators  $\Pi$  of the POVM which defines  $|\Phi_0\rangle$  via Eq. (20.20). The basis of this construction is the decomposition of the state transition performed by  $U$  on the initialized system into

$$U(|0\rangle \otimes |\Psi\rangle) = A^\dagger \left( \sum_{\ell=0}^{d^2-1} |\Phi_\ell\rangle\langle\ell| \otimes I_d \right) (|0\rangle \otimes |\Psi\rangle) = A^\dagger (|\Phi_0\rangle \otimes |\Psi\rangle).$$

This equation shows that the implementation of  $W$  is not necessary if the ancilla is initialized with the state  $|\Phi_0\rangle$  of Eq. (20.20), i.e., the initial POVM operator  $\Pi$  can be encoded into the state of the ancilla. Hence from Eqs. (20.19) and (20.20) it follows that it suffices to implement the unitary

$$(F_d^\dagger \otimes F_d^\dagger \otimes I_d) Z_{\text{div}} X_{\text{mod}}^\dagger (F_d^\dagger \otimes I_d \otimes I_d) \left( \sum_{q=0}^{d-1} |q\rangle\langle q| \otimes X_d^{-q} \otimes I_d \right) \quad (20.21)$$

if the ancilla state is described by

$$|\gamma\rangle := \sqrt{d} \sum_{j,k=0}^{d-1} \sqrt{\Pi_{jk}} |j\rangle \otimes |k\rangle \in \mathbb{C}^{d^2}.$$

The unitaries of Eq. (20.21) are the Fourier transform, the shift and the phase matrix. The shift and phase occur as controlled operations, i.e., for the state  $|j\rangle$  of the control system the operation  $X_d^j$  or  $Z_d^j$  is applied. The Fourier transform and the controlled shift and phase operations are natural operations on a  $d$ -dimensional system and we assume that they can be implemented efficiently.

A simple initialization of the ancilla follows for an operator  $\Pi = |\phi\rangle\langle\phi|/d$  of rank one with  $|\phi\rangle \in \mathbb{C}^d$  and  $\langle\phi|\phi\rangle = 1$ . Then we have the square root  $\sqrt{\Pi} = |\phi\rangle\langle\phi|/\sqrt{d}$  and the initial state

$$|\gamma\rangle = |\phi\rangle \otimes |\bar{\phi}\rangle.$$

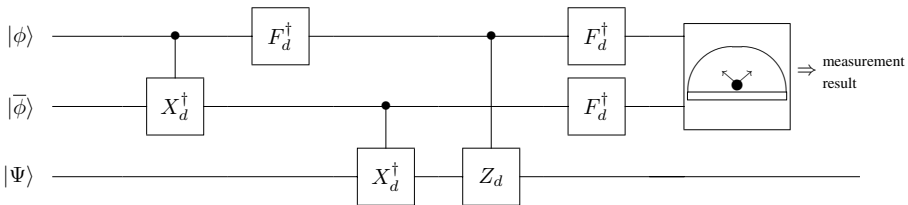


**Fig. 20.2** Implementation scheme for Heisenberg-Weyl symmetric POVMs. The  $j$ th power of an operation is performed for the state  $|j\rangle$  of the control wire. Both upper systems are measured in the computational basis.

This shows that an efficient preparation scheme for the states  $|\phi\rangle$  and  $|\bar{\phi}\rangle$  implies an efficient implementation of the POVM with initial operator  $\Pi = |\phi\rangle\langle\phi|/d$ . An implementation scheme for this POVM is shown in Fig. 20.2.

## 20.6 Conclusions and Outlook

The construction of a minimal-disturbing implementation of a symmetric POVM can be systematically studied with the theory of symmetric matrices. The POVM can be reduced to a symmetric unitary transform and an orthogonal measurement in the computational basis. For some families of symmetric POVMs this general scheme leads to efficient implementations on a quantum computer.

An interesting issue for further research is the implementation of POVMs for solving hidden subgroup problems [34, 35]. For many non-abelian groups it is not known how to solve this important problem efficiently. However, it has been shown that a poly-logarithmic number of POVM measurements is sufficient to solve a particular hidden subgroup problem [1]. The problem is that it is not yet known how to implement the POVMs efficiently.

### Acknowledgement

This work was supported by Landesstiftung Baden-Württemberg gGmbH (AZ 1.1422.01). The authors acknowledge fruitful discussions with Dominik Janzing and Frank Schmüser.

## References

- 1 D. Bacon, A. M. Childs, and W. van Dam, Optimal measurements for the dihedral hidden subgroup problem, preprint quant-ph/0501044 (2005).
- 2 T. Decker, D. Janzing, and M. Rötteler, J. Math. Phys. **46**, 012104 (2005).
- 3 V. Bužek, R. Derka, and S. Massar, Phys. Rev. Lett. **82**, 2207–2210 (1999).
- 4 A. Peres and P. F. Scudo, Phys. Rev. Lett. **86**, 4160–4162 (2001).
- 5 E. B. Davies, IEEE Trans. Inf. Th. **24**, 596–599 (1978).
- 6 A. Peres and W. K. Wootters, Phys. Rev. Lett. **66**, 1119–1122 (1991).
- 7 M. A. Nielsen and I. L. Chuang, Quantum Computation and Quantum Information (Cambridge University Press, Cambridge, 2000).
- 8 P. Wocjan, D. Janzing, T. Decker, and Th. Beth, Measuring 4-local n-qubit observables could probabilistically solve PSPACE, preprint quant-ph/0308011 (2003).
- 9 M. Grassl, Electronic Notes in Discrete Mathematics **20**, 151–164 (2005).
- 10 G. Zauner, Quantendesigns: Grundzüge einer nichtkommutativen Designtheorie, Dissertation, Universität Wien (1999).
- 11 D. Janzing and T. Decker, Minimally disturbing Heisenberg–Weyl symmetric measurements using hard-core collisions of Schrödinger particles, J. Math. Phys. **47**, 082102 (2006).
- 12 H. N. Barnum, Information-disturbance tradeoff in quantum measurement on the uniform ensemble, preprint quant-ph/0205155 (2002).
- 13 H. N. Barnum, Quantum information theory, Dissertation, University of New Mexico (1998).
- 14 K. Kraus, States, Effects, and Operations (Springer, Berlin, 1983).
- 15 A. Barenco, C. H. Bennett, R. Cleve, D. P. DiVincenzo, N. Margolus, P. Shor, T. Sleator, J. A. Smolin, and H. Weinfurter, Phys. Rev. A **52**, 3457–3467 (1995).
- 16 G. Cybenko, Comput. Sci. Eng. **3**, 27–32 (2001).
- 17 M. Möttönen, J. J. Vartiainen, V. Bergholm, and M. M. Salomaa, Phys. Rev. Lett. **93**, 130502 (2004).
- 18 S. Egner and M. Püschel, J. Symb. Comput. **37**, 157–186 (2004).
- 19 S. Egner and M. Püschel, IEEE Trans. Signal Process. **49**, 1992–2002 (2001).
- 20 M. Püschel, M. Rötteler, and Th. Beth, Fast quantum Fourier transforms for a class of non-abelian groups, Lecture Notes in Comp. Sci. Vol. 1719 (Springer, Berlin, 1999), pp. 148–159.
- 21 C. W. Curtis and I. Reiner, Representation theory of finite groups and associative algebras (Wiley-Interscience, New York, 1962).
- 22 J.-P. Serre, Linear Representations of Finite Groups (Springer, Berlin, 1977).
- 23 L. Dornhoff, Group Representation Theory, Part A (M. Dekker, New York, 1971).
- 24 S. Sternberg, Group theory and physics (Cambridge University Press, Cambridge, 1994).
- 25 C. W. Helstrom, Quantum Detection and Estimation Theory (Academic Press, New York, 1976).
- 26 A. S. Holevo, Statistical Structure of Quantum Theory (Springer, Berlin, 2001).
- 27 Th. Beth, Verfahren der schnellen Fourier-Transformation (Teubner, Stuttgart, 1984).
- 28 M. Sasaki, S. M. Barnett, R. Jozsa, M. Osaki, and O. Hirota, Phys. Rev. A **59**, 3325–3335 (1999).
- 29 M. Ban, K. Kurokawa, R. Momose, and O. Hirota, Int. J. Theor. Phys. **36**, 1269–1288 (1997).
- 30 Y. C. Eldar and G. D. Forney, IEEE Trans. Inf. Theory **47**, 858–872 (2001).
- 31 D. Coppersmith, An Approximate Fourier Transform Useful for Quantum Factoring, Technical Report RC 19642, IBM Research Division, Yorktown Heights, NY (1994).
- 32 E. B. Davies, Quantum theory of open systems (Academic Press, London, 1976).
- 33 A. Terras, Fourier Analysis on Finite Groups and Applications, (Cambridge University Press, Cambridge, 1999).
- 34 A. Yu. Kitaev, Quantum measurements and the Abelian Stabilizer Problem, preprint quant-ph/9511026 (1995).
- 35 M. Rötteler and Th. Beth, Polynomial-time solution to the hidden subgroup problem for a class of non-abelian groups, preprint quant-ph/9812070 (1998).

## 21

# Full Counting Statistics of Interacting Electrons

*D. A. Bagrets, Y. Utsumi, D. S. Golubev, and Gerd Schön*

### 21.1

#### Introduction

Solid-state quantum information systems based on electronic spin or charge degrees of freedom offer a number of intrinsic advantages and drawbacks. Among the former are the fast operation times, the possibility to scale the systems to large size, and the relative ease to integrate them into electronic control and read-out circuits. Probably the most serious disadvantage is the fact that, in general, solid state devices suffer strongly from noise due to internal and external degrees of freedom as well as material-specific fluctuations. They lead to relaxation and decoherence processes. Hence, one of the major tasks in the field is the understanding and control of noise and decoherence. In this article we will concentrate on the analysis of fluctuations which arise due to the discrete nature of the electron charge. They lead to what is denoted as *shot noise*. Its analysis reveals information about electron correlations and entanglement [1].

In many circumstances the fluctuations are Gaussian distributed and fully characterized by their power spectrum. In order to get further information in the general case, e.g. about correlations and entanglement, the theory of *full counting statistics* (FCS) [2] of electrons has been developed. It concentrates on the probability distribution for the number of electrons transferred through the conductor during a given period of time. It yields not only the variance, but all higher moments of the charge transfer as well, and thus also contains information about rare large fluctuations.

The FCS has its historical roots in quantum optics, where the counting statistics of photons has been used to characterize the coherence of photon sources [3]. Photons detected by the photo-counter are correlated in time, reflecting the Bose statistics of the particles involved. For electronic currents the Fermi statistics is the relevant one, but the first attempts to derive the FCS of electrons [4] revealed some fundamental interpretation problems, related to subtleties

of the quantum measurement process. We are interested in the probability that the outcome of a measurement of the charge is  $q$ . According to textbook definitions of projective measurement this quantity can be expressed by  $\langle n | \delta(q - \hat{Q}) | n \rangle$ , where  $\hat{Q}$  is the operator for the transmitted charge, and  $| n \rangle$  denotes the quantum state. It is tempting to relate the transferred charge to the current operator,  $\hat{Q} = \int_0^{t_0} \hat{j}(\tau) d\tau$ . However, in quantum transport problems one has to pay attention to the fact that the electric current  $\hat{j}(\tau)$  is an operator, which, in general, does not commute at different times. This property led to severe interpretation problems within the original work. They were resolved in the later work of Levitov and Lesovik [2], which invokes explicitly an extra degree of freedom, namely the detector degree of freedom. The paradigm of projective measurement is then applied to this detector degree of freedom.

In the meantime the theory of FCS in mesoscopic transport has developed into a mature field; some achievement are summarized in [1, 5]. However, the experimental analysis of the FCS remains a challenge. First measurements of the third cumulant of charge transfer through a tunnel junction have been reported in [6, 7] and, very recently, the FCS of a semiconductor quantum dot (QD) has been investigated by a real-time detection of single-electron tunneling via a quantum point contact [8]. Furthermore, threshold type of measurements of the FCS using an array of over-damped Josephson junctions has been elaborated theoretically in [9].

In this paper we will review our recent results on the FCS of interacting electrons in a QD and low-dimensional diffusive conductors. The QDs are basic constituents of most solid-state quantum information systems. For example, superconducting single Cooper-pair boxes [10] and, similarly, a double-dot system formed in a semiconductor 2DEG [11] have been shown to operate as charge qubits. A metallic QD or single-electron transistor (SET) can serve as an electro-meter to measure the quantum states of a charge qubit [12]. Since all these devices are based on the charge measurements, a thorough understanding of the fluctuating properties of charge becomes crucial for progress in this field.

Recently further links became apparent between the FCS of electron transport and the field of solid-state quantum information processing. One of these is related to the use of electron entangled states for these purposes. Most of the work on entanglement has been performed in optical systems with photons [13], cavity QED systems [14] and ion traps [15]. By now several ideas have been put forward how to generate, manipulate and detect electronic entangled states [16]. It turns out that in solid state systems entanglement is rather common, the nontrivial task remaining its control and detection. For mesoscopic conductors, the prototype scheme of such detection was discussed in [17]. It has been shown that the presence of spatially separated pairs of entangled electrons, created by some *entangler*, can be revealed by using a

beam splitter and by measuring the correlations of the current fluctuations in the leads. If the electrons are injected in an entangled state, bunching and anti-bunching of the cross-correlations of current fluctuations should be found, depending on whether the state is a spin singlet or triplet. In [18] the FCS of entangled electrons has been analyzed in detail. The FCS depends not only on the scattering properties of the conductor but also on the correlations among the electrons that compose the incident beam. In [19] the Clauser-Horne inequality test for the FCS in the multi-terminal structures has been proposed in order to detect the entanglement in the source flux of electrons.

A second link is the intrinsic relation between FCS and detector properties of a quantum point contact. QPCs were suggested as charge detectors in [20] and have been studied experimentally in [21]. Recently they have been used as detectors for the state of quantum-dot qubits [22–24]. The operating principle of the QPC detector relies on the dependence of the electron current  $I$  through the QPC on the state of the two-level system. In [25] the detector properties of the QPC have been calculated beyond linear-response for arbitrary energy-dependent transparency and coupling. This is the case of interest since for maximum detector sensitivity typical measurements are done in the regime of high QPC transparency,  $D \simeq 1/2$ , and for coupling that is not weak [22]. It was found that both the back-action dephasing rate  $\Gamma$  and the measurement rate  $W$  are determined by the electron FCS.

A further motivation to study FCS arises from the need to understand the effect of interaction on electron transport in disordered low-dimensional conductors. Disorder enhancement of Coulomb interaction, together with quantum coherence effects strongly influence the transport properties of these systems. The FCS analysis of this long-standing problem provides a deeper insight into the question. Typically the Coulomb interaction leads to a suppression of the conductance of mesoscopic samples at low temperatures and bias voltages. It has been demonstrated [26–28] that the strength of this suppression in various types of mesoscopic conductors is related to their noise properties. Frequently we find the simple rule: the higher the shot noise the stronger is the Coulomb suppression of the conductance. The reason is that both shot noise and Coulomb corrections to the transport current are manifestations of the discreet nature of the electric charge. Beyond that, it was shown that the Coulomb correction to the shot noise scales with the third moment of the current in the absence of interactions [29]. Furthermore, it was demonstrated by renormalization group studies of the FCS of short coherent conductors [30] and of quantum dots [31] in the presence of Coulomb interaction that the interaction correction to the  $n$ -th moment of the current is determined by  $n + 1$ -th moment evaluated in the absence of interaction. Further developing these ideas we show in the present paper that Coulomb interaction may substantially enhance the probability of large current fluctuations in low dimensions,

leading to the appearance of long correlated ‘trains’ in the transferred charge. This effect is most pronounced when the system size matches the dephasing length due to Coulomb interaction. Such coincidence is not accidental and comes from the presence of the soft diffusive modes in the system which strongly renormalize the bare interaction.

The structure of this article is as follows: In the next section we introduce some basic definitions and concepts of the FCS in mesoscopic transport. We discuss the paradigm of quantum measurement by using a spin 1/2 as galvanometer and consider some simple illustrative examples. In the main part we concentrate on our own contributions to the field, discussing the effects of Coulomb interaction onto the shot noise and FCS in interacting quantum dot systems (Sect. 3) and in low-dimensional diffusive interacting conductors (Sect. 4).

## 21.2

### Concepts of FCS

We start this section by introducing some definitions and general formulae of the FCS approach to mesoscopic transport. The central quantity is the probability distribution,  $P_{t_0}(N)$ , for  $N$  electrons to be transferred through the conductor during a time interval  $t_0$ . The detection time  $t_0$  is assumed to be much larger than the inverse current frequency  $e/I$ , which ensures that on average  $\bar{N} \gg 1$ . This probability distribution  $P_{t_0}(N)$  is related to the cumulant generating function (CGF),  $\mathcal{F}(\chi)$ , via a discrete Fourier transform

$$e^{-\mathcal{F}(\chi)} = \sum_{N=-\infty}^{+\infty} P_{t_0}(N) e^{iN\chi}. \quad (21.1)$$

The auxiliary variable  $\chi$  is usually called “counting field”. From the CGF one readily obtains the “cumulants” (irreducible moments)

$$C_k = \langle\langle N^k \rangle\rangle = -(-i)^k \frac{\partial^k}{\partial \chi^k} \mathcal{F}(\chi) \big|_{\chi=0}. \quad (21.2)$$

The first four of the irreducible moments, defined by

$$\begin{aligned} C_1 &= \bar{N} = \sum_N N P_{t_0}(N), & C_2 &= \overline{(N - \bar{N})^2}, & C_3 &= \overline{(N - \bar{N})^3}, \\ C_4 &= \overline{(N - \bar{N})^4} - 3C_2^2, \end{aligned} \quad (21.3)$$

denote the mean, variance, asymmetry (“skewness”) and kurtosis (“sharpness”), respectively. They characterize the peak position, width of the distribution and further details of the shape of the distribution  $P_{t_0}(N)$ , as illustrated in Fig. 21.1.

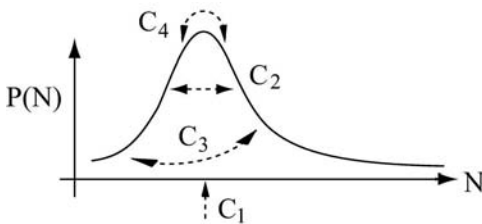


**Fig. 21.1** The distribution of the number of transmitted electrons  $N$ . The mean  $C_1$ , the variance  $C_2$ , the skewness  $C_3$  and the kurtosis  $C_4$  characterize the peak position, the width, the asymmetry and the sharpness of the distribution, respectively.

In order to provide a quantum mechanical definition of the CGF of electrons we will follow the approach proposed by Levitov and Lesovik [2]. The key step is to include the measurement device in the description. As a *gedanken* scheme a spin-1/2 system is used as a galvanometer for the charge detection. This spin is placed near the conductor and coupled magnetically to the electric current. Let the electron system be described by the Hamiltonian  $\mathcal{H}(\mathbf{q}, \mathbf{p})$ . We further assume that the spin-1/2 generates a vector potential  $\mathbf{a}(\mathbf{r})$  of the form  $\mathbf{a}(\mathbf{r}) = \frac{1}{2}\chi \nabla f(\mathbf{r})$ . Here the function  $f(\mathbf{r})$  smoothly interpolates between 0 and 1 in the vicinity of the cross-section at which the current is measured, and  $\chi$  is an arbitrary coupling constant so far. It will be shown below that it plays a role of “counting field”. If one further restricts the coupling of the current to the  $z$ -component of the spin then the total Hamiltonian of the system takes the form  $\hat{\mathcal{H}}_\sigma = \mathcal{H}(\mathbf{q}, \mathbf{p} - \mathbf{a}\hat{\sigma}_z)$ .

In the semiclassical approximation, when the variation of  $\nabla f(\mathbf{r})$  on the scale of the Fermi wave length  $\lambda_F$  is weak, it is possible to linearize the electron spectrum at energies near the Fermi surface. Thus one arrives at the Hamiltonian  $\hat{\mathcal{H}}_\sigma = \mathcal{H}(\mathbf{q}, \mathbf{p}) + \hat{\mathcal{H}}_{\text{int}}$ , where

$$\hat{\mathcal{H}}_{\text{int}} = -\frac{1}{e}\hat{\sigma}_z \int_{-\infty}^{+\infty} d^3\mathbf{r} \mathbf{a}(\mathbf{r})\mathbf{j}(\mathbf{r}) = -\frac{\chi}{2e}\hat{\sigma}_z I_S. \quad (21.4)$$

Here  $\mathbf{j}(\mathbf{r})$  is the current density and  $I_S = \int d^3\mathbf{r} \mathbf{j}(\mathbf{r}) \nabla f(\mathbf{r})$  the total current across a surface  $S$ . On the quasi-classical level Eq. (21.4) shows that a spin linearly coupled to the measured current  $I_S(t)$  will precess with a rate proportional to the current. If the coupling is turned on at time  $t = 0$  and switched off at  $t_0$  the precession angle  $\theta = \chi \int_0^{t_0} I_S(t)dt/e$  of the spin around the  $z$ -axis is proportional to the transferred charge through the conductor. In this way the spin-1/2 turns into analog galvanometer.

To proceed with the fully quantum mechanical description let us consider the evolution of the spin density matrix  $\hat{\rho}_S(t)$ . We assume that initially the density matrix of the whole system factorizes,  $\hat{\rho} = \hat{\rho}_e \otimes \hat{\rho}_S(0)$ , with  $\hat{\rho}_e$  being the initial density matrix of electrons. Then the time evolution of  $\hat{\rho}(t)$  is given

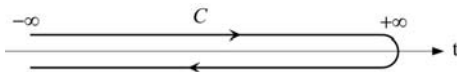


**Fig. 21.2** Keldysh contour  $C$ , used for evaluation of the cumulant generating function (CGF) .

by

$$\hat{\rho}(t) = \text{Tr}_e \left( e^{-i\hat{\mathcal{H}}_\sigma t} \hat{\rho} e^{i\hat{\mathcal{H}}_\sigma t} \right), \quad (21.5)$$

where  $\text{Tr}_e$  denotes the trace over electron states. Since, by construction, the evolution operator  $e^{-i\hat{\mathcal{H}}_\sigma t}$  is diagonal in the basis of  $\hat{\sigma}_z$ , the spin density matrix takes the form

$$\hat{\rho}_S(t_0) = \begin{bmatrix} \hat{\rho}_{\uparrow\uparrow}(0) & \mathcal{Z}(\chi)\hat{\rho}_{\uparrow\downarrow}(0) \\ \mathcal{Z}(-\chi)\hat{\rho}_{\downarrow\uparrow}(0) & \hat{\rho}_{\downarrow\downarrow}(0) \end{bmatrix}, \quad \mathcal{Z}(\chi) = \text{Tr}_e \left( e^{-i\mathcal{H}_\chi t} \hat{\rho}_e e^{i\mathcal{H}_{-\chi} t} \right), \quad (21.6)$$

where the Hamiltonian  $\mathcal{H}_\chi = \mathcal{H}(\mathbf{q}, \mathbf{p}) - \frac{\chi}{2e} I_S$  acts on the electron degrees of freedom only. It becomes clear now that the non-diagonal elements of the density matrix (21.6) contain the information about the distribution of precession angles of the spin during time  $t_0$ . To make it explicit we use the transformation rule of the spin-1/2 density matrix corresponding to a rotation around the  $z$ -axis by the angle  $\theta$ ,

$$\mathcal{R}_\theta(\hat{\rho}) = \begin{bmatrix} \hat{\rho}_{\uparrow\uparrow} & e^{i\theta}\hat{\rho}_{\uparrow\downarrow} \\ e^{-i\theta}\hat{\rho}_{\downarrow\uparrow} & \hat{\rho}_{\downarrow\downarrow} \end{bmatrix}. \quad (21.7)$$

One now can identify  $\mathcal{Z}(\chi)$  with the CGF introduced in Eq.(21.1), i.e one sets  $\mathcal{Z}(\chi) = e^{-\mathcal{F}(\chi)}$ , and the spin density matrix  $\hat{\rho}_S(t_0)$  can be represented as a superposition of the form

$$\hat{\rho}_S(t_0) = \sum_{N=-\infty}^{+\infty} P_{t_0}(N) \mathcal{R}_{\theta=N\chi}(\hat{\rho}), \quad (21.8)$$

where  $P_{t_0}(N)$  has a meaning of the probability to observe the precession at angle  $\theta = N\chi$ . For a classical spin a precession angle  $\theta = \chi$  corresponds to a current pulse carrying an elementary electron charge,  $e = \int_0^{t_0} I_S(t) dt$ . Using the correspondence principle we conclude that the quantity  $P_{t_0}(N)$  can be interpreted as the probability of transfer the multiple charge  $Ne$ . This consideration suggest the use of  $\mathcal{Z}(\chi)$  as the microscopical quantum mechanical definition for the CGF.

Using a cyclic permutation under the trace,  $\text{Tr}_e$ , in Eq. (21.6) one can represent  $\mathcal{Z}(\chi)$  in the form of the Keldysh partition function

$$\mathcal{Z}(\chi) = e^{-\mathcal{F}(\chi)} = \left\langle T_K \exp \left\{ -i \int_C dt \mathcal{H}_\chi(t) \right\} \right\rangle. \quad (21.9)$$

Here the time integration is performed along the Keldysh contour  $C$ , as shown in Fig. 21.2, and  $T_K$  denotes the time ordering operator along the path  $C$ . The average  $\langle \dots \rangle$  is performed with the non-equilibrium electron density matrix  $\hat{\rho}_e$ . The interaction part of the Hamiltonian  $\mathcal{H}_\chi(t)$  reads  $\mathcal{H}_{\text{int}}(t) = \frac{1}{2e} \chi(t) I_S$ , where the “counting field”  $\chi(t^\pm) = \pm \chi$  is asymmetric on the upper and lower branches of the Keldysh contour.

The definition (21.9) for the CGF can be generalized to obtain the full frequency dependence of the current correlators of arbitrary order [32]. Consider a mesoscopic conductor as shown in Fig. 21.3 coupled to two leads such that lead 1 is grounded while lead 2 is biased with voltage  $V(t)$ . We assume that the current  $I(t)$  is measured in the lead 2. This set-up is described by the interaction Hamiltonian  $\mathcal{H}_{\text{int}}(t) = \varphi(t) I(t)/e$  with the phases  $\varphi^\pm(t) = \int_{-\infty}^t eV(\tau) d\tau \pm \frac{1}{2} \chi(t)$  defined on the lower/upper branches of the contour  $C$ , and Eq. (21.9) yields the generating functional  $\mathcal{Z}[\varphi^+(t), \varphi^-(t)]$  of the current fluctuations in the lead 2. In analogy with the definition (21.2) the higher-order derivatives of the functional yield the  $n$ -point irreducible correlation function of currents

$$e^n C_n(t_1, \dots, t_n) = (-ie)^n \frac{\delta}{\delta \chi(t_1)} \dots \frac{\delta}{\delta \chi(t_n)} \ln \mathcal{Z}[\varphi^+(t), \varphi^-(t)] \Big|_{\chi=0}. \quad (21.10)$$

For illustration we consider an **Ohmic resistor** with resistance  $R$  at temperature  $T$ . Its CGF is quadratic in  $\varphi^\pm(t)$  and reads

$$\mathcal{F}_R[\varphi^+(t), \varphi^-(t)] = \frac{1}{2\pi} \frac{R_Q}{R} \int_C dt_1 \int_C dt_2 \alpha(t_1 - t_2) \varphi(t_1) \varphi(t_2), \quad (21.11)$$

where  $R_Q = 2\pi\hbar/e^2$  is the quantum resistance and

$$\alpha(t) = \frac{\pi T^2}{2 \sinh^2(\pi t T)}. \quad (21.12)$$

If the times  $t_{1,2}$  lie on different branches of the contour  $C$  the kernel  $\alpha(t)$  is regularized by the shift into the complex plane,  $t^\pm \rightarrow t \pm i0$ ; otherwise it is understood as principal value. The quadratic form of  $\mathcal{F}_R$  reflects the Gaussian nature of current fluctuations in an Ohmic resistor with its well-known properties.

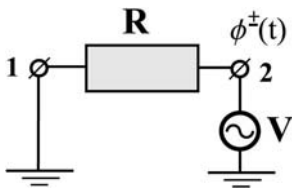


Fig. 21.3 Voltage biased mesoscopic conductor of resistance  $R$ .

The simplest example of a CGF for non-Gaussian processes is provided by a **tunnel junction**. In this case one has [33]

$$\mathcal{F}_T[\varphi^+(t), \varphi^-(t)] = -4\pi \frac{R_Q}{R_T} \int_C dt_1 \int_C dt_2 \alpha(t_1 - t_2) \sin^2 \left[ \frac{\varphi(t_1) - \varphi(t_2)}{2} \right], \quad (21.13)$$

where  $R_T$  is a tunnel resistance. For a constant applied voltage  $eV$  and stationary “counting field”  $\chi$  the corresponding CGF reduces to

$$\begin{aligned} \mathcal{F}_T(eV, \chi) &= -t_0 \left[ \Gamma_+ \left( e^{i\chi} - 1 \right) + \Gamma_- \left( e^{-i\chi} - 1 \right) \right], \\ \Gamma_{\pm} &= \pm \frac{1}{e^2 R_T} \frac{eV}{1 - e^{\pm eV/T}}. \end{aligned} \quad (21.14)$$

This result represents the CGF of a bidirectional Poissonian process with rates  $\Gamma_{\pm}$  corresponding to uncorrelated tunneling processes of the charge through the junction. At zero temperature and positive bias voltage the second term of Eq. (21.14) disappears. Then, performing the inverse Fourier transformation we obtain a simple Poisson distribution, corresponding to uncorrelated charge transfer

$$P(N) = \int_{-\pi}^{\pi} \frac{d\chi}{2\pi} \exp(\mathcal{F}_T(eV, \chi) - iN\chi) = \frac{\bar{N}^N e^{-\bar{N}}}{N!}, \quad \bar{N} = t_0 \Gamma_+. \quad (21.15)$$

As a further important example we consider a **quantum point contact** (QPC), shown in Fig. 21.4. It can be used as a quantum detector for the state of a quantum dot charge qubit. Its operating principle is based on the property that – due to the electrostatic coupling between the dot and the QPC – the scattering matrix  $\hat{S}_j = \begin{pmatrix} r_j & t_j^* \\ t_j & r_j^* \end{pmatrix}$  and thereby the current  $I$  of the QPC

depend on the state  $|j\rangle$  of the qubit. For a given realization  $\hat{S}$  of the scattering matrix the FCS has been calculated by Levitov et al. [2], with the result

$$\mathcal{F}(\chi) = -t_0 \int \frac{d\epsilon}{2\pi} \ln \det \left[ 1 + \hat{f} \left( \hat{S}^+(-\chi) \hat{S}(\chi) - 1 \right) \right] \quad (21.16)$$

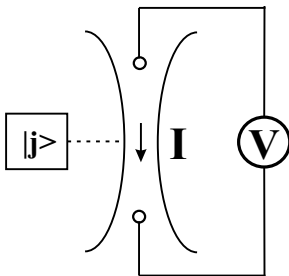


**Fig. 21.4** The principal scheme of the qubits readout using the quantum point contact (QPC). Due to electrostatic coupling the current  $I$  driven by the external voltage  $V$  is controlled by the state  $|j\rangle$  of the qubit.

where  $\hat{S}(\chi) = \begin{pmatrix} r_j & t_j^* e^{-i\chi/2} \\ t_j e^{i\chi/2} & r_j^* \end{pmatrix}$ , and  $\hat{f} = \text{diag}(f_L, f_R)$  is the diagonal density matrix of the leads. The explicit evaluation of Eq. (21.16) yields

$$\mathcal{F}(\chi) = -t_0 \int \frac{d\epsilon}{2\pi} \ln \left[ 1 + f_L(1 - f_R)D(e^{i\chi} - 1) + f_R(1 - f_L)D(e^{-i\chi} - 1) \right], \quad (21.17)$$

where  $D = |t|^2$  is a transmission coefficient. The physical interpretation of this result is that electrons can be transmitted either forward or backward with probabilities  $p_{R \leftarrow L} = f_L(1 - f_R)D$  and  $p_{L \leftarrow R} = f_R(1 - f_L)D$ , respectively, with the occupation factors accounting for the Pauli principle.

Recently, it has been realized that the quantum detector properties of the QPC are intrinsically related to its FCS [25]. The two basic quantities to be considered are the measurement-induced dephasing time of the qubit, and the time needed for the acquisition of information about the qubit's state. Keeping in mind the *gedanken* spin-1/2 measurement scheme for charge detection, described in the beginning of this section, we realize that in the quantum measurement process by a QPC the role of *gedanken* galvanometer is played by the qubit (or more generally by a many-level system). Then the analog of Eq. (21.6) describes the dephasing rate  $\Gamma$  of the qubit's density matrix  $\hat{\rho}(t)$  due to its interaction with the electron current in the QPC,  $\rho_{jk}(t) = \rho_{jk}(0) \langle e^{i\hat{H}_k t} e^{-i\hat{H}_j t} \rangle \simeq \rho_{jk}(0) e^{-\Gamma_{jk} t}$ . Here the average is taken over a stationary state of the QPC and  $\hat{H}_j$  and  $\hat{H}_k$  are electron Hamiltonians describing the propagation of electrons with scattering matrices  $\hat{S}_j$  and  $\hat{S}_k$ . In the long-time limit,  $t > \hbar/eV$ , the decay is exponential with rate

$$\Gamma_{jk} = - \int \frac{d\epsilon}{2\pi} \ln \det \left[ 1 + \hat{f}(\hat{S}_k^+ \hat{S}_j - 1) \right]. \quad (21.18)$$

The analogy with the expression (21.16) is striking. For a qubit at low temperature,  $T \ll eV$ , one obtains [25]

$$\Gamma_{12} = -\frac{eV}{2\pi\hbar} \ln |t_1 t_2^* + r_1 r_2^*|. \quad (21.19)$$

The second aspect of the measurement by the QPC is the rate of information acquisition. The information about the state  $|j\rangle$  of the qubit is encoded in the probability distribution  $P_t^{(j)}(N)$  for  $N$  electrons to be transferred via the QPC, given that the qubit is in the state  $|j\rangle$ . The mean value of this distribution,  $\bar{N}_j$ , and its width  $\sqrt{\langle \Delta N_j^2 \rangle}$  grow like  $t$  and  $t^{1/2}$ . This time dependence implies that only after a certain time, which we denote as the measurement time  $\tau_{\text{meas}}$ , the two peaks, corresponding to different states  $|j\rangle$  and  $|k\rangle$  emerge from a broadened distribution. Quantitatively this time can be defined by considering the statistical overlap of two distributions,  $M_{jk}(t) = \sum_N \left[ P_t^{(j)}(N) P_k^{(j)}(N) \right]^{1/2}$ . For long times,  $t > \hbar/eV$ , the decay should be exponential,  $M_{jk}(t) \propto \exp\{-W_{jk}t\}$ , with  $W_{jk} = 1/\tau_{\text{meas}}$  being the measurement rate. As it was shown in [25] it can be expressed in terms of the CGF as

$$W_{jk} = \frac{1}{2t_0} \min_{\chi} \chi \left[ \mathcal{F}_j(\chi) + \mathcal{F}_k(-\chi) \right] \quad (21.20)$$

In the case of quantum-limited detection the rates  $W_{jk}$  and  $\Gamma_{jk}$  coincide, while generally  $W_{jk} \leq \Gamma_{jk}$ , meaning that dephasing occurs faster than the information gain. One can show that a QPC can be operated as quantum limited detector with the rates

$$\Gamma_{jk} = W_{jk} = -\frac{eV}{2\pi\hbar} \ln \left[ (D_j D_k)^{1/2} + (R_j R_k)^{1/2} \right]. \quad (21.21)$$

where  $R_{j(k)} = 1 - D_{j(k)}$  are reflection coefficients.

The FCS of tunnel junction and quantum point contact represent the two simplest generic examples with non-Gaussian current fluctuations. In both cases the effects of electron-electron interaction were neglected. This is justified provided the conductance of the system is not too small,  $G \geq e^2/2\pi\hbar$ , and the length (size) of the system does not exceed the inelastic mean free path. Accounting for interaction effects on the FCS is no trivial task. This is the case, in particular, when electrons have an internal dynamics within the conductor, so that in the derivation of  $\mathcal{F}(\chi)$  the internal degrees of freedom have to be integrated out. Two examples of these calculations are considered in the following sections. In Sect. 3 we discuss the effects of Coulomb interaction onto the shot noise and FCS in interacting quantum dot systems, and in Sect. 4 we address the statistic of current fluctuations in the low-dimensional diffusive interacting conductors.

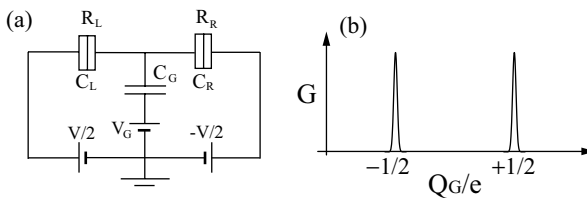


**Fig. 21.5** (a) The equivalent circuit of a metallic quantum dot. (b) The Coulomb oscillations.

## 21.3

### Full Counting Statistics in Interacting Quantum Dots

In this section we review the FCS of a single electron transistor (SET), which is shown schematically in Fig. 21.5 (a). It consists of a QD with strong local Coulomb interaction, which is coupled via two tunnel junctions (left and right) with tunneling resistances  $R_L$  and  $R_R$  and low capacitances  $C_L$  and  $C_R$  to two electrodes (source and drain). It is further coupled capacitively via  $C_G$  to a gate electrode which allows - by an applied gate voltage which determines the 'gate charge'  $Q_G = C_G V_G$  - to control the number of electrons inside the QD. In the systems of interest the total capacitance  $C_{\Sigma} = C_L + C_R + C_G$  is low and, hence, the single-electron charging energy  $E_C = e^2/2C_{\Sigma}$  typically in the range of 1K or above. If  $E_C$  exceeds the temperature and applied source-drain bias voltage,  $|eV|$ , the electron transfer through the QD is suppressed ("Coulomb blockade"). However, the Coulomb barrier can be tuned by the gate charge. For example, the energy difference between the charge zero state and the one with one excess electron in the QD depends on  $Q_G$  as  $\Delta_0 = E_C(1 - 2Q_G/e)$ . The voltage drops across the tunnel junctions are  $\mu_r = \kappa_r eV$ , where  $\kappa_{L/R} = \pm C_{R/L}(C_L + C_R)^{-1}$  and the subscript r stands for either L or R junction. If these voltages satisfy the condition  $\mu_R < \Delta_0 < \mu_L$  electrons can tunnel sequentially through the island. This mechanism leads to the typical oscillating behavior of the conductance as a function of the gate charge illustrated in Fig. 21.5 (b).

The first steps toward a theory of FCS in quantum dots with account of Coulomb interaction has been performed in [34] where the FCS of charge pumping in the limit of high transmission of the contacts was considered. Further progress was made by one of the authors and Nazarov [35], who derived the FCS in the frame of a Master equation. This approach is valid in the weak tunneling regime, where the parameter  $g \equiv R_Q/R_T$ , i.e., the ratio between the quantum resistance  $R_Q$  and the effective (parallel) resistance,  $R_T^{-1} = R_L^{-1} + R_R^{-1}$ , is much smaller than unity,  $g \ll 1$ . Applied to a quantum dot in the vicinity of the first conductance peak, the CGF is found to differ

from a simple Poissonian distribution. Rather it reads

$$\mathcal{F}^{(1)}(\chi) = t_0 \Gamma \frac{\sqrt{D(\chi)} - 1}{2}, \quad (21.22)$$

$$D(\chi) = 1 + \frac{4\Gamma_{\text{LI}}\Gamma_{\text{IR}}}{\Gamma^2} (e^{i\chi} - 1) + \frac{4\Gamma_{\text{RI}}\Gamma_{\text{IL}}}{\Gamma^2} (e^{-i\chi} - 1).$$

Here  $\Gamma = \Gamma_{\text{IL}} + \Gamma_{\text{IR}} + \Gamma_{\text{LI}} + \Gamma_{\text{RI}}$ , and the rates of electron tunneling into/out of the island through the junction  $r$  are given by Fermi's golden rule,

$$\Gamma_{\text{rI/Ir}} = \pm \frac{1}{e^2 R_r} \frac{\Delta_0 - \mu_r}{e^{\pm(\Delta_0 - \mu_r)/T} - 1}. \quad (21.23)$$

For special cases the CGF can be simplified: (i) Close to the threshold of the Coulomb blockade regime, e.g., for  $\Delta \approx \mu_L$ , and low temperatures  $T \ll |eV|$  the tunneling process through junction L becomes the bottleneck since  $\Gamma_{\text{LI}} \propto (\mu_L - \Delta_0)$  is much smaller than  $\Gamma_{\text{IR}}$ . In this case the CGF reduces to a Poissonian form,

$$\mathcal{F}^{(1)} \approx t_0 \Gamma_{\text{LI}} (e^{i\chi} - 1). \quad (21.24)$$

(ii) For a symmetric SET,  $R_L = R_R$  and  $C_L = C_R$ , at the conductance peak,  $\Delta_0 = 0$ , one finds for  $T = 0$  and  $eV > 0$

$$\mathcal{F}^{(1)} \approx 2 \bar{N} (e^{i\chi/2} - 1), \quad e\bar{N}/t_0 = V/2(R_L + R_R). \quad (21.25)$$

The extra factor  $1/2$  in the exponent leads to a sub-Poissonian value of the Fano factor, i.e., ratio between *dc* power spectrum and average current  $S_{II}/2e$   $\langle I \rangle \approx 1/2$ , indicating that tunneling processes through the two junctions are correlated. The distribution function in this case becomes

$$P(N) = \sum_{N_L, N_R=0}^{\infty} P_{\text{P}}(N_L) \cdot P_{\text{P}}(N_R) \delta_{N, (N_L + N_R)/2},$$

where the distributions of  $N_L$  and  $N_R$  transmitted electrons through the L and R junctions have a Poissonian form  $P_{\text{P}}(N) = \bar{N}^N e^{-\bar{N}}/N!$ . Both are constrained as indicated by the Kronecker  $\delta$ .

The Master equation approach captures the basic physics of the strong Coulomb correlations inside the QD, but it neglects non-Markovian effects, which become important for strongly conducting QDs, i.e., if the dimensionless conductance  $g$  is no longer small. This includes quantum fluctuations of the charge due to co-tunneling, i.e., simultaneous tunneling of two electrons through two junctions. This process dominates in the Coulomb blockade regime, i.e. far away from the conductance peaks. Recently Braggio et al. [36] considered these effects in second order perturbation theory in  $g$  in extension of the theory [35] using well established real-time diagrammatic techniques [37,38].

The CGF of a quantum dot in the limit of very strong tunneling,  $g \gg 1$ , has also been considered [31]. In this limit the Coulomb blockade almost disappears. Its weak precursor is caused by quantum fluctuations of the phase, which is the variable canonically conjugated to the island charge. The small negative correction to the conductance is logarithmic:  $\tilde{g} \approx g - 2 \ln(\Omega/T)$ , where  $\Omega = 1/(R_T C_\Sigma)$  is the inverse RC time [39].

Several further articles dealt with different setups. In [40] bosonization techniques were used to find the FCS of an open quantum dot coupled to reservoirs by single-channel point contacts in the presence of a strong in-plane magnetic field. Similarly, the CGF for the generalized two-channel Kondo model, which models a QD in the Kondo regime, has been derived [41]. In both cases the authors succeeded to fully account for Coulomb correlations, but the results are limited to a very special, exactly solvable case. Despite this work the understanding of the effects of quantum fluctuations on the FCS of interacting QDs is far from complete. In what follows we evaluate CGF for the regime of intermediate strength conductance.

### 21.3.1

#### FCS of a Set for Intermediate Strength Conductance

Here we consider a quantum dot single-electron transistor in the intermediate strength tunneling regime, where (introducing for convenience a new dimensionless conductance parameter)  $\alpha_0 \equiv g/(2\pi)^2 < 1$ . We assume that the inverse RC time is still smaller than the characteristic charging energy,  $\Omega \ll E_C$ , which ensures that the charge-state levels are well resolved. In the vicinity of the conductance peak, precisely for  $|\Delta_0|/E_C \ll 1$ , it is sufficient to restrict the attention to only two charge states of the quantum dot with charges differing by  $e$ . The Hamiltonian can then be mapped onto the ‘multi-channel anisotropic Kondo model’ [42]. Introducing a spin-1/2 operator  $\hat{\sigma}$ , which acts on the charge states, we have

$$\begin{aligned} \hat{H} = & \sum_{r=L,R,I} \sum_{kn} \varepsilon_{rk} \hat{a}_{rkn}^\dagger \hat{a}_{rkn} + \frac{\Delta_0}{2} \hat{\sigma}_z \\ & + \sum_{r=L,R} \sum_{kk'n} (T_r \hat{a}_{Ik'n}^\dagger \hat{a}_{rk'n} \hat{\sigma}_+ + \text{H.c.}) \end{aligned} \quad (21.26)$$

Here  $\hat{a}_{rkn}^\dagger$  creates an electron with wave vector  $k$  and channel index  $n$  (including spin) in the left or right electrode or island ( $r = L, R, I$ ). The tunneling matrix elements  $T_r$  are assumed to be independent of  $k$  and  $n$ . The junction conductances are  $1/R_r = 2\pi e^2 N_{ch} |T_r|^2 \rho_r \rho_r$ , with  $N_{ch}$  being the number of channels and  $\rho_r$  the electron DOS. We assume that energy and spin relaxation

times are fast so that electrons are distributed according to a Fermi distribution function  $f(\omega) = 1/[\exp(\omega/T) + 1]$  both in the island and in the leads.

In the intermediate conductance regime the main consequence of the quantum fluctuations of the charge is the renormalization of system parameters, specifically of the charging energy and the conductance. A perturbative two-loop renormalization group analysis for  $N_{\text{ch}} \gg 1$  predicts a renormalization of the conductance,  $\alpha_0 \rightarrow z_0 \alpha_0$ , and of the charging energy,  $\Delta_0 \rightarrow z_0 \Delta_0$ , to depend logarithmically on the low energy cut-off  $\Lambda = \max\{T, \Delta_0\}$  [42]

$$z_0 = \frac{1}{1 + 2\alpha_0 \ln(E_C/\Lambda)}, \quad (21.27)$$

Such a conductance renormalization has been confirmed by experiments [43], where the observed height of the conductance peaks has been suppressed as  $1/\ln T$ .

The logarithmic renormalization is typical for Kondo problem, in which one encounters logarithmic divergences in perturbation theory. Likewise, a perturbative treatment of quantum fluctuations in a quantum dot leads to logarithmic divergences. Handling these divergences remains a nontrivial task, especially in non-equilibrium transport problem. Schoeller and Schön [37] have formulated a real-time diagrammatic approach to this problem. Summing up a certain class of infinite order diagrams, they managed to remove the divergences and recover the renormalization factor (21.27). Furthermore, they derived non-linear current-voltage characteristics including low-bias Kondo anomalies. Recently the second cumulant of the current, i.e. the noise, has been evaluated in lowest [44] and second-order perturbation theory [45]. However, apart from the second-order analysis by Braggio et al. [36], the FCS of a quantum dot in the moderate tunneling regime has not been yet analyzed, in particular in situations where the finite-order perturbation theory fails and infinite order diagrams need to be included. Motivated by that, we addressed this problem in [46], where the FCS of a SET has been evaluated with the use of Majorana fermion representation [47–49]. This formulation enabled us to apply Wick's theorem and consequently the standard Schwinger-Keldysh approach [50–52]. Since practical calculations are rather technical, we will first summarize our main results, and postpone the sketch of the derivation to Sect. 21.3.3.

In the intermediate strength tunneling regime we obtained the CGF in the following form [46]

$$\begin{aligned} \mathcal{F}(\chi) \approx & \frac{t_0}{2\pi} \int d\omega \ln[1 + T^F(\omega) f_L(\omega) \{1 - f_R(\omega)\} (e^{i\chi} - 1) \\ & + T^F(\omega) f_R(\omega) \{1 - f_L(\omega)\} (e^{-i\chi} - 1)], \end{aligned} \quad (21.28)$$

where  $f_r(\omega) = f(\omega - \mu_r)$  is the Fermi distribution function for electrons in the lead  $r$ . This result looks similar to the Levitov-Lesovik formula for noninteracting systems [2], but the effective transmission probability  $T^F(\omega)$  accounts for the strong quantum fluctuations of the charge [46, 53],

$$T^F(\omega) = (2\pi)^2 \frac{\alpha_0^L \alpha_0^R (\omega - \mu_L)(\omega - \mu_R)}{|\omega - \Delta_0 - \sum_{r=L,R} \Sigma_r^R(\omega)|^2} \times \coth \frac{\omega - \mu_L}{2T} \coth \frac{\omega - \mu_R}{2T}, \quad (21.29)$$

$$\Sigma_r^R(\omega) = \alpha_0^r \left[ 2\text{Re} \psi \left( i \frac{\omega - \mu_r}{2\pi T} \right) - 2\psi \left( \frac{E_C}{2\pi T} \right) - \frac{2\pi T}{E_C} \right] - i\pi \alpha_0^r (\omega - \mu_r) \coth \frac{\omega - \mu_r}{2T}, \quad (21.30)$$

where  $\psi$  is the digamma function. For a symmetric SET at  $T = 0$  and  $|\omega| \ll eV$ , the self-energy becomes  $\sum_{r=L,R} \Sigma_r^R(\omega) \approx \alpha_0 \ln(2E_C/eV) \omega - i\Gamma/2$ . From the real-part of this expression one reproduces the logarithmic renormalization (21.27), and thus in this sense we accounted for leading logarithms. The imaginary part describes the effect of finite life-time of the charge state of the quantum dot in non-equilibrium situations. We also reproduce the average current predicted by Schoeller and Schön [37]. Furthermore, the second order expansion in  $\alpha_0$ ,  $\mathcal{F}^{(1)} + \mathcal{F}^{(2)}$ , with

$$\begin{aligned} \mathcal{F}^{(2)}(\chi) &= \partial_{\Delta_0} \{ \text{Re} \Sigma_c^R(\Delta_0) \mathcal{F}^{(1)}(\chi) \} + \mathcal{F}^{\text{cot}}(\chi), \\ \mathcal{F}^{\text{cot}}(\chi) &= t_0 \{ \gamma^+ (e^{i\chi} - 1) + \gamma^- (e^{-i\chi} - 1) \}, \end{aligned} \quad (21.31)$$

is consistent with the result of [36]. The first term in the expression for  $\mathcal{F}^{(2)}(\chi)$ , describes the renormalization (21.27) in lowest order perturbation theory. Corrections of this type for the current were derived earlier in [38]. The cotunneling correction to the CGF,  $\mathcal{F}^{\text{cot}}$ , describes a bidirectional Poissonian process governed by the cotunneling rates

$$\gamma^\pm = 2\pi \alpha_0^L \alpha_0^R \int d\omega \frac{(\omega - \mu_L)(\omega - \mu_R)}{(e^{\pm(\omega - \mu_L)/T} - 1)(1 - e^{\mp(\omega - \mu_R)/T})} \text{Re} \frac{1}{(\omega + i0 - \Delta_0)^2}.$$

This term dominates in the Coulomb blockade regime ( $|\Delta_0| > |eV/2|$  for a symmetric SET) and is consistent with the FCS theory of quasiparticle tunneling in the presence of many-body interaction [54].

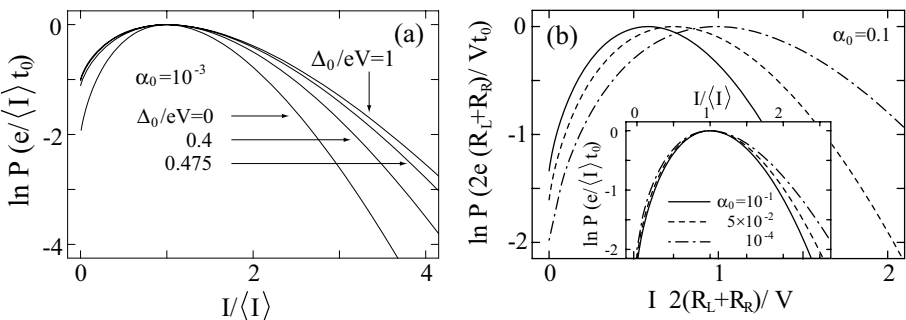


**Fig. 21.6** (a) The zero-temperature current distribution at  $eV = 0.2E_C$  for various values of  $\Delta_0$  ( $R_L = R_R$  and  $C_L = C_R$ ). (b) Plot of  $P$  at  $\Delta_0 = 0$  for various values of the conductance versus the current normalized to  $V/2(R_L + R_R)$ ; inset: the same distribution normalized to the average current  $\langle I \rangle$ .

### 21.3.2

#### Non-Markovian Effects: Renormalization and Finite Lifetime Broadening of Charge States

We present now some results. Fig. 21.6(a) shows the current ( $I = eN/t_0$ ) distribution for a symmetric SET and for several values of the Coulomb energy barrier  $\Delta_0$ . The conductance is chosen to be very small. As we sweep  $\Delta_0$  from the center of the conductance peak,  $\Delta_0/eV = 0$ , to the threshold of the Coulomb blockade regime,  $\Delta_0/eV = 0.5$ , the CGF gradually changes from the correlated Poissonian (21.25) to the uncorrelated one (21.24). Simultaneously the current distribution widens. With further increase of  $\Delta_0$  one enters into the Coulomb blockade regime, where the CGF smoothly crosses over to  $\mathcal{F}^{\text{cot}}$  and the non-Markovian co-tunneling processes becomes dominant.

As the conductance increases, quantum fluctuations are enhanced. We find that for  $z_0\Gamma \ll \Lambda$ ,  $[\Lambda = \max(|z_0\Delta_0|, 2\pi T, |eV|/2)]$ , the simple expression for CGF,  $\mathcal{F}^{(1)}$ , still holds provided the parameters are properly renormalized  $\alpha_0 \rightarrow z_0\alpha_0$ ,  $\Delta_0 \rightarrow z_0\Delta_0$ . The effect of this renormalization is illustrated in Fig. 21.6(b), where the current distribution for  $\Delta_0 = 0$  is plotted. Since  $z_0$  decreases with increasing  $\alpha_0$ , the mean value of the current, i.e. the position of the peak in the current distribution, shifts to lower values. The renormalization effect can be absorbed if we re-plot the same data with the current (horizontal axis) normalized by the average current  $\langle I \rangle$  rather than by  $V/2(R_L + R_R)$  [inset of Fig. 21.6(b)]. However, even after this procedure the three curves do not completely collapse to a single one. The remaining differences can be attributed to the non-Markovian effect of the broadening of the charge states due to their finite life time, which is described by the imaginary part of the self-energy, Eq. (21.30). We observe the following trend: the probability for current

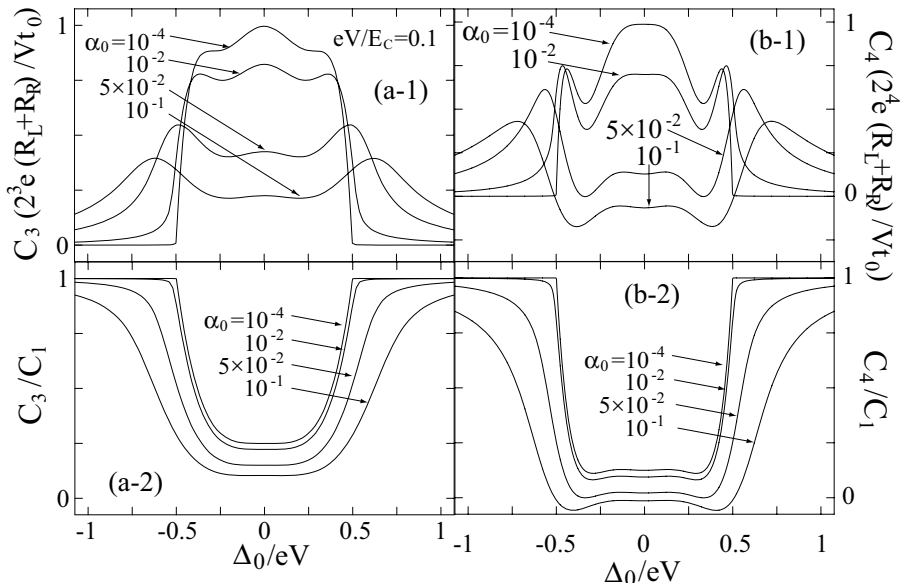


**Fig. 21.7** Panels (a-1) and (b-1) are the skewness and the kurtosis at  $eV = 0.1E_C$  and 0 K for various conductance. Panels (a-2) and (b-2) are those normalized by the average value.

much larger than the average value is suppressed and the current distribution shrinks with increasing  $\alpha_0$ .

Let us discuss the lifetime broadening effect quantitatively. At moderately large voltages,  $eV \gg T_K = E_C e^{-1/2\alpha_0} / 2\pi$ , and at  $T = 0$  the real part of the self-energy (21.30) is negligible and  $\sum_{r=L,R} \Sigma_r^R(\omega) \approx -i\pi\alpha_0 eV$ . Then the CGF at  $\Delta_0 = 0$  reads

$$\begin{aligned} \mathcal{F}(\chi) \approx & \mathcal{F}^{(1)}(\chi) - 4\bar{q}\alpha_0(e^{i\chi} - 1) \\ & + 2\bar{q}\pi^2\alpha_0^2(e^{i3\chi/2} - e^{i\chi/2}) + O(\alpha_0^3). \end{aligned} \quad (21.32)$$

It is evident from this formula that the higher order cumulants are suppressed with increasing  $\alpha_0$  due to lifetime broadening.

Figs. 21.7(a-1) and (b-1) show the skewness  $C_3$  and the kurtosis  $C_4$  as a function of  $\Delta_0$ . A double-peak structure growing with increasing conductance is observed. In general, we found that higher cumulants of the current depend on the gate charge in a complicated way and depend strongly on the conductance. E.g., the kurtosis even changes its sign for large values of  $\alpha_0$ . For the generalized ‘Fano factors’ defined as  $C_3/C_1$  and  $C_4/C_1$  [Figs. 21.6(a-2) and (b-2)], we observe a suppression with increasing  $\alpha_0$ .

## 21.3.3

**Keldysh Action and CGF in Majorana Representation**

In this section, we sketch our calculations [46, 53]. Since within the *Schwinger-Keldysh* approach the calculation of CGF is *formally* equivalent to the calculation of the partition function (21.9) on the closed time-path  $C$  (Fig. 21.2), we can apply the standard field theory methods. From the Hamiltonian (21.26) we obtain the path-integral representation of the Keldysh partition function (21.9) following the standard procedure. Tracing out the electron degrees of freedom, we obtain the effective Keldysh action, which is the sum of two parts: the charging part  $S_{\text{ch}}$  and the tunneling one  $S_t$  —  $S \equiv S_{\text{ch}} + S_t$ . They read

$$S_{\text{ch}} = \int_C dt \{ c^* (i\partial_t - \Delta_0) c + \frac{i}{2} \phi \partial_t \phi \},$$

$$S_t = - \sum_{r=L,R} \int_C dt dt' c^*(t) \phi(t) \alpha_r(t, t') \phi(t') c(t') + O(T_r^4).$$

Here  $c(t)$  and  $\phi(t)$  are Grassmann fields which correspond to Dirac fermionic operators  $\hat{c}$  and Majorana fermionic operators  $\hat{\phi}$ , respectively. The latter operators are defined by the following relations:  $\hat{\sigma}_+ = \hat{c}^\dagger \hat{\phi}$  and  $\hat{\sigma}_z = 2\hat{c}^\dagger \hat{c} - 1$ . The action  $S_t$  is equivalent to the tunneling action (21.13), defined earlier.

A particle-hole Green's function,  $\alpha_r$ , describing the tunneling of an electron between an electrode  $r = L, R$  and the island, is expressed in the Keldysh space as a  $2 \times 2$  matrix,

$$\tilde{\alpha}_r(\omega) = \begin{pmatrix} 0 & \alpha_r^A(\omega) \\ \alpha_r^R(\omega) & \alpha_r^K(\omega) \end{pmatrix}$$

$$= -i\pi\alpha_0^r \frac{(\omega - \mu_r) E_C^2}{(\omega - \mu_r)^2 + E_C^2} \begin{pmatrix} 0 & -1 \\ 1 & 2 \coth \frac{\omega - \mu_r}{2T} \end{pmatrix}, \quad (21.33)$$

where,  $\alpha_0^r = R_K / (4\pi^2 R_r)$  is the dimensionless junction conductance. Here we have introduced a Lorentzian cutoff function to regularize the UV divergence. The terms higher than  $T_r^4$  describe the *elastic* cotunneling process. They can be neglected in the limit of fixed  $\alpha_0$  but large number of channels,  $N_{\text{ch}} \gg 1$ . In this case  $T_r$  scales as  $\propto 1/\sqrt{N_{\text{ch}}}$  and thus the terms  $\propto T_r^4$  give only small corrections  $\propto 1/N_{\text{ch}}$ . In order to derive the CGF, we introduce the counting field  $\chi$  by means of the following rotation in the Keldysh space,

$$\tilde{\alpha}_r^\chi(\omega) = \exp(i\kappa_r \chi \tau_1/2) \tilde{\alpha}_r(\omega) \exp(-i\kappa_r \chi \tau_1/2). \quad (21.34)$$

Here  $\tau_1$  is the Pauli matrix. The CGF takes the following form

$$\mathcal{F}(\chi) = -\ln \int \mathcal{D}[c^*, c, \phi] \exp[i S(\chi)], \quad (21.35)$$

where  $S(\chi)$  is the effective action containing the rotated particle-hole Green's function (21.34). Tracing out the  $c$  fields, we obtain a term of fourth order in  $\phi$  in the action, which means that the path integration cannot be performed exactly. Therefore we proceed in a perturbative expansion in  $\alpha_0$  and resum a certain class of diagrams. Namely we take into account the contributions from free Majorana Green's function and Dirac Green's function with the bubble insertions formed by particle-hole Green's (21.34) function and free Majorana Green's function.

## 21.4

### FCS and Coulomb Interaction in Diffusive Conductors

In this section we consider the FCS of low-dimensional diffusive conductors, such as quasi-one-dimensional disordered wires and two-dimensional disordered films. It has been appreciated more than two decades ago that the interplay of interaction and phase coherence effects in these systems may drastically affect its transport properties [55,56]. Initially, the conductance was a main object of study, but more recently the trend moved toward the study of essentially non-equilibrium phenomena, like the quantum shot noise.

We consider short diffusive wires and films (with diffusion constant  $D$ ) where the Thouless energy  $E_{\text{Th}} = D/L^2$  is large compared to the applied voltage,  $E_{\text{Th}} \gg eV$ . In these systems the Fano factor, i.e. the ratio between shot noise and current,  $S = 2|e|IF$ , takes the value  $F = 1/3$  [57,58]. The condition for short conductors can be equivalently rewritten as  $\tau_D \ll 1/eV$ , where  $\tau_D = L^2/D$  is a typical diffusion time of electron through the system. Such short conductors are coherent and effectively zero-dimensional so that all effects of Coulomb interaction come from the external electromagnetic environment. It has been shown recently that the environment modifies the conductance, noise [26,29] and generally the FCS [30,31].

Much less is known about the role of Coulomb interaction onto the FCS in the quasi- 1D and 2D diffusive systems, when  $\tau_D \gg 1/eV$ . Under this condition the inelastic electron-electron scattering inside the conductor is important. This subject has recently attracted the attention in [59–61], where the so-called “hot electron” regime, was discussed. It is defined by  $\tau_D \gg \tau_E$ , with  $\tau_E$  being the energy relaxation time due to Coulomb interaction, and at the same time  $\tau_D \ll \tau_{e-\text{ph}}$ , with  $\tau_{e-\text{ph}}$  being the electron-phonon relaxation time. These two conditions imply that the size of the conductor is larger than the energy relaxation length due to electron-electron interaction, but the energy relaxation from the electron subsystem to phonons is negligible. In this situation the electron distribution function relaxes to the local Fermi distribution with a position dependent electron temperature along the conductor. This

changes the Fano factor  $F$  from  $1/3$  to  $\sqrt{3}/4$  [62], an effect that was confirmed experimentally [58].

**Tab. 21.1** The electron scattering times for low-dimensional (1D and 2D) diffusive conductors,  $E = \max\{T, eV\}$ . At  $T \leq \tau_\phi^{-1}(V)$ , we get  $\tau^* = \tau_\phi(V)$ .

d	$1/\tau_E$	$1/\tau_\phi$	$1/\tau^*, T \geq \tau_\phi^{-1}(V)$
1	$(E/D)^{1/2} \nu_1^{-1}$	$(E^2/D\nu_1^2)^{1/3}$	$(eV/T)^{1/2} \tau_E^{-1}(V)$
2	$E/g$	$(E/g) \ln g$	$\ln(eV/T) \tau_E^{-1}(V)$

The microscopic theory [63] of electron-electron interaction in low-dimensional disordered conductors predicts, however, in addition to  $\tau_E$  a further time scale, the dephasing time  $\tau_\phi$  (see Table 1). Both times are energy dependent and in the limit of good conductors  $g = G/G_Q \gg 1$ , which we wish to consider, differ parametrically from each other ( $\tau_\phi \ll \tau_E$ ). It is usually believed [64] that classical phenomena described by the Boltzmann equation are governed only by the energy relaxation time  $\tau_E$ , while the decoherence time  $\tau_\phi$  affects essentially quantum-mechanical phenomena. Since the FCS is a classical quantity, in the sense that it is proportional to the number of conducting channels, one might naively expect that it crosses over between the coherent and the “hot electron” regime on the scale  $\tau_D \sim \tau_E$ .

As we show below the time  $\tau_E$  is indeed responsible for a smooth crossover between the coherent and the “hot electron” limits if one is interested in the shot noise and the  $3^d$  cumulant of charge. However, this is not the case for the higher order cumulants of charge transfer in the shot noise limit  $eV \gg T$ . Moreover, in this limit the smooth crossover in the FCS does not exist. The Coulomb interaction drastically enhances the probability of current fluctuations for short conductors  $1/eV \ll \tau_D \ll \tau_E$ . We coined for this range of parameters the term “incoherent cold electrons” [65]. In what follows we will show that the tail of the current distribution for such electrons is exponential,  $P(I) \sim \exp(-\gamma|I|t_0/e)$ . The fluctuations are strongest for low temperatures,  $T \ll E_{\text{Th}}$ , and they reach the maximum on the scale  $\tau_D \sim \tau_\phi(V)$ . In this case  $\gamma \sim g^{-1/2}$  for 1D wire and  $\gamma \sim (\ln g/g)^{1/2}$  for 2D film. The FCS of this type can be understood as the statistics of a photocurrent which is generated by electron-hole pairs excited by classical low-frequency fluctuations of the electromagnetic field. It is remarkable that the time scale of optimal current fluctuations transforms to the scale  $\tau_\phi(T)$ , known as a decoherence time in the theory of weak localization [63], provided one identifies  $eV$  with  $T$ . Therefore, in strongly non-equilibrium situation the time  $\tau_\phi$  rather than  $\tau_E$  governs the crossover in the FCS between the coherent and the “hot electron” limits.

## 21.4.1

**Model and Effective Action**

We consider a quasi-one-dimensional (1D) diffusive wire of length  $L$  and a quasi- two-dimensional (2D) film of size  $L \times L$ , with density of states  $\nu_d$  per spin, diffusion coefficient  $D$  and large dimensionless conductance

$$g = 4\pi\nu_d D L^{2-d} \gg 1.$$

They are attached to two reservoirs with negligible external impedance which are kept at voltages  $\pm V/2$ . The current flows along the  $z$  direction and we concentrate on the incoherent regime,  $\max\{eV, T\} \gg E_{\text{Th}}$ .

To evaluate the CGF we have used the Keldysh technique and employed the low-energy field theory of the diffusive transport [66] which leads to the action

$$\begin{aligned} S[\chi, Q, \mathbf{A}] = & \int d^d \mathbf{r} \text{Tr} \left[ \frac{g L^{2-d}}{8} \left( \nabla Q - i[\hat{A}, Q] \right)^2 - 2\pi\nu_d \left( \partial_t Q \right) \right] \\ & - \frac{i}{8\pi e^2} \int d t \int d^3 \mathbf{r} \left( \dot{\mathbf{A}}_1^2 - \dot{\mathbf{A}}_2^2 \right). \end{aligned} \quad (21.36)$$

Here  $\hat{A} = \text{diag}(\mathbf{A}_1(t, \mathbf{r}), \mathbf{A}_2(t, \mathbf{r}))$  is the  $2 \times 2$  matrix in Keldysh space, where  $\mathbf{A}_{1,2}$  stand for fluctuating vector potentials in the conductor. We assume that  $\text{curl } \mathbf{A} = 0$ , thus neglecting relativistic effects. The matrix  $\hat{Q}(\mathbf{r}, t_1, t_2)$  accounts for diffusive motion of electrons and obeys the semi-classical constraint  $\hat{Q}(\mathbf{r}) \circ \hat{Q}(\mathbf{r}) = \delta(t_1 - t_2)$ . Boundary conditions are imposed on the field  $Q$  in the left (L) and right (R) reservoirs [67],  $Q|_{\mathbf{r}=R} = \hat{G}_R$  and  $Q|_{\mathbf{r}=L} = \hat{G}_L(\chi) = e^{i\chi \hat{t}_3/2} \hat{G}_L e^{-i\chi \hat{t}_3/2}$ . Here  $G_{L,R}$  are the Keldysh Green's functions in the leads.

With the action (21.36) the CGF should be evaluated as a path integral over all possible realizations  $\mathbf{A}_{1,2}$  and  $\hat{Q}$ . In general this is a complicated task. However, in the limit  $1/g \ll 1$  the problem simplifies. We employ the parameterization  $Q = e^{iW} \hat{G} e^{-iW}$ ,  $W\hat{G} + \hat{G}W = 0$ . Here the field  $W$  accounts for the rapid fluctuations of  $Q$  with typical frequencies  $\omega \sim eV$  and momenta  $q \sim \sqrt{eV/D}$ , while  $\hat{G}(\epsilon, \mathbf{r})$  is the slow stationary Usadel Green's function varying in space on the scale  $\sim L$ . As a first step we integrate out the field  $W$  in the Gaussian approximation to obtain the non-linear action  $\tilde{S}(\chi, \hat{G}, \mathbf{A})$  of the screened electromagnetic fluctuations in the media. We keep only quadratic terms in  $\tilde{S}$ , what is equivalent to the random phase approximation (RPA). As second step one can integrate out the photon field  $\mathbf{A}$  and reduce the problem to an effective action  $S_{\text{eff}}[\chi, \hat{G}]$ . Then the saddle point approximation,  $\delta S_{\text{eff}}[\chi, \hat{G}] / \delta \hat{G} = 0$  yields the kinetic equation for  $\hat{G}(\epsilon, \mathbf{r})$ . This program is very similar to that pursued in [66].

In the universal limit of a short screening radius,  $r^{-1} = (4\pi e^2 \nu_3)^{1/2} \gg \sqrt{eV/D}$ , we get the following result

$$S_{\text{eff}}[\chi, \hat{G}] = \frac{t_0}{8} g L^{2-d} \int d^d \mathbf{r} \int \frac{d\epsilon}{2\pi} \text{Tr} \left[ \nabla \hat{G}_\epsilon(\mathbf{r}) \right]^2 + \frac{t_0}{2} \int \frac{d^d \mathbf{r} d\omega d^d \mathbf{q}}{(2\pi)^{d+1}} \ln \left[ \frac{\text{Det} ||\mathcal{D}_\omega^{-1}(\mathbf{r}, \mathbf{q})||}{-(D\mathbf{q}^2)^2 - \omega^2} \right] \quad (21.37)$$

where  $\mathcal{D}_\omega$  is a  $2 \times 2$  matrix operator in Keldysh space corresponding to the non-equilibrium diffuson propagator,

$$\mathcal{D}_\omega^{\alpha\beta}(\mathbf{r}, \mathbf{q}) = \left[ D\mathbf{q}^2 \tau_1^{\alpha\beta} + (i/4) \int d\epsilon \text{Tr} \left( \gamma^\alpha \gamma^\beta - \gamma^\alpha \hat{G}_{\epsilon+\omega/2}(\mathbf{r}) \gamma^\beta \hat{G}_{\epsilon-\omega/2}(\mathbf{r}) \right) \right]^{-1}$$

with  $\gamma^0 = \hat{1}$ ,  $\gamma^1 = \hat{\tau}_3$ . The first term in  $S_{\text{eff}}$  is due to the diffusive motion of free electrons, while the second describes the real inelastic electron-electron collisions with energy transfer  $\omega \leq \max\{eV, T\}$ .

Minimizing the action  $S_{\text{eff}}$  under the constraint  $\hat{G}(\epsilon, \mathbf{r})^2 = 1$  one obtains a non-linear matrix kinetic equation for  $G(\epsilon, \mathbf{r})$ . It has a structure of the stationary Usadel equation

$$D \nabla \left( \hat{G}_\epsilon(\mathbf{r}) \nabla \hat{G}_\epsilon(\mathbf{r}) \right) = \left[ \hat{\mathcal{I}}_\epsilon(\mathbf{r}), \hat{G}_\epsilon(\mathbf{r}) \right] \quad (21.38)$$

with the extra matrix collision integral  $\hat{\mathcal{I}}_\epsilon$  in the r.h.s

$$\hat{\mathcal{I}}_\epsilon(\mathbf{r}) = \frac{i}{8\nu_d} \sum_{\alpha, \beta} \int \frac{d\omega d^d \mathbf{q}}{(2\pi)^{d+1}} \mathcal{D}_\omega^{\alpha\beta}(\mathbf{r}, \mathbf{q}) \left[ \gamma^\alpha \hat{G}_{\epsilon-\omega}(\mathbf{r}) \gamma^\beta + \gamma^\beta \hat{G}_{\epsilon+\omega}(\mathbf{r}) \gamma^\alpha \right] \quad (21.39)$$

This kinetic equation should be supplemented by the  $\chi$ -dependent boundary conditions at the interfaces with the leads, as described after Eq. (21.36). Since we consider the FCS at low frequencies,  $\Omega \ll E_{\text{Th}}$ , there is no time-dependent term in our kinetic equation similar to that of the usual time-dependent Usadel equation. In this limit the collision integral (21.39) guarantees the current conservation,  $\text{div } \mathbf{j} = 0$ , where  $\mathbf{j} \propto \int d\epsilon \text{Tr} \left( \hat{\tau}_3 \hat{G}_\epsilon(\mathbf{r}) \nabla \hat{G}_\epsilon(\mathbf{r}) \right)$ . The resulting CGF,  $\mathcal{F}(\chi)$ , can be found by evaluating the action (21.37) and solving the kinetic equation  $G_\epsilon(\chi, \mathbf{r})$ . In the absence of the field  $\chi$  our matrix kinetic equation reduces to the standard kinetic equation with a singular kernel  $K(\omega) \propto \omega^{d/2-2}$  in the collision integral [63, 64, 66].

To derive the action (21.37) we have used a local approximation, i.e. we neglected gradient corrections proportional to  $(\nabla \hat{G} \sim 1/L) \ll \nabla W$ . In this way we incorporate only classical effects of interaction into the FCS. The gradient terms would be responsible for quantum corrections to the CGF, coming from frequencies  $\omega \gg \max\{T, eV\}$ . They are small in the parameter  $1/g$  and are beyond the scope of this article.

So far our consideration was rather general. In the following we restrict the analysis to the most interesting shot-noise limit,  $eV \gg T$ . Then the further particular solution of kinetic equation strongly depends on the relative magnitude of the diffusion time  $\tau_D$  compared to the voltage dependent energy relaxation time  $\tau_E(V)$ . In the range of sufficiently high voltages, so that  $\tau_D \gg \tau_E(V)$ , the system is driven into the “hot electron” regime. In this limit the electron distribution function of electrons has the form of a local Fermi distribution with position dependent temperature  $T(\mathbf{r})$  set by the applied voltage  $eV$  and differing from the temperature  $T$  in the leads. For smaller voltages, so that  $1/eV \ll \tau_D \ll \tau_E(V)$ , the electrons are described by a strongly non-equilibrium two step distribution function, which results from the weighted average of the Fermi distribution functions in the left and right leads. We thus call this situation the regime of “cold electrons”. The behavior of the FCS is essentially different in these two regimes and we consider them separately in the following subsections.

#### 21.4.2

#### “Cold Electron” Regime

The cold electron regime is defined by relation  $E_{\text{Th}} \gg 1/\tau_E$ . Under this condition the collision term in the kinetic equation is small, and one can obtain the Green’s function perturbatively around the coherent solution obeying the Usadel equation  $\nabla_z \left( \hat{G}_\epsilon^0(z) \nabla_z \hat{G}_\epsilon^0(z) \right) = 0$ . Here  $0 < z < 1$  is a dimensionless coordinate along the current direction. This solution was found in [68] and at  $T \ll eV$  can be written as

$$\hat{G}_\epsilon^0(\chi, z) = L_\chi(z) \hat{G}_L(\epsilon, \chi) + R_\chi(z) \hat{G}_R(\epsilon) \quad (21.40)$$

$$L_\chi(z) = \frac{\sinh(1-z)\theta_\chi}{\sinh\theta_\chi}, \quad R_\chi(z) = \frac{\sinh z\theta_\chi}{\sinh\theta_\chi}, \quad \theta_\chi = \ln(u + \sqrt{u^2 - 1}),$$

where  $u = 2e^{i\chi} - 1$  for energies  $0 < \epsilon < eV$  and  $u = 1$  otherwise. In first order in  $\tau_D/\tau_E$  the CGF can be found by substituting  $\hat{G}^0$  in the action (21.37). The main contribution comes from frequencies  $T < \omega < eV$ . After some algebra we obtain

$$\mathcal{F}(\chi) = -(t_0 g/8\pi) \int d\epsilon \theta_\chi^2(\epsilon) + \mathcal{F}_{\text{Coll}}(\chi). \quad (21.41)$$

Here the first term is the CGF of non-interacting electrons, and  $\mathcal{F}_{\text{Coll}}(\chi)$  is the correction due to electron-electron interaction. It reads

$$\mathcal{F}_{\text{Coll}} = \frac{t_0 L^d}{2} \int_0^1 dz \int_{\omega^*}^{eV} \frac{d\omega d^d \mathbf{q}}{(2\pi)^{d+1}} \ln \left\{ 1 - \frac{N_\omega \omega^2 \Pi(\chi, z)}{(D\mathbf{q}^2)^2 + \omega^2} \right\} \quad (21.42)$$

$$\Pi(\chi, z) = -4 L_\chi(z) R_\chi(z) e^{i\chi} \{1 - L_\chi(z) - R_\chi(z)\}$$

$$- [zL_\chi(z) + (1-z)R_\chi(z)] (e^{i\chi} - 1) \Big\}$$

where  $N_\omega = (eV/|\omega| - 1)$ , and  $\omega^* = \max\{E_{\text{Th}}, T\}$ . The Thouless energy appears in the low frequency cut-off  $\omega^*$  due to finite-size effects while  $T$  takes into account the smearing of a step in the Fermi distribution. We also note two important properties of the function  $\Pi(\chi, z)$ , namely (i)  $\Pi(i\gamma, z) > 0$  for imaginary  $\chi = i\gamma$  and (ii)  $\Pi(\chi, z) = -P_2(z)\chi^2 + O(\chi^2)$  at  $\chi \ll 1$  where  $P_2(z) = \frac{8}{3}z^2(1-z^2)(1-z+z^2) > 0$ .

To estimate the range of validity of the result (21.42) we substitute a zero order distribution function  $f_0(\epsilon) = (1-z)f_F(\epsilon - eV/2) + zf_F(\epsilon + eV/2)$  into the collision integral,  $f_F(\epsilon)$  being equilibrium Fermi distribution. Then one estimates the 1<sup>st</sup> order correction to be

$$\delta f_{(1)}(\epsilon_\pm) \sim \frac{L^2/D}{\tau_E(V)} \int_{\epsilon_\pm}^{eV} \frac{d\omega}{\omega} \left( \frac{eV}{\omega} \right)^{(2-d)/2} \quad (21.43)$$

if  $\epsilon_\pm = |\epsilon \pm eV/2| \ll eV$  and  $\epsilon_\pm > \max\{E_{\text{Th}}, T\}$ . By virtue of Pauli's principle this correction may not exceed unity,  $\delta f_{(1)} \leq 1$ , which is true only for  $\epsilon_\pm \geq \epsilon^*$ , where the scale  $\epsilon^*$  is given by

$$\epsilon^*(V) \simeq \begin{cases} (eV)^2/g^2 E_{\text{Th}}, & \text{for } D = 1 \\ eV \exp\{-g E_{\text{Th}}/eV\}, & \text{for } D = 2. \end{cases} \quad (21.44)$$

This result shows that a simple perturbation theory is valid provided  $\epsilon^* < \max\{E_{\text{Th}}, T\}$ . Resolving this inequality we obtain the condition  $\tau_D < \tau^*$ , where the time scale  $\tau^*$  is presented in Table 1. The 1<sup>st</sup> order perturbation theory breaks down for higher voltages, when  $\tau_D > \tau^*$ . In this situation we can still obtain the result up to a factor of order of unity from Eq. (21.42) if we use as cut-off  $\omega^* \simeq \epsilon^*$ .

The result (21.41 - 21.42) with cut-off  $\omega^* = \max\{E_{\text{Th}}, T, \epsilon^*\}$  enables us to evaluate all irreducible cumulants  $C_k = -(-i)^k (\partial^k/\partial\chi^k) \mathcal{F}(\chi)$  of a number of electrons transferred. There is no correction to the current on the classical level. The interaction correction to the noise and the 3<sup>d</sup> cumulant is small in the parameter  $\tau_D/\tau_E$  and dominated by inelastic collisions with the energy transfer  $\omega \sim eV$ . On the contrary, the leading contribution to the higher order cumulants is due to Coulomb interaction and it is dominated by quasi-elastic collisions with low energy transfers  $\omega^* \leq \omega \ll eV$ . Up to a numerical constant the result is

$$C_{2k,2k+1} \propto \frac{\langle N \rangle}{g} \left( \frac{eV}{E_{\text{Th}}} \right)^{d/2} \left( \frac{eV}{\omega^*} \right)^{k-1-d/2}, \text{ for } k \geq 2 \quad (21.45)$$

where  $\langle N \rangle \gg 1$  is the average number of electrons transferred and  $\omega^* = \max\{E_{\text{Th}}, T, \epsilon^*\}$ .

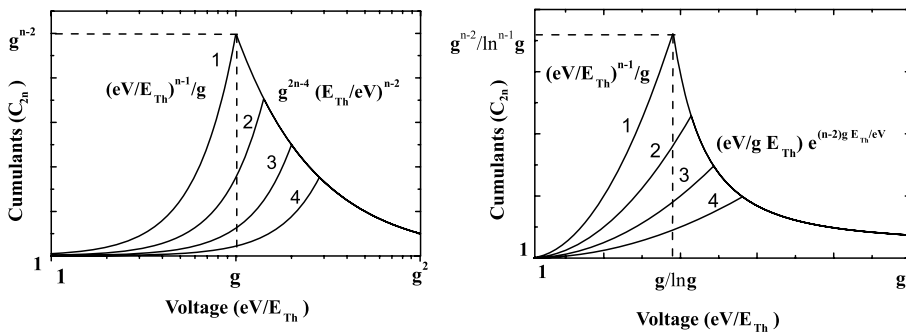


**Fig. 21.8** Sketch of the voltage dependence of the even cumulants of the charge transfer  $C_{2n}$  for  $n > 2$  for a 1D diffusive wire (left panel) and a 2D diffusive film (right panel). The curves 1,2,3,4 correspond to temperatures  $E_{\text{Th}} \sim T_1 < T_2 < T_3 < T_4$ .

The voltage dependence of the  $n^{\text{th}}$  cumulant with  $n \geq 4$  at different temperatures is sketched in Fig. 21.8. Eq. (21.45) shows that the  $n + 1$ st cumulant of the charge transfer is parametrically enhanced versus the  $k$ th one by the large factor  $eV/\omega^* \gg 1$ . It also follows from Eq. (21.45) that the higher cumulants grow with increasing voltage for  $E_{\text{Th}} > 1/\tau^*$  and decay for  $E_{\text{Th}} < 1/\tau^*$ , where the new time scale  $\tau^*(eV, T)$  is parametrically smaller than  $\tau_E$ ,  $\tau^* \ll \tau_E$ . (see Table 1). The current fluctuations are strongest if  $T \leq E_{\text{Th}} \sim 1/\tau_\phi(V)$ . In this case their maximum occurs at  $eV/E_{\text{Th}} \sim g$  for 1D and at  $eV/E_{\text{Th}} \sim g/\ln g$  for 2D. To clarify the physical origin of this strong amplification of the current fluctuations we present below a heuristic interpretation of the result (21.42) by relating it to the phenomenon of photo-assisted shot noise.

Photo-assisted shot noise has been theoretically predicted by Lesovik and Levitov [69]. They considered the mesoscopic scatterer with a single transmission channel  $\mathcal{T}$  biased by the AC voltage  $V(t) = V_\Omega \sin(\Omega t)$  (see Fig. 21.3). This voltage leads to an oscillating phase  $\varphi(t) = \int_{-\infty}^t eV(\tau)d\tau = \Phi_\Omega \cos \Omega t$  across the conductor with amplitude  $\Phi_\Omega = eV_\Omega/\hbar\Omega$ . It has been shown in [69] that such a phase modulation results in a zero-frequency non-transport shot noise due to the excitation of electron-hole pairs in the leads. At low temperatures,  $T \ll \hbar\Phi_\Omega$ , the noise is

$$S_2(\omega = 0) = \frac{e^2}{2\pi\hbar} \mathcal{T}(1 - \mathcal{T}) \sum_{n=-\infty}^{+\infty} |n\Omega| J_n^2(\Phi_\Omega) \quad (21.46)$$

where  $P_n = J_n^2(\Phi_\Omega)$  is the probability to excite an electron-hole pair with the absorption of  $n$  photons, and  $J_n(x)$  are Bessel functions. In the limit of weak phase oscillations,  $\Phi_\Omega \ll 1$ , the noise is quadratic in the amplitude,  $S_2 = G_Q \hbar\Omega \mathcal{T}(1 - \mathcal{T}) \Phi_\Omega^2$ .

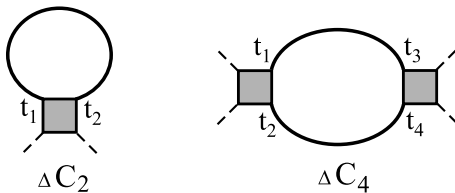


**Fig. 21.9** Diagrammatic representation of interaction corrections to the shot noise and  $C_4$ . Shaded blocks correspond to the imaginary part of diffuson, denoted as  $\tilde{D}_q(t)$ , and thick solid lines correspond to the screened propagator of the electromagnetic fluctuations  $\mathcal{B}(t)$ . Each vertex  $t_k$  brings time derivative  $\partial_{t_k}$ .

The physical origin of the interaction correction to the FCS in diffusive conductors has very much in common with the generation of photo-assisted shot noise. Exploiting the path integral formulation of quantum mechanics one can represent an interacting electron problem by a picture where a given electron is moving in a fluctuating electromagnetic field  $\mathbf{A}_{1,2}(\mathbf{r}, t)$  created by all other electrons (with indices  $j = 1, 2$  referring to a forward and a backward time evolution operator). Since the main effect of the interaction comes from low-frequency fields with  $\omega \ll eV$ , the classical part  $\mathbf{A} = (\mathbf{A}_1 + \mathbf{A}_2)/2$  is of main importance. The field  $\mathbf{A}_{\mathbf{q},\omega}$  leads to the excitation of electron-hole pairs, which, similar to photo-assisted shot-noise, produce corrections to the FCS of the form

$$\Delta\mathcal{F}(\chi, \mathbf{A}) = -\frac{gL^{2(1-d)}}{4\pi} \sum_{\mathbf{q}_1, \mathbf{q}_2} \frac{\omega^2}{(D|\mathbf{q}_1 + \mathbf{q}_2|^2/4)^2 + \omega^2} \int d^d\mathbf{r} \omega \tilde{\Pi}(\chi, z) \mathbf{A}_{\mathbf{q}_1, \omega} \mathbf{A}_{\mathbf{q}_2, \omega}^* e^{i(\mathbf{q}_1 - \mathbf{q}_2)\mathbf{r}} \quad (21.47)$$

Up to second order in  $\chi^2$  the polarization operator  $\tilde{\Pi}(\chi, z)$  agrees with  $\Pi(\chi, z)$  in Eq. (21.42). It is important that this correction is proportional to the total conductance  $g$  of the system. Thus it may become comparable with the non-interacting result for the CGF when the magnitude of phase fluctuation across the sample becomes of the order of unity.

In diffusive system with large conductance  $g \gg 1$  the fluctuation of  $\mathbf{A}_{\mathbf{q},\omega}$  are screened and can be considered as Gaussian with an Ohmic spectrum  $\mathcal{B}(\omega) = \langle |\mathbf{A}_{\mathbf{q},\omega}|^2 \rangle = N_\omega / (vD\omega)$ , where  $N_\omega \cong eV/|\omega|$  is a non-equilibrium distribution function of electromagnetic modes. Thus in order to obtain the interaction contribution to the CGF, the correction (21.47) has to be exponentiated and averaged over these fluctuations. Such considerations give exactly the result (21.42) with polarization operator calculated to accuracy  $\chi^2$ .

It is also instructive to consider the physical picture of photo-assisted current fluctuations in the time domain. To illustrate the main idea we compare

the interaction corrections to the shot noise  $C_2$  and the 4<sup>th</sup> cumulant  $C_4$  for a 1D wire. In the time representation they read

$$\begin{aligned}\Delta C_2 &= \int_0^1 P_2(z) dz \sum_q \int \tilde{\mathcal{D}}'_{t_1}(q, t_1 - t_2) \mathcal{B}'_{t_2}(t_2 - t_1) dt_1 dt_2 \quad (21.48) \\ \Delta C_4 &= 6 \int_0^1 P_2^2(z) dz \sum_q \\ &\quad \int \tilde{\mathcal{D}}'_{t_1}(q, t_1 - t_2) \tilde{\mathcal{D}}'_{t_4}(q, t_4 - t_3) \mathcal{B}'_{t_3}(t_3 - t_1) \mathcal{B}'_{t_2}(t_2 - t_4) dt_1 \dots dt_4\end{aligned}$$

where

$$\mathcal{B}(t) = \int_{1/\epsilon^*}^{+\infty} \frac{d\omega}{\pi} \frac{N_\omega e^{-i\omega t}}{\nu D\omega}, \quad \text{and} \quad \tilde{\mathcal{D}}(q, t) = \int_0^{eV} \frac{d\omega}{\pi} \text{Im} \left( \frac{1}{Dq^2 - i\omega} \right) e^{-i\omega t} \quad (21.49)$$

The corresponding Feynman diagrams are shown in Fig. 21.9. The correlation time of the diffuson propagator  $\tilde{\mathcal{D}}_q(t)$  is short, given by  $\tau_V \sim 1/eV$ , while the photon propagator  $\mathcal{B}(t)$  is strongly non-local in time with long correlation time  $\tau \sim 1/\epsilon^* \gg \tau_V$ . Therefore the time integral in  $\Delta C_2$  is dominated by the short range  $|t_1 - t_2| \sim \tau_V$  only, and the correction to shot noise is small. In contrast, when evaluating the correction to  $\Delta C_4$  both short,  $|t_1 - t_2| \sim |t_3 - t_4| \sim \tau_V$ , and long time intervals,  $|t_1 - t_3| \sim |t_2 - t_4| \sim 1/\epsilon^*$ , are essential. The same structure holds for higher cumulants  $C_{2n>4}$  which are expressed by one-loop diagrams with  $n$  diffusons and  $n$  propagators of the electromagnetic field. We thus see that a conversion of the long-time electromagnetic field correlations into the current of electron hole pairs is the reason for an enhancement of higher order cumulants in diffusive wires and films.

With the results (21.41, 21.42) we can also explore the current probability distribution

$$P(I) = \int_{-\pi}^{\pi} \frac{d\chi}{2\pi} \exp\{-\Omega(\chi)\}, \quad \Omega(\chi) = -\mathcal{F}(\chi) + i(It_0/e)\chi. \quad (21.50)$$

In the long-time limit,  $It_0/e \gg 1$ , this integral can be evaluated within the stationary phase approximation. For this analysis it is important that the action  $\mathcal{F}(\chi)$  has two branch points,  $\chi = \pm i\gamma$ , where  $\gamma \sim (\omega^*/eV)^{1/2} \ll 1$ . The points  $\pm i\gamma$  give two threshold currents,  $I^\pm = (e/t_0) \partial S / \partial \chi|_{\chi=\pm i\gamma}$ , which read  $(I^\pm - \langle I \rangle) / \langle I \rangle = \pm \gamma / 3$ .

Provided the fluctuations are small,  $I^- < I < I^+$ , the saddle point  $\chi^*$  of the function  $\Omega(\chi)$  lies on the imaginary axis and satisfies the condition  $|\chi^*| < \gamma$ . Thus with exponentially accuracy the probability distribution becomes  $P(I) \sim \exp\{-\Omega(\chi^*)\}$ . Due to the smallness of the parameter  $\tau_D/\tau_E$  we found that  $P(I)$  deviates only slightly from the probability  $P_0(I)$  of current fluctuations in the non-interacting limit. For larger current fluctuations,  $I < I^-$  or  $I > I^+$ ,

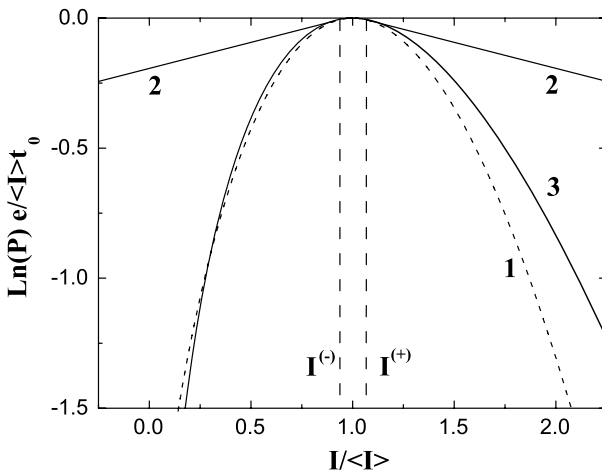


**Fig. 21.10** The log of probability to measure the big non-equilibrium current fluctuations ( $eV \gg T$ ). Curve (1), coherent regime; curve (2), incoherent “cold electron” regime,  $\gamma = 0.2$ ; curve (3), “hot electron” regime.

the potential  $\Omega(\chi)$  does not have a saddle point any more, and one should use the contour  $C_0$  of a zero phase,  $\text{Im } \Omega(\chi) \Big|_{\chi \in C_0} = 0$  for the asymptotic analysis of the integral  $P(I)$ . This contour is pinned by the branch point  $\chi = \pm i\gamma$ , which yields *exponential* tails in the current probability distribution

$$P(I) \approx \exp\{-\mathcal{F}(\pm\gamma) \mp \gamma It_0/e\}. \quad (21.51)$$

The results for the probability distribution are displayed in Fig. 21.10. The Coulomb interaction does not change the Gaussian fluctuations, but strongly affects the tails of  $P(I)$ . They describe long correlated “trains” in the transferred charge, in agreement with our previous discussion on the enhancement of higher order cumulants  $S_{n \geq 2(D+1)}$ .

One can also relate the statistics (21.42) to the photocounting statistics studied by Kindermann et al. [70]. In that work the FCS of incoherent radiation, which is passed through a highly transmitting barrier with transmission coefficient  $\mathcal{T} \leq 1$ , was studied. It was shown that a highly degenerate (or classical) source of radiation with bosonic occupation number  $f_\omega \gg 1$  produces long exponential tails in the photocounting distribution,  $P(n) \propto \exp(-n/f_\omega)$ . The tails of the distribution (21.51) are of the same bosonic nature. The classical electromagnetic field  $A_{\mathbf{q},\omega}$  with  $\omega \ll eV$  and large occupation number  $N_\omega \cong eV/|\omega|$  can excite electron-hole pairs with probability  $\mathcal{P} = \omega^2/((D\mathbf{q}^2)^2 + \omega^2)$ . This probability plays the role similar to the transmission coefficient  $\mathcal{T}$ . It is enhanced due to the diffusive motion of electrons and can be of order of unity. The polarization operator  $\Pi(\chi, z)$  describes the efficiency of the conversion of electromagnetic radiation into a current of electron-hole pairs.

## 21.4.3

**“Hot Electron” Regime**

In the “hot electron” regime,  $E_{\text{Th}} \ll 1/\tau_E$ , describing the regime of high applied voltages or long enough samples, the collision term in the kinetic equation (21.38) dominates. Thus the saddle point solution of the action (21.37) should make the collision integral vanish. To find this solution we note that the collision term in the action is invariant under the gauge transformation  $\tilde{G}_\epsilon(\mathbf{r}) = e^{-\hat{K}_\epsilon(\mathbf{r})} G_\epsilon(\mathbf{r}) e^{\hat{K}_\epsilon(\mathbf{r})}$ . Here  $\hat{K}_\epsilon(\mathbf{r}) = \frac{1}{2} \hat{\tau}_3 [\gamma(\mathbf{r}) + \beta(\mathbf{r})(\epsilon - \phi(\mathbf{r}))]$  and  $\gamma, \beta$  and  $\phi$  are arbitrary functions in space. In particular, this leads to the conservation of the current density,  $\text{div } \mathbf{j} = 0$ , and of the energy flow,  $\text{div } \mathbf{j}_E = 0$ , where  $\mathbf{j}_E \propto (2\pi)^{-1} \int \epsilon d\epsilon \text{Tr} \left( \hat{\tau}_3 \hat{G}_\epsilon(\mathbf{r}) \nabla \hat{G}_\epsilon(\mathbf{r}) \right)$ . It is well known that the physical Green function  $G(\epsilon, \mathbf{r})$  with a local Fermi distribution  $f_\epsilon(\mathbf{r}) = [e^{(\epsilon - \phi(\mathbf{r}))/T(\mathbf{r})} + 1]^{-1}$  makes the collision term in conventional kinetic equations vanish. Its gauge transform,  $\tilde{G}_\epsilon(\mathbf{r})$ , does the same for the generalized kinetic equation (21.38).

The four unknown functions  $\phi, \gamma, T$  and  $\beta$  can be found from the extremum of the simplified action  $S_{\text{hot}}$  which is obtained by substituting  $\tilde{G}_\epsilon(\mathbf{r})$  into the diffusive part of the action  $S_{\text{eff}}$ . For the rest of this discussion we restrict ourselves to a 1D wire, since for the 2D geometry shown in Fig.1, all results are identical to 1D. We write the action in the form  $S_{\text{hot}} = (2\pi)^{-1} g_0 t \int_0^1 dz S_{\text{hot}}(z)$ , where the spatial density  $S_{\text{hot}}(z)$  reads

$$S_{\text{hot}}(z) = -T(\nabla \gamma - \beta \nabla \phi)^2 + (\nabla \gamma - \beta \nabla \phi) \nabla \phi - \frac{\pi^2}{3} T^3 (\nabla \beta)^2 + \frac{\pi^2}{6} (\nabla T^2) \nabla \beta \quad (21.52)$$

Here  $T(z)$  and  $\phi(z)$  have a meaning of a local temperature and chemical potential, while  $\beta(z)$  and  $\gamma(z)$  are their quantum conjugate counterparts. The action (21.52) has to be minimized subject to the boundary conditions  $\phi(z)|_{z=0,1} = \pm eV/2$ ,  $T(z)|_{z=0,1} = T$ ,  $i\gamma(0) = \chi$  and  $\gamma(1) = \beta(0) = \beta(1) = 0$ .

The action  $S_{\text{hot}}$  possesses 4 integrals of motion. They are the physical current  $J = \partial S_{\text{hot}} / \partial \nabla \gamma$ , the “quantum” current  $M = \partial S_{\text{hot}} / \partial \nabla \phi$ , the energy current  $J_E = J\phi - \frac{2\pi^2}{3} T^3 \nabla \beta + \frac{\pi^2}{6} (\nabla T^2)$ , and the spatial density of the action  $S_{\text{hot}}(z)$ . Performing the Legendre transform, we can reduce the task to the boundary value problem for two functions  $T(z)$  and  $\beta(z)$ . Since it appears not to be possible to obtain an analytic solution of these equations for non-vanishing  $\chi$ , we solved them numerically. The results for the probability distribution  $P(I)$  are shown in Fig. 21.10. As in the previous section it can be evaluated using the saddle point approximation. We can see from Fig. 21.10 that the probability of positive current fluctuations,  $\Delta I > 0$ , is enhanced in the “hot electron” limit as compared to the coherent regime, while the probability of

negative fluctuations,  $\Delta I < 0$ , is affected to a lesser extent. The action (21.52) is equivalent to the actions of [60, 61] under the appropriate change of variables. A further increase of the voltage or the sample size will eventually bring the system into the macroscopic regime,  $L \gg L_{\text{e-ph}}$ . The conductor in this case displays only Nyquist noise  $S = 4k_{\text{B}}T/R$ , while higher order cumulants vanish and the probability of current fluctuations becomes Gaussian [61].

## 21.5

### Summary

To summarize, we have studied the full current statistics (FCS) of charge transfer in two important examples of the mesoscopic conductors taking into account the effects of Coulomb interaction. First, we derived the FCS for a single-electron transistor with Coulomb blockade effects in the vicinity of a conductance peak. Quantum fluctuations of the charge are taken into account by a summation of a certain subclass of diagrams, which corresponds to the leading logarithmic approximation. In lowest order in the tunneling strength our results reproduce the ‘orthodox’ theory, while in second order they account for renormalization and cotunneling effects. We have shown that in non-equilibrium situations quantum fluctuations of the charge induce lifetime broadening for the charge states of the central island. An important consequence is the reduction of the probability for currents much larger than the average value.

We further investigated the effect of Coulomb interaction onto the FCS in one- and two-dimensional diffusive conductors. We have found that Coulomb interaction essentially enhances the probability of rare current fluctuations for short conductors,  $1/eV \ll \tau_D \ll \tau_E$ , with  $\tau_D$  and  $\tau_E$  being the diffusion and energy relaxation times. The fluctuations are strongest at low temperatures,  $T \ll 1/\tau_D$ , and they reach the maximum when the sample size matches the voltage dependent dephasing length due to Coulomb interaction. We have shown that tails of the probability distribution of the transferred charge are exponential and they arise from the correlated fluctuations of the current of electron-hole pairs which are excited by the classical low-frequency fluctuations of the electromagnetic field in the media.

### Acknowledgement

This work is part of a research network of the Landesstiftung Baden-Württemberg gGmbH.

## References

- 1 Yu. V. Nazarov (ed.), *Quantum Noise in Mesoscopic Physics*, Vol. 97 of *NATO Science Series II: Mathematics, Physics and Chemistry* (Kluwer Academic Publishers, Dordrecht/Boston/London, 2003).
- 2 L. S. Levitov and G. B. Lesovik, *JETP Lett.* **58**, 230 (1993); L. S. Levitov, H.-W. Lee, and G. B. Lesovik, *J. Math. Phys.* **37**, 4845 (1996).
- 3 L. Mandel and E. Wolf, *Optical Coherence and Quantum Optics* (Cambridge University Press, Cambridge, 1995).
- 4 L. S. Levitov and G. B. Lesovik, *JETP Lett.* **55**, 555 (1992).
- 5 W. Belzig, in: *CFN Lecture Notes on Functional Nanostructures* Vol. 1, edited by K. Busch, A. Powell, C. Röthig, G. Schön, and J. Weissmüller, *Lecture Notes in Physics*, Vol. 658 (Springer-Verlag, Berlin, 2004).
- 6 B. Reulet, J. Senzier, and D. E. Prober, *Phys. Rev. Lett.* **91**, 196601 (2003).
- 7 Yu. Bomze, G. Gershon, D. Shovkun, L. S. Levitov, and M. Reznikov, *Phys. Rev. Lett.* **95**, 176601 (2005).
- 8 S. Gustavsson, R. Leturcq, B. Simovic, R. Schleser, T. Ihn, P. Studerus, K. Ensslin, D. C. Driscoll, and A. C. Gossard, *Phys. Rev. Lett.* **96**, 076605 (2006).
- 9 J. Tobiska and Yu. V. Nazarov, *Phys. Rev. Lett.* **93**, 106801 (2004).
- 10 Y. Nakamura, Yu. A. Pashkin, and J. S. Tsai, *Nature* **398**, 786 (1999).
- 11 T. Hayashi, T. Fujisawa, H. D. Cheong, Y. H. Jeong, and Y. Hirayama, *Phys. Rev. Lett.* **91**, 226804 (2003).
- 12 M. H. Devoret and R. J. Schoelkopf, *Nature* **406**, 1039 (2000).
- 13 A. Zeilinger, *Rev. Mod. Phys.* **71**, S288 (1999).
- 14 A. Rauschenbeutel, G. Nogues, S. Osnaghi, P. Bertet, M. Brune, J.-M. Raimond, and S. Haroche, *Science* **288**, 2024 (2000).
- 15 C. A. Sackett, D. Kielpinski, B. E. King, C. Langer, V. Meyer, C. J. Myatt, M. Rowe, Q. A. Turchette, W. M. Itano, D. J. Wineland, and C. Monroe, *Nature* **404**, 256 (2000).
- 16 C. W. J. Beenakker, [cond-mat/0508488](https://arxiv.org/abs/cond-mat/0508488).
- 17 G. Burkard, D. Loss, and E. V. Sukhorukov, *Phys. Rev. B* **61**, R16303 (2000).
- 18 F. Taddei and R. Fazio, *Phys. Rev. B* **65**, 075317 (2002).
- 19 L. Faoro, F. Taddei, and R. Fazio, *Phys. Rev. B* **69**, 125326 (2004).
- 20 M. Field, C. G. Smith, M. Pepper, D. A. Ritchie, J. E. F. Frost, G. A. C. Jones, and D. G. Hasko, *Phys. Rev. Lett.* **70**, 1311 (1993).
- 21 E. Buks, R. Schuster, M. Heiblum, D. Mahalu, and V. Umansky, *Nature* **391**, 871 (1998).
- 22 J. M. Elzerman, R. Hanson, J. S. Greidanus, L. H. Willems van Beveren, S. De Franceschi, L. M. K. Vandersypen, S. Tarucha, and L. P. Kouwenhoven, *Phys. Rev. B* **67**, 161308(R) (2003).
- 23 J. R. Petta, A. C. Johnson, C. M. Marcus, M. P. Hanson, and A. C. Gossard, *Phys. Rev. Lett.* **93**, 186802 (2004).
- 24 A. K. Huettel, S. Ludwig, K. Eberl, and J. P. Kotthaus, *Phys. Rev. B* **72**, 081310(R) (2005).
- 25 D. V. Averin and E. V. Sukhorukov, *Phys. Rev. Lett.* **95**, 126803 (2005).
- 26 D. S. Golubev and A. D. Zaikin, *Phys. Rev. Lett.* **86**, 4887 (2001).
- 27 D. S. Golubev and A. D. Zaikin, *Phys. Rev. B* **69**, 075318 (2004).
- 28 D. S. Golubev and A. D. Zaikin, *Phys. Rev. B* **70**, 165423 (2004).
- 29 A. V. Galaktionov, D. S. Golubev, and A. D. Zaikin, *Phys. Rev. B* **68**, 085317 (2003).
- 30 M. Kindermann and Yu. V. Nazarov, *Phys. Rev. Lett.* **91**, 136802 (2003).
- 31 D. A. Bagrets and Yu. V. Nazarov, *Phys. Rev. Lett.* **94**, 056801 (2005).
- 32 M. Kindermann and Yu. V. Nazarov, in [1].
- 33 G. Schön and A. D. Zaikin, *Phys. Rep.* **198**, 237 (1990).
- 34 A. V. Andreev and E. G. Mishchenko, *Phys. Rev. B* **64**, 233316 (2001).
- 35 D. A. Bagrets and Yu. V. Nazarov, *Phys. Rev. B* **67**, 085316 (2003).
- 36 A. Braggio, J. König, and R. Fazio, *Phys. Rev. Lett.* **96**, 026805 (2006).

- 37** H. Schoeller and G. Schön, Phys. Rev. B **50**, 18436 (1994).
- 38** J. König, H. Schoeller, and G. Schön, Phys. Rev. Lett. **78**, 4482 (1997); Phys. Rev. B **58**, 7882 (1998).
- 39** D. S. Golubev, J. König, H. Schoeller, and G. Schön, Phys. Rev. B **56**, 15782 (1997).
- 40** M. Kindermann and B. Trauzettel, Phys. Rev. Lett. **94**, 166803 (2005).
- 41** A. Komnik and A. O. Gogolin, Phys. Rev. Lett. **94**, 216601 (2005).
- 42** K. A. Matveev, Sov. Phys. JETP **72**, 892 (1991).
- 43** P. Joyez, V. Bouchiat, D. Esteve, C. Urbina, and M. H. Devoret, Phys. Rev. Lett. **79**, 1349 (1997).
- 44** A. Thielmann, M. H. Hettler, J. König, and G. Schön, Phys. Rev. B **68**, 115105 (2003).
- 45** A. Thielmann, M. H. Hettler, J. König, and G. Schön, Phys. Rev. Lett. **95**, 146806 (2005).
- 46** Y. Utsumi, D. S. Golubev, and G. Schön, Phys. Rev. Lett. **96**, 086803 (2006).
- 47** H. J. Spencer and S. Doniach, Phys. Rev. Lett. **18**, 23 (1967).
- 48** P. Coleman, L. B. Ioffe, and A. M. Tsvelik, Phys. Rev. B **52**, 6611 (1995).
- 49** A. Shnirman and Yu. Makhlin, Phys. Rev. Lett. **91**, 207204 (2003).
- 50** K.-C. Chou, Z.-B. Su, B.-L. Hao, and L. Yu, Phys. Rep. **118**, 1 (1985).
- 51** A. Kamenev, in: Nanophysics: Coherence and Transport (Les Houches, Volume Session LXXXI) edited by H. Bouchiat, Y. Gefen, S. Guérón, G. Montambaux, and J. Dalibard, NATO ASI (Elsevier, Amsterdam, 2005).
- 52** A. Kamenev, in: Strongly Correlated Fermions and Bosons in Low-Dimensional Disordered Systems, edited by I. V. Lerner et al., NATO Science Ser. II, Vol. 72 (Kluwer, Dordrecht, 2002).
- 53** Y. Utsumi, H. Imamura, M. Hayashi, and H. Ebisawa, Phys. Rev. B **67**, 035317 (2003).
- 54** L. S. Levitov and M. Reznikov, Phys. Rev. B **70**, 115305 (2004).
- 55** A. J. Efros and M. Pollak (eds.) Electron-Electron Interaction In Disordered Systems (Elsevier, Amsterdam, 1985).
- 56** P. A. Lee and T. V. Ramakrishnan, Rev. Mod. Phys. **57**, 287 (1985).
- 57** C. W. J. Beenakker and M. Büttiker, Phys. Rev. B **46**, 1889 (1992).
- 58** A. H. Steinbach, J. M. Martinis, and M. H. Devoret, Phys. Rev. Lett. **76**, 3806–3809 (1996).
- 59** D. B. Gutman and Y. Gefen, Phys. Rev. B **68**, 035302 (2003).
- 60** S. Pilgram, Phys. Rev. B **69**, 115315 (2004).
- 61** D. B. Gutman, A. D. Mirlin, and Y. Gefen, Phys. Rev. B **71**, 085118 (2005).
- 62** V. I. Kozub and A. M. Rudin, Phys. Rev. B **52**, 7853 (1995); K. E. Nagaev, Phys. Rev. B **52**, 4740 (1995).
- 63** B. L. Altshuler and A. G. Aronov, in: Electron-Electron Interaction In Disordered Systems, edited by A. J. Efros and M. Pollak (Elsevier, Amsterdam, 1985).
- 64** I. L. Aleiner and Ya. M. Blanter, Phys. Rev. B **65**, 115317 (2002).
- 65** D. A. Bagrets, Phys. Rev. Lett. **93**, 236803 (2004).
- 66** A. Kamenev and A. Andreev, Phys. Rev. B **60**, 2218 (1999).
- 67** W. Belzig and Yu. V. Nazarov, Phys. Rev. Lett. **87**, 197006 (2001).
- 68** Yu. V. Nazarov, Ann. Phys. (Leipzig) **8**, SI-193 (1999).
- 69** G. B. Lesovik, and L. S. Levitov, Phys. Rev. Lett. **72**, 538 (1994).
- 70** M. Kindermann, Yu. V. Nazarov, and C. W. J. Beenakker, Phys. Rev. Lett. **88**, 063601 (2002).

## 22

# Quantum Limit of the Carnot Engine

*Friedemann Tonner and Günter Mahler*

### 22.1

#### Introduction

Nanoscience is presently developing towards two diverging goals: The making of nanostructured materials [1] and the quest for functional machines [2,3] on the nanoscopic (or molecular) level. With respect to the latter pertinent questions are: (1) to what extent can the design principles of macroscopic machines be down-scaled? (2) Under what conditions and how might the function deteriorate? (3) Will alternative concepts become available, which in turn, would not be viable on the macroscopic limit [2,4–7]?

We will briefly return to question (3) in the conclusion section. In the following we mainly focus on the first two questions relating to a specific class of machines: the Carnot engine [8].

Machines are defined by their respective function. The physical representation of this function can often be decomposed into certain primitives. Typical examples are logical gates making up a computing network. If such a decomposition is not possible, the machine might be termed “primitive”. To carry out the function the machine has usually to respond to some external control (input). Physically this input can be regarded as a part of the initial conditions (state preparation).

The Carnot engine is considered to be a primitive machine. For a physical system  $M$  to operate as such a machine a number of conditions has to be met:

(1) There must be an environment  $C$ , which is kept in a non-equilibrium state (with regions of different temperatures  $T_L, T_U > T_L$ ). This state should survive for a sufficiently long time to be “useful”.

(2)  $M$  must be bipartite, i.e. consisting of a “mechanical” degree of freedom (the analogue of position  $x$  of the piston in a classical machine) and a thermal subsystem  $G$  (called the “working medium”). In the nanoscopic limit this amounts to saying that we are concerned with a few-particle system supporting collective modes of different character: One being weakly damped (almost

isolated from the environment) and becoming mechanical in the macroscopic limit, the others representing “thermal motion” (exchanging heat with the system’s environment).

(3) The system  $M$  has to be in controlled contact with that environment. In particular, the subsystem  $G$  should be able to interact with either temperature region of  $C$  (isothermal process) or else be isolated (adiabatic process). This selective coupling must, in turn, be synchronized with the cyclic motion of the mechanical coordinate  $x$ .

In the classical limit these various dynamical features do not pose any serious problems. Heat engines are part of our everyday life. In the quantum limit things change, though: (a) It may be difficult to maintain thermal non-equilibrium on small length scales and/or small environments [4]. (b) The distinction between thermal and mechanical degrees of freedom may become obscure in the nano-limit [9]. (c) The phase-sensitive control seems to call for a time-dependent Hamiltonian and damping, i.e. for a non-autonomous, essentially classical design [10–17].

Here we will assume that temperature gradients in the environment can be supplied down to the required length scale and the distinction between thermal and mechanical degrees of freedom will be taken as a constitutive part of our minimal model. It will then be shown that the phase-sensitive control does not require external driving but can phenomenologically be implemented as a static feature. This constitutes the concept of an autonomous Carnot engine down to the quantum limit, if at the cost of decoherence.

This paper is organized as follows: In Sect. 22.2 the pertinent Hamilton model is introduced, in Sect. 22.3 we discuss the master equation and the implementation of time slot operators. In Sect. 22.4 we supply tools to characterize the machine function (heat, work, efficiency, coherent energy), Sect. 22.5 contains the numerical results. Our conclusions are summarized and discussed in Sect. 22.6.

## 22.2

### Spin-oscillator Model

#### 22.2.1

##### Basic Definitions

Our machine  $M$  (see Fig. 22.1) consists of a spin as the “gas” system  $G$  or working medium and a mechanical system  $C$  (harmonic oscillator). As indicated by the two switches  $G$  is in thermal contact with two different baths at specific time slots controlled by the oscillator state. In addition  $G$  and  $C$  have a direct (mechanical) coupling by a corresponding Hamiltonian term.

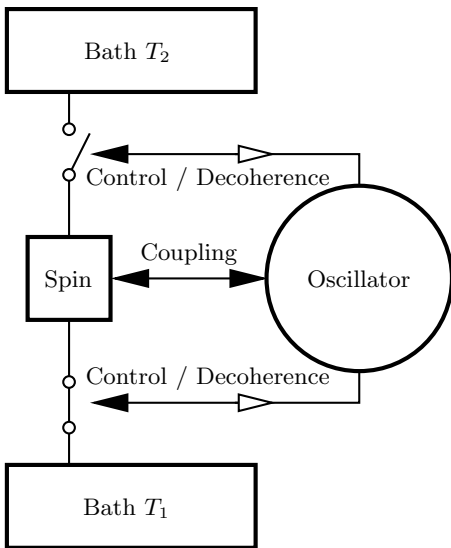


**Fig. 22.1** System diagram of autonomous quantum Carnot engines.

The Hamilton operator of the total system is

$$\hat{H} = \hat{H}_G + \hat{H}_C + \hat{H}_{GC} = \hat{H}_{GGC} + \hat{H}_C \quad (22.1)$$

with the local spin Hamilton operator

$$\hat{H}_G = C_G \hat{\sigma}_z \otimes \hat{1}, \quad (22.2)$$

the local harmonic oscillator Hamilton operator [18]

$$\hat{H}_C = \hat{1} \otimes C_C \left( \hat{b}^\dagger \hat{b} + \frac{1}{2} \right) = \hat{1} \otimes \frac{C_C}{2} (\hat{x}^2 + \hat{p}^2) \quad (22.3)$$

and the coupling

$$\hat{H}_{GC} = C_R \hat{\sigma}_z \otimes \hat{x} \quad (22.4)$$

between oscillator and spin. The (dimensionless) displacement  $\hat{x}$  of the oscillator herein controls (like a piston) the mean energy splitting of the spin, where  $\hat{x} = 2^{-1/2}(\hat{b}^\dagger + \hat{b})$  and  $\hat{p} = i \cdot 2^{-1/2}(\hat{b}^\dagger - \hat{b})$  are known as quadrature operators.

With the help of

$$\hat{H}_{GR}(\hat{x}) = C_G \hat{1} + C_R \hat{x} \quad (22.5)$$

we can write

$$\hat{H}_{GGC} = \hat{\sigma}_z \otimes \hat{H}_{GR}(\hat{x}) \quad (22.6)$$

and thus define an effective Hamilton operator for system  $G$

$$\hat{H}_{GGC}^{\text{eff}} = \overline{C_{\text{GR}}}(\langle \hat{x} \rangle) \hat{\sigma}_z \quad (22.7)$$

with

$$\overline{C_{\text{GR}}}(\langle \hat{x} \rangle) = \langle \hat{H}_{\text{GR}}(\hat{x}) \rangle = C_G + C_R \langle \hat{x} \rangle, \quad (22.8)$$

assuming  $\langle \hat{\sigma}_z \otimes \hat{x} \rangle \approx \langle \hat{\sigma}_z \rangle \cdot \langle \hat{x} \rangle$  (or the dimensionless measure  $\delta = \langle \hat{\sigma}_z \otimes \hat{x} \rangle / (\langle \hat{\sigma}_z \rangle \langle \hat{x} \rangle) - 1 \approx 0$ ) to be fulfilled. The effective energy splitting then is

$$\overline{\Delta E_G}(\langle \hat{x} \rangle) = 2\overline{C_{\text{GR}}}(\langle \hat{x} \rangle). \quad (22.9)$$

Here and in the following the overlines indicate mean values resulting from expectation values of unsharp quantum observables. The numerical value of  $\delta$  can be used as a quality measure for Eq. (22.9) to be a consistent concept. Typically (where the measure is not singular),  $\delta$  is in the low percentage range, as long as we set  $C_R/C_C$  to values in the same range. The validity of that effective Hamiltonian is only relevant for confirming our concepts of heat and work. Certainly we use for dynamical calculations the full Hamilton operator.

We take as initial state  $\hat{\rho}(t=0)$  of the machine the product state

$$\hat{\rho}(t=0) = \hat{\rho}_G \otimes \hat{\rho}_C \quad (22.10)$$

with  $\hat{\rho}_G = \begin{pmatrix} p & 0 \\ 0 & 1-p \end{pmatrix}$  being a mixed state in  $\hat{\sigma}_z$ -eigenbasis. For given energy splitting  $\Delta E_G$  the spin may be said to be in a canonical state with temperature  $T_G$ :

$$\frac{1-p}{p} = \exp\left(-\frac{\Delta E_G}{T_G}\right) \quad (22.11)$$

(for the isolated spin  $\Delta E_G = 2C_G$ ). Here and in the following all temperatures are in units of energy. The initial oscillator state is taken to be pure

$$\hat{\rho}_C = |\psi_C\rangle\langle\psi_C|, \quad (22.12)$$

where  $|\psi_C\rangle = |\alpha(\phi_0)\rangle$  is a coherent state [18, see, e.g.,] (excitation parameter  $\alpha(\phi_0) = |\alpha| \exp(-i\phi_0)$ ). For numerical reasons the state space of the oscillator will be truncated to the range  $n_l, n_{l+1}, \dots, n_{u-1}, n_u$ . In the simplest case  $n_l = 0$ . In general this range will reflect the initial state distribution. This distribution controls the energy splitting of the system  $G$  but also defines the phase-locked control of the bath coupling. The Hamiltonian system thus comprises  $N = 2(n_u - n_l + 1)$  states in total. The state (density operator  $\hat{\rho}$ ) of machine  $M$  lives in Liouville space of dimension  $N^2$ .

Represented in the truncated Fock basis  $|i\rangle$  of the oscillator we get

$$|\alpha(\phi_0)\rangle \approx C_N \sum_{i=n_l}^{n_u} \frac{\alpha(\phi_0)^i}{\sqrt{i!}} |i\rangle \quad (22.13)$$

with the normalizing constant  $C_N$ . By construction we thus have an oscillatory behavior for the mean displacement of the oscillator. The effective energy splitting becomes time dependent, we expect the splitting

$$\overline{\Delta E_G}(\langle \hat{x} \rangle) = \overline{\Delta E_G}(t) = 2C_G + 2\sqrt{2}C_R|\alpha| \cos(t + \phi_0) \quad (22.14)$$

for unitary dynamics and  $\omega = C_C = 1$ .

Note that – even without any bath coupling – the total system energy  $\overline{E} = \langle \hat{H} \rangle$  is defined here with some finite uncertainty only.

## 22.2.2

### Thermodynamic Variables for $G$

The instantaneous mean “effective” temperature of the spin  $G$  (cf. Eq. (22.11)) is taken to be

$$\overline{T_G} = -\frac{\overline{\Delta E_G}(\langle \hat{x} \rangle)}{\ln \left( \frac{\text{Tr}\{\hat{P}_{11}\hat{\rho}_G\}}{\text{Tr}\{\hat{P}_{00}\hat{\rho}_G\}} \right)} \quad (22.15)$$

with the reduced density operator  $\hat{\rho}_G$  of the system  $G$  and

$$\hat{P}_{ii} = |i\rangle\langle i|, \quad i = 0, 1. \quad (22.16)$$

Because the total system is interacting with the environment (baths), the (dimensionless) von Neumann entropy

$$S = -\text{Tr}\{\hat{\rho} \ln \hat{\rho}\} \quad (22.17)$$

can change. Here we need to consider also the reduced entropy [19]

$$S_G = -\text{Tr}\{\hat{\rho}_G \ln \hat{\rho}_G\}, \quad (22.18)$$

where  $\hat{\rho}_G = \text{Tr}_C\{\hat{\rho}\}$  is the reduced density operator of  $G$ .  $S_C$  is defined correspondingly.

Because the total system is in a mixed state (initial preparation: canonical state in the spin system) even initially, the entropies  $S_G, S_C$  are not equal. The von Neumann entropy  $S_G$ , after multiplying with the Boltzmann constant  $k_B$ , can be identified with the thermodynamical entropy (a bath induced transition between level 0 and 1 cannot generate coherences in system  $G$  and coherences between system  $G$  and  $C$  are not relevant for calculating the entropy of the system  $G$ ). This does even hold in the dynamical case, for which the system  $G$  is not in equilibrium with the bath in contact, but with a “virtual bath” of the temperature  $\overline{T_G}$  as introduced in Eq. (22.15).

## 22.3

### Master Equation

#### 22.3.1

#### Lindblad Superoperator

The dynamic evolution of a Hamilton system, weakly coupled under Markov conditions to a time independent environment, can be represented by a Lindblad superoperator  $\hat{L}$  [20,21]

$$\hat{L} = \hat{L}_{\text{coh}} + \sum_i \hat{L}_{\text{inc},i}, \quad (22.19)$$

which is constructed from a coherent part (Hamilton dynamics)

$$\hat{L}_{\text{coh}}\hat{\rho} = -i/\hbar[\hat{H}, \hat{\rho}] \quad (22.20)$$

and incoherent parts  $i$

$$\hat{L}_{\text{inc},i}\hat{\rho} = \hat{A}_i\hat{\rho}\hat{A}_i^\dagger - 1/2[\hat{A}_i^\dagger\hat{A}_i, \hat{\rho}]_+. \quad (22.21)$$

Here the action of the environment on the considered system is described by the environment operators  $\hat{A}_i$ .

The open system dynamics is then given by

$$\dot{\hat{\rho}} = \hat{L}\hat{\rho}. \quad (22.22)$$

with the formal solution

$$\hat{\rho}(t) = \exp(\hat{L}t)\hat{\rho}(0). \quad (22.23)$$

In our case we want to couple the spin alternatively to two baths of different temperature during different time slots, defined by the momentary oscillator state. The bath coupling has thus to be controlled by the state of the oscillator C in an autonomous fashion (i.e. explicitly time independent).

Under bath contact only the occupation of the spin states should change (quasi-isothermal step), whereas the control system itself should be disturbed in the least possible way.

The environment operators are thus taken to have the following general form:

$$\hat{A}_i = \hat{A}_{a_\pm^{(j)}, f^{(j)}, \pm} = a_\pm^{(j)} \cdot \hat{\sigma}_\pm \otimes \hat{\Pi}^{(j)}[f^{(j)}], \quad (22.24)$$

with the amplitudes  $a_\pm^{(j)}$  (giving the direction dependent transition rates of bath  $j$  with temperature  $T_j, j = U, L$  for the upper and lower temperature respectively), the transition operator  $\hat{\sigma}_\pm$  acting on the spin subspace and a “time slot operator”  $\hat{\Pi}^{(j)}[f^{(j)}]$  acting on the oscillator subspace. The index  $(j)$  indicating bath and time slot (see Fig. 22.2) is dropped in the following section for clarity.

## 22.3.2

## Time Slot Operators

The time slot operators should control an incoherent process (here with respect to the spin) by testing the momentary phase of an oscillator state. How can we generate an operator that reacts sensitively and autonomously to such a phase? Consider the fidelity [22]

$$F(t) = \text{Tr}\{\hat{\rho}_C(0)\hat{\rho}_C(t)\} \quad (22.25)$$

which is 1 at time  $t = 0$  and rapidly drops depending on the width of the oscillator state distribution. Eq. (22.25) thus tests the time dependent state  $\hat{\rho}_C(t)$  against its value at  $t = 0$ .  $F(t)$  is periodic with the oscillator frequency  $\omega = C_C$ .

We now introduce a time slot operator as the functional

$$\hat{\Pi}[f] = \hat{\Pi}[\theta(\tau)\hat{\rho}_C(\tau)] = N_{\Pi} \int_{\tau \in \Theta_{\omega}} \theta(\tau)\hat{\rho}_C(\tau) d\tau \quad (22.26)$$

with an arbitrary scalar control function  $\theta(\tau)$  defined on a single period, i.e. in the interval of length  $2\pi/\omega$ , e.g.  $\Theta_{\omega} = [0, \frac{2\pi}{\omega}]$ , and a (normalization) constant  $N_{\Pi}$ . Time is measured in units  $C_C^{-1}$ . Then

$$F(t) = \text{Tr}\{\hat{\Pi}[\theta(\tau)\hat{\rho}_C(\tau)]\hat{\rho}_C(t)\} \quad (22.27)$$

is a generalization of Eq. (22.25), which is recovered for

$$\theta(\tau) = \delta(\tau) \quad (22.28)$$

and  $N_{\Pi} = 1$ .

If we choose the uniform amplitude distribution over the Fock states of the oscillator, the definition of the time slot operator is least state dependent (independent of  $|\alpha|$  of the actual oscillator state there should be an overlap between the time evolved state and the integral over states used for defining the time slot operator)

$$|\psi_C(t)\rangle = \frac{1}{\sqrt{n}} \sum_{k=n_l}^{n_l+n-1} e^{-i\omega kt} |k\rangle. \quad (22.29)$$

Then we get for  $n_l = 0$

$$\hat{\rho}_C(t) = |\psi_C(t)\rangle\langle\psi_C(t)| = \frac{1}{n} \sum_{k=0}^{n-1} \sum_{l=0}^{n-1} e^{-i\omega(k-l)t} |k\rangle\langle l| \quad (22.30)$$

and thus the matrix representation of  $\hat{\Pi}$  reads in the Fock basis

$$\Pi_{kl}[f] = N_{\Pi} \int_{\tau \in \Theta_{\omega}} \theta(\tau) (\rho_C)_{kl}(\tau) d\tau$$

$$= \frac{N_{\Pi}}{n} \int_{\tau \in \Theta_{\omega}} \theta(\tau) e^{-i\omega(k-l)\tau} d\tau. \quad (22.31)$$

The time slot operator uses the basic resource of the oscillator, namely the multiples of a single frequency, to synthesize the desired control function, when the time slot operator is applied to an evolving oscillator state. If taken as part of an environment operator, it can therefore be used to control, for example, a state transition within another system as in Eq. (22.24).

Note that the environment operators act on the system all the time, the whole system is explicitly time independent (every ‘time dependence’ or machine function is engineered into the environment operators) – in contrast to the conventional use of gates (switched on and off by external classical control) in quantum computing [22]. Thus time slot operators are a means for incoherent state dependent autonomous control.

The time slot operator inherits its Hermitian property and its positivity via the definition over the density operator. It is not a projector, but a sum (integral) over projectors.

As the oscillator is also used as a work variable we do not want the time slot operators to change the mean energy of the oscillator substantially. Now, in the Lindblad time evolution terms of the type  $\hat{\Pi}|\psi_C\rangle$  for pure initial states of the oscillator occur. If we require

$$\left| \langle \psi_C | \hat{\Pi}^\dagger | \hat{H}_C | \hat{\Pi} \psi_C \rangle \right|^2 = \left| \langle \psi_C | \hat{H}_C | \psi_C \rangle \right|^2 \quad (22.32)$$

to hold for any  $|\psi_C\rangle$ , the application of  $\hat{\Pi}$  on  $|\psi_C\rangle$  will not change the mean occupation number directly, at least in an infinitesimally small time step.

This can be reached by suppressing unbalanced time dependencies between diagonal elements of  $\hat{\rho}_C$ , effectively leading to a “first order” correction in the Lindblad time evolution (“second order” effects are present via off-diagonal time dependencies). With the definition of Eq. (22.31), in which the absolute square of  $\Pi_{kl}$  is symmetric in  $k$  around  $k = 0$ , we require

$$\Pi'_{kl} = \begin{cases} \Pi_{kl} & \text{if } (|k - l| \leq l) \wedge (|k - l| \leq (n - 1) - l) \\ 0 & \text{otherwise} \end{cases} \quad (22.33)$$

Note that this cutoff procedure for the time slot operator destroys its Hermitian property, nevertheless the control function is not compromised severely.

As the bath coupling in Lindblad form is phenomenological, we have to put all its properties into the control function  $\theta(\tau)$ . This function should depend in our context on the parameters  $\overline{\Delta E_G}$ ,  $T$  and the transition direction.

If the coupling strength to the bath was large, the bath could “see”, in principle, the dynamics and changes in the spectrum of the system (timescale of system larger than that of the bath). If the coupling was weak, as in the present

case, the bath should see only an average spectrum (but it has always to see the time dependent phase of the oscillator).

## 22.4 Machine Cycles

### 22.4.1

#### Choice of Amplitudes $a_{\pm}^{(j)}$ and Control Functions $\theta^{(j)}(\tau)$

The general characteristics of the time slot operators acting on system  $C$  combined with transition operators in the system  $G$  do not yet completely define the system characteristics. The number and form of the control functions have to be specified.

The simplest way to define a thermodynamic machine in the quantum regime is to mimic a classical thermodynamic machine. Because we use canonical contacts to the baths and isolation from baths (steered by the control function), the analogous system is the Carnot machine [8]. A Carnot machine can run in two directions, as a heat pump and a heat engine, respectively, depending on the order in time of isothermal/adiabatic expansion/compression process steps.

The process steps are summarized in Table 22.1 and 22.2. Step 4 ends with time  $t_4$ , which is then identified with time  $t_0$  of the next cycle.

As our model is autonomous, we have to pre-calculate the time independent environment operators  $\hat{A}_i$  from an assumed (virtual) time evolution of the oscillator, which is taken to be unitary. Note that as the environment operators exhibit back-action on the oscillator, the actual time evolution is not unitary.

One simple way to define the control function on the time interval  $\Theta_{\omega} = [t_0 = 0, t_4 = 2\pi/\omega]$  is to use the normalized rectangular function  $\theta(\tau) = \text{rect}(\tau; \tau_a, \tau_b) \equiv h(\tau - \tau_a) - h(\tau - \tau_b)$ , where  $h(\tau)$  is the Heaviside step function and  $\tau_a$  and  $\tau_b$  are constants  $\tau_a < \tau_b$ . This means for a machine in contact with the bath  $T_j$  ( $j = U, L$ ):  $\theta^{(j)}(\tau) = \text{rect}(\tau; \tau_a^{(j)}, \tau_b^{(j)})$  with the constants for

**Tab. 22.1** Process steps of heat engine.

heat engine		step	start time
compression	isothermal $T_L$	1	$t_0$
	adiabatic	2	$t_1$
expansion	isothermal $T_U (> T_L)$	3	$t_2$
	adiabatic	4	$t_3$

**Tab. 22.2** Process steps of heat pump.

heat pump		step	start time
compression	adiabatic	1	$t_0$
	isothermal $T_U$	2	$t_1$
expansion	adiabatic	3	$t_2$
	isothermal $T_L (< T_U)$	4	$t_3$

$\theta_1(\tau), \theta_2(\tau)$  (dashed)

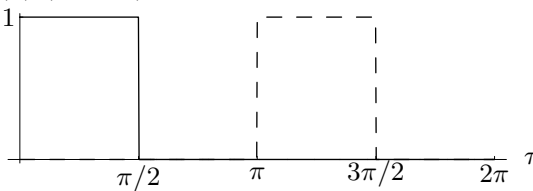


**Fig. 22.2** Control functions  $\theta^{(j)}(\tau)$  for switching on and off baths of temperature  $T_j$ , ( $j = U, L$ ) at different time slots (shown for the heat engine).

the heat engine:  $\tau_a^{(L)} = t_0$ ,  $\tau_b^{(L)} = t_1$ ,  $\tau_a^{(U)} = t_2$ ,  $\tau_b^{(U)} = t_3$  (cf. Fig. 22.2) and for the heat pump:  $\tau_a^{(U)} = t_1$ ,  $\tau_b^{(U)} = t_2$ ,  $\tau_a^{(L)} = t_3$ ,  $\tau_b^{(L)} = t_4$ .

We calculate the time slot operators  $\hat{\Pi}^{(j)}[\theta^{(j)}(\tau)\hat{\rho}_C(\tau)]$  for each bath  $j = U, L$  from these requirements (cf. Eq. (22.26)), apply the cutoff procedure (cf. Eq. (22.33)) and normalize them ( $N_{\hat{\Pi}}^{(j)} = 1/F^{(j)}(\tau_N^{(j)})$ ) with respect to the fidelity of Eq. (22.27) at time  $\tau_N^{(j)} = (\tau_a^{(j)} + \tau_b^{(j)})/2$ . We time average the energy splitting of Eq. (22.14) over the respective time slot

$$\widetilde{\Delta E_G}^{(j)} = \frac{1}{\tau_b^{(j)} - \tau_a^{(j)}} \int_{\tau_a^{(j)}}^{\tau_b^{(j)}} \overline{\Delta E_G}(\tau) d\tau \quad (22.34)$$

and calculate the corresponding occupation numbers (cf. Eq. (22.11)) from

$$\frac{1 - p^{(j)}}{p^{(j)}} = \exp \left( -\frac{\widetilde{\Delta E_G}^{(j)}}{T_j} \right) \quad (22.35)$$

to define the amplitudes of the environment operators of Eq. (22.24)

$$a_-^{(j)} = C_B \sqrt{p^{(j)}}, \quad a_+^{(j)} = C_B \sqrt{1 - p^{(j)}}. \quad (22.36)$$

where  $C_B$  is a global amplitude factor used for adjusting the total bath strength. This approach assumes that the baths only see the mean splitting during interaction.

## 22.4.2

**Heat and Work**

For a two-level system, restricted to states diagonal in its energy representation and subject to external control of its spectrum,  $E_i = E_i(x)$  (cf. Eq. (22.9)), the Gibbsian fundamental form

$$d\bar{E} = TdS + dW \quad (22.37)$$

does always apply, where  $dW = \xi dx$ ,  $\xi$  is an intensive parameter. In order to show this, consider

$$\bar{E} = \sum_i w_i E_i \quad (22.38)$$

$$\Rightarrow d\bar{E} = \sum_i dw_i E_i + \sum_i w_i dE_i \quad (22.39)$$

According to our assumptions we have

$$dE_i = \frac{\partial E_i}{\partial x} dx \quad (22.40)$$

$$d\bar{E} = \sum_i dw_i E_i + \underbrace{\sum_i w_i \frac{\partial E_i}{\partial x} dx}_{\xi} = \sum_i dw_i E_i + dW \quad (22.41)$$

On the other hand, the entropy is given by

$$S = - \sum_i w_i \ln w_i \quad (22.42)$$

so that

$$dS = - \sum_i dw_i \ln w_i - \sum_i w_i d(\ln w_i) \quad (22.43)$$

$$d \ln w_i = \frac{1}{w_i} dw_i, \quad \sum_i dw_i = 0 \quad (22.44)$$

$$\Rightarrow dS = - \sum_i dw_i \ln w_i \quad (22.45)$$

If the state is canonical with  $w_i = \frac{1}{Z} e^{-\beta E_i}$  (for a two-level system restricted to states diagonal in energy representation this form does always apply)

$$\ln w_i = -\beta E_i - \ln Z \quad (22.46)$$

$$\Rightarrow dS = \beta \sum_i dw_i E_i, \quad \beta = \frac{1}{T} \quad (22.47)$$

Finally, if the system is closed,  $d\bar{E} = 0$ , we conclude that  $dW = -TdS$ . This means per cycle:

$$\Delta W = - \oint T dS \quad (22.48)$$

As usual, the exchanged work can be calculated from the area in  $T(S)$ -space. In the present case,  $T$  will be the effective temperature,  $\bar{T}_G$ , which is not necessarily fixed by the external heat baths.

### 22.4.3

#### Energy Balance

The heat flowing into the spin-oscillator system  $M$  can be monitored by looking at the difference of  $\langle \hat{H} \rangle$  at the time of the beginning of an isothermal process step and at its end. Consider, e.g., for the heat engine (cf. Table 22.1)

$$\overline{\Delta E_{32}} = \langle \hat{H}(t_3) \rangle - \langle \hat{H}(t_2) \rangle. \quad (22.49)$$

$\overline{\Delta E_{32}} = \overline{\Delta Q_U}$  is the heat per cycle flowing from the bath with temperature  $T_U (> T_L)$  into the system  $G$ .

The energy gained per cycle remains in the total system (cf. Table 22.1),

$$\overline{\Delta E_{40}} = \langle \hat{H}(t_4) \rangle - \langle \hat{H}(t_0) \rangle. \quad (22.50)$$

The system  $G$  is quasi cyclic, so the work must completely be stored in the system  $C$  (oscillator). As confirmed numerically, this energy gain,  $\overline{\Delta E_{40}}$ , coincides (within tight limits) with the work  $|\overline{\Delta W}|$  according to expression (22.48).

Contrary to the classical case  $\overline{\Delta E_{40}}$  is not fully associated with coherent motion (increase of oscillator amplitude). In this sense the storage is not completely "mechanical".

Finally, the efficiency for the heat engine reads, defined as in the classical case [8],

$$\overline{\eta} = \frac{|\overline{\Delta W}|}{\overline{\Delta Q_U}}. \quad (22.51)$$

The analysis of the heat pump can be carried out correspondingly.

### 22.4.4

#### Fluctuations

Expectation values and variances of operators are defined with respect to a given quantum state. Heat and work, however, are defined with respect to a path (process step) [23]. Nevertheless, in addition to knowing the respective expectation values, Eqs. (22.49) and (22.50), one would also like to get access to the variances.

Fluctuations of heat and work have become subject of so-called fluctuation theorems, supposed to hold even away from equilibrium. These theorems are formulated for driven systems (quantum and classical) with or without contact to a heat bath [24,25]. The corresponding status for autonomous quantum machines is unclear, though. Here we will restrict ourselves to the definition

and numerical calculation of the quantum mechanical variances of  $\overline{\Delta W}$  and  $\overline{\Delta Q}$ . We leave open the question about observable consequences.

While the difference of expectation values at different times is defined in the Schrödinger as well as in the Heisenberg picture we need to introduce the Heisenberg picture for the definition of the respective variances:

With the Heisenberg operators  $\hat{H}(t_f)$ ,  $\hat{H}(t_i)$  and

$$\hat{D}(t_f, t_i) \equiv \hat{H}(t_f) - \hat{H}(t_i) \quad (22.52)$$

we can define both the expectation values (cf. Eqs. (22.49) and (22.50))

$$\overline{\Delta W} = \langle \hat{D}(t_4, t_0) \rangle, \quad \overline{\Delta Q} = \langle \hat{D}(t_3, t_2) \rangle \quad (22.53)$$

and the variances

$$\begin{aligned} \delta(\Delta W) &\equiv \langle \hat{D}^2(t_4, t_0) \rangle - \langle \hat{D}(t_4, t_0) \rangle^2, \\ \delta(\Delta Q) &\equiv \langle \hat{D}^2(t_3, t_2) \rangle - \langle \hat{D}(t_3, t_2) \rangle^2. \end{aligned} \quad (22.54)$$

For arbitrary times ( $t_f > t_i$ ) we find

$$\langle \hat{D}^2(t_f, t_i) \rangle - \langle \hat{D}(t_f, t_i) \rangle^2 = \delta(\hat{H}(t_f)) + \delta(\hat{H}(t_i)) \quad (22.55)$$

$$- \left[ \langle \hat{H}(t_f) \hat{H}(t_i) \rangle + \langle \hat{H}(t_i) \hat{H}(t_f) \rangle - 2 \langle \hat{H}(t_f) \rangle \langle \hat{H}(t_i) \rangle \right] \quad (22.56)$$

with the single time variances

$$\delta(\hat{H}(t_f)) \equiv \langle \hat{H}^2(t_f) \rangle - \langle \hat{H}(t_f) \rangle^2, \quad \delta(\hat{H}(t_i)) \equiv \langle \hat{H}^2(t_i) \rangle - \langle \hat{H}(t_i) \rangle^2. \quad (22.57)$$

Apart from the terms

$$\langle \hat{H}(t_f) \hat{H}(t_i) \rangle \quad \text{and} \quad \langle \hat{H}(t_i) \hat{H}(t_f) \rangle \quad (22.58)$$

Eq. (22.56) contains expectation values at a single time only. Observe that the resulting variance has to be real; in fact we can show that for complex valued two-time correlation functions as in Eq. (22.58)

$$\langle \hat{H}(t_f) \hat{H}(t_i) \rangle = \langle \hat{H}(t_i) \hat{H}(t_f) \rangle^*. \quad (22.59)$$

Thus we have to calculate only the real part of [26]

$$\langle \hat{H}(t_f) \hat{H}(t_i) \rangle = \text{Tr}\{\hat{H} \exp[\hat{L}(t_f - t_i)] \hat{H} \rho(t_i)\} \quad (22.60)$$

where  $\hat{H}$  is the Hamilton operator in the Schrödinger picture and  $\hat{L}$  the Lindblad operator. This two-time correlation function is measureable in principle; the complex quantum phase suggests, that a reference system, against which the phase is measured, is necessary in a concrete experimental situation [27].

We give numerical results for the variances of both heat and work in Sect. 22.5.1.

## 22.5

### Numerical Results

As we want to maximize the effect of the bath on the spin while minimizing the decoherence on the oscillator we choose the bath action  $C_B$  (Eq. (22.36)) to be approximately on the same time scale as the oscillator,  $C_C$ . Furthermore the mean energy splitting of the spin has to be large in relation to the oscillator energy  $C_C$  to fulfill the weak coupling condition to both the oscillator and the bath.

The operators  $\hat{A}_{a_+^{(U)}, f^{(U)}, +}$  and  $\hat{A}_{a_+^{(L)}, f^{(L)}, +}$  (and likewise  $\hat{A}_{a_-^{(U)}, f^{(U)}, -}$  and  $\hat{A}_{a_-^{(L)}, f^{(L)}, -}$ ) have zero overlap only approximately, but they are traceless.

The Lindblad superoperator  $\hat{L}$  is represented as a  $N^4 = 2^4(n_u - n_l + 1)^4$ -dimensional matrix. Sparsity of the matrix is made use of (only non-zero-elements are being held in memory).

The time evolution is calculated by the free software package “Expokit” [28], the package calculates  $\rho$  for some time steps  $t$ .

The stationary state is calculated using the SPOOLES library [29] and the ARPACK package [30].

The values of the constants  $\{n_l, n_u, C_R, C_G, C_C\}$  define the special Hamilton model of the machine  $M$ ,  $\{|\alpha|, \phi_0, \overline{T_G}\}$  its initial state. We use natural units ( $\hbar = k_B = 1$ ).

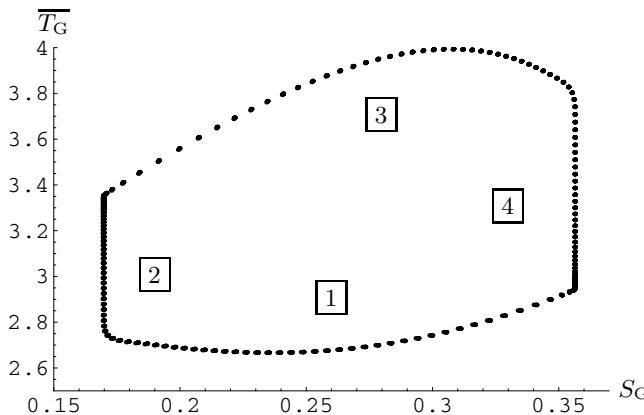
#### 22.5.1

##### Heat Engine

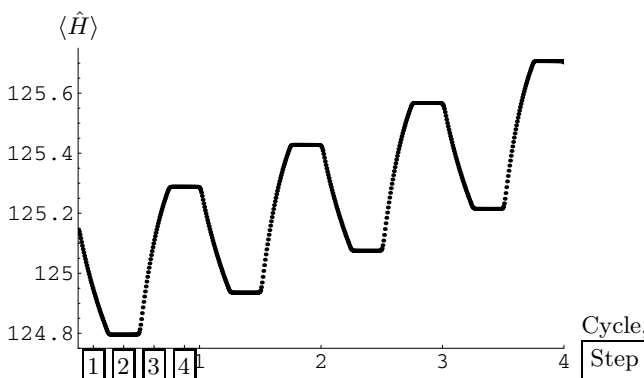
The heat engine  $M_1$  is defined by the parameters  $\{n_l = 91, n_u = 168, C_C = 1, C_G = 5, C_R = 0.05 \cdot \sqrt{2}, \alpha = 0.8 \cdot \sqrt{200} \approx 11.31, \phi_0 = \pi, T_L = 1, T_U = 5, C_B = 0.8, \text{initial } \overline{T_G} = 2.935\}$ .

The heat engine  $M_3$  is defined by the parameters  $\{n_l = 6, n_u = 29, C_C = 1, C_G = 5, C_R = 0.05 \cdot \sqrt{2}, \alpha = 0.8 \cdot \sqrt{30} \approx 4.38, \phi_0 = \pi, T_L = 5, T_U = 20, C_B = 0.8, \text{initial } \overline{T_G} = 10.445\}$ . This machine is even closer to the quantum limit and will thus exhibit strong decoherence effects.

To save computational time for large systems (especially machine  $M_1$ ) the harmonic oscillator is simulated in a state space truncated below a certain occupation number (if the occupation number in the initial state is smaller than 0.25 percent of the maximum occupation number, for machine  $M_1$  and  $M_3$ ). In this truncated space the cutoff procedure for the time slot operators, Eq. (22.33), has always been applied.



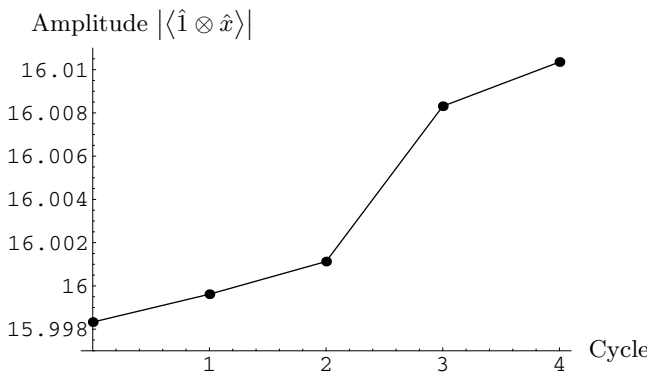
**Fig. 22.3** Autonomous quantum heat engine  $M_1$ : Temperature  $\overline{T}_G$  and entropy  $S_G$  (four cycles superimposed; each of the four steps marked by boxed numbers).  $\overline{T}_G$  is given in units of  $C_C$  (Eq. (22.3)),  $S_G$  is dimensionless.



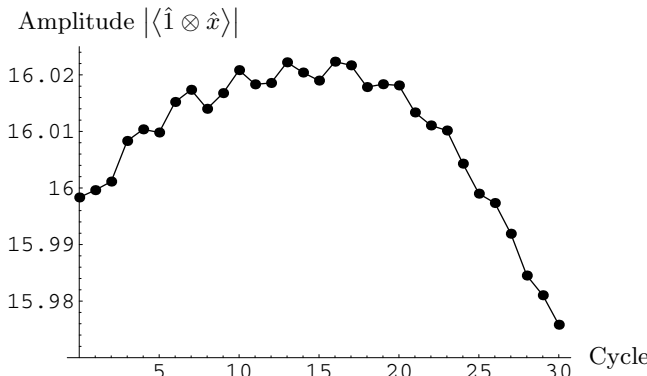
**Fig. 22.4** Autonomous quantum heat engine  $M_1$ : Average total system energy  $\langle \hat{H} \rangle$  over four machine cycles. Process steps are numbered (cf. Fig. 22.3). Energy in units of  $C_C$ .

Fig. 22.3 shows the quasi-cyclic behavior of the heat engine  $M_1$ . For the ideal Carnot engine this closed trajectory in  $\overline{T}_G/S_G$ -space would be rectangular; we see that the parts 1 and 3 deviate from isotherms. The ideal Carnot efficiency would be  $\eta_{\text{Carnot}} = 1 - T_L/T_U = 0.8$ . Here we find, mainly due to dynamical effects,  $\overline{\eta} = 0.29$ .

Fig. 22.4 shows the total system energy  $\langle \hat{H} \rangle$ : Note that our machine is freely running, so the mechanical energy piles up in the oscillator (cf. also Fig. 22.5). Alternatively the change in system energy per cycle can be calculated from the  $S_G \overline{T}_G$ -diagram (cf. Eq. (22.48)) with deviations of approximately one percent per cycle for machine  $M_1$  (stemming from the residual direct action of the time slot operators). This confirms the use of the von Neumann entropy as a



**Fig. 22.5** Autonomous quantum heat engine  $M_1$ : Dimensionless amplitude of oscillator  $C$  over four machine cycles. Note the coherence amplification for these parameters of the heat engine.



**Fig. 22.6** Same as Fig. 22.5, but over thirty machine cycles. Finally decoherence is stronger, the initial coherence amplification vanishes.

thermodynamic entropy. The increase of the oscillator amplitude  $\langle \hat{x} \rangle$  is finally reversed due to decoherence (Fig. 22.6).

System  $C$  performs a decohering dynamics (see, for example, machine  $M_3$  in Figs. 22.7, 22.8 and 22.9), it gains steadily in entropy and takes up energy from the baths via the system  $G$  (or the other way round for different running direction; heat pump). Only the bath transitions transfer energy to and from the oscillator  $C$  via its coupling to system  $G$ , because the coupling  $\hat{H}_{GC}$  (Eq. (22.4)) does not change the eigenstate-system of  $G$ . The amplitude  $\langle x \rangle$  indicating the coherent mechanical energy decreases, though (Fig. 22.9).

Work and heat have so far been introduced as expectation values over corresponding process steps. In the quantum limit one might expect that these parameters will become unsharp: According to Sect. 22.4.4 one, indeed, finds

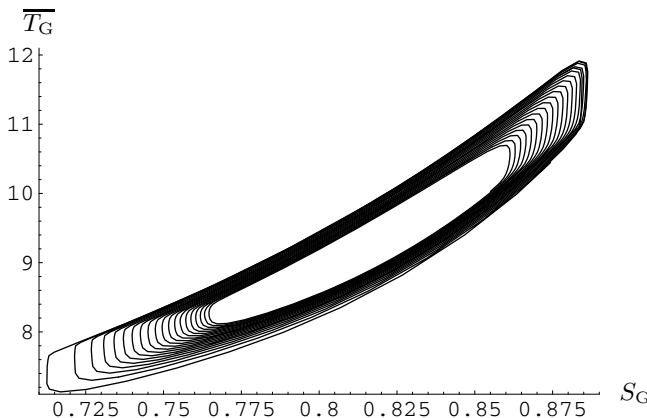


**Fig. 22.7** Autonomous quantum heat engine  $M_3$ : Temperature  $\overline{T_G}$  in units of  $C_C$  and entropy  $S_G$  (20 cycles superimposed). Spiraling in this plot is the effect of decoherence of the control operators on the oscillator.

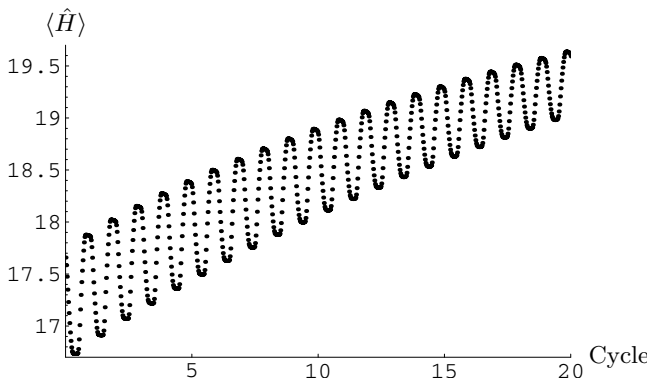


**Fig. 22.8** Autonomous quantum heat engine  $M_3$ : Average total system energy  $\langle \hat{H} \rangle$  in units of  $C_C$  over 20 machine cycles. Note that even with severe decoherence there is machine function left (increase in not coherently stored energy).

per cycle (first cycle of the respective simulation data)

$$\sqrt{\delta(\Delta W)/\Delta W} = 26.7, \quad \sqrt{\delta(\Delta Q_U)/\Delta Q_U} = 6.46 \quad (22.61)$$

for machine  $M_1$  and

$$\sqrt{\delta(\Delta W)/\Delta W} = 37.2, \quad \sqrt{\delta(\Delta Q_U)/\Delta Q_U} = 4.85 \quad (22.62)$$

for machine  $M_3$ . The work after one cycle is sharper for  $M_1$  than for  $M_3$ , mainly because  $M_1$  is farther away from the quantum limit. Note that the heat flux for  $M_3$  is sharper, because this machine works at a much larger temperature difference than  $M_1$ .

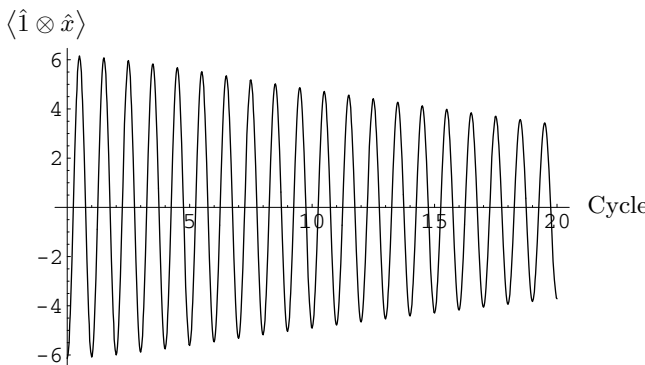


**Fig. 22.9** Autonomous quantum heat engine  $M_3$ : Dimensionless displacement  $\langle \hat{x} \rangle$  of oscillator C over 20 machine cycles. The coherently stored energy decreases.

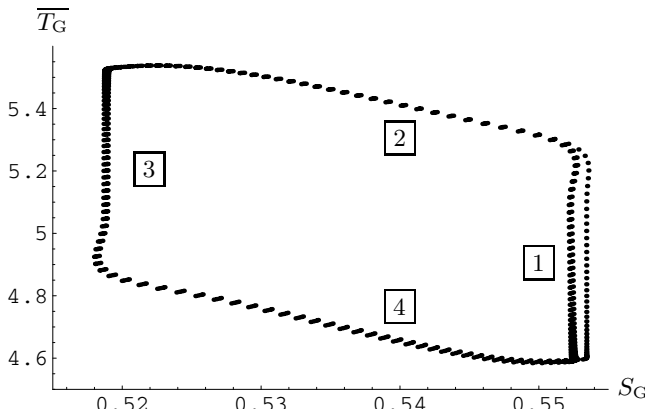


**Fig. 22.10** Autonomous quantum heat pump  $M_2$ : Temperature  $\overline{T}_G$  in units of  $C_C$  and entropy  $S_G$  (four cycles superimposed; each of the four steps marked by boxed numbers).

### 22.5.2

#### Heat Pump

The heat pump  $M_2$  is defined by the parameters  $\{n_l = 0, n_u = 58, C_C = 1, C_G = 5, C_R = 0.05 \cdot \sqrt{2}, \alpha = 6, \phi_0 = \pi, T_U = 5.1, T_L = 5, C_B = 0.8, \text{initial } \overline{T}_G = 4.596 \text{ (initial } \overline{T}_G = 5 \text{ for Fig. 22.13)}\}$ .

The quasi-cyclic behavior is shown in Fig. 22.10. Again, the trajectories deviate from the ideal rectangular form of an ideal Carnot engine. Fig. 22.11 shows the total system energy  $\langle \hat{H} \rangle$ . Note that the change in system energy during the adiabatic phases stems from the residual direct action of the time slot operators. The decrease of the oscillator amplitude  $\langle x \rangle$  is given in Fig. 22.12.

The total system is initially prepared in a mixed state for system  $G$  and a pure state for the system  $C$ . Normally, this state of the system  $G$  is not one

of the quasi cyclic states.. System  $G$  will therefore show an initial adaptive dynamics, until it relaxes to a quasi cyclic state, as long as the state space of  $C$  is large enough (see Fig. 22.13).

### 22.5.3

#### Longtime Limit

The stationary state and thus the long time behavior can be extracted from the eigenstate corresponding to the eigenvalue 0 of the Lindblad operator  $\hat{L}$ . All other eigenvalues are complex with negative real part, so they will die away in time.

Qualitatively, the stationary state represents energy transport through the machine induced by the external temperature difference (cf. [31,32]). The stationary state is approximately diagonal in the oscillator subspace, but depends on the original running direction of the machine. The asymptotic state for the spin is thermal with a temperature between those of the two baths ( $\overline{T_G} = 5.056$  for heat pump  $M_2$ ). The oscillator is in a non-thermal state: The heat engine produces a state with maximal occupation at some higher energy, with approximately a power law decay in occupation number to lower levels. In the case of the heat pump the steady state of the oscillator is a low energy state, with high occupation at the lowest level and approximately power law decay to higher energies.

### 22.5.4

#### Quantum Limit and Classical Limit

It is remarkable that this model is scalable, to both the quantum and the classical limit. The quantum limit is achieved for a single spin system (the least

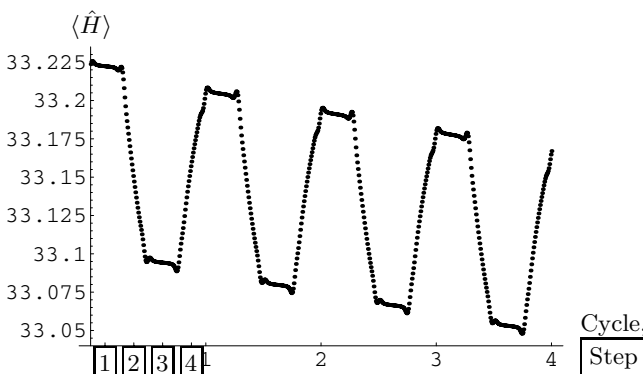


**Fig. 22.11** Autonomous quantum heat pump  $M_2$ : Average total system energy  $\langle \hat{H} \rangle$  in units of  $C_C$  over four machine cycles. Process steps are numbered (cf. Fig. 22.3).

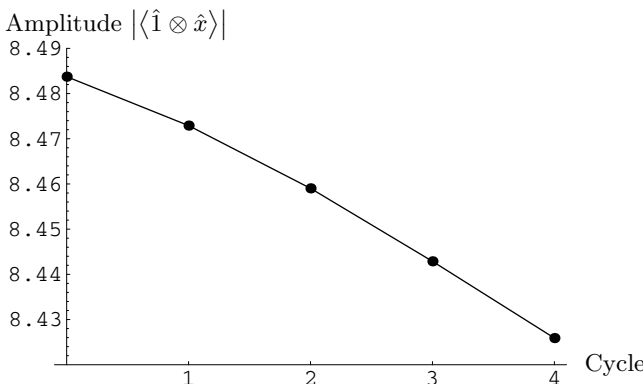


**Fig. 22.12** Autonomous quantum heat pump  $M_2$ : Dimensionless amplitude of oscillator  $C$  over four machine cycles. The amplitude decreases as coherently stored work is used to pump heat from the cold to the hot reservoir.

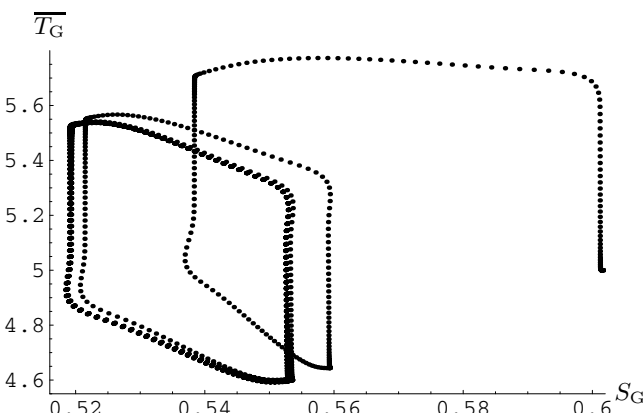


**Fig. 22.13** Autonomous quantum heat pump  $M_2$ : Initial adaptive dynamics in the plane of temperature  $\bar{T}_G$  and entropy  $S_G$  for 8 cycles until a quasi-cyclic state for  $G$  is established.

possible) and  $|\alpha| \approx 1$ . As the control system is then roughly of the same dimension as the system to control, any machine function tends to vanish in this limit.

The classical limit corresponds to the ordinary thermodynamic machine, in which the control is classical (no back-action on the control system) and the work remains coherent ("mechanical", no deterioration of work needs to be regarded). The full classical limit requires here to increase the number of spins  $n_v$  (qualitatively simulating the spectrum of a many body system as an

approach to a classical work medium):

$$\hat{H}_G = C_G \sum_{\nu=1}^{n_\nu} \hat{\sigma}_z(\nu) \quad (22.63)$$

$$\hat{H}_{GC} = C_R \sum_{\nu=1}^{n_\nu} \hat{\sigma}_z(\nu) \otimes \hat{x} \quad (22.64)$$

The environment operators are generalized accordingly:

$$\hat{A}_{a_\pm^{(j)}, f^{(j)}, \pm} = a_\pm^{(j)} \sum_{\nu=1}^{n_\nu} \hat{\sigma}_\pm(\nu) \otimes \hat{\Pi}^{(j)}[f^{(j)}] \quad (22.65)$$

Coupling and transition operators are thus replaced by their collective counterparts of the spin network. The classical limit is achieved as  $n_\nu \rightarrow \infty$  and  $|\alpha| \rightarrow \infty$ . As  $|\alpha|$  increases,  $C_R$  must decrease to keep the coupling energy constant. So it is easily seen that the eigensystem of the harmonic oscillator becomes part of the eigensystem of the total system in the classical limit. The suppression of back-action of the  $\hat{\Pi}$  operators on the oscillator has to be considered separately. Only for finite values of  $|\alpha|^2$  do we get decoherence. Thus in the classical limit the evolution of the harmonic oscillator system under the operator  $\hat{\Pi}$  in the incoherent Lindblad operator is, indeed, a purely coherent one.

The function  $F^2(t)$  according to Eq. (22.27) and (22.28) and can be viewed as sampling the control function  $\theta(\tau)$  more and more accurately as it becomes sharper. In the classical limit  $\theta(\tau)$  is sampled exactly, classical parametric control is recovered.

## 22.6

### Summary and Conclusions

In our quantum Carnot engine heat occurs in the “gas” system (the spin), mechanical energy (“work”) in the control system (oscillator). Contrary to intuition the state space of the thermal subsystem is thus smaller than that for the mechanical subsystem. Mechanical energy is of two kinds: Coherent (at the start and partially while running) and incoherent (only on the diagonal of the density matrix), while in the classical case all mechanical energy would be stored coherently. In fact,  $C$  has three functions: an effective “piston”, control of bath couplings, and work reservoir.

The present study has been based on the Lindblad approach for open quantum systems. Because of the dynamical modeling, the momentary temperatures in the gas system are never the quasi-static temperatures one would expect (this is not a quantum effect, it would likewise be found in the classical thermodynamic machine outside the quasi-static regime). The machine

operates in an irreversible way; its efficiency is considerably smaller than the Carnot efficiency.

After settling to a quasi periodic equilibrium (timescale of the “gas” system) the system shows machine function before finally reaching (timescale of the decoherence of the control system) its stationary state, which corresponds to energy transfer between the two baths (“leakage”).

Even a coherent increase of energy is observable (on a timescale smaller than that for the machine function to hold).

In the quantum limit (number of spins  $n_v = 1$ , coherent excitation of the oscillator  $|\alpha| \approx 1$ ) the back-action of the control on the control system is substantial and leads to decoherence. Heat and work are not sharp, the respective variances are substantial.

Let us finally return to the question of whether we might need to change machine concepts as we approach nanoscopic limits [2]. With respect to energy conversion it has been argued [4] that it should become preferable to convert chemical energy directly into potential energy (e.g. via molecular shape changes [5]) rather than first converting chemical energy to heat and then heat to mechanical energy. Such alternative modes of operation also underly Brownian motors [6, 7, 33]. One reason for this concept change might be the difficulty for maintaining temperature gradients on pertinent length scales, as cited already. Here we have explored a more fundamental limit: Contrary to Brownian motors, say, for autonomous heat engines decoherence becomes a major threat. This is why heat engines apparently do not exist in biological systems.

Our methods could also be used to study (autonomous) cellular automata [34]. Just like heat engines they also require cyclic control to be built in. The quantum limit of such machines would have to be distinguished from quantum cellular automata proper (see, e.g., [35]). The latter are concerned with the exploitation of quantum rules made available via explicitly time-dependent parameter control. Here we have been concerned with the problem of having such a parameter control be replaced by a full quantum description.

### Acknowledgement

We thank M. Hartmann, M. Henrich, M. Michel, H. Schmidt and M. Stollsteiner for fruitful discussions. This work has been supported by the Landesstiftung Baden-Württemberg.

## References

- 1 See, e.g., [36].
- 2 G. M. Whitesides, *Sci. Am.* **285** (9), 70 (2001).
- 3 Functional machines could be taken to include information processing systems, too. Examples would be molecular computing or even quantum computation. These issues are not discussed here.
- 4 R. A. L. Jones, *Soft Machines: nanotechnology and life* (Oxford University Press, Oxford, 2004), see also: <http://www.softmachines.org>.
- 5 A. J. Ryan, C. J. Crook, J. R. Howse, P. Topham, R. A. L. Jones, M. Geoghegan, A. J. Parnell, L. Ruiz-Pérez, S. J. Martin, A. Cadby, et al. *Faraday Discuss.* **128**, 55 (2005).
- 6 T. E. Humphrey, R. Newbury, R. P. Taylor, and H. Linke, *Phys. Rev. Lett.* **89**, 116801 (2002).
- 7 J. M. R. Parrondo and B. J. D. Cisneros, *Appl. Phys. A* **75**, 179 (2002).
- 8 B. Diu, C. Guthmann, D. Lederer, and B. Roulet, *Éléments de Physique Statistique* (Hermann Editions des Sciences et des Arts, Paris, 1989).
- 9 Cf. the flexural vibrations of thin beams, see [37].
- 10 T. Feldmann and R. Kosloff, *Phys. Rev. E* **68**, 016101 (2003), [quant-ph/0303046](http://arxiv.org/abs/quant-ph/0303046).
- 11 R. Kosloff and T. Feldmann, *Phys. Rev. E* **65**, 055102(R) (2002), [physics/0111098](http://arxiv.org/abs/physics/0111098).
- 12 E. Geva and R. Kosloff, *J. Chem. Phys.* **97**, 4398 (1992).
- 13 J. P. Palao, R. Kosloff, and J. M. Gordon, *Phys. Rev. E* **64**, 056130 (2002), [quant-ph/0106048](http://arxiv.org/abs/quant-ph/0106048).
- 14 M. O. Scully, *Phys. Rev. Lett.* **87**, 220601 (2001).
- 15 M. O. Scully, *Phys. Rev. Lett.* **88**, 050602 (2002).
- 16 C. M. Bender, D. C. Brody, and B. K. Meister, *Proc. R. Soc. Lond. A* **458**, 1519 (2002).
- 17 B. Lin and J. Chen, *Phys. Rev. E* **67**, 046105 (2003).
- 18 L. E. Ballentine, *Quantum Mechanics*, 2nd ed. (World Scientific, Singapore, 1998).
- 19 R. Alicki and M. Fannes, *Quantum Dynamical systems* (Oxford University Press, Oxford, 2001).
- 20 G. Lindblad, *Commun. Math. Phys.* **48**, 119 (1976).
- 21 U. Weiss, *Quantum dissipative systems*, 2nd ed. (World Scientific, Singapore, 1999).
- 22 M. A. Nielsen and I. L. Chuang, *Quantum Computation and Quantum Information* (Cambridge University Press, Cambridge, 2000).
- 23 G. E. Crooks, *Phys. Rev. E* **61**, 2361 (2000).
- 24 S. Mukamel, *Phys. Rev. Lett.* **90**, 170604 (2003).
- 25 C. Jarzynski and D. K. Wójcik, *Phys. Rev. Lett.* **92**, 230602 (2004).
- 26 C. W. Gardiner and P. Zoller, *Quantum noise*, Springer Series in Synergetics, 2nd ed., Vol. 56, Sect. 5.2 (Springer, Berlin, 2000).
- 27 C. Anastopoulos, *Quantum theory without hilbert spaces*, [quant-ph/0008126](http://arxiv.org/abs/quant-ph/0008126).
- 28 R. B. Sidje, *ACM Trans. Math. Softw.* **24**, 130 (1998).
- 29 C. Ashcraft and R. Grimes, *Spooles – an object oriented software library for solving sparse linear systems of equations* [www.netlib.org/linalg/spooles/](http://www.netlib.org/linalg/spooles/), 1999.
- 30 R. B. Lehoucq, D. C. Sorensen, and C. Yang, *ARPACK users guide: solution of large scale eigenvalue problems by implicitly restarted Arnoldi methods*, Philadelphia, SIAM (1998).
- 31 S. D. Franceschi and L. Kouwenhoven, *Nature* **417**, 701 (2002).
- 32 W. A. Goddard III, D. Brenner, S. E. Lyshevski, and G. J. Iafrate (eds.), *Handbook of Nanoscience, Engineering and Technology* (CRC Press, Boca Raton, FL, 2002), vol. 27 of Electrical Engineering Textbook Series, chap. M. Paulsson, F. Zahid, and S. Datta: Resistance of a Molecule, see also: [cond-mat/0208183](http://arxiv.org/abs/cond-mat/0208183).
- 33 F. C. Lombardo and P. I. Villar, *Phys. Lett. A* **336**, 16 (2005).
- 34 S. Wolfram, *Nature* **311**, 419 (1984).
- 35 B. Aoun and M. Tarifi, *Quantum cellular automata*, [quant-ph/0401123](http://arxiv.org/abs/quant-ph/0401123).
- 36 Y. Xia, P. Yang, Y. Sun, Y. Wu, B. Mayers, B. Gates, Y. Yin, F. Kim, and H. Yan, *Adv. Mater.* **15**, 353 (2003).
- 37 R. Lifshitz and M. L. Roukes, *Phys. Rev. B* **61**, 5600 (2000).



## Appendix Colour Plates

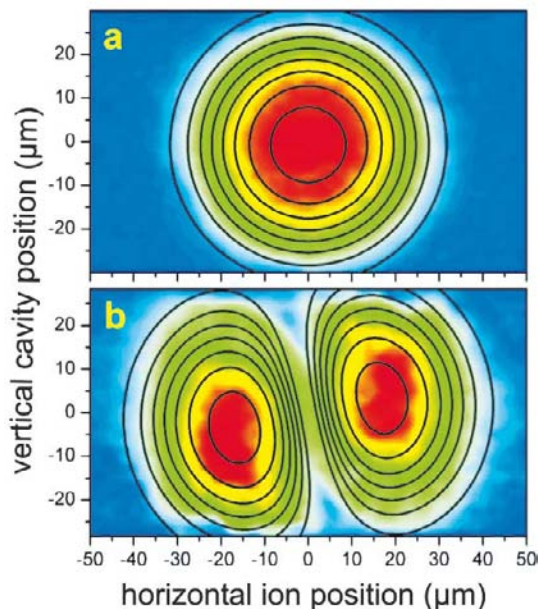


**Fig. 1.15** Two-dimensional images of the cavity field taken over an area of  $100 \times 60 \mu\text{m}^2$ . a)  $\text{TEM}_{00}$  mode. b)  $\text{TEM}_{01}$  mode. In the horizontal direction the ion was moved, while vertically the cavity position was changed relatively to the ion. False colors represent the measured fluorescence count rate; the contour lines indicate the theoretical fluorescence pattern.

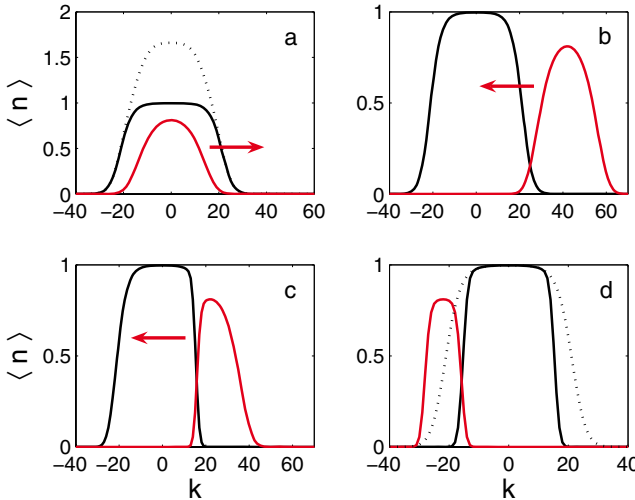


**Fig. 4.9** Illustration of the protocol. The state is initialized with the filter operation  $F_2$ . (a) Particles from doubly occupied sites are transferred to state  $|b\rangle$  (red) using operation  $U_{2,0}^{1,1}$ . (b) The lattice  $|b\rangle$  has been shifted  $2k_\epsilon$  sites to the right, so that the two distributions barely overlap. (c) Density distribution after  $k_s$  lattice shifts. After each shift doubly occupied

sites have been emptied. Afterwards lattice  $|b\rangle$  is shifted  $4k_\epsilon - k_s$  sites to the left and an analogous filter sequence is applied. (d) The final distribution of atoms in state  $|a\rangle$  is sharper compared to the initial distribution (dotted). Numerical parameters:  $N_i = 65$ ,  $s_i = 1$ ,  $U/b = 300$ ,  $k_\epsilon = 21$ ,  $k_s = 20$ ,  $N_f = 30.2$ ,  $s_f = 0.31$  (after equilibration).

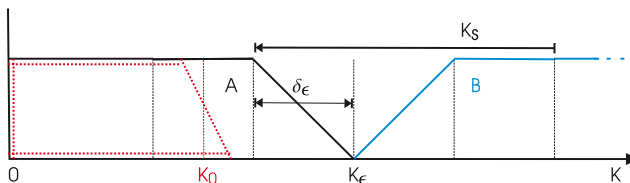


**Fig. 4.10** Schematic description of the initial state for lattice sites  $k \geq 0$ : Two identical density distributions for hard-core bosons, belonging to different species A (black) and B (blue), are shifted  $2k_\epsilon$  lattice sites apart. The region of non-integer filling has width  $\delta_\epsilon$ . In the course of the protocol the lattice of species B is shifted  $k_s = 3\delta_\epsilon$  sites to the left.

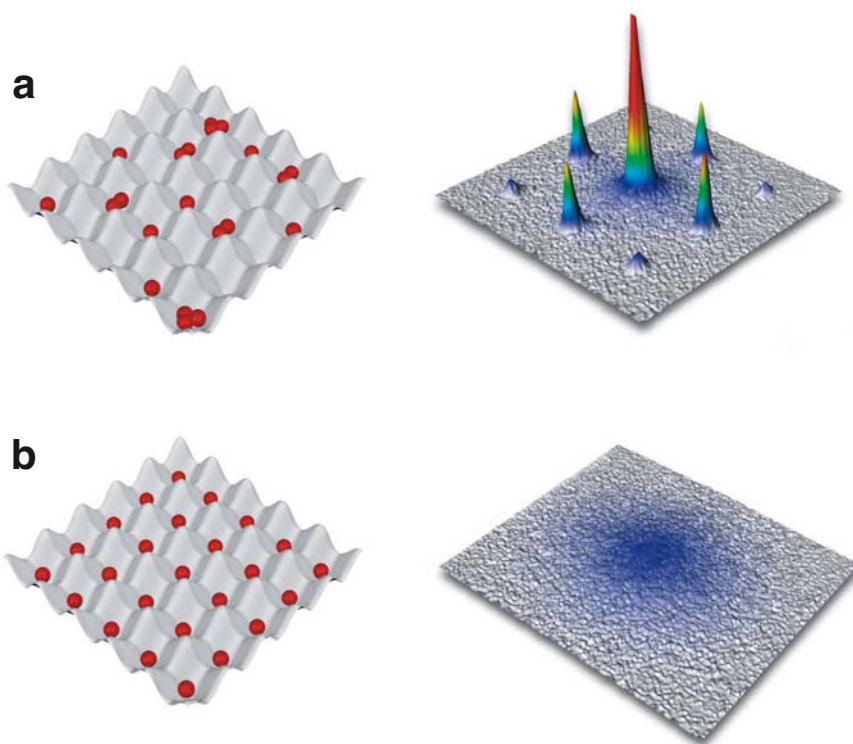


**Fig. 5.1** (a) In the superfluid state of a Bose-Einstein condensate, the underlying atoms can be described as a giant macroscopic matter wave. When such a condensate is released from the periodic potential a multiple matter wave interference pattern is formed due to the phase coherence between the atomic wavefunctions on different lattice sites. In this case the phase of the macroscopic matter

wave is well defined. However, the number of atoms at each lattice site fluctuates. (b) In the limit of a Mott insulating state, each lattice site is filled with a fixed number of atoms but the phase of the matter wave field remains uncertain. As a result, no matter wave interference pattern can be seen when the quantum gases are released from the lattice potential.

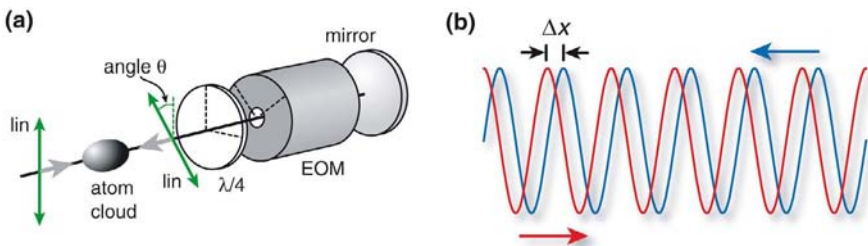


**Fig. 5.2** (a) Schematic experimental setup. A one dimensional optical standing wave laser field is formed by two counterpropagating laser beams with linear polarizations. The polarization angle of the returning laser beam can be adjusted through an electro-optical

modulator. The dashed lines indicate the principal axes of the wave plate and the EOM. (b) By increasing the polarization angle  $\theta$ , one can shift the two resulting  $\sigma^+$  (blue) and  $\sigma^-$  (red) polarized standing waves relative to each other.

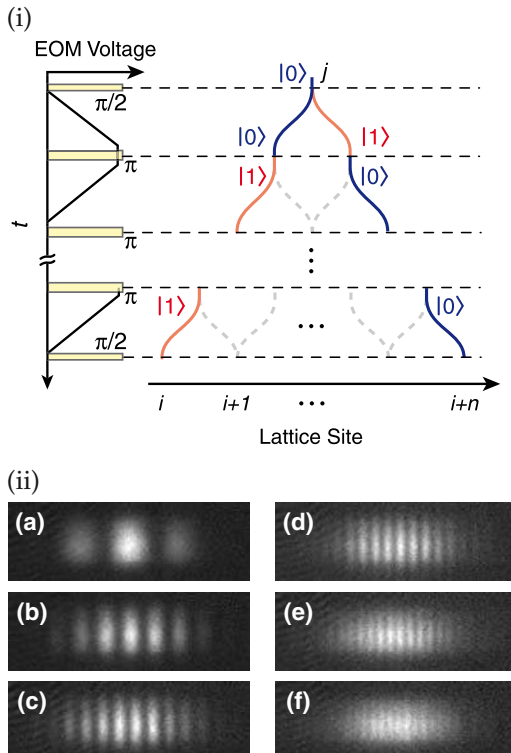


**Fig. 5.3** (i) Schematic sequence used for the quantum conveyor belt. A single atom on lattice site  $j$  can be transported over an arbitrary number of lattice sites depending on its spin state (marked as blue and red curves). (ii) This has allowed us to split the wave function of the atom in a coherent

way, such that a single atom simultaneously moves to the left and to the right. The coherence of the split wave-packets has been demonstrated in an interference experiment. For larger distances between the split wave-functions, the period of the interference pattern decreases.

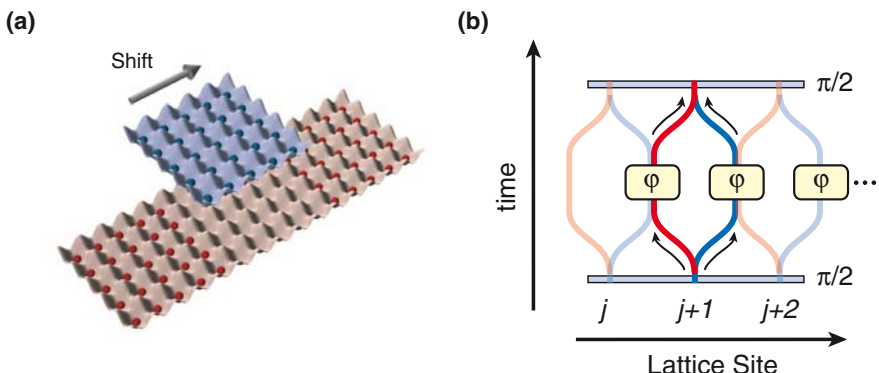


**Fig. 5.4** (a) Controlled interactions between atoms on different lattice sites can be realized with the help of spin-dependent lattice potentials. In such spin dependent potentials, atoms in a, let us say, blue internal state experience a different lattice potential than atoms in a red internal state. These lattices can be moved relative to each other such that two initially separated atoms can be brought into controlled contact with each other. (b) This can be extended to form a massively parallel quantum gate array. Consider a string

of atoms on different lattice sites. First the atoms are placed in a coherent superposition of the two internal states (red and blue). Then spin dependent potentials are used to split each atom such that it simultaneously moves to the right and to the left and is brought into contact with the neighbouring atoms. There both atoms interact and a controlled phase shift  $\varphi$  is introduced. After such a controlled collision the atoms are again moved back to their original lattice sites.

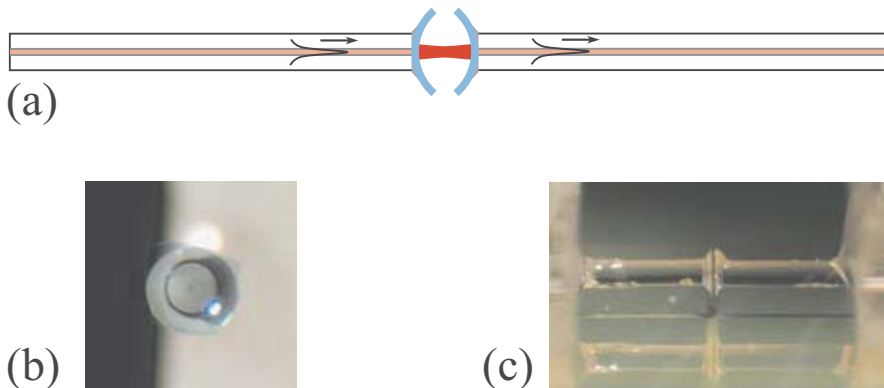


**Fig. 5.9** (a) Concept of the stable FFP cavity. The basic building block is an optical fiber functionalized with a concave dielectric mirror. Two such fibers, brought sufficiently close to each other, result in a stable Fabry-Perot cavity which can be interrogated remotely, either in transmission or in reflection, through

the two fibers (b) A single-mode optical fiber, total diameter 125  $\mu\text{m}$ , processed with a concave mirror. The mirror has radius 1000  $\mu\text{m}$  with a stopband centered at 780 nm. (c) A complete FFP cavity, realizing the configuration (a), mounted on an atom chip used in the detection of cold atoms (Fig. 5.11).

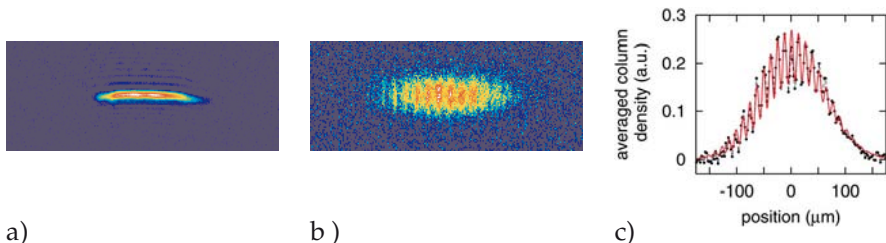


**Fig. 6.2** a) False-color absorption image of 20 microcondensates recorded shortly after switching off the  $\text{CO}_2$ -laser trapping potential. b) False-color absorption image of an interference pattern of 20 independently generated  $m_F = 0$  microcondensates released from a  $\text{CO}_2$ -laser optical lattice. This image

was recorded after a free expansion time of 15 ms. The field of view is  $350 \mu\text{m} \times 140 \mu\text{m}$ . c) Horizontal profile of image b) averaged over a vertical region of  $35 \mu\text{m}$ : Experimental data (dashed line with dots) and fitted fringe pattern (solid line).

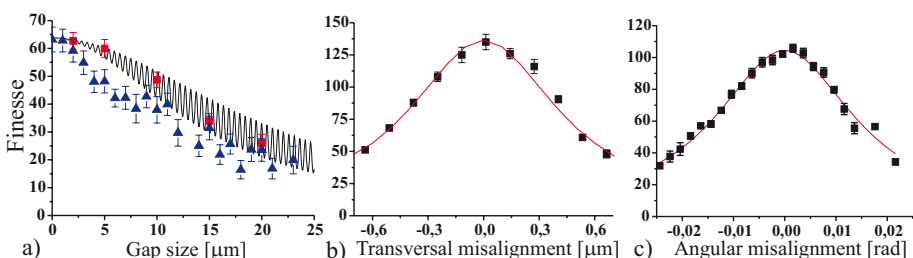


**Fig. 8.9** Measurement of the finesse of a fiber cavity as a function of the gap size is shown in a). The oscillating function shows the theoretical curve for the finesse with varying gap size. The oscillation of the finesse is due to the multiple reflections between the facets and the mirrors. The red squares correspond to the finesse measured for a cavity mounted

inside a SU-8 structure. The blue triangles correspond to a finesse measurement where the cavity is held by precision translation stages. Graph b) shows the finesse of a different cavity measured as a function of transversal misalignment. In c) the finesse is plotted as a function of angular misalignment.

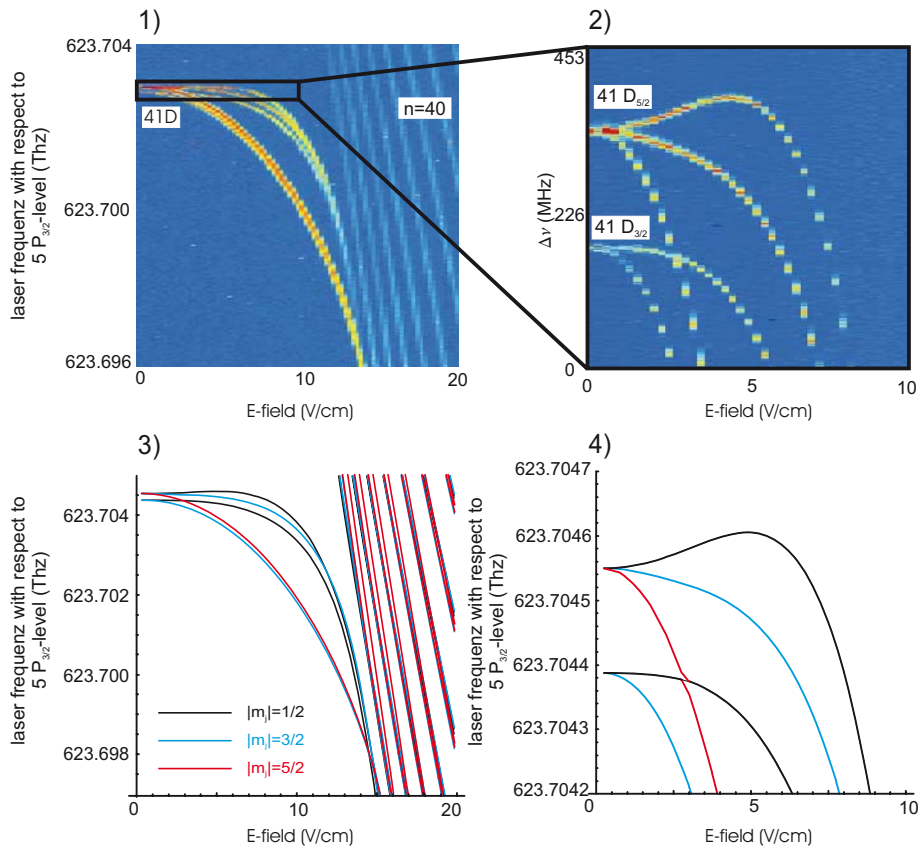


**Fig. 9.4** Example for the spectroscopic resolution of the laser system. On the upper left hand side (1) a Stark map scan is shown where the electrical field and the blue laser frequency is changed. On the upper right side a measurement of a smaller region with a higher resolution is shown, revealing the  $|m_j|$ -Splitting of the Rydberg states in the electrical

field. The two lower pictures (3,4) show the result of a numerical calculation with no free parameters. Only the atomic properties of <sup>87</sup>Rb are used. The different observed states can be assigned to the different  $|m_j|$  states. The color of the pictures indicates the signal strength (blue-low to red-high signal).

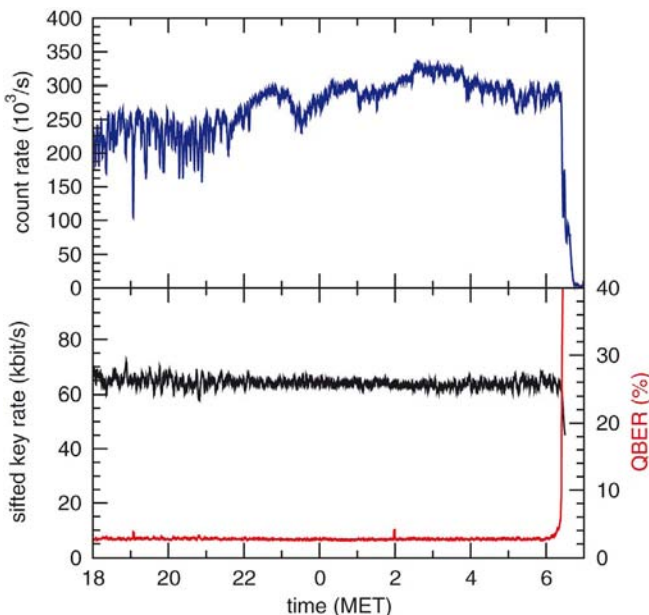


**Fig. 15.3** Counting rate, sifted key rate and quantum bit error rate of the measurement run starting November 27th. The increase of the QBER and the decrease of the counting rate in the morning is due to stray light hitting the detectors after sunrise, saturating them.

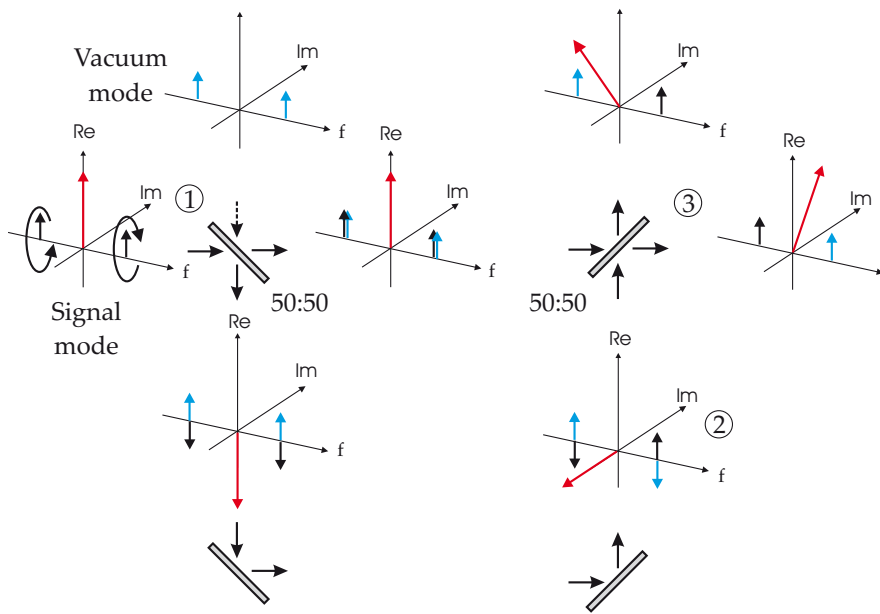


**Fig. 16.3** Pictorial diagram illustrating the function of the asymmetric interferometer in the sideband picture.



## Index

### **a**

AC Zeeman effect 132  
 Addressability 127  
 adiabatic limit 75  
 adiabatic suppression 75  
 adiabatic transport 86  
 algorithmic cooling 114, 383  
 algorithms 69  
 analogue complexity 390  
 analogue-to-digital conversion 388  
 anharmonic dispersion 59  
 annihilation and creation operators 79  
 approximate trajectories 86  
 array of microcondensates 150  
 aspect-ratio rule 87  
 associated Laguerre polynomials 77  
 asymmetric Mach-Zehnder interferometer 327  
 atom chip 127, 185  
     Bose-Einstein condensation 185  
     integrated optics 185  
 atom-surface distance 131  
 atom-surface interactions 131  
 Autler-Townes splitting 222  
 autoionization 240

### **b**

bang-bang operations 393  
 BB84 308  
 BB84 protocol 315  
 Bell state 250, 252, 288  
 BEM 66  
 Bessel function 345  
 bistability  
     one-atom maser 11  
 bit-flip noise 266  
 Bloch-Redfield approach 267  
 blockade 231, 239  
 Bose-Einstein condensate 122, 128, 145,  
     224, 483  
 Bose-Hubbard model 102  
 Boundary Element Method 66  
 Bragg scattering 176  
 Breidbart 308

### **c**

Carr-Purcel-Meiboom-Gill (CPMG) 261  
 cascade 320  
 cavity finesse 136, 138  
 cavity QED 136  
 cavity quantum electrodynamics 1  
     strong coupling 1  
 cavity-cooling 181  
 central limit theorem 149  
 cheating 308  
 chip surface 128, 131  
 chirped pulses 340  
 chromatic index 391  
 class number 360  
 class number formula 368  
 classical dynamics 72  
 classical energy transfer 77  
 cluster state 124  
 CNOT gate 275  
 CO<sub>2</sub>-laser 146  
 coherence lifetime 127, 131  
 coherence measurement 129  
 coherent collisions 124  
 coherent destruction of tunneling 272  
 coherent state 77, 80  
 collapse and revival 8, 26  
     one-atom maser 8  
 collective atomic recoil laser 156  
 collective coupling 157  
 collective instability 168  
 collisional interaction 127  
 collisional phase 126  
 collisional phase gate 133  
 collisional shifts 107  
 color centers 33  
 complementary error function 342  
 computational complexity 385  
 continuous complexity 390  
 continuous variable system 389  
 controlled collisions 124  
 conveyer belt 123  
 cooling 378, 383  
 cooperativity 136, 138  
 coplanar waveguide 133

correlation function 304, 306, 307  
 coupling strength 2  
 cryptography 303  
 cumulant generating function, CGF 428, 430

**d**

dark MOT 147  
 decoherence 29, 129, 260  
 density matrix 245, 246  
 dephasing time 444  
 depth 377  
 detection of atoms 186  
   absorption 187  
   cavity enhanced detection 189  
   cavity with small mode waist 205  
   fluorescence 186  
   refraction 189  
 Deutsch-Josza algorithm 246  
 dipole  
   blockade 228  
   induced 234, 240  
   interaction 228, 235  
   moment 235, 237  
   permanent 235, 240  
   resonant 236  
   trap 146, 160  
 dipole-dipole coupling 255  
 discrete ill-posed problem 89  
 discriminant 359  
 dispersion 77  
 dispersive detection 135  
 distance function 364  
 disturbance 404  
   minimal 404  
 double well potential 133  
 dragged quantum harmonic oscillator 78  
 dynamical decoupling 271

**e**

eavesdropping 307  
 Electron Nuclear Double Resonance (ENDOR) 251, 252  
 Electron Paramagnetic Resonance (EPR) 251, 252  
 electron spin echo 258  
 electron-electron interaction 434, 443  
 endohedral fullerene 251  
 ENDOR-spectrum 255  
 energy transfer 228, 236, 237, 240  
 ensemble quantum computation 108  
 entanglement 27, 378, 381  
   distillation 287  
   multiparticle 29  
   verification 331  
 EPR pulses 256  
 Ermakov equation 73

error correction 311, 319  
 error function transport 84  
 error rate 311  
 evaporative cooling 147  
 extended Gaussian wave packet dynamics 64

**f**

Fabry-Perot cavity 136, 137, 485  
 factoring algorithms 356  
 factorization 347  
 Fano-Mandel-Q parameter 6  
 FDM 66  
 FEM 66  
 fiber cavity 192  
   CQED 191  
   Fresnel reflections 197  
   loss mechanisms 193  
   miniaturization 191  
   strong coupling 191  
   transfer mirror coatings 192  
 fiber Fabry-Perot cavity 137, 485  
 fidelity 289  
 field ionization 216  
 filtering 107, 112  
 finesse 136  
 Finite Difference Method 66  
 Finite Element Method 66  
 finite resources 288, 293, 300  
 first and second order perturbation to transport 94  
 Floquet ladder 345  
 Floquet theory 269  
 Fock state 3  
   dynamical preparation 18  
   Rabi oscillations 21, 23  
 Fock state space 80  
 FORT 31  
 free induction decay (FID) 260  
 free space link 317  
 frequency standards 380  
 Fresnel transform 29  
 friction force 162  
 full counting statistics, FCS 425, 428  
 Förster 228, 236, 238, 240

**g**

gate fidelity 280  
 Gauss sum 339  
   periodicity of the 339  
 generalized invariant method 78  
 Generalized Riemann Hypothesis 367  
 generating function 77  
 geometry of numbers 357  
 GHZ 304  
 Green's function 74  
 Greenberger-Horne-Zeilinger state 250

group representation 407  
 equivalence 407  
 irreducible 408  
 projective 408  
 unitary 407

***h***

Hadamard transform 259  
 Hahn echo 260  
 Hallgren's algorithm 371  
 harmonic driving 279  
 harmonic potential 71  
 heat engine 378, 388  
 Heisenberg interaction 276  
 Heisenberg operators 79  
 Heisenberg picture 78  
 Heisenberg-Weyl group 419  
 heralded single photon source 310  
 high-finesse cavity 155  
 high-frequency limit 86  
 holonomic quantum computing 395  
 hot electron 453  
 hyperfine states 127  
 hyperfine structure 130  
 hyperfine tensor 255  
 hysteresis  
 one-atom maser 11

***i***

ideal minimum 362  
 information exchange 303  
 infrastructure 363  
 integer Factorization 356  
 integral elements 359  
 integral expansion 96  
 integrated optics 201  
 dipole trap 199  
 fiber cavities 201  
 mounting of fibers  
 SU-8 fiber splice 204  
 SU-8 resist 203  
 tapered lensed fiber 199  
 intercept/resend 308  
 interference pattern 122, 145, 483  
 intermediate entanglement 250  
 intertwining space 410  
 ion trap 34  
 ion-trap laser 34  
 ionization 232  
 Ising interaction 124, 276, 392  
 iterative process 294, 295

***j***

Jaynes-Cummings Hamiltonian 2, 389

***k***

Keldysh partition function 431, 442

Klyver's formula 149  
 knapsack problem 385  
 Kraus operator 402  
 Kuramoto model 174

***l***

Lüders' postulate 382  
 laser surface processing 138  
 lasing threshold 173  
 lattice shifts 107  
 Lewis-Riesenfeld method 72  
 limit cycle oscillator 174  
 line broadening 232  
 linewidth  
 one-atom maser 24  
 LOCC 288  
 long-range order 168

***m***

macrorealism 378, 380  
 macroscopic observables 380  
 magnetic field 128, 130  
 magnetic field fluctuations 129  
 magnetic microtrap 127  
 magnetic moment 129  
 magnetic near-field noise 129  
 magneto-optical trap 146, 212  
 majority function 383  
 many-body diffusion 239  
 matrix symmetry 410  
 matter wave 122, 483  
 mean energy 77  
 measurement  
 accuracy 386  
 disturbance 404  
 generalized 401  
 orthogonal 403  
 projective 403  
 von Neumann 403  
 measurements 379  
 microcavity 137  
 microcondensates 145  
 microfabrication 127  
 micromaser 1  
 micromotion 49  
 microtrap 127  
 microtraps 147  
 microwave 130  
 microwave current 133  
 microwave near-fields 132, 134  
 microwave potentials 132  
 mode volume 138  
 momentum-diffusion 173  
 MOT 212  
 Mott insulator 122, 483  
 MQE-tomography 260  
 multi-electrode structure 90

multi-quantum ENDOR (MQE) 255, 257,  
259  
multiple quantum ENDOR (MQE) 253

**n**

near-optimum transport 86  
neutral atoms 121  
NMR-experiment 350  
NP-complete problems 385  
number fields 357

**o**

on-chip atom detection 138  
on-chip fiber cavity 137, 485  
one-atom laser 30, 34  
one-atom maser 1  
bistability 11  
collapse and revival 8  
cyclic operation 17  
experimental set-up 3  
hysteresis 11  
linewidth 24  
phase transition 11  
phase-diffusion constant 25  
photon statistics  
steady state 5  
sub-Poissonian 9  
pump curve 7  
pump parameter 6  
quantum jumps 11  
single-atom-effect region 8  
spectrum 24  
threshold 6  
trapping states 13  
Wigner function 29  
optical cavity 135  
optical dipole force trap 31  
optical fiber 137, 485  
optical lattice 122  
optical lattice 147, 155, 224  
optical molasses 162  
optical potential 122  
optimal control method 55  
overdamped motion 173

**p**

$8\pi$  pulse sequence 262  
 $\pi$ -pulse 279  
parallel quantum gate array 126, 485  
parametric heating 59  
parametrically driven and forced harmonic  
oscillator 72  
particle transfers 106  
Paul trap arrays 69  
periodic potential 122, 483  
perturbation theory 344  
first order 344

second order 342  
phase diffusion 39  
phase estimation 379  
phase gate 28, 132  
phase modulation 251  
phase transition  
one-atom maser 11  
phase-locking 171  
phase-sensitivity of transport 84  
photon statistics  
one-atom maser 5  
Poissonian 6  
sub-Poissonian 6, 9, 31, 34  
super-Poissonian 6  
plasma 229, 233  
pointer 109  
Poissonian 77  
Poissonian process 432, 439  
positive operator-valued measure 379,  
403  
potential fluctuations 87  
potential optimization 51  
POVM 403  
symmetric 411  
prime number theorem 366  
privacy amplification 319  
pseudo-entangled state 252  
pseudo-pure state 248, 258  
PSPACE-complete problems 385  
pure state 245  
purity decay 268

**q**

2-qubit Deutsch-Josza algorithm 259  
3-qubit Deutsch-Josza algorithm 247  
QBER 311  
quadrature squeezing 326  
quantum communication 303  
quantum complexity 379  
quantum cryptography 315  
quantum dot 33, 282  
quantum gate 127  
quantum jumps  
one-atom maser 11  
quantum key distribution 303, 315  
quantum nondestructive-measurement  
28  
quantum phase gate 132  
quantum point contact 432  
quantum state engineering 69  
quantum-bus 253  
qubit register 122

**r**

Rabi oscillations 8, 130  
Fock state 21, 23  
Rabi splitting 32

- radio frequency 47, 130  
 Raman sideband cooling 229  
 Ramsey fringes 126, 131  
 Ramsey spectroscopy 131, 378, 380  
 random-walk model 148  
 Rayleigh scattering phase 180  
 recoil-induced resonances 165  
 reduced ideal 362  
 refrigeration 384  
 regularized trap-electrode waveforms 87  
 regulator 361  
 resonator mode 139  
 ring cavity 155  
 ring laser gyroscopes 171  
 rotary echo 260  
 rotating-wave approximation 273  
 Rubidium 130, 146  
 running time 392  
 Rydberg atom 2, 29, 211  
 Rydberg spectroscopy 211  
 Rydberg state  
     circular 26
- s**  
 S-bus concept 253  
 scalability 127  
 Schrödinger picture 80  
 Schrödinger cat 29  
 secret sharing 303  
 secular motion 49  
 security 307  
 self-organization 168  
 self-synchronization 168  
 sequential communication 306  
 shot noise 425, 444, 449  
 sideband entanglement 326  
 sideband picture 325  
 sideband separation 326, 327  
 sifting 319  
 simulation of Hamiltonians 392  
 sine transport 82  
 single crystal 255  
 single electron transistor 435  
 single qubit 306  
 single-atom detection 141  
 single-atom detector 135  
 single-atom preparation 141  
 single-photon generation 33  
 solid state 253  
 solid-state quantum information 426  
 SPDC 309, 310  
 spectrum  
     one-atom maser 24  
 spin 243  
 spin Echo Double Resonance (SEDR)  
     261  
 spin locking 260  
 spin-dependent periodic potential 123  
 spin-dependent potential 126, 485  
 squeezing 81  
 stability parameter 50  
 standing wave 124, 483  
 Stark map 212, 235  
 state preparation 378  
 state-dependent double well potential  
     134  
 state-dependent microwave potentials  
     132  
 state-selective potential 127  
 STIRAP 34  
 strong coupling regime 136  
 surface effects 131  
 system-bath model 266
- t**  
 thermodynamic machines 383  
 Tikhonov regularization 89  
 transition probabilities 77  
 transmission lines 134  
 transport 54  
 transport dynamics 69  
 transport function 71  
 trap frequency 47  
 trapped atoms 31  
 trapping states  
     one-atom maser 13  
 truncated density matrix 256  
 two-dimensional regime 149  
 two-photon transition 130
- u**  
 universal coupling 175
- v**  
 vacuum state 80  
 van der Waals interaction 230  
 vibrational modes 69  
 Vollmer's algorithm 373  
 von-Neumann measurements 379, 387
- w**  
 waveguide 130  
 wavepacket 54  
 weighted chromatic index 391  
 weighted depth 390  
 weighted graph 391  
 well-controlled regime 81  
 Wigner function 29  
     one-atom maser 29  
 work extraction 378
- z**  
 Zeeman shift 129, 130  
 Zeeman splitting 244  
 zero point energy 78, 80  
 Zeta-Function 366